

# Structural behaviour of concrete segmental lining tunnels: towards design optimisation



**Saleta Gil Lorenzo**

Department of Engineering

University of Cambridge

This dissertation is submitted for the degree of

*Doctor of Philosophy*

À minha família galega e italiana,  
e ao pequeno Minuncio também...

Quem vai em nau mercante ou pescadora  
não sulca o mesmo mar que o meu navio  
que não guarda porões e vai vazio  
de tudo o que se vende ou se penhora.

Vai cobrando distâncias hora a hora  
sem fundear em portos de medrio,  
o ganho comercial não é amorio  
que lhe enderece o leme nem a prora.

A minha nau só cobra no velame  
os ventos do Ideal, da Liberdade,  
do Anelo, da Beleza, da Ousadia.

Nunca se enrole nela quem não ame  
A Flor, a Estrela, o Sonho, a Saudade...  
nem aquele a que entala a cobardia.

JENARO MARINHAS DEL VALLE, *Invenção do mar*



## **Declaration**

I hereby declare that except where specific reference is made to the work of others in the text and Acknowledgements, this dissertation is the result of my own work and includes nothing which is the outcome of work done in collaboration with others. It is not substantially the same as any that I have submitted, or, is being concurrently submitted for a degree or diploma or other qualification at the University of Cambridge or any other University or similar institution. I further state that no substantial part of my dissertation has already been submitted, or, is being concurrently submitted for any such degree, diploma or other qualification at the University of Cambridge or any other University or similar institution. This dissertation contains 71,522 words including appendices, bibliography, footnotes, tables and equations and has 150 figures.

Saleta Gil Lorenzo

August 2018

# Acknowledgements

---

First, I would like to acknowledge all the people and parties involved in the Crossrail's Thames tunnel field trials, without whom the field data collection would not have been possible. I would like to thank Donal McGovern, Liam McGovern and all Shay Murtagh Precast staff who supported Peter Knott, Hyungjoon Seo, Matt Wilcock and myself during the segment instrumentation works, and later participated in the production of concrete samples for the creep tests. I also thank the contribution of the CUED team to the segment instrumentation. The involvement of Spliceteq Telecommunications with their assistance in the final design proposal and their work at the Thames tunnelling site was key to the success of the field trials and I would like to give a special thanks to Jothi Rajappan and Lee Allsop for their professionalism and availability in such a time-demanding project. I would like to thank Hochtief Murphy JV for supporting the instrumentation works and data collection at the tunnel site through the provision of access, specific machinery and human resources when required and reasonably practicable. I am particularly grateful for the help provided by Joerg Schippel, Dirk Sauer, Juergen Linhardt, Thomas Fuhrman, Irina Zolotareva, Michael Malone and John Lavin for the installation works in the tunnelling phase; John McElroy and Ian Kavanagh during the cross passage construction; and Phil, Barra, Don, Simone and many other site workers who have contributed to the overall installation works with great generosity. I would like to thank Frank Wiegand, Andreas Raedle and John Kinnear for facilitating the high level coordination and communications.

I would like to acknowledge the technical advice provided by Stephen Pooran and Grant Taylor from Geosense on tilt and VWSG instrumentation, Cedric Kechavarzi from the CSIC on BOTDR deployment essentials, Artur Guzik from Neubrex on BOTDR measurements, John Colton and Annette Colton from Lucid Optical Services on the assessment of FO connectors and splice quality during the installation works at the tunnel site and Jason Pedder from OFS on the feasibility of using bend-insensitive FO cables. I would like to thank Alistair Ross, Jeremy Penfold and the CUED workshop for producing ancillary devices for cable routing and DFOS protection during the cross passage construction.

I would like to thank the EPSRC and CH2M for their financial support of this research project, the latter represented by Mr. Peter Wright and the academic supervisor Dr. Mohammed Elshafie. I would like to thank the CSIC, particularly Dr. Jennifer Schooling, for lending the BOTDR interrogator and other additional resources to the Thames tunnel field trials.

I would like to express my great appreciation to the people at CUED that supported my research work. I would like to thank my advisor Prof. Kenichi Soga for lending his priceless time to discuss my research work at its early stages. I also thank Prof. Kenichi Soga and Dr. Krishna Kumar for helping setting up my HPC computer service account and letting me be part of the CB-Geo team. I would like to give my special thanks to Prof. Janet Lees for her kind support and guidance; our stimulating discussions have encouraged me immensely to drive my research forward. Dr. Andrea Giusti helped me with the replication of a grout flow model with the same enthusiasm as if it was one of his

## Acknowledgements

---

own projects, which I greatly appreciated. I would like to thank Dr. Loizos Pelecanos for sharing an example of BOTDR data processing, and Dr. Michael Williamson for MATLAB tips on data handling.

I am especially grateful to Joerg Schippel from Hochtief Ltd for his time and his efficient provision of information on the Thames tunnel, information that has definitely contributed to a more robust research work. I am also very thankful to Herrenknecht's technical support and Roy Slocombe in particular for his availability to explain, even with sketches, the basic configuration of current TBM thrust jacking systems. I would like to acknowledge Christophe Delus from Optimas-Sofrasar, previously Anixter, for his disposition to share technical data on the bolts and dowels deployed in the Thames tunnel, which turned out to be very valuable for my research. I cannot forget the kindness and generosity of C.B.M. (Kees) Blom, who met with me at Delft University and gave me a copy of his book "Design philosophy of concrete segmental linings for tunnels in soft soils", the bible of concrete segmental linings.

Finally, I would like to offer my special thanks to Wolfson college and my college tutors, Dr. Sally Church and Dr. Jane MacLarty, who helped me to reach a reasonable compromise between my sickness period and the expectations of those representing other interested parties. I will be eternally grateful for their support and kindness.

The deployment of engineering models and design methods divorced from the effect that mechanised shield tunnelling with tunnel boring machines (TBMs) has on concrete segmental linings (CSLs) can lead to either material waste or structural damage within the tunnel design life. Most research to date on CSL behaviour during construction neglects the sequential ring loading and TBM-lining transverse interactions, which this thesis proved to be key in the short and long term behaviour of CSLs and whose study is essential if the design and maintenance of CSL structures is ever to be optimised.

This thesis investigates the longitudinal and transverse behaviour of CSL structures simultaneously backfilled with bicomponent grouts (BGs) during tunnelling, and how this early response influences long term behaviour. The research work is drawn on three pillars that enable cross-validation of conclusions: analytical models, three-dimensional numerical simulations and the interpretation of the Crossrail's Thames tunnel (CTT) field data, which included distributed fibre optic strain (DFOS) data. A theoretical framework ranging from construction loading scenarios to the mechanisms underlying structural damage is described for the future development of limit state design methods. Analytical models of longitudinal behaviour are also proposed. The study of joint geometries, temporary spear bolts and DFOS sensing in CSL construction monitoring is included as ancillary research.

The solution developed for a sequential elastic rod subjected to a trilinear temperature profile and in shear interaction with the elastic ground predicts accurately the early tunnel pre-stressing relaxation caused by grout hardening, e.g.  $\approx 50\%$  in the CTT. The proposed sequential elastic beam model, which incorporates the effects of stage-varying net TBM moments, transverse loads and lining pressure gradients within the tunnel unsupported length, estimates satisfactorily the history of tunnel beam response during construction for a realistic expression of the lining stiffness. A potential damage assessment method for the early detection of tunnel sections prone to ring joint damage was proposed.

The TBM-lining transverse interaction determines the CSL ring behaviour at the early stages of tunnelling. The ring response resultant from this interaction is irrecoverable and contributes to the long term total deformations and internal forces; in tunnels excavated in grounds with  $K_o \approx 1$ , it becomes the major source of ring distortion. The main transverse actions are the sealing pressures, which are inversely related to the tail clearance, and the transverse load of oblique hydraulic jacks. When the non-bedded rings are eccentric with respect to the shield tail, the ring distortion increases the risk of cracking near the rear corners and spalling at the ram pad interspaces of constrained segments. The ring distortion is directly related to the pressure gradients, the unsupported length and the ring flexibility. When individual segments rotate outwards under the action of transverse ram loads, e.g. the outer springline segment during pronounced TBM steering around a horizontal curve, the localised action of the sealing pressures can result in longitudinal cracking at the intrados of the segment front.

This study represents a qualitative leap towards the optimisation of CSL design, shifting the attention of researchers and designers to TBM-lining transverse interactions as the most determinant factor of structural response during construction in CSLs simultaneously backfilled with BGs.

# Table of contents

<b>Table of contents .....</b>	<b>vii</b>
<b>List of figures .....</b>	<b>xiii</b>
<b>List of tables .....</b>	<b>xix</b>
<b>Nomenclature .....</b>	<b>xx</b>
<b>1. Introduction.....</b>	<b>1</b>
1.1. Simultaneously backfilled concrete segmental linings .....	1
1.2. Problem statement.....	2
1.3. Aims and objectives.....	3
1.4. Research strategy and thesis organisation.....	4
<b>2. Study on the geometry of longitudinal joints.....</b>	<b>7</b>
2.1. Introduction.....	7
2.2. Joint rotational models.....	8
2.2.1. Flat joints.....	8
2.2.2. Curved joints .....	10
2.3. Concrete damage modes .....	13
2.4. Bursting capacity .....	14
2.4.1. Current design practice .....	14
2.4.2. Proposed calculation method .....	15
2.4.3. Discussion .....	20
2.5. Gasket gap .....	24
2.6. Proposed method for joint design .....	25
2.7. In-plane contact imperfections .....	28
2.7.1. Input data.....	29
2.7.2. Results.....	30
2.8. Conclusions .....	32
<b>3. The role of spear bolts in gasketed joints.....</b>	<b>33</b>
3.1. Introduction.....	33

# Table of contents

---

3.2. Rotational models .....	34
3.2.1. Flat joints.....	34
3.2.2. Curved joints .....	36
3.2.3. Validation of mechanical models.....	37
3.3. Discussion.....	43
3.3.1. Moment capacity and gasket compression.....	43
3.3.2. Ring build.....	48
3.3.3. Construction stages .....	48
3.4. Conclusions.....	50
<b>4. 3D numerical study on the long term response of concrete segmental linings .....</b>	<b>52</b>
4.1. Introduction.....	52
4.2. Background.....	52
4.3. Description of numerical simulations .....	55
4.3.1. Input parameters and element types .....	56
4.3.2. Input loading .....	57
4.3.3. Simulation steps .....	58
4.3.4. Joint modelling.....	60
4.3.5. Modelling ground-structure interaction .....	64
4.4. Results.....	65
4.4.1. Isolated rings .....	65
4.4.2. Coupled rings .....	70
4.5. Global performance of CSLs with different joint geometry .....	77
4.6. Conclusions.....	78
<b>5. Thames tunnel SHM deployment study .....</b>	<b>80</b>
5.1. Introduction.....	80
5.2. Background on applied sensing technology .....	81
5.2.1. BOTDR technique.....	81
5.2.2. MEMS tilt sensors.....	83
5.3. Original proposal .....	83

# Table of contents

---

5.4. CTT SHM system .....	86
5.4.1. Stakeholders .....	86
5.4.2. Selection of parameters .....	89
5.4.3. Selection of instruments .....	90
5.4.4. Instrumentation layout .....	91
5.4.5. Gauge length and measurement accuracy .....	92
5.4.6. SHM system design.....	96
5.5. Data processing methods for CSLs.....	107
5.5.1. Nomenclature .....	107
5.5.2. Total strain and tilt .....	107
5.5.3. Mechanical strains.....	108
5.5.4. BOTDR data processing .....	122
5.5.5. Evaluation of concrete elastic properties .....	122
5.6. Comparative assessment of strain sensors .....	123
5.6.1. Temperature study.....	123
5.6.2. Strain study .....	127
5.7. Conclusions.....	140
<b>6. Thames tunnel field data interpretation: longitudinal response to sequential construction</b> .....	<b>141</b>
6.1. Introduction.....	141
6.2. Longitudinal pre-stressing of tunnel lining.....	141
6.2.1. Background .....	141
6.2.2. Analytical solution for thermal effect on longitudinal pre-stressing.....	142
6.2.3. Field data interpretation on longitudinal pre-stressing.....	145
6.3. Lining pressure gradients.....	155
6.3.1. Properties of cementitious grouts.....	155
6.3.2. Lining pressures in CSLs backfilled with MGs .....	157
6.3.3. Lining pressures in CSLs backfilled with BGs .....	160
6.3.4. Field data interpretation on pressure gradients .....	161

# Table of contents

---

6.4. Beam response on tunnel lining.....	164
6.4.1. Background .....	164
6.4.2. Enhanced analytical solution for tunnel beam response .....	165
6.4.3. Input data for analytical solution.....	168
6.4.4. Calibration of analytical model .....	170
6.4.5. Field data interpretation on tunnel beam response.....	172
6.5. Proposed method for potential damage assessment.....	174
6.6. Conclusions.....	176
<b>7. 3D numerical study on concrete segmental lining local response to simultaneous backfill grouting .....</b>	<b>177</b>
7.1. Introduction.....	177
7.2. Background.....	178
7.2.1. Previous research on sequential loading .....	178
7.2.2. FE analyses of CSL response to construction loads.....	178
7.2.3. TBM jacking systems.....	180
7.3. Description of numerical simulations .....	181
7.4. Parametric studies .....	183
7.5. Sequential loading under axisymmetric conditions .....	185
7.5.1. Lining structural response .....	185
7.5.2. Effect of ram loads on lining response.....	186
7.5.3. Effect of ram pad eccentricity on lining response.....	188
7.5.4. Membrane behaviour of standard segments.....	189
7.5.5. Longitudinal bending of standards segments .....	192
7.5.6. Potential damage during sequential loading .....	193
7.5.7. Influence of ring joint design on segment damage .....	195
7.6. The effect of ring selfweight on lining response .....	196
7.7. Validation of two-ring models .....	197
7.8. Sequential loading with vertical pressure gradients.....	198
7.8.1. Lining response with uniform ram pad-lining interface .....	198



# Table of contents

7.8.2. Lining response with uneven ram pad-lining interface .....	200
7.8.3. Potential damage during sequential loading.....	212
7.8.4. Influence of other parameters on lining response .....	213
7.9. Conclusions.....	216
<b>8. Thames tunnel field data interpretation: local CSL response to sequential construction</b> .....	<b>218</b>
8.1. Introduction.....	218
8.2. CSL loading scenarios during construction .....	219
8.3. Further considerations on processed field data .....	226
8.4. Field response to sequential assembly .....	227
8.4.1. CAM3 ring .....	227
8.4.2. CM4 ring .....	228
8.5. Field data interpretation on cycle 1 .....	234
8.5.1. CAM3 ring .....	235
8.5.2. CAM4 ring .....	247
8.6. Field data interpretation on cycle 2.....	258
8.6.1. CAM3 ring .....	258
8.6.2. CAM4 ring .....	264
8.7. Field data interpretation on following cycles.....	269
8.7.1. Lining pressures .....	269
8.7.2. Hoop membrane behaviour .....	273
8.7.3. Deformed shape, segment curvatures and vertical tilt .....	273
8.8. Conclusions.....	283
<b>9. Conclusions .....</b>	<b>285</b>
9.1. Findings .....	285
9.1.1. CSL behaviour .....	286
9.1.2. SHM systems for CSLs.....	292
9.1.3. Joints and bolts.....	292
9.1.4. Recommendations for joint design.....	293

## Table of contents

---

9.2. Future works .....	297
<b>References.....</b>	<b>300</b>
<b>Appendix 1.....</b>	<b>308</b>

# List of figures

1.1. Typical CSL configuration, frequent crack patterns during construction and tunnel construction interfaces .....	6
2.1. Flat joint models .....	10
2.2. Curved joint models.....	12
2.3. Concrete damage modes .....	13
2.4. Current design practice for bursting capacity check.....	15
2.5. Bursting capacity calculation procedure .....	17
2.6. Bursting capacity calculation for flat joints .....	18
2.7. Contact width and bursting capacity in curved joints .....	20
2.8. Factors influencing bursting capacity .....	22
2.9. Comparison with current design methods .....	23
2.10. Gasket gap in rotated joints .....	24
2.11. NR diagrams for different joint geometries .....	27
2.12. Joint geometry configurations .....	28
2.13. FE model for the study of 3D imperfections .....	29
2.14. Contact patches in curved joints at $N=4000\text{kN/m}$ , pressures in Pa.....	31
3.1. Concrete material model for rotational models .....	35
3.2. Gasket force-gap diagram .....	35
3.3. Force diagram for flat joints.....	36
3.4. Force diagram for curved joints .....	37
3.5. Experimental and analytical data of joints .....	39
3.6. Validation of analytical model against 2D FE models .....	41
3.7. FE and analytical MR curves for gasketed joints with soft and stiff bolts .....	43
3.8. MR curves, bolt force, gasket gap and neutral axis for gasketed flat joints .....	45
3.9. MR curves, bolt force, gasket gap and neutral axis for gasketed curved joints .....	46
3.10. Simplified force diagram for a two-segment system with boltless joint subjected to gasket force .....	47

## List of figures

---

3.11. Maximum initial rotations delimited by dowel misalignment .....	48
3.12. Boundary conditions and applied loads for sequential loading.....	49
3.13. Radial displacements [m] in ring subjected to sequential loading with 700KPa radial pressures	50
4.1. Hoop forces and maximum bending moments of closed-formed solutions .....	53
4.2. Optimization of longitudinal joint modelling.....	62
4.3. Anixter-Sofrasar lock-in dowel Sof-Fix Anix 60: Shear test (after Anixter, 2014) .....	63
4.4. Radial displacements in an isolated ring .....	66
4.5. Convergence in isolated rings .....	67
4.6. Joint behaviour in isolated rings.....	68
4.7. Internal forces in isolated rings .....	69
4.8. Coupling mechanism under ovalisation loads.....	71
4.9. Coupled rings-Vertical convergence .....	72
4.10. Coupled rings-Joints rotations.....	73
4.11. Coupled rings-Ring misalignment .....	74
4.12. Coupled rings-Hoop moments .....	76
4.13. $f_{CSL}$ in soft and hard ground .....	77
4.14. Global performance of CSLs with different joint geometry .....	78
5.1. Location of CTT instrumented rings .....	84
5.2. Tunnel cross-sections at instrumented rings .....	84
5.3. Original proposal.....	85
5.4. DFOS instrumentation layout of CSL segments .....	92
5.5. Relative strain measurement error.....	93
5.6. Ram load spread at lateral hoop section.....	94
5.7. Effect of concrete discontinuities on measurement accuracy.....	96
5.8. SHM physical architecture .....	98
5.9. IDEF diagram for implementation plan .....	102
5.10. Phase 3 installation works sequence .....	103
5.11. CTT robustness issues against double V-model (after Firesmith, 2011)–untested technology	105

## List of figures

---

5.12. CTT robustness issues against double V-model (after Firesmith, 2011)– Incomplete requirement set .....	106
5.13. Computation of CTT $\alpha_{Tc}$ and hysteresis under temperature cycles.....	110
5.14. Thermal response of a monitored cross-section in an isostatic beam under nonlinear temperature (after El-Tayeb et al., 2015) .....	110
5.15. Effect of hysteresis on $\Delta\epsilon_{mech}$ at $t=0$ .....	110
5.16. Segment response to temperature changes.....	111
5.17. Ring thermal expansion restrained by ground.....	111
5.18. Strain profiles due to CSL temperature increments .....	112
5.19. Initial mean hoop strains and absolute temperatures.....	114
5.20. Unrestrained thermal strain in longitudinal direction.....	115
5.21. Initial mean longitudinal strains and absolute temperatures .....	117
5.22. Initial hoop curvatures and absolute temperature gradients.....	119
5.23. Initial longitudinal curvatures and absolute temperature gradients.....	120
5.24. Restrained thermal curvatures.....	121
5.25. Concrete elastic properties .....	123
5.26. VWSG temperatures and thermal gradients.....	124
5.27. CAM4 BODTR temperature increments at central hoop and longitudinal sections .....	125
5.28. VWSG and BOTDR temperature increments at extreme fibres .....	127
5.29. CAM4 raw mechanical loop mean strains and curvatures .....	130
5.30. CAM4 raw mechanical hoop extreme fibre strains .....	131
5.31. CAM3 raw mechanical hoop mean strains and curvatures .....	132
5.32. CAM3 raw mechanical hoop extreme fibre strains.....	133
5.33. BOTDR damage and contact deficiency detection .....	134
5.34. CAM4 raw mechanical longitudinal mean strains and curvatures.....	136
5.35. CAM4 raw mechanical longitudinal extreme fibre strains.....	137
5.36. CAM3 raw mechanical longitudinal mean strains and curvatures.....	138
5.37. CAM3 raw mechanical longitudinal extreme fibre strains.....	139

## List of figures

---

6.1. Temperature loading states and boundary conditions for rod model .....	143
6.2. Validation of analytical rod solution for trilinear temperature profile .....	145
6.3. Selection of rod model parameters: ram loads .....	148
6.4. Selection of rod model parameters: packers.....	149
6.5. Selection of rod model parameters: creep effects .....	150
6.6. Thermal effects on longitudinal strains .....	152
6.7. Tunnel relaxation due to time-varying temperatures .....	153
6.8. Prediction of longitudinal force.....	154
6.9. Typical injection ports for MGs and BGs .....	157
6.10. Lining pressures in MGs backfilled CSLs (after Bezuijen et al., 2004).....	158
6.11. Example of vertical pressure gradients in BGs backfilled CSLs (after Talmon and Bezuijen, 2005) .....	161
6.12. CTT pressure gradients .....	163
6.13. Loading and boundary conditions of bedded beam model at construction stage <i>i</i> .....	167
6.14. Lining bending stiffness.....	168
6.15. Input data for beam model .....	170
6.16. CTT model calibration .....	171
6.17. CTT local longitudinal response .....	173
6.18. CTT global longitudinal response .....	174
6.19. PDA method for preliminary assessment.....	175
7.1. Longitudinal migration of sequential ovalisation loading (Blom, 2002) .....	178
7.2. Hydraulic jack system with fixing release during advance .....	180
7.3. Ring1 load share in two-ring systems subjected to uniform sequential loading .....	186
7.4. Relative position of hydraulic cylinders and packer .....	187
7.5. Effect of longitudinal loads on R1 response .....	188
7.6. Effect of ram pad eccentricity on R1 response.....	189
7.7. Membrane strains, MN trajectories and PM lines in standard segments.....	191
7.8. Longitudinal moments during uniform sequential loading .....	192

## List of figures

---

7.9. Contact quality during uniform sequential loading.....	194
7.10. Concrete spalling during sequential loading .....	194
7.11. Influence of ring joint design on segment damage.....	195
7.12. Validation of two-ring models .....	197
7.13. Convergence induced by vertical gradients in free TBM conditions .....	200
7.14. <i>3UAB</i> model: R1 deformed shape and ram pad reaction forces.....	201
7.15. FEA results- <i>3UAB</i> -R1 .....	202
7.16. FEA results- <i>3UAB</i> -R2.....	203
7.17. <i>3UEKL</i> model: R1 deformed shape and ram pad reaction forces .....	204
7.18. FEA results- <i>3UEKL</i> -R1 .....	205
7.19. FEA results- <i>3UEKL</i> -R2 .....	206
7.20. <i>3UKRA</i> model: R1 deformed shape and ram pad reaction forces .....	207
7.21. FEA results- <i>3UKRA</i> -R1 .....	205
7.22. FEA results- <i>3UKRA</i> -R2 .....	206
7.23. FEA results- <i>3UKR</i> -R1.....	207
7.24. FEA results- <i>3UKR</i> -R2.....	208
7.25. Damage modes in a CSL subjected to sequential loading with pressure gradients.....	213
7.26. Parametric study on local lining response .....	215
8.1. Parts of TBM wire brush seal (after Shandong East Machinery & Equipment Co., 2017) .....	220
8.2. Causes of variable clearance between tail skin and lining .....	221
8.3. Construction scenarios .....	225
8.4. CS3 loading and segment response .....	226
8.5. CAM3 hoop mean strains and curvatures prior to cycle1 .....	230
8.6. CAM3 raw hoop strains during sequential loading.....	231
8.7. CAM4 hoop mean strains and curvatures prior to cycle1 .....	232
8.8. CAM4 RAW hoop strains .....	233
8.9. Sealing pressures with swept distance.....	234
8.10. CAM3 and CAM4 general conditions.....	235

## List of figures

---

8.11. CTT field data: CAM3 Cycle1 .....	243
8.12. CAM3 MN trajectories in cycle1 .....	246
8.13 CAM3 segment rotation and change in tail clearance.....	246
8.14 CTT field data: CAM4 Cycle1 .....	254
8.15 CAM4 MN trajectories in cycle1 .....	257
8.16 CAM4 segment rotation and change in tail clearance.....	257
8.17 CTT field data: CAM3 Cycle2.....	262
8.18 CTT field data: CAM4 Cycle2.....	267
8.19 CAM4 grout injection pressures .....	269
8.20 History of the CTT lining pressures .....	272
8.21 History of the CTT hoop mean strains .....	273
8.22 CTT field data: CAM3 Cycle3.....	275
8.23 CTT field data: CAM3 Cycle8.....	277
8.24 CTT field data: CAM4 Cycle3.....	279
8.25 CTT field data: CAM4 Cycle8 .....	281
9.1 Future works .....	299



## List of tables

1.1. Research objectives .....	4
2.1. Input parameters for bursting capacity based on the CTT joints.....	18
2.2. Input parameters for joint models .....	30
2.3. Critical loads of joints with in-plane angularities .....	31
3.1. Spear bolt input parameters.....	41
3.2. Role of spear bolts against damage during construction.....	48
3.3. Summary of bolts functions .....	51
4.1. Material properties .....	57
4.2. Element types .....	57
4.3. Earth and water pressures at springline.....	57
4.4. Modelling steps .....	59
5.1. CTT SHM stakeholders.....	88
5.2. Relative measurement of maximum strain.....	93
5.3. BOTDR input specification for data acquisition.....	104
5.4. BOTDR standard deviation within a long term 24h period .....	127
7.1. Modelling steps .....	182
7.2. Nomenclature of FE models and R1 boundary conditions.....	184
7.3. Sequential loading under axisymmetric conditions.....	186
7.4. Effect of selfweight on lining response.....	196
7.5. Sequential loading with vertical pressure gradients and uniform ram -ad-lining interface.....	199
9.1. Construction loading scenarios representative of field conditions near the tail skin .....	291
9.2. Influence of longitudinal joint geometry on risk of concrete damage.....	295

## Nomenclature

### Roman symbols

$a$	contact width/width of anchor plate
$A_b$	bolt cross-sectional area
$A_c$	ring cross-sectional area
$a_{eq}$	equivalent contact width
$A_J$	cross-sectional area of circumferential joint
$A_r$	cross-sectional ring area
$A_{s,req}$	through-thickness reinforcement against tensile splitting
$b$	joint width/ratio between tangential and radial components of foundation modulus
$c$	Mohr-Coulomb cohesion
$C_\varepsilon$	BFS strain coefficient of strain sensing optical cable
$c_s$	speed of light in a vacuum
$C_T$	BFS temperature coefficient of strain sensing optical cable
$C_{TT}$	BFS temperature coefficient of loose tube optical cable
$C_{T,tilt}$	temperature coefficient of tiltmeter
$d_b$	location of the bursting force along the tendon path
$e$	eccentricity
$E_b$	bolt Young's modulus
$E_c$	concrete Young's modulus
$e_c$	load eccentricity at longitudinal joints
$e_{dowel}$	maximum eccentricity between dowel and socket
$err_\varepsilon$	relative strain measurement errors
$E_{ct}$	EC2 instantaneous concrete Young's modulus
$E_{cm}$	EC2 secant concrete Young's modulus
$E_p$	packer Young's modulus

# Nomenclature

---

$E_s$	ground stiffness
$EI$	longitudinal bending stiffness of lining
$EI_{eq}$	CSLs equivalent longitudinal bending stiffness
$EI_{eq,0}$	equivalent longitudinal bending stiffness of a CSLs with close circumferential joints
$E_{sc}$	ground constrained modulus of elasticity
$F$	total ground reaction activated by the displacement of a ring
$F_b$	bolt force
$F_c$	concrete compressive force
$F_g$	gasket force
$F_{st}$	steel capacity against splitting
$f_c$	compressive strength of concrete
$f'_c$	uniaxial compressive cylinder strength of concrete
$f_{CSL}$	CSL stiffness factor
$f_{ct}$	EC2 concrete tensile strength
$f_{ctm}$	concrete tensile strength
$F_g$	gasket force
$f_p$	packer yield stress
$f_{yk}$	characteristic tensile strength of steel
$g$	pressure gradient
$G$	ground shear stiffness
$H$	height of tunnel overburden
$h$	lining/segment depth
$h_j$	joint depth
$I_b$	bolt moment of inertia
$I_R$	ring moment of inertia
$I_J$	moment of inertia of a closed circumferential joint
$k_b$	bolt system stiffness
$k_c$	ring axial stiffness

# Nomenclature

---

$k_{Man}$	manufacturer's linear bolt system stiffness
$k_p$	packer axial stiffness
$K_r$	foundation modulus due to modulus of subgrade reaction
$k_r$	modulus of subgrade reaction
$k_s$	ground distributed shear spring stiffness along the tunnel axis
$K_t$	foundation modulus due to tangential shear stiffness
$K_\theta$	joint rotational capacity
$K_T$	concrete thermal gradient
$K_{tot}$	total foundation modulus
$K_o$	coefficient of lateral earth pressure at rest
$L$	segment length
$L_b$	bolt length
$L_c$	cracking spacing
$l_{cc}$	concrete length required for redistribution of joint stresses
$l_f$	influence length of a circumferential joint
$L_g$	BOTDR spatial resolution
$L_i$	rod length at stage $i$
$L_s$	sensor length
$l_s$	segment width (Liao's terminology)
$L_1$	rod length subject to first temperature gradient
$L_R$	rod length equal to ring width
$L_u$	unsupported length of two rings behind the TBM
$M$	bending moment
$m$	number of bedded rings
$M_i$	concentrated moment at the origin of the tunnel beam at stage $i$
$M_{Mi}$	internal moment in tunnel beam at stage $i$ caused by combined concentrated moments
$M_{Qi}$	internal moment in tunnel beam at stage $i$ due to combined concentrated shear forces
$M_v$	constant of proportionality between BFS and total strains in a fibre

# Nomenclature

---

$M_y$	longitudinal internal moment about the horizontal axis $y$
$M_z$	longitudinal internal moment about the vertical axis $z$
$M_o$	yield moment before immediate circumferential joint opening
$M_{CSL}$	CSL moment limits
$M_{CM}$	CM maximum moments in continuous linings
$\phi_{Mi}$	slope of tunnel beam at stage $i$ caused by combined concentrated moments
$\phi_{Qi}$	slope of tunnel beam at stage $i$ due to combined concentrated shear forces
$N$	normal force/load
$N_{target}$	target load or ultimate failure against tensile splitting
$n$	number of non-bedded ring
$n_b$	number of bolts per meter
$n_i$	total number of rings at stage $i$
$n_{Li}$	number of rings comprised in length $L_i$
$n_s$	refractive index of silica medium
$p$	normal pressure
$p_{1,i}$	UDL applied on the first ring of the tunnel beam at stage $i$
$p_{2,i}$	UDL applied on the second ring of the tunnel beam at stage $i$
$q$	UDL distributed over the founded length of the tunnel
$Q_{Mi}$	shear force in tunnel beam at stage $i$ caused by combined concentrated moments
$Q_{Qi}$	shear force in tunnel beam at stage $i$ due to combined concentrated shear forces
$R$	radius
$R_b$	bolt cross-sectional radius
$R_e$	external ring radius
$R_m$	mean ring radius
$R_l$	radius of curved joint
$R_{\Delta T}$	ratio of free thermal expansion prevented by the ground passive reaction
$R_{k,\Delta T}$	ratio of free thermal curvature prevented by the ground passive reaction
$R_2$	radius of rounded segment

# Nomenclature

---

$S_{dowel}$	spacing between dowels
$SD$	TBM swept distance
$S_u$	unconfined compressive strength
$T_s$	the cycle time in BOTDR
$T$	absolute temperature
$T_b$	bursting force
$t$	time
$t_p$	packer thickness
$u(x)$	longitudinal displacement of the rod at position $x$
$v_a$	acoustic velocity in silica fibre
$v_b$	Brillouin frequency shift
$v_{b0}$	Brillouin frequency shift at zero strain and reference temperature
$V_i$	transverse point load acting at the origin of the tunnel beam at stage $i$
$V_y$	transverse point load at the origin of the tunnel beam along the horizontal axis $y$
$V_z$	transverse point load at the origin of the tunnel beam along the vertical axis $z$
$w$	vertical tilt
$W$	segment width
$W_b$	pulse width of a pump signal
$y_b$	average gasket depth
$y_{beam,ni-k+1}$	tunnel beam deflection at ring $k$ in first TBM cycle after assembly
$y_{beam,ni-k+2}$	tunnel beam deflection at ring $k$ in second TBM cycle after assembly
$y_g$	bolt depth
$y_{Mi}$	deflection of tunnel beam at stage $i$ caused by combined concentrated moments
$y_{Qi}$	deflection of tunnel beam at stage $i$ due to combined concentrated shear forces

## Greek symbols

$\alpha$	bending stiffness ratio; square of stiffness factor (chapter 6)
$\alpha^2$	stiffness factor in rod models

# Nomenclature

---

$\alpha_j$	joint in-plane angularity
$\alpha_b$	bolt angle
$\alpha_{Tc}$	concrete coefficient of thermal expansion
$\alpha_{Tp}$	packer coefficient of thermal expansion
$\beta$	compressibility ratio
$\gamma$	load eccentricity ratio
$\gamma_s$	material safety factor
$\Delta$	average gasket gap
$\Delta_c$	local displacements at concrete joints
$\Delta k_h$	hoop curvature increment
$\Delta k_l$	longitudinal curvature increment
$\Delta \varepsilon_{ext}$	strain increments at extreme fibers of a cross section
$\Delta \varepsilon_{tot}$	total strain increments
$\Delta \varepsilon_s$	instantaneous strain increments due to structural loading
$\Delta \varepsilon_{creep}$	creep strain increments
$\Delta \varepsilon_{h,m}$	mean hoop strain increment
$\Delta \varepsilon_{l,m}$	mean longitudinal strain increment
$\Delta \varepsilon_{shr}$	shrinkage strain increments
$\Delta \varepsilon_{\Delta T}$	free thermal strain increments
$\Delta \varepsilon_{m,\Delta T}$	instantaneous mechanical strain increments due to restrained thermal deformations
$\Delta \varepsilon_{mech}$	mechanical strain increments
$\Delta C$	change in tail clearance
$\Delta L_b$	extension of the bolt system
$\Delta M_{b,bend}$	joint moment capacity enhancement due to bolt bending
$\Delta T$	temperature increment
$\Delta tilt_{tot}$	total tilt increment
$\Delta tilt_{app}$	apparent tilt increment measured by tiltmeter
$\Delta T_1$	temperature increment per ring in length $L_l$ at each stage
$\Delta T_2$	additional temperature increment per ring in lengths greater than $L_l$ at each stage
$\Delta \delta$	ring displacement after being fully founded on the ground

# Nomenclature

---

$\delta\epsilon_{C,s,crack}$	relative error in a strain measurement caused by cracking
$\epsilon$	total strain
$\epsilon_c$	concrete compressive strain
$\epsilon_{c0}$	yielding compressive strain
$\epsilon_{c,max}$	peak concrete strain at joint faces
$\epsilon_{cu}$	ultimate limit strain for concrete
$\epsilon_{C,s}$	average strain measured by a sensor at the sensor midpoint
$\epsilon_{unrest}$	thermal unrestrained strains in rod models
$\epsilon_{mech,th}$	thermally-induced mechanical strains in rod models
$\theta$	joint rotation
$\theta_0$	rotation at immediate opening of circumferential joint
$\theta_r$	radial rotation of segments
$\lambda$	pump pulse wavelength
$\nu$	Poisson's ratio
$\nu_s$	Poisson's ratio of the ground
$\sigma_{t,max}$	maximum bursting stress at imminent cracking
$\sigma_r'$	radial earth pressure components
$\sigma_t'$	tangential earth pressure components
$\varphi$	Mohr-Coulomb internal friction angle
$\varphi_w$	creep factor function of wood

## Subscripts

$i$	construction stage or number of a TBM cycle in the construction sequence of a tunnel
$j$	number of a construction stage previous to stage $i$
$k$	ring number counting from the free boundary at stage $i$



## Acronyms/Abbreviations

BFS	Brillouin Frequency Shift
BG	Bicomponent Grout
BGS	Brillouin Gain Spectrum
BOTDR	Brillouin Optical Time Domain Reflectometry
CM	Continuum Model 1 (Duddeck and Erdmann, 1982)
CSIC	Centre for Smart Infrastructure and Construction
CS	Construction Loading Scenario
CSL	Concrete Segmental Lining
CTT	Crossrail's Thames tunnel
DFOS	Distributed Fibre Optic Sensing/Sensor
EC2	Eurocode 2
FD	Finite Difference
FE	Finite Element
FEA	Finite Element Analysis
FO	Fibre Optic
FWHM	Full Width at Half Maximum
ID	Internal Diameter
IDEF	Icam DEFinition for Function Modelling
ILC	Isostatic Lines of Compression
LLK <sub>0</sub>	Longitudinal Load-Ovalisation
LS	Loading State
MEMS	Micro-Electro-Mechanical System
MN	In-plane Moment-Hoop Force
MR	Moment-Rotation
NR	Normal force-Rotation
OTDR	Optical Time Domain Reflectometry
PDA	Potential Damage Assessment

## Nomenclature

---

PM	Peak Moment
PFA	Point of coupling Force Application
SFRC	Steel Fibre Reinforced Concrete
SNR	Signal to Noise Ratio
SHM	Structural Health Monitoring
TBM	Tunnel Boring Machine
UDL	Uniformly Distributed Load
ULS	Ultimate Limit State
VWSG	Vibrating Wire Strain Gauge
2D	Two Dimensional
3D	Three Dimensional

# Chapter 1

## Introduction

Single-shell concrete segmental linings (CSLs) are the most popular tunnel structures in modern shield tunnelling with tunnel boring machines (TBMs) (Koyama, 2003). Recent technological advances in TBMs enabled the safe, versatile and efficient construction of tunnels with ever larger diameters and in adverse ground conditions that were impossible before (Koyama, 2003; Cavalaro, 2009). Despite the progress in TBM technologies, conventional lining design methods still rely on one-ring structural models subjected to load combinations representative of in situ ground conditions, without giving due consideration to the effects of shield tunnelling on the short and long term response of CSLs (Koyama, 2003). Indeed, field records have confirmed a general increase in lining damage events during construction that required repair (Sugimoto, 2006).

This thesis focuses on the influence that sequential ring loading and TBM-lining transverse interactions have on the short and long term response of CSLs simultaneously backfilled with bicomponent grouts (BGs), which has been widely neglected by designers and researchers to date. A theoretical framework ranging from construction loading scenarios (CSs) to the mechanisms underlying structural damage is described for the future development of limit state design methods; analytical models of longitudinal behaviour are also proposed. The study of joint geometries and temporary spear bolts is included as ancillary research.

### 1.1. Simultaneously backfilled concrete segmental linings

In the construction of grouted smooth bored tunnels, the thrust forces required to support the tunnel face and steer the TBM are provided by hydraulic jacks that push against the last assembled concrete segmental ring (see Figure 1.1.a). New rings are sequentially erected at the back of the shield tail between consecutive advances. The typical CSL configuration based on universal rings is shown in Figure 1.1.b.

The tail void between excavation line and lining extrados is backfilled to minimise ground settlement and provide early support to the flexible lining. Backfill grouting simultaneous with advance is common practice in full face shield machines (Maidl et al., 2012). The use of BGs in simultaneous backfilling has grown steadily in the last few decades given their advantageous properties of quick grout setting and early high strengths when compared to traditional mortars (Hashimoto et al., 2006).

Besides supporting the TBM thrust during construction, CSLs must safely sustain the surrounding ground and control, to a certain degree, groundwater ingress to enable tunnel operations. Thus, durability

and watertightness are key to lining design and must be delivered through appropriate material specification, lining depth and segment detailing (BTS, 2004). Damaged concrete in the form of cracking, flaking or chipping is more prone to material degradation. Likewise, contact deficiencies at segmental joints leading to poor gasket compression or misalignment (Shalabi, 2001) can undermine watertightness.

### 1.2. Problem statement

The deployment of engineering models and design methods divorced from the effects of mechanised shield tunnelling on the short and long term performance of CSLs can lead to either material waste or a higher risk of structural damage during the tunnel design life, which in turn have a negative impact on the total costs incurred and the environment.

In recent years, several statistical studies drawn from field observations were performed to identify the cause for segment cracking, chipping and spalling during CSL construction (see Figure 1.1.b). It was found that most damage occurred at the early stages of tunnelling. Chen and Mo (2009) quantified that half of the cracks were initiated before or during ring erection; subsequent cracking was mostly allocated to the skewed orientation between TBM and ring and to a lesser extent to uneven ram loads and grouting pressures. Sugimoto (2006) identified the two most common types of segment damage: intrados longitudinal cracks at segment sides and chipping of corners. The longitudinal cracks were associated with the position of segments in curved alignments and appeared during the TBM advance, either before or after the ring exiting the tail skin. It was suggested that such cracks could be caused by the contact of the segment with the tail skin. Sugimoto (2006) also stated that the chipping of corners was primarily triggered by ring erection.

Cavalaro (2009) conducted a thorough theoretical study on the structural behaviour of segments subjected to contact deficiencies, which could lead to either corner chipping or longitudinal cracks. Cavalaro (2009) proved that the longitudinal cracks could be caused by the redistribution of longitudinal loads in segments with uneven support at circumferential joints. Corner chipping was produced by the shear failure of laterally confined segments with severe initial angularities at longitudinal joints when hoop loaded. At moderate angular imperfections, the segments could develop bursting cracks near the stressed corners as a result of a reduction in the load-bearing capacity of the angled longitudinal joints. However, Cavalaro (2009) assumed uniform loading conditions, neglected the sequential nature of radial loading in simultaneously backfilled linings and TBM-lining interactions, and tackled flat joints only.

Based on field observations, Gruebl (2006) described a damage mechanism associated with sequential loading near the shield tail. The seal or grout pressures loaded progressively the rear of the newest ring during the TBM advance. The ring adopted an uneven shape with greater diameter at the unloaded front

than at the compressed rear. If the compressive strains at the stressed zones of the longitudinal joints were irreversible, the shape became permanent. Gruebl (2006) also pointed that the transverse component of ram loads in narrow curves, with radius smaller than 500m, could induce the shearing of ring joints with bituminous packers. Gruebl (2006) proved the existence of damage mechanisms that are entirely disregarded in the CSL design process, but without conducting further investigations; he also provided one of the scarce published examples in which the transverse interaction between ram pads and lining can result in structural damage.

Despite such evidence, most research to date on CSL behaviour during tunnelling focuses on the effects of grout pressures on the lining through geotechnical and structural models that can reach a high degree of complexity but neglect the TBM-lining transverse interaction and the sequential nature of ring loading (Gruebl, 2006), e.g. in Ninic et al. (2017).

It then follows that a thorough investigation on the impact of sequential ring loading near the tail skin and transverse TBM-lining interaction on the short and long term behaviour of CSLs is needed if the design and maintenance of CSL structures is ever to be optimised; an optimisation that will benefit tunnel designers and asset owners alike.

### 1.3. Aims and objectives

The main purpose of this study is to investigate the transverse and longitudinal behaviour of CSL structures simultaneously backfilled with BGs during tunnelling, and how this early response influences long term behaviour, in order to advance in the development of engineering models, limit state design methods and potential damage assessment (PDA) methods that capture the effects of radial ring loading and TBM-lining transverse interaction near the tail skin (**Research purpose 1**).

The research relies on the interpretation of a comprehensive data set on ring deformations measured during the construction of the Crossrail's Thames tunnel (CTT). The CTT field trials included the deployment of distributed fibre optic strain sensing (DFOS) embedded in the concrete segments with the Brillouin Optical Time Domain Reflectometry (BOTDR) technique. Given the novelty of this distributed sensors in CSL monitoring during tunnelling, the research works were designed to develop the practical use and assess the suitability of BOTDR sensing in CSL monitoring (**Research purpose 2**).

The CTT tunnel was designed with convex-convex longitudinal joints equipped with temporary spear bolts. Most of the published research on CSL behaviour and structural damage is, however, based on flat jointed CSLs while the functionality of the spear bolts in current CSLs is unclear (Harding et al., 2014). Consequently, this study aimed also at evaluating the impact of joint geometry on CSL performance and identifying the role of spear bolts in gasketed joints (**Research purpose 3**).

## 1.4. Research strategy and thesis organisation

The objectives of this thesis are listed in Table 1.1:

**Table 1.1: Research objectives**

<b>Purpose</b>	<b>Objectives</b>
<b>1</b>	<p><b>Longitudinal behaviour:</b></p> <ol style="list-style-type: none"> <li>1.1. To assess the longitudinal relaxation of CSLs during construction due to time-varying temperatures;</li> <li>1.2. To identify the governing factors in longitudinal CSL behaviour and subsequent damage mechanisms;</li> <li>1.3. To develop an analytical solution for the longitudinal relaxation of CSLs due to thermal effects;</li> <li>1.4. To refine existing analytical bedded-beam models for the prediction of CSL beam behaviour during construction;</li> <li>1.5. To propose a PDA method for the preliminary assessment of damage risk.</li> </ol> <p><b>Ring behaviour near the tail skin:</b></p> <ol style="list-style-type: none"> <li>1.6. To prove that the TBM-lining transverse interaction near the tail skin is a governing factor of ring behaviour in the short and long term;</li> <li>1.7. To identify CSs representative of field conditions;</li> <li>1.8. To identify and describe the ring behaviour and damage mechanisms associated with the CSs;</li> <li>1.9. To assess the influence of lining features on ring behaviour and risk of damage.</li> </ol>
<b>2</b>	<ol style="list-style-type: none"> <li>2.1. To develop installation procedures for BOTDR sensors in CSLs;</li> <li>2.2. To develop data interpretation methods for CSLs;</li> <li>2.3. To assess the performance of strain and temperature sensors in CSLs;</li> <li>2.4. To demonstrate the capability of DFOS for contact deficiency and crack detection.</li> </ol>
<b>3</b>	<ol style="list-style-type: none"> <li>3.1. To develop an analytical method to assess joint bursting capacity at imminent cracking as a function of joint geometry and rotations;</li> <li>3.2. To develop a method for the selection of longitudinal joint geometry integrating local joint performance and global CSL behaviour;</li> <li>3.3. To identify the functions of temporary spear bolts during construction;</li> <li>3.4. To propose recommendations for joint design, including joint geometry, bolts, dowels and packers.</li> </ol>

### 1.4. Research strategy and thesis organisation

The research work is drawn on three pillars that enable cross-validation of conclusions: the development and deployment of analytical models, three-dimensional (3D) numerical simulations and the interpretation of the CTT field data. The thesis organisation is outlined below. Further explanation on research methodologies is included in each chapter.

In **chapter 2**, the influence of joint geometry on the bursting and watertightness performance of longitudinal joints is investigated. An analytical method for joint design that can integrate CSL global behaviour is proposed.

In **chapter 3**, the role of temporary spear bolts in gasketed joints during construction is elucidated.

## 1.4. Research strategy and thesis organisation

---

In **chapter 4**, the effect of longitudinal joint geometry on the long term response of CSLs is examined with the aid of 3D finite element (FE) models.

In **chapter 5**, the CTT structural health monitoring (SHM) deployment study is described, including a detailed description of the installation works and the performance-based evaluation of the sensors deployed.

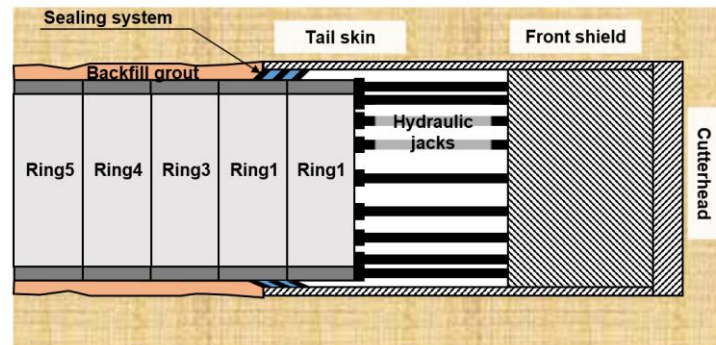
In **chapter 6**, the longitudinal response of the CTT to sequential construction is studied with the support of analytical models developed as required. A PDA method for the preliminary assessment of damage risk is proposed.

In **chapter 7**, a 3D numerical study on the CSL local response to sequential loading near the tail skin is conducted and damage mechanisms identified. The effect of uneven TBM-lining transverse interactions and pressure gradients is examined for linings with different features.

In **chapter 8**, the behaviour of the CTT instrumented rings at the early stages of tunnelling is thoroughly investigated and CSs representative of field conditions are proposed.

In **chapter 9**, the conclusions are summarised and the lines of research arising from this thesis outlined.

### a) CSL construction interfaces



### b) CSL terminology

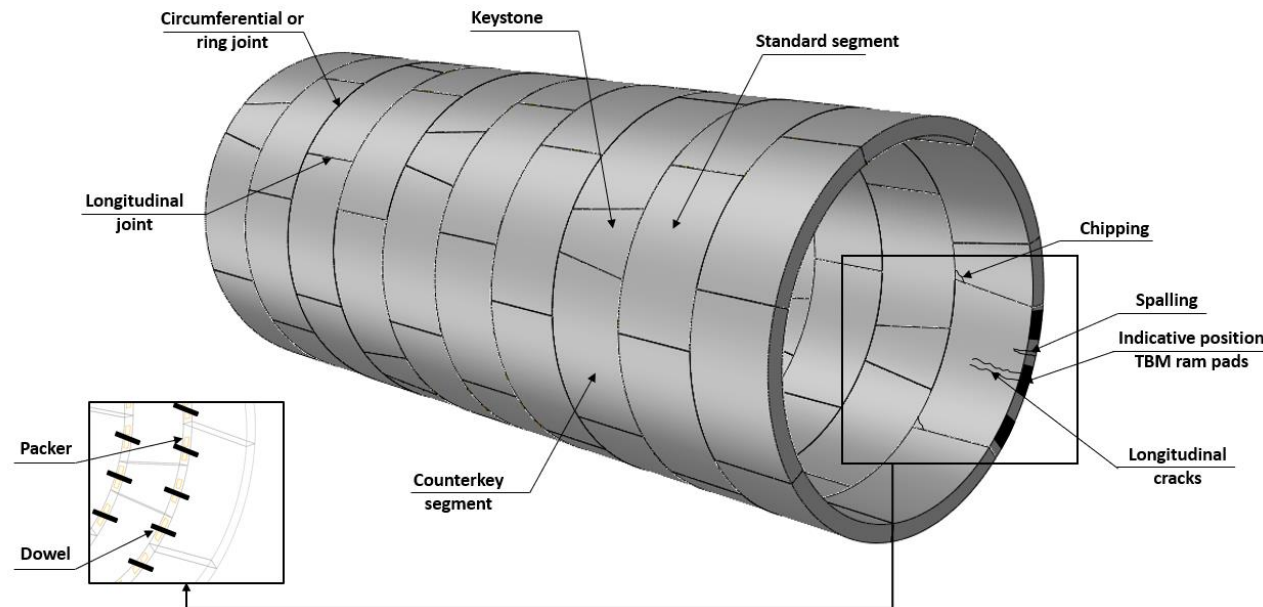


Figure 1.1: Tunnel construction interfaces, the typical configuration of CSLs and frequent crack patterns during construction



## Chapter 2

# Study on the geometry of longitudinal joints

### 2.1. Introduction

Joint detailing is key in CSL design (BTS, 2004). Joints are critical features for the watertightness of tunnels, must withstand concentrated loads and can become a governing factor in the global behaviour of tunnels. Tunnel designers must detail joint geometry, sealing and connections with the view to optimising CSL performance over its design life.

Longitudinal joints can be designed with convex-convex or flat bearing geometry (Vimalanathan, 2007). Craig and Muir-Wood (1978) categorised convex-convex joints as “articulated longitudinal joints” that transfer normal forces at low eccentricities and increase ring flexibility. A minimum number of ten to twelve segments was proposed at the time to avoid excessive hoop moments within the segment bodies. Convex-convex joints with radii around 3m were typically used in expanded linings of about 4m diameter constructed in London Clay (Craig and Muir-Wood, 1978), as these joints could cope with the larger offsets and rotations required to accommodate overbreaks and irregularities in the excavation line (Baumann, 1992). Conversely, their deployment was traditionally disregarded in smooth bore grouted linings (Craig and Muir-Wood, 1978).

Examples of emblematic projects with convex-convex longitudinal joints are the Channel Tunnel, with expanded CSL, and the Great Belt railway tunnel, with grouted and bolted CSL. Despite using different joint curvatures, 3.2m and 2.5m respectively (BTS, 2004), the reinforcement design was based on the same empirical equations developed for the Channel Tunnel project, which omitted joint curvature as a variable. Vimalanathan (2007) reported curved joints with a radius of 1.375m being deployed in the Heathrow Express tunnel.

Maidl et al. (2012) noted that the joint curvature was influenced by lining thickness, hoop thrust and allowable rotations. Baumann (1992) proposed certain guidelines in the applicability of flat and curved joints based on experimental results from full-scale joint tests. Flat joints were more suitable for low hoop compression and small allowable rotations, while curved joints could cope better with high hoop forces and large rotations.

In this chapter, the impact of bearing surface geometries on the local performance of longitudinal joints is examined. First, mechanical models of joints available in published literature are reviewed. Second, the main concrete damage modes near joints are summarised. Third, an analytical method for the evaluation of bursting capacity is proposed. Fourth, the expression of gasket gaps in rotated joints

is given. Fifth, a new method for joint design that can integrate the global CSL performance during and after construction is proposed. Finally, the impact of joint geometry on in-plane imperfections is briefly examined.

### 2.2. Joint rotational models

#### 2.2.1. Flat joints

The most common rotational models of flat joints are the Janssen and Gladwell models (see Figure 2.1). Luttikholt (2007) summarised the comparison of these analytical models against finite element analyses (FEA) undertaken by others and Hordijk and Gijsbers's moment-rotation (MR) curves derived from full-scale joint tests (Hordijk and Gijsbers, 1996).

The Janssen model represents the flat joint as a concrete element between two segments with a depth and width equal to the joint depth,  $h_j$ , thus capturing the effect of joint rotation,  $\theta$ , and local concrete deformations on the joint rotational stiffness,  $K_\theta$  (see Figure 2.1.b). It also assumes that the concrete material is linear elastic and that a linear distribution of normal compressive stresses develops at the contact surface. Consequently, the MR relationship is formulated with two equations:

$$M = \frac{E_c h_j^2 b}{12} \theta \quad \theta \leq \frac{2N}{E_c h_j b} \text{ or } M \leq \frac{N h_j}{6} \quad (2.1)$$

$$M = \frac{N h_j}{2} \left( 1 - \sqrt{\frac{8N}{9b h_j E_c \theta}} \right) \quad \theta > \frac{2N}{E_c h_j b} \text{ or } M > \frac{N h_j}{6} \quad (2.2)$$

where  $N$  is the normal force,  $M$  the bending moment,  $E_c$  the concrete Young's modulus and  $b$  the joint width. In Eq. 2.1, the joint is closed and  $K_\theta$  depends only on  $h_j$  and  $E_c$ . Once the joint opens, Eq. 2.2 applies, evidencing that  $K_\theta$  is not only dependant on joint geometry and material properties, but also on the normal force being transferred at the joint. Since the contact depth reduces as the joint opens,  $K_\theta$  decreases progressively and  $M$  approaches the asymptotic line of  $M = N h_j / 2$ , i.e. equivalent to a normal force acting as a concentrated load at the extreme fibre of the joint depth (see Figures 2.1.a and 2.1.b).

The Gladwell solution is based on the contact problem of a flat frictionless punch pressed asymmetrically on an elastic semi-space (see Figure 2.1.c) (Gladwell, 1980). MR curves converge towards the same asymptotic line more rapidly and the initial  $K_\theta$  is greater due to stress concentration at the punch edges (see Figure 2.1.a).

Blom (2002) refined the Janssen model to take into account concrete plasticity under compression through a bilinear stress-strain relationship. In this case, a third region in the MR space is defined

## 2.2. Joint rotational models

when concrete strains at the contact surface reach the elastic limit. The concrete compressive strength,  $f_c$ , becomes an additional variable.

Ding et al. (2013) and Li et al. (2015) developed comprehensive rotational models based on an elastoplastic stress-strain relationship for concrete. The total normal concrete displacement at the most loaded edges of the bearing surfaces,  $\Delta_c$  (see Figure 2.1.d), were calculated with Eq. 2.3:

$$\Delta_c = 2l_{cc}\varepsilon_{c,max} \quad (2.3)$$

where  $l_{cc}$  is the length of concrete segment needed to redistribute the concentrated stresses to the full lining depth,  $h$ , and  $\varepsilon_{c,max}$  is the peak concrete compressive strain at the joint faces. Ding et al. (2013) determined the  $l_{cc}/h$  ratio of surface loads as a function of the load eccentricity and depth from two-dimensional (2D) FEA of elastoplastic concrete joints. The Janssen model is equivalent to the Ding's solution if a linear elastic concrete constitutive model is adopted and  $l_{cc}$  assumed to be equal to  $h/2$ .

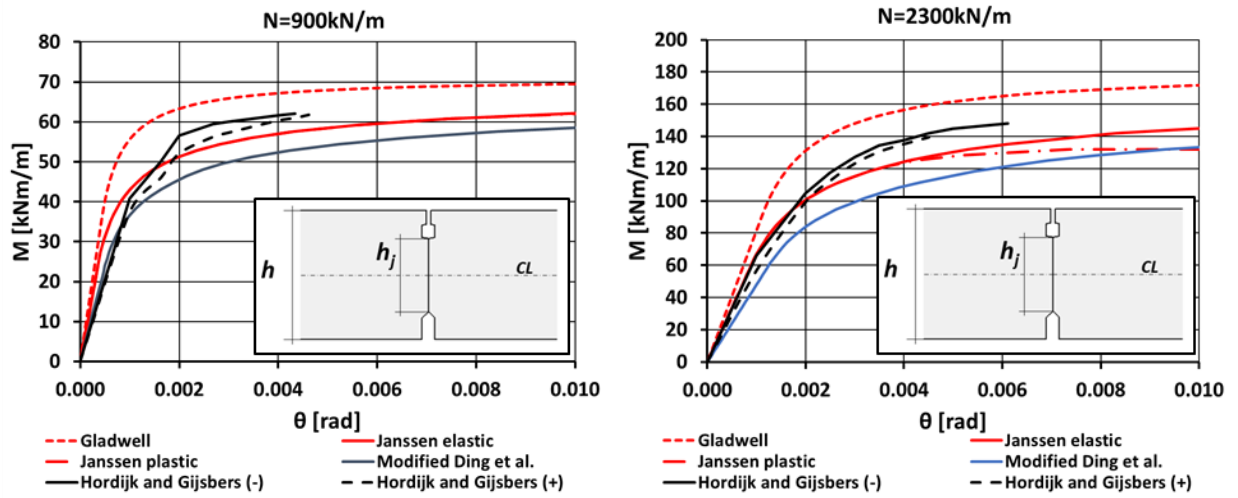
In Figure 2.1.a, Hordijk and Gijsbers' (1996) test results on flat joints are plotted against MR curves inferred from the above solutions and the joint geometry of their full-scale tests. Ding's model is formulated with no concrete plasticity but using Ding's  $l_{cc}/h$  ratios (Ding et al., 2013).

The graphs evidence that the Gladwell solution is an upper limit of the experimental MR curves. Numerical studies have shown that the Gladwell relation reflects with great accuracy the rotational behaviour of 2D FE models of flat joints with  $h_j/h$  ratios typically used in joint design (Luttikholt, 2007), suggesting that the latter must also result in an overestimation of the experimental  $K_\theta$ .

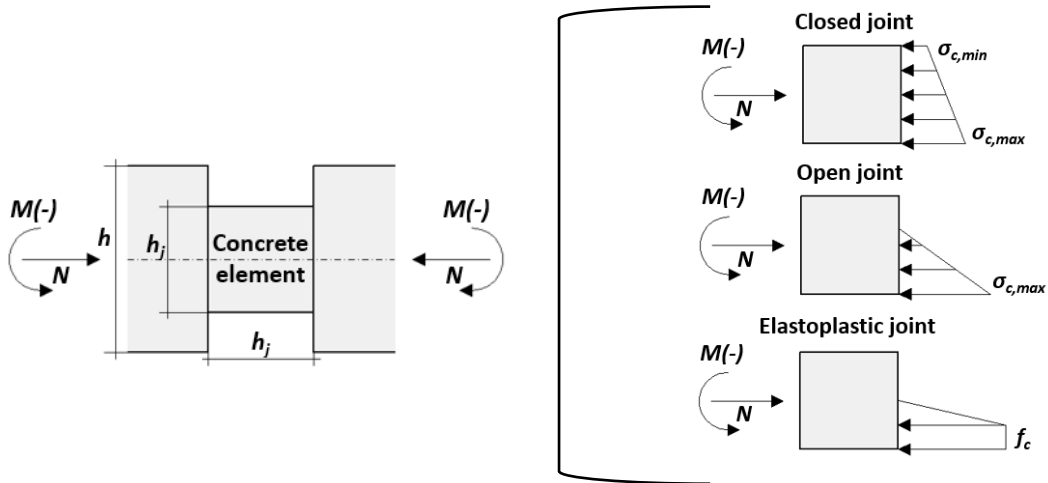
The Janssen model approaches the experimental MR curves with slightly smaller moment capacity from about 0.002rad onwards. The elastoplastic version of the Janssen model underestimates moment capacities at high axial forces as the development of surface stresses is limited by the  $f_c$  of choice. Middendorf suggested an allowable bearing stress in concrete contact patches of at least three times the cylinder compressive strength due to local concrete confinement before reaching failure by wedging (Ibell, 1992). Yielding at the joint surfaces may then only be experienced at large rotations in highly normally loaded joints. Consequently, the Janssen model is deemed an adequate lower bound for serviceability states.

Hordijk and Gijsbers (1996) showed that the initial  $K_\theta$  at low axial forces was smaller than predicted by the Janssen model, and attributed the data scatter to joint imperfections whose relative effect decreased with normal force. Conversely, the modified Ding's model results in a better approximation of initial stiffness when the joints are subjected to moderate normal loads. It leads, however, to lower values of moment capacity, particularly at the non-linear branch of the MR curves. This underestimation may be caused by the adoption of an elastoplastic concrete constitutive model for the computation of  $l_{cc}/h$  ratios, that results in overestimated  $l_{cc}$  and  $\Delta_c$ .

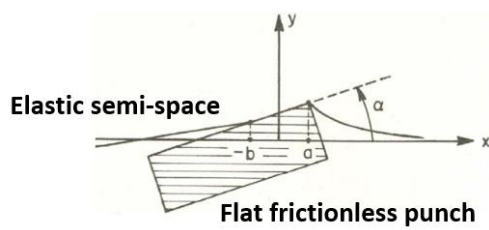
### a) MR curves



### b) Janssen model



### c) Gladwell model (after Gladwell, 1980)



### d) Definition of $l_{cc}$ (after Ding et al., 2013)

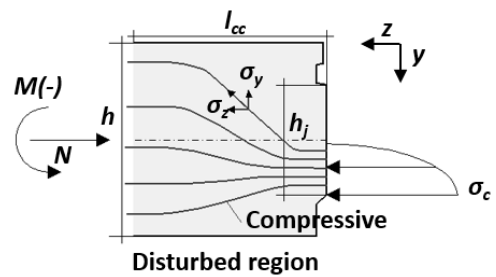


Figure 2.1: Flat joint models

### 2.2.2. Curved joints

The mechanical behaviour of curved joints has been a less prolific topic in the published literature. The surface stresses of a curved joint can be estimated through Hertz's theory for nonconforming surface contacts, which assumes that surfaces are frictionless and continuous, strains are small and curved bodies are linear elastic (Williams, 2005). Joints with constant bearing curvature can be approximated to the Hertzian solution for two cylinders with parallel axes as long as the contact area is small compared to the cylinders curvature (see Figure 2.2.a) (Young and Budynas, 2002). According to Hertz, the pressure distribution described at the contact strip is semi-elliptical. The contact strip shifts with stress distribution as the segments rotate relative to each other. Consequently, for a given normal load, the rotational behaviour of curved joints working within the elastic region of concrete and not subjected yet to edge effects is determined exclusively by the radius of the joint surfaces:

$$K_{\theta} = \frac{Ne_c}{\theta} = \frac{NR \sin(\theta/2)}{\theta} \approx \frac{NR}{2} \quad \theta \leq \frac{h_j}{2R} \quad (2.4)$$

where  $e_c$  is the eccentricity of the normal force and  $R$  the joint radius. This expression is also valid for initially misaligned joints, given that the Hertzian model assumes each curved body as an elastic cylinder, and thus the distinction between aligned and offset bodies is not relevant as long as the contact strip is not narrowed by the joint edges (see Figure 2.2.b).

If edge effects are neglected, the joint rotational behaviour can be described through a family of bilinear curves with normal force as the family parameter (see Figure 2.2.c). In the first branch, the moment increases linearly with rotation until reaching the maximum moment of  $M = Nh_j/2$ . From this rotation onwards, the joint yields and it can be assumed that the moment is kept constant. In reality, there is a transitional stage, where the contact strip narrows from the Hertzian to an infinitesimal width.

There are no analytical solutions for contact problems in elastoplastic materials and their characterisation is generally approached through FEA (Williams, 2005). In the case of curved joints with elastoplastic concrete, the joint surfaces tend to flatten without significant influence on  $e_c$  (see Figure 2.2.d). Consequently, the effect of concrete plasticity on  $K_{\theta}$  is very limited.

## 2.2. Joint rotational models

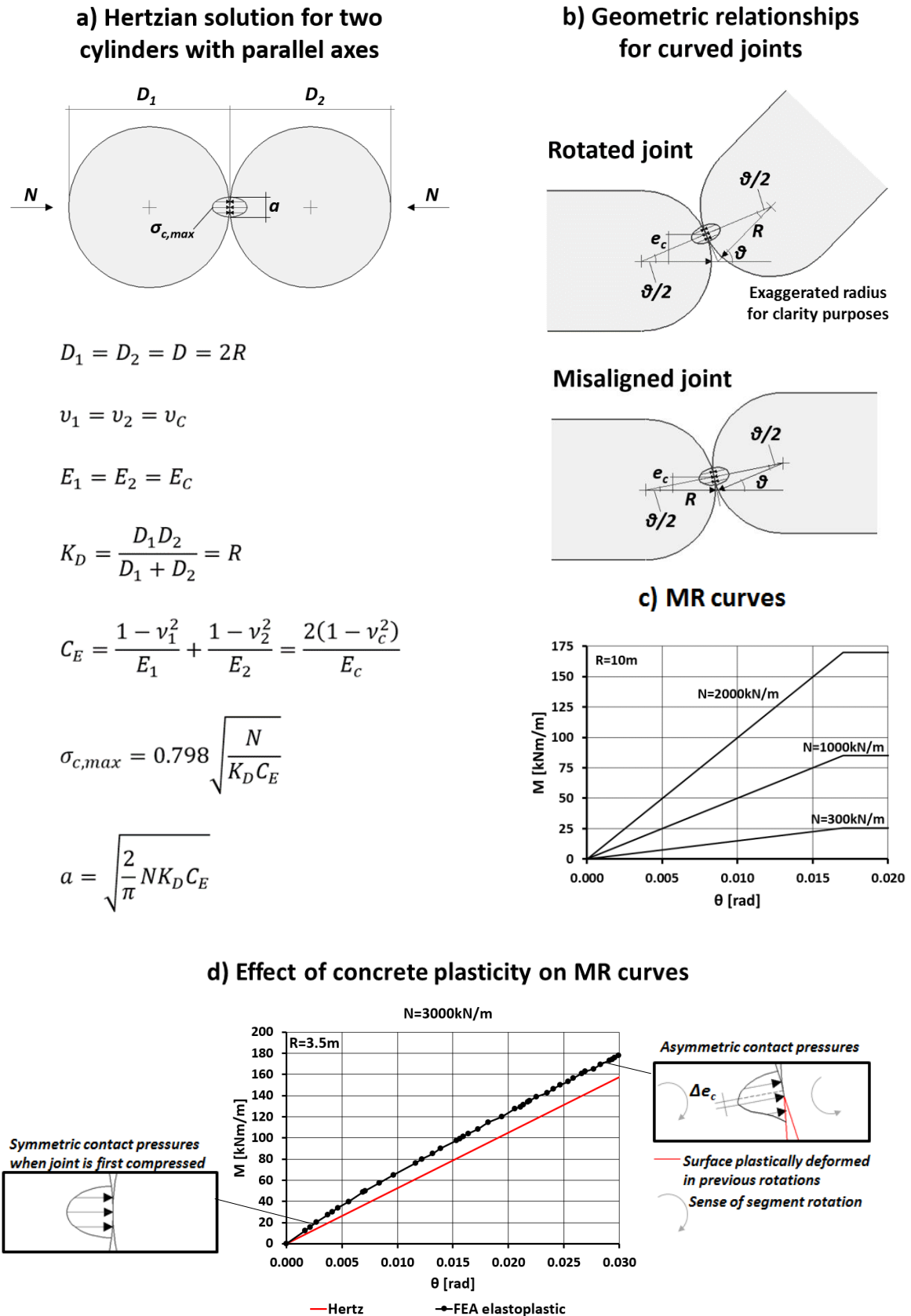


Figure 2.2: Curved joint models

### 2.3. Concrete damage modes

At longitudinal joints, the hoop thrust is transferred through surface loads concentrated over a limited contact depth that depends on joint geometry and rotation. The spread of such concentrated load towards a linear distribution of compressive stresses along the lining depth generates transverse tensile stresses in the disturbed zone: bursting stresses near the joint along the axis of the concentrated load and spalling stresses at the sides of the loaded surface (see Figure 2.3.a).

In typical longitudinal flat joints with reduced joint depths, centrally loaded and subjected to moderate in-plane angularities up to  $0.2^\circ$ , the load bearing capacity of joints at service loads is determined by the crack width limit of bursting cracks, whilst, at higher angular imperfections, the critical load is governed by shear failure of the loaded corner (see Figure 2.3.b) (Cavalaro, 2009).

Full-scale tests on curved joints without in-plane angularities conducted by various authors over the years (Baumann, 1992; Swartz et al., 2002; BSI, 2004) showed that the tensile splitting caused by bursting stresses was the most onerous damage mode as opposed to low-angle shearing, particularly at serviceable load eccentricities. Indeed, in his study of anchorage zones for prestressed concrete, Ibell (1992) concluded that in centrally strip loaded concrete specimens, bursting cracks were formed at the centreline of the loaded area either prior to or contemporarily to ultimate failure due to low-angle wedging (see Fig. 2.3.c). Simultaneous failure was observed only for highly concentrated surface loads.

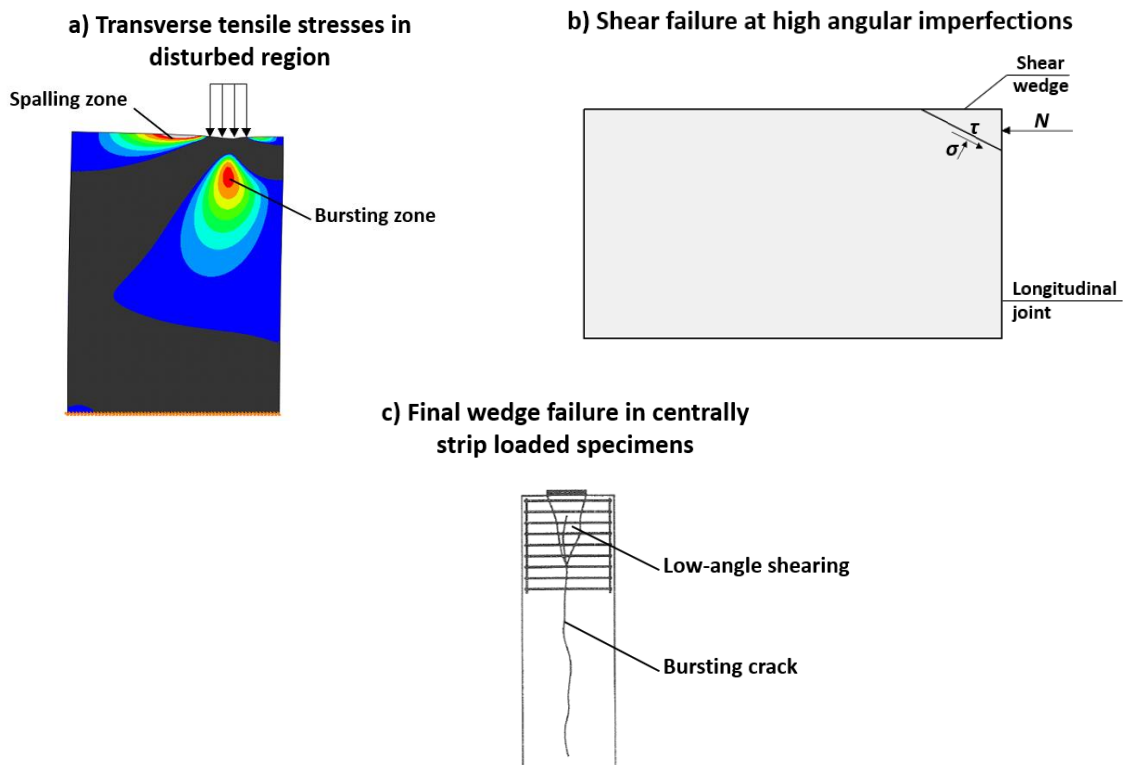


Figure 2.3: Concrete damage modes

### 2.4. Bursting capacity

#### 2.4.1. Current design practice

In current design practice, the quantity of through-thickness reinforcement required to prevent tensile splitting near flat joints,  $A_{s,req}$ , is generally computed with Eq. 2.5:

$$A_{s,req} = \frac{T_b}{f_{yk}\gamma_s} \quad (2.5)$$

where  $T_b$  is the bursting force,  $f_{yk}$  is the characteristic tensile strength of steel and  $\gamma_s$  is the material safety factor. The bursting force is calculated with the empirical formula for concentric anchorage zones in post-tensioned concrete (see Figure 2.4.a), which was derived from experimental tests and FEAs and has been adopted by several concrete codes (Zhou et al. 2015):

$$T_b = 0.25N \left(1 - \frac{a}{h}\right) \quad (2.6)$$

where  $a$  is the width of the anchor plate along the beam depth and  $h$  is the depth of the concrete member. The location of the bursting force along the tendon path,  $d_b$ , is given by:

$$d_b = 0.5(h - 2e_c) \quad (2.7)$$

The expression of the bursting force for concentric and uniform surface loads is applied to the case of flat joints with eccentric and triangular surface loads with the following amendments: the width of the triangular surface load  $a$  is converted to the width of a uniform surface load with equal eccentricity  $a_{eq}=h_j-2e_c$ ;  $h$  is reduced to the depth centred with respect to the surface load  $h_{eq}=h-2e_c$  (see Figure 2.4.b) (DAUB, 2013); so that  $T_b$  is:

$$T_b = 0.25N \left(1 - \frac{h_j - 2e_c}{h - 2e_c}\right) \quad (2.8)$$

Therefore, the current design method for flat joints is based on the calculation of the bursting force by adopting equivalent surface loads and joint dimensions and ignores the contribution of the concrete tensile strength,  $f_{ct}$ , to bursting resistance.

In the case of curved joints, the design method against splitting failure is fundamentally empirical. Designers infer rebar quantities from published design charts of joint bursting capacity against reinforcement ratio obtained from joint tests conducted for previous tunnel projects, which may be validated with project-specific laboratory tests (Swartz et al., 2002). The bursting capacity of joints is defined as the maximum normal load that longitudinal joints can withstand before reaching a certain limit state. Figure 2.4.c shows experimental data on bursting capacity at first visible crack and ultimate



## 2.4. Bursting capacity

failure against tensile splitting, i.e. target load  $N_{target}$ , gathered from the 3.2m radius joint tests conducted for the Channel tunnel (Swartz et al., 2002). The empirical equation for  $N_{target}$  includes the contribution of  $f_{ct}$  but the influence of joint curvature and load eccentricity is omitted:

$$N_{target} = 4.45f_{ct}hb + 4.0F_{st} \quad (2.9)$$

where  $F_{st}$  is the steel capacity against splitting (Swartz et al., 2002).

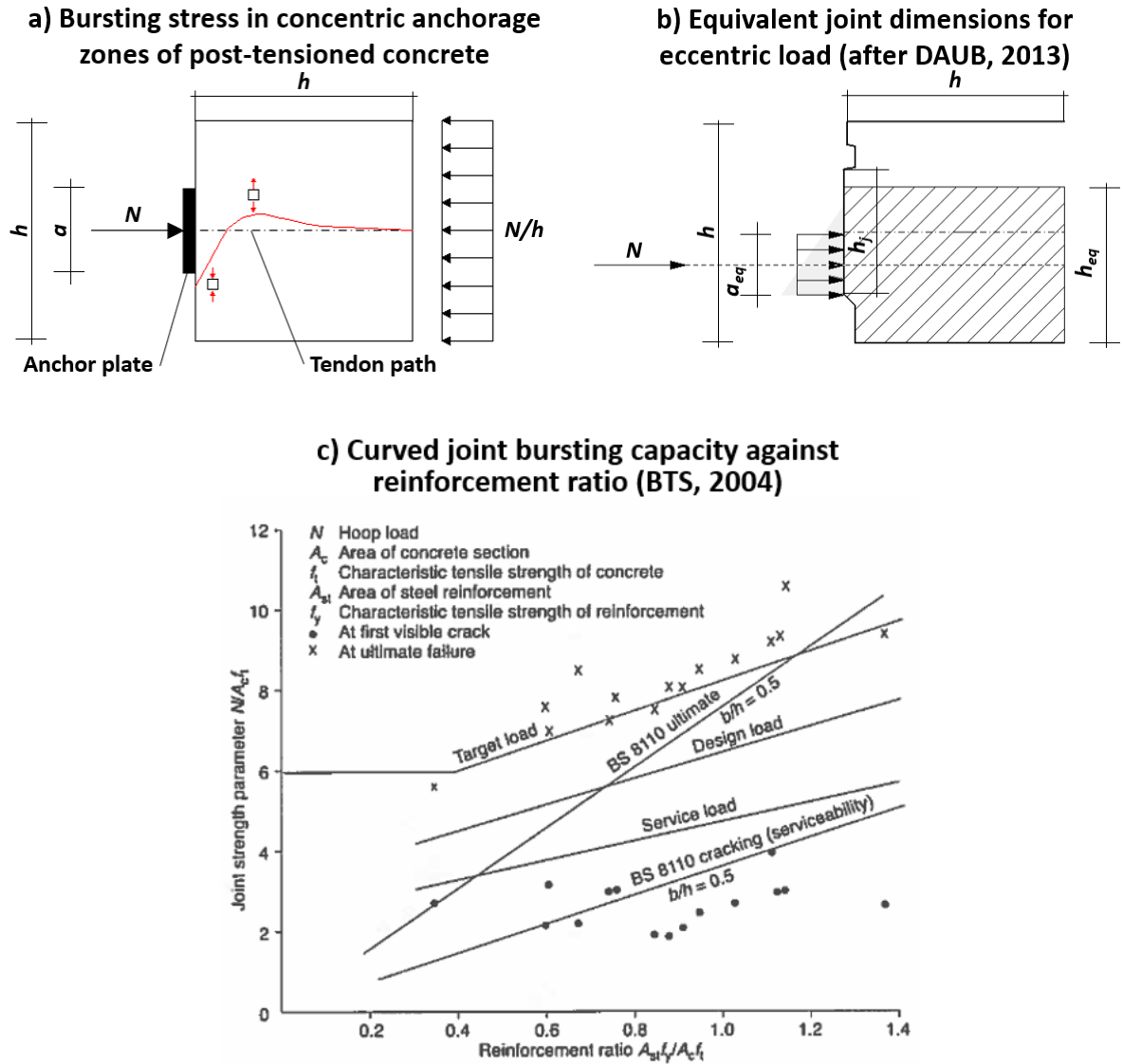


Figure 2.4: Current design practice for bursting capacity check

### 2.4.2. Proposed calculation method

The standard formulation of bursting forces at end zones of concrete members subjected to concentrated surface loads given by Eq. 2.6 and Eq. 2.7 has been drawn from numerical methods and experimental tests due to the lack of theoretical solutions (Zhou et al., 2015). However, in the last

## 2.4. Bursting capacity

decade, several authors have proposed mathematical models of surface load dispersion based on Guyon's (1953) concept of main isostatic lines of compression (ILCs), i.e. load trajectories of equal load share (see Figures 2.5.a and 2.5.b). The ILCs were approximated by polynomials that were to fulfil certain boundary conditions. In the most recent development by Zhou et al. (2015), the boundary conditions were drawn from the equations of the plane stress elastic problem. The bursting stresses were then proportional to the ILCs curvatures.

The method proposed here for the calculation of bursting capacity at variable rotations of longitudinal joints combines Zhou's (2015) solution for eccentric surface loads with the rotational models of joints. The bursting capacity is regarded as the maximum normal load that joints can withstand at imminent tensile cracking.

In Zhou's (2015) analytical method, peak bursting stresses,  $\sigma_{t,max}$ , along the centreline of an eccentric and uniformly distributed surface load are computed with Eq. 2.10:

$$\sigma_{t,max} = \frac{0.6N}{bh(1-\gamma)} \left(1 - \frac{a}{h}\right) \quad (2.10)$$

where  $b$  is the concrete member width,  $a$  the contact width along the member depth and  $\gamma=2e_c/h$  the load eccentricity ratio.  $T_b$ , is equal to:

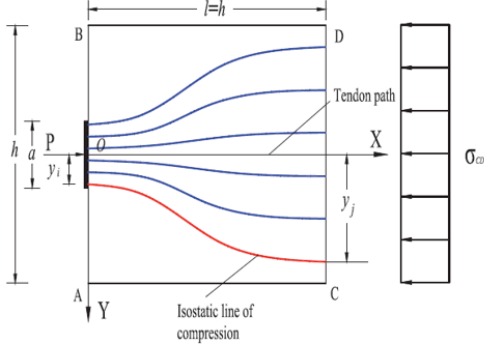
$$T_b = 0.25N(1+\gamma)^2 \left(1 - \gamma - \frac{a}{h}\right) \quad (2.11)$$

and is located at:

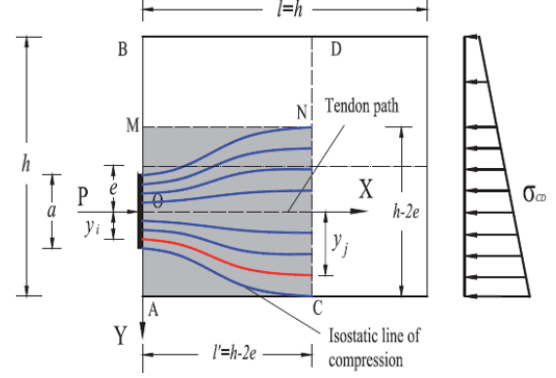
$$d_b = 0.48h(1-\gamma) = 0.48(h - 2e_c) \quad (2.12)$$

Figure 2.5.c outlines the bursting capacity calculation procedure adopted here. For a given  $N$  and  $\sigma_{t,max}$ , the  $e_c$  at which bursting cracks are first experienced is derived from Eq. 2.10 and an equivalent contact width,  $a_{eq}$ , that in turn depends on joint geometry and eccentricity. Once  $e_c$  is calculated by solving the system of two equations,  $M$  can be easily computed. The bursting capacity curve for a certain value of  $\sigma_{t,max}$  can be represented in the normal force-rotation (NR) space with the aid of joint moment-rotation relationships. The maximum  $T_b$  and  $d_b$  corresponding to the bursting capacity curves can be calculated with Eq. 2.11 and Eq. 2.12.

**a) ILCs and bursting stresses in the concentric anchorage zone (after Zhou et al., 2015)**



**b) ILCs in the eccentric anchorage zone (after Zhou et al., 2015)**



**c) Proposed calculation procedure**

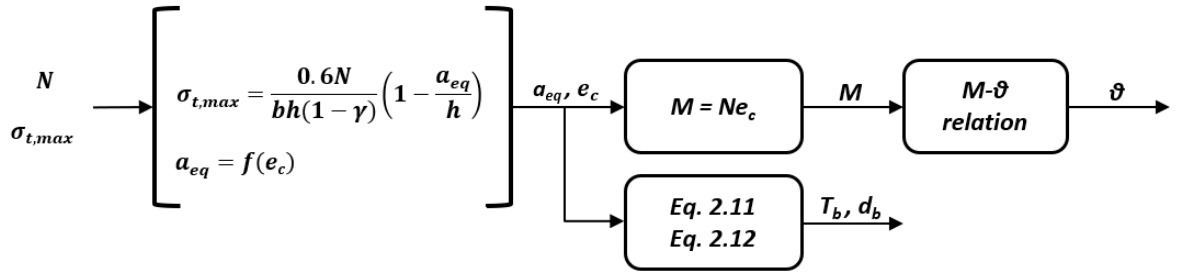


**Figure 2.5: Bursting capacity calculation procedure**

### 2.4.2.1. Flat joints

With the Janssen model, the joint bearing stresses are linear. The contact width of an equivalent uniformly distributed load (UDL) with equal eccentricity is  $a_{eq}=h_j-2e_c$ . Figure 2.7.a compares Zhou's unitary  $\sigma_{t,max}$  calculated for the above UDL with those obtained from 2D FE linear elastic models of flat joints subjected to equivalent uniform or triangular surface loads, for  $e_c$  ranging from 0 to  $h_j/2$ . The input parameters are listed in Table 2.1.

Zhou's  $\sigma_{t,max}$  increases with  $e_c$ , from 0.25 to 1.40 times the average axial stress while in both numerical analyses with triangular and uniform loads it varies from 0.20 to 1.1 only. The triangular surface loads lead to  $\sigma_{t,max}$  marginally smaller than those given by the uniform numerical solution.

Figure 2.6.b shows the evolution of  $a_{eq}$  with  $e_c$  in Zhou's solution and the numerical analyses, the latter calculated with Eq. 2.10 and the  $\sigma_{t,max}$  obtained from the FE models. The correction factors,  $f_{corr}$ , can be used to convert Zhou's  $\sigma_{t,max}$  to the numerical  $\sigma_{t,max}$  or a  $\sigma_{t,max}$  that is corrected only for the linear distribution of the surface loads.

The analytical bursting capacity curves in the NR space calculated with and without contact width correction for various  $\sigma_{t,max}$  are illustrated in Figure 2.6.c. In both cases, the joint capacity against bursting is extremely high at small rotations but drops sharply as the joint opens. Triangular distributions lead to slightly higher bursting capacities, particularly for greater  $\sigma_{t,max}$ . However, at

## 2.4. Bursting capacity

moderate rotations, they can expand the usability of flat joints to larger rotations, e.g. when  $\sigma_{t,max}=9\text{MPa}$  and  $N=2750\text{kN/m}$ , the allowable rotations increase from  $0.010\text{rad}$  to  $0.015\text{rad}$  if the triangular distribution of surface loads is accounted for.

Given that Zhou's overestimation of  $\sigma_{t,max}$  increases with  $e_c$ , up to two times the numerical  $\sigma_{t,max}$  for  $e_c/(h_j/2)=0.7$ , the FE bursting capacity curves are expected to present a smoother decline with rotations.

Table 2.1: Input parameters for bursting capacity based on the CTT joints

Input parameters			
Name	Symbol	Units	Value
Joint width	$b$	m	1
Lining depth	$h$	m	0.3
Joint depth	$h_j$	m	0.17
Radius of curved joint	$R$	m	3.5
Concrete Young's modulus	$E_c$	GPa	38

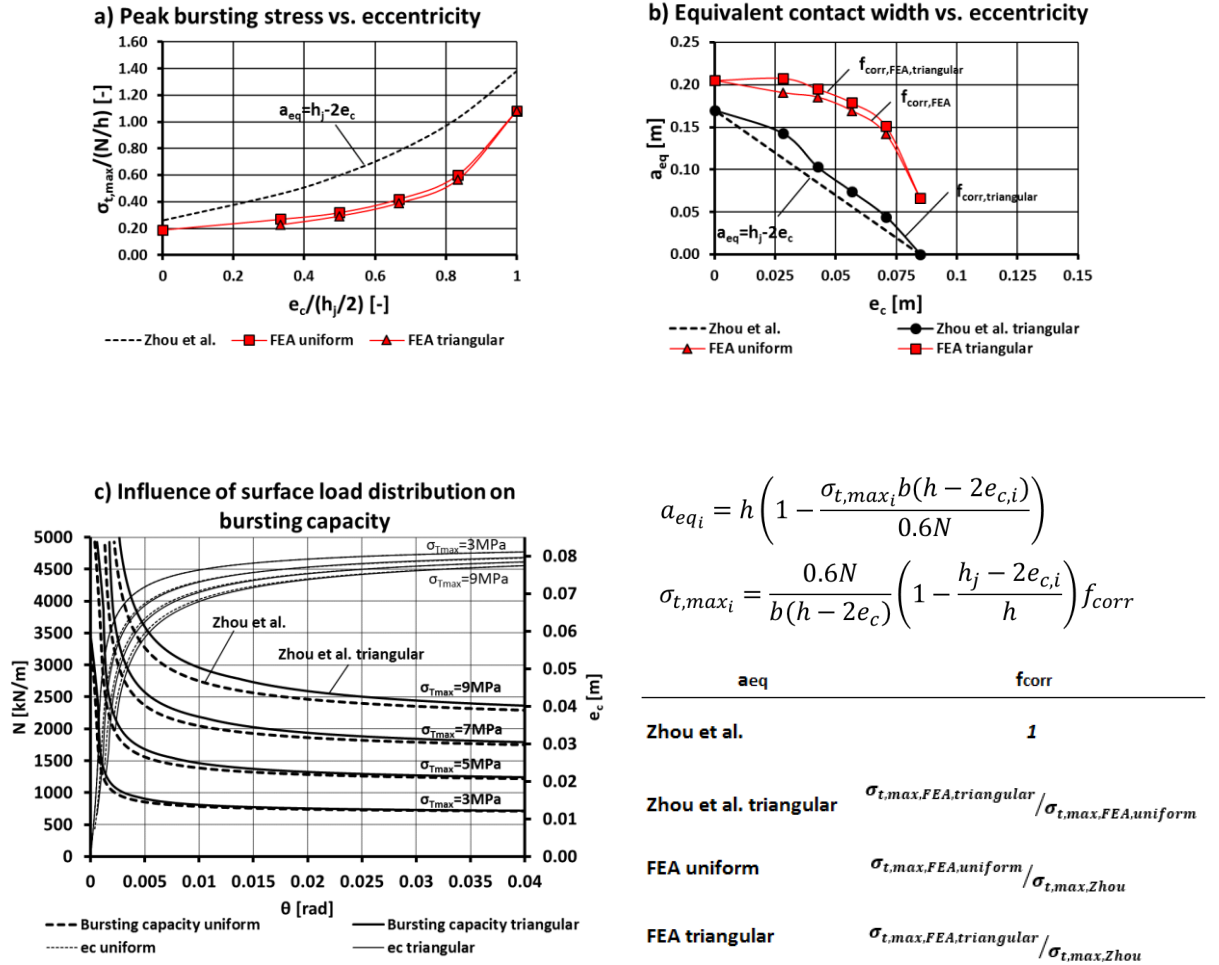


Figure 2.6: Bursting capacity calculation for flat joints

### 2.4.2.2. Curved joints

Baumann (1992) measured the contact width of curved joints, unaffected by edge effects, for two different values of axial force. These experimental widths were greater than the Hertzian widths (see Figure 2.7.a), which means that the joint bearing surfaces were partially plasticized near the contact width.

The lack of elastoplastic solutions to the contact of nonconforming surfaces imposes some difficulty in the calculation of bursting capacity envelopes. However, the proposed Eq. 2.13, with the first term proportional to the elastic solution and the second term varying linearly with the normal load  $N$ , fits Hertz's widths at low axial forces and Baumann's experimental data:

$$a_{eq} = A\sqrt{NK_d C_E} + BN \quad (2.13)$$

where  $K_d$  is the effective curvature and  $C_E$  the effective elastic modulus given in Figure 2.2 (Young and Budynas, 2002). When the contact width is close to the joint edges, it becomes again  $a_{eq}=h_j-2e_c$  if a symmetric pressure distribution is assumed (see Figure 2.7.b).

Figure 2.7.b shows the bursting capacity curves in the NR space of elastic and elastoplastic curved joints with  $R=3.5m$ . Both families present three distinctive linear branches. At low rotations, with the contact strip away from the joint edges, the contact width is fully developed. Plasticity increases bursting capacity slightly, particularly with high values of  $\sigma_{t,max}$  and  $N$  as a larger proportion of the contact width is plasticized. The second linear branch describes bursting capacity at large rotations, i.e. greater than 0.04rad, when the contact width is constrained by the joint edge. Wider contact strips at higher  $\sigma_{t,max}$  experience edge effects at slightly lower rotations. The third branch represents infinite joint yielding with normal forces acting as a concentrated load at the joint extreme fibre. Overall, it could be inferred that elastic contact widths provide a satisfactory estimation of bursting capacity.

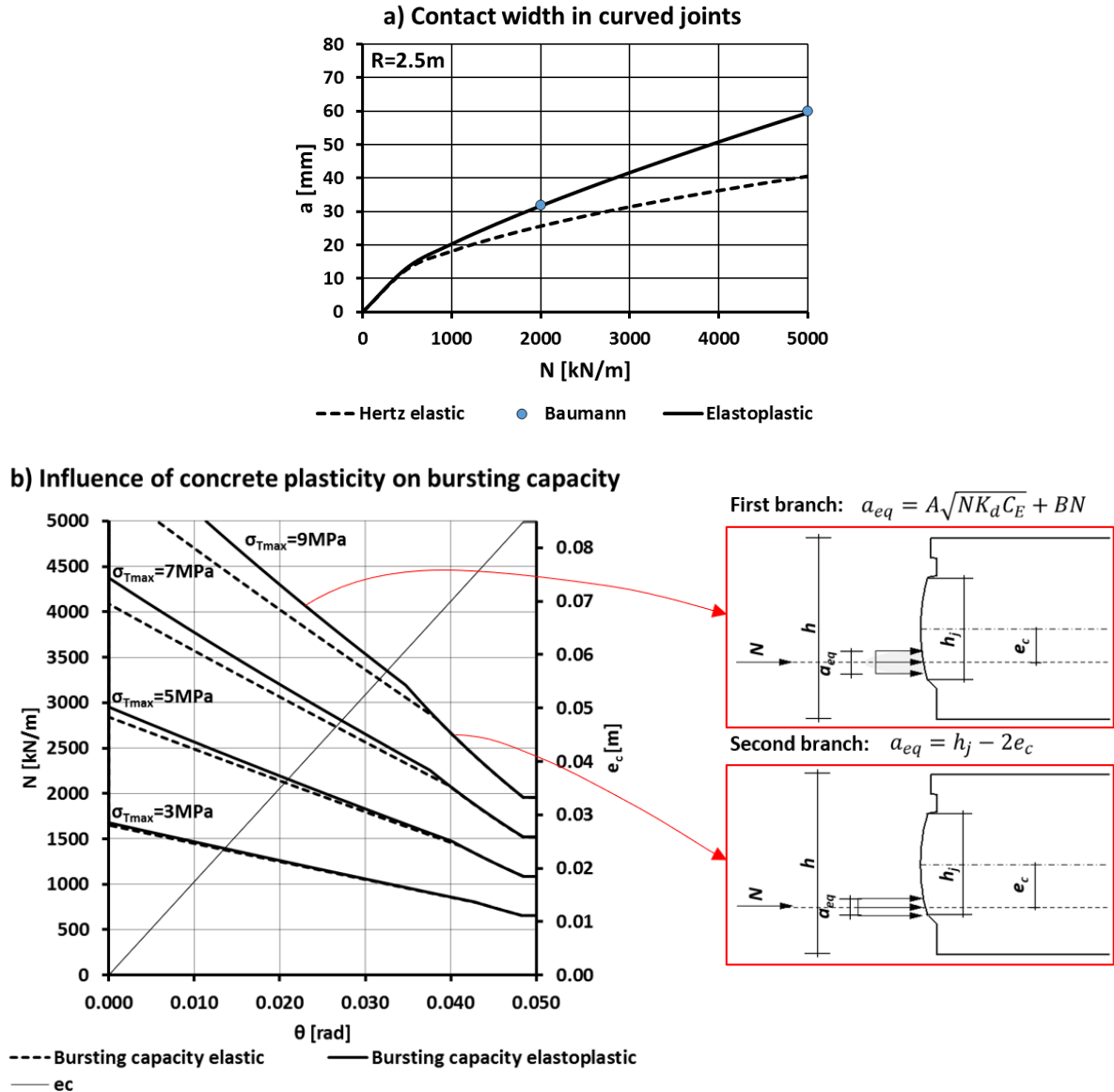


Figure 2.7: Contact width and bursting capacity in curved joints

### 2.4.3. Discussion

#### 2.4.3.1. Factors influencing bursting capacity

##### a) Effect of joint geometry

Figures 2.8.a and 2.8.b illustrate the bursting capacity curves of flat and 3.5m radius curved joints for concrete grades defined by the approximate secant Young's modulus,  $E_{cm}$ , and tensile strength,  $f_{ctm}$ , given by the Eurocode 2 (EC2) (BSI, 2010).

It is evidenced that the bursting capacity limits are greatly influenced by joint geometry. Flat joints deliver high bursting capacities for quasi-centred loads but their performance drops drastically with  $\theta$ , particularly in joints with low strength concrete. The sensitivity of the flat joint bursting capacity to rotations entails that small initial rotations resulting from ring erection can undermine bursting capacity and its predictability.

## 2.4. Bursting capacity

---

Curved joints present a more steady bursting performance against rotations. The radius determines the correlation between load eccentricity and rotation, and subsequently the gradient of the bursting capacity limit in the NR space. Curved joints with radii in the order of 3.5m, as generally used in design, tolerate large rotations better than flat joints, particularly in the range of 0.002rad to 0.040rad.

The figures also prove that  $e_c$  increases much more rapidly in flat joints than in 3.5m curved joints: at 0.01rad, the eccentricity of a 3.5m radius joint still lies within the middle third of the joint depth; in flat joints it already approaches the joint edge. Consequently, the splitting cracks of curved joints are generally centred with respect to the joint depth unless extremely large rotations have taken place. In flat joints, the splitting cracks are prone to develop at the joint edges, which may lead to concrete flaking, as reported by Baumann (1992), and loss of gasket confinement. In conventionally reinforced segments with flat joints, the offset cracking or flaking can expose the reinforcement near the joint and trigger steel corrosion. At very large rotations, flat joints must experience wedge failure earlier than curved joints, which was again empirically attested by Baumann (1992).

### ***b) Effect of concrete grade***

The use of high strength concrete improves the bursting capacity of both joint types. For instance, at  $\theta=0.010$ rad, a C80/95 concrete grade, with  $E_{cm}=42$ GPa and  $f_{ctm}=4.8$ MPa, doubles the bursting capacity of flat and curved joints with a C25/30 concrete grade, with  $E_{cm}=31$ GPa and  $f_{ctm}=2.6$ MPa. The enhancement in bursting performance is caused by the increase in concrete tensile strength associated with a greater concrete grade.

### ***c) Effect of concrete tensile strength***

The tensile strength of mature concrete,  $f_{ct}$ , generally ranges between 0.05 and 0.10 times its compressive strength (Chen, 1982). Figures 2.8.c and 2.8.d. present the bursting capacity limit of normal and high strength concretes with upper and lower values of  $f_{ct}$ .

Normal and high strength concretes with equal  $f_{ct}$  and  $E_{cm}$  of 35GPa and 41GPa respectively yield very similar bursting capacity curves in flat joints, which denotes that the influence of  $E_{cm}$  is negligible. In curved joints,  $E_{cm}$  is not a variable for bursting capacity.

An increase of  $f_{ct}$  boosts the bursting capacity limit of joints. In flat joints, the decay with rotation is smoother for higher  $f_{ct}$ ; in curved joints, the bilinear decline becomes more accentuated although the bursting capacity still remains greater than in curved joints. The difference between upper and lower capacity curves is more notable for high strength concretes given that the range of  $f_{ct}$  is proportional to the compressive strength.

## 2.4. Bursting capacity

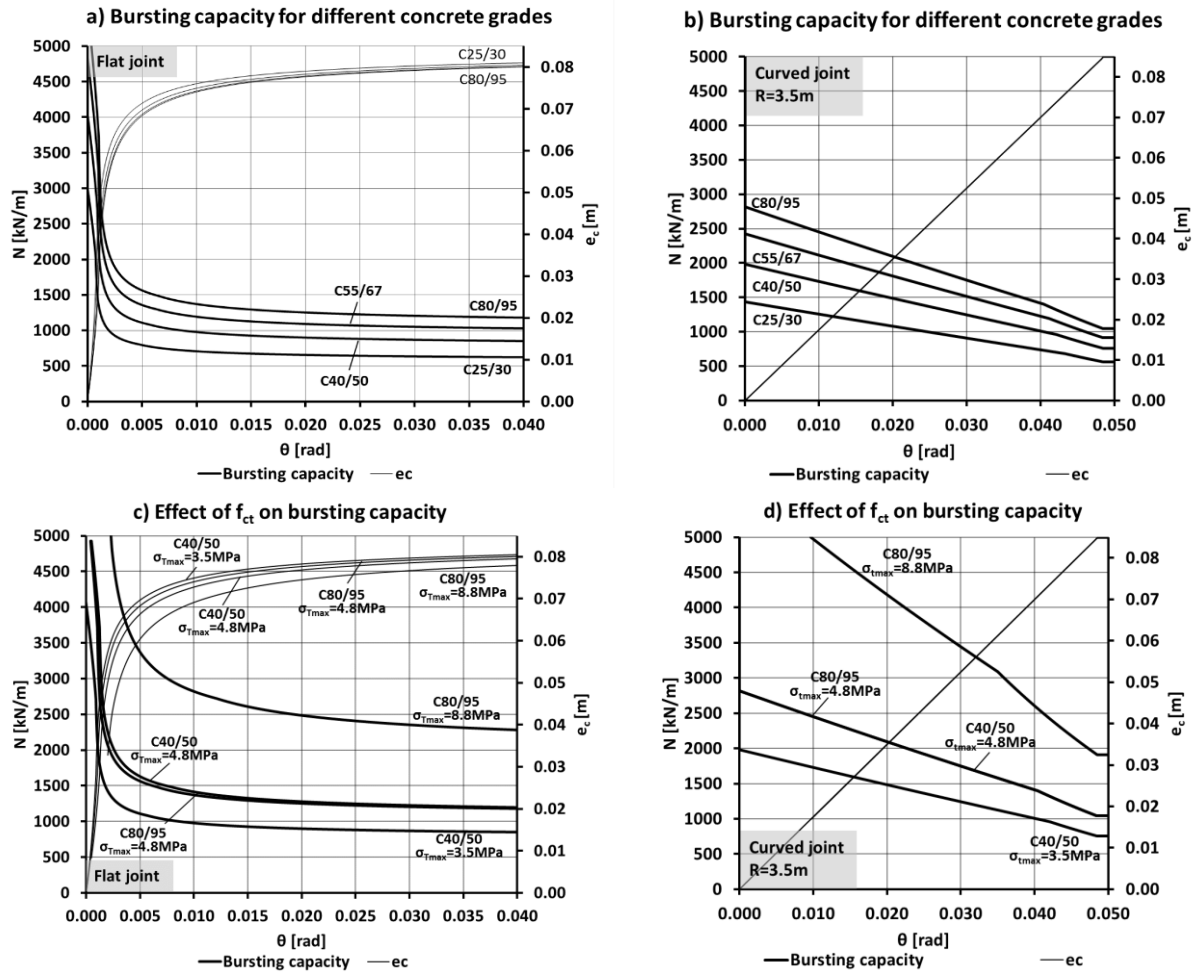


Figure 2.8: Factors influencing bursting capacity

### 2.4.3.2. Comparison with current design methods

In current design methods, the contribution of  $f_{ct}$  to the bursting capacity at imminent cracking of flat joints is dismissed while the empirical equation at ultimate bursting capacity of curved joints ignores the influence of joint curvature and load eccentricity or joint rotations. If a more demanding analysis is required, designers must resort to time-consuming FE analyses or costly full-scale joint tests, which can have an impact on the project budget.

The proposed analytical method enables the inexpensive computation of the bursting capacity and the maximum bursting force that an uncracked concrete joint can withstand for variable joint geometries and rotations, based on the input parameters of  $h$ ,  $h_j$ ,  $R$ ,  $E_c$  and  $f_{ct}$ .

Figures 2.9.a and 2.9.b show the normalised bursting capacity of flat and 3.5m radius curved joints for different  $f_{ct}$ . It is clear again that the curved joints outperform the flat joints regardless of  $f_{ct}$ . The differences in normalised bursting capacity curves for the  $f_{ct}$  examined are minor, with higher  $f_{ct}$  enabling a wider range of permissible rotations.

The analytical normalised capacity of curved joints with null rotations agrees with the Channel tunnel experimental data on bursting capacity at first visible crack of centrally loaded joints (see Figure



## 2.4. Bursting capacity

2.4.c), both in the order of 2. Given that the proposed solution reveals a drop in normalised capacity with joint rotations, the reinforcement ratio calculated with Eq. 2.9 may need to be increased for tunnels where large rotations are expected.

Figures 2.9.c and 2.9.d present the allowable bursting forces of uncracked concrete joints against the bursting forces developed for given values of  $N$ . If it is assumed that the total bursting capacity of reinforced joints is given by the contribution of both  $f_{ct}$  and reinforcement as suggested by Eq. 2.9, the analytical calculation of bursting forces can help designers to reduce the quantity of transverse reinforcement required, particularly in flat joints, based on estimated axial forces and joint rotations.

This analytical approach to the estimation of bursting capacity and forces can be a powerful design tool, as it can help designers to minimise or avoid the need for costly full-scale tests and FE analyses and identify opportunities to reduce or eliminate bursting reinforcement in accordance with the expected global behaviour of the tunnel. However, the method proposed here relies on Zhou's (2015) polynomial approximation to ILCs, which overestimates  $\sigma_{t,max}$  in eccentrically loaded joints. The development of more accurate analytical expressions for transverse stresses is needed and should be encouraged in future research.

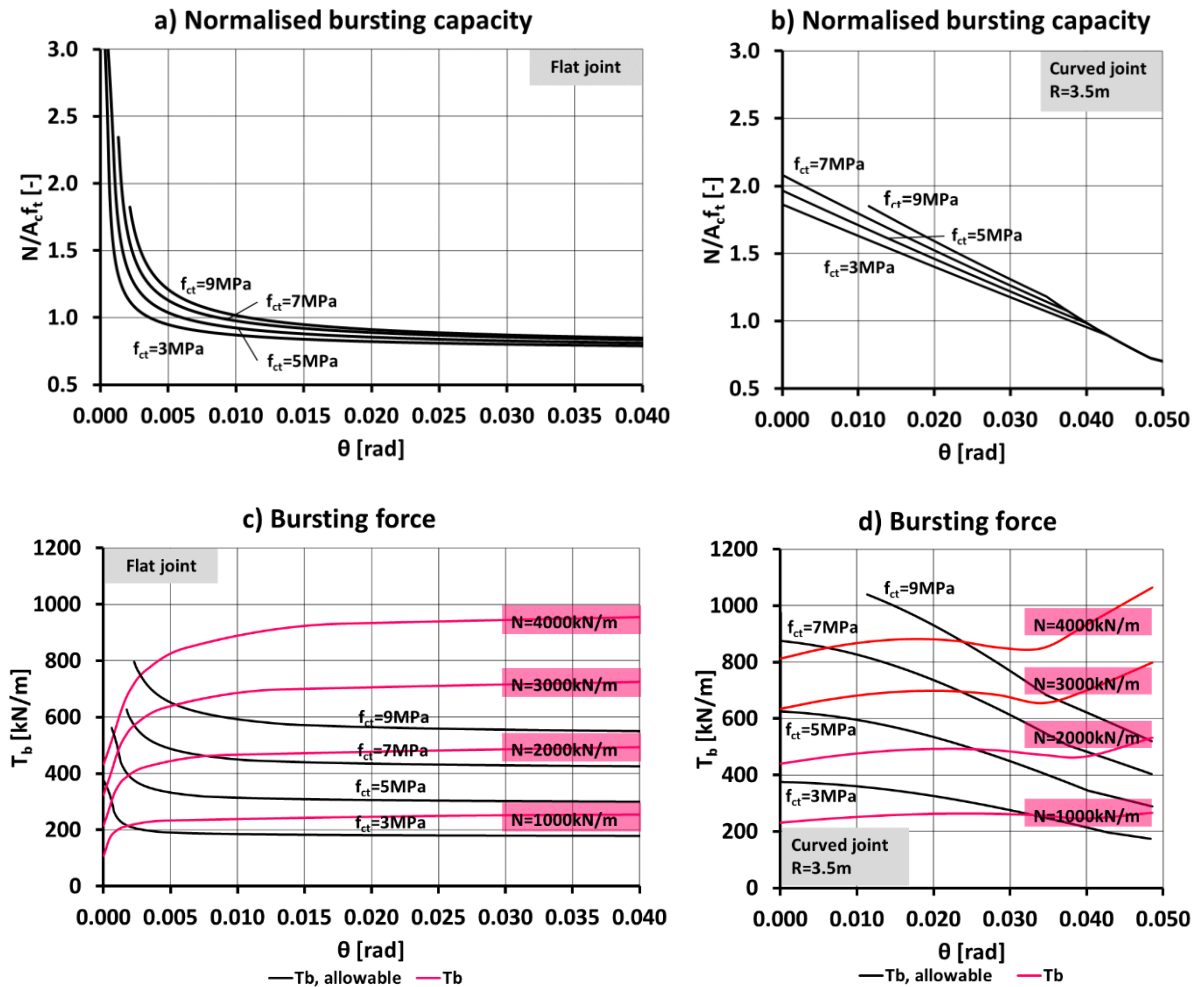


Figure 2.9: Comparison with current design methods

## 2.5. Gasket gap

The degree of watertightness required in a tunnel depends on its function and maintainability. Permissible leakage rates or tightness classes are a design requirement for CSLs. Concrete segments, gaskets and drainage systems must be designed accordingly (Haack, 1991). In transportation tunnels, some groundwater leakage is permitted although it can affect humidity in the tunnel, leading to either greater ventilation demands or condensation on the lining surface (BTS, 2004). Small groundwater leakages can cause structural damage in the long term via progressive degradation of the concrete quality (BTS, 2004). In more severe scenarios, the wash-through of soil particles could even initiate a tunnel collapse (Grose et al., 2005).

Compression gaskets are a prominent element in a CSL's watertight system. Their sealing capability against groundwater pressures depends on the applied compression and the quality of the gasket-gasket and gasket-concrete contact (Shalabi, 2001). The average gasket gap,  $\Delta$ , is the main parameter to measure the quality of gasket performance in aligned joints.

The gasket gap of rotated joints can be calculated with Eq. 2.14 and Eq. 2.15:

$$\Delta_{flat} = \theta \left( h_j + \frac{(h - h_j)}{2} - y_g - y_c \right) \quad (2.14)$$

$$\Delta_{curved} = -2 \left( \frac{h}{2} - y_g - e_c \right) \frac{e_c}{R} - \Delta_{comp} \quad (2.15)$$

where  $\Delta_{comp}$  is the decrement in the gasket gap of curved joints caused by the normal load  $N$  and  $R$  is the curved joint radius. The remaining parameters are illustrated in Figure 2.10;  $y_g$  is equal to 50mm.

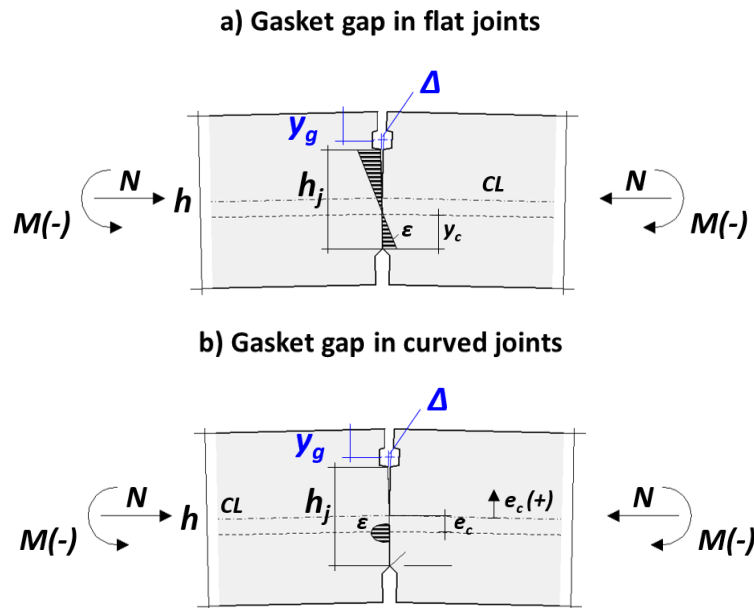


Figure 2.10: Gasket gap in rotated joints

## 2.6. Proposed method for joint design

The isolines in the NR space with equal  $\Delta$  are the gasket gap limits, as shown in Figure 2.11. In both joints, for a given  $\theta$ , an increase in the normal force reduces  $\Delta$ ; thus the isolines present a minor positive gradient in the NR space.

In curved joints,  $\Delta$  is the result of the local concrete deformation due to normal compression,  $\Delta_{comp}$ , and joint rotation. The calculation of  $\Delta_{comp}$ , assumes uniform contact stresses, which may underestimate concrete displacements and lead to conservative  $\Delta$ , particularly in lightly loaded joints.

Curved joints allow larger rotations for a given gasket gap limit because the distance between the gasket depth and the joint neutral axis is smaller in curved than in flat joints.

### 2.6. Proposed method for joint design

To date, the selection of joint curvatures in joint design has been based on general guidelines supported on past in situ performance and full-scale experiments (Baumann, 1992; BSI, 2004). The NR envelopes of bursting capacity and gasket gap limit can be used as a rational method where the joint design is integrated with the global CSL performance during and after construction. Two examples of how to use the proposed method are presented here:

**a) *Selection of joint geometry based on global structural analysis:***

Figure 2.11. shows the NR diagrams of CTT joints with variable curvature: flat, 10m and 3.5m radius curved joints. The most onerous combination of  $N$  and  $\theta$  obtained from a long term analysis of CSL behaviour is also plotted in Figures 2.11.a and 2.11.c (see chapter 4).

The graphs evidence that a flat joint requires a  $f_{cr}=5\text{MPa}$  to prevent the formation of bursting cracks while gaskets with  $\Delta<1\text{mm}$  need to meet the watertightness criteria. A 3.5m curved joint with  $f_{cr}=3\text{MPa}$  performs satisfactorily against bursting, despite undergoing larger rotations under the same long term tunnel conditions. Both technical solutions are viable; the option selection could be made on the basis of other criteria such as ring misalignment, cost or environmental impact.

Figure 2.11.b illustrates that the benefits of curved joints disappear with greater radii.

**b) *Selection of joint geometry including construction effects on CSL performance:***

The total joint rotations in a built tunnel comprise those originated during construction. In the CTT tunnel, the  $\theta$  associated with tunnelling reached a peak of about 0.005rad, although the initial  $\theta$  due to ring erection was excluded from the measurements (see chapter 5). If these rotations were added to those predicted by the long term analysis, then the required  $f_{cr}$  would not change but the maximum  $\Delta$  with acceptable watertightness would increase to  $1\text{mm}<\Delta<2\text{mm}$  for both joints.

## 2.6. Proposed method for joint design

---

The proposed method can cope with initial misalignments by amending the joint depth parameters appropriately. However, the effect of random in-plane contact imperfections resulting from the ring erection and sequential loading near the tail skin cannot be accounted for.

## 2.6. Proposed method for joint design

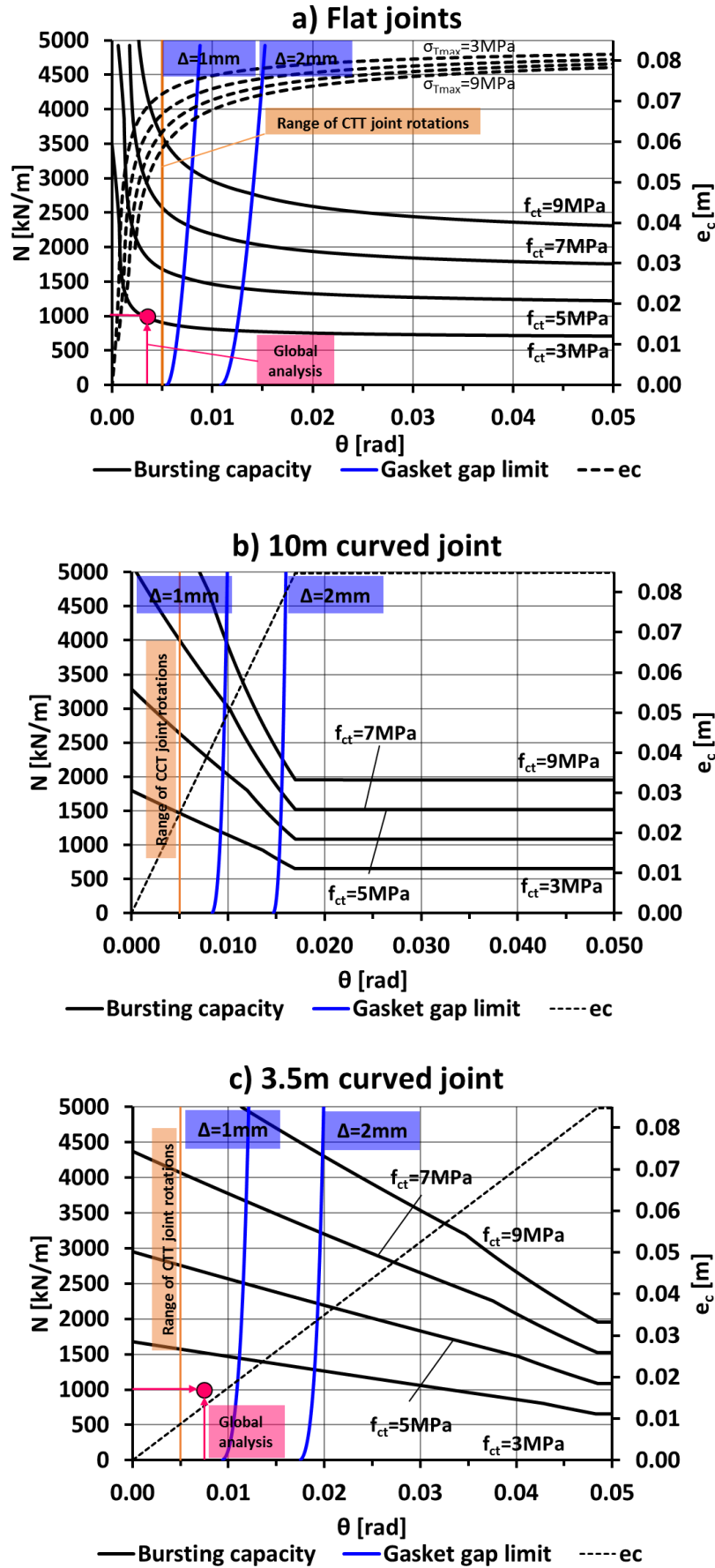


Figure 2.11: NR diagrams for different joint geometries

### 2.7. In-plane contact imperfections

When two segments with an in-plane angularity,  $\alpha_j$ , are externally loaded in hoop direction, a moment is induced at the contact between segments due to stress eccentricity. Equilibrium is reached through segment deformation and lateral confinement activated by segment rotation, which progressively increases the contact length between joint faces as the hoop load is applied (Cavalaro, 2009).

The resilience of longitudinal joint geometries to  $\alpha_j$  is investigated here through FEA. Four different joint geometries are considered, i.e. flat and curved joints combined with straight or rounded shapes along the segment width (see Figure 2.12). In-plane angularities of  $\alpha_j=0.0^\circ$  and  $\alpha_j=0.4^\circ$  are examined.

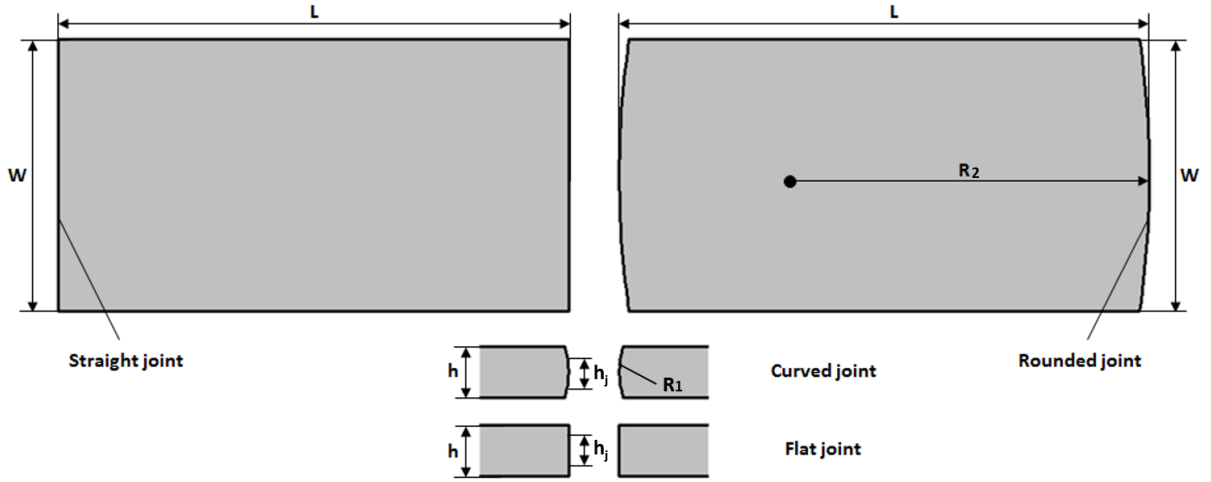


Figure 2.12: Joint geometry configurations

The resilience to  $\alpha_j$  of each configuration is evaluated on the basis of the critical hoop load that segments can sustain without the joint experiencing bursting or shear failure. Bursting failure is assumed to occur at first cracking when  $f_{ct}$  is reached to enable the comparison of FE and analytical results.

Figure 2.13 illustrates the general arrangement of the numerical models with two straight segments and contact interactions at their longitudinal joint. One segment is fixed at one end in the hoop direction and the other is free to rotate in all directions. Cavalaro (2009) demonstrated that in-plane rotations and contact lengths are not influenced significantly by variations in lateral confinement stiffness ranging from  $10^2$  to  $10^{10}$  N/mm<sup>3</sup>. In this model, the lateral restraint is provided by half segments laterally fixed at opposite sides. The contact between segments and confining units is made through packers. For simplicity, the rounded curved joints are formed by segments with one curvature at alternative axis,  $y$  or  $z$ , that is twice the nominal value. The solid elements are meshed with hexahedral elements of first order with reduced integration.

## 2.7. In-plane contact imperfections

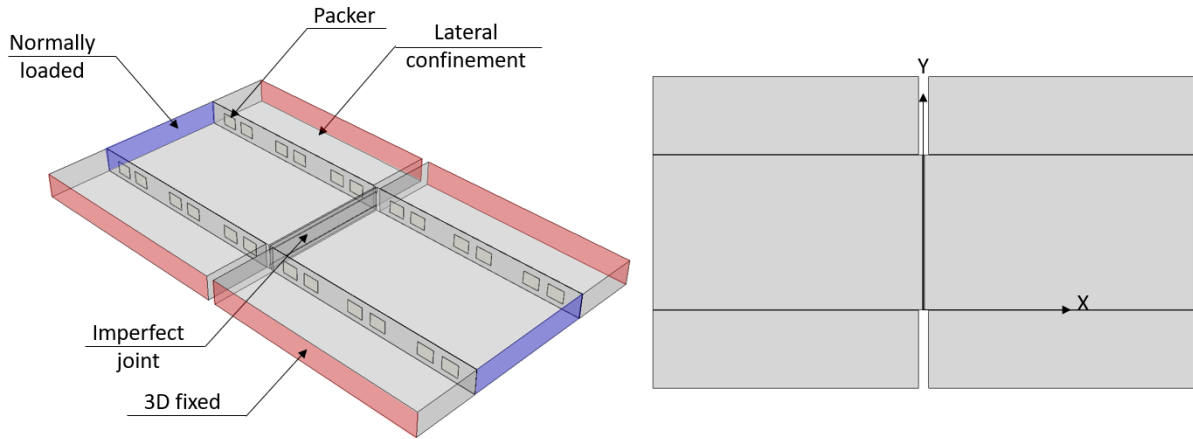


Figure 2.13: FE model for the study of 3D imperfections

### 2.7.1. Input data

The input parameters are listed in Table 2.2. The curvature of rounded joints was selected so that the maximum initial clearance between bearing surfaces in perfect joints would not undermine gasket confinement. Records on British expanded linings designed in the 70's with 600mm wide segments evidenced that  $R_2$  ranged between 10m and 20m in doubly convex-convex joints (Craig and Muir-Wood, 1978), i.e. much smaller than the  $R_2=240$ m adopted here.

Given that the strain softening of confined concrete contributes to a wider contact area between segments, the concrete was simulated with a linear elastic perfectly plastic model with the Mohr-Coulomb failure criterion (Chen, 1982) defined by the concrete internal friction angle,  $\varphi$ , of  $37^\circ$  and a cohesion  $c$  derived from:

$$f'_c = \frac{2c \cos \varphi}{1 - \sin \varphi} \quad (2.16)$$

where  $f'_c$  is the uniaxial compressive cylinder strength of C55/67 concrete. The Young's modulus prior to plastic yielding was calculated in accordance with the EC2 guidance for elastoplastic concrete with a bilinear stress-strain relationship (BSI, 2010). The hoop loads applied in the models were limited to 4000kN/m.

## 2.7. In-plane contact imperfections

Table 2.2: Input parameters for joint models

Input parameters		
Name	Symbol	Value
Geometry		
Segment length [m]	$L$	2.784
Segment width [m]	$W$	1.6
Lining depth [m]	$h$	0.3
Joint depth [m]	$h_j$	0.17
Radius of curved joint [m]	$R_1$	3.5m
Radius or rounded segment [m]	$R_2$	240m (120m in model)
Packer thickness [m]	$t_p$	3mm (6mm in model)
Concrete–Mohr Coulomb model		
Young's modulus [GPa]	$E_c$	30.5
Poisson ratio [-]	$\nu$	0.167
Cohesion [MPa]	$c$	13.75
Angle of friction [°]	$\phi$	37°
Maximum bursting stress [MPa]	$\sigma_{t,max}$	3
Packer–von Mises model		
Young's modulus [GPa]	$E_p$	13.3
Yield stress [MPa]	$f_p$	8.5

### 2.7.2. Results

Table 2.3 summarises the critical loads at which each failure mode was initiated for each case. There is good agreement between the numerical and analytical bursting capacity of straight joints centrally loaded.

The bursting capacity and critical load associated with shearing of straight joints is dramatically reduced at  $\alpha_j=0.4^\circ$  in both joint types. The capacity loss, however, is greater than Cavalaro's prediction for flat straight joints mainly because this study omits the concrete rebar and uses a different constitutive model. The spalling stresses at the bearing surfaces of curved joints exceed  $f_{ct}$  earlier than the bursting stresses.

The rounded joints are more resilient to  $\alpha_j$ . No shear failure is experienced by imperfect flat joints while the curved joints exhibit only a modest improvement in shear capacity. The rounded flat joints retain 55% of the bursting capacity at  $\alpha_j=0.4^\circ$  as opposed to a 17% residual capacity of the straight flat joints. The bursting capacity of rounded curved joints is only enhanced at zero angularity by a partially plasticized contact area (see Figure 2.14).

Overall, the rounded flat joints exhibit the best resilience against high  $\alpha_j$ , followed by joints with single curvature. However, if the rounded flat joints were also rotated by certain  $\theta$ , it is likely that their resilience would be deteriorated to the levels of rounded curved joints in the best case.



## 2.7. In-plane contact imperfections

Table 2.3: Critical loads of joints with in-plane angularities

Joint geometry	Critical loads [kN/m]			
	$\alpha_j=0.0^\circ$		$\alpha_j=0.4^\circ$	
	Shear failure	Bursting failure at $\sigma_{Tmax}=3\text{MPa}$	Shear failure	Bursting failure at $\sigma_{Tmax}=3\text{MPa}$
Flat	>4000	3500	52	684
Curved	1795	1584	52	156
Flat and Round	>4000	2137	>4000	1926
Curved and Round	3600	2237	655	156

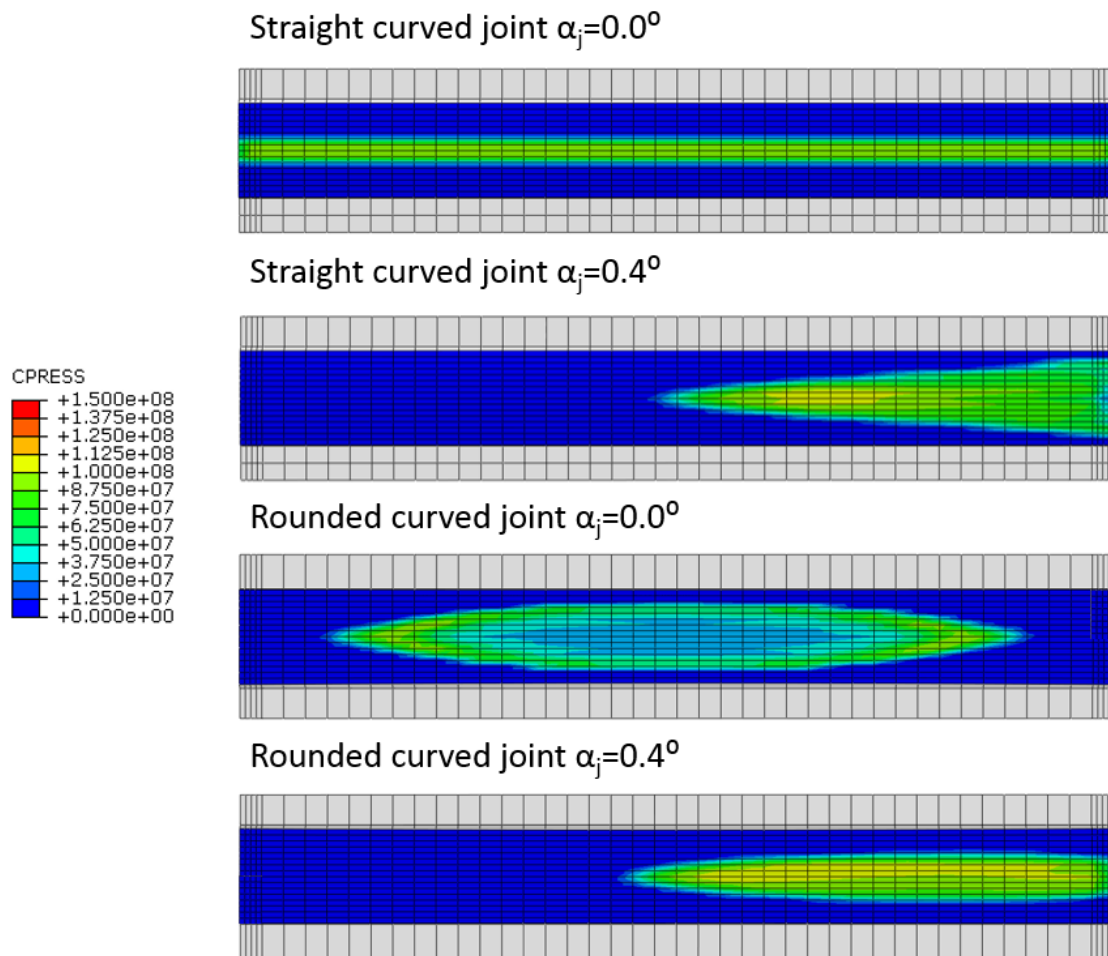


Figure 2.14: Contact patches in curved joints at  $N=4000\text{kN/m}$ , pressures in Pa

## 2.8. Conclusions

Nowadays, the selection of longitudinal joint curvatures is based on generic published guidelines supported on past in situ performance and experimental evidence (Baumann, 1992; BSI, 2004). A new analytical method for joint design that predicts joint performance against bursting and watertightness for variable rotations was proposed in this chapter. This inexpensive method enables tunnel designers to make rational decisions on the geometry of longitudinal joints by inserting the results of global CSL structural analysis on the proposed NR diagrams. When more than one option is possible, then the evaluation of other criteria such as cost or the impact on the environment can be pondered.

The analytical estimation of bursting capacity and forces at imminent cracking can be a powerful tool in the preliminary stages of joint design, as it can help designers to minimise or avoid the need for costly full-scale tests and FE analyses and identify opportunities to reduce or eliminate bursting reinforcement in accordance with the expected global behaviour of the tunnel. However, the method proposed here relies on Zhou's (2015) polynomial approximation to ILCs, which overestimates  $\sigma_{t,max}$  in eccentrically loaded joints. The development of more accurate analytical expressions for transverse stresses is needed and should be encouraged in future research.

The bursting capacity before cracking depends mainly on the joint curvature and  $f_{ct}$ . Curved joints with radius in the order of 3.5m tolerate larger rotations than flat joints. The splitting cracks in flat joints tend to develop near the joint edge, which can trigger rebar corrosion and loss of gasket lateral confinement. Conversely, the splitting cracks of curved joints would tend to be close to the joint mid depth. High strength concretes, with generally superior  $f_{ct}$ , ensure a greater bursting capacity before cracking.

The influence of joint geometry on the resilience to in-plane imperfections was briefly investigated through flat and curved joints with either a straight or rounded extrusion. The straight joints with high in-plane angularity,  $\alpha_j=0.4^\circ$ , failed in shear when subjected to low hoop forces, regardless of the joint out-of-plane curvature. Overall, the rounded flat joints exhibited the best resilience to high  $\alpha_j$ , followed by joints with one single curvature. However, in rotated rounded flat joints, the critical loads may be reduced again to low values.

## Chapter 3

# The role of spear bolts in gasketed joints

### 3.1. Introduction

Mechanical connections in British grouted smooth bore CSLs were first introduced at a time when ring assembly was performed manually (Harding et al., 2014) to provide ring self-support in tunnels subjected to adverse ground conditions (Winterton, 1994). Gaskets were first deployed in bolted CSLs at a later time to replace the traditional sealing methods that contained asbestos (Winterton, 1994). Since then, gasketed CSL rings have been consistently equipped with at least temporary mechanical connectors (Winterton, 1994),

Nowadays, spear bolts are installed at longitudinal joints during ring erection and removed once the effects of TBM tunnelling on the lining response are expected to have dissipated, i.e. about ten rings behind the TBM, even if their function during construction is not clear to neither designers nor manufacturers (Harding et al., 2014). The temporary use of spear bolts, however, increases material and manpower costs and entails the risk of localised cracking of concrete segments near the bolt pockets (Chen and Mo, 2009).

Nevertheless, there appears to be a lack of detailed studies on the role of spear bolts during construction. The BTS guidance on tunnel design conveys the importance of fixings between segments in ensuring adequate gasket performance by closing or holding the joint together against gasket forces without specifying fixing types (BTS, 2004). Herrenknecht and Bappler (2003) stated two functions of temporary bolts at longitudinal joints: ring build accuracy and preserving longitudinal gasket compression prior to grouting. Harding et al. (2014) examined qualitatively the function of bolts without long term moment capacity, i.e. spear and curved bolts. Their limited rotational resistance and inability to contribute to shear resistance in a serviceable context was evidenced: the former due to their joint position close to mid depth; the latter caused by the clearance between the bolt shaft and the segment body. Harding et al. (2014) concluded that perhaps the only function of such bolts in normal conditions was “to hold the joint closed under gasket loads”; in the accidental case of TBM rams failure, bolts might also “hold segments of partially built rings together”.

With the advent of modern dowelled connectors, which can improve ring build accuracy (Kolic et al., 2000) and connectivity between adjacent rings, it becomes even more necessary to investigate the role of spear bolts in current lining configurations. Apart from shear resistance in ultimate limit state (ULS) scenarios (Harding et al., 2014), the possible mechanisms of interaction between joint and bolt are

through rotational resistance against eccentric loading, i.e. gasket loads or segment moments, and tensile resistance against pure tension. The former is important to examine the function of holding the gaskets closed at joints with low or null hoop compression. The latter may be relevant in retaining the shape of poorly compressed rings and limiting contact deficiencies.

In this chapter, rotational models of flat and curved joints fitted with spear bolts and one-gasket sealing are proposed. The approach to spear bolt modelling is validated through published test results on full-scale flat joints with spear bolts (Hordijk and Gijsbers, 1996) and FEA. These models, together with complementary calculations, are then used to clarify the role of spear bolts in retaining gasket compression and enhancing ring build quality. Finally, their ability to mitigate concrete damage during construction is reviewed with the aid of 3D FE simulations. All the analyses are based on the CTT CSL (see Figure 1.1).

### 3.2. Rotational models

The rotational models for gasketed bolted joints are computed in accordance with ITA guidelines (ITA, 2000) and published two-dimensional mechanical models that successfully predicted experimental joint behaviour. Ding et al. (2013) developed an analytical solution specific to bolted flat joints provided with cast iron panels and moment-resistant bolts for a water conveyance tunnel. Li et al. (2015) proposed a joint model to investigate ULS behaviour of flat gasketed joints equipped with moment-resistant bolts. The same basic assumptions considered by the authors above apply to the analytical solutions presented here:

1. Deformations and joint rotations are very small;
2. Normal strains along the rotated joint are linear (only valid for flat joints);
3. Bolts cannot bear compressive forces and concrete resists compressive stresses only.

#### 3.2.1. Flat joints

The flat joint model copes with linear and bilinear stress distributions at the concrete faces in contact. Local concrete displacements are calculated with Eq. 2.3. The rotational model is based on the Janssen model, i.e.  $l_{cc}=h_j/2$ , and incorporates concrete plasticity (Blom, 2002). Thus, concrete stresses at the joint faces are:

$$\sigma_c = \begin{cases} E_c \varepsilon_c & \varepsilon_c \leq \varepsilon_{c0} \\ f_c & \varepsilon_{c0} < \varepsilon_c \leq \varepsilon_{cu} \end{cases} \quad (3.1)$$

where  $\varepsilon_{c0}$  is the yielding compressive strain and  $\varepsilon_{cu}$  the ultimate limit strain of concrete (see Figure 3.1).

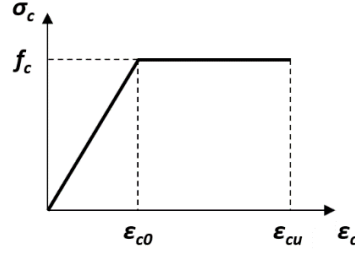


Figure 3.1: Concrete material model for rotational models

The gasket action is simulated as a compression spring with variable stiffness resulting from the polynomial interpolation of the manufacturer's gasket force-gap curve. As the gasket deployed in the CTT is unknown to the author, the Phoenix M 385 41a type "Tokio" (Phoenix, 2014) gasket force-gap diagram is adopted here and is approximated with Eq. 3.2 (see Figure 3.2).

$$F_g = \begin{cases} 0.048\Delta^4 - 0.854\Delta^3 + 5.853\Delta^2 - 20.907\Delta + 44.53 & 0 \leq \Delta \leq 7\text{mm} \\ -0.077\Delta^3 + 1.863\Delta^2 - 14.838\Delta + 46.573 & 7\text{mm} < \Delta \leq 13\text{mm} \end{cases} \quad (3.2)$$

where  $F_g$  is the gasket force in kN/m and  $\Delta$  is the average gasket gap in mm.

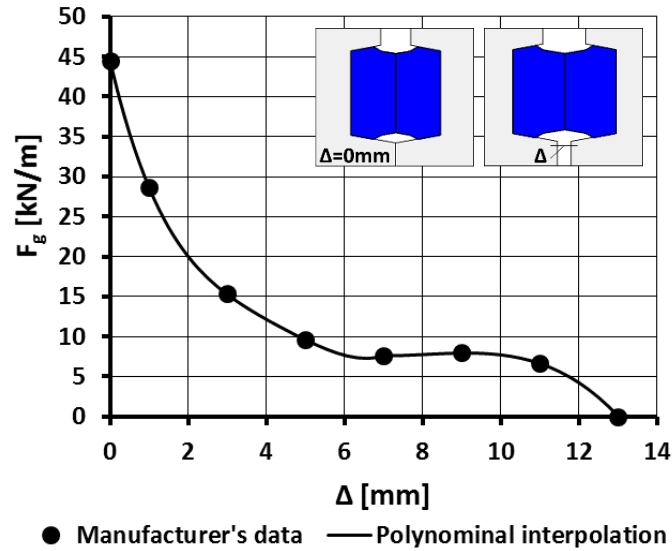


Figure 3.2: Gasket force-gap diagram

Bolts are modelled via a tension spring normal to the joint and located at a depth  $y_b$ , i.e. the depth at which the spear bolt crosses the joint. Pull-out tests of spear bolt assemblies evidenced that failure in tension occurs due to thread-stripping (Harding et al., 2014) before reaching bolt yielding (Anixter, 2014). The spring representing the bolt system is linear elastic, with a stiffness derived from pull-out tests specific to the CTT bolts. Then, the bolt force is:

$$F_b = k_b \Delta L_b = n_b \cdot \min\left(\frac{E_b A_b}{L_b}, k_{Man}\right) \cdot \cos(\alpha_b) \Delta L_b \quad (3.3)$$

where  $F_b$  is the bolt force,  $n_b$  is the number of bolts per metre,  $k_b$  is the bolt system stiffness,  $\Delta L_b$  the extension of the bolt system,  $E_b$ , the bolt Young's modulus,  $A_b$  the bolt cross-sectional area,  $L_b$ , the bolt length,  $k_{Man}$  the manufacturer's linear stiffness and  $\alpha_b$  the bolt angle.

The MR curves are obtained by solving the equilibrium equations of the joint section, ensuring compatibility of deformations (see Figure 3.3):

$$N = F_c + F_g - F_b \quad (3.4)$$

$$M = F_c e_c + F_g \left( \frac{h}{2} - y_g \right) + F_b \left( \frac{h}{2} - y_b \right) \quad (3.5)$$

where  $F_c$  is the concrete compressive force,  $e_c$  is the eccentricity of the concrete force and  $y_g$  the average depth of the gasket (see Figure 3.33).

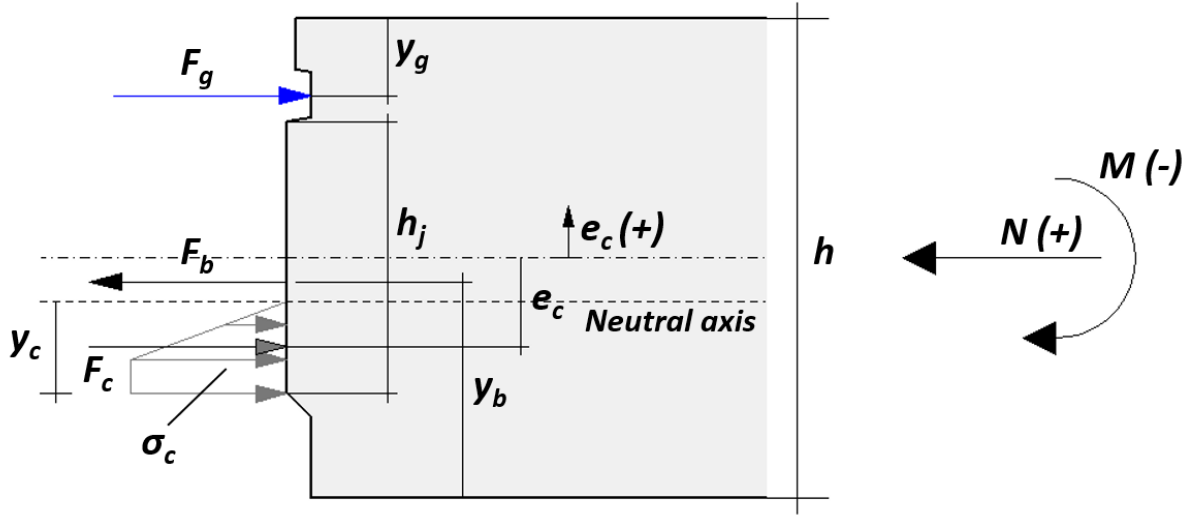


Figure 3.3: Force diagram for flat joints

Unlike in cast iron linings, the contribution of bolt bending to moment capacity,  $\Delta M_{b,bend}$ , computed with Eq. 3.6 is negligible given the usual slenderness of spear bolts, their large spacing and the possible deformation of the plastic socket.

$$\Delta M_{b,bend} = \frac{E_b I_b}{L_b} \theta = \frac{E_b n_b \pi R_b^4}{L_b 4} \theta \quad (3.6)$$

where  $I_b$  is the bolt moment of inertia and  $R_b$  the bolt cross-sectional radius. Bolt pre-tightening and 2D imperfections, i.e. initial misalignment and rotations, can be included in the model, the latter by modifying the input geometry and loosening the bolt accordingly.

### 3.2.2. Curved joints

Like in the joints without gaskets and bolts, hereafter named bare joints, the cross-sectional displacements are the result of local concrete deformations and joint rotations (see chapter 2). Bolt and

gasket effects are considered through Eq.3.1 to Eq.3.5 and the compatibility of deformations between gasket, bolt and the contact strip (see Figure 3.4). For example, in Figure 3.4  $\Delta$  can be calculated as:

$$\Delta = \Delta_{\theta} - \Delta_{comp} = -2 \left( \frac{h}{2} - y_g - e_c \right) \frac{e_c}{R} - \Delta_{comp} \quad (3.7)$$

where  $\Delta_{\theta}$  and  $\Delta_{comp}$  are the gasket gap components caused by the joint rotation and axial compression respectively.  $\Delta_{comp}$  can be computed from  $N$  with the expression of  $a_{eq}$  proposed in Eq. 2.13.

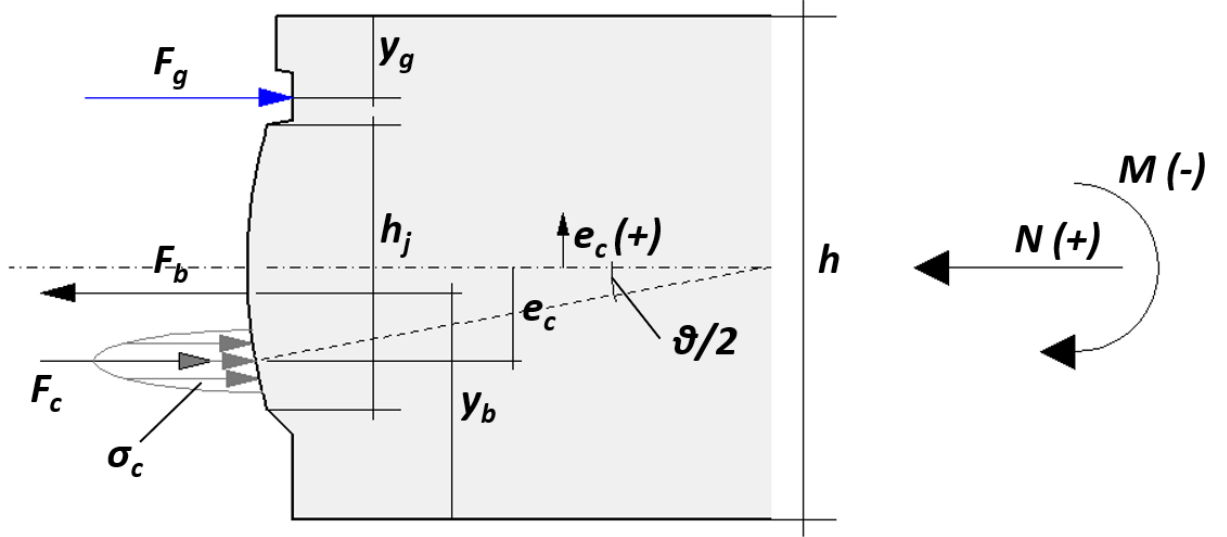


Figure 3.4: Force diagram for curved joints

### 3.2.3. Validation of mechanical models

The validation of bolt and gasket simulation techniques is conducted on flat joints only, given that both joint geometries share the same modelling approach to these two features and that the experimental test results on spear bolted joints were only available for flat geometries.

#### 3.2.3.1. Validation against full-scale tests

The full-scale joint tests performed by Hordijk and Gijsbers (1996) revealed that, overall, “the effect of spear bolts on MR curves is not significant and decreases with an increase in axial force”. Figure 3.5 illustrates the experimental MR curves at various normal loads and the analytical solutions obtained from the geometry and bolt pre-tightening of the tested joints. The stiffness of the tested bolt system was not reported and thus it is assumed equal to that of the CTT bolts (see Table 3.1) despite the bolt diameter being 14mm rather than 20mm. However, given that the bolt system stiffness is determined by the bolt interface with the plastic socket (Anixter, 2014), it is reasonable to assume that it may be of similar magnitude in both cases. The scatter in experimental data and the bolt contribution in positive and negative bending are also included in the graphs.

The dispersion in the experimental data of bare joints has a more prominent role in lightly loaded joints, up to 25% of the moment capacity at 200kN/m as opposed to roughly 10% at 2300kN/m.

Hordijk and Gijbsers (1996) associated the data scatter with initial contact imperfections at joints. The bolt contribution to dispersion is very small at 200kN/m, but becomes greater with higher normal loads.

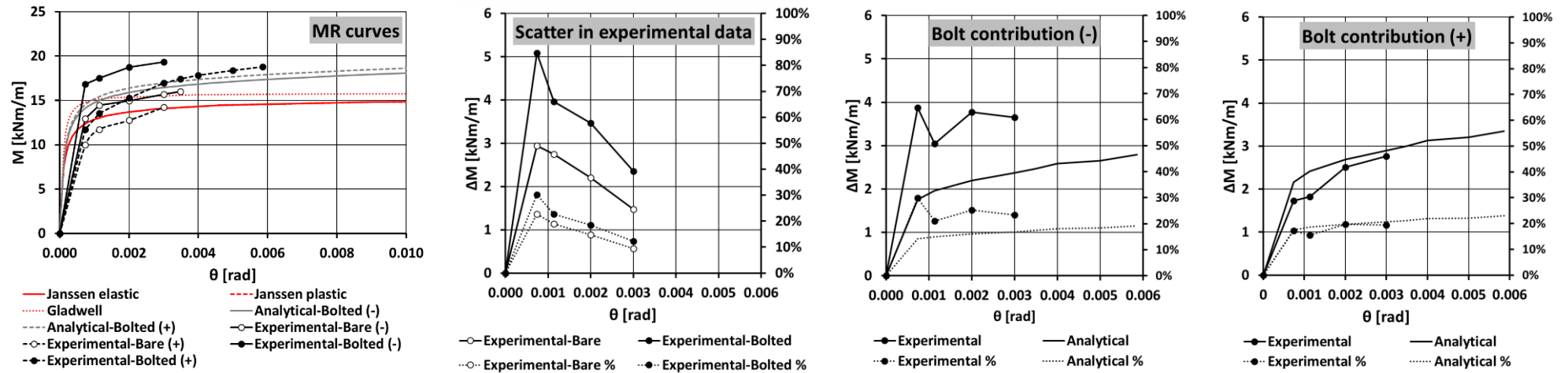
At  $N=200\text{kN/m}$ , there is a good correlation between the bolt contribution of the test results and the analytical predictions, particularly at positive bending. The greater discrepancies at negative bending are in the order of 5% of the total moment capacity. Even changes in the trend of bolt contribution with joint rotations are well captured by the rotational models.

At higher normal forces, the experimental and analytical results do not agree well. However, the bolt contribution is small and thus the differences oscillate by about 10% of the total moment capacity, that is, in the order of the data scattering found in bolted joints.

Overall, the experimental data suggested that the bolt contribution to moment capacity, which is mostly provided by the initial pre-tightening (see section 3.3.1), is only relevant at low normal forces and may be sensitive not only to contact deficiencies but also to the relaxation of bolt pre-tightening with loading cycles.



a)  $N=200\text{kN/m}$



b)  $N=900\text{kN/m}$

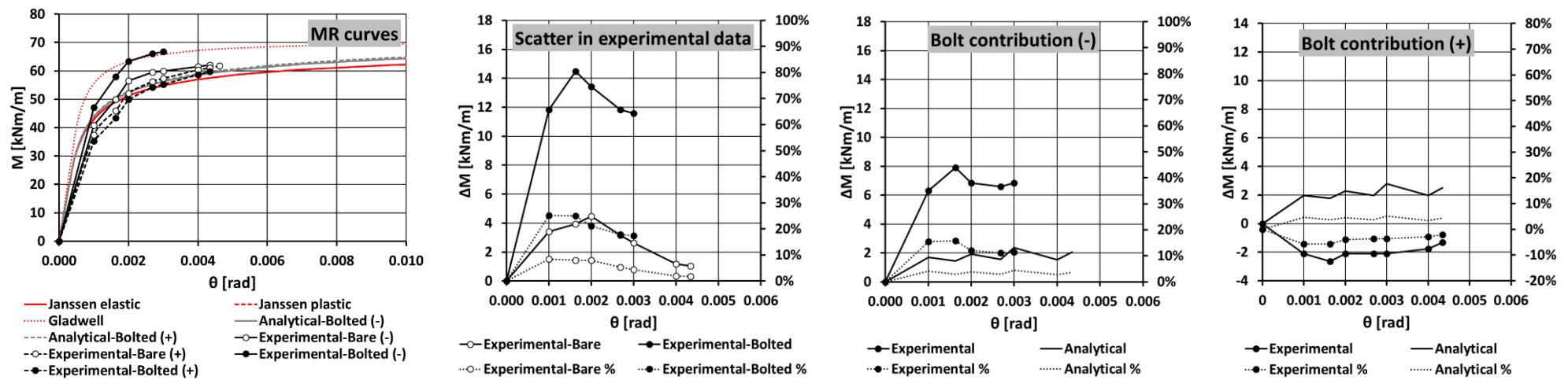
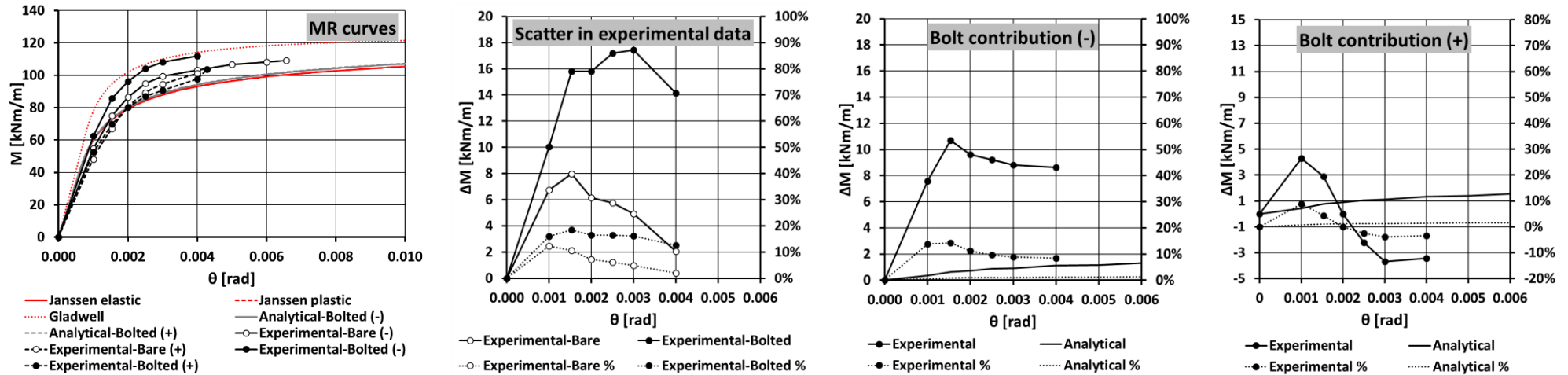


Figure 3.5: Experimental and analytical data of joints

c)=N=1600kN/m



d)=N=2300kN/m

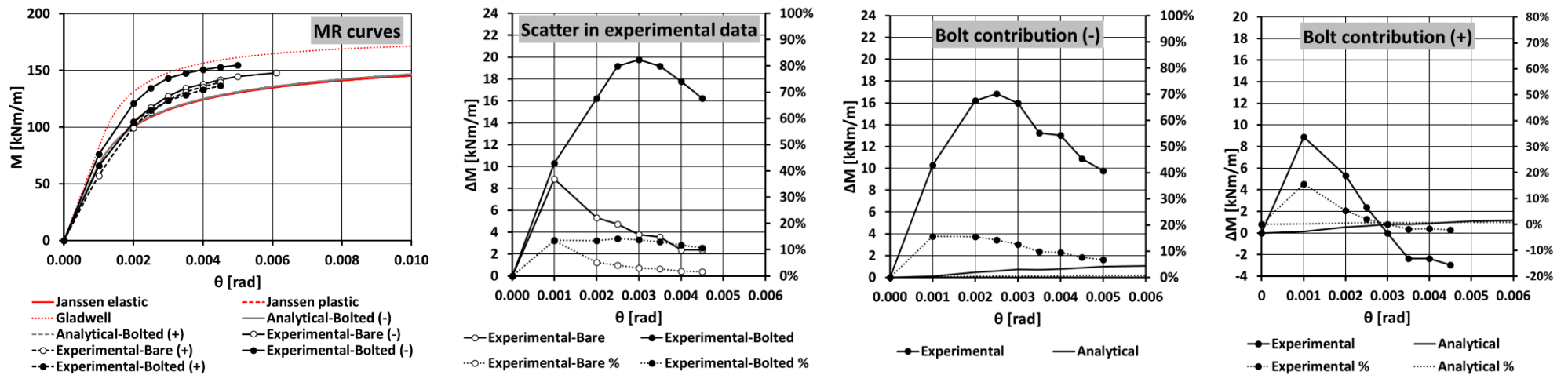


Figure 3.5 (continued)

### 3.2.3.2. Validation against FE analysis

The FE modelling of flat joints implies an overestimation of moment capacity caused by stress concentration at the edges of closed joints (see chapter 2). However, the rotational model can be validated against 2D FEA if the joint is open prior to the application of an external moment, which entails that  $N$  must be not greater than the maximum gasket force. The flat joint geometry was summarised in Table 2.1 and spear bolt input parameters are listed in Table 3.1. The bolts were modelled by a single tension spring with  $k_{Man}$  system stiffness and no pre-tightening.

**Table 3.1: Spear bolt input parameters**

Description	Value
Average gasket depth, $y_g$ [mm]	50
Bolt depth, $y_b$ [mm]	140
Bolting system stiffness, $k_{Man}$ [kN/mm/bolt]	9.184 (Anixter, 2014)
Bolt angle, $\alpha_b$ [°]	28°
Number of bolts/metre, $n_b$ [-]	1.25

Figure 3.6 evidences an excellent agreement between analytical and numerical models in both bolted and boltless joints. Unfortunately, as far as the author knows, there are no experimental MR curves of bolted and boltless joints subjected to normal loads smaller than maximum gasket forces.

At null rotation, the moment is equal to that exerted by the fully closed compression gasket, i.e. 4.453kNm/m. At negative rotations, the eccentric force of the compression gasket opens the joint until the compressive stress developed at the contact strip, plus the bolt tension in bolted joints, can restore equilibrium. At such small normal loads, the moment transfer is palpably affected by the reduction in gasket force. At pure compression, with  $M=0$ kNm/m, the flat joint experiences a rotation in the order of -0.01rad, slightly smaller in the bolted joint, and the gasket gap is about 2mm.

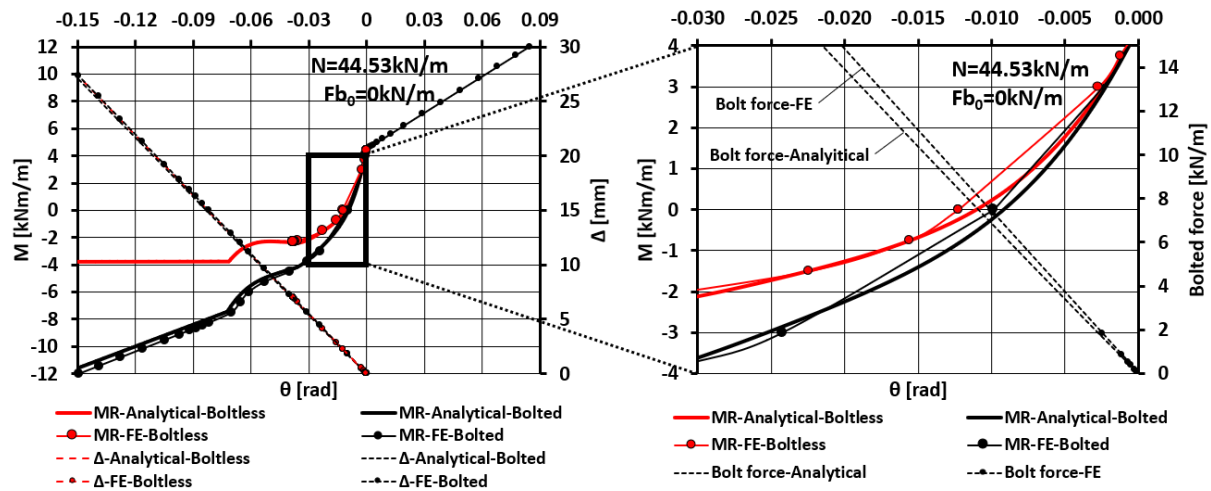


**Figure 3.6: Validation of analytical model against 2D FE models.**

The use of appropriate techniques for bolt modelling in lining joints has been widely debated. Li (2014) investigated several configurations of group springs in 3D models of cast iron joints to capture the enhancement in  $K_\theta$  provided by bolts. Li (2014) found that a group of nine springs equally distributed in a rectangular grid circumscribed to the bolt cross section was a good compromise between accuracy and numerical efficiency. Wang et al. (2012) conducted a study on bolt modelling techniques for concrete joints with moment-resistant bolts subjected to bending. The bolts were modelled in three different ways: solid elements, a single spring and the group spring recommended by Li (2014). It was concluded that the single spring substantially underestimated the bolt contribution to moment capacity, whilst the group spring yielded MR curves similar to those of continuum bolts.

Consequently, the 2D FE models used in the validation of the analytical solutions must be checked against solid models of gasketed flat joints with single and group spring bolts. Figure 3.7 compares the MR curves of boltless and bolted joints in positive and negative bending. The usual mismatch between analytical and FE solutions caused by edge effects is visible, particularly at negative bending. However, the post-linear gradients agree in both bending directions. The effect of spear, or soft, bolts is almost negligible and there is practically no difference in behaviour between 2D (1 and 3 springs) and 3D (3 and 9 springs) FE models, which contradicts the findings from previous authors.

With moment-resistant or stiff bolt systems, the bolt contribution to bending capacity is obvious in analytical and 2D FE (1 and 3 spring) solutions. In 3D simulations, single spring models cannot capture the bolt effect, which is, this time, consistent with published research. Group spring models, however, can simulate satisfactorily bolt contribution up to rotations of 0.002rad in positive bending and 0.010rad in negative bending. Beyond these values, the discrepancy between 2D and 3D simulations increases. It could be inferred that the difficulty in capturing bolt effects in 3D joint models with spring techniques resides in the connectivity between solid elements and springs. When this connectivity improves through group spring enhancement, 3D models tend to resemble better the 2D solutions.

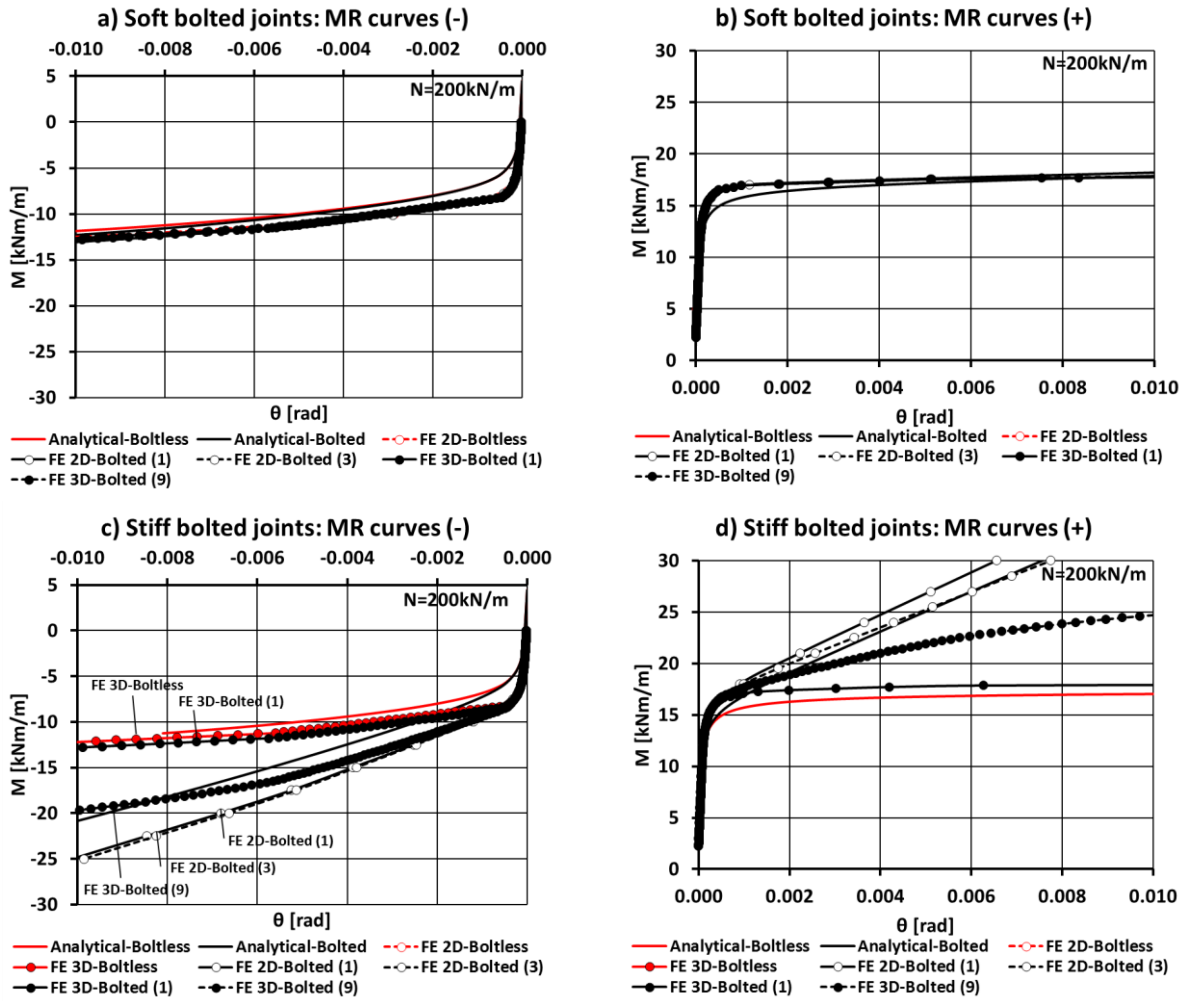


Figure 3.7: FE and analytical MR curves for gasketed joints with soft and stiff bolts

### 3.3. Discussion

The role of spear bolts has been investigated with regards to (i) contribution to joint moment capacity; (ii) preservation of gasket compression; (iii) ring build quality; and (iv) ring shape retention during construction. The CTT joint is taken as the reference joint. Input parameters are given in Table 2.2, Table 3.1 and  $E_c=38\text{GPa}$ .

#### 3.3.1. Moment capacity and gasket compression

##### 3.3.1.1. Rotational behaviour of joints

The analytical models reveal that, at normal forces greater than the maximum gasket force, there is contact between concrete faces for all equilibrium states, and the restoring mechanism against gasket force is realised through rotational resistance (see Figure 3.8.a). When the normal force is lower than the maximum gasket compression (see Figure 3.8.b), there are two modes of equilibrium in opened joints. In negative bending, the equilibrium states are again reached by rotational resistance. In positive bending, there is no contact between joint faces and the bolt and gasket are the only active

elements in the system. Bolt tension is the only restoring force that can compensate gasket force, leading to one single equilibrium state at a small rotation.

The joints that are subjected to normal loads greater than the maximum gasket force are herein called “closed” joints and those under smaller loads are named “open” joints. This terminology is not entirely correct as “closed” joints can be open. “Open” joints, however, cannot be closed.

#### *a) Flat joints*

Figure 3.9.a evidences that the contribution of bolts without pre-tightening to the moment capacity of “closed” joints is negligible. In “open” joints, the bolt reduces the  $\theta$  required for equilibrium: for example, at  $N=20\text{kN/m}$  and  $M=0\text{kNm/m}$  (see Figure 3.8.b),  $\theta$  and  $\Delta$  decrease from  $-0.028\text{rad}$  and  $5\text{mm}$  to  $-0.018\text{rad}$  and  $3.3\text{mm}$  respectively. The lower rotation limit,  $\theta_{lim}$ , also drops from  $-0.011\text{rad}$  to  $-0.007\text{rad}$ .

Bolt pre-tightening improves the effectiveness of bolt resistance against joint rotations in both cases. Hordijk and Gijsbers (1996) applied in their tests pre-tightening forces comprised between  $20\text{kN/bolt}$  and  $30\text{kN/bolt}$ , noting that larger pre-tightening forces were not practicable. Figures 3.8.c and 3.8.d present the MR curves of “closed” and “open” joints with  $30\text{kN/m}$  of bolt pre-tightening. The relaxation of pre-tightened bolts with time is not considered in steel bolts with a temporary function. The moment capacity of “closed” joints subjected to low normal forces is increased with pre-tightened bolts, e.g.  $22.7\%$  at  $-0.002\text{rad}$  and  $200\text{kN/m}$ , although the total capacity remains small, about  $10\text{kNm/m}$ . In “open” joints,  $\theta$  and  $\Delta$  at  $20\text{kN/m}$  pure compression are further reduced to  $-0.0085\text{rad}$  and  $1.6\text{mm}$  respectively, whilst  $\theta_{lim}$  lowers to less than  $-0.001\text{rad}$ . With null normal forces and moments (see Figures 3.8.e and 3.8.f), bolt pre-tightening halves  $\theta$  and  $\Delta$ , resulting in  $-0.015\text{rad}$  and  $2.7\text{mm}$  respectively.

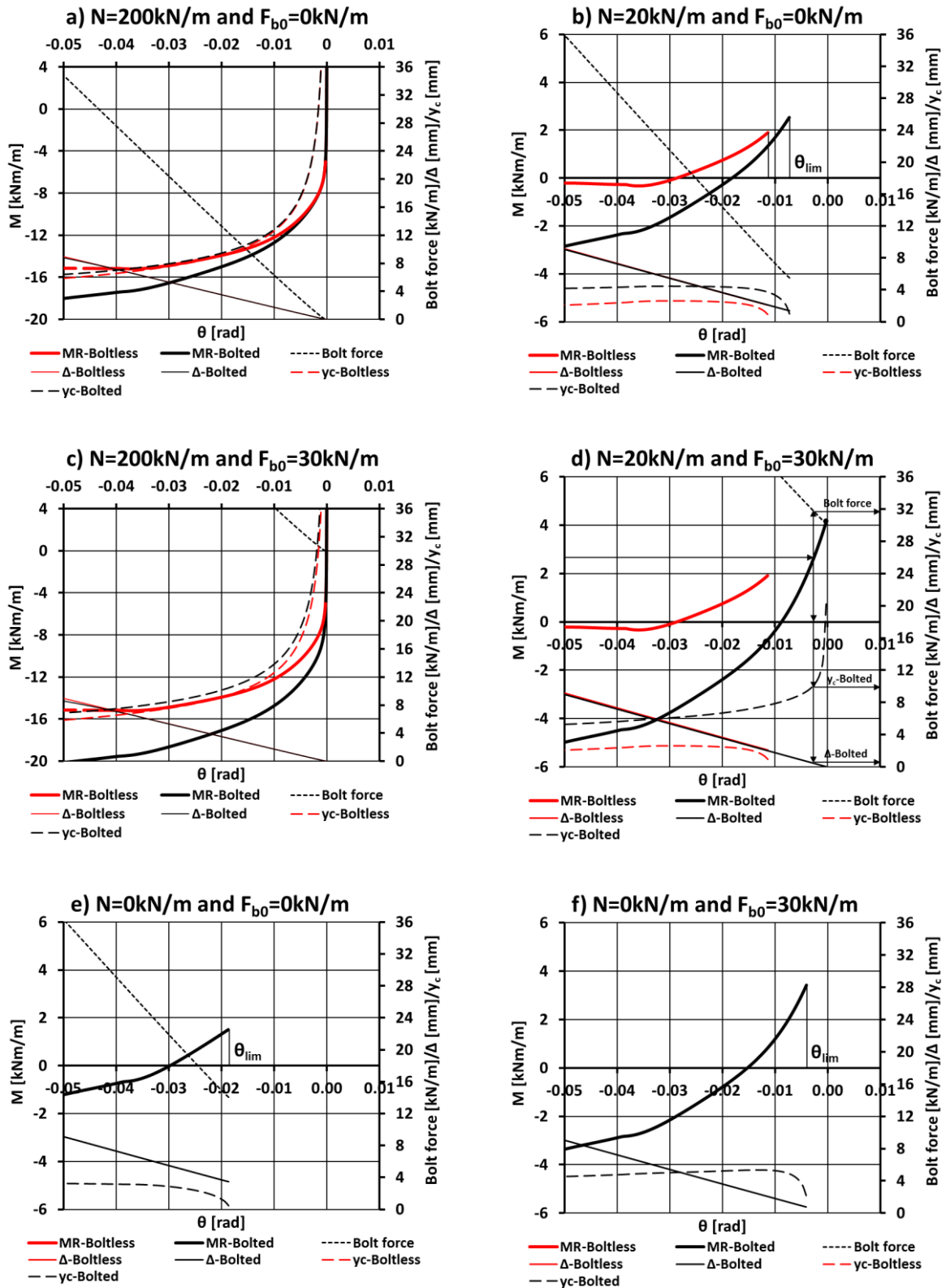


Figure 3.8: MR curves, bolt force, gasket gap and neutral axis for gasketed flat joints

#### a) Curved joints

In curved “open” joints, the  $\theta$  in boltless joints is higher but of magnitude similar to flat joints (see Figure 3.9). For instance, when  $N=20\text{kN/m}$  and  $M=0\text{kNm/m}$ , the curved boltless joint reaches a  $\theta=-0.036\text{rad}$  as opposed to the  $\theta=-0.028\text{rad}$  exhibited by flat joints. In curved bolted joints, the spear bolt is less effective in preventing rotations, as the eccentricity of the contact strip remains relatively small even for large rotations. Thus, the bolt forces developed at curved joints are also lower. Conversely,  $\Delta$  still increases more rapidly in flat than in curved joints (see chapter 2). A  $30\text{kN/m}$  bolt pre-tightening improves the moment capacity of “open” curved joints, but  $\theta$  is still significant: for example, when  $M=0\text{kNm/m}$ , the  $\theta$  required to balance the gasket force is  $-0.024\text{rad}$ .

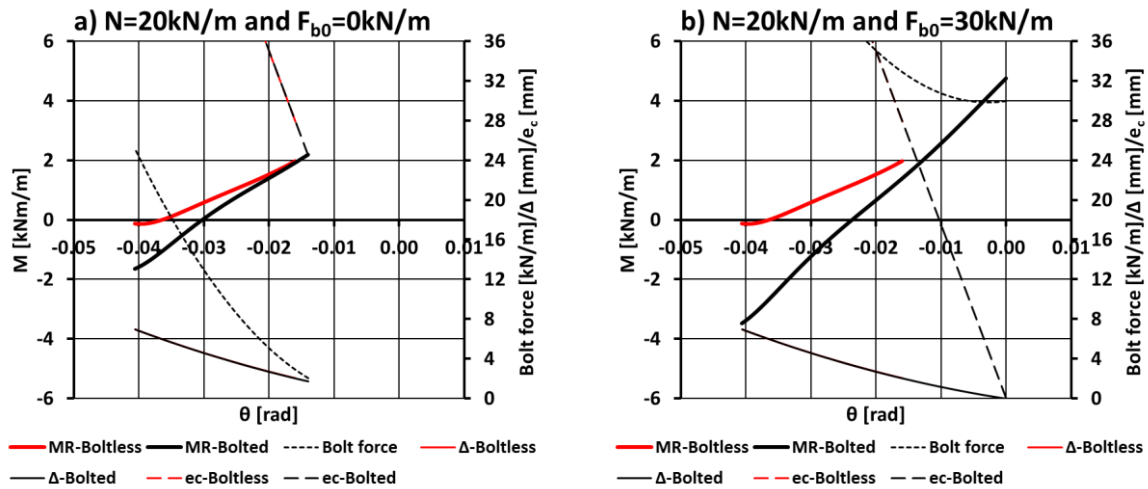


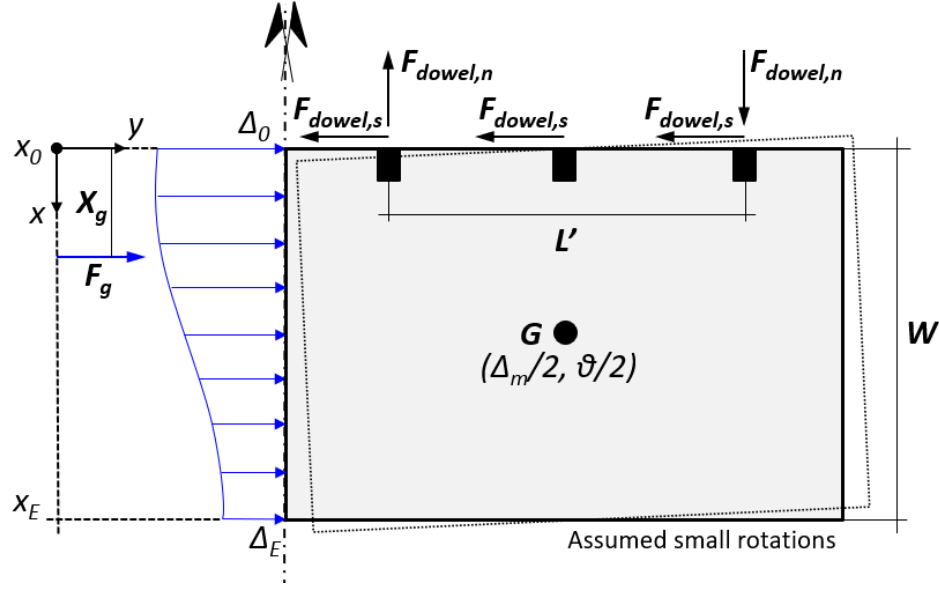
Figure 3.9: MR curves, bolt force, gasket gap and load eccentricity for gasketed curved joints

#### 3.3.1.2. Gasket compression

It can be inferred from the above that, in “closed” joints, the spear bolts can improve the joint moment capacity at low normal loads and serviceable rotations through significant bolt pre-tightening, while  $\theta$  and  $\Delta$  can be reduced in “open” joints with spear bolts, particularly when pre-tightened, to values that, however, are not minor. Bolt pre-tightening in field conditions, however, cannot be as reliable as in the controlled environment of a laboratory. Consequently, in assembled segments or rings with “open” joints, e.g. during ring erection, the equilibrium against gasket forces may be reached through shear and normal resistance at the circumferential joint before the rotational resistance of bolts is even activated.

Figure 3.10 illustrates the equilibrium mechanism of a two-segment system subjected to gasket forces. The gasket force originates a lateral load and moment in the segments, which translate along the  $y$  axis and rotate around the  $x$  and  $z$ . The rotation around the  $x$  axis is ignored in this system with the assumption that it will be in any case small. The translation in the  $x$ -axis activates the dowels in shear. The pull-out reaction of dowels and the compression of packers oppose the  $z$ -axis rotation; the reaction of the ram loads is ignored, which should result in a conservative calculation.





$$F_{dowel,s} = k_{dowel,s} \frac{\Delta_0}{2}$$

$$F_{dowel,n} = k_{dowel,n} \frac{\Delta_E - \Delta_0}{W} \frac{L'}{4}$$

$$F_g = \int_{x_0}^{x_E} f_g(x) dx = \frac{W}{\Delta_E - \Delta_0} \int_{\Delta_0}^{\Delta_E} f_g(\Delta) d\Delta$$

$$X_g = \frac{\int_{x_0}^{x_E} f_g(x) x dx}{\int_{x_0}^{x_E} f_g(x) dx} = \frac{W^2}{F_g(\Delta_E - \Delta_0)^2} \left[ \int_{\Delta_0}^{\Delta_E} f_g(\Delta) \Delta d\Delta - \frac{F_g \Delta_0 (\Delta_E - \Delta_0)}{W} \right]$$

$$\sum F_y = 0 \Rightarrow F_g = 3F_{dowel,s}$$

$$\sum M = 0 \Rightarrow F_g X_g = F_{dowel,n} L'$$

Figure 3.10: Simplified force diagram for a two-segment system with boltless joint subjected to gasket force

The shear stiffness of CTT dowels at small displacements,  $k_{dowel,s}$ , is 29kN/mm (Anixter, 2014) and the pull-out stiffness,  $k_{dowel,n}$ , 18.75kN/mm. If the 200x150mm<sup>2</sup> packers are assigned a conservative stiffness of 13.3MPa/mm, the lateral confinement per packer pair would be 800kN/mm. However, given that the packer can only withstand compressive forces, the equivalent  $k_{dowel,n}$  of the packers could be taken as 400kN/mm.  $L'$  is close to 1.86m and the remaining input parameters can be found in Table 2.2 and Table 3.1.

The above system yields values of  $\Delta_0 \approx 1\text{mm}$  and  $\Delta_E \approx 1.2\text{mm}$ , which are already smaller than the 2.7mm gasket gap of bolted flat joints with 30kN/m bolt pre-tightening and null  $N$  and  $M$ . The bolted two-segment system delivers similar gasket gaps of  $\Delta_0 \approx 0.8\text{mm}$  and  $\Delta_E \approx 0.9\text{mm}$ . It can then be inferred that the principal restoring mechanism against gasket loads is provided by the interaction with the circumferential joint. The bolt action to hold the gasket close is either insufficient or not used.

### 3.3.2. Ring build

Bolts can delimit excessive longitudinal joint misalignments during ring assembly. However, their lack of shear resistance at serviceable displacements (Harding et al., 2014), implies that subsequent lipping must be resisted mainly through friction between concrete segments or by connectors at circumferential joints.

In addition, bolts cannot prevent initial rotations. Dowelled connectors are again the primary elements delimiting rotations. For a given maximum eccentricity between dowel and socket,  $e_{dowel}$ , the maximum initial rotation allowable,  $\theta_{max}$ , is:

$$\theta_{max} = \frac{2e_{dowel}}{s_{dowel}} \quad (3.8)$$

where  $s_{dowel}$  is the spacing between dowels. For the CTT, a  $e_{dowel}=8\text{mm}$  yields initial rotations not greater than 0.017rad (see Figure 3.11).

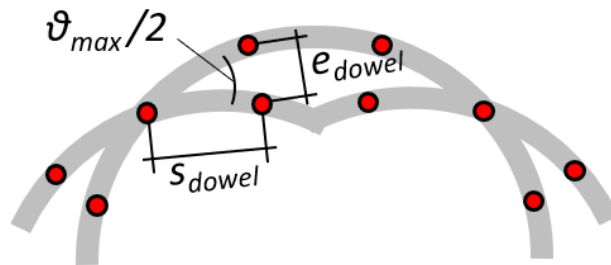


Figure 3.11: Maximum initial rotations delimited by dowel misalignment

### 3.3.3. Construction stages

In this section, the capability of spear bolts to alleviate damage during tunnel construction is investigated by reviewing the most frequent damage events associated with the construction stages (see Table 3.2).

Table 3.2: Role of spear bolts against damage during construction

Stage	Contact deficiency	Action	Damage	Bolt function
Ring assembly	Joints not fully closed	Forcing key installation with rams due to tight space	Chipping and gasket stripping at keystone	Very limited
Ring loaded longitudinally	Uneven packer support	Ram loads	Longitudinal cracks	None
Near tail skin	Angular imperfections at longitudinal joints	Tulip effect due to eccentric compression	Local splitting or chipping	Tensile resistance
Outside tail skin	Circumferential joint lipping	TBM interaction in curves Uneven settlement	Gasket underperformance	None

Gruebl (2006) identified the forced insertion of a tight keystone as the cause of the most frequent damage during ring erection, i.e. chipping of keystone corners and gasket stripping. Gruebl (2006) associated it with either poor ring erector operation or deformations in previous rings inhibiting the full closure of longitudinal joints during ring assembly. Since spear bolts have at best a secondary role in keeping lateral gaskets closed, their use has a minor impact on this damage.

The initial angular imperfections that trigger the chipping of longitudinal joints under hoop compression (see chapter 1 and 2) cannot be mitigated by spear bolts that are installed after the segment assembly. Likewise, bolts cannot prevent the longitudinal cracks produced by the longitudinal compression of segments with uneven packer support (see chapter 1).

Despite their minor role in holding gaskets close prior to any hoop compression, the spear bolts could indeed contribute to resist the opening of longitudinal joints when the rings are loaded with eccentric radial pressures near the tail skin during TBM advance. This scenario is further examined in section 3.3.3.1. Once the ring is fully compressed, the bolts become loose and can be removed.

#### 3.3.3.1. Role of bolt during sequential loading with uniform radial pressures

The action of spear bolts during sequential loading was examined through the solid model of a ring subjected to a 700kPa radial pressure applied gradually from the ring rear until covering the entire ring width (see Figure 3.12). The concrete segments were simulated with first order hexahedral elements with reduced integration and a linear elastic constitutive model. The longitudinal joints were modelled with hard contact interactions.

Figure 3.12 details the boundary conditions and loads applied in the modelling sequence. The tangential and longitudinal displacements at packer positions were fixed. It was assumed that the TBM hydraulic jacks did not impose any restraints to ring displacements.

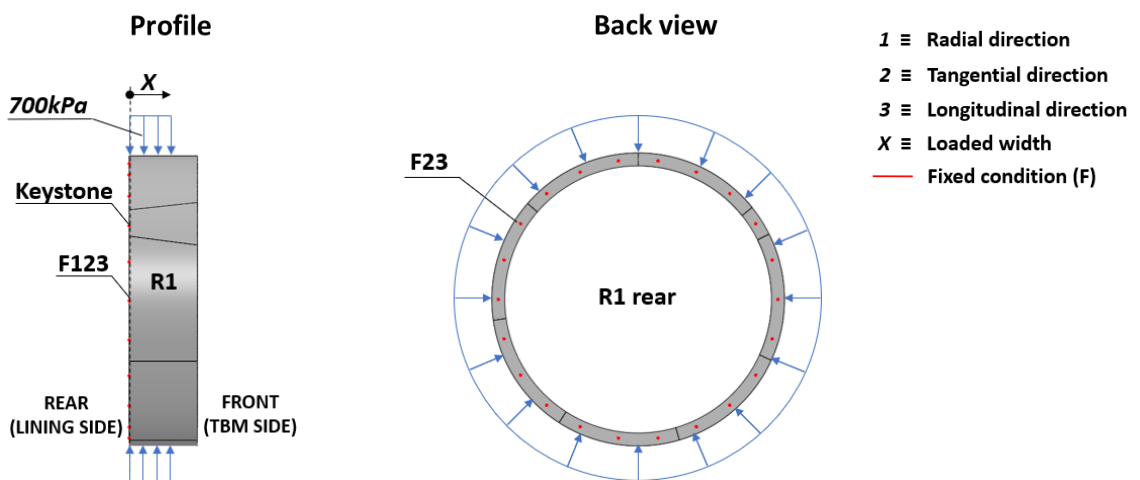


Figure 3.12: Boundary conditions and applied loads for sequential loading

Figure 3.13 illustrates the radial displacements when the ring is loaded over a 0.1m width and by the end of the loading sequence, with full compression. Under eccentric radial pressures, the segments tend to rotate radially and the longitudinal joints open as a consequence. The joints close gradually with the increase of the loaded width.

In boltless rings, the keystone exhibits a residual radial rotation of 0.0025rad that results in 3mm front displacements. The tensile resistance of the spear bolts installed at least at the keystone joints can prevent the residual rotation of keystones, leading to uniform ring displacements after sequential loading.

The spear bolts can also reduce peak radial rotations, particularly of keystones, within the loading sequence, in this case study from 0.003rad to 0.0018rad. Thus, the risk of chipping of segment corners and the uneven plastic deformations of longitudinal joints that can lead to permanent “tulip” ring shapes (see Figure 3.13.a) can be mitigated with the use of spear bolts.

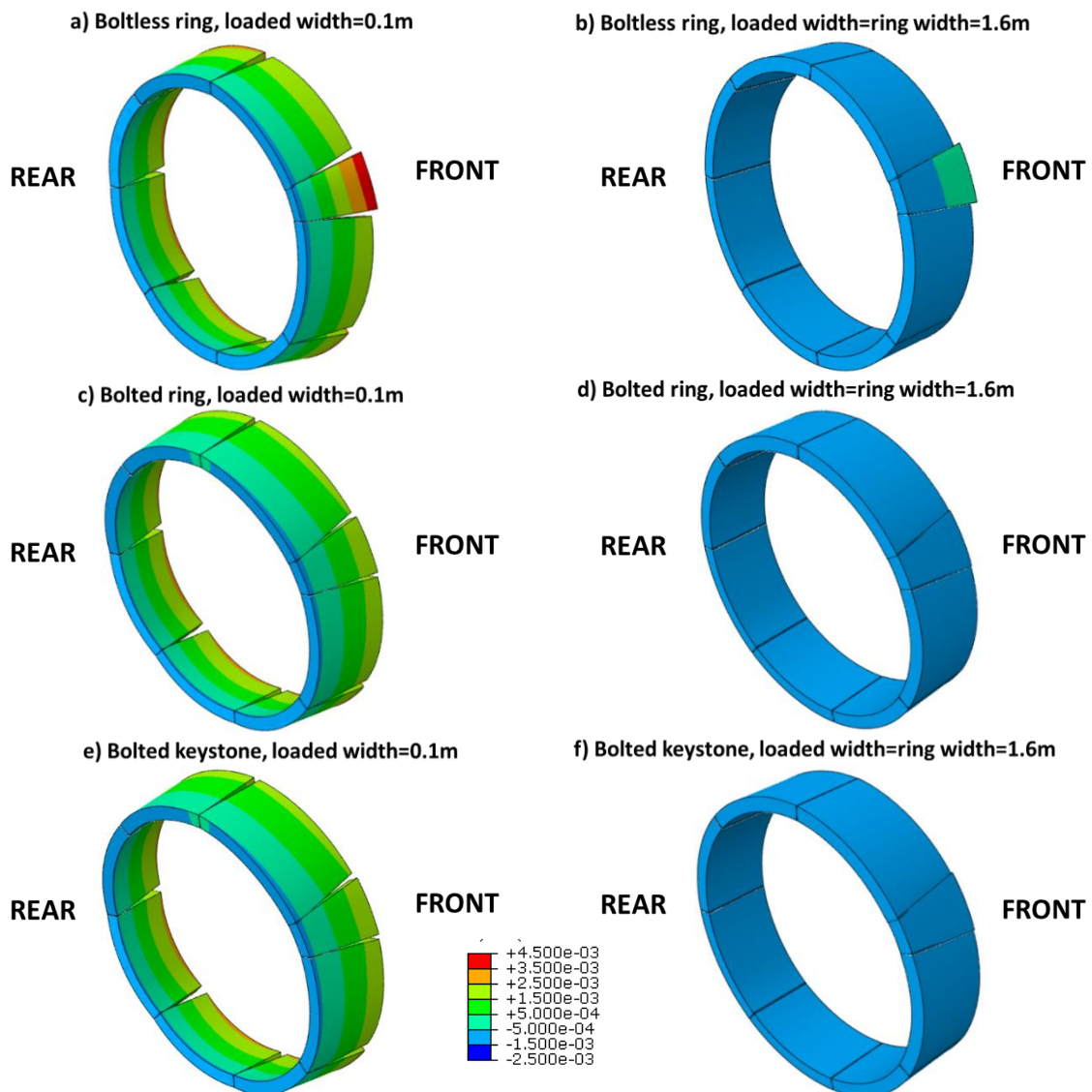


Figure 3.13: Radial displacements [m] in ring subjected to sequential loading with 700kPa radial pressures

### 3.4. Conclusions

The function of temporary spear bolts in current CSL configurations is not clearly understood by neither tunnel practitioners nor manufacturers (Harding et al., 2014), who, in the absence of detailed studies, propose them as conventional features of CSL design.

The role of spear bolts in gasketed joints with regard to joint moment capacity, preservation of gasket compression, ring build quality and retention of ring shape during construction has been thoroughly examined in this chapter with the support of 2D analytical models of bolted gasketed joints and two-segment systems, plus ring numerical models.

Table 3.3 summarises the identified functions regarding structural capacity and damage prevention.

**Table 3.3: Summary of bolt functions**

<b>Function</b>	<b>Bolt performance</b>
Enhancement of moment capacity (“closed joints”)	Minor only for low normal forces when pre-tightened.
Resistance to gasket force (“open joints”)	Minor and insufficient.
Prevention of initial imperfections	<b>Delimits longitudinal joint misalignments.</b> No action against initial angularities.
Retention of ring shape during construction	<b>Limits residual deformations and risk of corner chipping during sequential loading</b>
Enhancement of joint shear capacity	Only ULS capacity

First, the effect of spear bolts on moment capacity is null for “closed” joints without bolt pre-tightening due to the low stiffness of the bolt system. Second, their capability of resisting gasket forces at longitudinal joints is minor and insufficient, being the lateral confinement of circumferential joints the primary mechanism for keeping the gaskets closed. Third, spear bolts can prevent excessive initial misalignments in longitudinal joints, but their shear resistance is only activated after the development of substantial joint lipping. Fourth, the tensile resistance of spear bolts can limit residual deformations, particularly around keystones, and mitigate the risk of corner chipping as a result of sequential loading.

In summary, spear bolts have two main functions in current CSL configurations, either with or without gasketed joints: (i) to be a physical constraint to longitudinal joint lipping during ring assembly; and (ii) to mitigate the risk of contact imperfections and corner chipping near the tail skin at the expense of increasing the risk of localised cracking around the bolt pockets (Chen and Mo, 2009).

It stems from this study that a more cost-effective design of connectors may be possible and that boltless CSLs could be adopted in favourable tunnelling conditions and appropriate lining configurations with the benefit of removing bolt pockets in concrete segments and cutting costs. However, the above decisions require a better understanding of the CSL behaviour near the tail skin (see chapters 7 and 8).

## Chapter 4

# 3D numerical study on the long term response of concrete segmental linings

### 4.1. Introduction

In general long term conditions, the uniform and deviatoric components of earth pressures around deep tunnels cause the uniform compression and ovalisation of linings respectively (Muir-Wood, 1975; Curtis, 1976). The ovalisation of CSLs is accommodated through segment curvatures, longitudinal joint rotations and, eventually, the flexural cracking of segments if the ovalisation loads are sufficiently high (Blom, 2002; Lutikholt, 2007; Arnau, 2012). Unless heavily reinforced with bolts or steel connectors, longitudinal joints in conventional CSLs are less stiff than the full cross section of segments and therefore lining deformations tend to concentrate at joint positions.

In this chapter, the effect of longitudinal joint geometry on the long term response of CSLs is investigated through FE solid models of ten tunnel rings based on the CTT design, provided with either flat or curved longitudinal joints. A simplified ground modelling typical of conventional design models (Duddeck and Erdmann, 1982) is adopted here and further research on this matter is left for future endeavours.

First, past research on CSL global behaviour is reviewed and structural mechanisms outlined. Second, the FE model and modelling strategy are thoroughly described. Third, the results of the parametric study are presented and discussed, focusing first on the behaviour of isolated rings and later on the mechanics of coupled rings. Closed-form solutions are used as reference models to provide a comparative framework against current design. Finally, the scope of the use of flat and curved joints applicable to this case study is defined with recommendations on the selection of joint geometry.

### 4.2. Background

A vast body of research has been devoted to the study of joint mechanical behaviour and the influence of longitudinal joints on the global response of tunnel structures. It has been found over the years that the importance of joint rotational capacity on lining performance depends on other factors, mainly the degree of ground support provided, the magnitude of ovalisation loads applied and the possibility of ring coupling (Blom, 2002; Lutikholt, 2007; Arnau, 2012).

Traditional structural design models based on plane strain solutions of a circular tunnel in elastic ground represent the lining as a thin ring with uniform rigidity (Duddeck and Erdmann, 1982). A review of these closed-form solutions evidenced that the correlation between lining and ground

## 4.2. Background

stiffness, given by compressibility,  $\beta$ , and bending stiffness,  $\alpha$ , ratios, was a governing factor in lining performance (Duddeck and Erdmann, 1982):

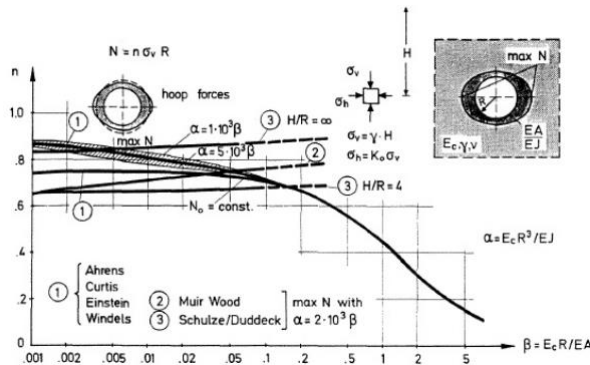
$$\alpha = \frac{E_s R_m^3}{E_c I_R} \quad (4.1)$$

$$\beta = \frac{E_s R_m}{E_c A_c} \quad (4.2)$$

where  $E_s$  is the ground Young's modulus,  $R_m$  is the tunnel mean diameter,  $E_c$  is the concrete stiffness and  $A_c$  and  $I_R$  are the cross-sectional area and moment of inertia of the tunnel. Duddeck and Erdmann (1982) indicated that the typical values of  $\alpha$  in constructed tunnels range between 5 and 200, from soft to stiff ground relative to the lining, while no information was provided on the usual values of  $\beta$ .

Stiffer grounds, relative to the tunnel structure, allowed for a greater redistribution of stresses within the soil mass, and reduced the proportion of both uniform pressures and deviatoric stresses effectively sustained by the lining (see Figure 4.1). The ratio  $\alpha$  had a definite influence on peak moments and radial displacements;  $\beta$  governed the maximum hoop thrust.

a) Hoop forces for continuum model and tangential slip,  $\nu=0.3$  and  $K_0=0.5$  (Duddeck and Erdmann, 1982)



b) Maximum bending moment as a function of  $\alpha$ , Continuum model with  $\nu=0.3$  (Duddeck and Erdmann, 1982)

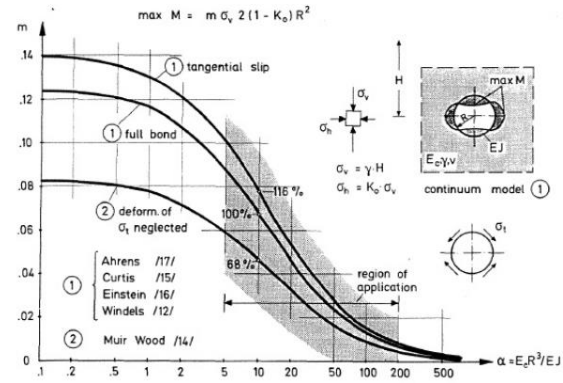


Figure 4.1: Hoop forces and maximum bending moments of closed-formed solutions

The effect of longitudinal joints on continuous rings was introduced by Muir Wood (1975) through the concept of smeared lining flexibility and his empirical formula on effective bending stiffness:

$$I_R = \frac{1}{12} h^3 \left( \frac{4}{n_J} \right)^2 + I_J \quad (4.3)$$

where  $h$  is the lining depth,  $n_J$  the number of joints in a segmental ring and  $I_J$  the longitudinal joint stiffness.

The effect of flat longitudinal joints on the long term behaviour of ground-bedded isolated rings was investigated by means of analytical and numerical methods by several authors:

- a) Do et al. (2013) conducted a parametric study to investigate the effects of joint stiffness,  $E_s$  and the lateral earth pressure coefficient at rest,  $K_o$ , on the lining behaviour of a shallow tunnel by means of 2D finite difference (FD) models. The rotational stiffness of longitudinal joints was approximated to a bilinear relation derived from the popular Janssen rotational model of flat joints. Rotational stiffness ratios, i.e. joint stiffness relative to lining stiffness, of 1, 0.1 and 0.01 were examined for a range of  $E_s$  comprised between 10MPa and 500MPa and a  $K_o=0.50$ . Overall, radial displacements were mainly determined by ground stiffness, except for very soft ground, and low rotational stiffness ratios produced minor increments in radial displacements. A reduction in maximum hoop moments was observed with the softening of joints providing that  $E_s < 200\text{MPa}$ , i.e.  $\alpha < 100$  for the equivalent continuous ring.
- b) Blom (2002) examined the effect of flat joints on isolated rings in soft ground subjected to increasing ovalisation. It was concluded that the non-linearity in joint behaviour increased radial displacements slightly and that the maximum moment capacity of joints delimited peak moments in rings subjected to high ovalisation ratios. Joints eventually failed by concrete crushing, i.e. when the normal contact strains reached the ultimate limit strain of concrete,  $\epsilon_{cu}$ , at which point almost the entire ovalisation load was supported by the ground.

In watertight tunnels, ring linings with staggered joints are the norm in order to avoid excessive water leakage through cruciform joints. Uncoupled rings, even subjected to equal earth pressures, deform differently due to rotations of joints at staggered positions. Recent research confirmed that when there is ring coupling through shear resistance of compressed packers or dowelled connectors placed at circumferential joints, the rings adopt similar displacement profiles and the ring internal forces are redistributed longitudinally:

- a) Blom (2002) explored the effects of ring interaction on bedded linings through his analytical model of two rolled rings with constant segment stiffness coupled by axial springs at longitudinal joint positions. The reference value of coupling stiffness was validated against full-scale tests of three rings subjected to serviceable loads, although the magnitude of working longitudinal loads is unknown to the author.

It was found that ring coupling increased the overall stiffness of the tunnel structure leading to a substantial rise in hoop moments, up to three times, but only minor reductions in ring convergence. The moments were governed mainly by the coupling stiffness and, to a lesser extent, by flat joint non-linearity, which implied a moderate decrease in ring stiffness.

From Blom's investigation, two possible damage modes of bedded tunnels subjected to high ovalisation loads were inferred: with high ring interaction, extreme peak moments within the segment body may result in the flexural cracking of concrete; with low ring interaction, excessive rotation of flat joints could lead to local joint damage by concrete crushing.



### 4.3. Description of numerical simulations

---

- b) These mechanisms were further examined by Luttikholt (2007) through full-scale tests of three non-bedded rings subjected to high and low longitudinal loads so that, in the absence of ground support, the structural response against ovalisation loads was magnified, which helped to identify structural interactions.

In a tunnel section made of strongly coupled rings, the coupling forces originated by disparities in deformed shapes of neighbouring rings resulted in the longitudinal migration of hoop moments to the segment bodies of adjacent rings, predominantly at coupling positions placed near longitudinal joints. When the moments were sufficiently large and the concrete segments cracked at critical cross sections, the circumferential redistribution of hoop moments within rings was greatly amplified. The circumferential moment distribution at low ovalisation loads was not affected by the degree of coupling.

In tunnel sections subjected to low longitudinal loads, the coupling capacity of circumferential joints was exhausted at small ovalisation loads, giving rise to partial slip between rings and poor longitudinal redistribution of hoop moments. Large joint rotations were experienced prior to failure without significant segment cracking.

- c) Arnau (2012) investigated the structural response of an eleven ring CSL model with flat joints subjected to a wide range of ovalisation ratios, ground stiffness and longitudinal loads. Coupling effects on bending moments were only significant for tunnels with moderate or low  $\alpha$  subjected to high ovalisation. For example, at  $E_s=75\text{MPa}$ , i.e. equivalent to  $\alpha\approx 100$  for a continuous ring, the ring interaction was effective for  $K_o\leq 0.50$  while at  $E_s=150\text{MPa}$ ,  $\alpha\approx 200$ , the range of influence was limited to  $K_o\leq 0.3$ . At the worst combined conditions in the study, with  $\alpha\approx 33$ , the peak moments reached values of 180% higher than in isolated rings.

Arnau demonstrated that the rotational stiffness of longitudinal joints was an important factor in the development of coupling moments. However, the progressive cracking of segments attenuated the ring interaction, and decreased the peak moments, as the bending stiffness of the cracked sections and the flat joints approached (Luttikholt, 2007).

### 4.3. Description of numerical simulations

An adequate modelling strategy should enable the comparative analysis of long term lining behaviour with different joint geometries. A thorough examination of the lining response demands the use of models focused on the tunnel structure, from which important indicators such as ring convergence, joint rotations and gasket openings, lining forces and ring misalignments can be derived. Bedded models are especially suited for the assessment of CSLs subjected to multiple load combinations.

The hyperstatic reaction method simulates the ground-structure interaction by means of both external loads applied onto the lining structure and Winkler springs acting as ground supports when the tunnel

## 4.3. Description of numerical simulations

---

deforms. Its main limitation is that the active and passive actions of the ground are uncoupled and disconnected from stress and deformational fields, which means that the selection of parameters to characterise the ground-structure interaction must be made with a certain degree of uncertainty. Analytical bedded models represent the lining structure in a simplified manner, as isolated or groups of 1D rings made of beam elements interconnected by springs (Duddeck and Erdmann, 1982; Blom, 2002). Bedded numerical models are more versatile and allow for a detailed depiction of the tunnel structure if required.

Accordingly, this parametric study is based on FE analyses of ten bedded ring models performed with ABAQUS/Standard. Segments and packers at circumferential joints are simulated via solid elements with hard contact interactions established at structural interfaces. With this approach, the modelling priority is given to joints which are replicated with high precision. Dowels are modelled by means of group springs and temporary spear bolts are excluded.

Contact interactions numerically entail the introduction of severe nonlinearities in the analyses (ABAQUS, 2012). Plastic and cracking features of concrete behaviour must be sacrificed to make the simulations viable, and a linear elastic concrete model is adopted. However, it could be even argued whether concrete plasticity and cracking are deemed necessary in a comparative study of lining global response with different joint geometries. At serviceable loads, (i) the flexural cracking of segments should be of secondary importance in the prediction of radial deformation and internal forces, as exemplified by Blom's investigation (2002) based on full-scale tests of three rings instantaneously loaded to serviceable levels; (ii) the plasticity experienced by joints has a negligible effect on joint rotational behaviour (see chapter 2); and (iii) the local bursting in the vicinity of joints is irrelevant at a global scale and could be predicted through the NR diagrams developed in chapter 2 if desired.

### 4.3.1. Input parameters and element types

The geometry and material properties of the lining were based on the CTT tunnel (see Figure 1.1, Table 2.2 and Table 4.1). The CTT 6.2m internal diameter (ID) lining was made of tapered universal rings with seven segments and a keystone.

The parametric study focuses on the long term CSL behaviour under soft ground conditions, i.e. when the CSLs yield at least moderate values of  $\alpha$ , given that the effect of joint rotational stiffness in hard ground, or high  $\alpha$ , is expected to be negligible (Arnau, 2012). For the CTT lining configuration, a  $E_s=50\text{MPa}$  results in  $\alpha=65$  and  $\alpha=160$  for curved and flat jointed rings using Eq. 4.3 and it is deemed to represent the soft ground condition. When  $E_s$  approximates the stiffness of chalk, 163MPa,  $\alpha$  far exceeds the value of 200 for both CSL types. Nevertheless, numerical analyses for this hard ground condition were performed to validate Arnau's (2012) conclusion, particularly in regard to curved jointed CSLs.

## 4.3. Description of numerical simulations

**Table 4.1: Material properties**

<b>Material property</b>	<b>Value</b>	
Modulus of elasticity [MPa]	Soft ground	50
	Hard ground (Chalk)	162.74
Poisson ratio [-]	0.2	
Concrete Young's modulus [GPa]	38 (see chapter 5)	
Packer Young's modulus [MPa]	100	
Packer-concrete friction coefficient [-]	0.4	
Dowel properties [-]	See section 4.3.1.2	

The segments and packers were modelled with first-order hexahedral elements with reduced integration; dowels with two-node springs acting in a fixed direction and the ground-structure interaction with one-node springs between node and ground acting in fixed directions (ABAQUS, 2012). The element types are listed in Table 4.2.

**Table 4.2: Element types**

<b>Feature</b>	<b>Element type</b>	
Segment	C3D8R	
Packer	C3D8R	
Dowels	SPRING2	
Ground-structure interaction	Radial	SPRING1
	Tangential	SPRING1

### 4.3.2. Input loading

Uniform and ovalisation loads were inferred following Blom's third approach on long term normal load cases for bedded models, which ignores floating effects (Blom, 2002). The impact of the CSL selfweight on a substantially radially compressed tunnel is negligible and it was excluded.

Table 4.3 shows the assumed primary vertical pressures at the springline of the CTT instrumented rings and the vertical pressures adopted for the FE analysis. The latter is based on the CAM3/CAM4 water pressures and the 300kPa total crown pressures obtained from hoop strain measurements sensed 24h after ring erection and which are near the primary in situ stresses (see chapter 5).

**Table 4.3: Earth and water pressures at springline**

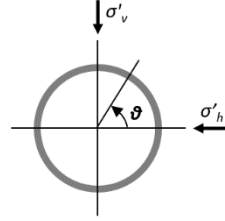
	<b>CAM1</b>	<b>CAM2</b>	<b>CAM3/CAM4</b>	<b>FE model</b>
<b>Total vertical pressure <math>\sigma_v</math> [kPa]</b>	363.3	358.5	345.9	300.0
<b>Water pressure <math>p_w</math> [kPa]</b>	254.1	271.7	<b>183.0</b>	180.0
<b>Effective vertical pressure <math>\sigma'_v</math> [kPa]</b>	109.2	86.7	162.9	120.0

## 4.3. Description of numerical simulations

In the FE simulations,  $K_o$  decreased from 1.00 to 0.00 with the progress of ovalisation loads. The mathematical expression of the radial,  $\sigma_r'$ , and tangential,  $\sigma_t'$ , earth pressure components input as external loads is:

$$\sigma_r' = \sigma_v' \left( \frac{1 + K_o}{2} + \frac{K_o - 1}{2} \cos 2\theta \right) \quad (4.4)$$

$$\sigma_t' = \sigma_v' \left( \frac{K_o - 1}{2} \sin 2\theta \right) \quad (4.5)$$



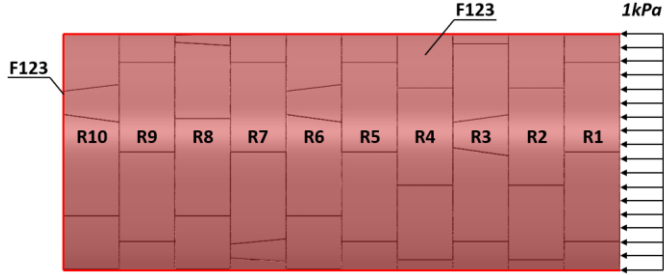
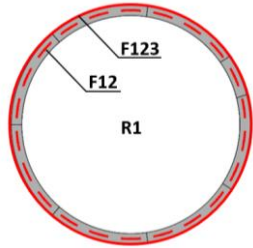
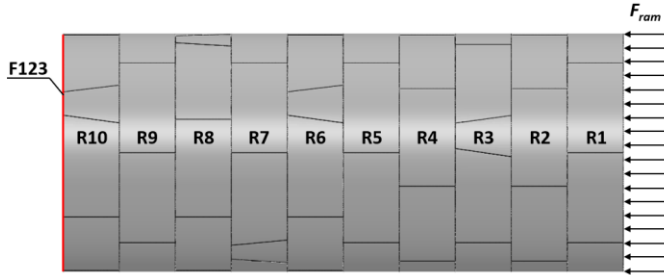
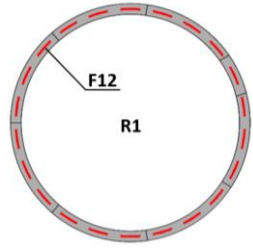
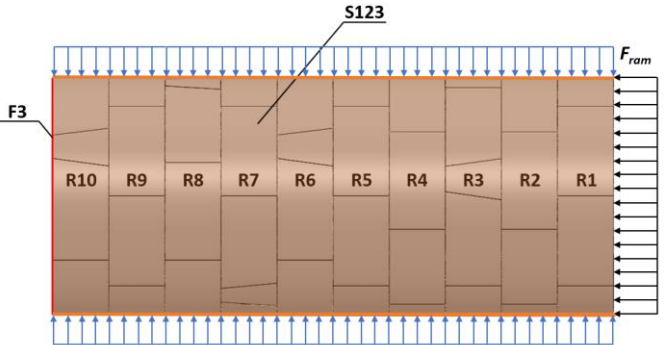
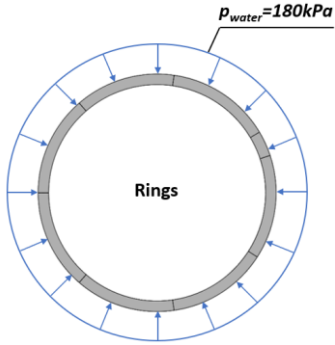
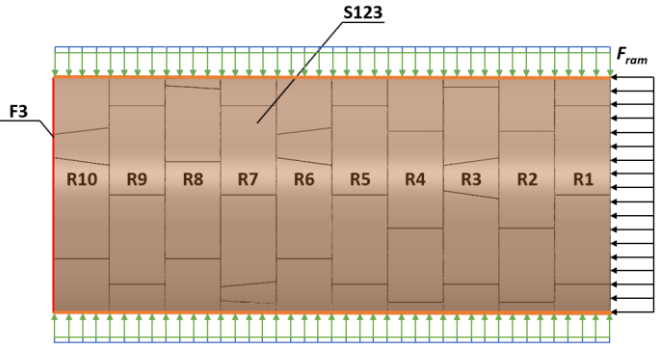
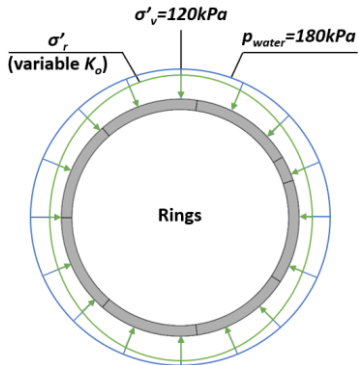
The uniform longitudinal loads ranged from 0bar/ram to 200bar/ram.

### 4.3.3. Simulation steps

Table 4.4 describes the loading and boundary conditions of each simulation step. At the first step, the contact interactions were initialised with the application of 1kPa ram pressures and restraint displacements at the outer CSL boundaries. The total ram loads were applied in step 2 with full constraints at the opposite side. In step 3, the ring plane fixities were replaced with spring supports and the uniform radial compression was applied at the lining extrados. In the final steps, the ovalisation loads were introduced gradually with constant vertical effective stress at the vertical axis and  $K_o$  variable from 1.00 to 0.00.

## 4.3. Description of numerical simulations

Table 4.4: Modelling steps

Step	Loading and boundary conditions	
1		
2		
3		
4 to 7		 <p><math>\sigma'_t</math> not represented for clarity</p>

- 1  $\equiv$  Radial direction
- 2  $\equiv$  Tangential direction
- 3  $\equiv$  Longitudinal direction
- Fixed condition (F)
- Spring support (S)

### 4.3.4. Joint modelling

#### 4.3.4.1. Longitudinal joints

A preliminary study on joint modelling at a local scale was conducted to optimise the accuracy and the convergence of the global lining models (see Figure 4.2). The joints were modelled through the geometry of joint surfaces and the definition of contact pairs between adjoining surfaces. The contact surfaces covered the joint height.

##### 4.3.4.1.1. Curved joints

ABAQUS offers two types of contact discretisation: node to surface, where each slave node interacts with its normal projection on the master surface; and surface to surface, where contact constraints are imposed on regions of the slave surface instead of slave nodes. The advantage of surface to surface over node to surface discretisation for contact pairs with well-defined surfaces is generally accepted (ABAQUS, 2012). Surface to surface discretisation tends to provide more accurate and smoother stress fields as penetrations are resisted over finite surface regions rather than by nodes, especially for coarse meshes (ABAQUS, 2012). In this study, however, the primary criterion for selection of contact discretisation was the accuracy in rotational behaviour delivered by the contact pair, with precision in contact stresses being of secondary importance.

The performance of both discretisation techniques was investigated through local models of curved joints with detailed geometry and very refined meshes (see Figure 4.2.a). Figure 4.2.b shows an example of the MR curves obtained with surface to surface and node to surface formulations against the Hertzian-based expression (see chapter 2). Overall, both modalities followed the analytical solution, although there was a greater tendency to staggered behaviour with surface to surface discretisation as a result of an uneven transition in effective contact with rotation. The staggering became noticeable also in node to surface contact pairs at very low values of applied normal load. At serviceable normal forces and rotations, the node to surface contact discretisation replicated better the rotational behaviour of curved joints. Figure 4.2.b also shows that the finite sliding node to surface contact pairs were insensitive to master surface smoothing.

The efficiency of the numerical simulations in large tunnel models was enhanced through the simplification of the joint geometry and the mesh optimisation, envisaged as a trade-off between accuracy in rotational behaviour and available computer capabilities (see Figures 4.2.a and 4.2.c). The MR curves obtained for model 3, characterised by the local geometry and mesh deployed in the global models, verified that the deviations in  $K_\theta$  from the theoretical solution were small and within the allowance defined by the reference model, model 1. The adopted element depths (along the joint depth) were within the order of magnitude of the element size in reference models.

## 4.3. Description of numerical simulations

---

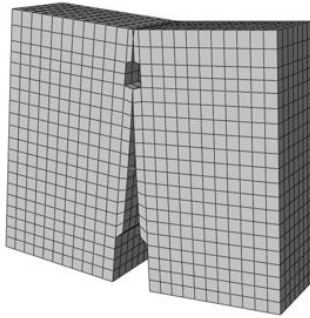
### 4.2.1.1.1. *Flat joints*

The same optimisation procedure was implemented in joints with flat bearing surfaces with a similar outcome in geometry and mesh optimisation.

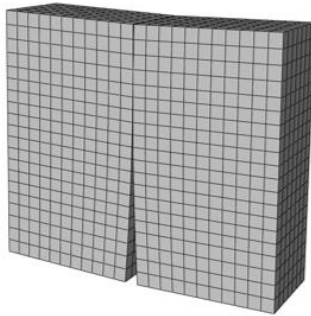
## 4.3. Description of numerical simulations

### a) Optimisation of curved joint models

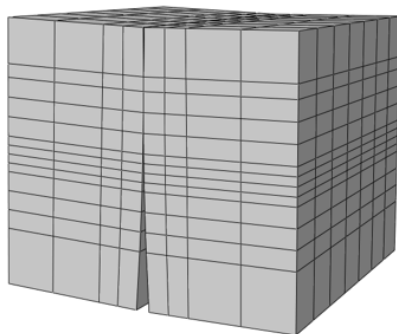
**Model 1:**  
Original geometry, refined mesh



**Model 2:**  
Simple geometry, refined mesh



**Model 3:**  
Simple geometry, mesh for  
large scale model

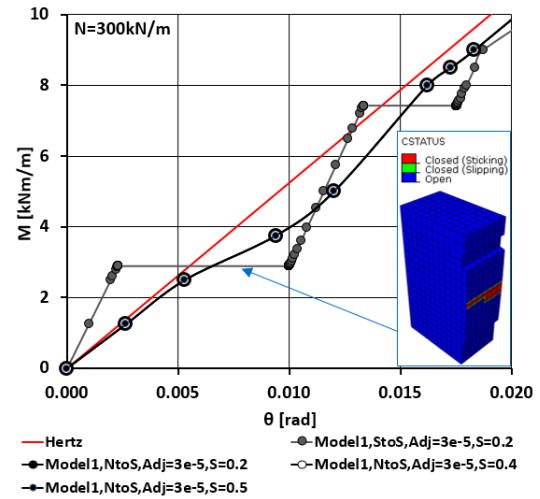


StoS  $\equiv$  Surface to Surface  
NtoS  $\equiv$  Node to Surface

Adj  $\equiv$  Strain-free adjustment  
S  $\equiv$  Surface smoothing



### b) Effect of contact discretisation on MR curves



### c) Effect of joint geometry and mesh on MR curves

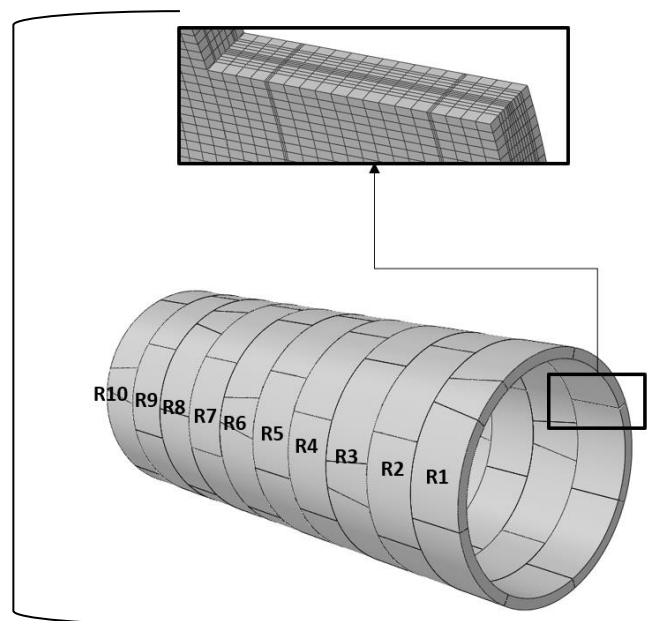
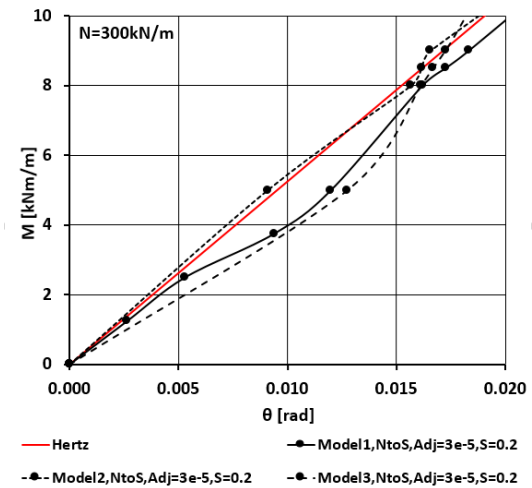


Figure 4.2: Optimisation of longitudinal joint modelling



## 4.3. Description of numerical simulations

### 4.3.4.2. Circumferential joints

The CTT circumferential joints were flat joints equipped with plywood packers and dowels. Packers are small sheets made of relatively soft material aligned with the circumferential position of TBM rams (see Figure 1.1). Their primary function is to distribute longitudinal forces roughly uniformly over the packer surface to minimise stress concentration in concrete segments, particularly if these are subjected to contact imperfections (Cavalaro, 2009).

Gijsbers and Hordijk (1997) conducted experimental short-term shear tests on flat joints equipped with packers. They found that plywood packers were able to transfer significant shear with peak friction coefficients varying from 0.4 to 0.7 with decreasing normal load, and declining up to 75% of these maximum values with increasing deformation. In the solid model, one side of the packers was tied to the circumferential face of an adjacent ring. A surface to surface contact interaction between packers and ring with friction equal to 0.4 was defined on the other packer side.

In the CTT, lock-in dowels were installed between standard rings whilst shear dowels were used near cross passages. In the numerical study, the dowels were simulated by radial and tangential linear elastic nine spring groups circumscribed to the dowel perimeter. Numerical simulations were conducted for two non-linear spring stiffnesses: one with stiffness equal to that of the Anixter CTT dowel (see Figure 4.3) and another with doubled stiffness. The pull-out resistance of dowels is irrelevant when rings are longitudinally compressed along their entire circumference; hence, it was excluded from the models.

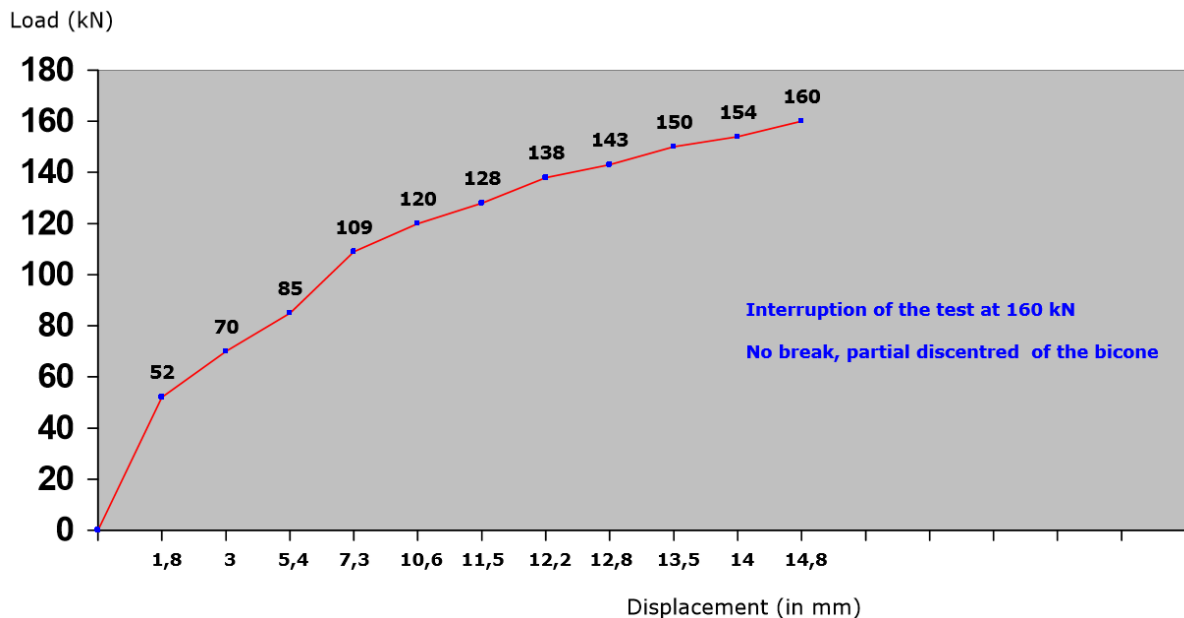


Figure 4.3: Anixter-Sofrasar lock-in dowel Sof-Fix Anix 60: Shear test (after Anixter, 2014)

## 4.3. Description of numerical simulations

### 4.3.5. Modelling ground-structure interaction

In the hyperstatic reaction method, the bedding support of the ground is modelled through normal springs with a stiffness,  $k_r$ , deemed representative of the modulus of subgrade reaction. The most extended formulation is computed from a circular cavity expansion model in elastic ground subjected to uniform radial pressure (Kolymbas, 2005), which is adopted here:

$$k_r = \frac{E_s}{R(1 + \nu_s)} \quad (4.6)$$

where  $E_s$  and  $\nu_s$  are the modulus of elasticity and Poisson's ratio of the ground. Further refinements on normal spring stiffness, such as bilinear curves derived from the Mohr-Coulomb failure criterion for soils, are questionable since the ground-structure interaction in bedded structural models is inherently simulated with certain arbitrariness (Kolymbas, 2005).

Since in the CTT, the tunnel overburden  $H$  is less than  $3D$ , being  $D$  the tunnel diameter, (see chapter 5, p.84) "a model without reduction of ground pressure at crown (...) may be appropriate" (Duddeck and Erdmann, 1982), and thus compressive-only springs are used in this study. Further discussion is beyond the scope of this research work.

The importance of the tangential interaction at the ground-structure interface had already been acknowledged by Curtis (1976). He demonstrated that the transmission of shear stresses at this interface increased the ground radial deformations and, consequently, hoop bending moments in the lining were very much reduced.

In 2D elastic continuum closed-form solutions, full slip and full bond limited by shear strength can be considered at the interface. Full shear interaction is recommended as best practice to avoid overdesign.

In bedded models, the tangential interaction between the ground and the lining is determined by the stiffness of the tangential springs and the applied tangential loads. In full slip conditions, neither tangential springs nor loads are applied. In full bond, it is widely accepted that the tangential spring stiffness is one third of the radial compressive spring stiffness (USACE, 1997). Arnau (2012) confirmed that such a value led to the best fit of his beam spring model to in situ loading tests of a ring embedded in hard ground and experiencing arch behaviour when point loaded at the crown.

#### 4.3.5.1. CTT full bond condition

The ability of the ground-structure interface to transfer shear stresses depends mainly on the construction procedures and ground properties. The full bond condition should imply no shear sliding at both grout-lining and ground-grout interfaces, and no shear failure within the grout layer.

The CTT geotechnical investigations revealed that the unconfined compressive strength,  $S_u$ , of chalk at the tunnel depth of the monitored rings was in the order of 1MPa (Crossrail, 2014). Since the  $S_u$  of dry intact chalk is about twice that of saturated chalk (Lord et al., 2002), the  $S_u$  of chalk under the Thames river bed may be around 0.5MPa. Considering the CIRIA's diagram on shear strength of sawtooth

interfaces between machine-cut intact chalk and in situ concrete (Lord et al., 2002) and the CTT in situ dry density of about  $1.6\text{Mg/m}^3$ , the shear strength of the ground-grout interface after grout hardening may be around 630kPa, not far from the  $S_u$  in saturated chalk.

Moreover, the failure envelope computed from drained compressive triaxial tests may imply that for an in situ mean effective pressure of about 200kPa, similar to that experienced at relevant tunnel depths, the effective strength of chalk is 115kPa, which is in the order of the  $S_u$  developed in BGs 1h after injection. Although the 1h compressive strength of grout was not measured in the CTT, BGs can reach 1h strengths of 250kPa (Hashimoto, 2006), again not dissimilar from the  $S_u$  of saturated chalk. Besides, the 24h compressive strength of CTT grout fluctuated around 1MPa, which is definitely greater than the  $S_u$  of saturated chalk.

Given that the duration of a typical TBM advance during the CTT tunnel drive was around 1h and the comparable strengths of 1h old grout and chalk, a strong bond between the grout and the ground is deemed very likely. Consequently, the full bond condition can be assumed and the tangential component of ground action and reaction,  $k_t$ , is included in these models.

## 4.4. Results

The results are generally extracted from R6 (see Table 4.3), unless otherwise stated, in order to avoid edge effects of model boundaries in coupled rings. Positive moments imply tensile and compressive strain increments at the lining extrados and intrados respectively.

The results are compared when relevant with the outcome of the continuum model 1 (CM) presented by Duddeck and Erdmann (1982) (see Figure 4.1), applied with and without reduced lining flexibility in accordance with Eq. 4.3.

### 4.4.1. Isolated rings

#### 4.4.1.1. Ring deformation and joint rotations

In this study, the deformation of isolated rings is governed by segment curvatures and the rotation of longitudinal joints, as segment cracking was excluded from the analyses. Figure 4.4 presents an example of radial displacements. Since the segment deflection caused by the same ovalisation loads must be equal in both ring types regardless of joint stiffness (Blom, 2002), the deformed shape of flat and curved jointed rings is analogous, although the contribution of joint rotations to radial displacements is more prominent in rings with curved joints.

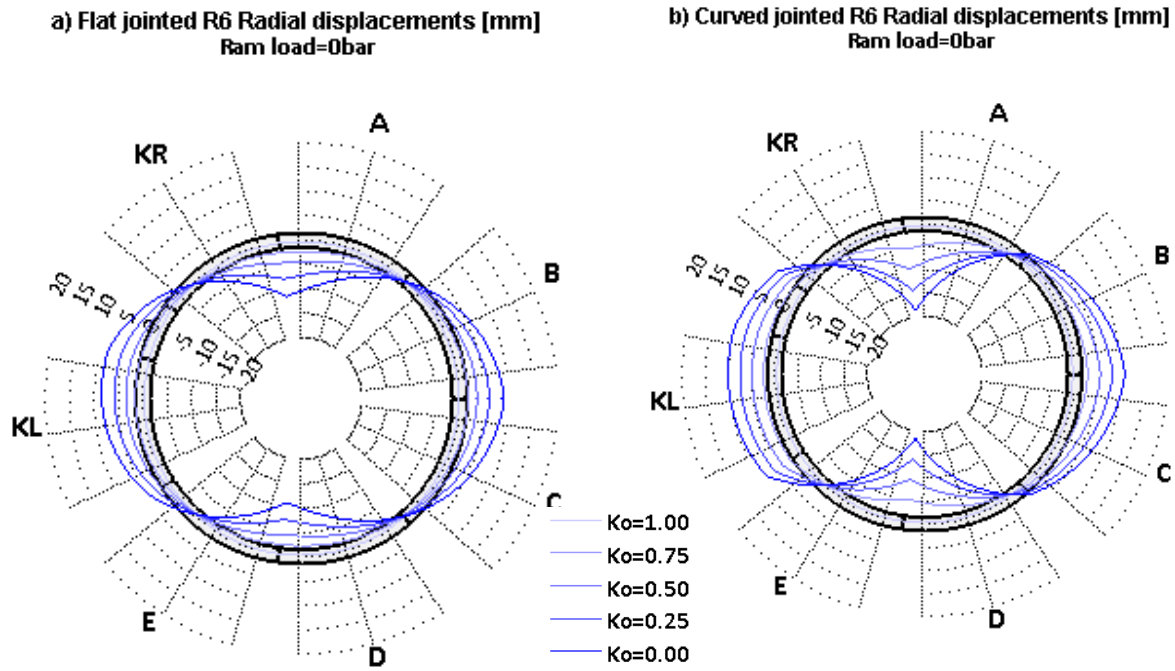


**Figure 4.4: Radial displacements in an isolated ring**

In a squatted continuous ring, the maximum hoop moments develop at the symmetry axes of the deviatoric pressure (Curtis, 1976). When longitudinal joints are placed near the vertical axis, i.e. crown or invert, the joint rotations induced by the transfer of peak moments are amplified (see Figure 4.5.a). Vertical convergence is greatest in rings with joints situated both at the crown and the invert (see Figure 4.5.b).

The maximum vertical convergence in hinged rings, about 40mm at  $K_\theta=0$ , roughly doubles that of flat jointed rings, about 20mm. Arnau (2012) noted that the moment capacity of crown joints in isolated rings becomes fully utilised from a certain ovalisation ratio threshold, given by  $E_s$  and  $K_\theta$ . Since the stiffness of curved joints is negligible at serviceable rotations, these are free to rotate even for low ovalisation loads, and ring deformations are only prevented by lateral ground support. Conversely, compressed flat joints can undertake substantial moments at low rotations and therefore increase the ring bending stiffness. Consequently, joint rotations and radial displacements at the vertical axis of hinged rings are significantly larger and more sensitive to ring rolling.

At the spring line, the ring partially relies on the passive bedding of the ground for equilibrium. The horizontal convergence is thus dictated by the ground stiffness. The position of joints or the joint stiffness has a minor influence on the ring response (see Figure 4.5.c).

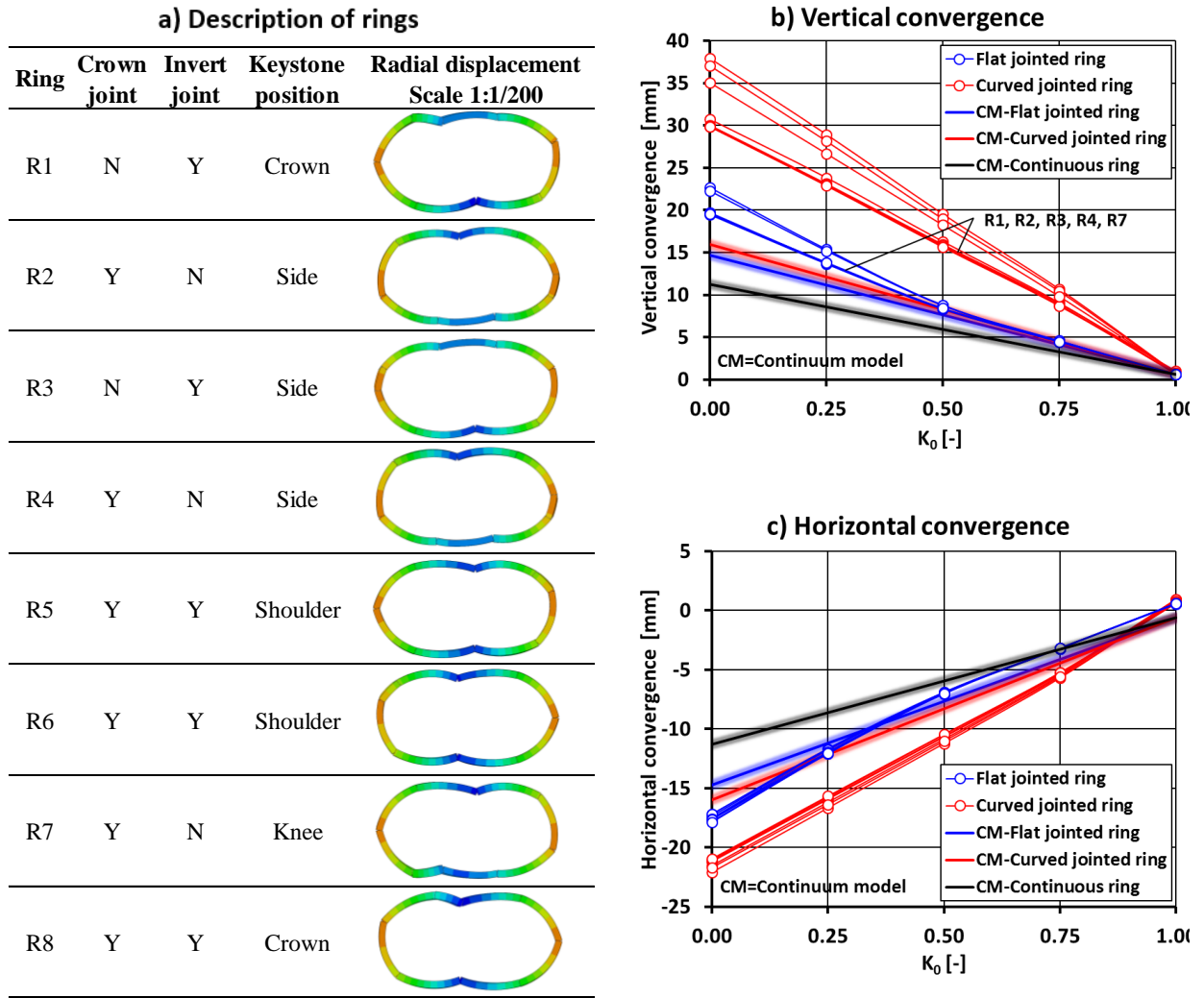


**Figure 4.5: Convergence in isolated rings**

Figures 4.6.a and 4.6.b illustrate the maximum inward and outward rotations of rings with flat and curved joints. The peak inward rotations take place at the joint closest to the vertical axis, and maximum outward rotations at the adjacent shoulder or knee.

When  $K_0 > 0.75$ , all flat joints are fully closed and joint rotations, radial displacements and ring convergence follow a linear pattern. At  $K_0 = 0.75$ , some joints begin to open, entering the non-linear branch of their rotational capacity curve. This progressive joint softening increases radial displacements (see Figure 4.4).

Isolated rings with curved joints present an almost perfectly linear behaviour for the full range of  $K_0$ , resembling their MR curves at serviceable rotations. Minor deviations may be caused by keystones with flat faces.

Overall, peak rotations are much larger in curved than flat joints. For example, when  $K_0 = 0$ , inward rotations are about 0.015rad and 0.0045rad in curved and flat joints respectively. Outward rotations are smaller but curved joints still rotate almost double than flat joints, 0.0075rad against 0.0035rad.

Despite this, the magnitude of gasket openings for both ring types is quite comparable, e.g. 0.5mm in flat joints as opposed to 0.7mm in curved joints at  $K_0=0$  (see Figure 4.6.c), given that the distance between the gasket and the joint neutral axis is smaller in curved than in flat joints (see chapter 2).

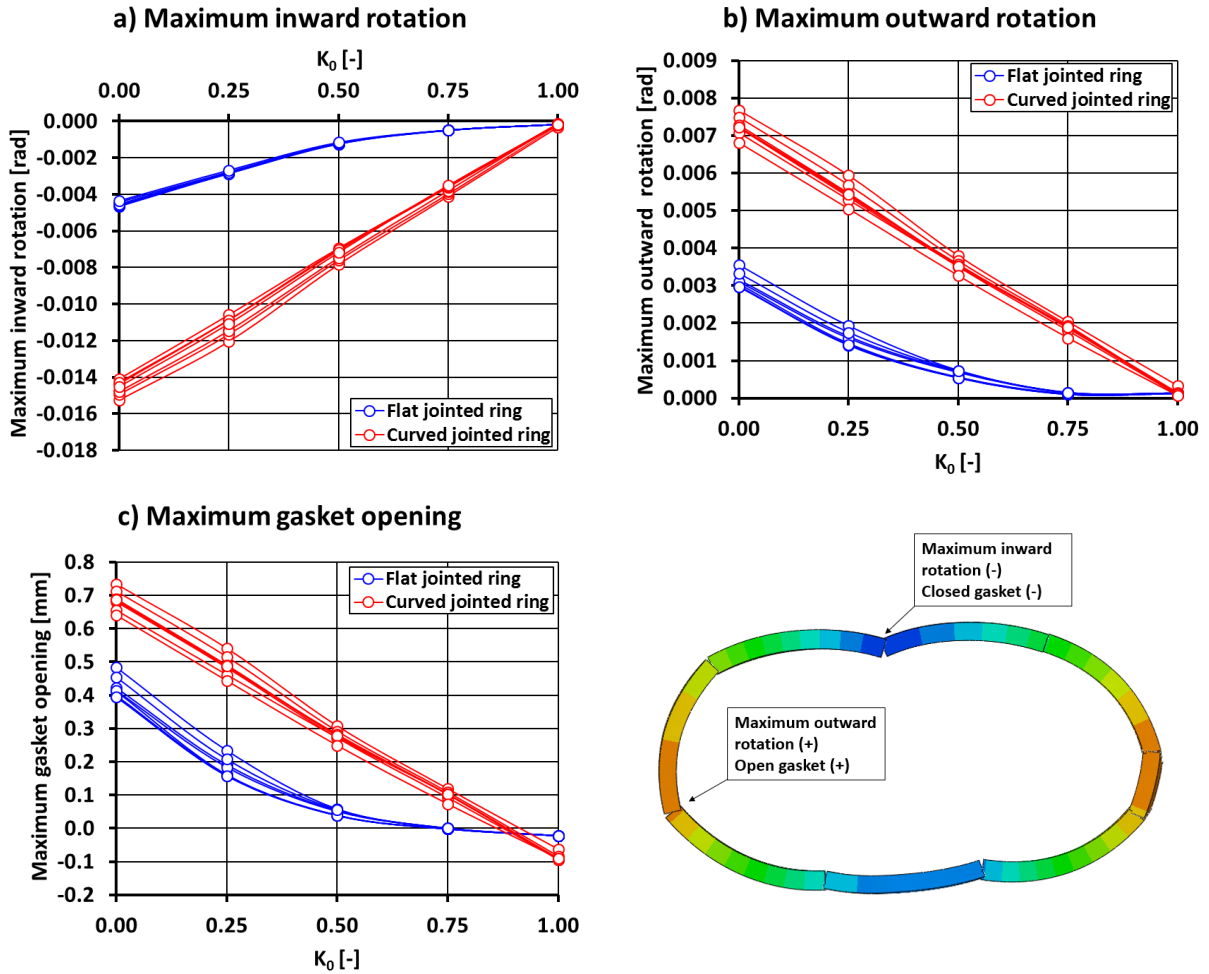


Figure 4.6: Joint behaviour in isolated rings

### 4.4.1.2. Lining forces

Figures 4.7.a and 4.7.b show that the maximum hoop moments occur within the segment bodies regardless of joint type. The moment capacity of curved joints is extremely low and, even for small ovalisation loads, the moment distribution is conditioned by the position of joints. Moments within the segments are only due to their own deflection and are therefore small, up to -40kNm/m. In flat jointed rings, the hoop moments depend on the ring rolling so that the rings with segments crossing the vertical axis experience peak values of -100kNm/m as opposed to -70kNm/m (see Figure 4.7.c).

Given the low bending moments experienced by the isolated curved jointed rings, the whole structure works almost in pure compression for the range of  $K_0$  examined. Conversely, with flat joints, peak tensile stresses invariably arise at the intrados of sections crossing the vertical axis and, like negative moments, are highly dependent on ring rolling. Again, segments centred with the vertical axis reach peak tensile strains of 3.5MPa.

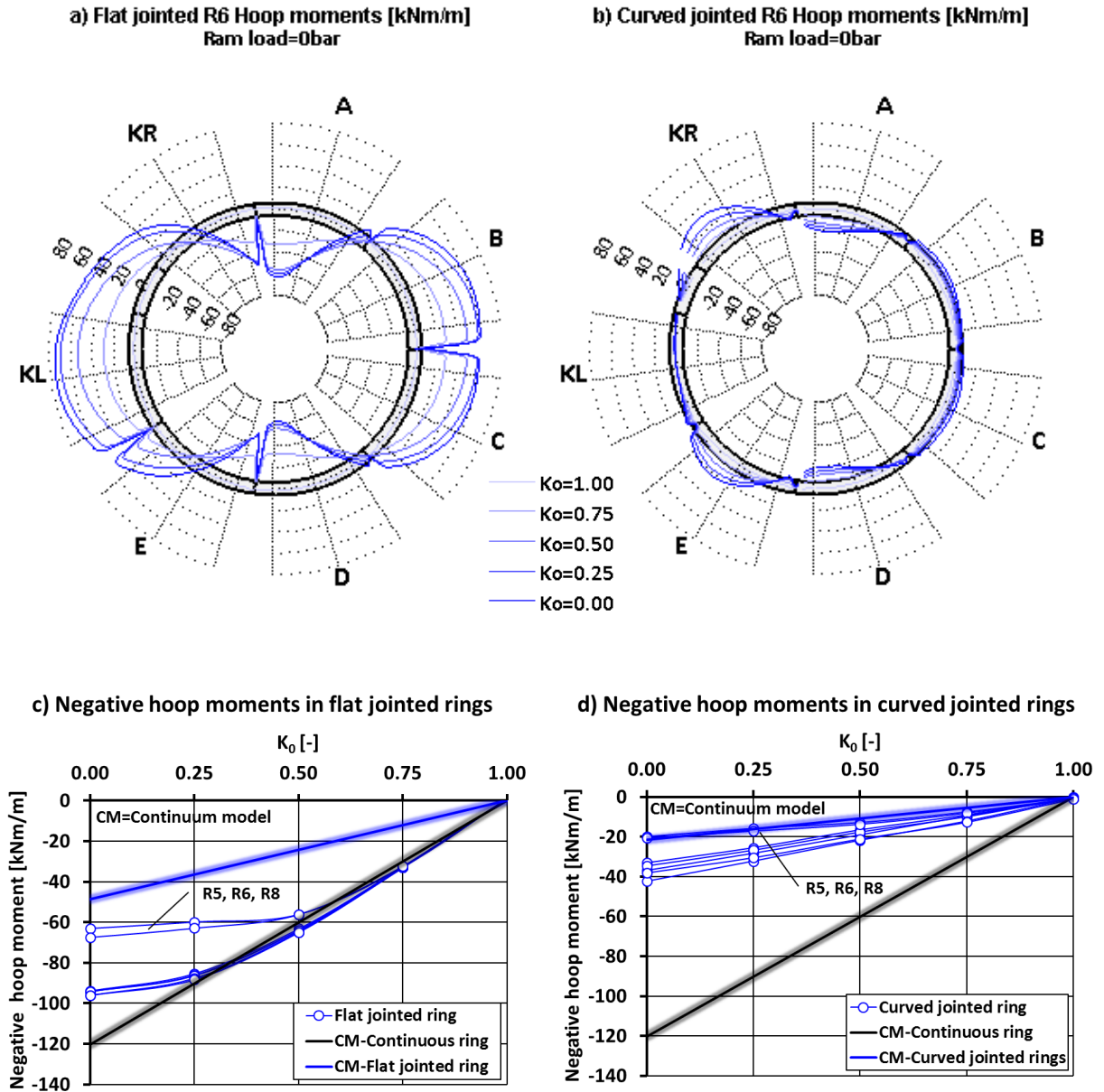


Figure 4.7: Internal forces in isolated rings

### 4.4.1.3. Ring misalignment

Ring misalignments are the result of disparities in the deformation of adjacent rings with different rolling (see Figure 4.5.a). Since the deformation mode of curved and flat jointed rings is analogous, ring misalignment profiles present similar patterns for both joint types. Maximum misalignments occur at the position of joints closer to the vertical axis where radial displacements are largest and sensitive to joint position. When joints and segment centres crossing the vertical axis are alternated, then peak misalignments reach their highest values (see Figure 4.8.a). The magnitude of lipping in circumferential joints is by far greater in curved jointed rings: whilst peak misalignments in flat jointed rings reach 3.5mm at  $K_0=0$  with the most onerous joint staggering, in curved jointed rings these approach 11mm.

### 4.4.1.4. Comparison with continuum model

The CM, even when applied with a smeared lining stiffness, tends to underestimate the convergence of jointed rings with low joint stiffness, i.e. curved joints or open flat joints (see Figure 4.5). The discrepancies are greater at the vertical axis.

Hoop moments are predicted well by the CM in curved jointed rings outside the influence zone of keystones and in flat jointed rings as long as the joints are not substantially opened, i.e. until  $K_0=0.50$  (see Figure 4.7). In the former case, the continuous ring is modelled with the smeared lining stiffness.

### 4.4.2. Coupled rings

#### 4.4.2.1. Coupling mechanism

The analyses confirm that the ring interaction entails the longitudinal migration of hoop forces and moments through coupling forces developed at circumferential joints. Coupling forces are shear forces concentrated at the position of packers and dowelled connectors, activated by, and opposing to, differential deformation between rings (see Figure 4.8.d). Ring misalignment, originated by the rotation of staggered joints, is prevented by pairs of radial coupling forces acting on adjacent rings in opposite directions.

The magnitude of radial coupling forces follows the pattern of misalignment between uncoupled rings (see Figures 4.8.a and 4.8.b). Peak values take place at those packers, or dowels, closer to crown or invert joints of a neighbouring ring. Consequently, the segments bend unevenly, exhibiting high concentration of lateral hoop moments where the peak coupling forces align with the overall ring deflection, i.e. for a squatted ring, inward and outward coupling forces at vertical axis and springline respectively.

The moments smoothen progressively towards the segment centreline as the effect of the coupling forces declines with distance. The peak moments are therefore experienced at the long sides of the segments.

When the joints of the neighbouring rings near the symmetry axes are alternated, the radial coupling forces at each ring side share the same distribution. However, if the adjacent joints adopt different positions, the distribution of coupling forces at each side may be different, which can induce torsion in the segments.

The ring interaction also influences the distribution of hoop compression through the development of tangential coupling forces at packers and connectors (see Figures 4.8.c and 4.8.d). For example, in a squatting tunnel, when the crown segment of a ring centred with the vertical axis cannot match the inward displacements of a neighbouring joint near the vertical axis, tangential lipping occurs at the circumferential joint. Similar to the mechanics of a guiding rod, the packers or connectors in the



misaligned region transfer tensile hoop stresses to the deflected segment, which decreases its total hoop compression.

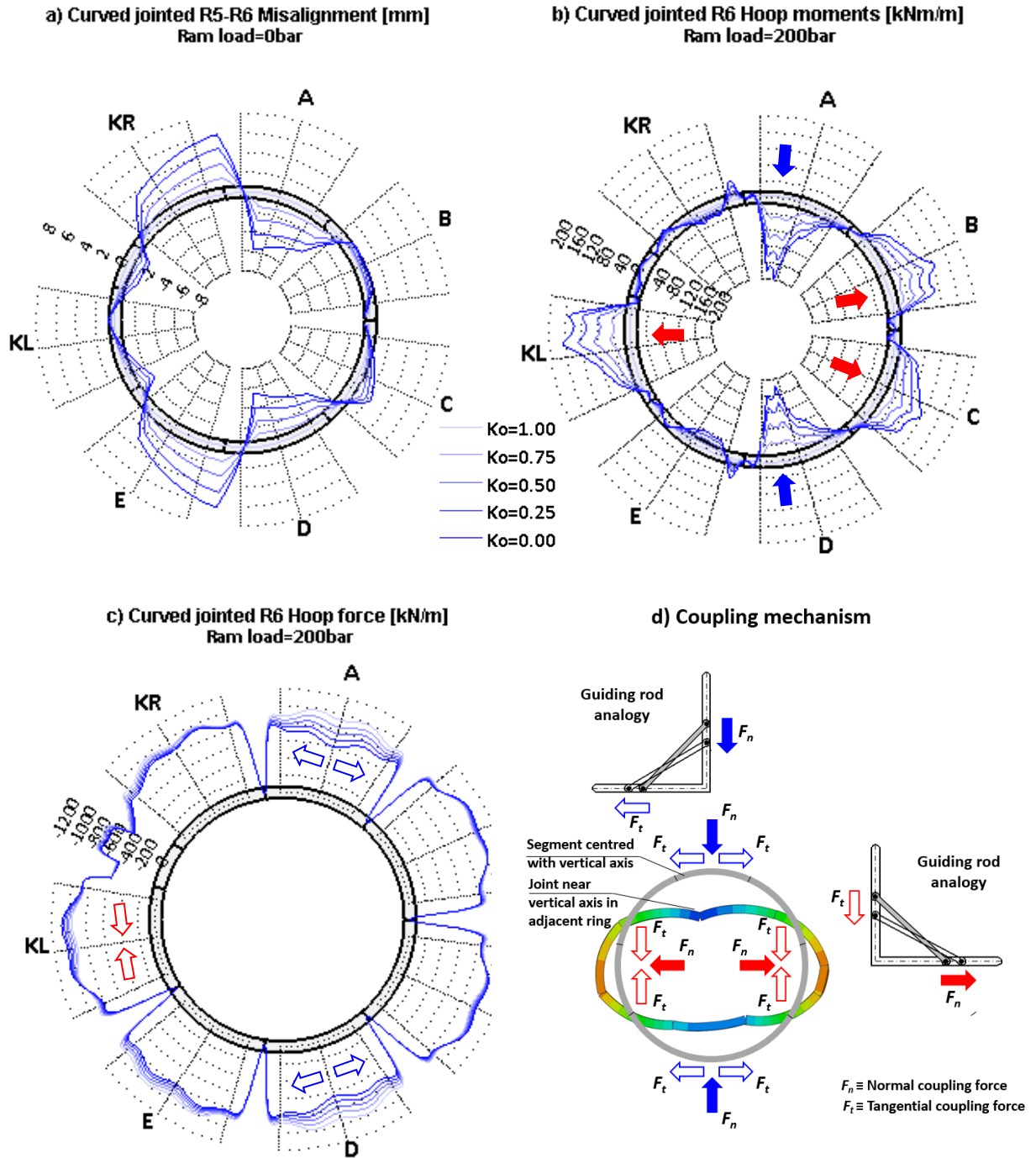


Figure 4.8: Coupling mechanism under ovalisation loads

### 4.4.2.2. Ring deformation

With robust coupling, the vertical and horizontal convergence reach similar values for both joint types (see Figure 4.9). In linings with curved longitudinal joints, the ring interaction can halve the vertical convergence, e.g. at  $K_0=0$ , it falls from 37mm to 20mm. Small longitudinal loads, up to 50bar/ram, are

able to produce significant reductions in vertical convergence, 75% of the total. The dowels are most active in the absence of ring interaction through packers, e.g. they can decrease the vertical convergence by 20% at null longitudinal loads. However, their action becomes negligible for longitudinal loads greater than 25bar/ram.

In flat jointed rings, the reduction in vertical convergence is minor, up to 25% from 22mm to 16mm, with the strongest ring interaction. The horizontal convergence is barely sensitive to ring coupling, particularly for flat joints. The action of dowels is in this case negligible.

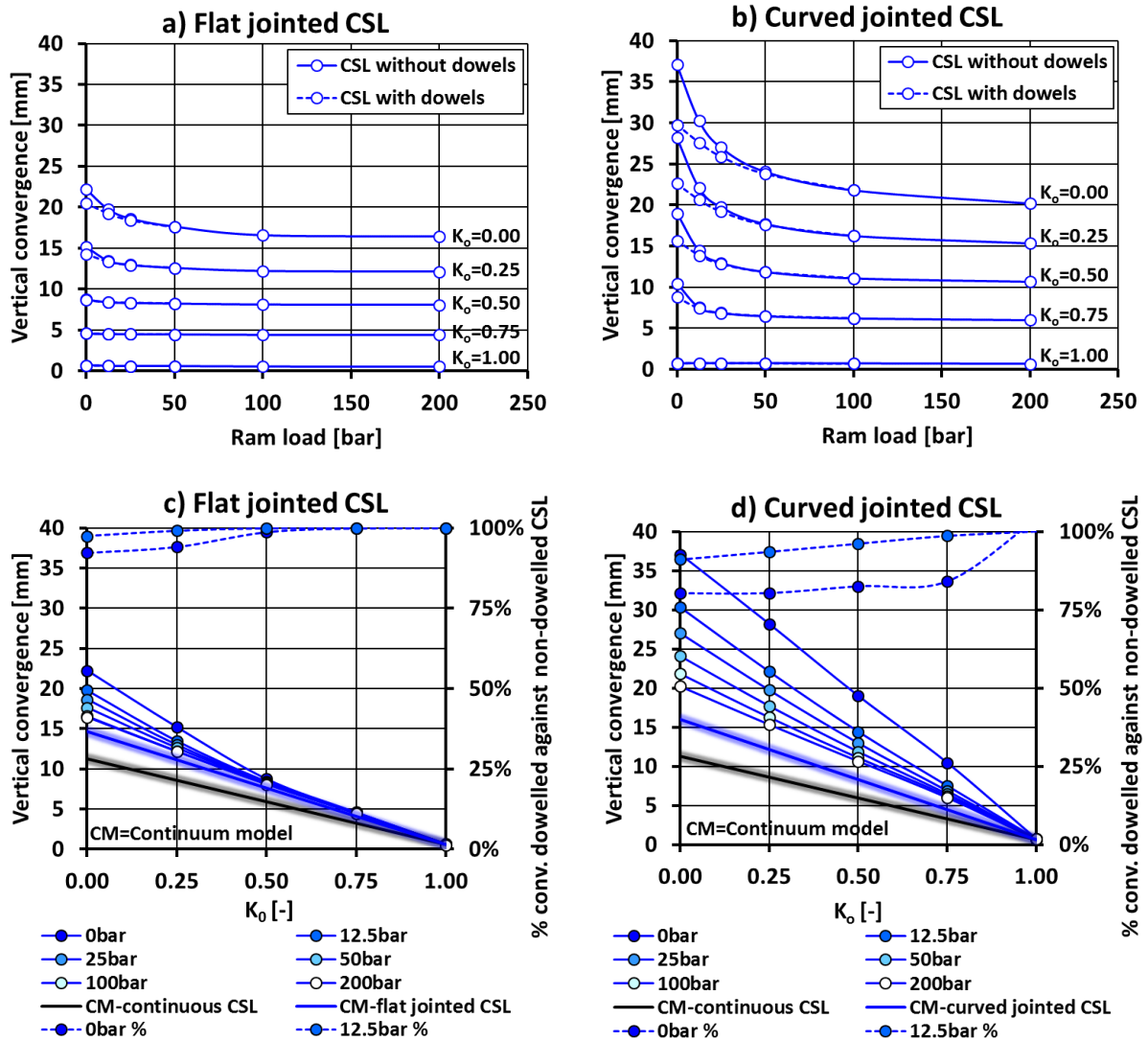


Figure 4.9: Coupled rings-Vertical convergence

### 4.4.2.3. Joint rotations

The maximum inward rotations of curved joints closest to the vertical axis are dramatically reduced with ring coupling (see Figure 4.10). At  $K_0=0$ , peak rotations decrease from 0.014rad to 0.0045rad when the longitudinal loads rise up to 200bar/ram. The benefits of ring interaction are more notable at low longitudinal loads but are still visible when these are further increased, e.g. from 100bar/ram to 200bar/ram and  $K_0=0$ , joint rotations become 0.001rad smaller. Conversely, dowels are only effective

against joint rotations for longitudinal loads up to 25bar/ram and at null packer compression can reduce total rotations by 70%.

With flat joints, the inward rotations are already small, i.e. the maximum peak value is 0.0045rad, and improvements caused by ring interaction are modest, reaching a plateau at longitudinal loads in the order of 50bar/ram. The effect of dowels on joint rotations in linings with flat jointed rings is negligible.

The same trends are observed for outward joint rotations, although total rotations are significantly smaller, 0.0075rad and 0.0035rad for curved and flat joints respectively. Despite curved joints roughly doubling the rotations of flat joints, again the magnitude of gasket opening is similar for both joint geometries, especially when ring coupling is involved.

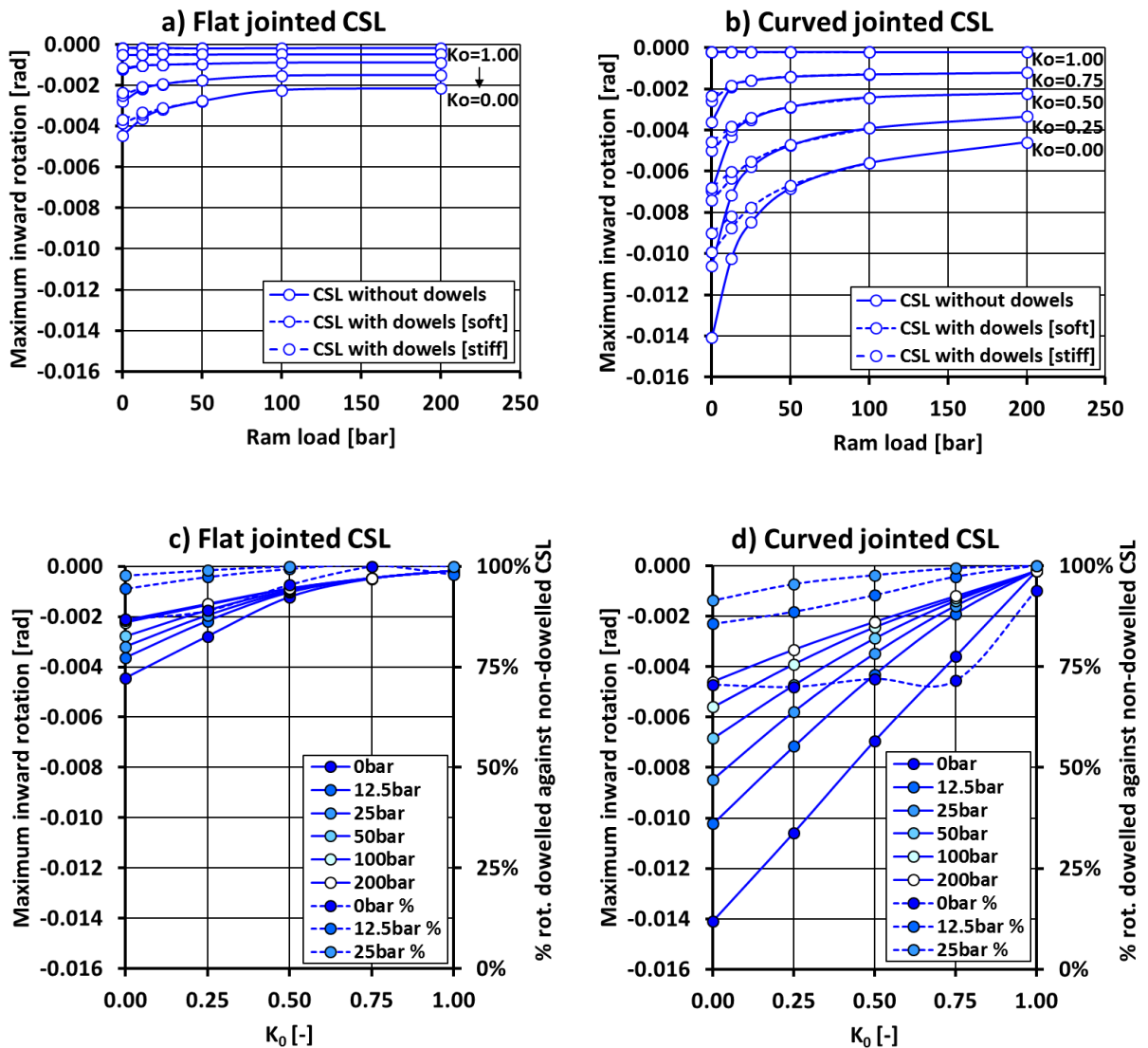


Figure 4.10: Coupled rings-Joint rotations

## 4.4.2.4. Ring misalignment

Ring coupling is extremely effective in limiting lipping at circumferential joints (see Figure 4.11). Rings subjected to high longitudinal loads experience ring misalignments in the order of 1mm for curved joints and 0.5mm for flat joints, which roughly correspond to a reduction factor of six against uncoupled rings. At low longitudinal compression, tunnels with curved joints can benefit substantially from the use of dowels, although joint lipping between rings subjected to high ovalisation loads can still be significant, i.e. 3mm for the most onerous conditions. In linings with flat joints, the uncoupled rings deform quite similarly due to the limited rotations experienced by longitudinal joints. In this case, the action of dowels is almost negligible even at null longitudinal loads.

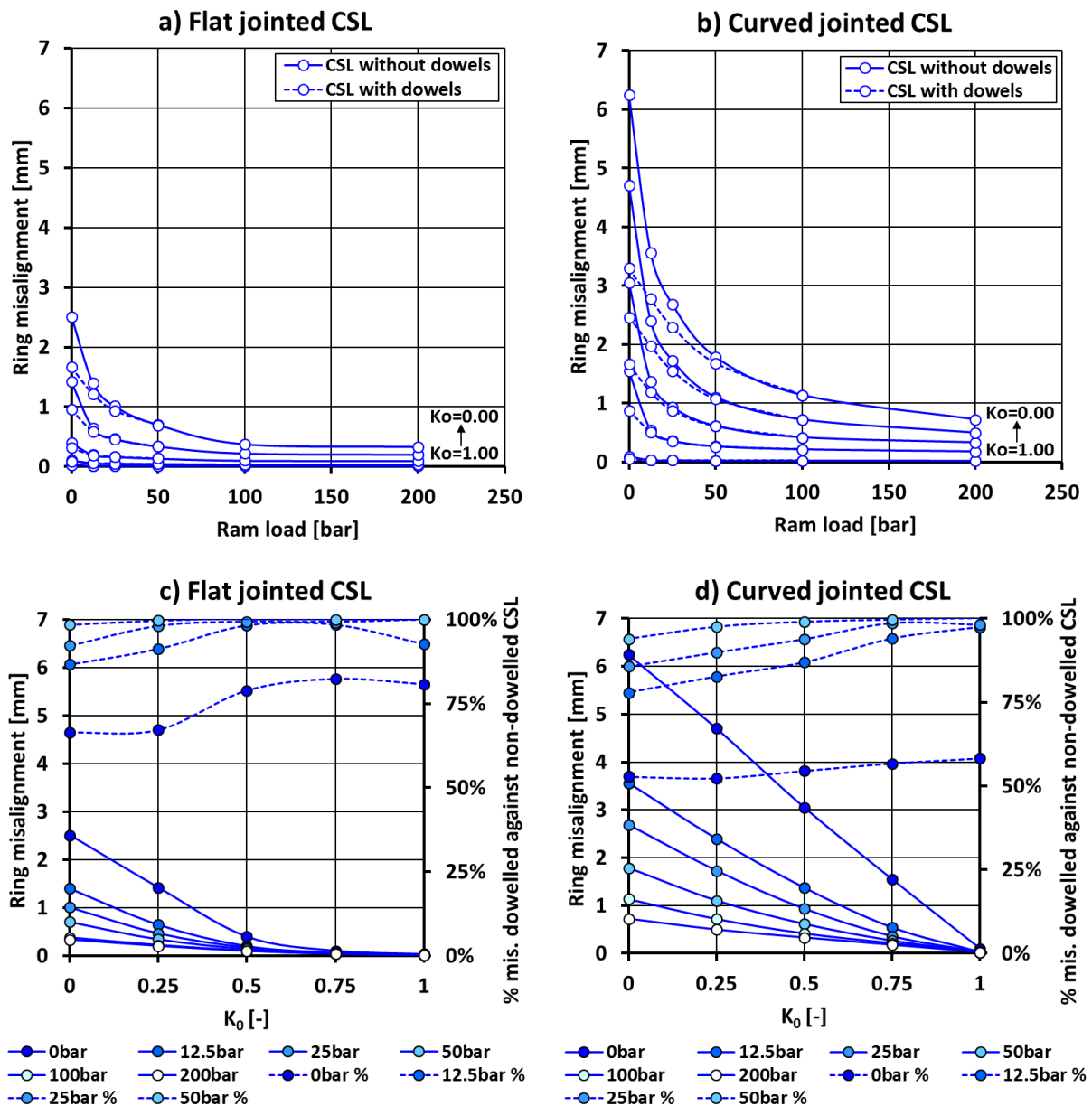


Figure 4.11: Coupled rings-Ring misalignment

### 4.4.2.5. Lining forces

In tunnel linings with curved longitudinal joints, the hoop moments are clearly governed by ring interaction given the limited moments developed in isolated rings. Figure 4.12.a shows that the -40kNm/m peak moments at the centreline of uncoupled rings with curved joints at maximum ovalisation are magnified to values in the order of -150kN/m when the longitudinal loads are 200bar/ram.

In flat jointed rings, the coupling forces also produce a significant increase in peak hoop moments, for example from roughly -70kNm/m to -140kNm/m at  $K_0=0$  (see Figure 4.12.b). At about 100bar/ram, the hoop moments reach a plateau denoting that ring interaction is fully developed.

Figures 4.12.c and 4.12.d present the peak hoop moments as a function of ovalisation. As explained in section 4.4.1, when flat jointed rings are uncoupled, the peak moments grow linearly with ovalisation until the joints open and the moments flatten. Ring coupling leads to a more uniform deformation of rings with staggered joints, which delays the opening of the flat joints.

The hoop moments increase progressively with ring coupling and reach an upper bound limit where the coupling capacity is fully utilised and the slipping of compressed packers becomes negligible. The system stiffness in fully coupled rings, i.e. with infinite longitudinal compression, remains constant. Like in the CM (see section 4.4.1.2), the upper bound limit is linearly proportional to the deviatoric pressures,  $(1-K_0)$ , with a constant of proportionality that depends on ground conditions and the lining flexibility ratio  $\alpha$ .

However, given the uneven distribution of bending stiffness within the CSLs, the moment envelope allows for peak moments greater than in the CM. The greater the disparities in stiffness amongst lining parts, the more dramatic the variations in hoop moments within the structure, and the higher the peak moments experienced.

The bending stiffness of closed flat joints is quite comparable to that of the lining cross section and hence the hoop moment envelope is not distant from the CM moments. Curved joints subjected to serviceable hoop compression are effectively hinges with null bending stiffness and demand for strong ring interactions to reach the upper limit state. Consequently, allowable peak moments in strongly coupled rings with curved joints are higher and the hoop moment envelope becomes wider.

The effect of dowels on hoop moments is only significant for longitudinal loads up to 25bar/ram in curved jointed rings (see Figures 4.12.a and 4.12.b). With dowelled connectors, the curve of maximum negative moments becomes of similar magnitude for rings with different joint type. Doubling the shear stiffness of dowels leads only to a minor improvement in ring interaction.

Maximum hoop tensile stresses take place at the intrados of those sections with peak negative moments, i.e. in crown or invert segments. Peak tensile stresses developed in strongly coupled rings

are hardly affected by joint geometry. For example, at the greatest ovalisation and longitudinal loads, tensile stresses at segment centreline are 8.4MPa and 7.3MPa for curved and flat jointed CSLs respectively. Tensile stresses at segment sides are influenced by the spalling stresses near packers which leads to tensile stresses of about 11MPa in both CSL types.

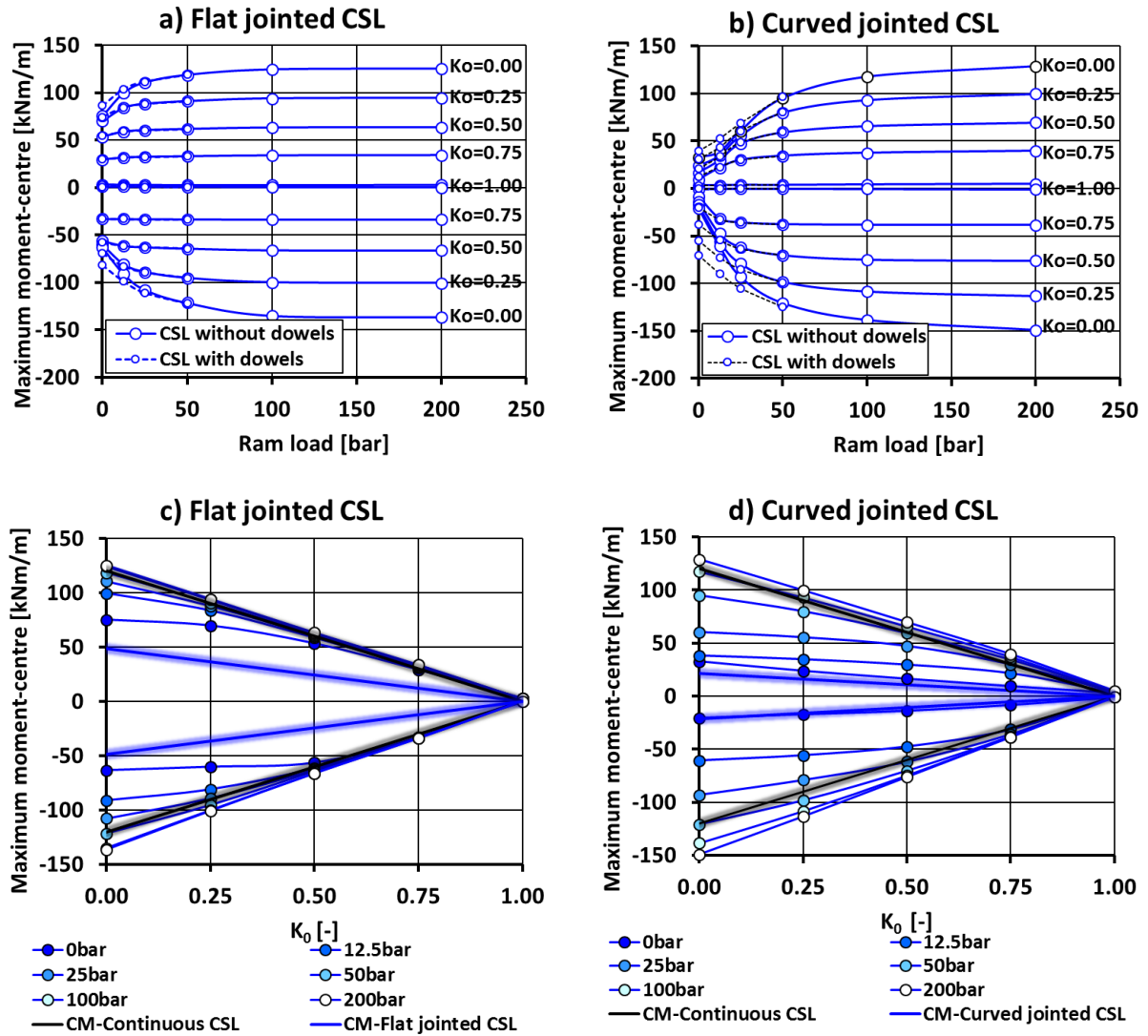


Figure 4.12: Coupled rings-Hoop moments at centreline

### 4.4.2.6. Comparison with continuum model

The ring interaction brings ring deformations closer to the CM predictions calculated with reduced lining stiffness (see Figure 4.9) at the expense of increasing the hoop moments (see Figure 4.12).

Given the linear correlation of hoop moments in both the CM and infinitely coupled CSLs with  $(1-K_0)$ , a CSL stiffness factor,  $f_{CSL}$ , can be defined as the ratio between CSL moment limits,  $M_{CSL}$ , and CM maximum moments in continuous linings,  $M_{CM}$ , subjected to the same ground conditions:

## 4.5. Global performance of CSLs with different joint geometry

$$f_{CSL} = \frac{M_{CSL}}{M_{CM}} \quad (4.7)$$

which is independent from  $K_o$ .

Figure 4.13 shows the evolution of  $f_{CSL}$  with the initial joint rotational stiffness ratio or the initial ring bending stiffness in soft and hard ground. In soft ground, the  $f_{CSL}$  is the greatest at joint rotational stiffness ratios close to zero, i.e.  $f_{CSL}=1.30$  and  $f_{CSL}=1.73$  at the ring centreline and sides respectively, and decays rapidly as the joint stiffness grows. In hard ground, the  $f_{CSL}$  exhibit higher peak values that decline gradually with stiffer joints. However, in this case the CM moments are small and therefore  $M_{CSL}$  is still minor.

It is also evidenced that, in CSLs with soft longitudinal joints,  $M_{CSL}$  at the ring sides can exceed by far those at the centreline, revealing that flexural concrete cracking will tend to initiate laterally.

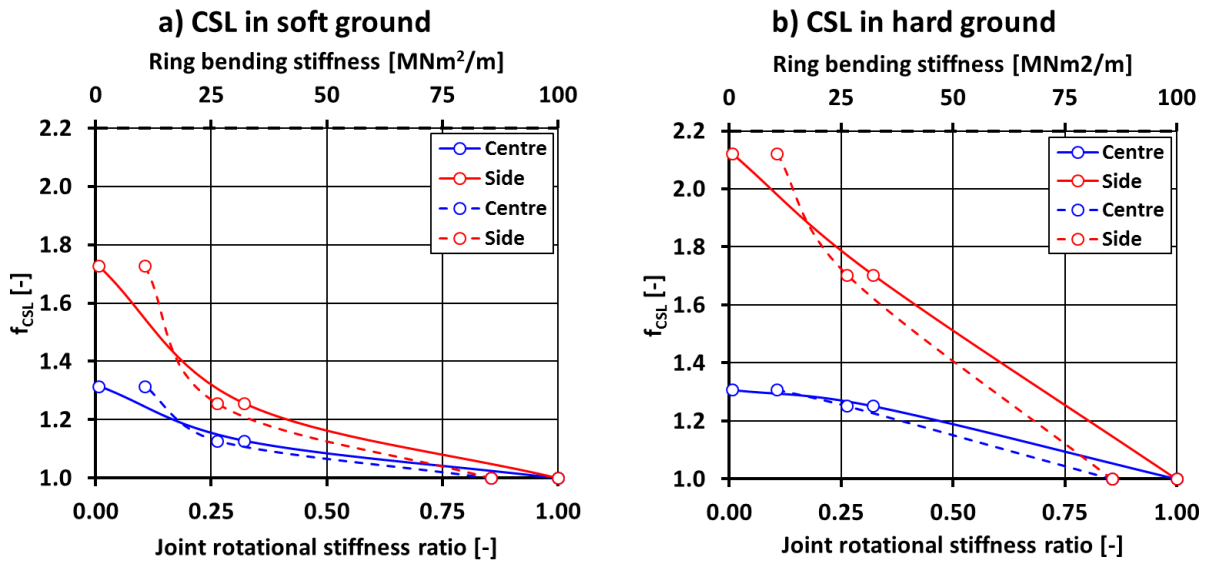


Figure 4.13:  $f_{CSL}$  in soft and hard ground

## 4.5. Global performance of CSLs with different joint geometry

The parametric study enabled the identification of domains indicative of CSL global performance in the longitudinal load-ovalisation (LLK<sub>0</sub>) space (see Figure 4.14). It follows from previous sections that the key indicators are lateral flexural cracking of segment bodies and ring misalignment.

Curved jointed CSLs may not be recommendable in watertight tunnels excavated in soft ground subjected to high ovalisation and small longitudinal loads, particularly if the gasket tolerance to ring misalignment is very low. The initial longitudinal pre-stressing of CSLs relaxes with time (see chapter 6), which can aggravate water leakage at circumferential joints. The provision of shear dowels can expand the scope of use of curved jointed CSLs to less favourable long term conditions.



The flexural tensile stresses of segments delimit the usability of CSLs subjected to high ovalisation and high longitudinal loads, the latter load being representative of short term conditions. Limit curves of both flat and curved jointed CSLs are similar, particularly when  $f_{ct}$  is low. Curved joints may be more advantageous in soft ground CSLs with  $f_{ct} > 7\text{MPa}$  when subjected to high ovalisation and medium longitudinal loads, as long as the tunnel remains watertight.

In hard ground conditions, both joint geometries are suitable for the full range of long term general conditions examined, with only minor ring misalignment restrictions in curved jointed CSLs when there is no ring interaction.

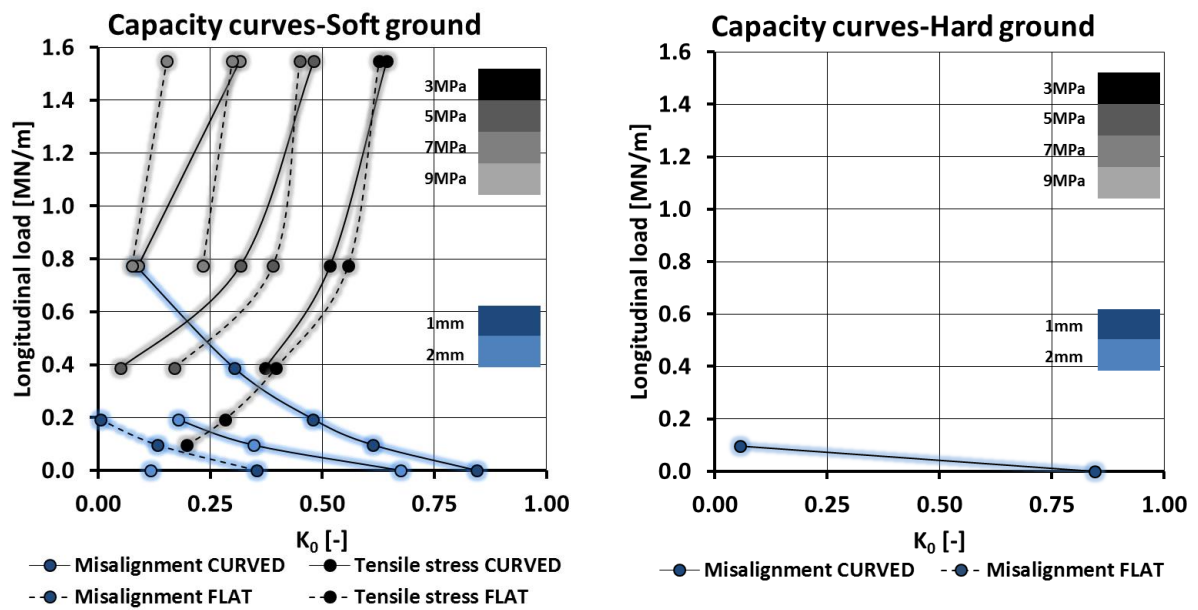


Figure 4.14: Global performance of CSLs with different joint geometry

## 4.6. Conclusions

### a) Isolated rings:

The geometry of longitudinal joints has an impact on the structural behaviour of isolated rings, i.e. ring deformation, lining forces and ring misalignment. The most relevant aspects in lining performance to ensure a competent and durable structure are the integrity of the segment body and watertightness. From a global perspective, the study of the isolated rings' structural response working under a wide range of ovalisation loads has revealed that, of all indicators representative of lining performance in the long term, flexural tensile stresses (or strains) and ring misalignment are the most affected by joint geometry. Although the vertical ring convergence is also influenced by the moment capacity of joints, it is assumed that it might be of importance only for tunnels with specific functions, such as railway tunnels, so they are omitted from the assessment.



Curved jointed rings have the advantage of dramatically reducing flexural tensile stresses in segments, but ring misalignments can become prohibitive when subjected to high ovalisation. Conversely, the main concern regarding isolated rings with flat joints working under high ovalisation loads lies on the flexural cracking of concrete segments.

The ring rolling of isolated rings where crown or invert segments are centred at the vertical axis yields the greatest negative moments in segments, particularly in flat jointed rings. Squatted rings with alternating segments centred with the vertical axis and joints near the vertical axis lead to peak ring misalignments.

The CM solution underestimates ring convergence and gives a good estimation of maximum hoop moments for flat jointed rings without substantial joint opening and for curved jointed rings, in the latter case when applied with the smeared lining stiffness.

### ***b) Coupled rings:***

Vertical convergence, joint rotations and ring misalignment of curved jointed CSLs are very sensitive to ring coupling through either compressed packers or dowels, particularly when subjected to high ovalisation loads. In flat jointed rings, the impact of effective ring interaction is much lower.

In both curved and flat jointed CSLs, the vertical convergence approaches the CM predictions with ring coupling. The upper limit of CSL hoop moments at infinite ring coupling is linearly correlated with the CM peak moments through a CSL stiffness factor  $f_{CSL}$  that is independent from  $K_o$ . The  $f_{CSL}$  is the greatest for the ring sides of curved jointed CSLs and is inversely related to the longitudinal joint stiffness.

At low longitudinal loads up to 25bar/ram, curved jointed CSLs can benefit significantly from the shear reaction of dowels. However, ring misalignments may still remain excessive depending on the required degree of watertightness. The reduction in lipping of circumferential joints is not linear with dowel shear stiffness.

### ***c) Scope of use of joint geometries:***

The selection of joint geometry has an impact on the risk of excessive ring misalignments and flexural cracking in CSLs excavated in soft ground. i.e. tunnel systems with at least moderate  $\alpha$ .

Overall, the CTT study revealed that curved joints may undermine long term watertightness of soft ground tunnels subjected to high ovalisation loads. Dowels can expand the use of curved joints to somewhat less favourable long term conditions. Flat jointed CSLs in soft ground subjected to high ovalisation loads may require the use of concrete with high  $f_{ct}$ .

## Chapter 5

# Thames tunnel SHM deployment study

### 5.1. Introduction

The CTT SHM system installed by Cambridge University in collaboration with Crossrail Ltd and Hochtief Ltd was first conceived as a research tool to gather CSL field monitoring data at the CTT. The CTT field trials were conducted in consecutive phases for about a year starting in November 2013. The purpose and objectives were refined and expanded throughout all the monitoring project stages, from planning through installation to interpretation of the sensed data.

The CTT monitoring project was regarded by the University of Cambridge and Centre for Smart Infrastructure and Construction (CSIC) as a research opportunity to test BOTDR distributed strain sensing with embedded fibre optic (FO) sensors in CSL tunnel monitoring. FO SHM methods have emerged in the last few decades and many research efforts have been made to develop their practical use in geotechnical applications (CSIC, 2016). This monitoring project belongs to a suite of case studies which showcase the DFOS capabilities and develop solutions for in situ deployments.

The CTT field trials were also part of a research project with the intent to investigate in situ CSL behaviour, and as such, it was designed to produce field monitoring data on ring deformations in a CSL tunnel subjected to different conditions: (i) mechanised tunnelling with simultaneous backfilling; (ii) short term action of permeable chalk with tidal fluctuations in water level; and (iii) construction of adjacent cross passages.

Webb et al. (2015) proposed a system categorisation for SHM deployments drawn on their ultimate purpose, where superior categories might provide greater benefit at the expense of higher complexity in producing valuable information. Following Webb's classification system and the objectives fulfilled in this research work, the CTT deployment falls within (i) Category 2-Sensor deployment studies and (ii) Category 3-Model validation, and provides examples of (iii) Category 5-Damage detection.

In this chapter, the CTT SHM deployment study is explained, the field data processing methods specific to CSL are discussed and the strain sensing techniques evaluated. First, the non-conventional monitoring technologies deployed are described. Second, the original proposal inherited by the author is summarised. Third, the CTT SHM system and implementation plan finally adopted are detailed. The main challenges faced during the installation works are reviewed and lessons learnt reported for future SHM deployments in CSLs of a similar type. Fourth, the data processing is tackled with particular attention to the effect of temperature changes on mechanical strains and curvatures. Finally, the BOTDR

## 5.2. Background on applied sensing technology

deployment study is completed through a comparative assessment of field data quality against vibrating wire strain gauges (VWSGs). Examples of BOTDR damage detection are also presented.

### 5.2. Background on applied sensing technology

#### 5.2.1. BOTDR technique

BOTDR is a distributed sensing technique that exploits the linearity of measured Brillouin frequency shift (BFS) with strain and temperature changes in FO sensors. When a pump pulse with a given wavelength  $\lambda$  propagates through a silica fibre, the signal attenuates with time as a result of light being backscattered through the optical fibre. If the pump pulse has sufficient intensity, the phenomenon of inelastic Brillouin scattering is triggered by the interaction of thermally excited acoustic waves in the silica fibre, i.e. phonons, with the pump signal (Glišić and Inaudi, 2007). The Doppler effect caused by the phonon periodic motion gives rise to both Stokes and anti-Stokes Brillouin Gain spectra (BGSs) (Rogers, 1999) with a frequency shift  $\nu_b$ , i.e. frequency at BGS peak intensity, equal to:

$$\nu_b = \pm \frac{2n_s \nu_a}{\lambda} \quad (5.1)$$

where  $n_s$ =refractive index of silica medium;  $\nu_a$ =acoustic velocity in silica fibre; and  $\lambda$ = pump pulse wavelength. The acoustic velocity  $\nu_a$  of phonons is inversely related to the density of the solid medium, which in turn is inversely related to strain and temperature in the optical fibre. Thus, the BFS at a position  $z$  along the optical sensor,  $\nu_b(z)$ , can be expressed with Eq. 5.2:

$$\nu_b(z) = \nu_{b0} + M_v \varepsilon(z) \quad (5.2)$$

where  $\nu_{b0}(z)$  is the BFS at zero strain and reference temperature;  $M_v$  is a constant of proportionality and  $\varepsilon(z)$  is the total strain increment in the fibre at position  $z$ .

In BOTDR systems, like in Optical Time Domain Reflectometers (OTDRs), backscattered BGSs are detected as a function of the time  $T_s$  taken for a pump pulse to propagate to and back from a certain position  $z$  along the optical fibre. BGSs are measured by scanning a range of beat frequencies at a given frequency interval (Brown et al., 1999; Li et al., 2015). Through the frequency sweep method (Li et al., 2015), measurements at each BGS frequency data point are repeated by the selected average count and averaged. The position  $z$  in the optical sensor corresponding to time  $T_s$  can be derived from Eq. 5.3:

$$z = \frac{c_s T_s}{2n_s} \quad (5.3)$$

where  $c_s$ =speed of light in a vacuum and  $T_s$ =the cycle time. Given that the pump signal is injected with a pulse width  $W_b$ , the BGS at position  $z$  and time  $T_s$  encompasses the light backscattered in a preceding fibre section of length  $L_g$ , named spatial resolution, which can be obtained from Eq. 5.3 with  $T_s=W_b$  (Brown et al., 1999). Thus, the spatial resolution  $L_g$  is the gauge length characteristic of BOTDR reflectometers.

## 5.2. Background on applied sensing technology

---

Phonons have a lifetime in the order of 10ns (Brown et al., 1999), and if the total strain in an optical fibre is uniform, the phonon exponential decay with time results in BGS shapes that fit a Lorentzian curve (Zhao et al., 2014). The conventional method of peak gain detection is a single peak-fitting method that calculates the centroid of a least-square fit curve to BGS spectra (Deif et al., 2010; Brown et al., 1999). Quadratic fitting of Brillouin spectrum is commonly implemented in algorithms of BOTDR systems (Li et al., 2015; Soto and Thévenaz, 2013).

It follows that, with the single-peak method, the average total strain measured at  $z$  by the centroid frequency coincides with the local strains experienced within the spatial resolution  $L_g$  as long as axial strain gradients within  $L_g$  remain constant, including uniform total strains with zero gradient (Shang et al., 2009). However, the differential strain within the spatial resolution broadens the Brillouin spectrum with significant decay of the peak power gain. The drop in signal intensity limits the length of optical sensor, and wider BGSs hamper the identification of the BFS which in turn increases random errors in total strain measurements (Shang et al., 2009). Total strain profiles with variable gradient within the spatial resolution result in both asymmetric and broadening Brillouin spectra (Deif et al., 2010), breaking the identity between average and local strains. In this case, systematic errors must be added to random errors in the accuracy of strain measurements.

The physical principles underlying the BOTDR technique limit the maximum spatial resolution achievable at acceptable measurement accuracy. With a fine spatial resolution, systematic errors induced by variable true strain profiles can be reduced in detriment of random errors, which increase due to weaker Brillouin scattering (Brown et al., 1999). In strain profiles with constant gradient, there is a trade-off between random errors originated by differential strains in coarse spatial resolutions and random errors caused by weakening and broadening of Brillouin scatter with fine spatial resolutions (Shang et al., 2009). In general terms, the maximum spatial resolution  $L_g$  of 500mm has been proven to be feasible in current sensing applications (Brown et al., 1999), which makes BOTDR systems very suitable for global structural rather than local material monitoring, particularly in inhomogeneous materials such as concrete.

Nonetheless, recent research efforts have focused on the development of advanced signal processing methods with the view to enhancing the spatial resolution of total strain measurements in strain profiles with either gradual changes or step variations as in cracking concrete (Murayama et al., 2005; Brown et al., 1999; Deif et al., 2010; Li et al., 2016; Li et al., 2015; Kim et al., 2002).

There are other input parameters in BOTDR operations which have an impact on measurement uncertainty of total strains. Soto and Thévenaz (2013) proposed a propagation error equation to characterise measurement errors of centre frequencies computed with the quadratic-least square fitting method and under uniform total strain conditions. Frequency errors were inversely proportional to

signal-to-noise ratio (SNR) and directly proportional to the square root of frequency sampling step and the full width at half maximum (FWHM), i.e. broadening of Brillouin scatter.

The SNR can be improved by increasing the average count of swept frequencies, although systematic errors may be amplified by longer acquisition times if true strains are time-varying. Smaller frequency intervals in spectral analysis can help to reduce uncertainty in the computation of BFS, but may require again longer acquisition times. Soto and Thévenaz (2013) suggested, however, that using larger frequency intervals with a greater number of time averages may be more time effective.

Finally, cumulative power losses due to attenuation or fibre discontinuities such as splices, connectors or macrobends result in lower SNR and greater FWHM, doubly degrading the quality of centre frequency measurements. In field applications with demanding optical budgets, i.e. low total power losses in the optical circuit, the pump power can be increased to improve repeatability as long as nonlinear effects are not triggered.

### 5.2.2. MEMS tilt sensors

Micro-electro-mechanical system (MEMS) instrumentation was introduced in geotechnical monitoring in the late 2000s (Dunnicliff, 2008). Since then, multiaxial MEMS accelerometers have been deployed in applications such as inclinometers, tiltmeters and tilt beams. Within the MEMS accelerometer family, RST instruments have developed a profile monitoring system for CSLs which works on the principle of the Basset convergence system (Bassett, 2012) and measures tilt changes in segments in two vertical planes, one comprising a ring cross-section and another parallel to the tunnel axis.

The advantages of MEMS accelerometers are their small size, long-term stability, high linearity and angular accuracy within operating ranges (Sheahan et al., 2008). MEMS tilt sensing in tunnel profile monitoring systems enables the possibility of measuring segment rigid body movements soon after ring erection without interference with the TBM envelope.

## 5.3. Original proposal

The original design proposal inherited by the author envisaged the monitoring of four rings at the CTT twin-tunnel (see Figure 5.1), which was driven in chalk under the river Thames. The topography and geology varied along the route, with overburden depths ranging between 12.8m to 20m. At the centre of the river channel, and tunnel deepest point, the weathered chalk had been partially excavated to facilitate fluvial traffic in the past. The channel was later refilled with river terrace deposits and alluvium clay, leaving an overburden depth of chalk of only 4m. Figure 5.2. presents the tunnel cross-sections at the location of the instrumented rings.

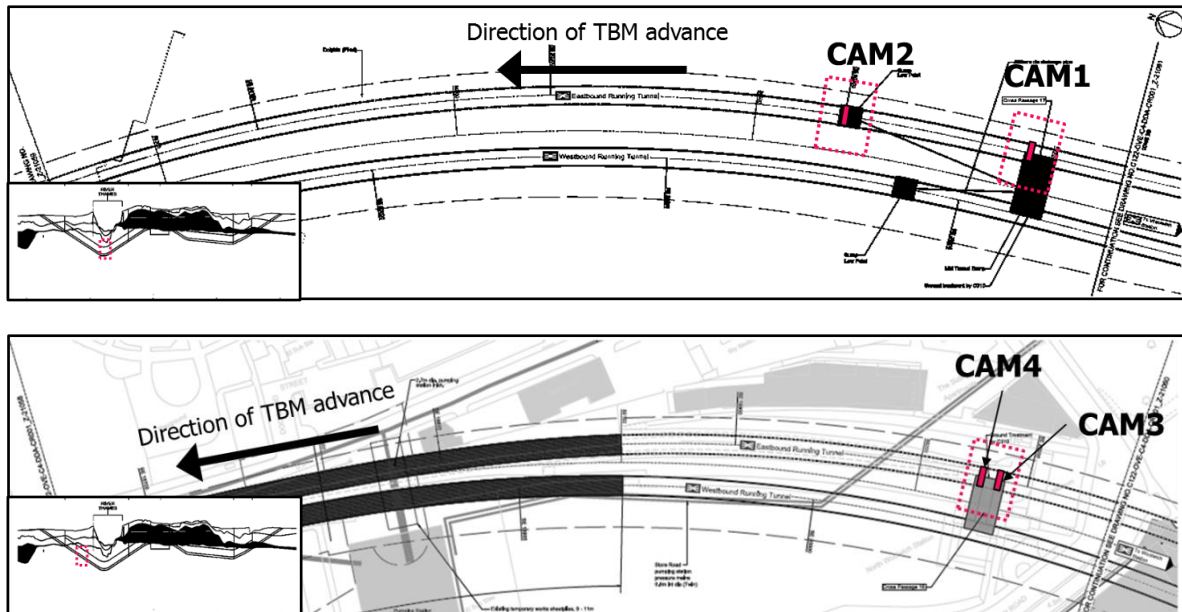


Figure 5.1: Location of CTT instrumented rings

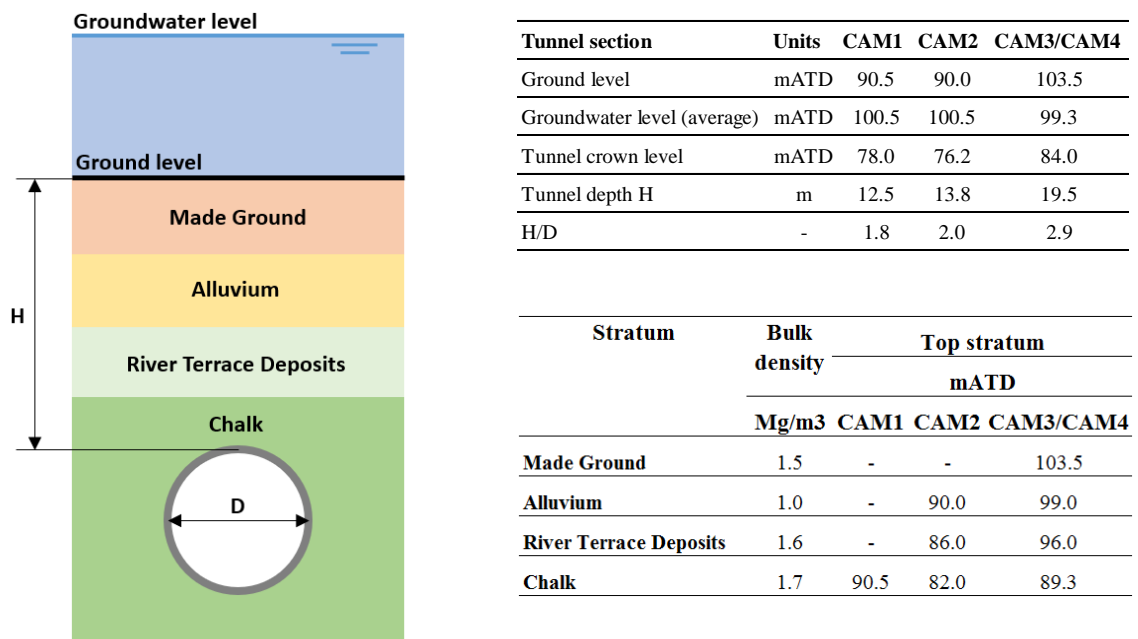


Figure 5.2: Tunnel cross-sections at instrumented rings

The original proposal projected the strain monitoring of ring segments in the hoop direction with parallel topology by deploying BOTDR sensing in all segments except the keystone and embedment VWSGs in four segments per ring (see Figure 5.3). Separate strain and temperature DFOS ring circuits were to be completed immediately after ring erection in what was assumed to be a quick connection of segment sensors with novel Diamond ODVA connectors, which in turn would have been previously spliced to the sensors' ends. The DFOS and VWSG cables of each instrumented segment would be terminated in cast-in box outs connected to channels that would enable the completion of the sensing circuits.

## 5.3. Original proposal

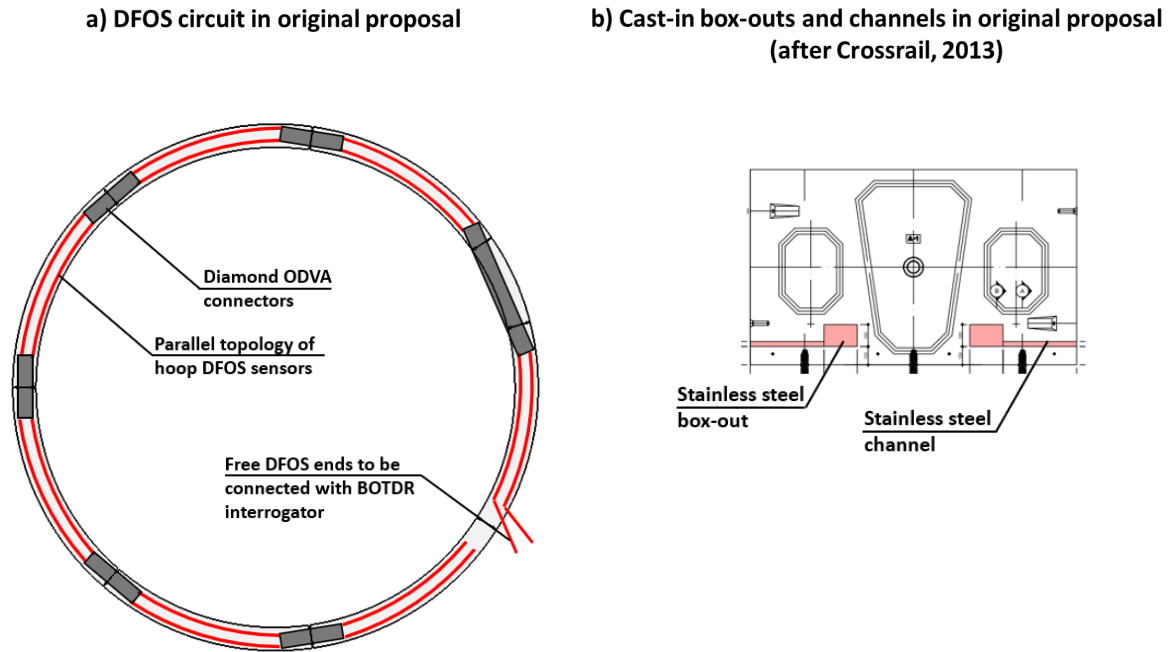


Figure 5.3: Original proposal

The CAM1 and CAM2 segment instrumentation proceeded in Shay Murtagh's concrete plant in November 2013 in accordance with the above design concept, each DFOS terminated in short ends that were to be spliced to the ODVA connectors. The author contributed to the segment instrumentation works as part of the Cambridge team, with four members. The author also proposed the location of three of the four instrumented rings at cross passages to capture ring behaviour during tunnelling and cross passage construction with the same instrumented rings; and designed the instrumentation layout, which enabled strain measurements in the longitudinal direction and the identification of rational primary sections (see section 5.4.4).

Subsequent in-house laboratory tests demonstrated that power losses induced by the ODVA connectors were excessive for the proposed ring circuits,  $\approx 0.7\text{dB}/\text{connector}$  in a laboratory environment, and highly sensitive to dust and dirt, leading to the conclusion that they were not sufficiently robust or reliable for a construction environment (Colton, 2013). When the replacement of such connectors with conventional arc fusion splices was proposed to the main stakeholders, Crossrail and HMJV raised their Health and Safety concerns on performing splicing activities near the tail skin.

In addition, there was no provision in the proposal for the integration of the SHM requirements with the constraints imposed by the TBM passage and tunnelling activities and the harsh environment of a tunnel site constructed with a slurry TBM.

Following a stakeholders' meeting on 18<sup>th</sup> December 2013, it was agreed that a new design solution was to be developed on the principles that (i) all splicing within the tunnel was to be conducted in a safe work area, i.e. the first TBM bridge gantry; and (ii) the duration of the installation works within the tunnel requiring the interruption of the TBM advance was to be minimised. The above principles entailed

a profound change in the design process from system requirements analysis onwards with the constraint that all DFOS lengths had already been cut and CAM1 and CAM2 segments instrumented in accordance with the original proposal.

### **5.4. CTT SHM system**

Best-practice guidance and worldwide expertise confirm that the success of monitoring projects relies on adequate planning and design (BTS, 2011; Dunnicliff, 1993). The monitoring process should follow a rational approach from inception up to detailed specification of installation procedures, data collection and interpretation, which should ideally be completed prior to any installation works (Dunnicliff, 1993). For clarity, the description of the adopted SHM system presented here follows the key steps in planning a monitoring program (Dunnicliff, 1993; BTS, 2011) relevant for research monitoring projects. Unfortunately, such systematic approach was not fully implemented in the CTT case study (see section 5.3 and 5.4.6.4). Planning activities and design decisions inevitably concurred with the instrumentation works, which compromised project risk. The lessons learnt are explained in section 5.4.6.4.

#### **5.4.1. Stakeholders**

Table 5.1 summarises the stakeholders engaged in the SHM project with direct participation on monitoring tasks. The author managed the Cambridge team from December 2013 onwards and was responsible for the completion of the monitoring program in cooperation with the other parties involved. The team composition changed with time: three university staff members and students for the CAM3 and CAM4 segment instrumentation works at Shay Murtagh's concrete plant (phase 1); two Spliceteq staff members in average for the works undertaken at Crossrail's site yard (phase 2) and one Spliceteq employee for the works conducted within the tunnel (phase 3). All the planning, design, procurement and coordination with stakeholders required to develop and deliver the physical architecture and implementation plan described hereafter were undertaken by the author, except for the features inherited from the original plan. The author was also a full-time member of the site team undertaking the installation works in all the phases.

The monitoring plan was thoroughly coordinated with Crossrail and the construction contractor, HMJV, with the imperative of Health and Safety and Fire Safety regulations compliance and the prerogative of minimising disruptions to construction activities on site, particularly TBM tunnelling. Modifications in segment design required to facilitate instrumentation were consulted with the lining designer, ARUP, for structural integrity and with the concrete segment plant, Shay Murtagh, to ensure easy manufacture, as part of the original proposal. The specialist subcontractor, Spliceteq, contributed with their expertise in FO installations to the adoption of a technical solution satisfactory to all stakeholders. Other parties with no direct interest in the field monitoring trials such as FO manufacturers (OFS Ltd), instrument



## 5.4. CTT SHM system

---

distributors (Geosense Ltd) and BOTDR analyser manufacturer (Neubrex Ltd) were consulted during the planning stage of this monitoring program.

The installation of the CTT SHM system was achieved by a joint effort of Cambridge University with Spliceteq Communications Ltd. HMJV actively supported instrumentation and data collection through the provision of access, specific machinery and human resources when required and reasonably practicable.

Table 5.1: CTT SHM stakeholders

Task	CTT SHM Stakeholders					
	Crossrail	Cambridge University	Specialist subcontractor (Spliceteq)	Construction contractor (HMJV)	Lining designer (ARUP)	Concrete segment manufacturer (Shay Murtagh)
Plan monitoring program	•	•	•	•	•	•
Procure instruments and make factory calibrations		•				
Install instruments		•	•	•		•
Maintain and calibrate instruments on regular schedule		•				
Establish and update data collection schedule		•				
Collect data		•		•		
Process and present data		•				
Interpret and report data		•				

### 5.4.2. Selection of parameters

#### 5.4.2.1. Total strains in concrete segments

The prerequisite that DFOS sensing was to be tested in CSL structures automatically determined strain as a primary measurand in lining response characterisation. Nevertheless, strain measurements are predominant over stress measurements in SHM systems targeting CSL structural response, partly because of limitations in stress sensing performance (Dunnicliff, 1993), but also due to the versatility of strain measurements in data interpretation.

Pressure cells are insensitive to tension, cumbersome to install and rarely ensure an effective contact with the surrounding concrete (Dunnicliff, 1993). Conversely, strain sensing instruments enable measurements of tensile and compressive strains, and the installation quality tends to be more reliable and predictable.

Mechanical strains are a good performance indicator of concrete failure. Indeed, it has been noted that (i) “there are strong indications that the real criterion (in concrete failure) is the limiting (mechanical) strain” (Neville and Brooks, 2010), given that concrete failure in either compression or tension is caused by crack propagation (Neville and Brooks, 2010); and that (ii) “(concrete) failure occurs at limiting (mechanical) strain, regardless of whether this strain is reached by a rapidly applied high stress or a lower sustained stress” (Neville et al., 1983). Moreover, yield tensile strains, ultimate and yield compressive strains are similar for a wide range of concrete strengths (BSI, 2010; Chen, 1982), e.g. yield tensile strains lie within a narrow  $[100-200]\mu\epsilon$  strain interval (Neville and Brooks, 2010). Project specific limiting strains can be inferred from standard concrete tests.

In addition to the strain sensing capacity for damage detection, if concrete mechanical strains are spot mapped within a concrete structure, then the structural loads may be inferred if the nature of loading states can be anticipated.

Nonetheless, there are a number of sensor and concrete features that may hinder the identification of mechanical strains and further computation of structural loads. First, sensors affected by temperature changes provide measurements of apparent measurand, which is the combination of the quantity to be measured, i.e. total strains, and sensor thermal sensitivity. Second, embedded strain sensors capture total strains in monitored structures, which implies that mechanical strains can only be known provided that concrete volume changes due to thermal deformations and shrinkage can be identified. Third, concrete creeps with time under sustained load and incurs in lateral deformations due to the Poisson effect.

It then follows that information on influence parameters is needed for adequate data interpretation. The evaluation of total strains demands temperature sensing in non-isothermal conditions and shrinkage characterisation must be regarded in the assessment of mechanical strains. The estimation of operating structural loads compels the knowledge of concrete elastic properties and creep characterisation.

Consequently, temperature sensors with the same strain topology were incorporated and creep and shrinkage tests were conducted in parallel to the field trials. However, the prediction of time-dependent deformations in tunnel conditions is not easy and laboratory tests in concrete samples can only be expected to narrow the range of in situ creep and shrinkage despite relative humidity having been measured in the CTT tunnel (see chapter 8).

### 5.4.2.2. Segment tilt

Tunnel deformations in CSLs are the combination of segment strains and relative movements between segments. Joints can have a dominant role in the structural response of CSLs. For example, rotations in longitudinal joints are the main component of ring deformations and tunnel convergence. TBM forces and sequential loading may cause the tilt of individual segments in non-bedded rings, and longitudinal tunnel deflections concentrate at circumferential joints through rotation and shearing. Additionally, the relative movements between segments during construction may indicate the propensity of the lining to contact deficiencies.

Accordingly, and given that the original proposal prescribed the monitoring of individual rings, segment tilt measurements were incorporated to capture the CTT ring response during construction activities and in the long term.

### 5.4.3. Selection of instruments

The strain instruments adopted were inherited from the original proposal. DFOS sensing was enabled through the installation of FO sensing cables embedded in the instrumented segments and the deployment of a BOTDR analyser, Neubrescope-5000X, for data acquisition.

The loose tube method (CSIC, 2016) was deployed to facilitate strain and temperature sensing. In this way, parallel sensing of strain and temperature was achieved through a pair of cables: (i) the Fujikura reinforced JBT-03813 optical cable, a tight buffer cable with a flat nylon cable sheath reinforced with steel wires; and (ii) a standard gel-filled loose tube telecommunication cable. The former allows the full transfer of strains from the cable jacket to the optical fibre and is sensitive to temperature and external strains (CSIC, 2016). The latter targets temperature sensing only as the gel interlayer isolates the fibre from external strains (CSIC, 2016).

Geosense VWS-2100 embedment VWSGs, with built-in thermistors, became the benchmark sensors of choice. The selection criteria for the BOTDR interrogator and the VWSG model in the original proposal might have been governed respectively by resource availability and precedent use in monitoring projects.

RST MEMS tilt sensors, including thermistors, were adopted on the basis of their sensing performance, small size and operational readiness soon after erection of instrumented rings. They enabled biaxial sensing which added the possibility of measuring vertical tilt parallel to the tunnel axis.

The manufacturer's technical specifications are collected in Appendix 1.

### 5.4.4. Instrumentation layout

Each ring sensor network consisted of a cell sensor topology repeated in all instrumented segments (see Figure 5.4). Parallel sensor topologies were adopted in the two principal directions of expected axial loading and bending, i.e. hoop and longitudinal directions. In parallel topologies, pairs of sensors, of equal gauge length, are oriented parallel to the neutral axis of the monitored cross section and situated at different offsets, preferably at either side of the section centroid (Glišić and Inaudi, 2007). This arrangement enables the computation of mean strain and curvature.

The primary instrumented sections were selected with consideration of expected behaviour and project budget. With sequential loading near the tail skin, the time-varying eccentric hoop compression of rings was anticipated (see chapters 3 and 6 to 8). Thus, three hoop cross sections were included in the layout: a central section at one side of the grout hole near the segment centroid; two lateral sections at about  $0.5h$  of the circumferential joints to avoid excessive local effects.

Only a central longitudinal cross section was proposed as primary section since longitudinal strains in segments with relatively even packer support were expected to be uniformly distributed along the segment centreline.

One optical cable circuit swept all selected primary sections in each segment. The ten channel DT2055B data logger for strain gauges limited their number to five per segment: two pairs of strain gauges, hoop and longitudinal, were positioned near the segment centroid and a single longitudinal strain gauge was placed laterally at the lining thickness midpoint.

Disparate lining depths and cross-sectional offsets between the strain gauges and the DFOS were given by demands in installation procedures and to prevent concrete void formation around the sensors.

One of the two box-outs cast in the instrumented segments was used to house the MEMS tilt sensor, fixed at its base. The instrument was properly oriented to match tilt measurements against the two primary vertical planes.

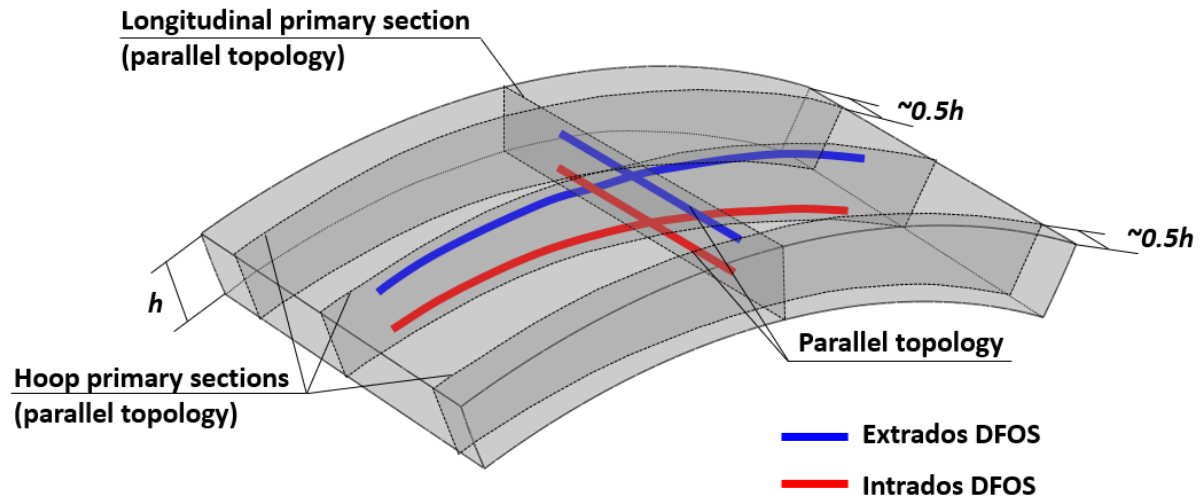


Figure 5.4: DFOS instrumentation layout of CSL segments

### 5.4.5. Gauge length and measurement accuracy

Structural monitoring is generally concerned with global structural response and damage assessment or detection (Glišić and Inaudi, 2007). Structural engineering theories rely on the adoption of mechanical properties that characterise the structural behaviour of inhomogeneous members by integrating the effects of material discontinuities in the global structural response. This is valid even in advanced constitutive models such as the recently popular smeared cracking concrete models.

Point sensing in concrete structures can only provide measurements representative of structural behaviour if the local effects of concrete discontinuities are bypassed by long gauge lengths (Glišić, 2011). However, averaged strains over too long gauge lengths will differ from strains at attributed sampling points if the strain distribution within the gauge length is nonlinear (Glišić, 2011).

According to the above, the impact of the adopted gauge length on the measurement accuracy of strain sensing techniques selected for the CTT segments is investigated here in regards to the load distribution expected in the segments and the concrete discontinuities.

#### 5.4.5.1. Segment loads

Glišić (2011) developed a method for the calculation of relative strain measurement errors,  $err_e$ , caused by variable strains within a sensor gauge length,  $L_s$ , in homogeneous beams subjected to various loading types and for sensors positioned at a distance from the member extremities either greater or smaller than the beam depth (see Figure 5.5).

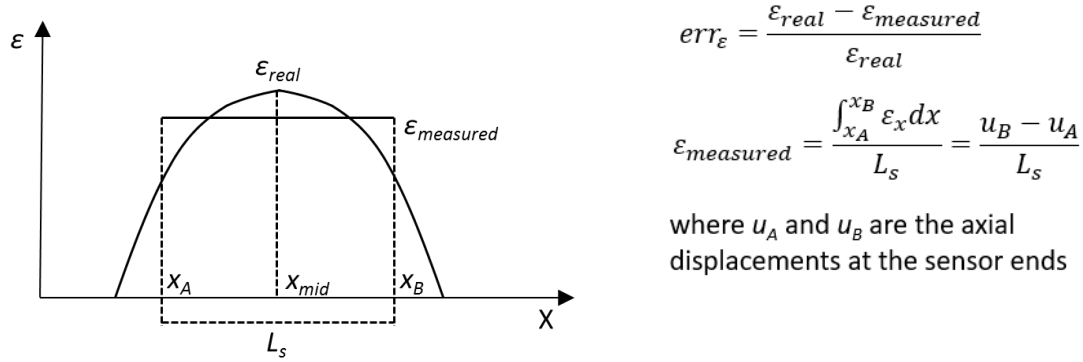


**Figure 5.5: Relative strain measurement error**

In CSL tunnels, the radial pressures tend to be smoothly distributed except perhaps near the tail skin (see chapter 8). For the purpose of this discussion, it can be assumed that the lining pressures will exhibit a linear distribution with depth during construction (see chapter 7) or a sinusoidal distribution in the long term (see chapter 4) that can be approximated to a quadratic distribution. In both situations,  $err_{\epsilon}$  can be computed in accordance with Glišić's (2011) load case for a polynomial load and a sensor away from the member extremities.

Table 5.2 summarises the VWSG and the BOTDR  $err_{\epsilon}$  associated with the maximum strains attributed to the above type of distributed loads in hoop and longitudinal directions. The VWSGs with  $L_s=150\text{mm}$  yield  $err_{\epsilon}<1\%$  in all cases, while the BOTDR, with  $L_s=500\text{mm}$ , results in peak  $err_{\epsilon}\approx 7.5\%$ . The computation of measured strains in BOTDR measurements based on a frequency representative of the BGS may not conform to Glišić's (2011) formulae. However, the BOTDR  $err_{\epsilon}$  here obtained can be taken as an indication that a detailed examination of BOTDR measurement accuracy in members subjected to variable strains is required.

**Table 5.2: Relative measurement error of maximum strain**

Strain sensor	Distributed loads		
	Uniform	Linear	Quadratic
VWSG hoop centre	0.1	0.2	0.3
VWSG long centre	0.3	0.6	0.9
BOTDR hoop centre	1.5	1.9	2.8
BOTDR hoop side	1.5	1.9	2.8
BOTDR long centre	3.3	5.4	7.4

Boundary loads in CSL segments typically are longitudinal normal loads acting on packers, coupling forces at packers or dowels, and concentrated normal loads at longitudinal joints.

The longitudinal compression of ram loads is applied over the packers' area and spreads longitudinally and radially towards the segment centreline. Figure 5.6 shows that at central positions, the ram load

spread is fully developed and strain fluctuations are minor while, at lateral hoop sections, the incomplete spread of ram loads over the segment length results in wider fluctuations of hoop strain.

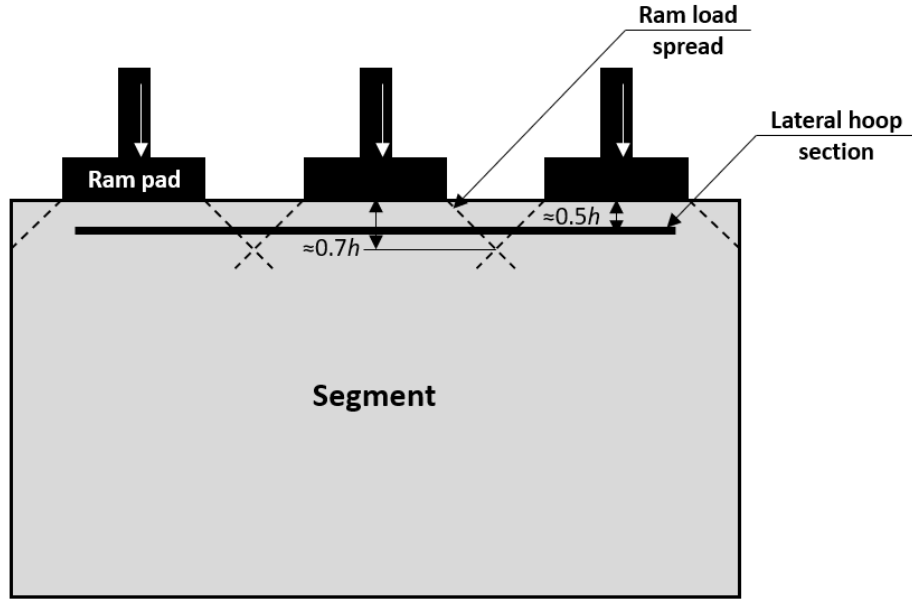


Figure 5.6: Ram load spread at lateral hoop section

All the strain sensors, except at lateral hoop sections, were installed at a distance greater than the lining depth  $h$  from the point of coupling force application (PFA), which implies that the bending strains caused by the coupling forces near the sensors present a smooth distribution that could be equated to the polynomial loading case. For the lateral sensors, Glišić's (2011) solution for rectangular beams with strain sensors positioned at  $0.5h$  distance from the PFA and  $L_s > h$  yields  $err_\epsilon = 3.6\%$  and  $err_\epsilon = 2.9\%$  when coupling forces act at  $1/4$  and  $1/2$  of the segment length respectively.

Finally, all BOTDR usable lengths and strain gauges are outside the disturbed zone of the longitudinal joints, i.e. at a distance greater than  $h$  from the longitudinal boundaries, which implies that the hoop strains are linearly distributed with lining depth and unaffected by transverse strains (see chapter 2).

### 5.4.5.2. Concrete discontinuities

In the analysis of RC structures, the concrete is tackled as a homogeneous material (Glišić, 2011): the curvature required for the computation of bending moments or deflections is the curvature averaged over the crack spacing,  $L_c$ , and the flexural crack width is computed through the product of maximum  $L_c$  and the mean tensile strain in the reinforcement (BSI, 2010).

Glišić (2011) estimated the relative error in a strain measurement caused by cracking,  $\delta\epsilon_{C,s}^{crack}$ , as:

$$\delta\epsilon_{C,s}^{crack} \approx \pm \epsilon_{C,s} \frac{L_c}{L_s} \quad (5.4)$$

where  $\epsilon_{C,s}$  is the average strain measured by the sensor at the sensor midpoint (see Figure 5.7.a).



The maximum  $L_c$  calculated with the Lofgren's method for load-induced cracking (Lofgren, 2007) for the CTT concrete is about 180mm and 140mm in hoop and longitudinal directions respectively; thus the total strains measured with 150mm and 500mm strain sensors may incur in relative errors of up to 120% and 36% each.

The 150mm VWSGs embedded in cracked regions may not provide reliable strain measurements for the structural monitoring as their certainty depends on the sensor position (see Figure 5.7.a). However, this conclusion does not necessarily apply to DFOS since, given that averaged strain data is retrieved at small sampling intervals, e.g. 50mm, cracks may be detected and averaged tensile strains estimated even for spatial resolutions smaller than  $L_c$ .

In this case study, the FO cables were point-fixed with loose cable ties to the steel corrugated bars of segment reinforcement cages. With this arrangement, it can be assumed that in uncracked regions the cable sheath is bonded to the steel bar, which in turn is bonded to the surrounded concrete.

In cracked regions, with partial slip between concrete and steel bar over a certain transfer length,  $l_t$  (see Figure 5.7.b), the strains transmitted to the cable sheath and optical fibre must either (i) reproduce the strains in concrete, if there is full bond between the optical cable and the concrete; (ii) follow the steel strain profile in the case of the optical cable fully bonding with the steel bar; or (iii) describe a uniform distribution of averaged strain if there is no cable bond over the transfer length (see Figure 5.7.c).

The first case is physically impossible given that the FO cable bridges the opened crack. In the third case, if the BOTDR spatial resolution is smaller than  $L_c$ , there must be at least one data point with the correct measurement of average steel strain, which is required for the computation of crack width and averaged curvature. Otherwise, crack detection would still be possible with the centroid method if  $L_c > 0.5L_s$  or through the secondary peak method if  $L_c < 0.5L_s$  (Glišić and Inaudi, 2007). Finally, in the second case, crack detection would depend on the steel strain distribution, becoming increasingly difficult with higher concentration of tension at the crack location.

Overall, it follows that the attachment method of optical sensors can determine the system capability for crack detection and average steel strain measurement in cracked concrete. Spatial resolutions smaller than  $L_c$  ensure the accurate measurement of average steel strain in unbonded optical cables. In this case study and assuming unbonded optical sensors, the detection of cracks spaced over a 180mm distance with 500mm BOTDR spatial resolution would be close to the sensitivity boundaries of centroid and secondary peak methods.

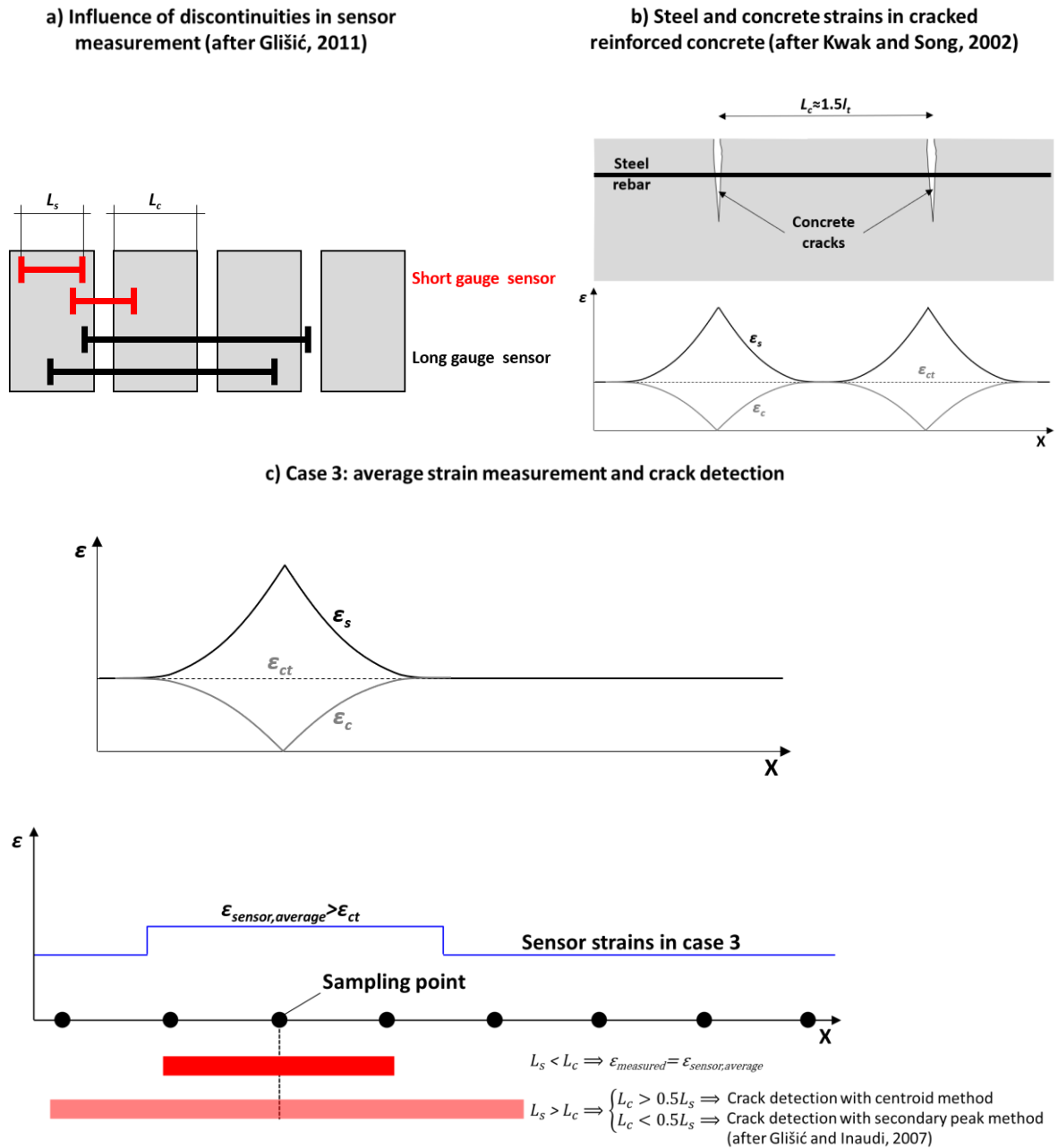


Figure 5.7: Effect of concrete discontinuities on measurement accuracy

### 5.4.6. SHM system design

The SHM design was conducted through the integrated development of three interdependent elements: the physical architecture, the implementation plan and the data acquisition programme.

A wide range of system engineering tools were deployed during the design process, such as feasibility studies of the installation works, Icam DEFinition for Function Modelling (IDEF) diagrams, risk assessments, method statements, and requirements and cost analyses.

The constraint requirements and the novelty of DFOS in tunnel construction environments demanded significant planning efforts with preliminary laboratory sessions, spaceproofing analysis, regular communication with all stakeholders at relevant phases and almost daily coordination with the main

contractor and the construction programme. The design described herein is the solution finally adopted for the last two instrumented rings, CAM3 and CAM4. Robustness issues and lessons learnt derived from this SHM deployment are also explained.

### 5.4.6.1. Physical architecture

The system was delivered in phases with a view to conducting as many installation tasks outside the tunnel as possible and thus minimising disruptions to the tunnelling activities. This solution also integrated the segment instrumentation works of the original proposal completed prior to the design of this phased configuration (see section 5.2).

***a) Phase 1: Segment instrumentation at Shay Murtagh's concrete plant (see Figure 5.8.a):***

The first phase entailed the segment instrumentation with the DFOS and the embedment VWSGs. The instrumented segments were furnished with two covered stainless steel box-outs cast at the segment intrados: one housing the VWSG data loggers and a pair of strain and temperature cable loose ends; the other, another pair of DFOS ends.

***b) Phase 2: Preparatory works at Crossrail's site yard (see Figure 5.8.b):***

This phase comprised all preparatory works that could take effect prior to ring erection. The physical architecture at the end of this stage consisted in a segment circuit of strain and temperature FO sensors spliced in series to 20m of connecting optical pigtailed terminated in connectors, which enabled the data acquisition with the BOTDR interrogator for the first time.

The segment instrumentation was completed with the addition of the tilt sensors and their data loggers.

***c) Phase 3: Works at Crossrail's tunnel during tunnelling (see Figure 5.8.c):***

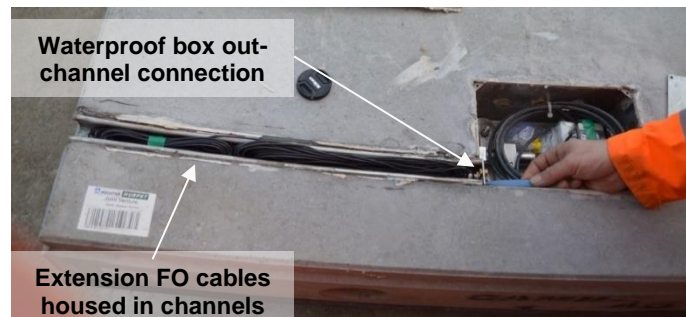
A DFOS ring circuit with two free ends terminated in connectors was delivered by splicing the loose ends of the connecting FO cables, after being routed to a terminal box where all intersegment splices were housed.

This configuration, with extended FO free cable ends when appropriate, enabled simultaneous automated data acquisition in all ring segments during the TBM passage and at future construction stages, e.g. cross passage construction. It also delivered the best DFOS technical performance of all the options examined in terms of accessibility for data acquisition, system verification and repairs, optical budget and readiness time for automated measurements. The terminal box facilitated partial access to the FO splices and DFOS circuit ends. The estimated optical budget of the ring circuit, 2.1dB, was well within the capabilities of the selected BOTDR interrogator. The automated measurements in the ring circuit were expected to start about 15h after ring erection, and individual measurements in the segment circuits 6h after ring erection.

### a) Phase 1: Shay Murtagh concrete plan



### b) Phase 2: CTT site yard



Box out A: FO cable ends



Box out B: VWSG logger



Box out A: Tilt system, splice to extension FO cable



Box out B: VWSG logger, splice temperature-strain DFOS



Figure 5.8: SHM physical architecture

## c) Phase 3: CTT tunnel during tunnelling

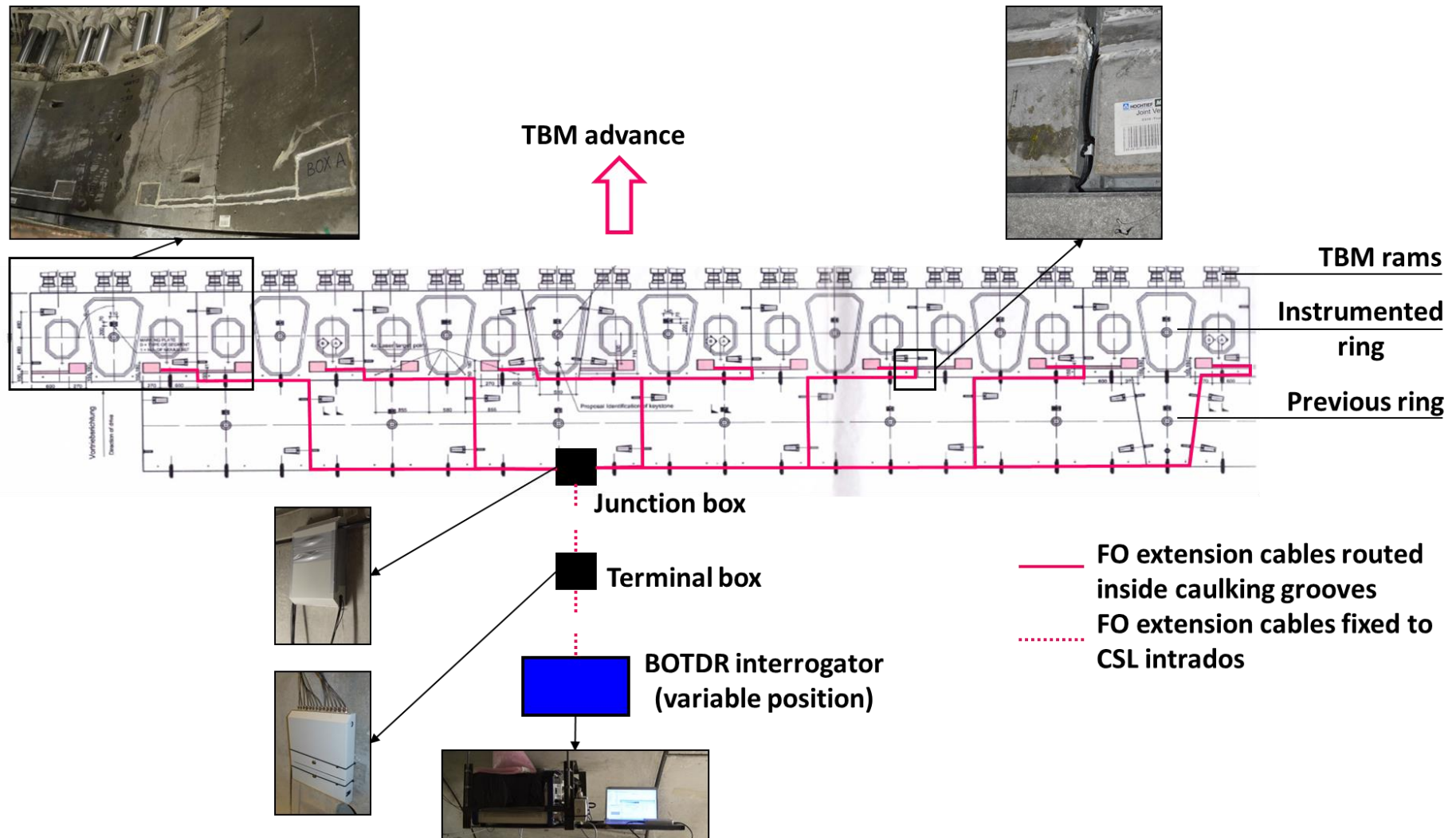


Figure 5.8 (continued)

### 5.4.6.2. Implementation plan

Figure 5.9 shows the IDEF diagram of the installation works, highlighting the main tasks accomplished in each phase.

The installation of strain gauges was completed in the first phase, which enabled automated measurements from this phase onwards.

The tilt sensors were attached to each segment in the second phase, but the required adjustment of the hoop reference plane was performed in the third phase, once the segment position in the erected ring was known. Consequently, automated measurements became meaningful only after the tilt adjustment.

The DFOS circuit was adapted to the physical and site constraints of each phase:

- a) In the second phase, the initial layout was modified to a segment circuit with connecting optical cables in preparation for the following stage and to perform baseline measurements of segment circuits in unloaded conditions.

The risk of power loss induced by local defects in non-bedded optical fibres, such as breakages or macrobending, was minimised through the use of splice trays and bend-insensitive connecting optical cables.

All splices were housed in standard splice trays for telecommunication applications, which in turn were fixed onto the box-out walls.

The 3.0mm EZ-bend ruggedized optical pigtails were provided with EZ bend insensitive single mode fibres, especially manufactured for high macrobending performance and yet suitable for harsh environments.

The macrobending properties of the connecting cables allowed their temporary fold within the covered stainless steel channels without optic fibre breakage or permanent damage, which ensured cable integrity during segment transportation and ring erection. These cast-in channels had been originally foreseen as conduits for intersegment sensor splicing (see section 5.3), and hence were part of the first phase installation works.

- b) In the third phase, the same macrobending properties enabled the safe routing of connecting cables within the lining caulking grooves up to the junction box. The total macrobending attenuation due to the fifty six 90° corners encountered in each ring circuit was estimated to be 0.14dB, which assumed cable radii of 20mm achievable with the aid of spacers.

It is noteworthy that bend-insensitive optical fibres are manufactured with a mode field diameter slightly different from single mode fibres in optical sensors, and therefore the average power loss per splice in the estimation of ring optical budget was increased to 0.05dB, which included this hybrid splicing.

After cable routing to a collection box, the DFOS installation works in the third phase encompassed: (i) mounting a temporary support frame for the BOTDR interrogator to enable

ring measurements during TBM passage (see Figure 5.10.a); (ii) routing all connecting cables from the junction box to a terminal box (see Figure 5.10.b); (iii) splicing the connecting optical cables to complete the ring circuit and housing the splice trays containing the new thirteen splices in the terminal box (see Figure 5.10.c); (iv) fixing surface optical cables to the concrete lining (see Figure 5.10.e); (v) checking segment and ring circuit integrity from a temporary workstation for the BOTDR interrogator (see Figure 5.10.d and 5.10.f); (vi) performing segment measurements with the BOTDR interrogator (see Figure 5.10.d); and (vii) programming automated ring measurements during TBM passage (see Figure 5.10.g).

CAM3 and CAM4 instrumented rings were four rings apart. CAM3 automated ring measurements were interrupted to verify the CAM4 ring circuit. Automated measurements were resumed afterwards for both ring circuits, making use of the two ports in the Neubrescope-5000X analyser.

After about 70m of TBM passage, the BOTDR interrogator was relocated to a shelf fixed to the concrete lining on top of the slurry pipes at the back of the TBM equipment, which remained the data acquisition point for future measurements (see Figure 5.10.h).

One major concern from the second phase onwards was the protection of (i) equipment sensitive to water submersion, such as data loggers, and (ii) bare optical fibres held in splice trays that could be damaged by slurry or grout entering the box-outs during tunnelling or cross passage construction respectively. Waterproofing layers were added to the non-waterproof cast-in box-outs and channels as appropriate and with consideration of applicable site constraints.

The installation works delivered 5.8dB and 3.0dB optical budgets for CAM3 and CAM4 rings, slightly higher than the estimated values but within the BOTDR allowance. Segment measurements and ring measurements were completed about 6h and 8h after ring erection for the above rings, which exceeded the initial expectations. The duration of the third phase installation works oscillated between 24h and 12h per ring, with a clear improvement in installation time with experience.

A fourth phase for the additional protection of monitoring instrumentation during cross passage construction works was also implemented.



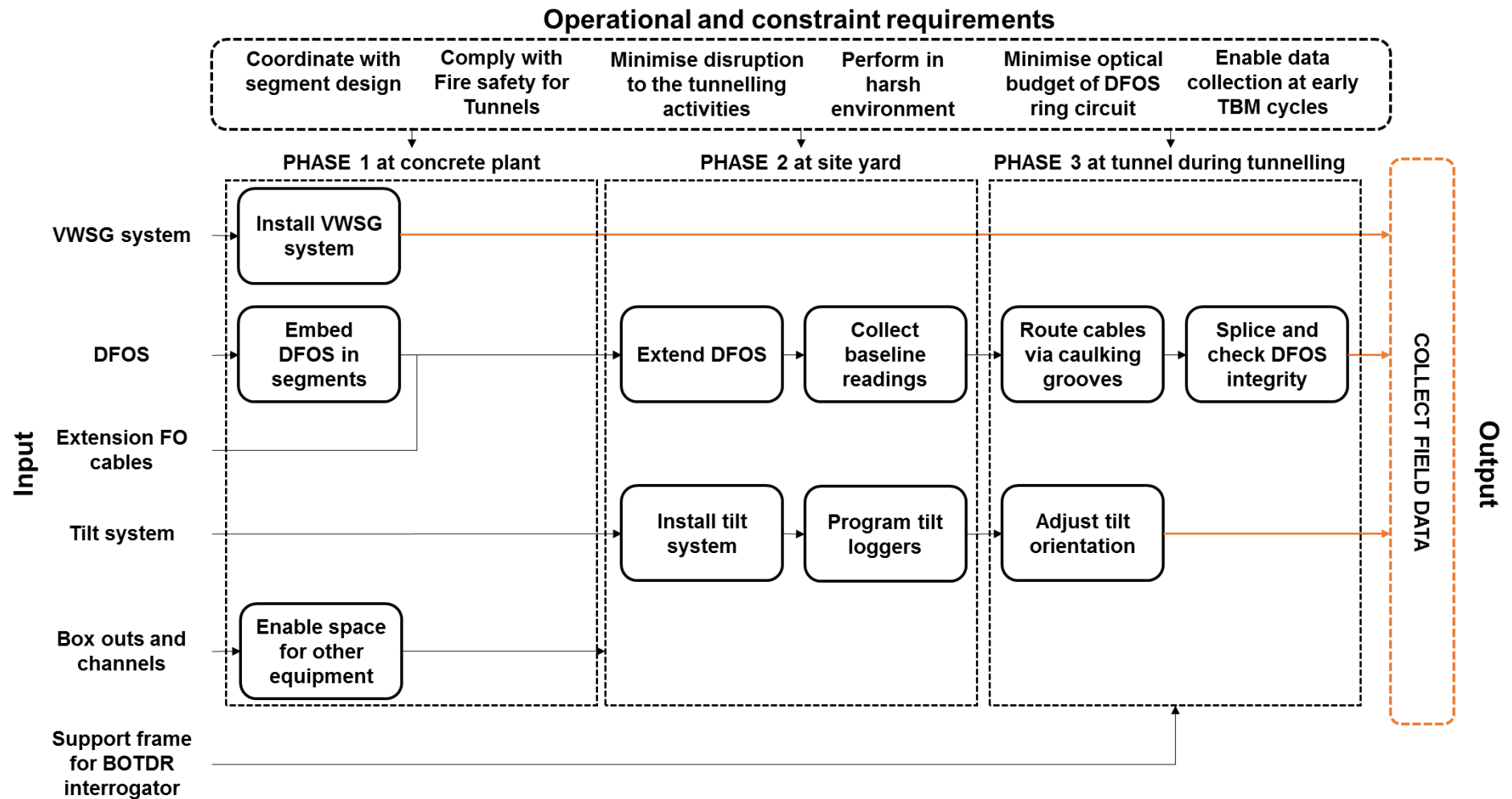


Figure 5.9: IDEF diagram for implementation plan



## 5.4. CTT SHM system

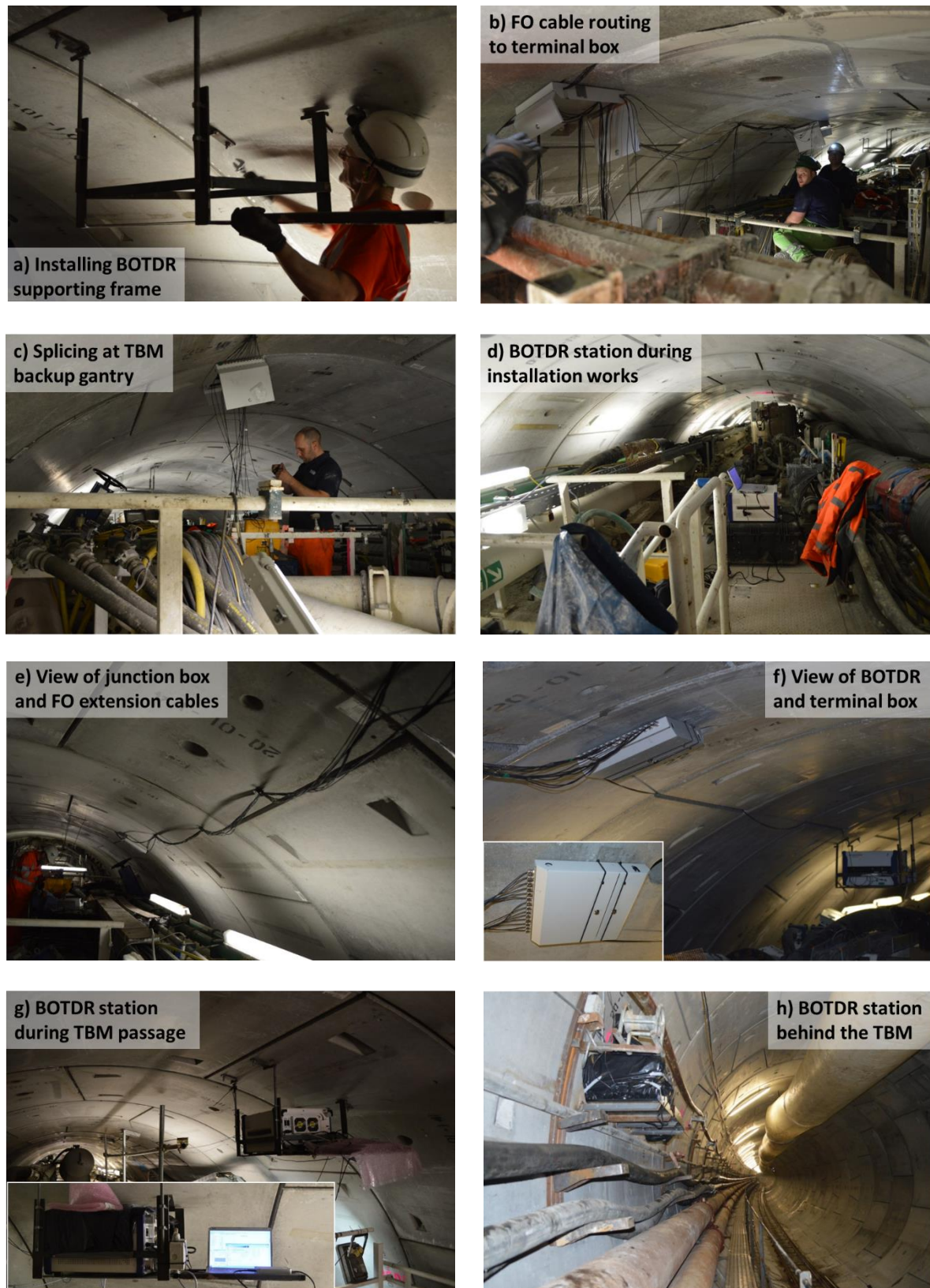


Figure 5.10: Phase 3 installation works sequence

### 5.4.6.3. Data acquisition

Table 5.3 shows the BOTDR input specification for data acquisition. Time and distance maps of the measurements are shown in chapter 8.

**Table 5.3: BOTDR input specification for data acquisition**

<b>CTT input parameters</b>	
Laser wavelength	1550 $\pm$ 2nm
Distance range	$\approx$ 700m
Measurement frequency range	[10.3-11.4GHz]
Measurement frequency scan step	5MHz
Readout resolution	5cm
Sampling points	220
Average count settings	2 <sup>16</sup>
Pulse Width	5ns
Spatial resolution	50cm
Optical budget	$\approx$ 6dB
Operating conditions	10-35°C/R.H.<85%

### 5.4.6.4. Robustness issues and lessons learnt

The reliance on untested technology and the incomplete identification of site requirements at the early stages of the design process, i.e. the original proposal, increased the risk of project failure:

***a) Reliance of original proposal on untested technology:***

Despite the magnitude of the works, in the original proposal, the project depended entirely on the use of the novel Diamond connectors (see section 5.3). There was no alternative plan in case the connectors failed, as they did, the unit tests designed to validate the operational requirement of an acceptable ring optical budget in a harsh environment such as the CTT tunnel (see Figure 5.11).

The in-house laboratory tests on the connectors were conducted late in the design process, November 2013, so that the results were reported once CAM1 and CAM2 segments had been already instrumented and the DFOS of CAM3 and CAM4 segments cut.

When the Cambridge team proposed the replacement of the connectors with splices in 18<sup>th</sup> December 2013, Crossrail and HMJV rejected it on the basis of Health and Safety compliance and requested a design that minimised the installation time within the tunnel and enabled all splicing activities to be conducted in a safe work area of the TBM.

Consequently, the new design solution, comprising the procurement of materials and the completion of the installation works, had to be delivered within the tight timeframe of less than three months determined by the CTT construction programme.

The CTT experience confirms that profound design changes at late stages in a project life cycle can lead to (i) greater demands in equipment and materials; (ii) deterioration of working conditions and overtime; and (iii) higher risk of project failure (Blanchard and Fabrycky, 2011).

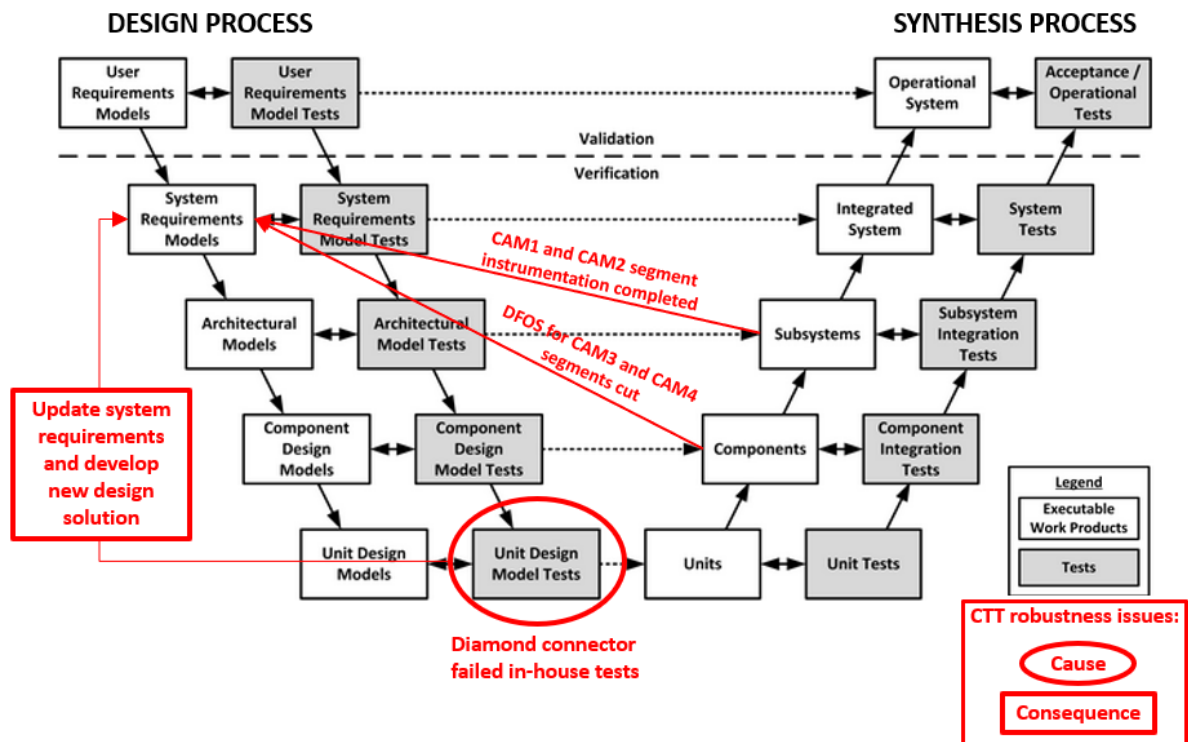


Figure 5.11: CTT robustness issues against double V-model (after Firesmith, 2011)-untested technology

**b) Incomplete identification of site requirements at early stages:**

Two further changes in the initial proposal were required to harmonise the new SHM system with the features inherited from the original proposal and site, particularly tunnelling conditions, activities and regulations (see Figure 5.12).

First, some VWSG data loggers housed in non-waterproof box-outs were damaged by rainwater entry during segment stacking. Site visits to the tunnel also evidenced that the rings used to be cleaned with pressurised water after erection; that slurry was poured regularly over the tunnel invert during slurry pipe extensions, which later solidified and formed a layer of variable depth; that construction waste accumulated at the tunnel invert during cross passage construction; and that the intrados of cross passage rings was grouted as part of the temporary works. Appropriate waterproofing layers were included at each stage of the new solution.

Second, the original splice protection method, commonly applied in previous geotechnical projects, consisted in a flexible plastic tube, housing the splice sleeve and bare fibres, with its ends sealed with heat shrinks. The review of the BOTDR measurements for system verification in the days following CAM1 ring erection revealed that there was a progressive deterioration in splice quality, which led to total data loss over time. CAM2 ring erection was imminent at the time and therefore

a full investigation of the problem was postponed. Tests conducted at the site yard on the CAM3 splices confirmed that, even with slight curvatures of the protecting tube, the high macrobending attenuation was caused by the tight bending of the optical fibres at the tips of the splice sleeves. It was concluded that the splice protection method was not appropriate given that its straight alignment could be disrupted by the limited box-out size, water or slurry entry in the boxes, cable selfweight and vibrations during advance. In the absence of a CSIC splice protection case at that time, commercial splice trays for telecommunication applications were deployed instead. The tray models that fitted in the box-outs left the splice bare fibres exposed; therefore the uncontrolled entry of external substances in the box-outs had again to be prevented.

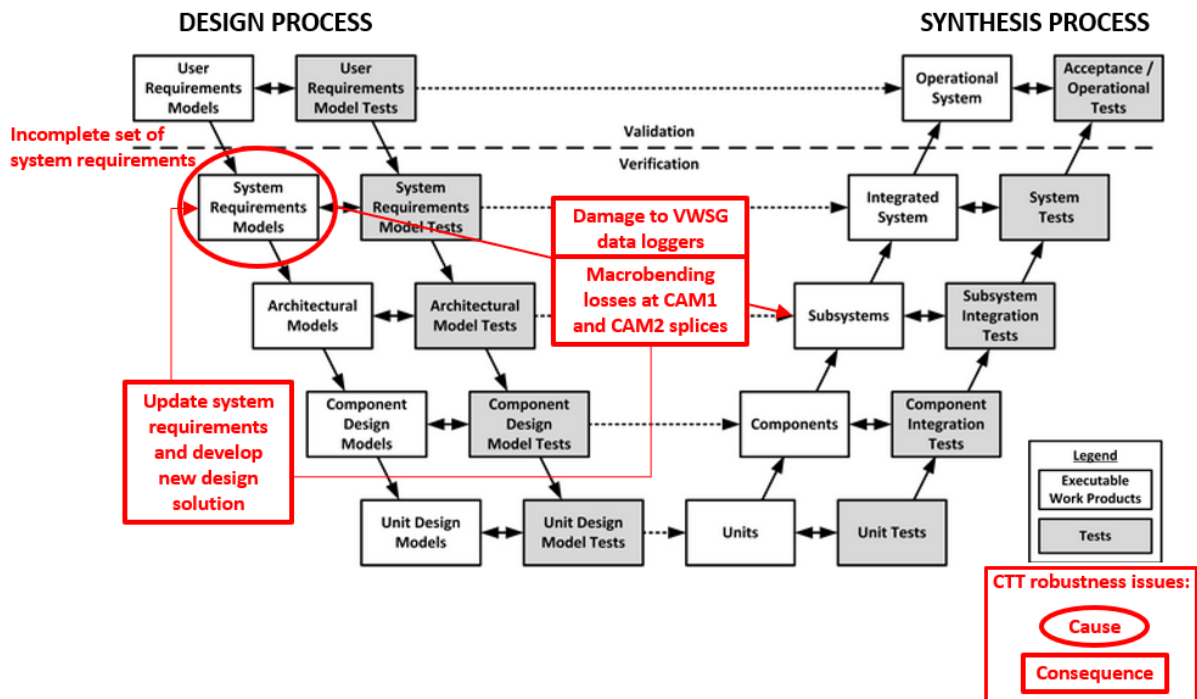


Figure 5.12: CTT robustness issues against double V-model (after Firesmith, 2011)-incomplete requirements set

The acquisition of a complete field data set starting immediately after ring erection was pursued in the development of the new solution in order to enable a comprehensive characterisation of the lining performance during construction: early BOTDR ring measurements after ring erection and over 70m of the TBM passage, were facilitated by the use of the BOTDR interrogator temporary support, produced at the site workshop; vertical tilt measurements were added to capture the global performance of segmental rings; all the segments cast in January 2014, i.e. CAM3 and CAM4 segments, were equipped with a full set of strain gauges each.

### 5.5. Data processing methods for CSLs

#### 5.5.1. Nomenclature

*Apparent strains* are the sum of total strains in the monitored structure and strain quantities induced by the sensor thermal sensitivity.

*Total strains*,  $\Delta\epsilon_{tot}$ , are the sum of all strains in the monitored structure:

$$\Delta\epsilon_{tot} = \Delta\epsilon_{str} + \Delta\epsilon_{creep} + \Delta\epsilon_{shr} + \Delta\epsilon_{\Delta T} + \Delta\epsilon_{mech,\Delta T} \quad (5.5)$$

where  $\Delta\epsilon_{str}$  are instantaneous strains due to structural loading;  $\Delta\epsilon_{creep}$  are creep strains under sustained load;  $\Delta\epsilon_{shr}$  are shrinkage strains;  $\Delta\epsilon_{\Delta T}$  are thermal strains and  $\Delta\epsilon_{mech,\Delta T}$  are instantaneous mechanical strains caused by restrained thermal deformations.

*Net mechanical strains*, hereafter named *mechanical strains*, are the strains produced by structural loading, thus excluding thermal effects and shrinkage strains. CTT shrinkage tests confirmed that shrinkage strains of concrete specimens after months of being cast were negligible.

*Net structural strains*, from here on referred as *structural strains*, are the instantaneous strains produced by structural loading, i.e. mechanical strains minus creep strains.

*Total mechanical strains* are strains produced by structural loading and restraints in thermal deformation.

*Total structural strains* are instantaneous strains produced by structural loading and restraints in thermal deformation.

*Raw strains* are absolute strain measurements.

*Initial strains* are strain increments measured from  $t=0$ .

*Zeroed strains* are strain increments measured after ring erection.

The same categorisation can apply to combined quantities such as curvatures.

#### 5.5.2. Total strain and tilt

##### 5.5.2.1. BOTDR total strains

With the loose tube method, temperature increments,  $\Delta T$ , can be estimated from the BFS detected in temperature sensors,  $(\Delta v_b)_{loose}$ , with Eq. 5.6:

$$(\Delta v_b)_{loose} = C_{TT} \Delta T \quad (5.6)$$

where  $C_{TT}$  is the BFS temperature coefficient of the loose tube cable (CSIC, 2016). Then, total strains in the FO strain sensor can be inferred from Eq. 5.7, as long as the BFS temperature and strain coefficients,  $C_T$  and  $C_\epsilon$ , are known (CSIC, 2016):

## 5.5. Data processing methods for CSLs

$$\Delta v_b = C_\varepsilon \Delta \varepsilon_{tot} + C_T \Delta T \quad (5.7)$$

For a 1550nm nominal laser wavelength, CSIC collated published  $C_{TT}$  values ranging from 1.0 to 1.1MHz/°C, whilst  $C_\varepsilon$  could vary between 0.0483 and 0.0506MHz/ $\mu\varepsilon$  (CSIC, 2016). CSIC recommendations on BFS coefficients for this particular case study were  $C_{TT}=1.08\text{MHz}/^\circ\text{C}$ ,  $C_T=1.00\text{MHz}/^\circ\text{C}$  and  $C_\varepsilon=0.04846\text{MHz}/\mu\varepsilon$ .

### 5.5.2.2. Total tilt

Total tilt  $\Delta tilt_{tot}$  in tilt sensors can be calculated with the following expression:

$$\Delta tilt_{tot} = \Delta tilt_{app} - C_{T,tilt} \Delta T \quad (5.8)$$

where  $\Delta tilt_{app}$  is the apparent tilt measured and  $C_{T,tilt}$  is the temperature coefficient of the tiltmeter, which can be obtained through linear regression of the tilt measurements against temperature changes under stable tilt conditions.

### 5.5.3. Mechanical strains

Temperature changes in tunnels are generally small when compared to overground structures, except during mechanised tunnelling with backfill grouting. In grouted smooth bored tunnels, the exothermic hydration of grout injected in the tail void generates heat that is transferred to the lining and can increase lining temperatures by 20°C, as measured in the CTT.

With temperature compensation of total strains, it is assumed that thermal strains in the instrumented structure are not restrained and, consequently, the total value of free thermal strains  $\Delta \varepsilon_{AT}$ , produced by a temperature increment  $\Delta T$  is subtracted to obtain the mechanical strains,  $\Delta \varepsilon_{mech}$ :

$$\Delta \varepsilon_{mech} = \Delta \varepsilon_{tot} - \Delta \varepsilon_{AT} - \Delta \varepsilon_{mech, \Delta T} \approx \Delta \varepsilon_{tot} - \alpha_{Tc} \Delta T \quad (5.9)$$

where  $\alpha_{Tc}$  is the concrete coefficient of thermal expansion. The applicability of temperature compensation thus understood can only be guaranteed in isostatic concrete structures subjected to slow thermal changes so that linear temperature distributions can develop within structural cross-sections. In statically indeterminate structures such as CSLs, partial or total constraints might be imposed by segment boundaries, and a sound examination of lining response to thermal variations is required to either validate temperature compensation or to assess additional measurement uncertainty introduced by thermal restraints.

#### 5.5.3.1. Coefficient of thermal expansion

The coefficient of thermal expansion in hardened concrete depends on intrinsic factors such as the water/cement ratio, age (Berwanger and Sarkar, 1976) and thermal properties of aggregates whose thermal coefficients can oscillate between 5.4 and 12.6 $\mu\varepsilon/^\circ\text{C}$  (Gambhir, 2013). In SFRC, the steel fibres embedded in the concrete mix tend to hinder concrete thermal expansion, even in small volume fractions (Purkiss, 1987). External factors such as extreme ambient temperatures also influence  $\alpha_{Tc}$ . For example, concrete in freezing conditions presents greater thermal coefficients (Bishnoi and Uomoto, 2008). It is,



## 5.5. Data processing methods for CSLs

---

therefore, necessary to evaluate  $\alpha_{Tc}$  for the particular concrete mix of CTT segments and with consideration of site temperatures.

Strain and temperature daily fluctuations experienced by unloaded CTT concrete segments exposed to ambient temperature at the site yard were used to compute averaged linear coefficients of thermal expansion. Figure 5.13 illustrates total strain increments and absolute temperatures measured by longitudinal VWSGs in a concrete segment over the week prior to ring erection. There is a strong linear correlation between temperature and total strains with the typical hysteresis caused by daily temperature cycles.

The poor thermal diffusivity of concrete causes transient nonlinear temperature distributions in concrete members subjected to rapid thermal variations (Bishnoi and Uomoto, 2008; El-Tayeb et al., 2015). Surface fibres are heated or cooled much faster than central fibres at the structural core. With such nonlinear temperature variations in a member cross-section, thermal strains are partially inhibited by internal restraints and self-equilibrating thermal stresses develop (El-Tayeb et al., 2015).

For instance, when the external temperature increases, surface fibres reach greater temperatures than central fibres during heat transfer (see Figure 5.14.a). Since plane cross-sections tend to remain plane, surface strains are partially constrained and consistently smaller than free thermal strains at measured temperatures (see Figure 5.14.b). Conversely, thermal strains at core fibres are furthered by the thermal expansion of surface fibres. The strain deviation from the free thermal expansion produces compressive stresses at the surface and tensile stresses at the centre (see Figure 5.14.c).

Overall, strains measured near the surface of a cross-section in the heating (thawing) and cooling (freezing) path are smaller and greater than the steady strains respectively, leading to a hysteresis whose amplitude is directly related to that of the temperature cycles. In all cases, thermal curvatures are smoother than those expected from external temperature differences.

The thermal expansion coefficients were derived through linear regression of measured actual strains and temperature for each VWSG. The expected value, standard deviation and hysteresis of  $\alpha_{Tc}$  inferred from all segments were larger in hoop than in longitudinal direction, possibly due to hoop strain gauges being closer to the surface and concrete rebar. Consequently, separate  $\alpha_{Tc}$  were adopted in longitudinal and hoop directions,  $(9.2 \pm 0.5) \mu\epsilon/^\circ\text{C}$  and  $(10.1 \pm 0.6) \mu\epsilon/^\circ\text{C}$  respectively, so that the standard uncertainty of thermal strains, excluding hysteresis effects, was reduced by three times. In the absence of sufficient BOTDR measurements prior to ring erection, the same  $\alpha_{Tc}$  values were assumed for DFOS, even though these were attached to the concrete rebar.

Measurement uncertainty and hysteresis associated with cyclic temperature fluctuations lead to apparent residual strains after temperature compensation, which have an impact on the evaluation of initial mechanical strains (see Figure 5.15).

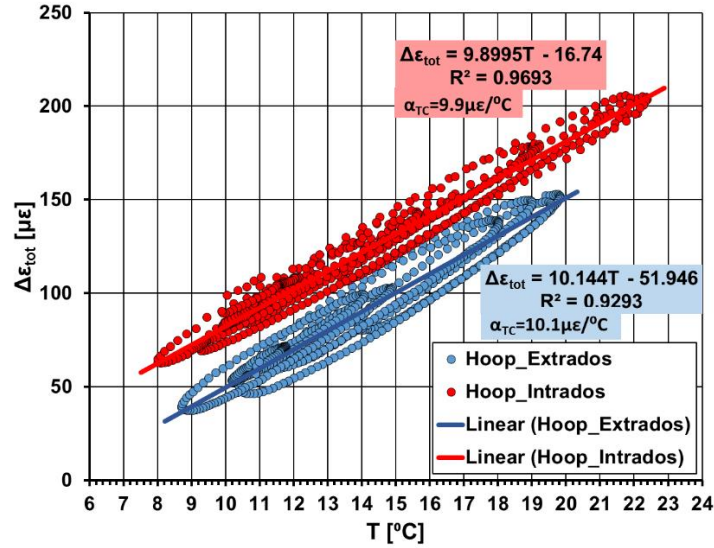


Figure 5.13: Computation of CTT  $\alpha_{TC}$  and hysteresis under temperature cycles

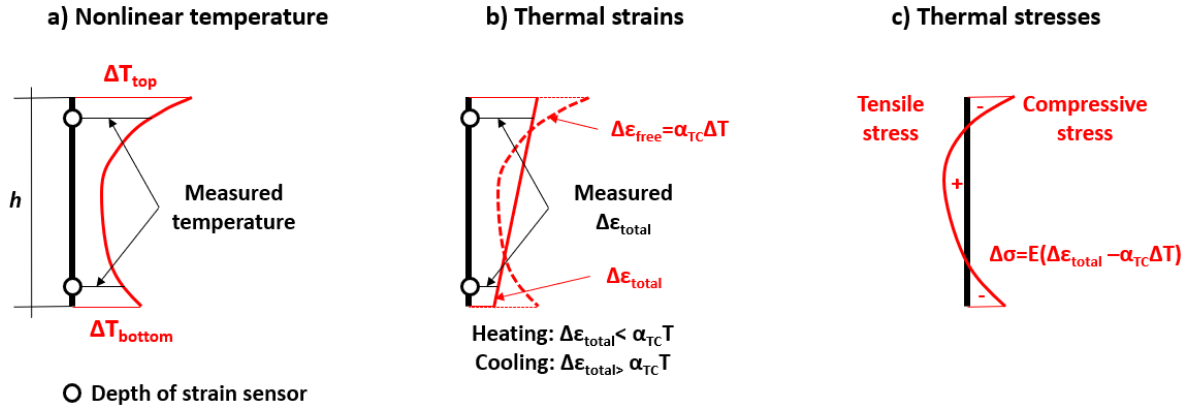


Figure 5.14: Thermal response of a monitored cross-section in an isostatic beam under nonlinear temperature (after El-Tayeb et al., 2015)

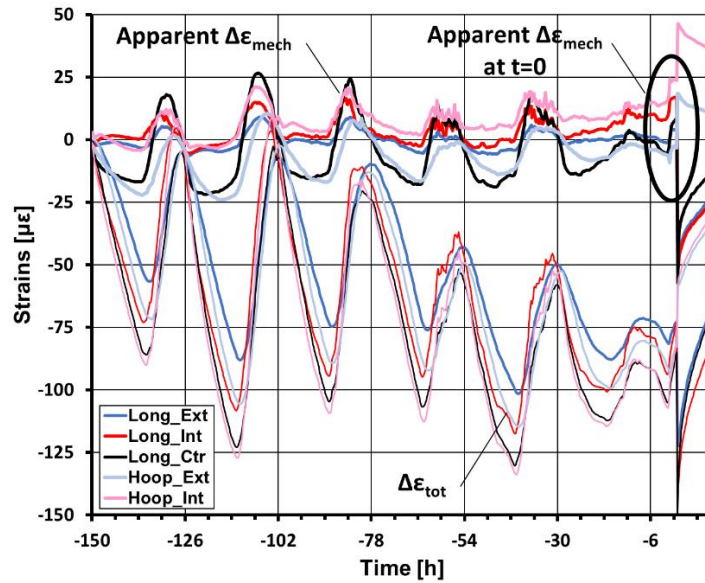


Figure 5.15: Effect of hysteresis on  $\Delta\epsilon_{\text{mech}}$  at  $t=0$



### 5.5.3.2. CSL response to mean temperature changes

#### a) Changes in mean hoop temperature

If a non-bedded segmental ring is subjected to uniform temperature changes applied at a low rate, the ring contracts and expands uniformly as a continuous ring. Each segment behaves as a simply supported curved beam with free radial displacements at the supports (see Figure 5.16), and thermal strains can develop fully without producing concrete thermal stresses. If the temperature distribution varies significantly along the ring perimeter, then the thermal expansion of individual segments may be, at least, partially hindered by adjacent segments.

Since the CTT temperature data demonstrated that mean temperature increments along the ring circumference remain roughly uniform and vary smoothly with time (see Figure 5.27, p.125), the condition of free thermal response is deemed representative of real segment boundaries.

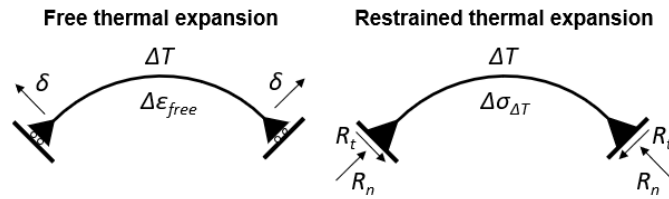
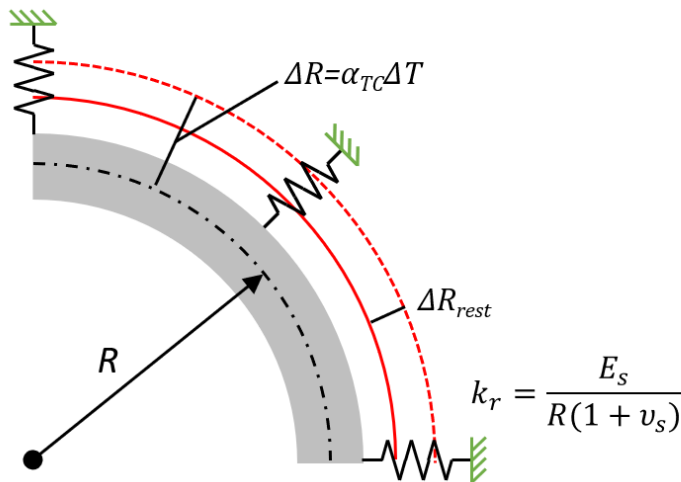


Figure 5.16: Segment response to temperature changes

When a bedded ring is subjected to a uniform temperature increase, the proportion of free thermal expansion,  $R_{\Delta T}$ , prevented by the ground passive reaction can be approximated with Eq. 5.10, which assumes linear elastic behaviour of the ground and the concrete (see Figure 5.17):

$$R_{\Delta T} = \frac{-\Delta \varepsilon_{rest, \Delta T}}{\Delta \varepsilon_{\Delta T}} = \frac{1}{1 + \left( \frac{E_c(1 + \nu_s)A_r}{E_s R} \right)} \quad (5.10)$$

where  $R$  is the ring radius and  $A_r$  is the cross-sectional ring area.



$$\Delta \varepsilon_l = \frac{\Delta L}{L} = \frac{\Delta R}{R} = \Delta \varepsilon_r$$

$$p_k = \frac{-E_s(\Delta R - \Delta R_{rest})}{R(1 + \nu_s)}$$

$$N = p_k R = E_c A_r \frac{-\Delta R_{rest}}{R}$$

Figure 5.17: Ring thermal expansion restrained by ground

## 5.5. Data processing methods for CSLs

For the ground conditions encountered at the location of the instrumented rings, constrained thermal strains are less than 5% of those realised in non-bedded rings. The steel thermal expansion coefficient,  $12.2\mu\epsilon/^\circ\text{C}$ , slightly higher than  $\alpha_{Tc}$ , ensures the non-interference of spear bolts on CSL thermal strains inside the tunnel.

Following the thermal curves derived from field monitoring data (see section 5.6.1, p.123), the mean concrete temperature increases at a nonlinear rate after grout backfilling for several TBM cycles. The rings experience a cumulative thermal expansion for several advances so that ring thermal strains may be affected by deformations in adjacent rings.

Figure 5.18 illustrates the typical profile of free thermal strains, proportional to temperature increments, exhibited by the instrumented segments with peak temperature increments per advance of about  $5^\circ\text{C}/\text{advance}$  in the second advance. The temperature profile in this advance could be approximated to a square roof function.

The axisymmetric problem, ignoring the staggered position of longitudinal joints, could be viewed as that of a thin-walled cylinder subjected to a nonlinear temperature profile. Given the short width of the rings, it could be assumed that the nonlinear temperatures are accommodated by the sequence of ring cross-sections, each exhibiting nearly linear radial strains along their ring width. Following El-Tayeb's analytical method for the calculation of self-equilibrating stresses in cross sections that remain plane when subjected to nonlinear temperatures (El-Tayeb et al., 2015), the restrained thermal strains in an instrumented ring cross section by the end of its second advance could be estimated.

It emerged that the predicted peak restrained strains were less than  $2.5\mu\epsilon$  and  $20\mu\epsilon$ , i.e. 5% and 40% of free thermal strains, at the centroid and DFOS side position respectively. Although the above deviations certainly contribute to measurement uncertainty, their magnitude remains small when contextualised, given that VWSGs were installed in the vicinity of segment centroids and that both values are lower than the BOTDR repeatability achieved in this case study (see section 5.6.2, p.127).

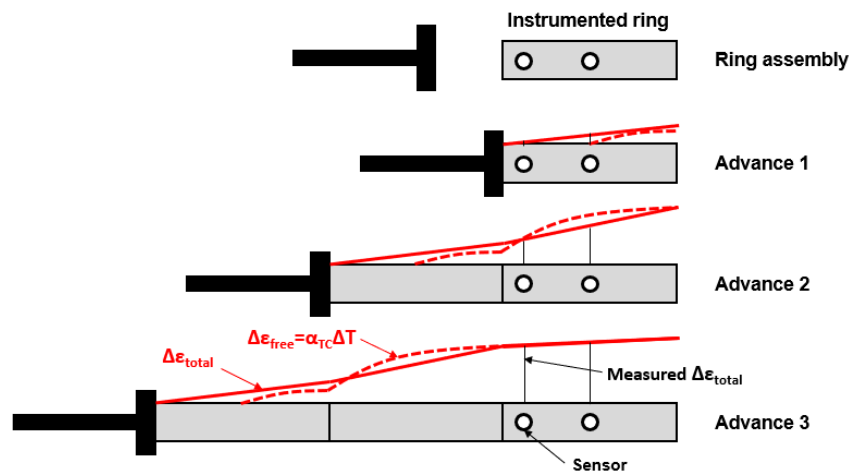


Figure 5.18: Strain profiles due to CSL temperature increments

## 5.5. Data processing methods for CSLs

---

Overall, about 95% of the concrete thermal strains can develop freely in the hoop direction at centroid positions and restrained strains at the side positions may only be significant during the second advance.

Accordingly, the temperature compensated strains in Figure 5.19 reflect rational patterns in the mechanical deformations of CSLs. For example, during tunnelling, the compensated strains show a progressive lining compression from the first advance onwards, whilst, in the long term, they increase gradually with monotonic trends that resemble time-dependent concrete creep deformations under sustained compression. Conversely, total strains are positive for the 200h following ring erection and adhere to temperature changes once tunnelling effects become negligible.

## 5.5. Data processing methods for CSLs

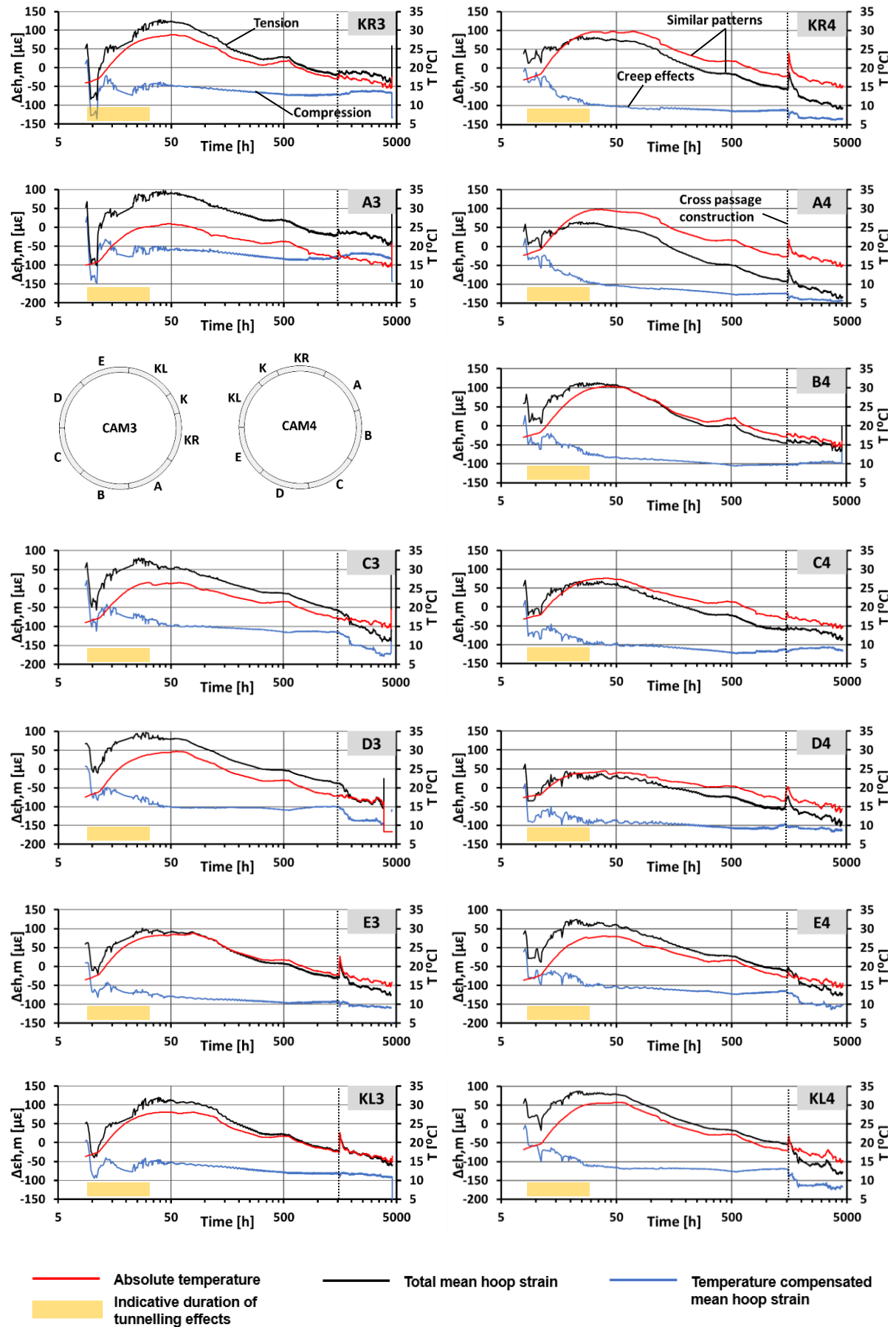


Figure 5.19: Initial mean hoop strains and absolute temperatures

### *b) Changes in mean longitudinal temperature*

Given the typical temperature changes experienced by simultaneously backfilled CSLs, the tunnel tube must also experience a sequential tendency to longitudinal thermal expansion. The suitability of temperature compensation is treated here through a simplified spring model (see Figure 5.20). A more realistic analytical model with due consideration of sequential construction and soil-structure interaction is developed in chapter 6 to further explain the effect of temperature variations on CSL longitudinal response.

The spring system is made of two springs in series with fixed nodes at its ends. One spring represents the row of  $n$  rings, packers included, behind the TBM that undergo a temperature increase,  $n$  being in the order of six according to field data. The second spring accounts for the subsequent row of  $m$  rings with constant temperature that are allowed to move longitudinally. The ratio of restrained thermal strains in a concrete ring within the group of  $n$  rings can be calculated with Eq. 5.11:

$$R_{\Delta T} = \frac{n}{n+m} \frac{\alpha_{Tc}W + \alpha_{Tp}t_p}{\alpha_{Tc}W} \frac{1}{1 + \frac{k_c}{k_p}} \quad (5.11)$$

where  $\alpha_{Tp}$  is the thermal expansion coefficient of packers equal to  $28\mu\epsilon/^\circ\text{C}$ ;  $k_c$  is the ring axial stiffness,  $k_p$  is the packer axial stiffness,  $W$  the ring width and  $t_p$  the packer thickness of 2mm. Figure 5.20 illustrates the proportion of free thermal strains that can develop in such a system, with and without packers, for various values of  $n$  and  $m$ . In a lining provided with packers and with  $n=6$ , the longitudinal stiffness of 20 subsequent rings enables the development of 80% of free thermal strains, and 90% is attained at  $m \approx 60$ . A reduction in  $n$  increases the proportion of unrestrained thermal strains even for a small number of  $m$  rings. Packers play a secondary role, although soft packers contribute to release the longitudinal constraints for thermal expansion.

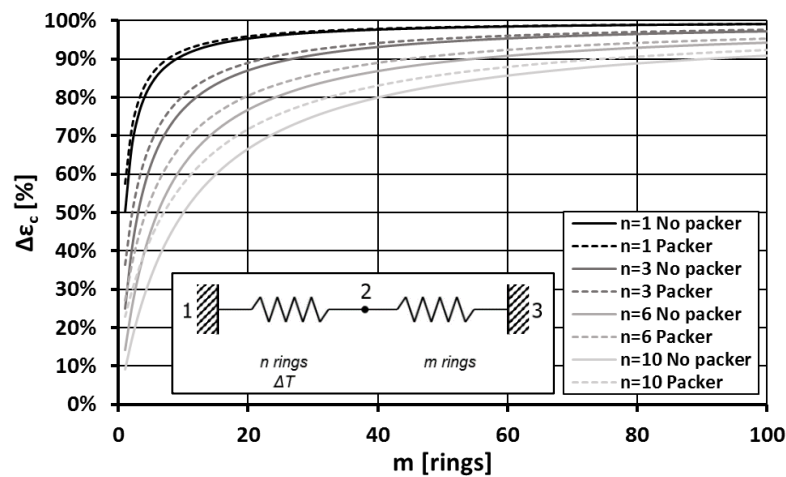


Figure 5.20: Unrestrained thermal strain in longitudinal direction

## 5.5. Data processing methods for CSLs

---

Figure 5.21 shows the evolution of absolute temperatures and strain increments derived from longitudinal VWSG measurements, and calculated strain increments inferred from average ram loads applied to each segment (which were available from TBM data). In all the segments, there is a good correlation between calculated and temperature compensated strain increments for at least the first TBM cycle after ring erection. This is clearly not the case for the total strains, which consistently display smaller compression or even tension in some segments.

The above suggests that thermal strains can develop in free conditions at the early stages of tunnel construction while instrumented rings are not fully bedded in the ground. The effect of soil-structure interaction and sequential uneven loading is more evident in subsequent data with the apparent divergence of field strains from the calculated strains.

The longitudinal CSL response will be fully addressed in chapter 6 with further consideration of thermal effects. For the moment, it has been proven that temperature compensation of mean longitudinal strains can be validated in non-bedded rings and that thermal strains may be partially restrained in bedded rings due to soil-structure interaction.

## 5.5. Data processing methods for CSLs

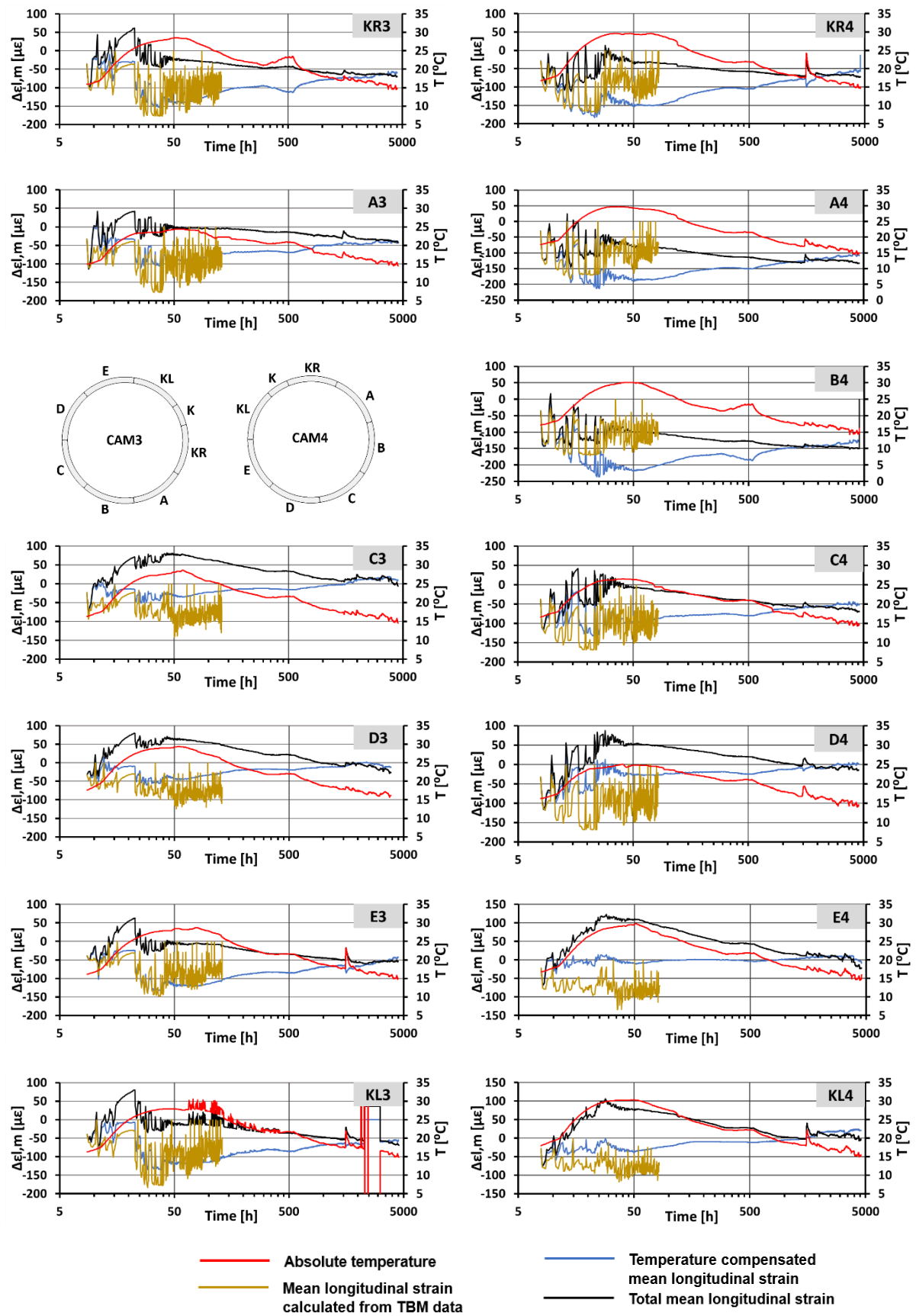


Figure 5.21: Initial mean longitudinal strains and absolute temperatures

### 5.5.3.3. Lining response to temperature gradients

Figure 5.22 illustrates total and temperature compensated initial hoop curvatures, plus thermal gradients,  $k_t$ , measured with hoop VWSGs. The curvatures are different only within the first 50h. Total curvatures are consistently greater than temperature compensated curvatures from the second advance,  $t \approx 11$ h, until  $t = 50$ h.

During tunnelling and the long term stages, the total hoop curvatures are insensitive to minor spikes in  $k_t$ , suggesting that thermal curvatures must be restrained. Besides, the long term pattern of constant curvature gradient is reached earlier in total than in compensated curvatures,  $t \approx 25$ h and  $t \approx 50$ h respectively. The former time correlates well with the estimated duration of tunnelling effects (see chapter 6). Only hoop curvatures at invert segments exhibit stepped changes that coincide with TBM advances for a longer period. Similar trends can be observed in initial longitudinal curvatures (see Figure 5.23).



## 5.5. Data processing methods for CSLs

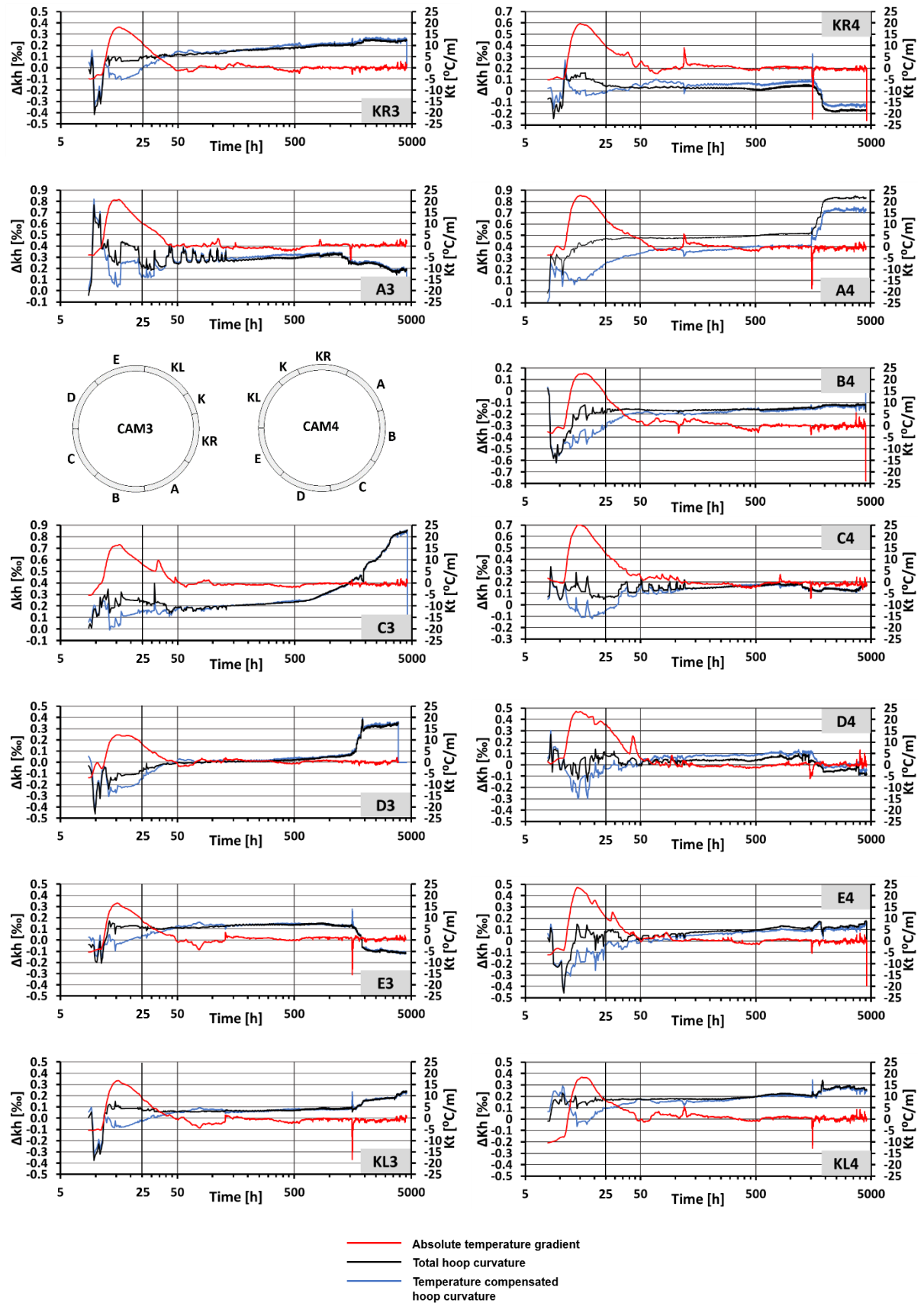


Figure 5.22: Initial hoop curvatures and absolute temperature gradients

## 5.5. Data processing methods for CSLs

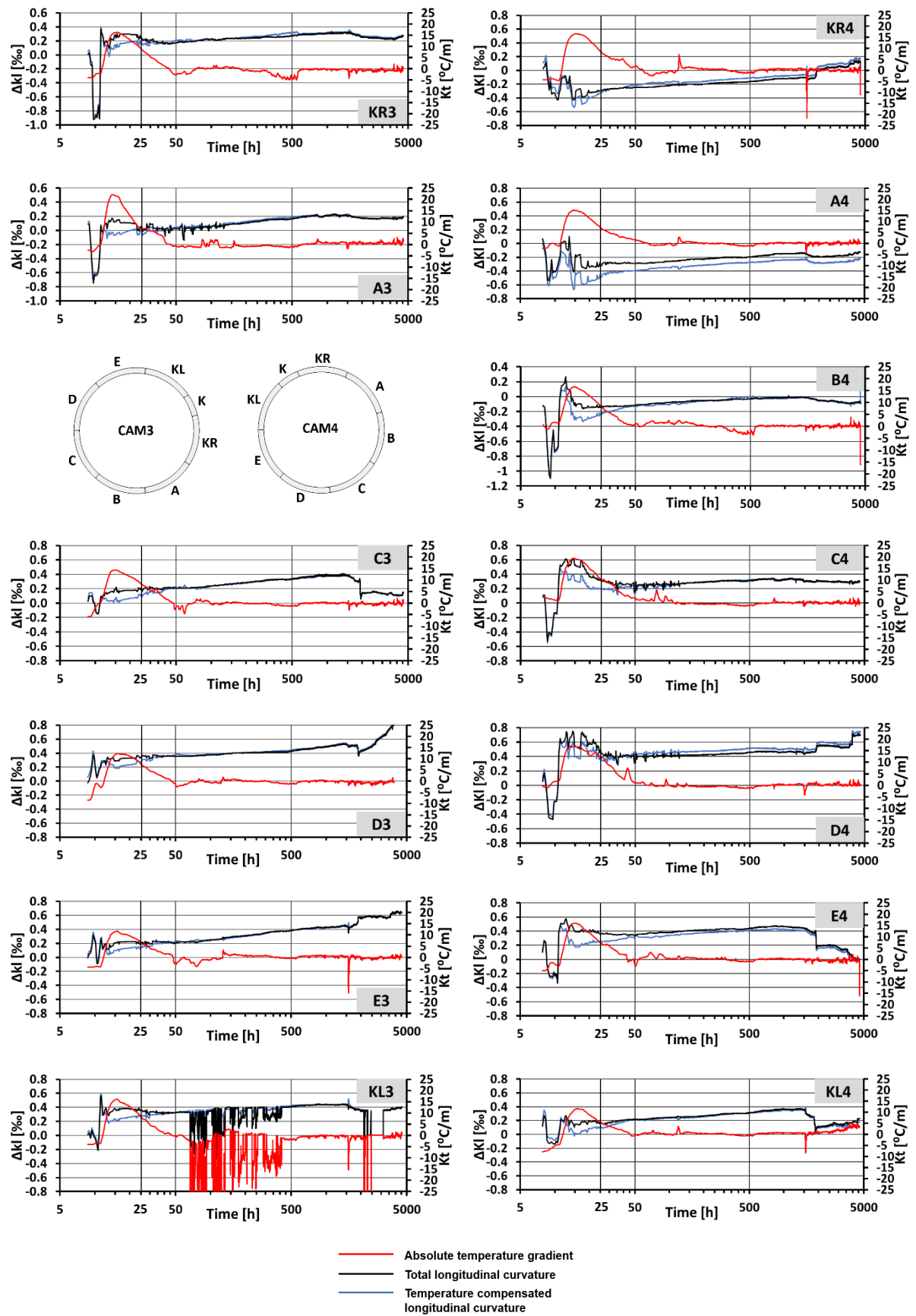


Figure 5.23: Initial longitudinal curvatures and absolute temperature gradients

## 5.5. Data processing methods for CSLs

The theoretical explanation of constrained thermal gradients is not obvious. Solving the elastic problem of a bedded straight segment subjected to thermal curvatures (see Figure 5.24.a), the restrained component,  $R_{k,\Delta T}$ , is given by Eq. 5.12:

$$R_{k,\Delta T} = \frac{1}{1 + \frac{2E_c I_c R(1 + \nu_s)}{E_s \left( \frac{x^4}{4} - \frac{Lx^3}{3} \right)}} \quad (5.12)$$

where  $I_c$  is the segment moment of inertia in  $m^4/m$  and  $L$  the segment length for hoop curvatures.

This expression leads to restrained thermal curvatures at the segment centroid of about 32% in typical CTT conditions. Coupling forces at circumferential joints may also oppose the development of thermal curvatures that could lead to differential displacements between adjacent rings with staggered joints (see Figure 5.24.b). Thus, the ground restraint and coupling forces add to the thermal strains restrained in cross-sections subjected to nonlinear temperature profiles (see section 5.5.3.1).

Despite the lack of complete theoretical grounds, total curvatures in both longitudinal and hoop directions appear to be more representative of CSL mechanical curvatures, and therefore will be used for the CTT field data interpretation.

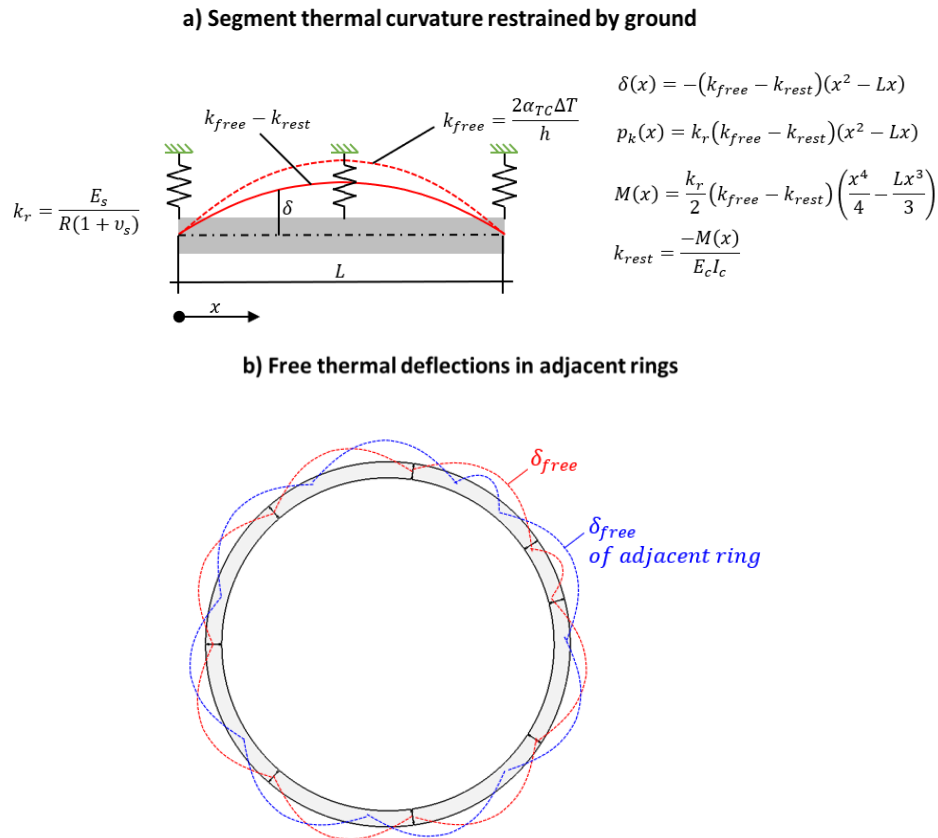


Figure 5.24: Restrained thermal curvatures

### 5.5.4. BOTDR data processing

With each measurement, the BOTDR interrogator provides a quadratic estimation of the BGS centre frequency shift for each sampling point along the FO circuit. The raw centre frequency data must be converted into interpretable data, which in strain sensing of parallel topologies subjected to non-isothermal conditions are at least total strains, total curvatures, temperatures and thermal gradients measured in the primary sections of each instrumented segment. Then, mechanical or structural strains and curvatures can be obtained as required.

The general steps for data processing in geotechnical applications are outlined by CSIC (2016), being these spatial shifting, filtering and breakdown of sensor segments. The author developed a customised Matlab® code for the CTT optical circuit that enables the automatic calculation and display of BOTDR strains, curvatures and temperatures in comprehensive dashboards (see Figure 5.27, p.125), also combined with VWSG and tilt data (see chapter 8).

Given the lack of local cable pre-tensioning in this case study, which is commonly used to provide reference positions in the optical circuits of fully bonded installations (CSIS, 2016), the author innovated a double cross-correlation method for the identification and alignment of segment sensors based on normalised BFS and BFS increments. Filtering was omitted to avoid masking real patterns of variable strains.

### 5.5.5. Evaluation of concrete elastic properties

Figure 5.25.a compares the initial mean longitudinal strains and mean strain decrements at segment centroids with average ram loads per segment during the first advance, AD1, and the segment unloading during CAM4 ring assembly, AS0, respectively. The theoretical correlation between ram loads and strains derived from the EC2 secant,  $E_{cm}=38\text{GPa}$ , and tangent,  $E_c=39.9\text{GPa}$ , moduli of C55/C67 concrete grades are also presented. This calculation is based on the assumption of a uniform load spread at the hoop centreline of the segment, which has been corroborated with plane stress models of linear elastic segments. The graph shows that the field data agrees with the linear relation inferred from both  $E_c$  and  $E_{cm}$ . The value of  $E_{cm}=38\text{GPa}$  is selected for future data interpretation.

Mean longitudinal and hoop strains at segment centroids are also plotted in Figure 5.25.b to estimate the Poisson's ratio,  $\nu_c$ . The second data set of AD1, AD1\_2, is dismissed as the hoop strains are already affected by the lining pressures. A  $\nu_c=0.18$  provides a best fit to the remaining data points, which is consistent with typical values obtained from static tests (Neville and Brooks, 2010), and long term  $\nu_c$  (Bazant and Murphy, 1995).

## 5.6. Comparative assessment of strain sensors

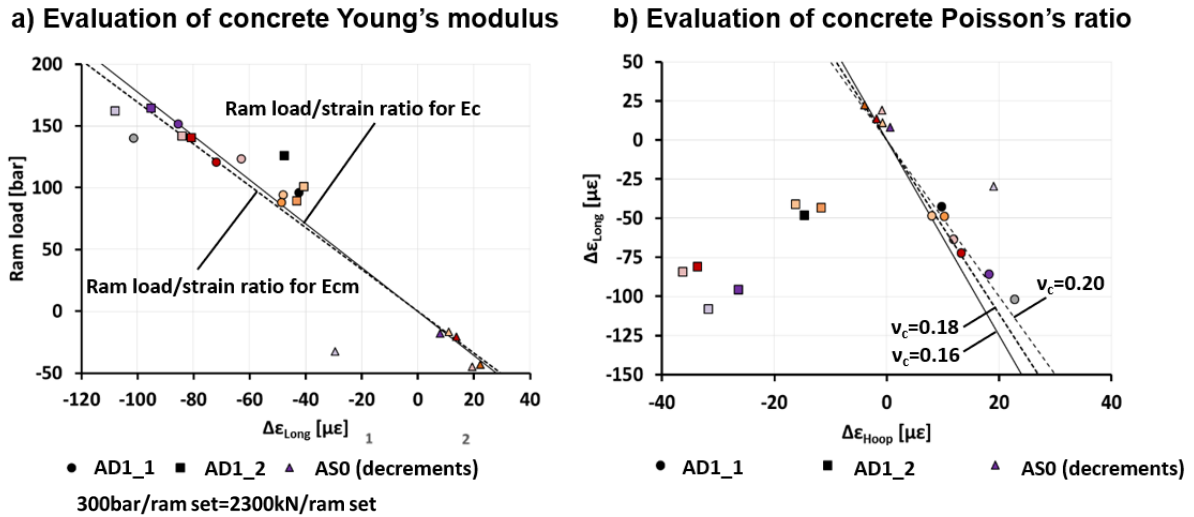


Figure 5.25: Concrete elastic properties

## 5.6. Comparative assessment of strain sensors

### 5.6.1. Temperature study

#### 5.6.1.1. Absolute temperatures

VWSG thermistors provided local measurements of absolute temperatures within concrete segments. Figure 5.26.a shows the evolution of the absolute temperature distribution in a segment until 90h after ring erection. Given that the temperature field at fixed lining depths remains relatively constant regardless the position of the sensing points (see Figure 5.27), it can be assumed that the VWSG measurements are representative of the temperature distribution with depth in a single segment location.

When the segment enters the tunnel, the concrete temperatures rise uniformly, from 12°C in this case to the ambient temperature in the tunnel of about 18°C, retaining the initial thermal profile. During the second advance, AD2, there is a rapid increase in concrete temperature driven by grout hydration. The temperature profile at time  $t=18h$  evidences a change in temperature distribution with a minor lag in temperature increase at the intrados caused by the poor diffusion of extrados heat. At  $t=90h$ , the segment cross-section exhibits uniform temperature.

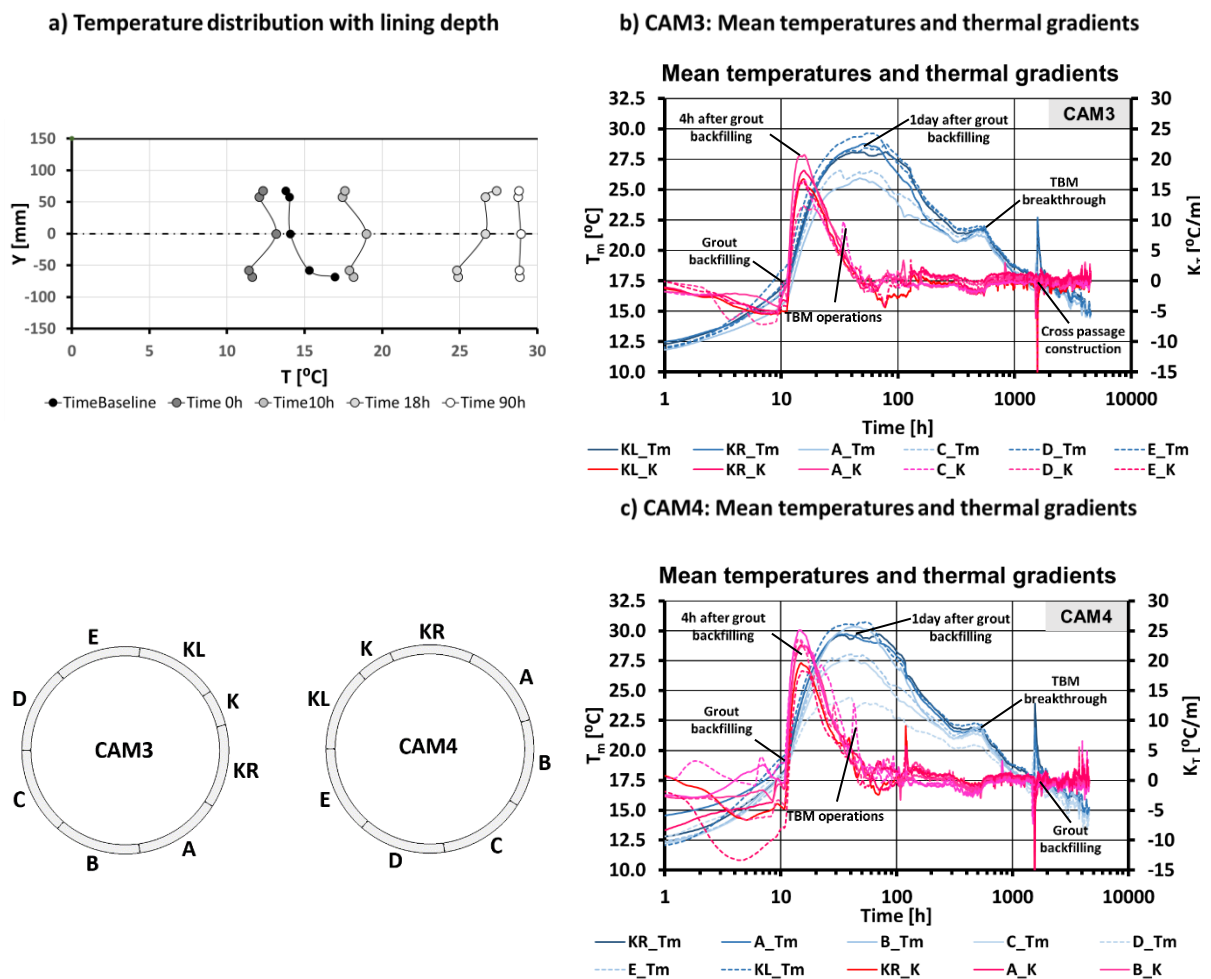
Nonlinear temperature profiles in segment cross-sections during tunnelling imply that mean temperatures and thermal gradients inferred from pairs of temperature sensors depend on their depth of installation. This dependency tends to be more pronounced in invert segments given the additional cooling effect of water or slurry sitting on top of them. The maximum discrepancies in mean temperatures and thermal gradients are about 3°C and 5°C/m respectively, which result in free thermal strain differences of approximately  $30 \pm 7.5 \mu\epsilon$  at cross-sectional extreme fibres.

Figures 5.26.b and 5.26.c illustrate the mean absolute temperatures and thermal gradients of the instrumented rings, computed from hoop strain gauge thermistors. All segments repeat temperature

## 5.6. Comparative assessment of strain sensors

patterns which are distinctive of tunnel operations. Grout hardening and slurry storage at the invert determine the lining mean temperature and thermal gradient distribution. Positive thermal gradients reach a peak of around  $20^{\circ}\text{C}/\text{m}$  after 4h of grout backfilling, and mean temperatures start deflating one day after grout hardening with maximum values of  $30^{\circ}\text{C}$  at crown and  $25^{\circ}\text{C}$  at the invert. By then, the thermal gradients become practically zero, and from this point onwards mean temperatures decrease smoothly at negligible gradients.

Besides grout hardening, a number of tunnel operations can be identified from lining thermal characterisation. First, the average lining temperature appears to settle to about  $22^{\circ}\text{C}$  at  $t \approx 300\text{h}$ . However, a further decrease is observed from  $t \approx 520\text{h}$  up to the end of the monitoring period when the mean temperature reaches  $15^{\circ}\text{C}$  roughly. This change in pattern may correspond to the TBM breakthrough. Second, the hardening of the grout between CSL and cross passage temporary works produces sudden spikes in mean temperature and thermal gradient, the latter of opposite sign to that developed by annular grout hardening. Third, secondary gradient peaks at the invert segments of both rings may suggest local cooling of the tunnel invert by pouring slurry during slurry pipe extension.



## 5.6. Comparative assessment of strain sensors



Figure 5.27: CAM4 BOTDR temperature increments at central hoop and longitudinal sections



## 5.6. Comparative assessment of strain sensors

---

### 5.6.1.2. Comparative performance of temperature sensing

BOTDR absolute temperatures can only be computed if at least one BOTDR measurement, e.g. the baseline, is performed at known absolute temperature distributions, preferably a field of uniform steady temperatures. Since baseline measurements were conducted on individual segments at ambient conditions, the BOTDR measurements enabled only the calculation of temperature increments relative to the baseline. Consequently, the comparison between the BOTDR and the VWSG temperature sensing capabilities is undertaken in terms of temperature increments.

Figure 5.28.a and 5.28.b presents VWSG and BOTDR temperature increments at the extreme fibres of the segment centroid in two segments, derived from hoop VWSGs and the central hoop temperature FO sections opposite to the position of the hoop VWGSs. The VWSG data was linearly interpolated against BOTDR measurement times and both the VWSG and the BOTDR temperatures converted to extreme fibre temperatures. The figures show the segments with the best, C4, and worst, B4, agreement between measurements.

The graphs evidence the lack of BOTDR data over certain periods of time due to the temporary unavailability of the BOTDR interrogator.

The dispersion of BOTDR measurements, characterised by a 99% confidence level of  $\pm 1.25^{\circ}\text{C}$ , or standard deviation of about  $\pm 1^{\circ}\text{C}$ , introduce an evident element of uncertainty in temperature sensing. However, the CTT measurement specification resolved temperature sensing with high precision relative to the instrument capabilities, given that the repeatability attained in standard laboratory tests at constant temperatures is  $\pm 1^{\circ}\text{C}$  (Neubrex, 2015).

BOTDR and VWSG temperatures evolved in a similar fashion but appeared to diverge by a fairly constant gap, more evidently in segment B4 than C4. This shift in temperature captured by sensors located at different lining depths could be explained by the nonlinear temperature distribution with depth of baseline measurements (see Figure 5.26.a).

Accordingly, a mean temperature difference was calculated over a 24h period with relatively constant temperature to calibrate the BOTDR against the VWSG temperatures. After temperature correction, the agreement between the BOTDR and the VWSG temperature increments was greatly improved, particularly B4 (see Figure 5.28.c and 5.28.d).

Nevertheless, given the nonlinear profile of baseline temperatures, the corrected values of BOTDR measurements are only useful to assess the BOTDR performance in regards to temperature sensing. The original temperature increments must be input for the computation of the BOTDR strains.



## 5.6. Comparative assessment of strain sensors

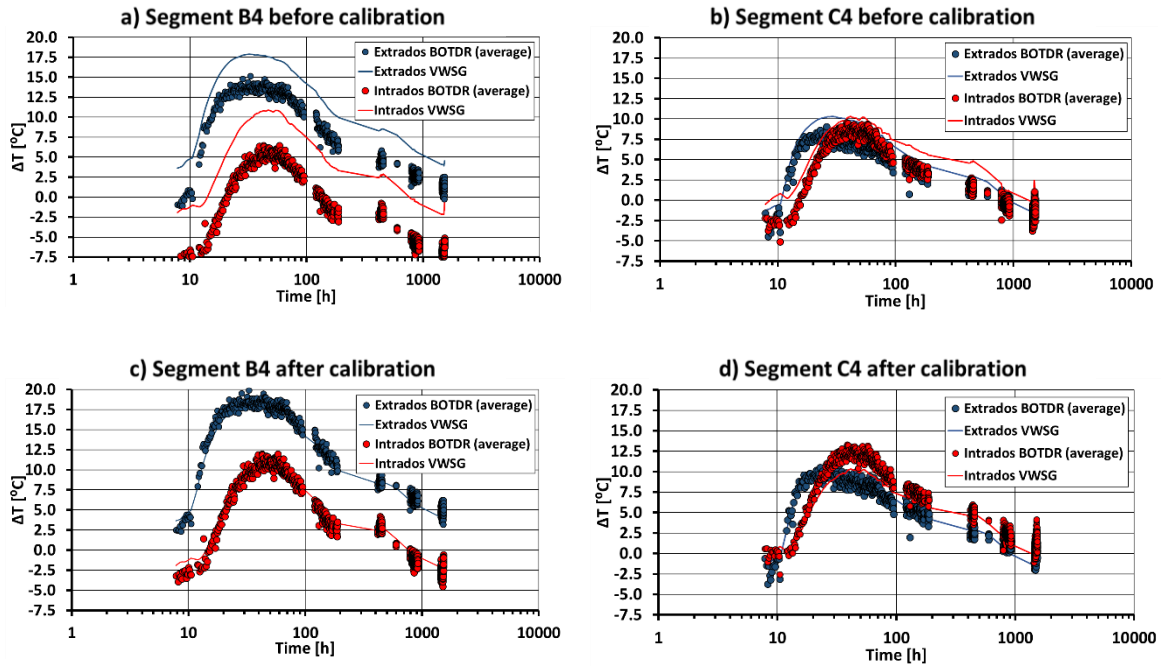


Figure 5.28: VWSG and BOTDR temperature increments at extreme fibres

### 5.6.2. Strain study

Given the lack of BOTDR measurements at time  $t \approx 0$ h, the comparison of strain sensing performance between VWSGs and BOTDR must be drawn on raw strain increments. Figures 5.29 to 5.34 show mean strains, curvatures and strains at extreme fibres captured at CAM3 and CAM4 by BOTDR and VWSGs in hoop and longitudinal directions. Except for the BOTDR profiles of Figure 5.33, the BOTDR quantities are mean values of raw strain data measured over 150mm length of usable sensor segments opposite to VWSG positions.

The BOTDR strain measurements and combined quantities exhibit a manifest degree of dispersion. Table 5.4 summarises the mean, maximum and minimum standard deviations derived from a 24h period of long term measurements in CAM3 and CAM4 segments. The average values are consistent with the Neubrescope-5000X repeatability of  $\pm 20 \mu\epsilon$ , which indicates that, again, the CTT measurement specification was adequate. The increase in CAM3 optical budget caused by a 2dB local power loss within one of its instrumented segments resulted in a peak standard deviation of  $\pm 35 \mu\epsilon$ , which exemplifies the sensitivity of strain repeatability to optical budget.

Table 5.4: BOTDR standard deviation within a long term 24h period

Standard deviation	CAM3					CAM4				
	Long.	Hoop Centre	Hoop Side	Max.	Min.	Long.	Hoop Centre	Hoop Side	Max.	Min.
$\Delta \epsilon_{\text{ext}} [\mu\epsilon]$	$\pm 21$	$\pm 21$	$\pm 22$	$\pm 35$	$\pm 16$	$\pm 22$	$\pm 20$	$\pm 21$	$\pm 25$	$\pm 17$
$\Delta \epsilon_{\text{m}} [\mu\epsilon]$	$\pm 10$	$\pm 10$	$\pm 10$	$\pm 16$	$\pm 8$	$\pm 10$	$\pm 9$	$\pm 10$	$\pm 12$	$\pm 8$
$\Delta k [\text{‰}]$	$\pm 0.12$	$\pm 0.12$	$\pm 0.13$	$\pm 0.21$	$\pm 0.10$	$\pm 0.13$	$\pm 0.12$	$\pm 0.12$	$\pm 0.15$	$\pm 0.10$

## 5.6. Comparative assessment of strain sensors

---

The figures also show that there is no significant increase in the dispersion of strain measurements conducted under transient temperatures. However, with typical field strain and curvature data comprised within  $[-300, +150]\mu\epsilon$  and  $[-1.5, +1.5]\%$  intervals, the standard deviation of the BOTDR data represents more than 10% of peak strain quantities.

Besides the measurement uncertainty introduced by calibration coefficients, the comparison of BOTDR and VWSG strain accuracy is hampered by several factors inherent to this particular deployment: (i) measurement uncertainty in BOTDR temperature increments; (ii) different gauge length, position and depth of strain gauges and DFOS at segment centroids in combination with nonuniform strain and temperature fields; (iii) attachment method of strain sensors in cracked regions of concrete; and (iv) uncertainty in the identification and alignment of DFOS usable sensor segments during data processing. Consequently, data correction methods such as the BOTDR data calibration applied to temperature increments (see section 5.6.1.2) are not appropriate for strain variables.

The comparison between the VWSG and BOTDR strain sensing must be qualitative and is based on strains detected at segment centroids:

### *a) Hoop strains and curvatures:*

In CAM4 segments, there is generally good agreement between BOTDR and VWSG hoop mean strains and curvatures, including side BOTDR strains, once tunnelling effects are dissipated (see Figure 5.29). In the tunnelling stage, differences in mean strains measured along the segment width are caused by the sequential loading of rings with simultaneous backfill grouting, whilst divergent curvatures may be the result of radial TBM or coupling forces acting along the ring circumference (see chapters 4, 7 and 8).

The mismatch between the VWSG and BOTDR strain quantities in segment B4 can be explained by the longitudinal cracking detected with the DFOS (see Figure 5.33.a). The BOTDR strain profiles in the first TBM cycle exhibit a progressive tension increase at the intrados of the segment midpoint. Peak tensile strains of  $+250\mu\epsilon$  and  $+300\mu\epsilon$  at central and lateral profiles respectively clearly exceed the  $+130\mu\epsilon$  yield tensile strain of the CTT concrete. Such high tensile strains were not captured by the VWSGs situated about 300mm away from the BOTDR central section (see Figure 5.30). The B4 strain mapping reveals that (i) at least a longitudinal crack was initiated near the midpoint of the circumferential face in contact with the ram pads and (ii) the longitudinal crack propagated beyond the position of the BOTDR central section.

In the long term, the BOTDR intrados strains reached a plateau at null values (see Figure 5.30), which may suggest that the crack closed at least partially with time. Conversely, the long term VWSG intrados strains in the uncracked concrete experienced a progressive increase in compression with time, possibly due to concrete creep.

## 5.6. Comparative assessment of strain sensors

---

It is important to highlight here that BOTDR strain measurements are strain increments developed from a reference measurement, not absolute strains. Additionally, concrete is an inhomogeneous material whose mechanical properties, including the yield tensile strain, entail a certain degree of dispersion.

Consequently, the crack detection in BOTDR strain profiles may be also driven by the combination of certain strain patterns rather than only absolute thresholds of tensile strains. For example, the bell shape and peak tensile strains greater than  $+100\mu\epsilon$  of A4 lateral BOTDR strain profiles comprised between  $t=24\text{h}$  and  $t=96\text{h}$  may suggest the presence of a moderate longitudinal crack, in this occasion, at the extrados of the segment midpoint (see Figure 5.33.b).

This longitudinal crack may explain the constant value of  $+50\mu\epsilon$  in long term lateral BOTDR extrados strains (see Figure 5.30), which in turn leads to mean strains and curvatures greater than those measured with strain gauges (see Figure 5.29). The reduction in lining stiffness induced by the longitudinal crack may have triggered the longitudinal migration of hoop moments towards the central BOTDR section, resulting in curvatures slightly greater than those at the segment side.

In the CAM4 invert segments, the BOTDR hoop curvatures differ from the VWSG hoop curvatures from  $t=10\text{h}$  onwards (see Figure 5.29), with the BOTDR curvatures presenting the same pattern of increase and decrease with time in both segment C4 and D4. It is not entirely clear the cause for such divergence, although it could be related to a delayed adjustment in coupling forces induced by changes in longitudinal moments. The sharp fluctuations in curvature measured with the VWSGs until  $t=50\text{h}$  are masked by the dispersion of the BOTDR data.

In the CAM3 segments, the permanent gaps between mean hoop strains measured at different segment width positions evidence that the effect of sequential loading persisted over time in segments C3 to KL3 without affecting the hoop curvatures (see Figure 5.31).

The B3 VWSG data logger was damaged and thus the retrieved field data is not reliable (see Figures 5.31 and 5.32). Further examination of the BOTDR strain profiles revealed that B3 was subjected to an extremely variable hoop strain field developed from the ring assembly onwards (see Figure 5.33.c), thus suggesting that it may be related to contact imperfections. A more in-depth examination is tackled in chapter 8.

## 5.6. Comparative assessment of strain sensors

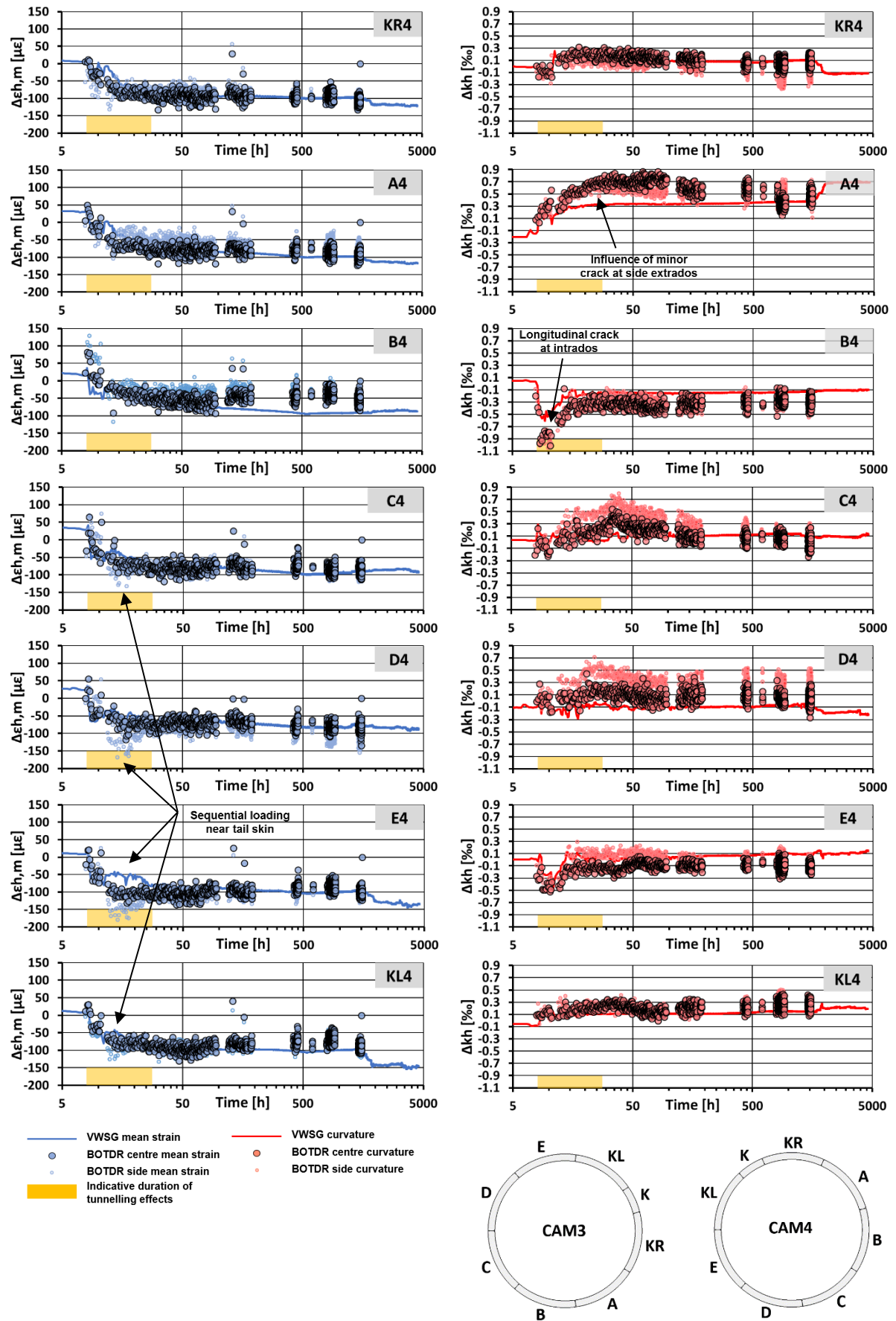


Figure 5.29: CAM4 raw mechanical hoop mean strains and curvatures

## 5.6. Comparative assessment of strain sensors

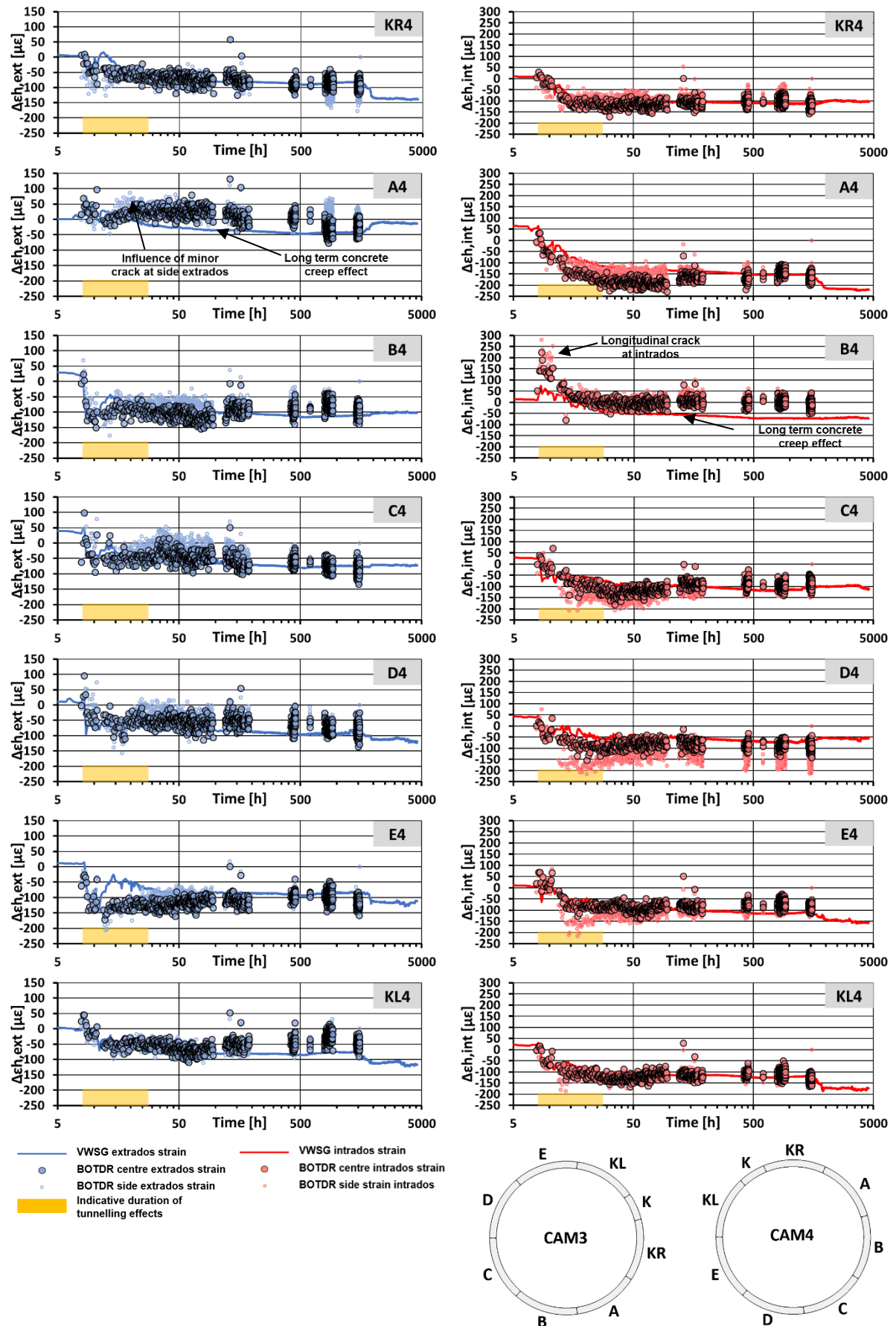


Figure 5.30: CAM4 raw mechanical hoop extreme fibre strains

## 5.6. Comparative assessment of strain sensors

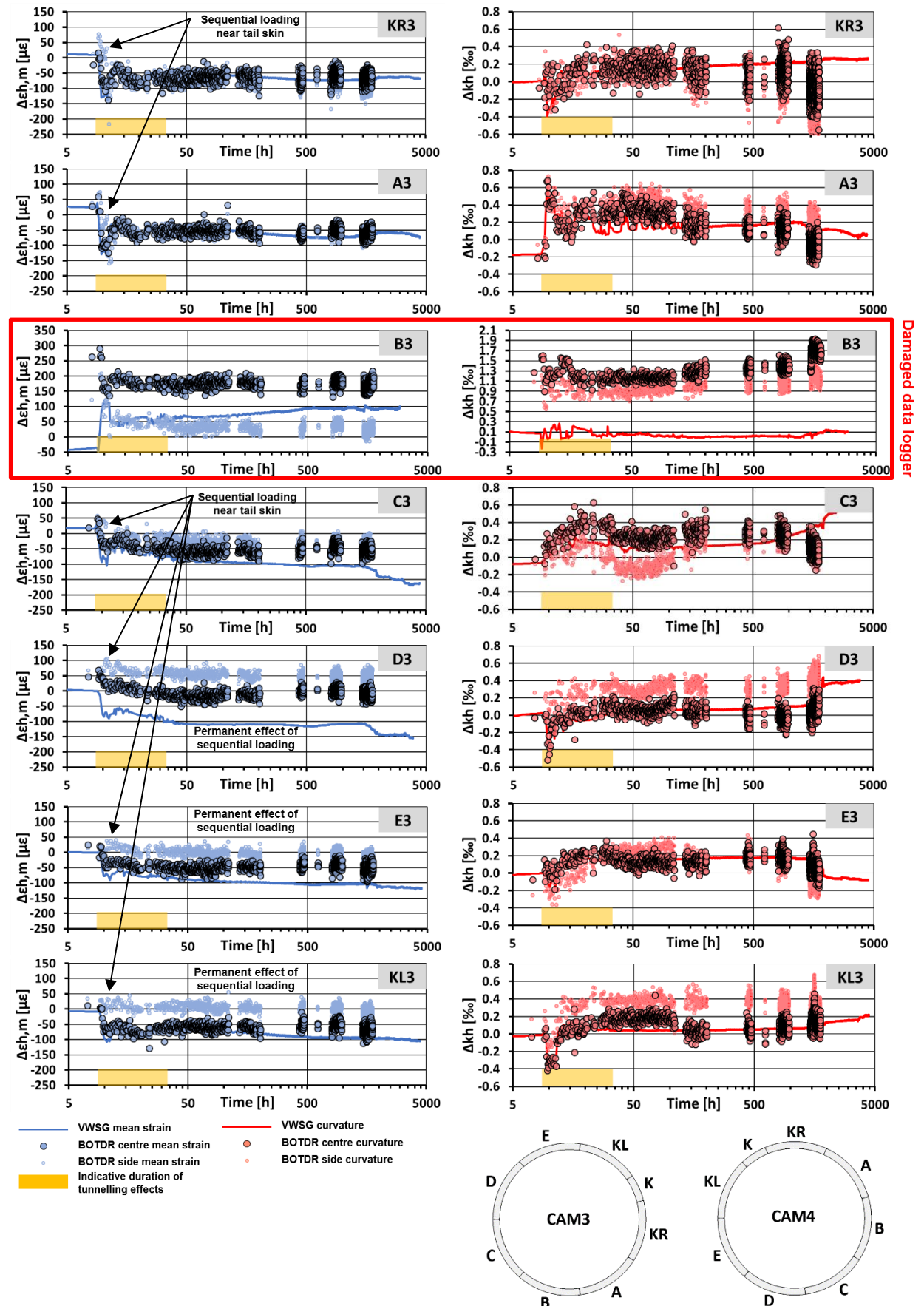


Figure 5.31: CAM3 raw mechanical hoop mean strains and curvatures



## 5.6. Comparative assessment of strain sensors

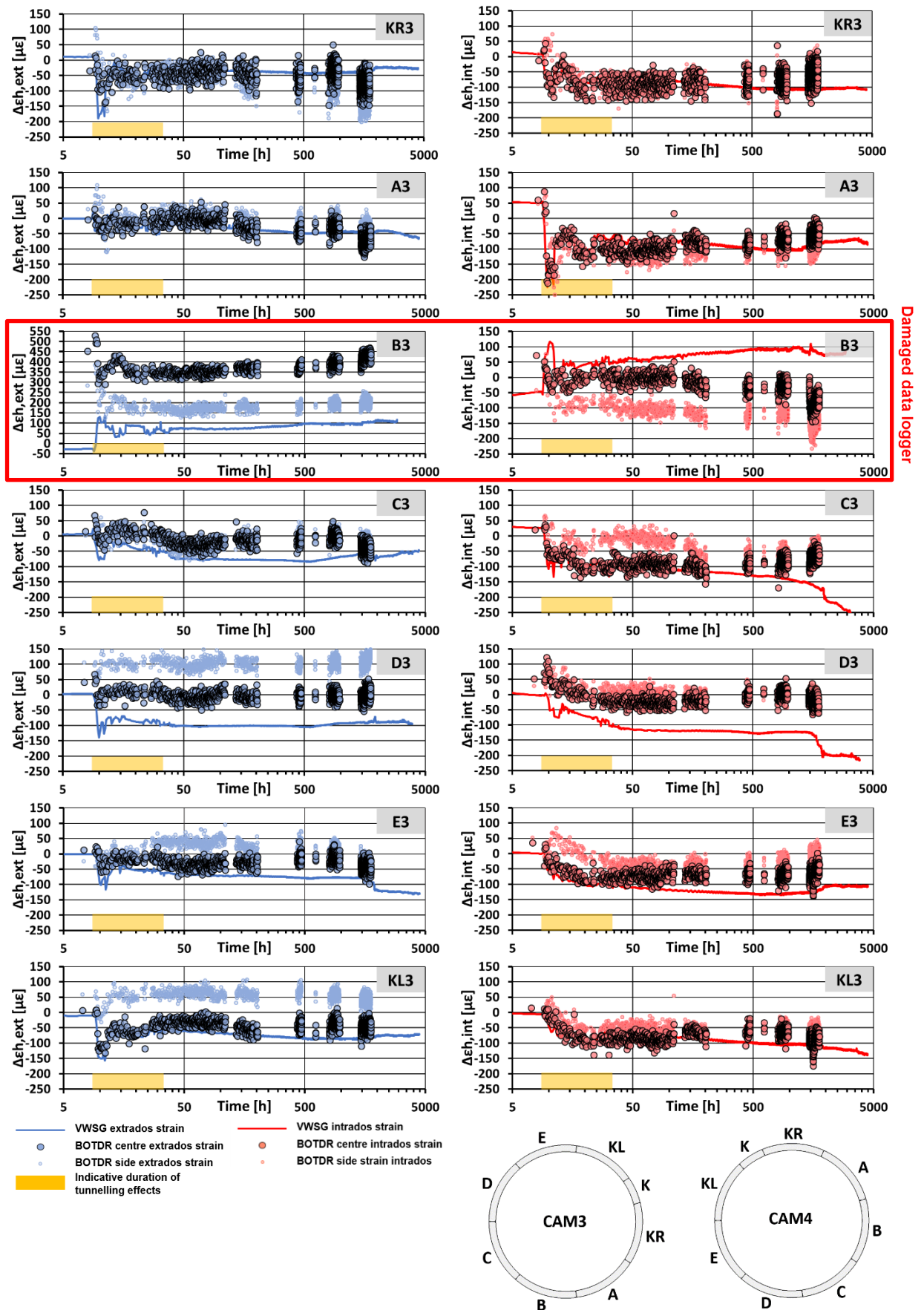


Figure 5.32: CAM3 raw mechanical hoop extreme fibre strains

## 5.6. Comparative assessment of strain sensors

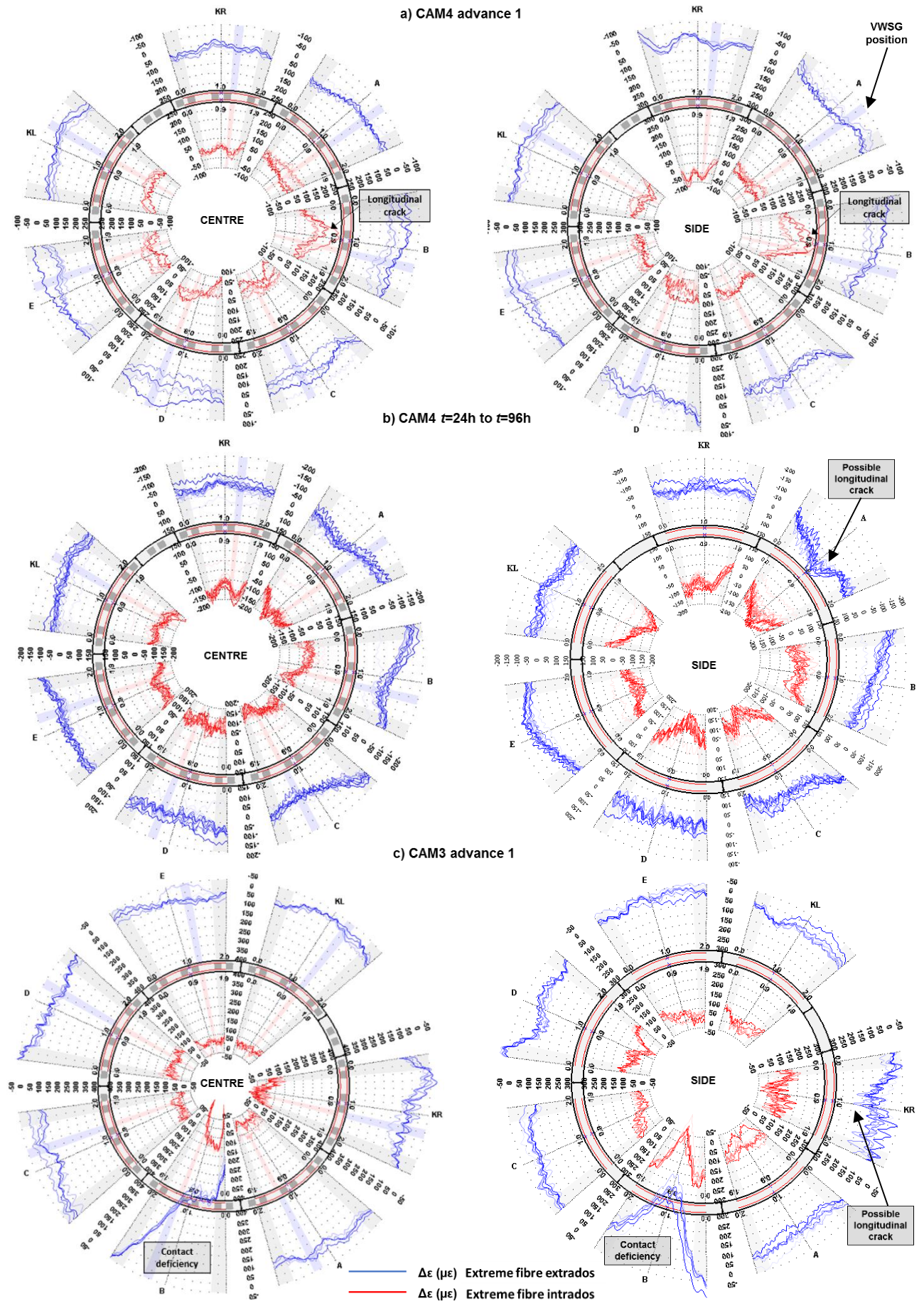


Figure 5.33: BOTDR damage and contact deficiency detection



## 5.6. Comparative assessment of strain sensors

---

### *b) Longitudinal strains and curvatures:*

BOTDR and VWSG longitudinal strains at extreme fibres of CAM4 segments follow almost reverse trends, with the BOTDR mean strains presenting consistently greater tension and short term BOTDR curvatures being disproportionately larger and of opposite sign (see Figures 5.34 and 5.35). Since VWSG mean strains describe adequately the longitudinal CSL behaviour (see chapter 6), such notable disparities in all longitudinal measurements must stem from a common physical cause.

The optical cables for the hoop loops were routed on the inside of the hoop bars with their ends detached from any reinforcement. In the longitudinal direction, however, the loops were fixed externally around the shear links. It would appear that the attachment method of the longitudinal loops forced them to mimic the shear link deformations, including those caused by splitting forces and ram pressures at the shear link ends, thus leading to the greater tension and reverse trends observed in the BOTDR measurements.

There is a better agreement between the BOTDR and VWSG mean strains in CAM3 than CAM4 segments although the BOTDR mean strains still present an additional tensional component (see Figure 5.36). The CAM3 BOTDR curvatures are substantially different from those obtained from VWSGs, particularly after several TBM cycles when the tunnel is subjected to high longitudinal TBM moments during TBM steering around a horizontal curve (see chapter 6). This trend gives further evidence that the measurement mismatch is associated with local deformations caused by the concentrated transfer of longitudinal loads.

## 5.6. Comparative assessment of strain sensors

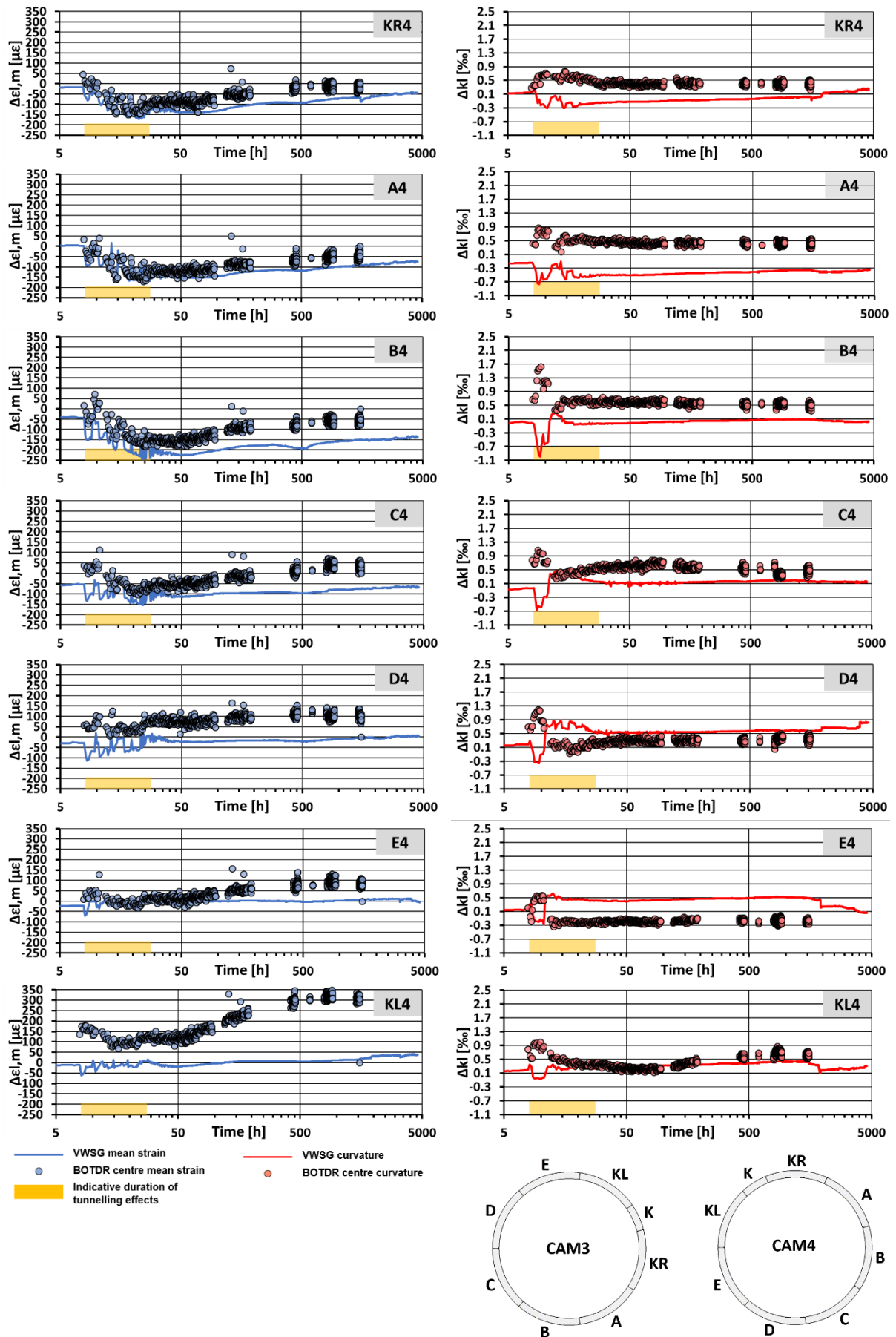


Figure 5.34: CAM4 raw mechanical longitudinal mean strains and curvatures

## 5.6. Comparative assessment of strain sensors

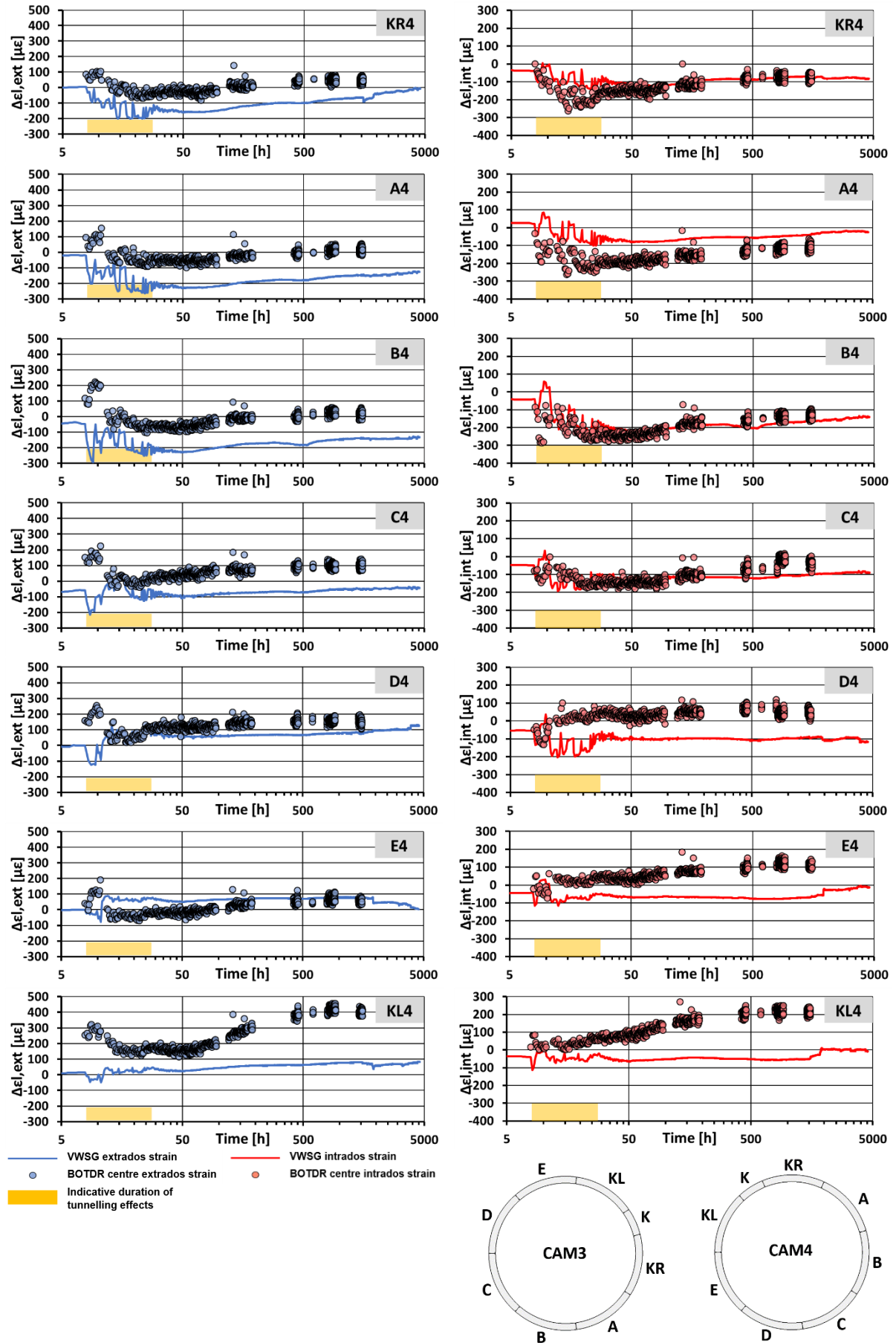


Figure 5.35: CAM4 raw mechanical longitudinal extreme fibre strains

## 5.6. Comparative assessment of strain sensors

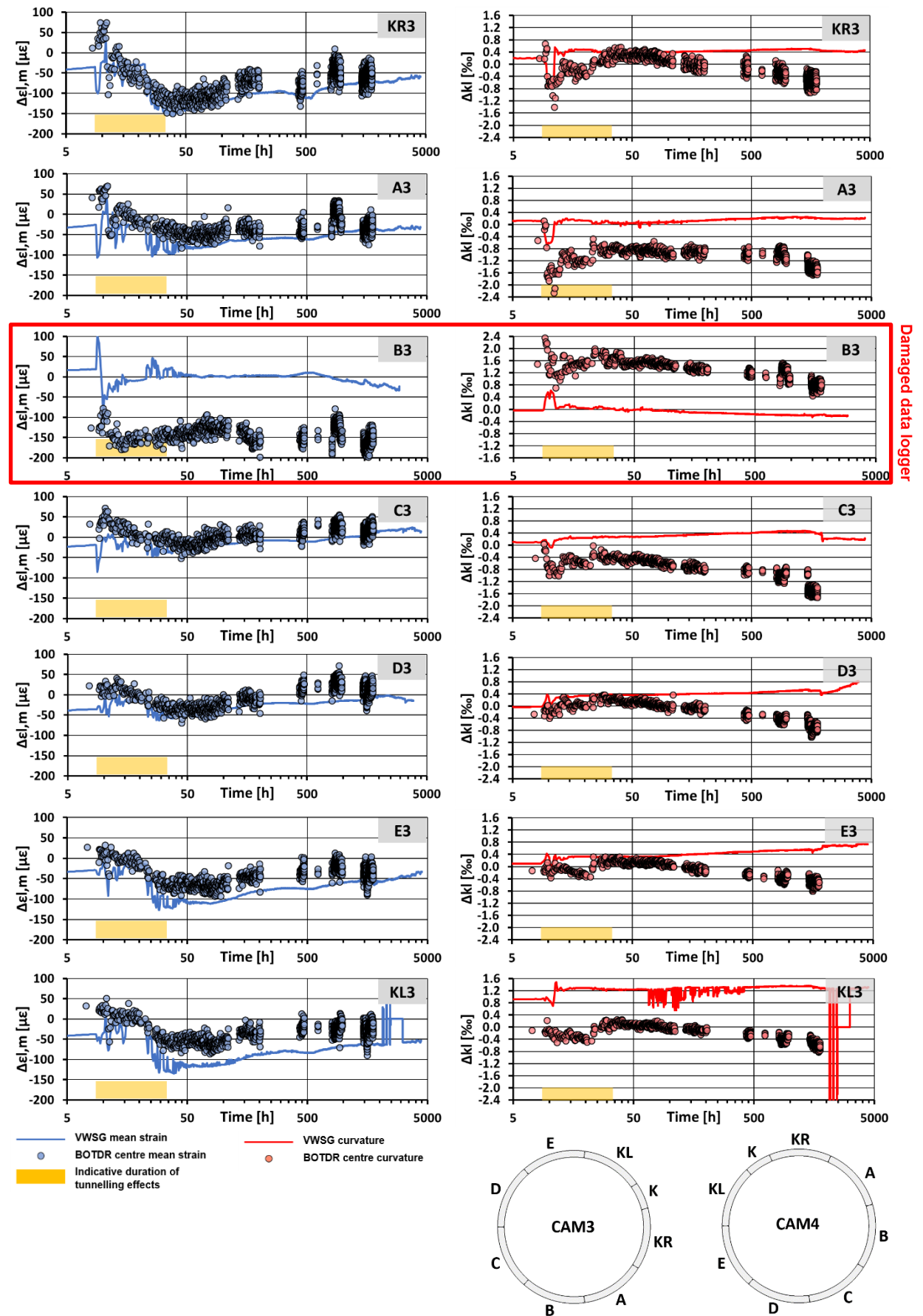


Figure 5.36: CAM3 raw mechanical longitudinal mean strains and curvatures

## 5.6. Comparative assessment of strain sensors

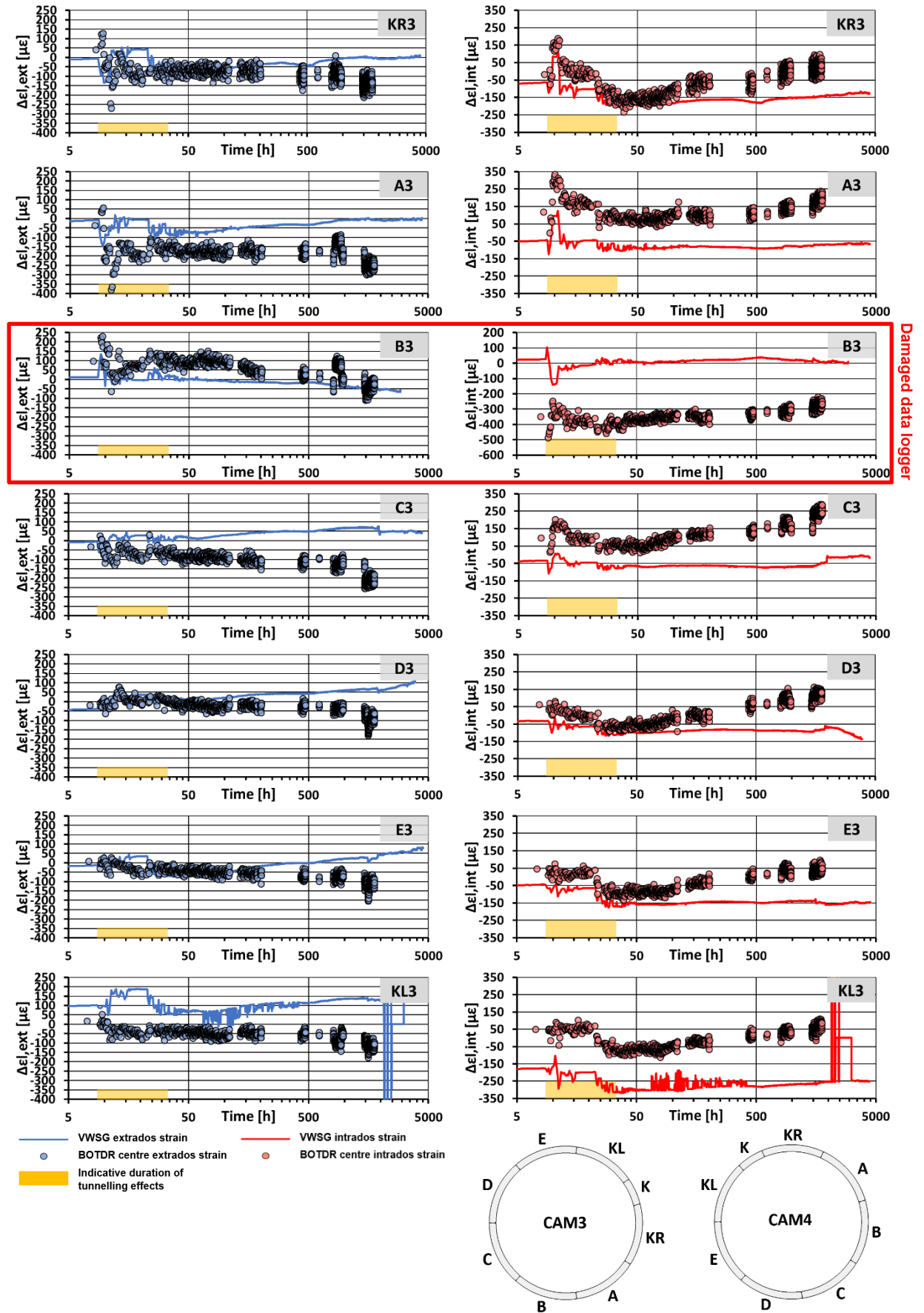


Figure 5.37: CAM3 raw mechanical longitudinal extreme fibre strains

### 5.7. Conclusions

The issues encountered in this SHM case study demonstrated the importance of a structured approach to SHM systems design from early design stages, through the identification and analysis of system requirements and site constraints. When a design solution relies on technology whose performance has not been previously attested, alternative solutions must be designed in parallel to satisfactory detail so that the project risk can be controlled in case of test failure, and the design and installation works can be completed sequentially within rational deadlines. These conclusions are particularly relevant for SHM systems where maturing technology such as DFOS is deployed in new working environments, and would definitely contribute to lower costs and the risk of project failure.

It was also evidenced that an in-depth study of BOTDR measurement accuracy that tackles the effect of nonlinear strains and concrete cracks is needed. The impact of attachment methods of embedded DFOS on crack detection and average steel strain measurement should also be examined.

The lack of local cable pre-tensioning during the installation of DFOS in CSL segments to facilitate data processing can be addressed with the new double cross-correlation method based on normalised BFS and BFS increments.

In CSLs with staggered joints, temperature compensated mean strains represent net mechanical strains in hoop direction and total mechanical strains in longitudinal direction. Total curvatures represent better the net mechanical curvatures.

Based on the evaluation of the BOTDR performance in the CTT deployment, it can be concluded that (i) the measurement specification was adequate for the optical budget of ring optical circuits; (ii) the dispersion in BOTDR data determined by the deployed interrogator was excessive for the range of measurements typical of CSLs and therefore future deployments targeting lining behaviour must select BOTDR interrogators with higher repeatability; (iii) BOTDR strain data outperformed the  $\pm 50\mu\epsilon$  measurement accuracy expected from instrument specifications; (iv) the 500mm gauge length enabled crack detection through the centroid fitting method; (v) distributed strain sensing can detect effectively structural damage in concrete at serviceability states; (vi) in CSLs, DFOS in parallel topologies must not surround shear links; and (vii) a more precise performance-based assessment of BOTDR strain sensing would require DFOS and VWSGs with equal gauge length to be installed at the same position and lining depth and with equivalent attachment methods.

# Chapter 6

## Thames tunnel field data interpretation: longitudinal response to sequential construction

### 6.1. Introduction

In grouted smooth bore tunnels, CSLs are subjected to the effects of TBM operations through the direct interaction with various TBM parts and the impact that those operations have on lining pressures and ground support behind the tunnel face (see Figure 1.1.a). The tunnel tube is axially pre-stressed through the thrust forces exerted by the TBM hydraulic jacks during both excavation and standstill. The TBM ring erector assembles a new ring within the tail skin at the end of every advance, which leaves an annular gap between the excavation line and the lining extrados once the TBM moves forward. Like in the CTT tunnel, the tail void is generally backfill grouted simultaneously with the TBM advance to minimise ground settlement and provide early support to the lining.

In this chapter, the longitudinal response during and after tunnelling of the CTT near the instrumented rings is studied in detail. Analytical rod and beam models that consider the sequential construction and loading of the tunnels are developed to optimise the field data interpretation. A PDA method for the identification of areas at risk of ring joint damage is also proposed.

### 6.2. Longitudinal pre-stressing of tunnel lining

#### 6.2.1. Background

In a theoretical scenario where there is no longitudinal ground-structure interaction, the total longitudinal force remaining in a tunnel tube would be the last applied by the TBM rams or restrained by the TBM shove frames, at the end of tunnelling. However, longitudinal movements in the lining after grout hardening can induce the migration of the tunnel pre-stressing forces to the ground, as long as the shear yield strength of the ground-lining interface is not exceeded (Arnau, 2012; Koek, 2005a). The lining movements can be caused by fluctuations in the magnitude of pre-stressing forces due to tunnelling, or time-dependent deformations of longitudinal lining components, i.e. concrete segments and packers (Arnau, 2012). The latter includes volumetric changes in packers due to material degradation (Koek, 2005a).

Koek (2005a; 2005b) developed an analytical model to estimate longitudinal pre-stressing during TBM construction based on the sequential assembly of a pre-stressed elastic rod in shear interaction

## 6.2. Longitudinal pre-stressing of tunnel lining

with elastic ground. The solution was based on the superposition of loading states in a sequentially extended rod that could be resolved with the second order differential equation below and pertinent boundary conditions (Koek, 2005a):

$$\frac{d^2 u(x)}{dx^2} - \alpha^2 u(x) = 0 \quad (6.1.)$$

$$\alpha^2 = \frac{k_s}{E_c A_c} \quad (6.2)$$

where  $u(x)$  is the longitudinal displacement of the rod at position  $x$ ,  $\alpha^2$  is a stiffness factor,  $k_s$  is the ground distributed shear spring stiffness and  $A_c$  is the rod cross-sectional area. The analytical solution assumed a continuous rod with no ring joints, although Koek (2005a) verified that the effect of ring joints could be accounted for with relative accuracy by the adoption of an equivalent rod stiffness (Koek, 2005a). Koek (2005a) proposed that  $k_s$  could be approximated to  $\pi G$ ,  $G$  being the ground shear stiffness. Arnau (2012) confirmed that the stiffness of the annular grout had a negligible effect on the axial pre-stressing of the lining.

### 6.2.2. Analytical solution for thermal effect on longitudinal pre-stressing

In chapter 5, it was recognised that the longitudinal free thermal strains, caused by the exothermic reaction of the annular grout or changes in ambient temperatures after the TBM breakthrough, were partially restrained by the longitudinal interaction between lining and ground. Koek's approach can be implemented to estimate the thermally-induced strains,  $\Delta \varepsilon_{mech,th}$ , arising in the staged construction of a tunnel lining subjected to temperature variations.

An analytical solution is presented here with a trilinear temperature profile that displaces and develops with the sequential assembly of the elastic rod. Figure 6.1 shows the basic loading states representative of previous stages  $j$  that must be superimposed to solve a given construction stage  $i$ . Loading state 1 applies when the rod length  $L_j$  is smaller than  $L_1$ , loading state 2 when  $L_1 < L_j < L_2$  and loading state 3 when  $L_j > L_2$ .



## 6.2. Longitudinal pre-stressing of tunnel lining

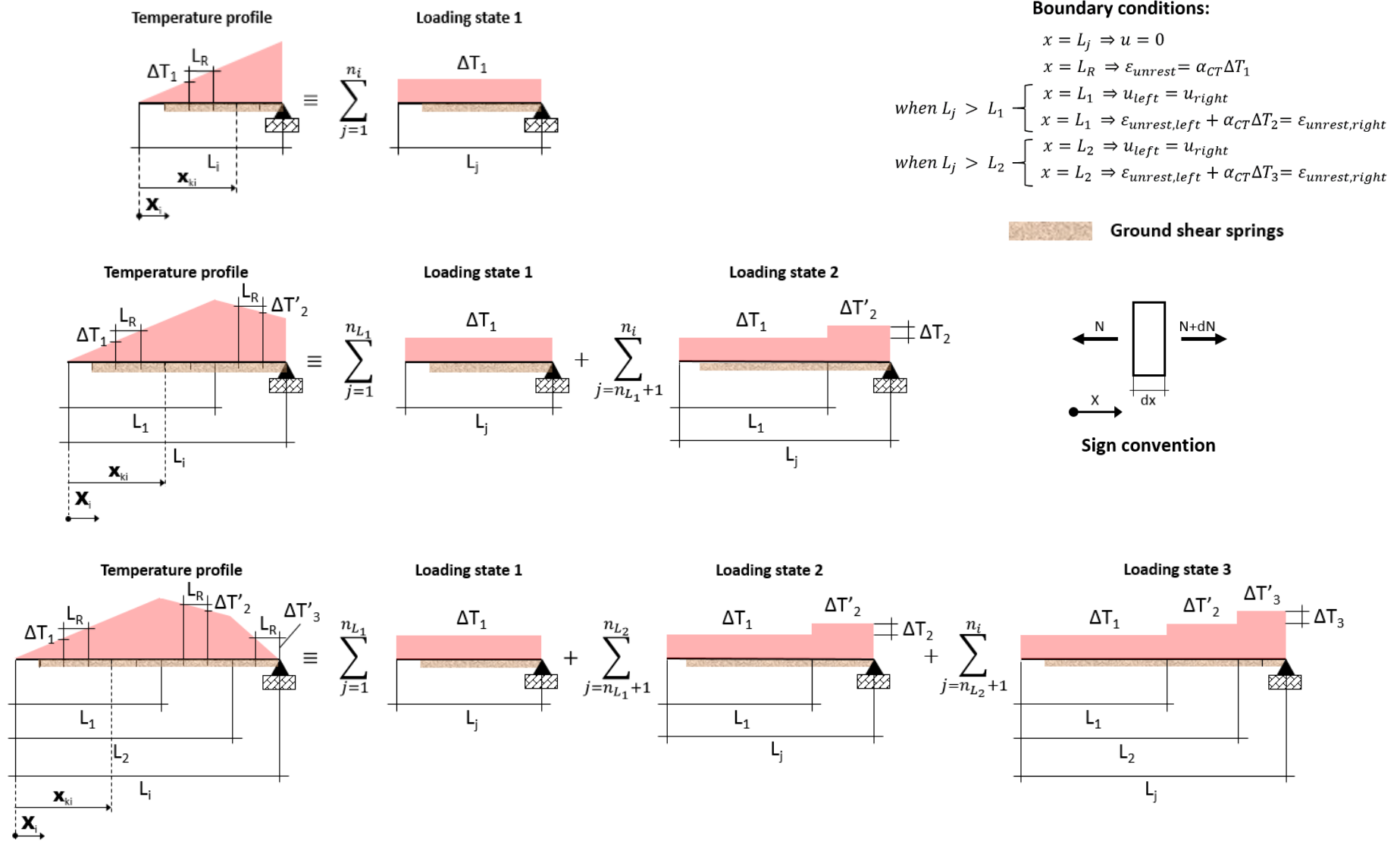


Figure 6.1: Temperature loading states and boundary conditions for rod model

## 6.2. Longitudinal pre-stressing of tunnel lining

The unrestrained strains at construction stage  $j$  are given by the following equations. When the temperature profile is linear:

$$\varepsilon_{unrest}(x) = \alpha_{CT}\Delta T_1 \quad \text{when } x \leq L_R \quad (6.3)$$

$$\varepsilon_{unrest}(x) = C_1\alpha e^{\alpha x} - C_2\alpha e^{-\alpha x} \quad \text{when } L_R < x \leq L_j \quad (6.4)$$

where:

$$C_1 = \frac{\alpha_{CT}}{\alpha(1 + e^{2\alpha(L_j - L_R)})} (\Delta T_1 e^{-2\alpha L_R}) \quad (6.5)$$

$$C_2 = -C_{1,1} e^{2\alpha L_j} \quad (6.6)$$

When the profile is bilinear:

$$\varepsilon_{unrest}(x) = \alpha_{CT}\Delta T_1 \quad \text{when } x \leq L_R \quad (6.7)$$

$$\varepsilon_{unrest}(x) = C_3\alpha e^{\alpha x} - C_4\alpha e^{-\alpha x} \quad \text{when } L_R < x \leq L_1 \quad (6.8)$$

$$\varepsilon_{unrest}(x) = C_5\alpha e^{\alpha x} - C_6\alpha e^{-\alpha x} \quad \text{when } L_1 < x \leq L_j \quad (6.9)$$

where:

$$C_5 = \frac{\alpha_{CT}}{\alpha(1 + e^{2\alpha(L_j - L_R)})} \left( \Delta T_1 e^{-\alpha L_R} + \frac{\Delta T_2}{2} (e^{-\alpha(L_1)} + e^{\alpha(L_1 - 2L_R)}) \right) \quad (6.10)$$

$$C_6 = -C_5 e^{2\alpha L_j} \quad (6.11)$$

$$C_4 = -C_5 e^{2\alpha L_j} + \frac{\alpha_{CT}}{2\alpha} \Delta T_2 e^{\alpha L_1} \quad (6.12)$$

$$C_3 = C_4 e^{-2\alpha L_R} + \frac{\alpha_{CT}}{\alpha} \Delta T_1 e^{-\alpha L_R} \quad (6.13)$$

When the profile is trilinear:

$$\varepsilon_{unrest}(x) = \alpha_{CT}\Delta T_1 \quad \text{when } x \leq L_R \quad (6.14)$$

$$\varepsilon_{unrest}(x) = C_7\alpha e^{\alpha x} - C_8\alpha e^{-\alpha x} \quad \text{when } L_R < x \leq L_1 \quad (6.15)$$

$$\varepsilon_{unrest}(x) = C_9\alpha e^{\alpha x} - C_{10}\alpha e^{-\alpha x} \quad \text{when } L_1 < x \leq L_2 \quad (6.16)$$

$$\varepsilon_{unrest}(x) = C_{11}\alpha e^{\alpha x} - C_{12}\alpha e^{-\alpha x} \quad \text{when } L_2 < x \leq L_j \quad (6.17)$$

where:

$$C_{11} = \frac{\alpha_{CT}}{\alpha(1 + e^{2\alpha(L_j - L_R)})} \left( \Delta T_1 e^{-\alpha L_R} + \frac{\Delta T_2}{2} (e^{-\alpha(L_1)} + e^{\alpha(L_1 - 2L_R)}) + \frac{\Delta T_3}{2} (e^{-\alpha(L_2)} + e^{\alpha(L_2 - 2L_R)}) \right) \quad (6.18)$$

$$C_{12} = -C_{11} e^{2\alpha L_j} \quad (6.19)$$

$$C_{10} = -C_{11} e^{2\alpha L_j} + \frac{\alpha_{CT}}{2\alpha} \Delta T_3 e^{\alpha L_2} \quad (6.20)$$

$$C_9 = C_{11} - \frac{\alpha_{CT}}{2\alpha} \Delta T_3 e^{-\alpha L_2} \quad (6.21)$$

$$C_8 = -C_{11} e^{2\alpha L_j} + \frac{\alpha_{CT}}{2\alpha} \Delta T_3 e^{\alpha L_2} + \frac{\alpha_{CT}}{2\alpha} \Delta T_2 e^{\alpha L_1} \quad (6.22)$$

## 6.2. Longitudinal pre-stressing of tunnel lining

$$C_7 = C_8 e^{-2\alpha L_R} + \frac{\alpha_{CT}}{\alpha} \Delta T_1 e^{-\alpha L_R} \quad (6.23)$$

$L_R$  is the ring width;  $\Delta T_1$ ,  $\Delta T_2$  and  $\Delta T_3$  are the additive temperature increments per ring at each stage when  $x > L_1$ ,  $L_2$  and  $L_3$  respectively. The thermally-induced mechanical strains in ring  $k$  at stage  $i$  are:

$$\varepsilon_{mech,th}(x_{ki}) = \sum_{j=n_i-k+1}^{n_i} \varepsilon_{unrest}(x_{kj}) - k\Delta T_1 \quad \text{when } n_i \leq n_{L_1} \quad (6.24)$$

$$\varepsilon_{mech,th}(x_{ki}) = \sum_{j=n_i-k+1}^{n_i} \varepsilon_{unrest}(x_{kj}) - k\Delta T_1 - (k - n_{L_1})\Delta T_2 \quad \text{when } n_{L_1} < n_i \leq n_{L_2} \quad (6.25)$$

$$\varepsilon_{mech,th}(x_{ki}) = \sum_{j=n_i-k+1}^{n_i} \varepsilon_{unrest}(x_{kj}) - k\Delta T_1 - (k - n_{L_1})\Delta T_2 - (k - n_{L_2})\Delta T_3 \quad \text{when } n_i > n_{L_2} \quad (6.26)$$

where  $n_i$  is the total number of rings at stage  $i$ ;  $k$  is the ring number of interest counting from the free boundary at stage  $i$ ;  $n_{L_1}$  and  $n_{L_2}$  are the number of rings comprised in lengths  $L_1$  and  $L_2$  respectively. The formulae above are verified with an ABAQUS beam spring model where each of the twenty rings is represented by a two element B21 (two-node linear) beam with appropriate cross-sectional and material properties (see chapter 2); the shear interaction with the ground is simulated with elastic SPRING1 springs centred with respect to each beam; and the beams are interconnected with longitudinal, shear and rotational SPRING2 springs of very high stiffness in order to produce rigid connections. Figure 6.2 compares the analytical and numerical  $\Delta \varepsilon_{mech,th}$  when  $x_{ki} = L_i$  corresponding to a fictitious temperature profile, revealing an excellent agreement between both solutions.

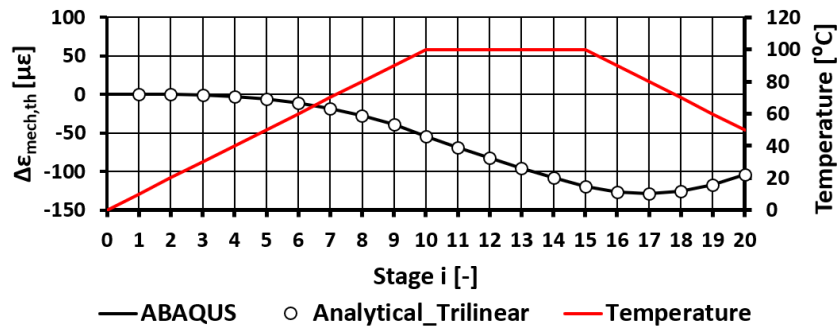


Figure 6.2: Validation of analytical rod solution for trilinear temperature profile

### 6.2.3. Field data interpretation on longitudinal pre-stressing

Following Saint Venant's principle, the stress distribution in the cross-section of an elastic cylinder subjected to concentrated longitudinal loads at its ends is equal to that produced by statically equivalent loads as long as the cross-section is sufficiently far from its extremities. In continuous cylinders, the distance to the load application area required to verify the above statement would be a

## 6.2. Longitudinal pre-stressing of tunnel lining

few times their mean diameter. In CSLs, the length of the transition zone from the individual longitudinal compression of segments to the longitudinal bending of a monolithic ring is less clear, given that the load transfer is realised through friction at the longitudinal joints of radially compressed rings, and via the staggered configuration of longitudinal joints in adjacent rings.

For the CTT study on longitudinal pre-stressing, the elastic rod solution is first applied individually to each instrumented segment. Early divergences between predicted and measured longitudinal strains may indicate either contact deficiencies between adjacent segments or a notable effect of longitudinal bending, which is excluded from the rod model. Then, the predicted and field mean longitudinal strains of instrumented rings are compared.

The total mechanical strains derived from VWSG measurements were corrected (i) to match the longitudinal strains inferred from the TBM axial compression of instrumented segments after ring assembly, thus removing the initial impact of assembly imperfections; and (ii) to eliminate the Poisson effect associated with hoop pressures in a multiaxially loaded lining based on zeroed hoop strains, in turn previously corrected against transverse deformations caused by longitudinal strains.

### 6.2.3.1. Selection of input loads

The longitudinal ram loads applied onto the lining undergo sharp changes within each TBM advance; hence, the impact of the input load selection criterion on the prediction of mechanical strains must be examined. The load sets under consideration are average and last ram loads per advance acting on individual segments, together with loads that compute a TBM moment equal to the last loads but with a plane distribution, i.e. representative of a monolithic ring subjected to longitudinal bending and away from the transition zone.

Figure 6.3 illustrates the evolution with time of field longitudinal strains, longitudinal strains computed from TBM ram loads and longitudinal strains calculated through a CTT sequential rod model subjected to the load sets described above that excludes thermal effects. For the analytical solution, the cross-sectional properties of the standard CTT segments were adopted (see chapter 2),  $E_c$  was taken as 38GPa and the ground Young's modulus  $E_s$  was 200MPa, which laid within the CTT's range of variability.

The analytical strains calculated from average, last and last equivalent loads are quite similar, with peak discrepancies of about 25µε. They tend to be responsive to ram load changes and are comprised within the bandwidth defined by the ram loads for the first 48h, after which the analytical strains are kept constant.

The measured strains also become less sensitive to ram load changes with time. However, the analytical strains fail to predict accurately the field strains in most segments. For example, in the least longitudinally loaded segments situated on the left side of the tunnel horizontal curve, i.e. C3, D3, E4,

## 6.2. Longitudinal pre-stressing of tunnel lining

---

KL4, the measured strains become small in the second TBM cycle, exhibiting values occasionally close to zero. The early gap between analytical and measured strains remains roughly constant in the following cycles, which suggests that it may be linked to the higher risk of contact imperfections in poorly longitudinally compressed segments as evidenced by published numerical studies (Mayer et al., 2009). The incidence of contact imperfections in the CTT rings will be further discussed in chapter 8.

Conversely, the strains measured in the right side segments either agree with or exceed the analytical predictions. The discrepancies, encountered mainly in CAM4, tend to increase as the TBM steers around the left curve, particularly between cycle 4 and cycle 7, even after considering the redistribution of uneven ram loads through the equivalent last load set. The divergences developed with time after several advances are associated with the longitudinal bending of the tunnel, which will be tackled in section 6.4.

At about 48h after the first advance, the field strains of all segments exhibit a gradual reduction in compression over time that mirrors the in situ temperature profiles, indicating that the thermal deformations caused by time-varying temperatures must be partially constrained (see chapter 5). The effect of lining temperature changes typical of simultaneously backfill grouted tunnels on its longitudinal pre-stressing will be examined in the following subsections.

The accurate prediction of E3 in situ strains before 48h suggests that this crown segment is free from contact imperfections and situated near the bending axis of the tunnel tube, which makes it a satisfactory baseline for the selection of the most representative load set. Despite the minor differences in the analytical strains computed, the last load set provides a better approximation to the in situ strains and will be used hereafter.

## 6.2. Longitudinal pre-stressing of tunnel lining

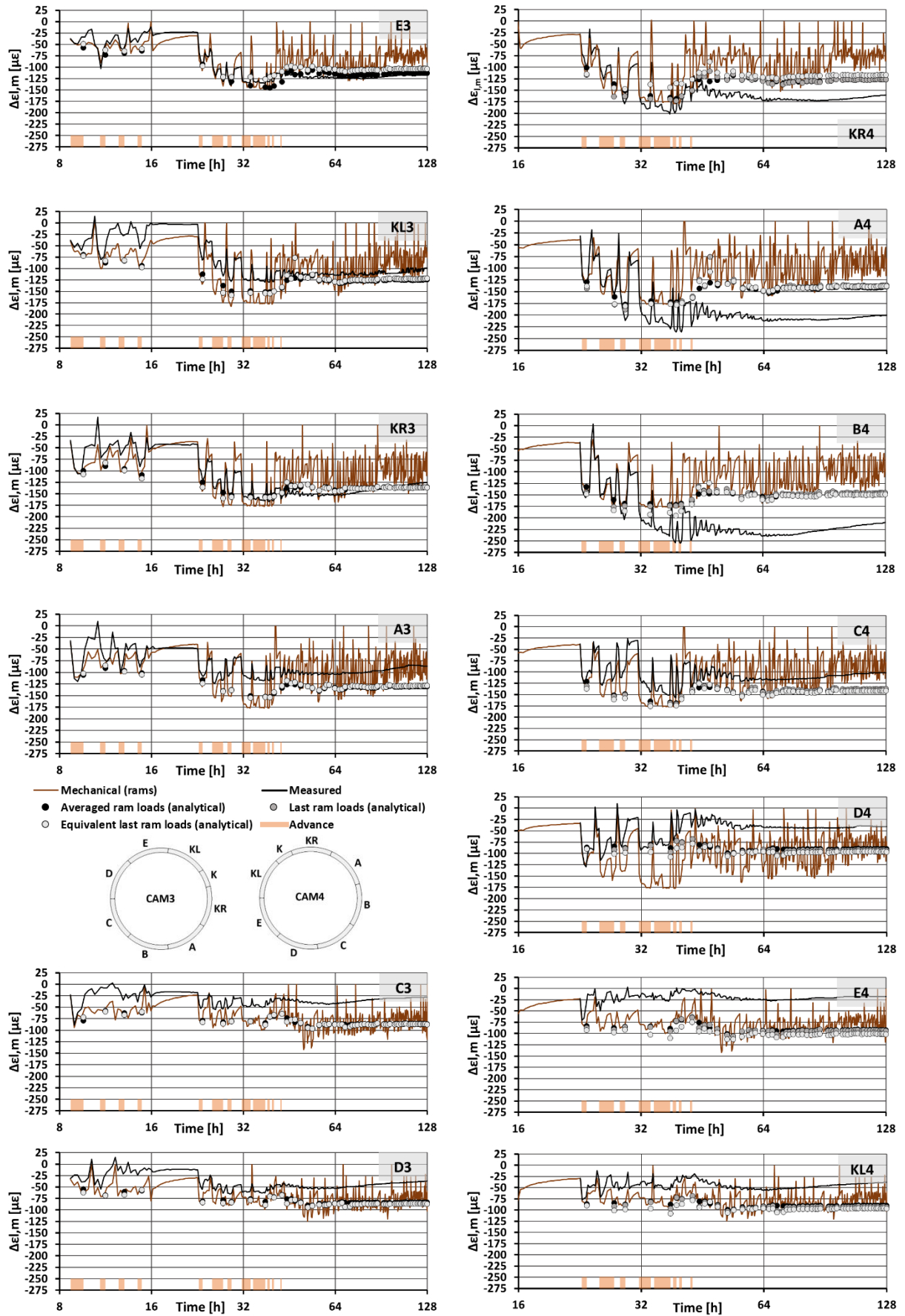


Figure 6.3: Selection of rod model parameters: ram loads

## 6.2. Longitudinal pre-stressing of tunnel lining

### 6.2.3.2. Selection of rod model parameters

Before focusing on the effect of temperature changes, a sensitivity analysis on  $k_s$ ,  $E_c$  and packer stiffness,  $E_p$ , is conducted to identify the set of input parameters that enable the most accurate prediction of in situ strains.

Neither the expected range of uncertainty of  $E_s$ , between 136MPa and 250MPa (Crossrail, 2014), nor the consideration of instantaneous or secant concrete modulus, 38GPa and 39.9GPa respectively (EC2), signify a noticeable change in analytical strains,  $10\mu\epsilon$  at most.

The effect of the packer stiffness can be considered in Koek's solution through the adoption of an equivalent rod stiffness (Koek, 2005a). The influence of either stiff packers,  $E_p=275\text{MPa}$ , or soft packers,  $E_p=88\text{MPa}$ , is limited (see Figure 6.4). The analytical strains become less responsive to changes in longitudinal loads.

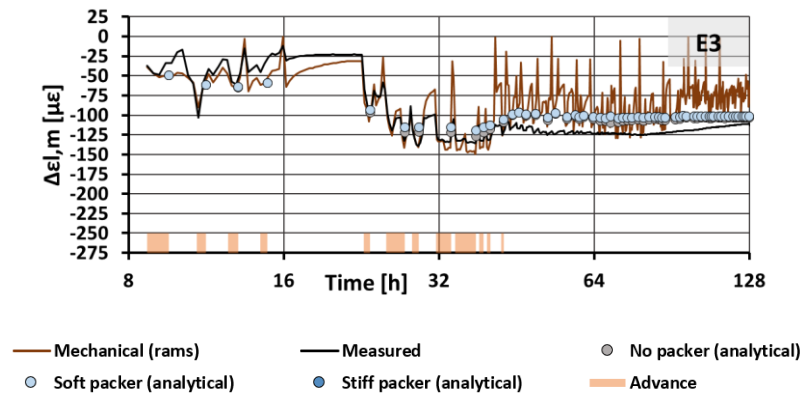


Figure 6.4: Selection of rod model parameters: packers

The incidence of concrete and packer creep is investigated by comparing the field strains with those obtained from ABAQUS rod models. The segments and packers were simulated with two-node linear beams interconnected through very stiff translational and rotational springs. Creep effects were tackled through the so-called reduction stiffness method (Neville et al., 1983). Despite this method implying the application of the deferred load increments onto softer material, it is deemed sufficient for the study of CSL longitudinal pre-stressing, given that the loading magnitude of initial advances is comparable to following loads.

The concrete creep is approximated through the general EC2 creep model for a C55/67 concrete grade and outside conditions (BSI, 2010). The creep function of plywood packers,  $\varphi_w$ , was obtained from the calibration of a typical logarithmic formula for wood creep (Holzer et al., 1989) to Bengtsson's lowest compression creep tested in wood at 90% relative humidity (Bengtsson, 2000):

$$\varphi_w(t) = \frac{0.75}{\log 11} \log(t + 1) \quad (6.27)$$

where  $t$  is the time elapsed in days from load application.

## 6.2. Longitudinal pre-stressing of tunnel lining

The comparison of field and predicted strains in segment A4 (see Figure 6.5) evidences that the numerical models including concrete creep, as opposed to the models with constant concrete stiffness, overestimate the early in situ strains. Indeed, the CTT concrete mix exhibited a low initial creep rate (see chapter 8).

The rod models without packers that consider the effects of time-varying temperatures result in strain variations after 48h that are in excellent agreement with the field data. Conversely, the presence of packers without creep flattens the long term response. The packer creep reverses the trend back to decreasing compression, although with patterns that diverge from those experienced in situ.

It can be inferred from the above that concrete creep may not be relevant for the evolution of the CTT longitudinal pre-stressing and that the contribution of previously compressed plywood packers to longitudinal force equilibrium must be negligible, possibly as a result of compression stiffening. Consequently, the rod models with  $E_c=38\text{GPa}$ ,  $E_s=200\text{MPa}$  and no packers are considered the models that can reproduce better the evolution of the CTT longitudinal pre-stressing during construction and under time-varying temperatures.

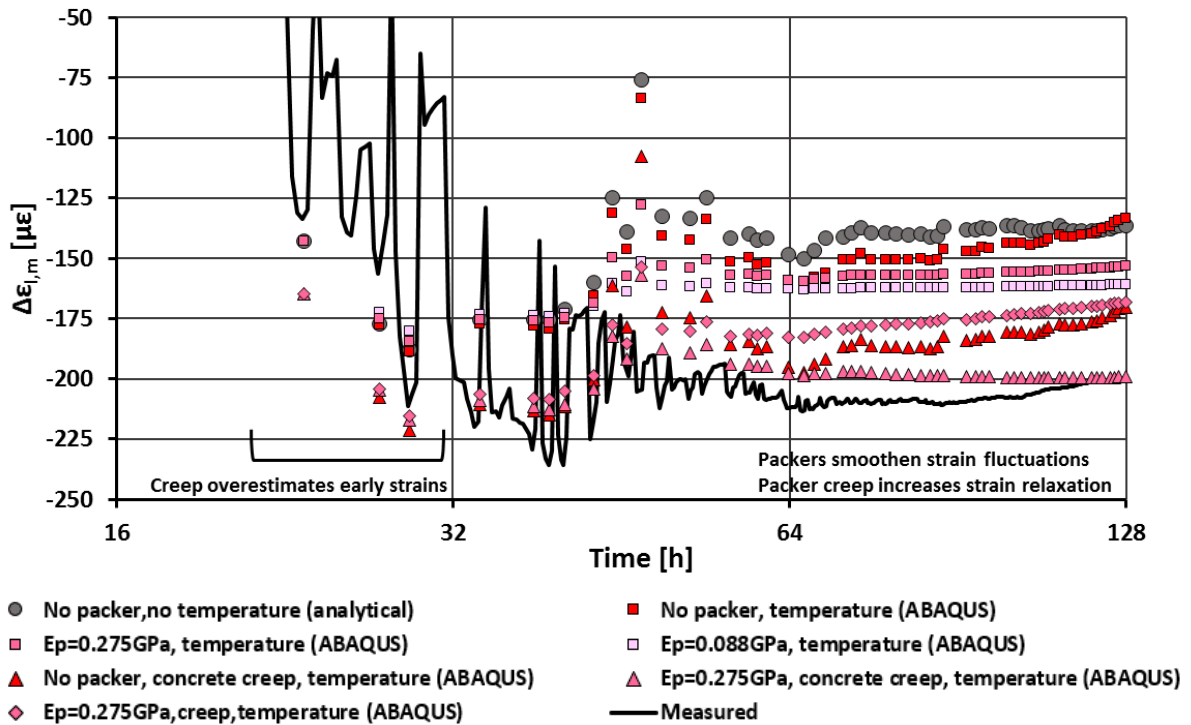


Figure 6.5: Selection of rod model parameters: creep effects

### 6.2.3.3. Relaxation of longitudinal pre-stressing at varying temperature

The thermal effects of time-varying temperature on the CTT longitudinal pre-stressing are examined first on individual segments (see Figure 6.6) and then on the rings altogether (see Figure 6.7).



## 6.2. Longitudinal pre-stressing of tunnel lining

---

The rod numerical models of segmental sections with rigid packers, no concrete creep and subjected to in situ temperature profiles predict with excellent accuracy the longitudinal decompression that arises in all segments after 48h and for the following 3.5days. The simulations stop at  $t \approx 128\text{h}$  due to the unavailability of following TBM records. However, it is confirmed that the gradual relaxation of compressive strains within the tunnelling phase is solely caused by the temperature changes in the lining.

The mean in situ longitudinal strains of both instrumented rings show that the temperature profile typical of simultaneously backfill grouted tunnels during tunnel construction leads to significant longitudinal pre-stressing relaxation in the months following construction until the high temperatures produced by grout hardening are lowered to ambient levels. For a given tunnel, the extent of the relaxation depends only on the ground stiffness and the temperature profile given by the grout mix and the tunnel ambient temperature. For example, in the CTT, total compressive strain reductions of  $25\mu\epsilon$  and  $50\mu\epsilon$ , equivalent to 43bar/ram and 85bar/ram, are exhibited by both rings before and after the tunnel breakthrough. The final tunnel relaxation corresponds to 40% and 50% of the early pre-stressing experienced by CAM3 and CAM4 respectively.

## 6.2. Longitudinal pre-stressing of tunnel lining

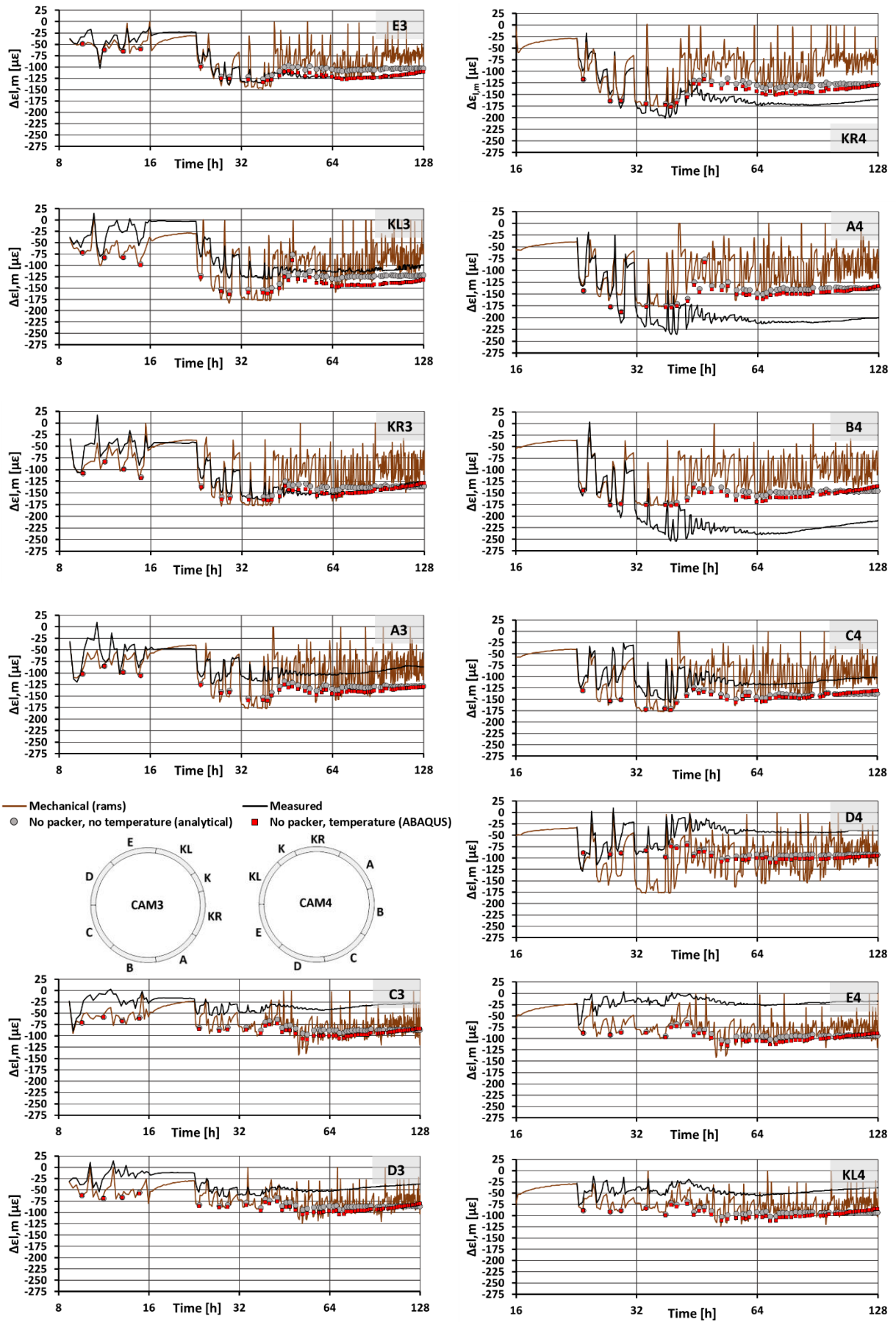
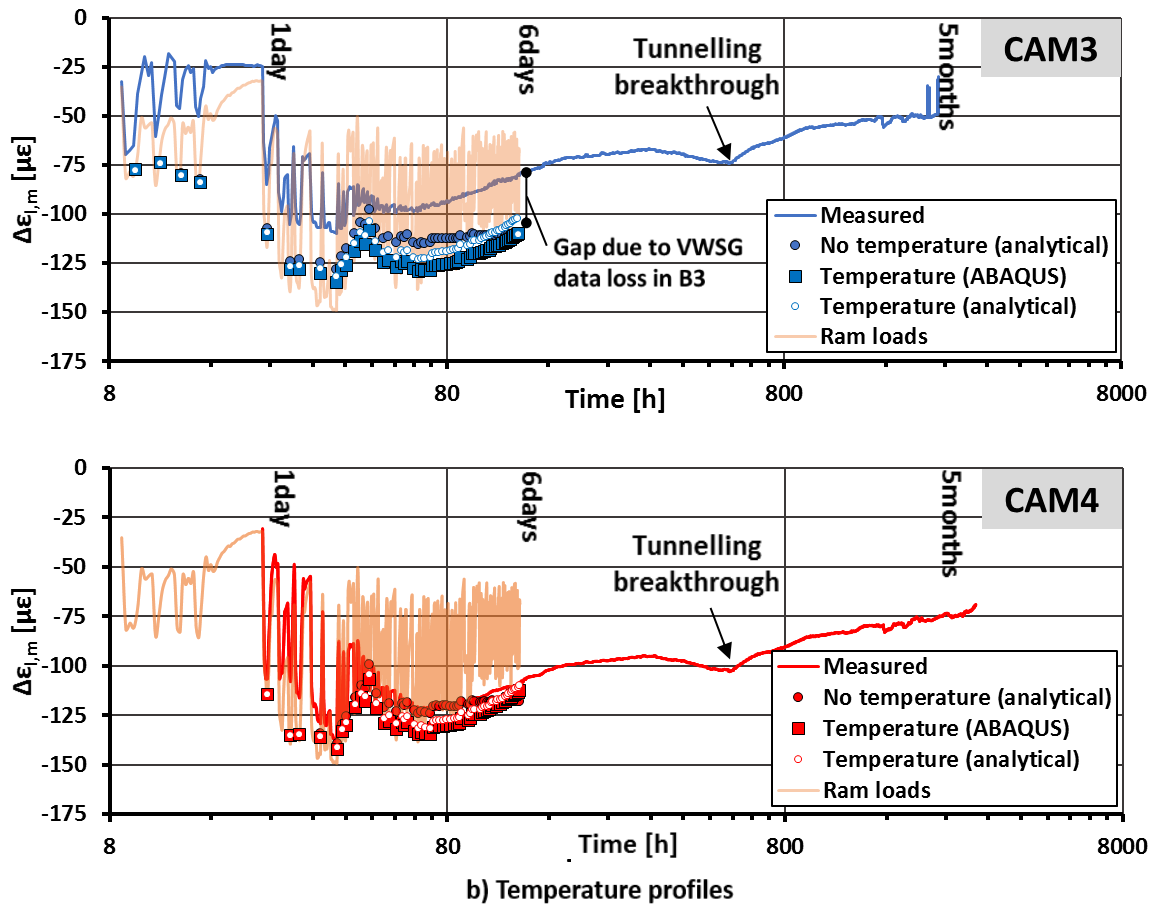


Figure 6.6: Thermal effects on longitudinal strains

## 6.2. Longitudinal pre-stressing of tunnel lining

a) Field and predicted mean longitudinal strains



b) Temperature profiles

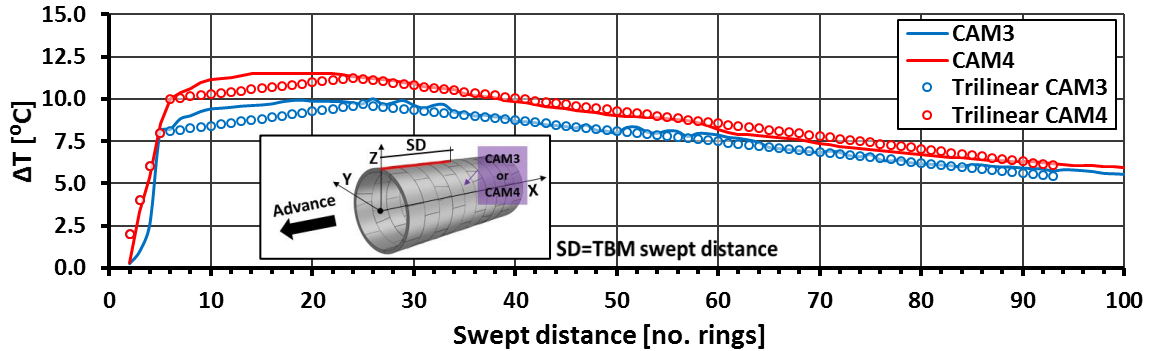


Figure 6.7: Tunnel relaxation due to time-varying temperatures

If the long term tunnel relaxation at constant strain due to creep (Arnau, 2012) is added, it is reasonable to expect that the longitudinal force in the long term will be small and the ring interaction limited. Thus, the performance of CSLs subjected to significant ovalisation loads should deteriorate with the progress of tunnel relaxation (see chapter 4).

The analytical solution for an approximate trilinear temperature profile reproduces with great accuracy the numerical strains based on the CTT in situ temperatures and can be used as an effective tool for the prediction of residual longitudinal strains after tunnel construction. Consequently, the deployment of this analytical solution enables the asset owner to assess the longitudinal strains remaining in the structure at a given age, providing that in situ temperatures have been monitored during tunnel

## 6.2. Longitudinal pre-stressing of tunnel lining

construction and TBM records on ram loads are made available (see Figure 6.8). The longitudinal force can be derived once the long term creep effects are evaluated with Arnau's (2012) solution.

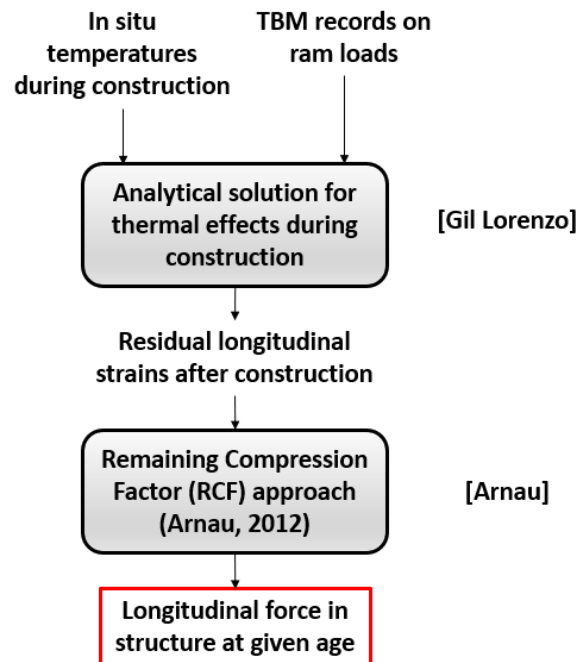


Figure 6.8: Prediction of longitudinal force

### 6.3. Lining pressure gradients

The history of lining pressures during construction defines the radial loading state supported by a tunnel that, together with its boundary conditions and the TBM loads, determines its 3D structural response. The evolution of lining pressure gradients is, in particular, key to the longitudinal beam behaviour of the tunnel.

In this section, the CTT pressure gradients are analysed with the support of published literature to date on lining pressures in CSLs simultaneously backfilled with cementitious grouts. Given that the in situ measurements of lining pressures around CSLs grouted with BGs are scarce in the published literature as opposed to the detailed research conducted on grout pressures of CSLs backfilled with mortar grouts (MGs), the background comprises a brief summary on material properties of both MGs and BGs relevant to tail void pressures followed by a review of the theoretical framework developed for MGs and the trends in field annular pressures of BGs in past projects.

#### 6.3.1. Properties of cementitious grouts

##### 6.3.1.1. Traditional grouts

Traditional grouts are bentonite-cement mortars made of sand, fly-ash, cement, bentonite and additives (Henn, 2003) with densities in the order of  $2000\text{kg/m}^3$ . The bentonite reduces bleeding and permeability, which in turn enhances mix homogeneity in detriment of flowability and compressive strength (Peila et al., 2011). Bentonite-cement grouts require several injection ports to prevent void formation (see Figure 6.9.a) and gain strength slowly with hardening times.

Movement in fluid and plastic grouts is initiated only if the shear stress exceeds the initial yield value at zero shear rate, i.e. initial shear strength or cohesion, and the shear stress required to sustain the flow increases with the shear rate (Henn, 2003). In Bingham fluids such as grouts subjected to the low velocities realised in the tail void, the wall shear strength and the grout density are the most relevant parameters for the prediction of grout flow (Talmon et al., 2001).

Talmon et al. (2002) investigated the rheology of MGs with various laboratory experiments. Bespoke experiments resembling flow conditions in the tail void were conducted to obtain wall shear stresses for a wide range of velocities prior to grout hardening. It was found that the external shear stresses at the grout-lining interface were small, around 50Pa, due to the formation of a thin lubricating film. Lubrication was caused by the segregated flow of the liquid component through the sand grains in the vicinity of the wall. At the soil-grout interface, however, it was argued that the penetration of cementitious fluid onto the ground could create a compact and irregular ring around the tail void where a lubricating film could not be formed. It was expected for wall stresses at the grout cake to be higher but in the same order of the grout yield stress, i.e. several kPa.

The early strength of the grout at the tail void determines its capability to deliver lining support at the back of the tail skin as the TBM advances. Bezuijen and Talmon (2005) proposed a full-scale consolidation test to evaluate consolidation in confined MGs subjected to external pressures and possibly undergoing hardening. This test confirmed that grout consolidation in permeable soils substantially increases the early strength of MGs prior to hardening. In impermeable soils, however, the early strength is defined by the hardening time, in the order of 4h, and the compressive strength curve.

### 6.3.1.2. Bicomponent grouts

BGs were introduced in Japan in the eighties and since then their market share has grown steadily due to their advantageous properties against traditional mortars (TAC Corporation, 2017; Feddema et al., 2006; Antunes, 2012; Peila et al., 2011).

These highly mobile grouts are made of a superfluid grout, i.e. the A component, which is stabilised to ensure workability until an accelerator, i.e. the B component, is added at the injection port (Peila et al., 2011). BGs have been specifically designed for quick grout setting and very high early strengths, which dramatically shorten the unsupported length of tunnels,  $L_u$ . In addition, superfluid BGs are generally injected from two ports, one at each tail skin shoulder like in the CTT tunnel (see Figure 6.9.b). With specific densities close to 1000kg/m<sup>3</sup>, the buoyancy forces also decrease.

BGs undergo a phased chemical reaction after mixture. In the liquid state, the grout presents very low viscosity and can flow around the ring circumference very effectively (Talmon et al., 2001), reducing the likelihood of voids in the grout annulus. The liquid grout gels in some seconds and acquires a plastic clay-like consistency with relatively constant shear strength (Peila et al., 2011). Gel times found in the literature range between 10s and 60s (Talmon et al., 2002; Peila et al., 2011), depending on the test method and grout mix.

The shear strength before hardening reaches values in the order of kPas, although it is highly influenced by the test method. For example, the shear strength of a certain mix was estimated to be about 10kPa with pocket penetrometers tests, 1kPa with vane tests and 0.1kPa with vane tests on remoulded samples (Talmon et al., 2001; 2002).

Grout hardening can be initiated in minutes, typically in half an hour (Antunes, 2012; Peila et al., 2011). Depending on the grout mix and homogeneity, the compressive strength can range between 30kPa and 300kPa in an hour (Antunes, 2012; Peila et al., 2011) and reach 1MPa in 24h (Hashimoto et al., 2006, Talmon et al., 2002). Talmon et al. (2002) experiments evidenced the formation of a lubrication film in the flow of BGs by mechanical rupture of the grout chemical structure at the grout-lining interface, resulting again in wall shear stresses in the order of 50Pa. At the grout-soil interface, static drained experiments on confined saturated layered samples of grout and sand subjected to

## 6.3. Lining pressure gradients

normal pressures confirmed that fluid loss was significantly smaller in BGs, thus enhancing settlement control.

In this respect, the CTT grout properties routinely tested fit the general characteristics of BGs: density of about 1250kg/m<sup>3</sup>, gel time around 15s and 24h compressive strength between 1.5MPa and 2.0MPa (Crossrail, 2014).

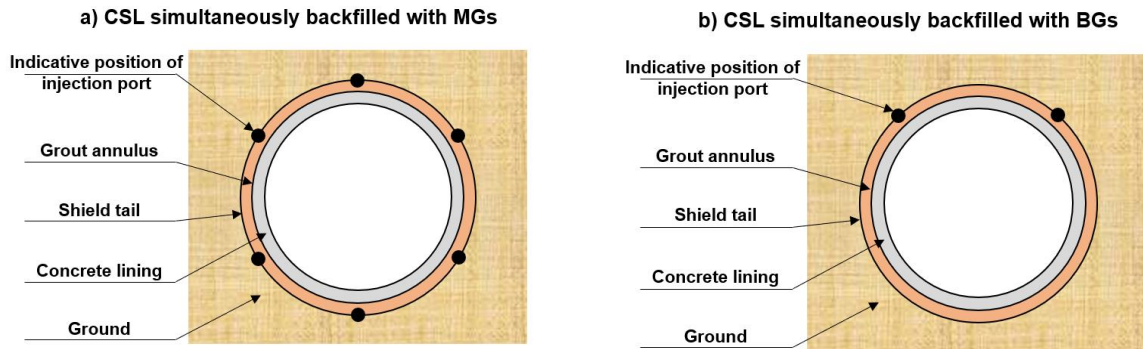


Figure 6.9: Typical injection ports for MGs and BGs

### 6.3.2. Lining pressures in CSLs backfilled with MGs

Dutch researchers developed theoretical models of grout behaviour within the tail void, supported and validated with laboratory tests and field monitoring experiences. The aim of their research was to improve settlement control reliability and to investigate the influence of backfill grouting on lining behaviour during construction, when most segment damage occurred (Bezuijen et al., 2004).

Short-term lining pressures were measured in several tunnels with pressuremeters installed at the extrados of the monitoring rings. It was found that, during each advance, the crown pressures remained close to the injection pressure at upper grout ports for several advances and then dissipated with time down to values slightly higher than hydrostatic pressures (see Figure 6.10.a). In early advances, the pressures in the annular gap increased with the progress of active backfilling. A sudden drop of grout pressures consistently occurred at the beginning of each advance, induced by the delayed activation of the grout pumps.

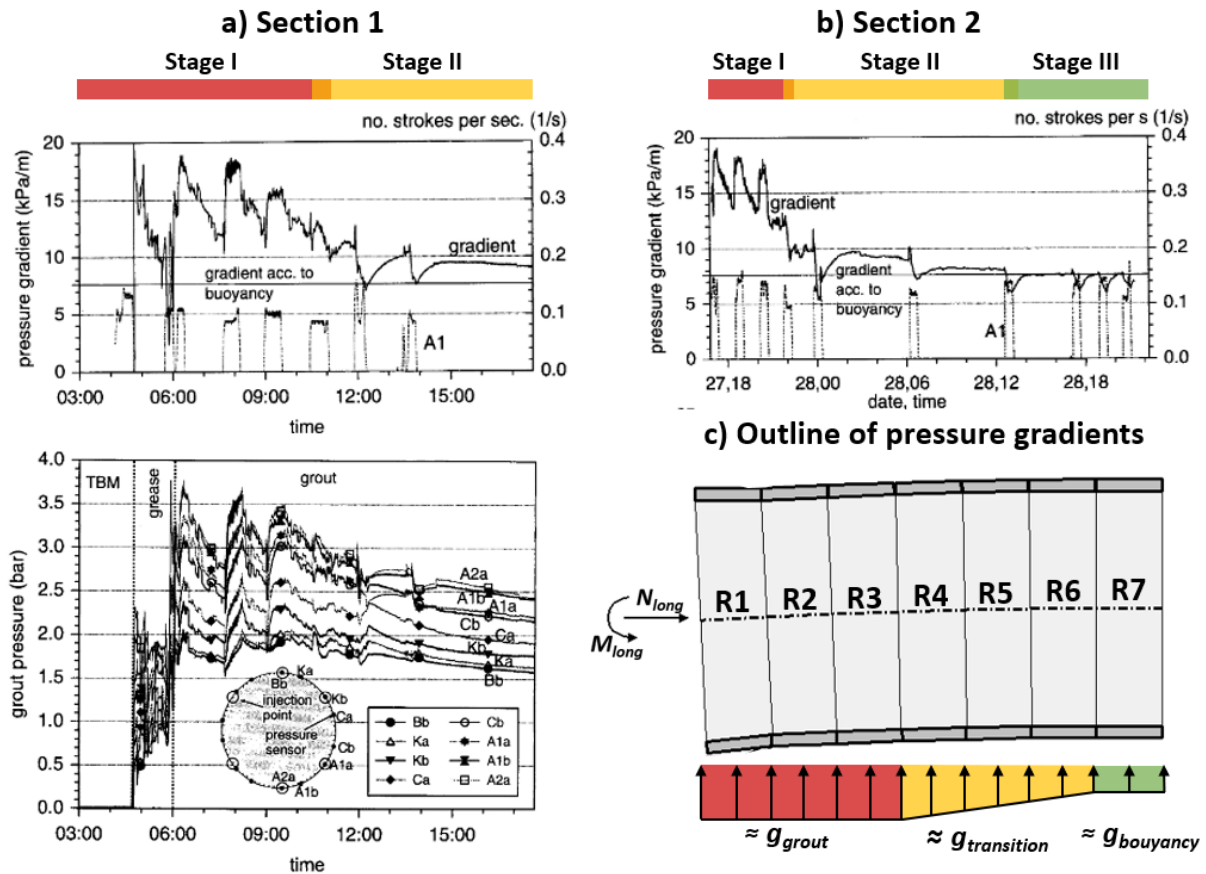


Figure 6.10: Lining pressures in MGs backfilled CSLs (after Bezuijen et al., 2004)

When the grout was injected with equally distributed flow rates around the ring perimeter, e.g. in the Sophia tunnel, the lining pressures were roughly linear with depth in each measurement. At early advances, the vertical pressure gradients,  $g_v$ , first rose up to grout static values and then decayed slightly due to the downward grout flow (see Figure 6.10.a and 6.10.b). After several advances, the above trends during backfilling were reversed. Overall, however, the vertical gradients decreased over time from values close to grout static to lower than hydrostatic gradients.

The research evidenced the interdependency between backfill process, grout material, and lining response in early stages of the lining design life. Bezuijen et al. (2004) distinguished three stages in the history of lining pressures driven by different mechanisms (see Figure 6.10.c):

a) **Stage 1 near the TBM:**

During backfilling, the lining pressures were predominantly governed by the flow of fresh grout. During standstill, grout consolidation led to progressive pressure decay.

b) **Stage 2 between stage 1 and 3:**

The pressure gradients were affected by the ground deformations and the lining deflections caused by the longitudinal bending of the tunnel, the latter triggered by the action of the uplift forces and TBM ram loads.

c) **Stage 3 far from the TBM:**



The grout yield stresses were sufficiently high to counteract the uplift forces through ring vertical equilibrium.

### **6.3.2.1. Theoretical models for the prediction of grout pressures in stage 1**

Talmon et al. (2001) proposed a grout flow model to predict and estimate grout pressures near the TBM and during active backfilling. The model assumed a steady shallow flow in a two-dimensional space with constant thickness moving with the TBM; thus changes in flow rate during TBM advance were not contemplated. The model confirmed that the injection protocol, the wall shear strength of the grout, the tail void thickness and the grout density determine the distribution of lining pressures while the grout is workable (Talmon et al., 2001).

Numerous examples validated with field data (Talmon et al., 2001; Bezuijen et al., 2004) showed that the number and location of injection ports and the injection flow rates affected the pressure distribution in the first metres of TBM advance. Equally distributed flow rates led to nearly hydrostatic pressures. This was not the case for asymmetric or uneven flow due to either the injection strategy or clogging of the grout ports (Talmon et al., 2001).

Bezuijen and Talmon (2009) argued that when the grout injection is resumed, the soil deforms elastically and the tail void formerly grouted widens and receives the fresh grout, which disrupts the development of shear stresses with time. Consequently, the vertical gradients keep increasing in every advance until the grout has sufficiently hardened.

The grout consolidation during standstill is only possible under the following conditions: (i) there is an excess pore pressure in the grout layer; (ii) the grout material and soil interface are permeable; (iii) the grout is not fully hardened (Talmon and Bezuijen, 2009b). The grout consolidation is initiated by fluid loss at the permeable soil-grout interface, which leads to the progressive formation of a consolidated grout layer, the grout cake. An indication that grout consolidation ended is that the lining pressures become stable in a complete TBM cycle (Talmon and Bezuijen, 2009b).

In standstill, the volume loss in the grout layer due to bleeding unloads the soil at the grout-soil interface and the excess pore pressure decays as grout consolidation progresses. Pressure dissipation occurs quicker in stiffer soils as small ground deformations incur in high reductions of interface pressures. Talmon and Bezuijen (2009b) developed a one-dimensional consolidation model valid to predict decay and grout cake thickness, which is important to characterise the overall stiffness and yield strength of the grout layer (Talmon and Bezuijen, 2006). The effect of grout consolidation on yield strength is relevant for grout flow and lining support prior to grout setting in tunnels constructed in permeable soils only (Bezuijen and Talmon, 2009).

### 6.3.2.2. Theoretical models for the prediction of grout pressures in stage 3

Vertical pressure gradients around a fully founded tunnel are dictated by net buoyancy forces. Vertical equilibrium is first reached through the frictional forces developed at the annular grout along the ring circumference. The restoring downward pressures are proportional to the average wall shear stress that can develop at grout-lining and grout-ground interfaces. Bezuijen et al. (2004) model enabled the calculation of theoretical peak vertical pressure gradients which agreed well with those regressed from field data measured away from the TBM. The average wall shear stress, and subsequently the grout yield strength (Talmon et al., 2002), required for the two-dimensional balance of uplift forces could also be estimated. It then followed that, if the grout yield strength curve with time was known for a given tunnel excavated at a certain speed, the tunnel unsupported length,  $L_u$ , could also be evaluated.

### 6.3.2.3. Theoretical models for the prediction of grout pressures in stage 2

The numerical modelling of the tail void grout, with consideration of grout flow, grout hardening and consolidation, vertical lining movements and soil deformations confirmed the smooth evolution of pressure gradients characteristic of this stage, which could be approximated to a linear decline for structural models (Talmon and Bezuijen, 2006).

### 6.3.3. Lining pressures in CSLs backfilled with BGs

In this case, the field measurements in past projects have not always conformed to the MGs' theoretical framework. For instance, Talmon and Bezuijen (2005) reported vertical pressure gradients in the first advance of a Botlek tunnel monitoring ring greater than 40kPa/m, followed by an instantaneous drop to gradients below -10kPa/m (see Figure 6.11). From the second to the third advance, at which point the measurement reliability was jeopardised by grout hardening, the gradients were stabilised to 5kPa/m. It was interpreted that a 5kPa/m constant gradient indicated that vertical equilibrium was achieved at the second advance. It was also suggested that the marked fluctuations detected in the first advance could be the result of lining movements at the exit of the tail skin conflicting with hardened grout previously injected.

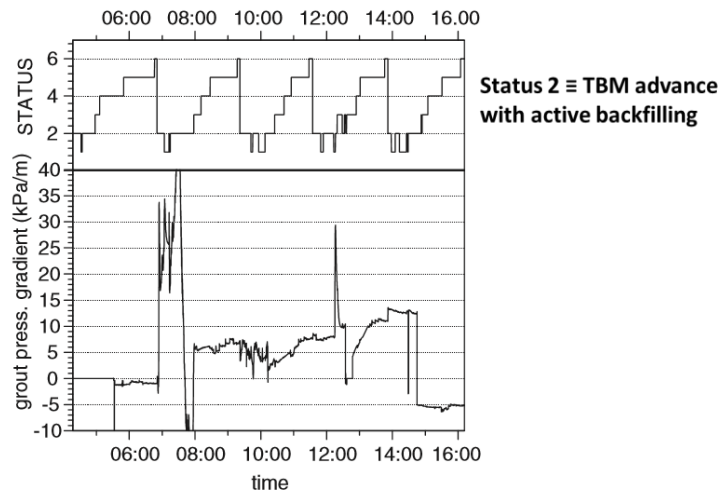


**Figure 6.11: Example of vertical pressure gradients in BGs backfilled CSLs (after Talmon and Bezuijen, 2005)**

Conversely, Hashimoto et al. (2002; 2006) noted that lining pressures measured during simultaneous backfilling were quite uniform along the ring circumference, leading to small pressure gradients without dramatic oscillations. This uniformity in lining pressures was attributed to the plastic state and homogeneity of BGs before hardening. Asymmetric distributions occurred when backfilling was conducted with one lateral injection port, although lining pressures converged progressively to a more uniform distribution with time.

Koyama (2003) pointed that high injection pressures could lead to uneven lining pressures in the short term, but associated the latter to the contact of rings with steel wire brushes while exiting the tail skin. Feddema et al. (2006) counted more damage events in rings grouted with BGs than with MGs without providing an explanation for such difference.

### 6.3.4. Field data interpretation on pressure gradients

Figure 6.12 shows the pressure gradients in both rings developed with time and TBM swept distance, *SD*, measured in number of rings. The pressure gradients are calculated from the mean lining pressures of crown and invert segments in the case of vertical gradients and springline segments for horizontal gradients. The lining pressures are computed from field strain data, as explained in section 8.3, p.226, and thus the pressure gradients include not only the effect of the external pressures but also the influence of the ring selfweight and the tangential stresses at the grout interfaces.

The evolution of vertical gradients in the two rings is comparable to that observed in the Botlek tunnel (see Figure 6.11), which increases the confidence on the reliability of the CTT field pressures.

The CTT vertical gradients are near zero by the end of the second advance, AD2, in both rings, with a deviation in CAM3 when *SD* lies between 3ring and 5ring. There are minor fluctuations in both rings when  $SD \approx 12$ ring. Null steady gradients of strain derived pressures indicate that there is vertical ring equilibrium.

## 6.3. Lining pressure gradients

---

Ring equilibrium is typical of fully founded linings. The grout annulus enables the interfacing frictional forces and transfers the passive ground reaction that can counteract the uplift forces. It can be inferred that the instrumented rings reach a full bedding condition at about  $SD \approx 2\text{ring}$ , i.e. 3.2m away from the TBM, which agrees with the expected completion rates of BG hardening 12h after injection.

The horizontal gradients of the fully founded rings converge to constant absolute values in the order of 15kPa/m as a result of the tunnel deflection caused by the TBM steering around the horizontal curve.

During the passage of the instrumented rings through the shield tail, both rings exhibit vertical gradients that far exceed the grout static value of 12.3kPa/m. For example, in the first advance, AD1, the vertical gradients peak to near 60kPa/m and 20kPa/m in CAM3 and CAM4 respectively and, in the first half of AD2, the gradients are still kept at 40kPa/m and 20kPa/m. The vertical gradients decrease during AD2 and approach zero once the rings are outside the tail skin, i.e. by the end of AD2.

During the first assembly, AS1, the rear of the rings is already subjected to grout pressures while the front is still surrounded by the sealing system. The pressure gradients oscillate around the values beyond grout static: in CAM3 there is a sharp drop to 40kPa/m followed by a period of constant gradients; in CAM4 the gradients fluctuate around 20kPa/m. These variations, particularly in CAM4, indicate that either the contribution of grout pressures to the pressure gradients is small or that the grout consolidation is negligible or uniform. The fluctuations may be associated with segment movements during erection of the next ring.

Similarly to the vertical gradients, the horizontal gradients grow to absolute peaks near 20kPa/m in the first TBM cycle, fall to almost null values by end of AD2 and remain constant during AS1 at least for CAM3.

Overall, the magnitude of vertical gradients beyond grout static during the ring passage through the tail skin, the sudden pressure gradient dissipation afterwards and the rough preservation of gradients during AS1 suggest that the high gradients in the first two cycles, namely stage 1, are caused by the physical interaction of the rings with the TBM, more specifically the sealing system, rather than grout flow.

There is an intermediate stage, stage 2, where both vertical and horizontal gradients transition smoothly towards the steady state. The general changes within this stage can be linked to the tunnel deflections caused by the uplift forces and the ram loads required to steer the TBM around the horizontal curve. The tunnel beam response and its effect on lining pressures will be studied in full detail in section 6.4 and chapter 8. The decrease with  $SD$  in the amplitude of pressure gradient oscillations during assembly supports the idea that in this region the changes in tunnel deflections still affect the lining pressures.

## 6.3. Lining pressure gradients

The minor fluctuations captured in the vertical gradients of both rings between  $SD=11$ ring and  $SD=13$ ring may reflect the local impact of the backup trail wheels passing over the rings.

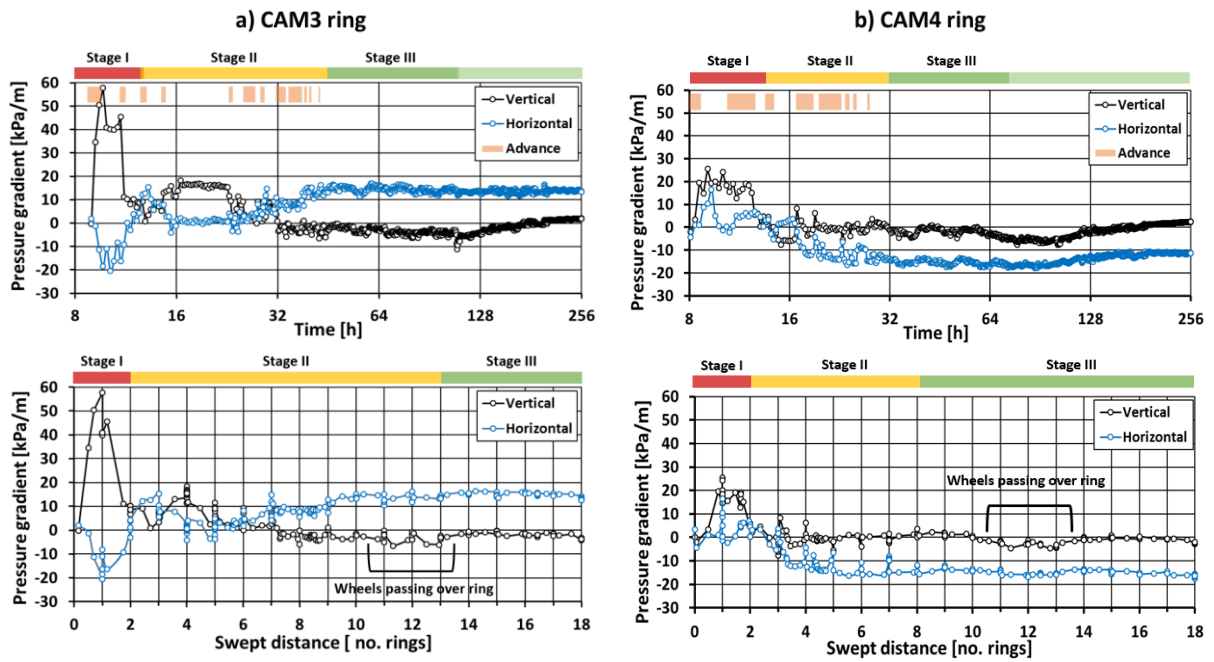


Figure 6.12: CTT pressure gradients

### 6.4. Beam response of tunnel lining

In this section, the longitudinal beam response of the CTT tunnel is examined with the aid of an existing analytical beam model, enhanced to consider the change in TBM ram loads with construction stage. The expression of a realistic input bending stiffness for CSLs with closed ring joints is also derived and validated with 3D FE joint models.

The model calibration against the CTT field data offers an excellent opportunity to validate the analytical model as a reliable tool for the prediction of CSL longitudinal behaviour. The field data interpretation is an example of how the calibrated model can be deployed to infer the in situ longitudinal response of TBM-built tunnels during construction and to identify tunnel sections prone to structural damage during and after tunnelling, enabling the asset owner to plan inspections and maintenance works in a more rational manner.

#### 6.4.1. Background

Bogaards and Bakker (1999) developed an analytical model to evaluate the beam response of a sequentially assembled semi-infinite elastic beam on a uniform elastic foundation based on the superposition of internal forces and deformations produced at each assembly step. The solutions encompassed the action of UDLs representing buoyancy forces, and constant point transverse loads and moments representing TBM forces.

The cumulative internal forces thus calculated confirmed that the sequential construction was responsible for a constant bending moment remaining in the lining at distances far from the tunnel face, which had already been observed in the Second Heinenoord tunnel pilot project (Bogaards and Bakker, 1999). It was also proved that transient internal forces estimated within the influence zone of mechanised tunnelling were greater in sequential than simultaneous models (Hoefsloot, 2009). The residual moment may have an impact on the quality of long term ring coupling; the construction moments and shear forces may lead to concrete damage or gasket performance degradation (Bakker, 2003).

Over the years, Bogaards and Bakker (1999) analytical solutions have been enhanced with corrections verified through bedded-beam numerical models (Hoefsloot, 2007), completed with solutions for UDLs over limited lengths (Hoefsloot, 2007) and combined with grout theories to estimate lining pressures affected by vertical displacements of the lining (Debrauwer et al., 2003). However, the lining bending stiffness and the modulus of subgrade reaction usually needed to be tweaked to convenient values so as to obtain good approximations to in situ measurements, even if all the other input parameters were well known (Hoefsloot, 2009; Talmon et al., 2009c).

### 6.4.2. Enhanced analytical solution for tunnel beam response

The following analytical model provides a solution for a sequentially assembled and loaded semi-infinite elastic beam supported on a uniform elastic foundation with a free boundary at the TBM-lining interface and an unsupported length,  $L_u$ , of two rings behind the TBM. Following Bogaards' approach, the solution consists in the summation of structural responses to various loading states repeated over the beam construction sequence with the novelty that the magnitude of TBM loads can vary with construction stage.

Figure 6.13.a illustrates the set of structural loads that can act on the bedded beam at a given construction stage  $i$ . The origin of the beam axis is situated at the free end. The loads under consideration are a concentrated moment,  $M_i$ , and transverse point load,  $V_i$ , acting at the origin; a UDL,  $q$ , distributed over the founded length of the tunnel; and UDLs,  $p_{1,i}$ , and  $p_{2,i}$ , applied on  $L_u$ .

$M_i$  and  $V_i$  are the moments and transverse forces exerted by the TBM on the lining. The UDLs represent the unbalanced component of lining pressures at stage  $i$  of lining pressures before any interaction with the ground. For example, in the vertical direction,  $q$  is equal to:

$$q = g_w \pi R_e^2 - g_c 2\pi R_m h \quad (6.28)$$

where  $g_w$  is the water specific weight,  $R_e$  is the external tunnel radius,  $g_c$  is the concrete specific density,  $R_m$  is the mean tunnel radius and  $h$  is the lining thickness. In the horizontal direction  $q$  is zero. The net pressure gradients resulting from the tunnel beam deflection are an output of the beam model.

The UDLs within  $L_u$  are expressed in a similar manner, although the effect of selfweight is already included in the in situ lining pressure gradients. For instance:

$$p_{1i} = g_{1i} \pi R_e^2 \quad (6.29)$$

where  $g_{1i}$  is the pressure gradient in a given direction acting on ring  $k=1$  at stage  $i$ .

The weight of the TBM backup trail in the CTT is unknown by the author and not considered in this model.

The load combination typical of a construction stage  $i$  is subdivided into recurrent loading states (LSs) repeated throughout the sequential tunnel construction (see Figure 6.13.b), which enable the application of stage-varying loads with the exception of  $q$ . Within  $L_u$ , the internal forces for each LS can be easily calculated. Within the bedded-beam, the analytical solutions for loading state 1 (LS1) and 2 (LS2) rely on Young and Budynas (2002) formulae for semi-infinite beams on elastic foundations with a concentrated transverse load and moment acting at the free end. Loading state 3 (LS3) combines the above solutions with Hoefsloot's equations for a semi-infinite beam on an elastic foundation subjected to a UDL over a limited length (Hoefsloot, 2007). The sequential superposition of loading state 4 (LS4) is resolved through Bakker's approximate solution (Hoefsloot, 2007). The internal forces, slope and deflection within the fully bedded beam section at construction stage  $i$

## 6.4. Beam response of tunnel lining

resulting from the sequential application of combined point loads or moments in LS1, LS2 and LS3 can be computed from the equations below:

$$M_{Mi}(x_{ki}) = \sum_{j=n_i-k+3}^{n_i} M_j e^{-\beta(x_j-2L_R)} \left( \cos(\beta(x_j-2L_R)) + \sin(\beta(x_j-2L_R)) \right) + M'_{n_i-k+2} \quad (6.30)$$

$$Q_{Mi}(x_{ki}) = 2 \sum_{j=n_i-k+3}^{n_i} M_j \beta e^{-\beta(x_j-2L_R)} \sin(\beta(x_j-2L_R)) \quad (6.31)$$

$$y_{Mi}(x_{ki}) = - \sum_{j=n_i-k+3}^{n_i} y_j + \Delta\varphi_{n_i-k+2} L_R + \Delta\varphi_{n_i-k+1} L_R + y_{beam,n_i-k+2} + y_{beam,n_i-k+1} \quad (6.32)$$

$$M_{Qi}(x_{ki}) = \sum_{j=n_i-k+3}^{n_i} \frac{Q_j}{\beta} e^{-\beta(x_j-2L_R)} \left( \sin(\beta(x_j-2L_R)) \right) \quad (6.33)$$

$$Q_{Qi}(x_{ki}) = \sum_{j=n_i-k+3}^{n_i} Q_j e^{-\beta(x_j-2L_R)} \left( \cos(\beta(x_j-2L_R)) - \sin(\beta(x_j-2L_R)) \right) + Q'_{n_i-k+2} \quad (6.34)$$

$$y_{Qi}(x_{ki}) = \sum_{j=n_i-k+3}^{n_i} \frac{Q_j}{2EI\beta^3} e^{-\beta(x_j-2L_R)} \cos(\beta(x_j-2L_R)) \quad (6.35)$$

$$M_j = M_{Mj} - M_{Mj-1} + M_{Vj} + M_{pj} = M_{Mj} - M_{Mj-1} + (2Q_{1j} - Q_{1j-1})L_R + (3p_{1j} + p_{2j} - p_{1j-1})\frac{L_R^2}{2} \quad (6.36)$$

$$Q_j = Q_{Vj} - Q_{Vj-1} + Q_{pj} = Q_{Vj} - Q_{Vj-1} + (p_{1j} + p_{2j} - p_{1j-1})L_R \quad (6.37)$$

$$y_j(x_{ik}) = -\frac{M_j}{2EI\beta^2} e^{-\beta(x_j-2L_R)} \left( \sin(\beta(x_j-2L_R)) - \cos(\beta(x_j-2L_R)) \right) \quad (6.38)$$

$$M'_{n_i-k+2} = M_{Mn_i-k+2} + 2Q_{Vn_i-k+2}L_R + (3p_{1,n_i-k+2} + p_{2,n_i-k+2})\frac{L_R^2}{2} \quad (6.39)$$

$$Q'_{n_i-k+2} = Q_{Vn_i-k+2} + (p_{1,n_i-k+2} + p_{2,n_i-k+2})L_R \quad (6.40)$$

$$\Delta\varphi_{n_i-k+2} = \frac{y_{n_i-k+4} - y_{n_i-k+3}}{L_R} \quad (6.41)$$

$$\Delta\varphi_{n_i-k+1} = \frac{y_{n_i-k+3} - y_{n_i-k+2}}{L_R} \quad (6.42)$$

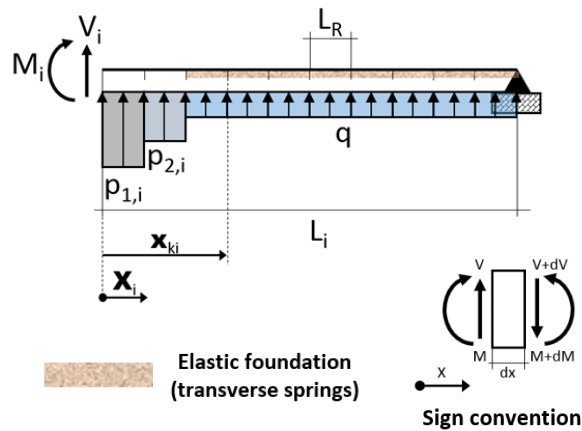
$$x_j = (j - n_i + k)L_R \quad (6.43)$$

$$\beta = \sqrt[4]{\frac{K_{tot}}{4EI}} \quad (6.44)$$

where  $k$  is the ring number counting from the origin at the construction stage  $i$  of interest;  $x_{ki}$  is the distance of ring  $k$  from the origin at stage  $i$ ;  $M_{Mi}$ ,  $Q_{Mi}$ ,  $\varphi_{Mi}$  and  $y_{Mi}$  are the moment, shear, slope and deflection caused by the succession of combined concentrated moments;  $M_{Qi}$ ,  $Q_{Qi}$ ,  $\varphi_{Qi}$  and  $y_{Qi}$  are the moment, shear, slope and deflection caused by the succession of combined concentrated shear forces;  $x_j$  is the position of ring  $k$  at a precedent construction stage  $j$ ;  $y_{beam,n_i-k+1}$  and  $y_{beam,n_i-k+2}$  are deflections produced at ring  $k$  in first and second stages after ring  $k$  assembly;  $K_{tot}$  is the foundation modulus and  $EI$  is the lining bending stiffness. The outline of the matrix solution for spreadsheets is also given in Figure 6.13.



a) Load combination and boundary condition at construction stage  $i$



Matrix solution for spreadsheets:

$$\begin{pmatrix} u_{11} & \cdots & u_{1i} & \cdots & u_{1n} \\ 0 & \ddots & \vdots & \ddots & \vdots \\ 0 & 0 & u_{ki} & \cdots & u_{kn} \\ 0 & 0 & 0 & \ddots & \vdots \\ 0 & 0 & 0 & 0 & u_{nn} \end{pmatrix}$$

where  $u_{ki} = \sum_{j=1}^{n_i} f(x_{n_i-k,i})$

and  $f$  is a variable of structural response given by the basic loading states

b) Basic loading states at construction stage  $i$

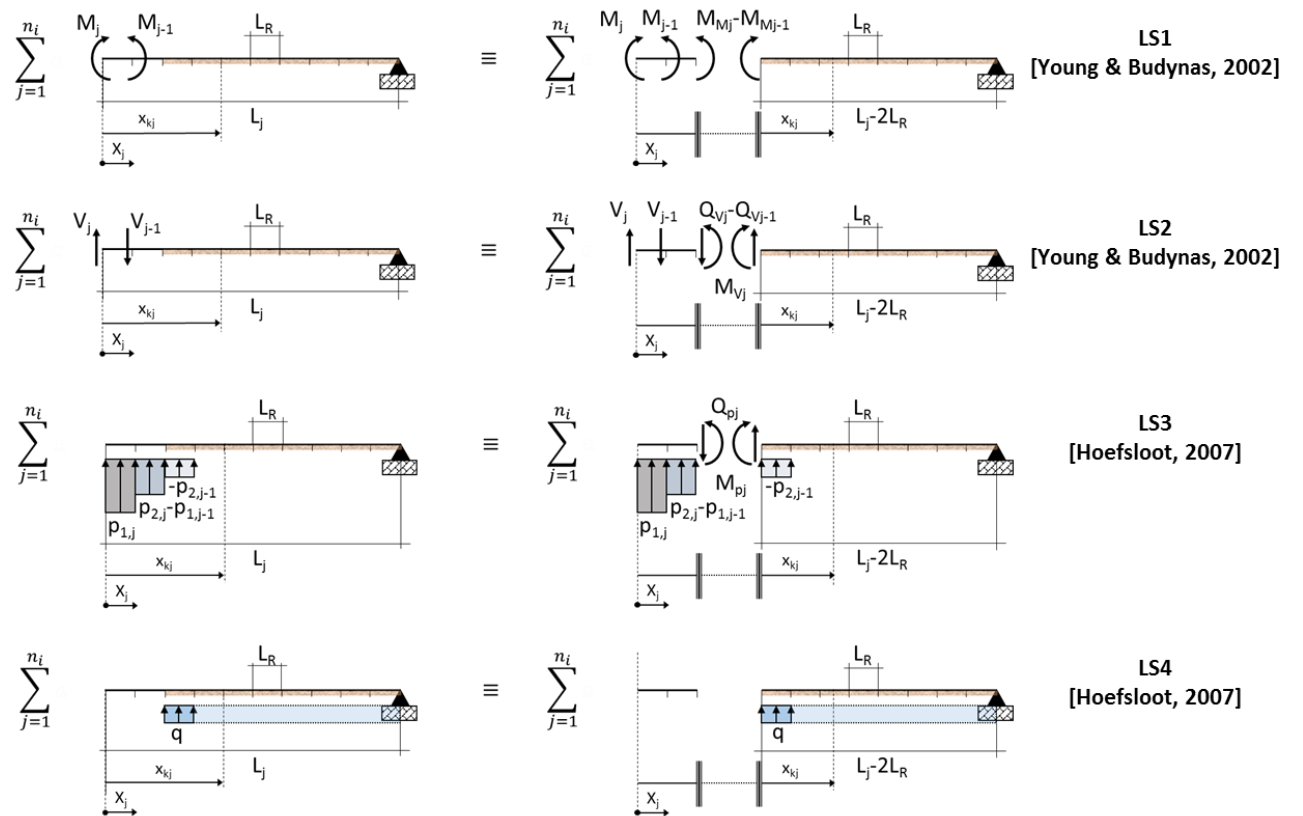


Figure 6.13: Loading and boundary conditions of bedded beam model at construction stage  $i$

### 6.4.3. Input data for analytical solution

#### 6.4.3.1. Expression of lining bending stiffness

An equivalent bending stiffness  $EI_{eq}$  of the lining must consider the softening effect of circumferential joints, whose behaviour is analogous to that of flat longitudinal joints (see chapter 2). ABAQUS FE simulations of a free linear elastic ring rotating against a fully fixed ring after initial pre-stressing were performed to evaluate  $EI_{eq}$  (see Figure 6.14).

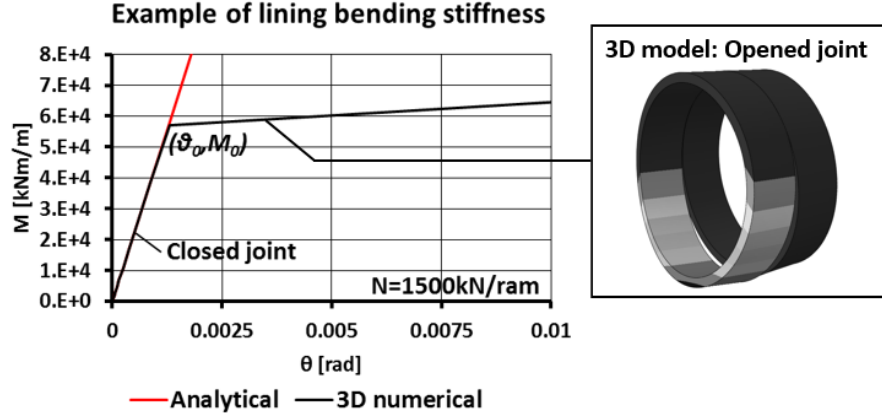


Figure 6.14: Lining bending stiffness

It was assumed that the nominal contact area at the circumferential joint was a ring with thickness equal to that of the packers. The MR curves derived were representative of combined joint and ring behaviour. It was corroborated that the stiffness remains constant until reaching a yield moment  $M_o$  at imminent joint opening. Once the circumferential joint opens, the instantaneous stiffness decreases progressively and MR curves approach an asymptotic moment with infinite rotation.

$M_o$  can be expressed as:

$$M_o = \frac{NI_J}{A_J R_m} \quad (6.45)$$

where  $I_J$  is the moment of inertia of the close joint,  $A_J$  is the cross-sectional area of the joint,  $R_m$  is the mean ring radius and  $N$  is the initial pre-stressing force. The corresponding eccentricity  $e_o$  depends only on joint geometry. Using Liao et al. (2008) nomenclature, the total rotation  $\theta$  induced by a moment  $M < M_o$  can be expressed as:

$$\theta = \frac{Ml_s}{EI_{eq,0}} = \frac{Ml_s}{EI_R} + \frac{Ml_f}{EI_J} \quad (6.46)$$

where  $I_R$  is the moment of inertia of the ring,  $l_s$  is the segment width and  $l_f$  is the influence length of the circumferential joint. The FE simulations confirmed that  $l_f = 4R_m$ . The longitudinal bending stiffness of a lining with close joints  $EI_{eq,0}$  can then be formulated by:

$$EI_{eq,0} = \frac{EI_R}{1 + \frac{I_R l_f}{I_J l_s}} \quad (6.47)$$

and the joint rotation at imminent opening,  $\theta_0$ , is:

$$\theta_0 = \frac{M_o l_s}{EI_{eq,0}} \quad (6.48)$$

### 6.4.3.2. Expression of foundation modulus

The foundation modulus  $K_{tot}$  in a fully founded tunnel with full bond at the soil-structure interface can be obtained by integrating over the ring perimeter the local ground reaction stresses produced by the lining displacement in a given direction.  $K_{tot}$  is then equal to:

$$K_{tot} = \pi R(k_r + k_t) = \frac{E_s \pi}{1 + \nu_c} (1 + b) \quad (6.49)$$

where  $k_r$  and  $k_t$  are radial and tangential spring stiffnesses respectively (see chapter 4),  $E_s$  is the ground Young's modulus,  $\nu_c$  is the ground Poisson's ratio and  $b$  is the ratio between tangential and radial stiffness.

### 6.4.3.3. CTT input data

The input parameters for the CTT analytical model are tabulated in Figure 6.15.a. Given the linearity of the analytical solution,  $EI_{eq,0}$  is adopted as the constant lining stiffness. The model proved to be insensitive to  $b$  so that variations between  $b=0$  and  $b=1/2$  led to imperceptible changes in longitudinal moments and changes of about 1mm in tunnel deflections.

The stage-varying concentrated moments, transverse forces and pressure gradients within  $L_u$  are shown in Figures 6.15.b to 6.15.d, where the origin corresponds to the construction stage at which CAM3 is erected.

The axial loads  $N$  are required for the calibration of the model and, together with the concentrated moments, were computed from TBM records.

The transverse forces are the result of model calibration (see section 6.4.4).

## 6.4. Beam response of tunnel lining

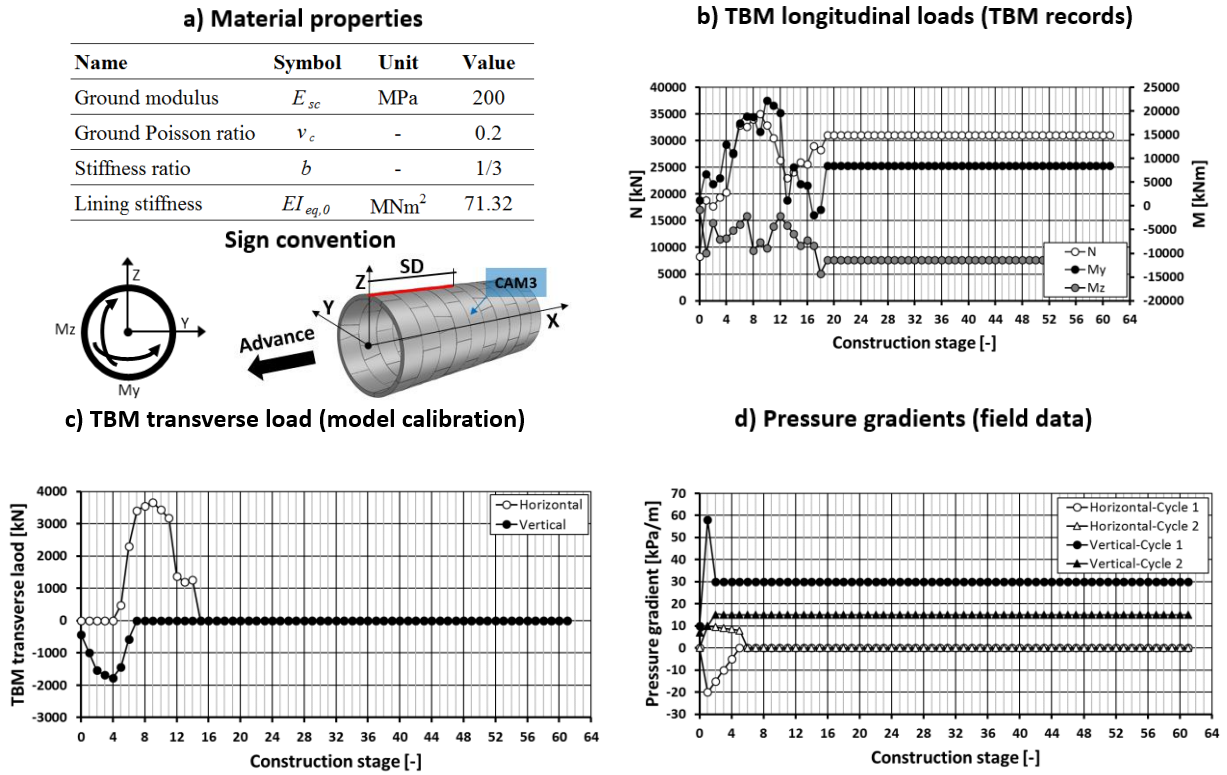


Figure 6.15: Input data for beam model

### 6.4.4. Calibration of analytical model

The tunnel beam model is calibrated against the eccentricity  $e$  of the longitudinal mean strains (or force) measured in both instrumented rings. Figures 6.16 presents the evolution of measured  $e$  and analytical  $e$  after calibration. The origin of  $SD$  is set at the CAM3 rear (see Figure 6.15.a): CAM3 is first loaded at  $SD=1$ ring and CAM4 at  $SD=5$ ring. The wide oscillations at early construction stages caused by changes in ram loads within the TBM cycles and in the contact quality of segments during assembly cannot be accounted for in this model.

#### a) Horizontal direction:

Given that both rings are situated in a 500m horizontal curved section, the hydraulic jacks exert a horizontal moment  $M_y$  on the lining to enable the steering of the shield. The moment applied to CAM3 at  $stage=1$ ,  $SD=ring1$ , is about 5000kNm and escalates to almost 25000kNm until  $SD=12$ ring. It drops then to null values that are partially recovered at  $SD=19$ ring, where  $M_y$  approaches 8000kNm.

The analytical horizontal eccentricity  $e_y$  calculated with the TBM axial load  $N$  yields a better approximation to the measured  $e_y$  than the analytical  $e_y$  computed with the in situ axial force of CAM3, given that the CAM3 VWSG strain data set was incomplete (see chapter 5). In CAM4, the difference between the two analytical  $e_y$  is small. Consequently, the  $e_y$  obtained from the TBM loads is taken hereafter as the calibrated  $e$ .

## 6.4. Beam response of tunnel lining

Excluding the sharp changes at early stages, CAM3  $e_y$  is moderate, reaching a 0.75m peak at  $SD=13$  that is far below the CTT  $e_0$  of 1.63m and that decays progressively to a steady  $e_y$  of 0.6m. The calibrated model reveals that most of the  $e_y$  is caused by the TBM moments: the lining pressures near the tail skin have a minor influence and the transverse action of the hydraulic jacks is required only from  $SD=5$ ring mainly to reproduce CAM4  $e_y$ .

In the case of CAM4,  $e_y$  increases rapidly to a maximum value of 1.80m at  $SD=13$ ring. Then,  $e_y$  decreases up to 1.40m at  $SD=19$ ring, from which point it remains roughly constant. The eccentricity during advance exceeds  $e_0$  from  $SD=10$ ring to  $SD=17$ ring, which indicates that the adjacent ring joints open temporarily. The calibrated model shows that the contribution of the TBM moments to  $e_y$  is greater than in CAM3: the peak at  $SD=13$ ring is 0.8m as opposed to the 0.5m of CAM3. However, the model also proves that significant transverse point loads are required to replicate the measured  $e_y$  so that the eccentricity allocated to the transverse ram loads becomes comparable to that of TBM moments.

### b) Vertical direction:

In the vertical direction, the vertical TBM moments and transverse loads counteract the uplift of the buoyancy forces. Downward transverse ram loads are required immediately after CAM3 to compensate the high vertical gradients of the lining pressures. Peak eccentricities during construction are however moderate in both rings, lower than 0.75m, and residual values are small,  $e_z \approx 0.0$ m and  $e_z \approx 0.5$ m for CAM3 and CAM4 respectively.

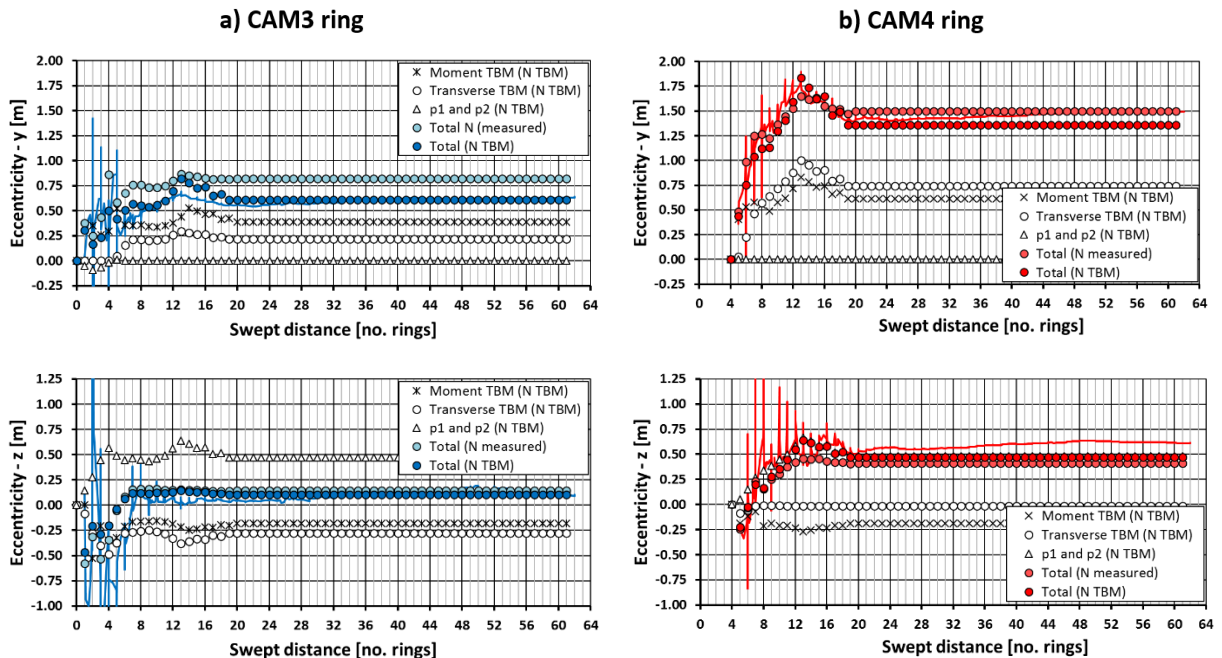


Figure 6.16: CTT model calibration

### 6.4.5. Field data interpretation on tunnel beam response

The analytical model enables the estimation of the history of the CTT structural response during construction within a tunnel section comprising the instrumented rings.

#### 6.4.5.1. Local lining response (Lagrangian)

Figure 6.17 illustrates the evolution of displacements, slope and shear force of the instrumented rings with the progress of construction.

The ring displacements become stable at  $SD=16$ ring, although the most dramatic changes in flexural deflection occur in the first seven TBM cycles after ring erection. In the horizontal direction, the opposite trend in the displacements of the two rings is the result of longitudinal tunnel bending when subjected to the TBM concentrated loads (see section 6.4.5.2). In the vertical direction, both rings move upwards due to the uplift forces: CAM4 reaches a plateau at about 5.0mm while CAM3 at 1.6mm only due to the pronounced downward action of the hydraulic jacks.

The calibrated model replicates well the general trend in measured vertical tilt for both rings, particularly of those situated at the crown, although the field data includes the effect of individual segment rotations typical of sequential loading near the tail skin, which results in an in situ vertical tilt dispersion of up to 0.002rad.

The shear forces increase gradually in the first seven TBM cycles towards a residual peak value. The strength of the adjacent ring joints is calculated from the measured axial force assuming a friction coefficient of 0.4. In the horizontal direction, the maximum shear forces are moderate, 3000kN and 6000kN for CAM3 and CAM4 respectively, and there is no horizontal joint lipping. In the vertical direction, the shear force peaks to 10,000kN and 12,500kN in CAM3 and CAM4. The shear strength is exceeded at early TBM cycles after ring erection. The ring joints may undergo shearing from the first and third cycle of each ring onwards.

The progressive reduction of joint shear strength with the longitudinal relaxation of the tunnel suggests that the tendency of ring joints to shearing grows as the structure ages.

## 6.4. Beam response of tunnel lining

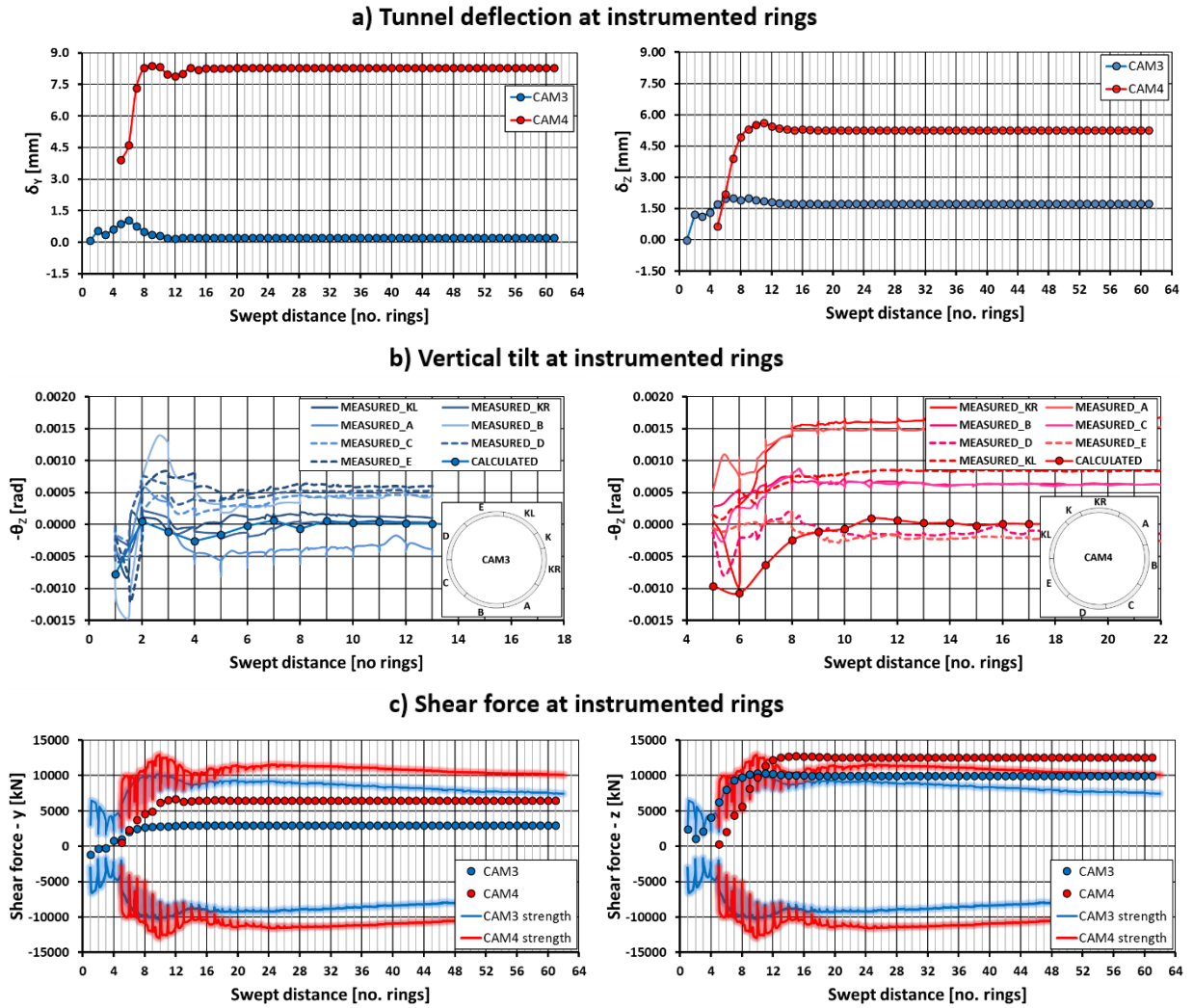


Figure 6.17: CTT local longitudinal response

### 6.4.5.2. General lining response (Eulerian)

Figure 6.18 shows the evolution of deflections, joint rotations and shear forces within the modelled tunnel length, referred to a fixed abscissa positioned at  $SD=-32$ ring.

The residual tunnel deflections at  $stage=61$  are generally the greatest of the entire lining history for both directions. The high concentrated TBM actions required to steer the shield, particularly after CAM4 erection, bend the tunnel horizontally in such a way that CAM4 shifts gradually towards the outer side of the curve while CAM3 moves in the opposite direction to accommodate the horizontal curvature. The peak outer displacements of +12mm are experienced two rings after CAM4,  $X_{eulerian}=37$ ring, at the ring subjected to the highest concentrated moment and transverse load when it is first founded in the ground. The uplift forces cause moderate vertical displacements less than 7mm.

The history of ring joint rotations and shear forces allows the identification of tunnel sections at risk of ring joint opening and shearing respectively during construction and in the long term by comparing the predicted quantities with the limits given by the longitudinal pre-stressing force. The CTT field data evidence that the tunnel section near the monitored rings is more prone to joint opening in the



## 6.5. Proposed method for potential damage assessment

horizontal direction, as the TBM steering causes the lining to bend. The cumulative uplift forces make joint shearing more likely in the vertical direction.

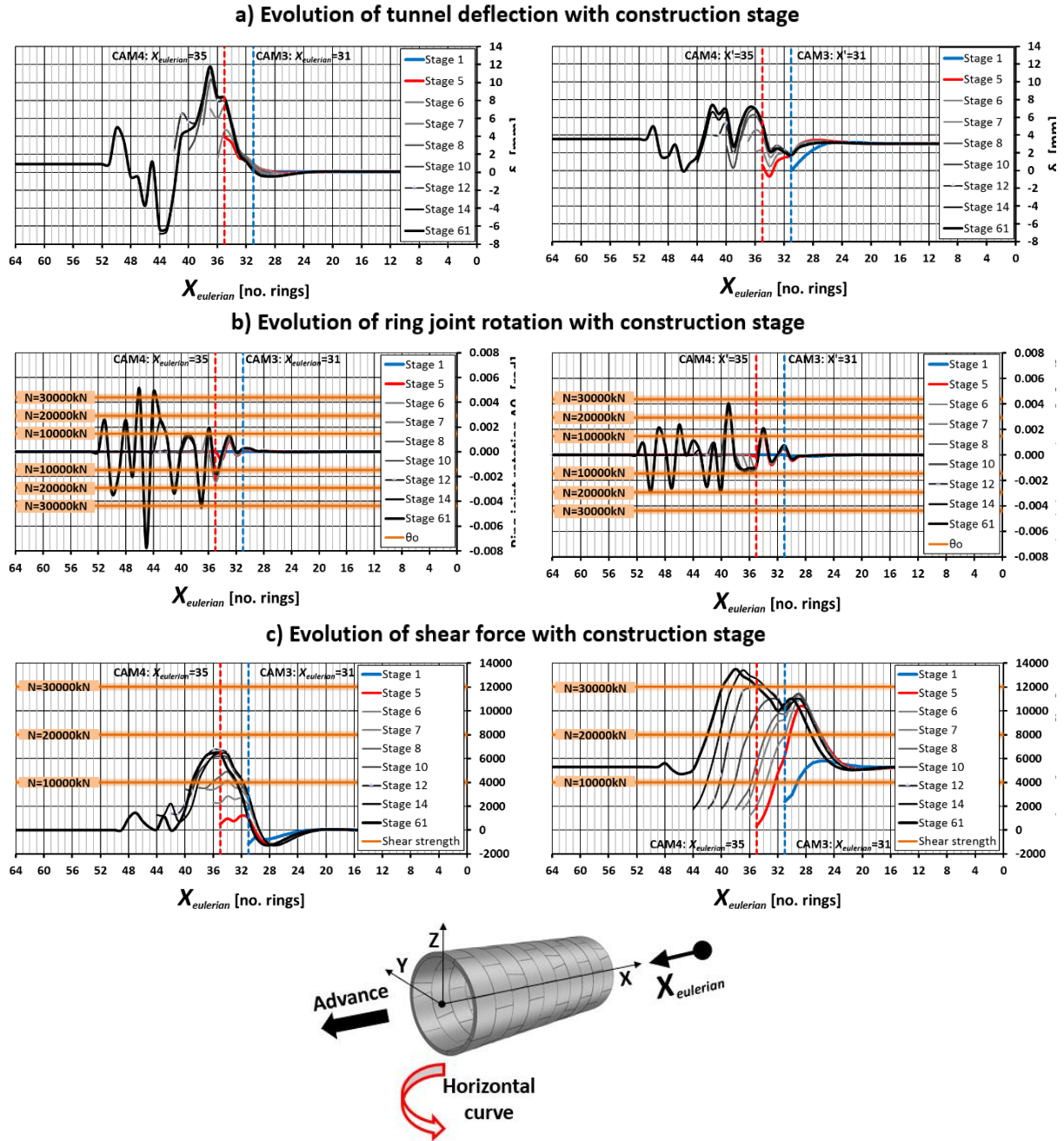


Figure 6.18: CTT global longitudinal response

## 6.5. Proposed method for potential damage assessment

The development of reliable analytical models that can estimate the history of the tunnel longitudinal pre-stressing force and beam response lead to the proposal of a PDA method that can identify tunnels sections at risk of ring joint damage and estimate when such damage may be imminent (see Figure 6.19). The method, however, requires to know beforehand the history of ram loads, net TBM-lining transverse interactions during construction and the in situ temperatures during and after construction.



## 6.5. Proposed method for potential damage assessment

Of the above inputs, ram loads and in situ temperatures can be easily obtained from TBM records and conventional temperature sensors respectively. However, the monitoring of TBM transverse actions would require the development of a monitoring system built in the tail skin for either direct or indirect measurements (see section 9.2 for a proposed design concept). Nevertheless, the effort could be invaluable for asset owners that can then target the problematic areas in their monitoring, inspection and maintenance plans.

If the above inputs could be predicted by engineering models on the basis of the proposed tunnel drive, including alignment and geology, and foreseeable TBM operations, then tunnel designers could follow a similar workflow to customise ring joint design to the predicted risk of structural damage.

Although the lining shear stiffness has a minor influence on the internal forces (Hoefsloot, 2007), given that the tunnel beam model is based on the Euler-Bernoulli beam solution, it is convenient to remark that this PDA method should be used for the identification of problematic areas in preliminary assessments. Then, asset owners can focus on the detailed analysis of these areas with more sophisticated methods.

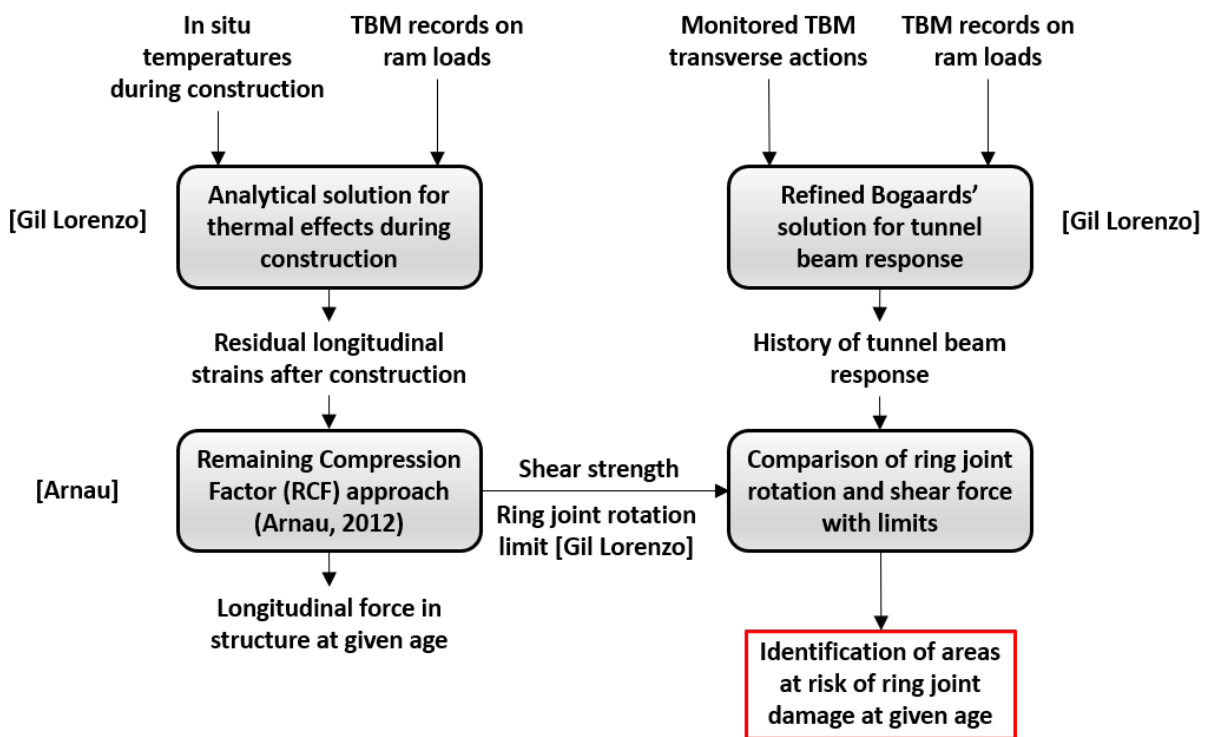


Figure 6.19: PDA method for preliminary assessment

## 6.6. Conclusions

The study of the CTT longitudinal response during construction revealed that CSLs simultaneously backfilled with cementitious grouts undergo an early relaxation of the longitudinal pre-stressing force due to the temperature changes induced by grout hardening. The extent of relaxation depends mainly on the temperature profile given by the grout mix and the ambient temperatures. In the CTT tunnel, backfilled with BGs, the mean strains were reduced by 50%, equivalent to 85bar/ram, in the months following ring erection. If creep effects associated with the loading time are added to this early relaxation, it is expected that the longitudinal force in the long term will be small and the ring interaction limited.

It was also found that the residual moments and shear forces resulting from sequential CSL construction are highly dependent on the TBM moments and transverse actions near the tail skin. The lining responds to pronounced TBM steering around curves through longitudinal bending and to uplift forces through shear. The inherited internal forces may lead to deferred structural damage in the form of ring joint opening or lipping as a consequence of the loss of tunnel pre-stressing.

The deployment of analytical models enhances the field data interpretation: the development of the solution for a sequential elastic rod subjected to trilinear temperature and in shear interaction with the elastic ground enables the accurate prediction of tunnel relaxation caused by grout hardening; the refined Bogaards' solution, incorporating the effects of stage-varying net TBM moments, transverse loads and lining pressure gradients within  $L_u$ , can estimate satisfactorily the history of tunnel beam response during construction for the derived expression of  $EI_0$ .

Following the validation of these two models as effective tools for the prediction of longitudinal lining response, a PDA method for the early detection of tunnel sections prone to ring joint damage was proposed. The method requires that the TBM is equipped with transducers that can measure the transverse loads and lining pressures near the tail skin, the TBM records on the above loads and ram loads are available and the in situ lining temperatures are either monitored from early construction or estimated. With this PDA method, the asset owner can identify the problematic areas in a tunnel immediately after its construction and develop monitoring, inspection and maintenance plans that target these areas.

Tunnel designers could benefit from the deployment of rod and beam models by giving them the opportunity of customising ring joint design in accordance with the predicted history of longitudinal lining response. However, a reliable method for the prediction of TBM ram loads and net transverse TBM-lining interactions based on the knowledge of the proposed tunnel drive, i.e. possibly alignment and geology, and foreseeable operations would be needed.

# Chapter 7

## 3D numerical study on the CSL local response to sequential loading near the tail skin

### 7.1 Introduction

The need for coordination between the design of CSLs, the TBM technology deployed and the in situ TBM operations has been pointed out in the past (Blom, 2002; Koyama, 2003). The interactions between the TBM and the tunnel structure in the construction phase are not fully understood and therefore their effects cannot be properly accounted for in the design process of both TBM and lining. The fact that nowadays most of the damage in CSLs takes place at the early stages of mechanised shield tunnelling either before or while the ring is exiting the tail skin (Chen and Mo, 2009; Sugimoto, 2006) may be a symptom of such lack of design harmonisation.

The CTT field data interpretation conducted in chapter 6 confirmed that the TBM operations can determine the longitudinal CSL response during construction. Mean lining pressures with vertical gradients greater than grout-static and not null horizontal gradients can arise during sequential loading near the tail skin. Such gradients dissipate abruptly once the ring is fully surrounded by the annular grout. Additionally, net TBM transverse loads can be required to either achieve lining stability in the vertical direction or to replicate the in situ longitudinal response of CSL tunnels in curved alignments. Nevertheless, the local effects of TBM-lining transverse interaction on ring behaviour immediately behind the TBM have been hardly examined in previous research.

In this chapter, the CSL local response to sequential loading near the tail skin during one TBM advance is discussed through a 3D numerical study where TBM-lining transverse interactions are simplified but still representative of the field conditions that can be found in CSLs simultaneously backfilled with BGs, e.g. the CTT tunnel. The analysis is approached from less to more complexity: first, the structural performance of rings subjected to axisymmetric sequential compression and boundary conditions is examined; then, selfweight, pressure gradients and uneven TBM-ram pad transverse interactions are gradually incorporated into the study. The numerical simulations with axisymmetric radial loading may represent a lining that is concentric with the tail skin; those where radial pressures are applied with a certain gradient may correspond to a lining eccentrically positioned against the shield tail (see chapter 8).

## 7.2 Background

### 7.2.1. Previous research on sequential loading

In chapter 3, the response of an isolated ring to eccentric radial compression was briefly discussed to identify the role of spear bolts in the prevention of permanent ring distortions and segment damage during sequential loading. The numerical model evidenced the tendency of concrete segments to radial tilt and partial opening of longitudinal joints, particularly for the keystone.

Blom (2002) investigated the response of CSLs subjected to sequential loading through full-scale tests where three rings were initially compressed in axial direction, and uniform and deviatoric pressures were later applied in the radial direction, first in two adjacent rings and then in the remaining ring.

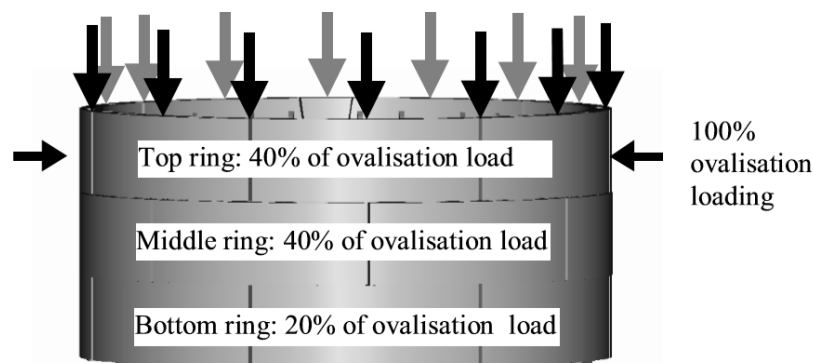


Figure 7.1: Longitudinal migration of sequential ovalisation loading (Blom, 2002)

The experimental results and numerical analyses confirmed that, at the end of the sequential loading, the ovalisation loads applied to the latter ring were shared with the former rings in a proportion of 40% to 60% respectively (see Figure 7.1), whilst there was no redistribution of uniform pressures amongst rings. The longitudinal migration of ovalisation loads was produced by coupling forces in turn triggered by differential radial deformations amongst rings. Successive loading resulted in coupling forces of opposite sign acting at each side of a ring, which affected moment distribution within segments. The uneven distortion of coupled rings also led to segment torsion, particularly in those segments situated at  $45^\circ$  from the symmetry axes of ovalisation. The influence length of sequential loading in this study was limited to three rings.

Blom (2002) explained the mechanics of CSLs under sequential loading, but it was based on the underlying assumption that individual rings were radially loaded at one time rather than progressively. The effects of unbalanced pressures were not examined.

### 7.2.2. FE analyses of CSL response to construction loads

The longitudinal response of CSLs under transient construction loads and boundaries is enabled by the local interaction of neighbouring rings. In this respect, three-dimensional FE models are the most effective tools to investigate the full effects of typical construction processes and imperfections on the

structural behaviour of CSLs behind the TBM (Blom et al., 1999), although analytical solutions may be adequate to describe certain aspects such as longitudinal bending or prestressing relaxation (see chapter 6).

With current computer capabilities, the degree of sophistication of numerical models in terms of concrete constitutive models, lining joints, soil-structure interaction, TBM interactions, simultaneous backfill grouting, ring assembly and lining imperfections depends on the objective of the simulations. Bedded numerical models are deemed to be the most appropriate technique for a detailed examination of global structural response in CSL construction (Blom et al., 1999; Mashimo and Ishimura, 2005; Mayer et al., 2009; Ishimura et al., 2013).

Blom et al. (1999) performed a wished-in-place numerical simulation of a twelve ring solid model subjected to assumed input TBM longitudinal loads, radial pressures transitioning from grout-static to typical long term distributions and variable spring support. The packers were represented as four bilinear springs, the longitudinal joints were modelled with interface elements and the concrete behaviour was simulated with a linear elastic constitutive model. The effect of backfill grouting on the hoop stress distribution of CSLs with coupled rings was ascertained, and it was found that the mechanical properties of packers had a strong influence on the nature and magnitude of the longitudinal response.

Mashimo and Ishimura (2005) examined the lining behaviour under construction loads by comparing the bending moments obtained from a beam-spring model of two coupled rings with field data. The two rings were passively supported by a circular retainer simulated with compressive springs. One ring was subjected to tail seal pressures whilst the other only to selfweight. The latter was modelled in either a complete or incomplete assembly state. It was concluded that selfweight and tail pressures governed the lining internal forces in the construction stage.

Mayer et al. (2009) investigated the response of one and two ring solid models subjected to uniform, asymmetric and eccentric ram loads. The longitudinal joints were simulated with hinge elements and plywood packers by means of solid elements with a Mohr-Coulomb constitutive model. The 3D numerical analyses revealed that the ram pad eccentricity is critical for concrete spalling and that asymmetric ram loads may increase ring deformations in the unloaded perimeter due to the absence of vertical support through ring coupling.

Ishimura et al. (2013) studied the effect of TBM ram loads, tail and backfill grouting pressures on peak stresses of concrete segments and bolt shear forces in ring joints through a wished-in-place forty two ring shell model. The longitudinal joints were simulated with rotational, axial and shear springs and the ring joints with tensile and shear springs only. The input construction loads were obtained from field data on lining pressures and TBM data. It was concluded that the asymmetry of construction loads, particularly TBM thrust, greatly increased the likelihood of concrete damage and bolt shearing at circumferential joints.

Overall, the reviewed FE models disregarded sequential loading and oversimplified either the tunnel structure, e.g. Mashimo & Ishimura (2005); the input loads, e.g. excluding the effects of tail seal pressures, (Blom et al., 1999), or radial pressures altogether, (Mayer et al., 2009); or the nature of ram pad-lining interfaces (Ishimura et al., 2013).

### 7.2.3. TBM jacking systems

According to a technical consultation with Herrenknecht, the jacking systems currently in use can be classified in two types depending on the rod support during advance (see Figure 7.2).

In simple systems with permanent bulkhead fixings, the rams may be subjected to bending and thus the ram pads can transfer transverse loads to the lining. However, it is common practice to release and reposition the hydraulic jacks while steering the TBM in order to prevent the permanent damage of the rods.

In sophisticated systems, the fixings at the rear of the bulkhead are released at the beginning of the TBM advance. The rams are relatively free to pivot against the spherical hinge on the shield end as long as rotations remain small and there is no contact with the intermediate wall. In this system type, the hydraulic jacks are only subjected to axial loads and the ram pads can exert transverse loads onto the lining if the hydraulic jacks are inclined with respect to the lining. In this case, the transverse loads must be proportional to the inclination and axial load of the rams providing that there is sufficient friction between the pads and the lining.

In any case, the common assumption in 3D FE models of fully constrained ring plane displacements at the ram pad-lining interface would be at least arguable.

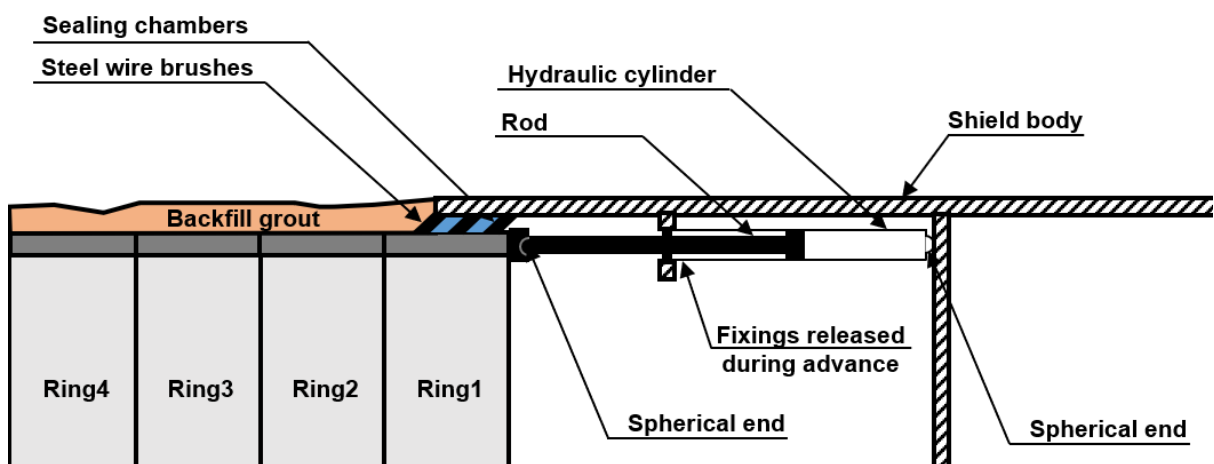


Figure 7.2: Hydraulic jack system with fixing release during advance

## 7.3. Description of numerical simulations

---

### 7.3. Description of numerical simulations

The numerical study is designed to target the structural behaviour of CSLs subjected to the sequential loading of one TBM advance and gives particular attention to the effects of high pressure gradients and uneven ram pad-lining interactions.

The FE models are wished-in-place solid models of multiple rings that share ring geometry, element types, mesh, concrete constitutive models, material properties and modelling techniques for discrete lining joints with the 3D models described in chapter 4. The loading sequence, the extent of ground-structure interaction, the boundary conditions and the modelling sequence are modified to suit representative construction environments during the TBM advance. Given that the study focuses on the CSL response to sequential loading in one TBM advance, the wished-in-place approach is deemed sufficient. The effects of potential contact deficiencies originated in previous TBM cycles are thus omitted.

Table 7.1 describes the loading and boundary conditions of each simulation step. At the first step, the contact interactions are initialised with the application of 1kPa ram pressures and restraint displacements at the outer CSL boundaries. The total ram loads are applied in step 2 with full constraints at the opposite side. The eccentricity of ram loads or the selfweight of the first ring, R1, can be added in optional steps. In the next steps, from step 3 up to step 7, the radial pressures are sequentially applied from the mid width of the second ring, R2, up to the mid width of R1 after the replacement of ring plane fixities with spring supports acting within the tunnel supported length. The sequence may be completed with the full compression of R1, i.e. when the loaded width is 2.4m.

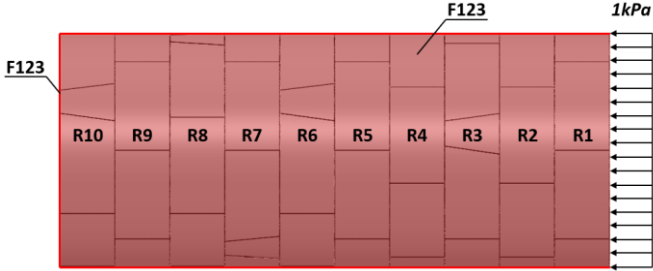
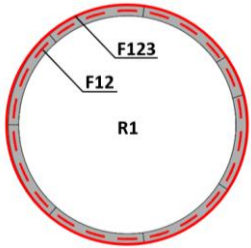
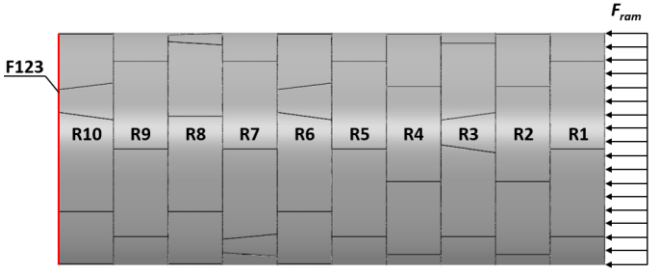
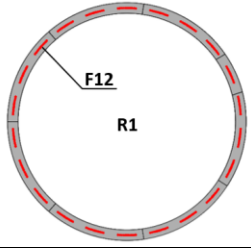
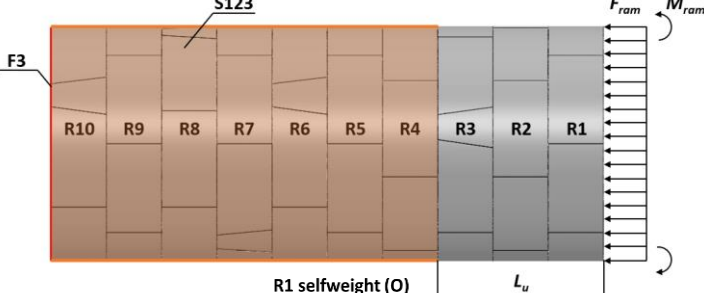
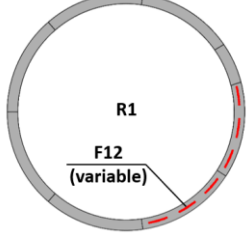
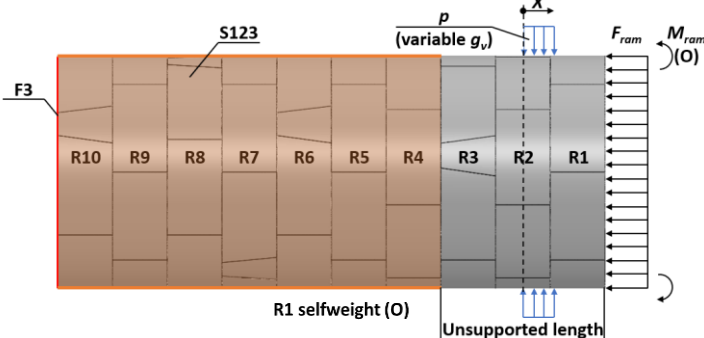
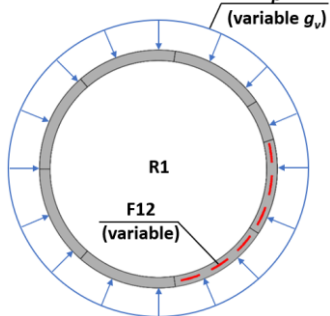
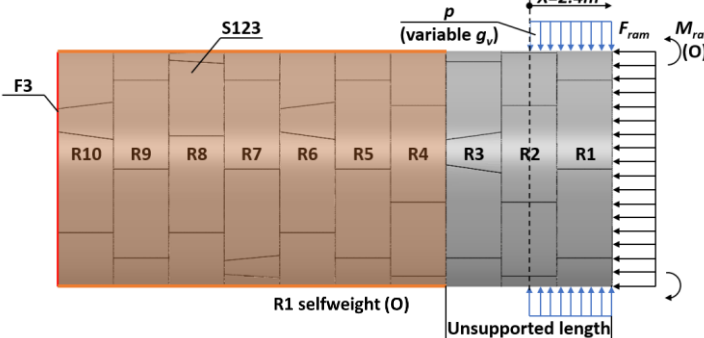
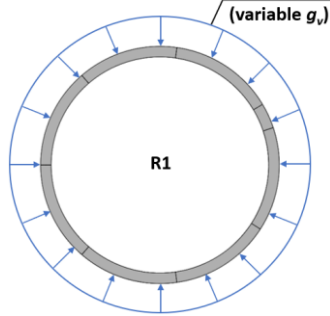
The radial pressures that would act on the tunnel structure prior to the R1 assembly, i.e. AS0, are disregarded in the wished-in-place model in order to avoid the unrealistic propagation of lining deformations developed prior to R1 erection. This is considered to be a good approximation in the case of axisymmetric loading or in CSLs where the moment capacity of longitudinal joints in previously erected rings is not significantly affected by the development of hoop forces, e.g. curved jointed CSLs or flat jointed CSLs with out-of-plane angularity at their longitudinal joints.

The radial pressures are uniformly distributed along the longitudinal axis, somewhat equivalent to mean lining pressures. This simplified sequential loading still enables the identification of the mechanisms governing lining response behind the TBM and will prove useful for the interpretation of the CTT field data.

The transverse interaction between ram pads and lining is simulated through ring plane fixity at the mid lining depth of the ram pad positions within the restrained arc of choice (see Tables 7.1 and 7.2).

## 7.3. Description of numerical simulations

Table 7.1: Modelling steps

Step	Loading and boundary conditions	
1		
2		
2a (O)		
3-7		
8 (O)		

$X \equiv$  Loaded width

$p \equiv$  Radial pressure

$g_v \equiv$  Vertical pressure gradient

1  $\equiv$  Radial direction

2  $\equiv$  Tangential direction

3  $\equiv$  Longitudinal direction

Fixed condition (F)

Spring support (S)

O  $\equiv$  Optional



### 7.4. Parametric studies

The parametric studies are undertaken in three phases:

**a) Sequential loading of two coupled rings under axisymmetric conditions:**

Here the study focuses on the effects of the magnitude of input loads, ram pad eccentricity, the tunnel unsupported length,  $L_u$ , and the quality of ram pad-lining interface on the CSL structural response. Two extreme conditions at the boundary with the ram pads are considered: ring plane full fixity or free ring plane displacements. The former represents the boundary generally assumed in numerical simulations; the latter corresponds to the academic case where there is no transverse interaction with the ram pads. The impact of lining features such as packers or longitudinal joint geometry is also examined.

**b) Sequential loading of two coupled rings under axisymmetric radial pressures and ram pad-lining boundaries plus R1 selfweight;**

**c) Sequential loading of ten coupled rings under radial pressures with vertical gradient, variable ram pad-lining interface and R1 selfweight:**

This part of the study is conducted in two stages.

First, the impact of the ram pad-lining interface on the response of a curved jointed CSL subjected to lining pressures with high vertical pressure gradients is investigated.  $L_u$  is 1.5 times the ring width, the pressure gradient close to 80kPa/m, the ram loads 150bar/ram and the ring roll of R1 equal to that of CAM3. The above parameters are deemed to be roughly representative of the in situ conditions encountered by CAM3 on its first advance, AD1, if it is assumed that, after the 8h of TBM standstill required for the field trials works, the previously grouted tunnel length is fully founded on the ground; and that the field lining pressure gradients in AD1 are an average of the radial pressures acting over the ring width (see chapter 6). Table 7.2 lists the models analysed, illustrating the boundary conditions at their ram pad-lining interface.

Second, the influence of features other than the ram pad-lining interface is evaluated. The 3UKRA model developed for the previous stage is regarded as the reference model. The parameters under consideration are: the magnitude of ram loads,  $L_u$ , the R1 ring rolling, the longitudinal joint geometry and the action of spear bolts. This time, the angled bolts are modelled by means of not only tension but also shear group springs to consider the added resistance to joint lipping given by the bolt elongation. The bolt shear stiffness is the stiffness component tangential to the joint.

## 7.4. Parametric studies

Table 7.2: Nomenclature of FE models and R1 boundary conditions

Model name	Boundary condition at ram pad interface
3UFR	
3UFX	
3UAB	
3UEKL	
3UKRA	
3UKLKKR	
3UKR	
3UKRAB	
3UKLKKRA	

## 7.5. Sequential loading under axisymmetric conditions

---

### 7.5. Sequential loading under axisymmetric conditions

#### 7.5.1. Lining structural response

In chapter 3, the tulip effect of an isolated ring was exemplified through a one-ring model subjected to sequential loading and a free TBM boundary. The compatibility of deformations entailed the radial rotation of segments and the partial opening of longitudinal joints (see Figure 3.14). For a given tunnel diameter, the segment length governed the magnitude of radial tilt and hoop tension experienced at the unloaded regions. Shorter segments such as keystones presented a greater tendency to tilt and negligible hoop tension.

In a system of two coupled rings, when one ring is compressed, the change in ring diameter near the circumferential joint induces the development of radial coupling forces that in turn drag the adjacent ring into partial compression. Consequently, the second ring contributes also to the equilibrium of the two-ring system (see Table 7.3). The ability of the unloaded ring to share radial compression depends on the magnitude of the applied pressures, the loaded width and the boundary condition at the ram pad-lining interface while it is hardly influenced by the geometry of longitudinal joints (see Figure 7.3).

For example, during sequential loading in free conditions, while  $X \approx 0.8\text{m}$  and most of the radial pressure acts on R2, the coupling forces at the ring joint lead to the eccentric compression of R1 with the subsequent development of segment rotation and hoop tension. The proportion of radial compression sustained by R1 depends on the compressed length of the opened longitudinal joints and thus it increases with the magnitude of radial pressures. If the radial pressures are not sufficiently high, the radial rotation of segments typical of the “tulip effect” results in a negative balance of hoop membrane stresses (see Figure 7.3.a).

With fixed conditions and  $X \approx 0.8\text{m}$ , the opening of the longitudinal joints at the front of R1 is prevented by the ram pads through radial inward reactions and R1 is more evenly compressed. The total load share of R1 reaches values of about 30% regardless the magnitude of radial pressures (see Figure 7.3.b).

At  $X = 1.6\text{m}$ , both rings are loaded in the same proportion, R2 at its front and R1 at its rear. In free conditions, the response of the two rings mirror each other and there is an equal share of the total load. The smaller eccentricity of the total hoop force in R1 causes the segment rotation to decline. In fixed conditions, the R1 total load share grows to 60% as the rotation of segments is still constrained.

At  $X = 2.4\text{m}$ , the R1 total load share approaches 67%, i.e. 100% of the load directly applied on R1 and the segment rotation is negligible, regardless of previous boundary conditions, which agrees with Blom's (2002) conclusions.

## 7.5. Sequential loading under axisymmetric conditions

Table 7.3: Sequential loading under axisymmetric conditions

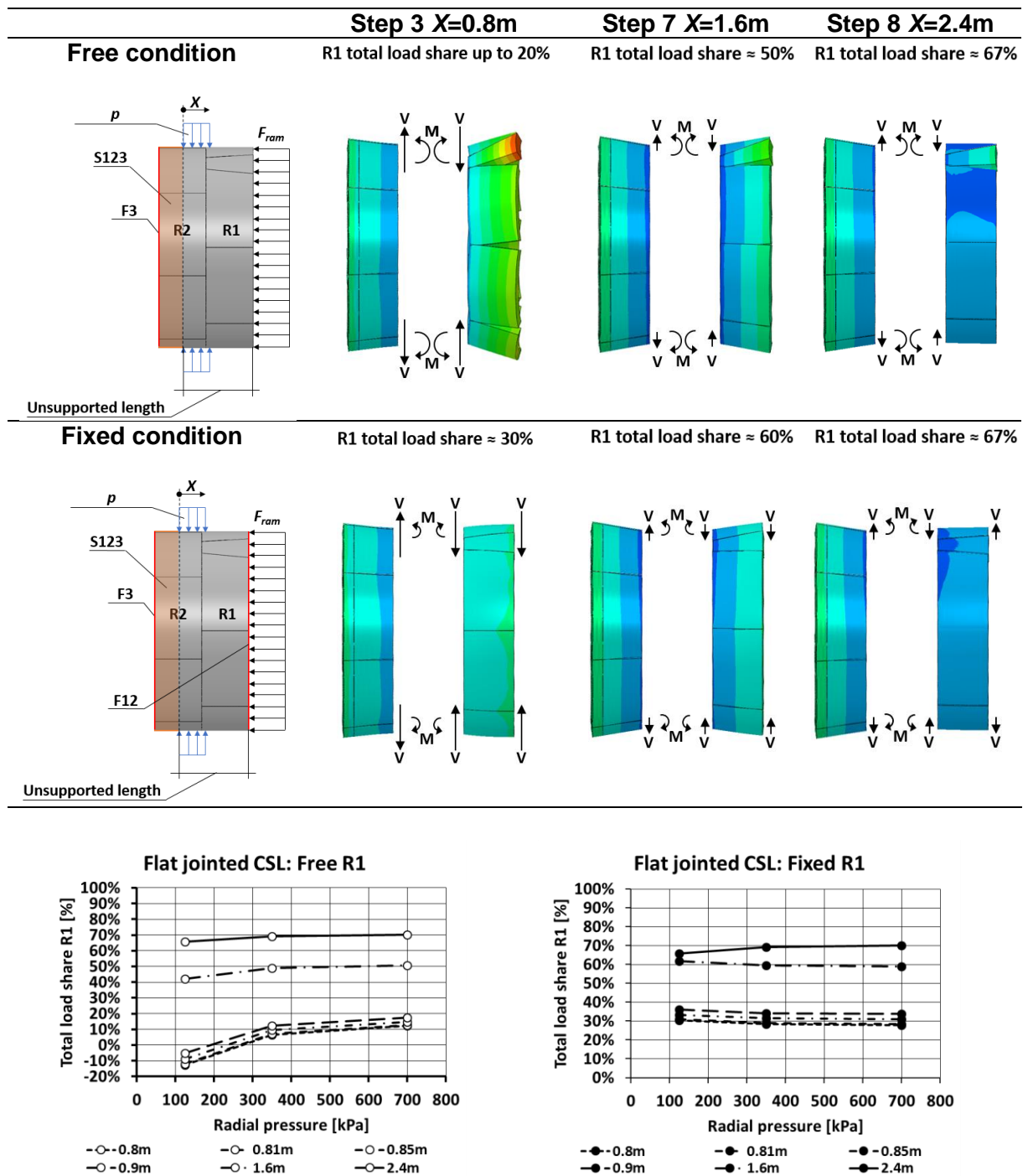


Figure 7.3: R1 load share in two-ring systems subjected to uniform sequential loading

### 7.5.2. Effect of ram loads on lining response

In the CTT, the hydraulic cylinders were nominally positioned in alignment with the lining mid depth (see Figure 7.4). The packers were, however, fitted at the intrados edge of the ring joints, giving rise to a -10mm offset between centred jacks and packers. This implies that both the sequential loading and the nominal offset between packers and jacks cause the rotation of segments under axisymmetric conditions and centred ram loads in the FE models.

## 7.5. Sequential loading under axisymmetric conditions

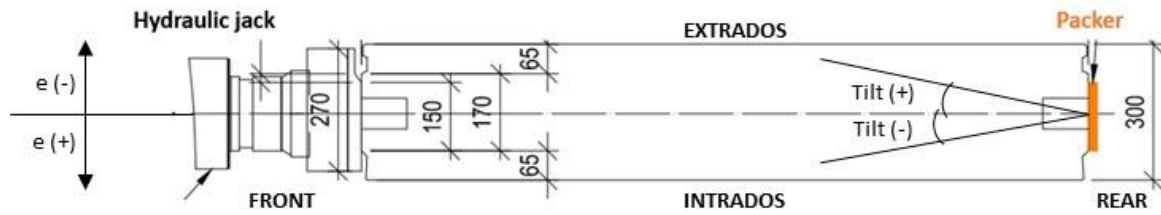


Figure 7.4: Relative position of hydraulic cylinders and packer

Figures 7.5.a and 7.5.b show the outward segment rotations and radial displacements at the front of R1 standard segments under free conditions. At intermediate longitudinal loads of 150bar/ram, the peak values of both variables increase with the magnitude of radial pressures. The rotation at 125kPa pressures of  $0.05^\circ$  is more than half that reached with 700kPa, which suggests that the relative offset of the ram loads produce rotations comparable to those associated with sequential loading.

With high longitudinal loads of 300bar/ram, the segments exhibit the greatest peak rotations and displacements,  $0.12^\circ$  and 3mm respectively, since the resultant longitudinal moment at the ring joint is proportional to the magnitude of the ram loads applied.

At low longitudinal loads of 12.5bar/ram, the longitudinal moment acting on the segments is small. In addition, the ring interaction is compromised by the limited friction capability of lightly compressed segment-packer interfaces. Consequently, peak rotations are less than  $0.025^\circ$ .

Given that the longitudinal migration of hoop forces depends on the development of coupling forces at the ring joint and the contact length of longitudinal joints, the magnitude of longitudinal loads has an influence on the total load share of R1 during sequential loading (see Figure 7.5.c and 7.5.d). With poor ring coupling, there is partial slip at the ring joint and the two rings tend to deform more independently; thus, the total share load is similar in both free and fixed conditions. Under high longitudinal compression, the greater segment rotations in free conditions can undermine slightly the total load share of R1.

## 7.5. Sequential loading under axisymmetric conditions

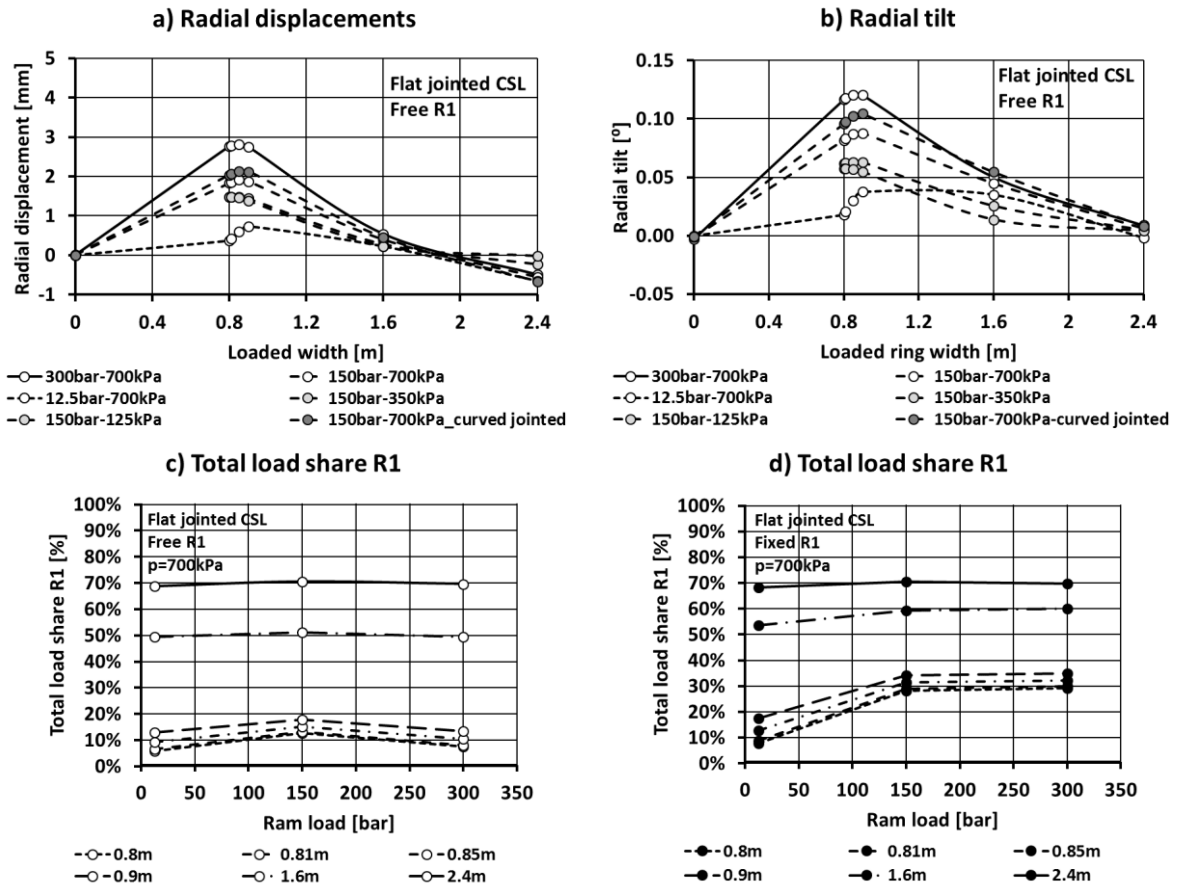


Figure 7.5: Effect of longitudinal loads on R1 response

### 7.5.3. Effect of ram pad eccentricity on lining response

When the ram loads are applied with negative eccentricity, i.e. towards the segment extrados, the maximum outward rotations of segments are exacerbated (see Figures 7.6.a to 7.6.d). For example, in a standard segment, a -25mm offset of the ram pads yields peak displacements and rotations of 6mm and 0.2° respectively before the application of any radial compression in the system. These numbers roughly double the peaks caused by centred 300bar/ram loads. In keystones, with a smaller moment of inertia at their circumferential joint, the maximum values rise to 20mm and 0.7°.

At  $X=1.6\text{m}$ , both displacements and rotations are minor and hardly influenced by ram pad eccentricity in standard segments, while keystones subjected to negative ram pad eccentricities exhibit substantial permanent rotations, e.g. a -25mm eccentricity results in residual 7.5mm displacements and 0.3° rotations.

Conversely, when the ram pad eccentricity is positive, the peak radial deformations tend to decrease and remain close to zero through the whole loading sequence, which suggests that the positioning of ram pads with moderate inward offsets could mitigate the potential damage associated with the opening of joints described by Gruebl (2006).

## 7.5. Sequential loading under axisymmetric conditions

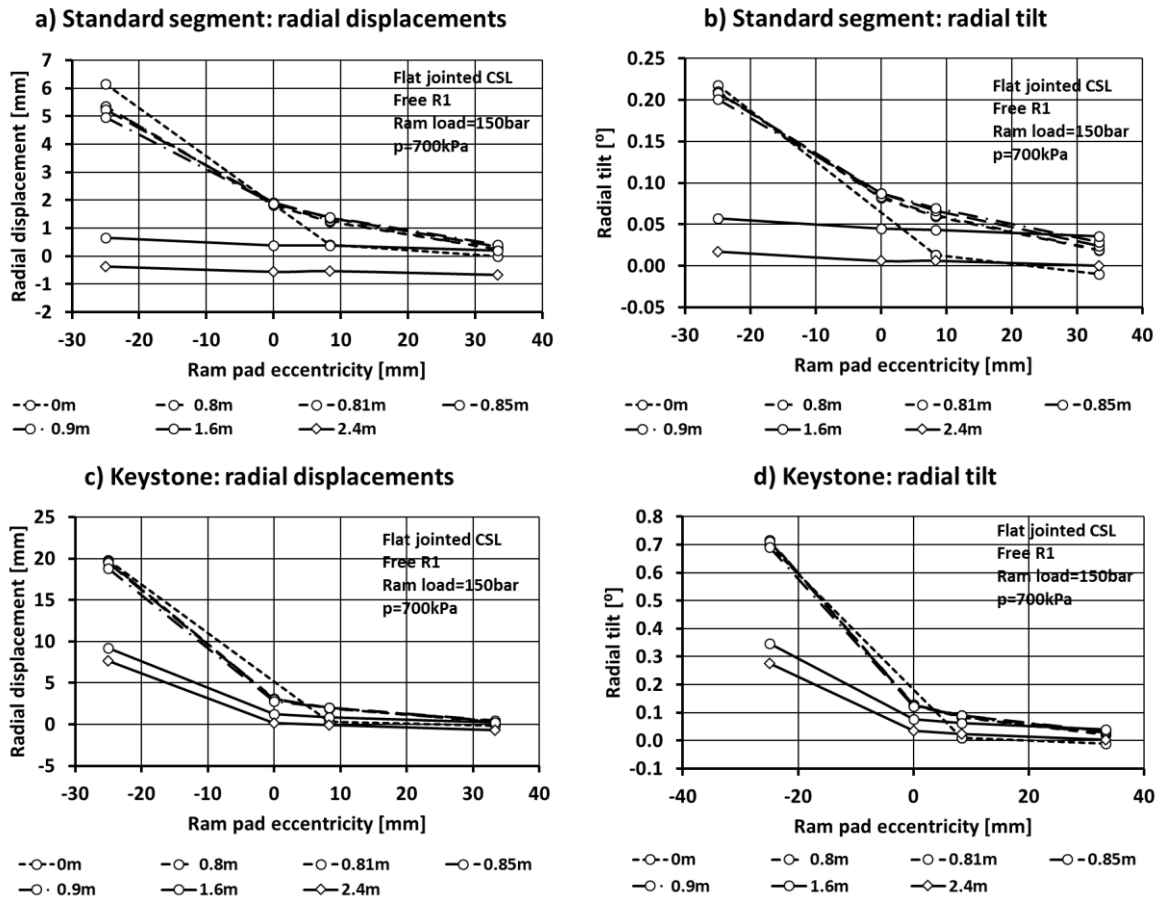


Figure 7.6: Effect of ram pad eccentricity on R1 response

### 7.5.4. Membrane behaviour of standard segments

The R1 standard segments can be regarded as curved deep beams subjected to both longitudinal and eccentric hoop compression. The contribution of shear deformations to deep beam deflections and the spread of concentrated loads necessarily imply that cross sections do not remain plane after deformation.

In free conditions, the distribution of hoop strain increments, i.e. from step 3 onwards, follows the strain field described by Cavalaro (2009) for segments subjected to in-plane angularities at the longitudinal joints, with the difference that here the distribution of contact stresses at the longitudinal joints is invariably triangular given the linear elasticity of the modelled concrete (see Figure 7.7.a).

The neutral axis of the longitudinal cross sections shifts along the segment width from side to centre: at lateral sections, there is a narrow compressive zone with triangular strain distribution while the rest of the cross section remains undeformed; at the centre, the cross sections show a linear distribution of hoop strain increments with a wider compressed region and a tensile zone with moderate peak values, e.g. about  $+50\mu\epsilon$  for 700kPa pressures.

In free conditions, the rotation of R1 segments changes the distribution of hoop strains along the segment length (see Figure 7.7.b). When a standard segment tilts outwards, the neutral axis at the circumferential joint shifts upwards which, given the curved geometry of the segment, entails the central packer bearing

## 7.5. Sequential loading under axisymmetric conditions

---

more longitudinal loading than the side supports. The simple strut and tie model (STM) in Figure 7.7.b evidences the tensile hoop stresses, or strains, that develop near the central ram pad as a result of the longitudinal load spread in a rotated segment. The same mechanism causes a compressive region near the central packer. The distribution of FE hoop strains, i.e. from step 2 onwards, in a segment subjected to -25mm eccentric ram pads agrees with the patterns described by the STM model.

In fixed conditions, the segment rotations are negligible and the longitudinal joints remain fundamentally closed within the modelling sequence. The entire segment is hoop compressed with a more uniform field of hoop strain increments.

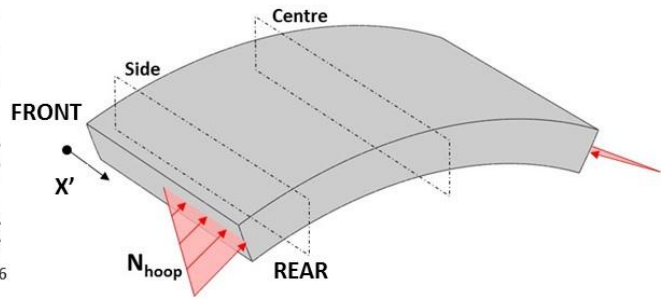
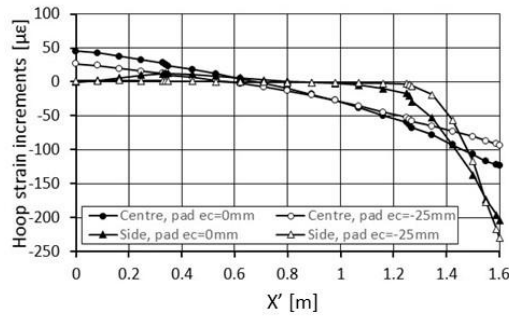
Figures 7.7.c and 7.7.d show the in-plane moment-hoop force (MN) paths at central and lateral cross sections derived from the hoop strain increments. The internal forces at  $X=1.6\text{m}$ , when the in-plane moments are highest, are directly proportional to the magnitude of radial pressures in both free and fixed conditions and define the herein called peak moment (PM) lines in the MN space. The evened distribution of hoop strains in fixed conditions results in peak in-plane moments lower than in free conditions, e.g. 630kNm/m against 800kNm/m for 700kPa radial pressures.

Figures 7.7.e and 7.7.f confirm that reasonable changes in ram pad eccentricity or joint geometry have a minor effect on the correlation of peak hoop forces, which remain within the umbrella delimited by the PM lines.

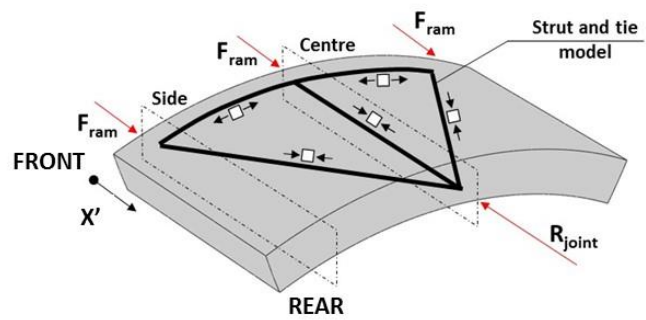
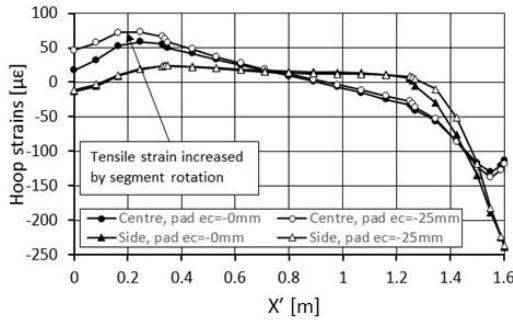


## 7.5. Sequential loading under axisymmetric conditions

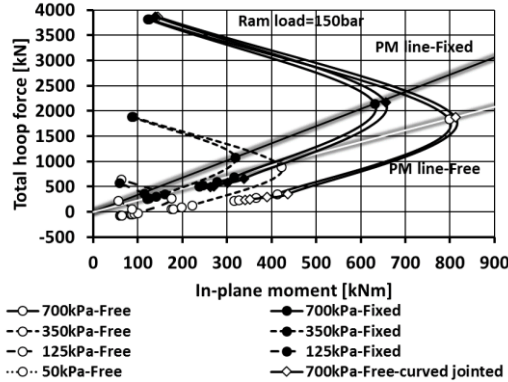
a) Hoop membrane strain increments in segments with eccentric hoop compression



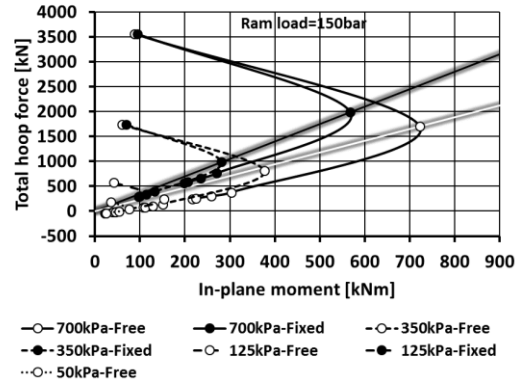
b) Influence of segment rotation on hoop membrane strains



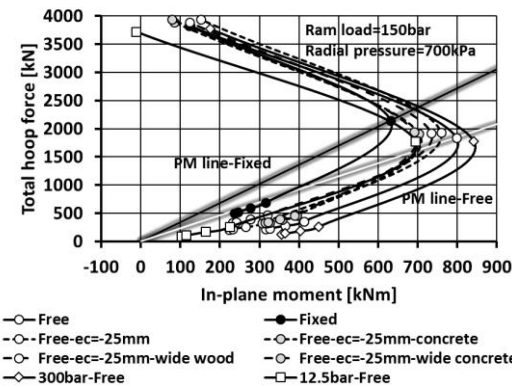
c) MN trajectories: Central section



d) MN trajectories: Lateral section



e) MN trajectories: Central section



f) MN trajectories: Lateral section

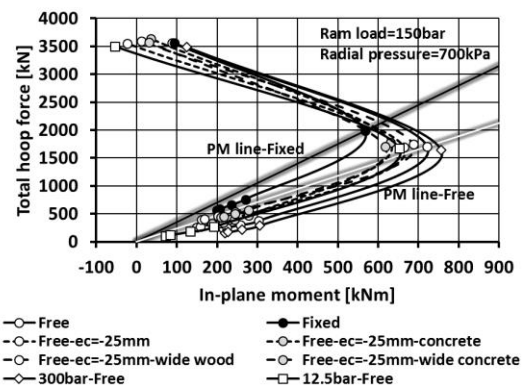


Figure 7.7: Membrane strains, MN trajectories and PM lines in standard segments

## 7.5. Sequential loading under axisymmetric conditions

### 7.5.5. Longitudinal bending of standard segments

The initial longitudinal moments at the segment centroid prior to any radial compression vary linearly with the magnitude of longitudinal loads and also ram pad eccentricity (see Figure 7.8.a). However, Figure 7.8.b evidences that the sequential compression of rings yields changes in longitudinal moments.

The effect of sequential loading on the longitudinal bending of standard segments can be explained with the beam analogy outlined in Figure 7.8.c. When  $X \approx 0.8\text{m}$  and most of the radial pressures are applied on R2, the coupling forces at the ring joint are significant and lead to positive moment increments. When  $X=1.6\text{m}$ , the migration of hoop compression between the two rings is virtually null and the coupling forces must be negligible. The increments in longitudinal moments drop to null or even negative values in the case of free conditions.

The mechanism underlying the changes in longitudinal moments caused by sequential loading suggests that these are independent of the magnitude of longitudinal loads. However, under low longitudinal compression, the poor ring interaction limits the development of coupling forces and subsequently longitudinal moment increments.

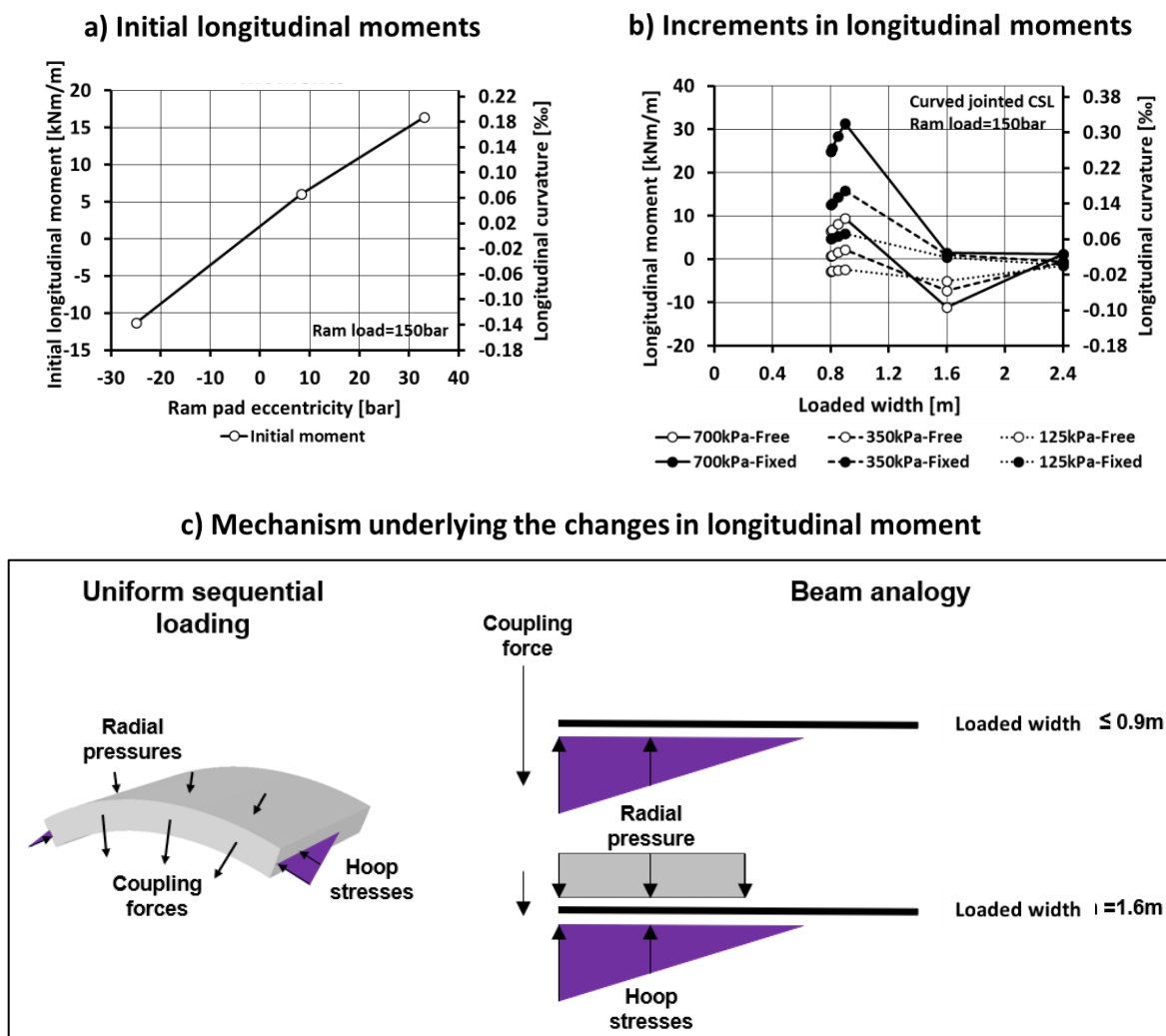


Figure 7.8: Longitudinal moments during uniform sequential loading

## **7.5. Sequential loading under axisymmetric conditions**

---

### **7.5.6. Potential damage during sequential loading**

It has become apparent in previous sections that, in a CSL structure where the concrete behaviour remains within the elastic region, the only ring imperfection produced by sequential loading under axisymmetric conditions is the residual rotation of the keystone, which increases the risk of contact deficiencies with neighbouring segments and rings. However, the development of numerical strains that exceed the compressive or tensile elastic limits within the loading sequence indicates that the real structure can undergo additional permanent deformations which in turn may lead to concrete damage.

Under axisymmetric loading conditions, the concrete damage is caused by load concentration at the rear corners of segments or ring joints. In the load cases examined, the hoop membrane tension at the R1 front does not reach the elastic limit of C55/67 plain concrete, i.e.  $+130\mu\epsilon$ . However, it may contribute to concrete damage when combined with other mechanisms such as spalling between ram pads.

#### **7.5.6.1. Damage at the rear corners of segments**

It was discussed in chapter 2 that the concentration of hoop forces at the corners of longitudinal joints due to angular imperfections increases the risk of local concrete damage: at moderate in-plane angularities, the load bearing capacity of joints at serviceable states is determined by the crack width limit of bursting cracks; at high angularities, the critical load is governed by the shear failure of the loaded corner, generally known as chipping of corners.

With the eccentric radial compression of rings characteristic of sequential loading, the transfer of hoop forces is concentrated at the rear corners of longitudinal joints. Such concentration may initiate concrete damage during the loading sequence of the TBM advance, or yield irreversible in-plane angularities that can raise the risk of damage after construction, particularly in deep tunnels subjected to high hoop compression or in CSLs subjected to high ovalisation loads.

The tendency of the longitudinal joints to concrete damage can be assessed by comparing the peak contact stresses experienced during the loading sequence with those exhibited under uniform ring compression, i.e.  $X=2.4\text{m}$ . The contact length by the end of the advance, at  $X=1.6\text{m}$ , can be also an indicator of propensity to in-plane angularities.

Figures 7.9.a and 7.9.b reflect that, at curved joints, the hoop forces are transferred over a narrow contact strip so that the contact stresses are higher than in flat joints, although the load is distributed over a longer contact length. The peak contact stresses in curved joints are virtually equal to those developed under uniform compression and are insensitive to the magnitude of longitudinal loads, ram pad eccentricity or ram pad-lining interface.

The peak contact stresses of flat joints are influenced by the radial rotation of segments and thus can reach values comparable to those of curved joints, e.g. 60MPa in flat joints at 700kPa, 150bar/ram and a -25mm ram pad eccentricity and 85MPa in curved joints. However, the peak stresses in flat joints are

## 7.5. Sequential loading under axisymmetric conditions

concentrated at the extrados of the segment corners, as opposed to the joint mid depth position exhibited at curved joints, which increases the susceptibility of flat joints to concrete damage during sequential loading, particularly under imperfect conditions such as ram pad eccentricity or assembly imperfections.

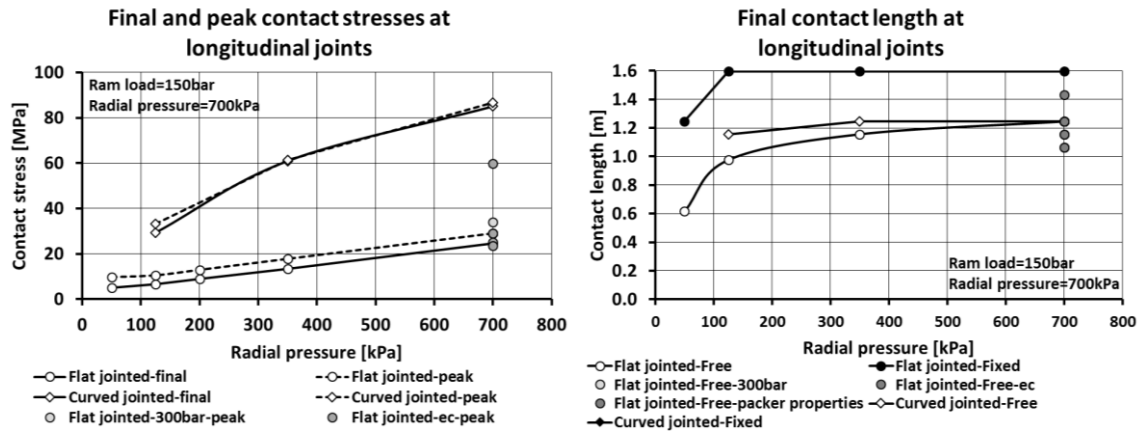


Figure 7.9: Contact quality during uniform sequential loading

### 7.5.6.2. Concrete spalling at ring joints

The discontinuous longitudinal compression of standard segments through ram pads causes the development of transverse tensile stresses, called spalling stresses, at the ram pad interspaces. In free conditions, the tensile strains between ram pads grow with the sequential loading due to the contribution of hoop membrane strains. The peak strains are experienced at  $X=1.6m$ .

Figure 7.10 illustrates the hoop tensile strains for  $X=1.6m$  when the longitudinal loads are (a) 150bar/ram , (b) 150bar/ram with a -25mm pad eccentricity and (c) 300bar/ram. It is evidenced that in the last two cases the tension at the intrados of the ram pad interspaces exceeds the elastic limit of  $+130\mu\epsilon$ .

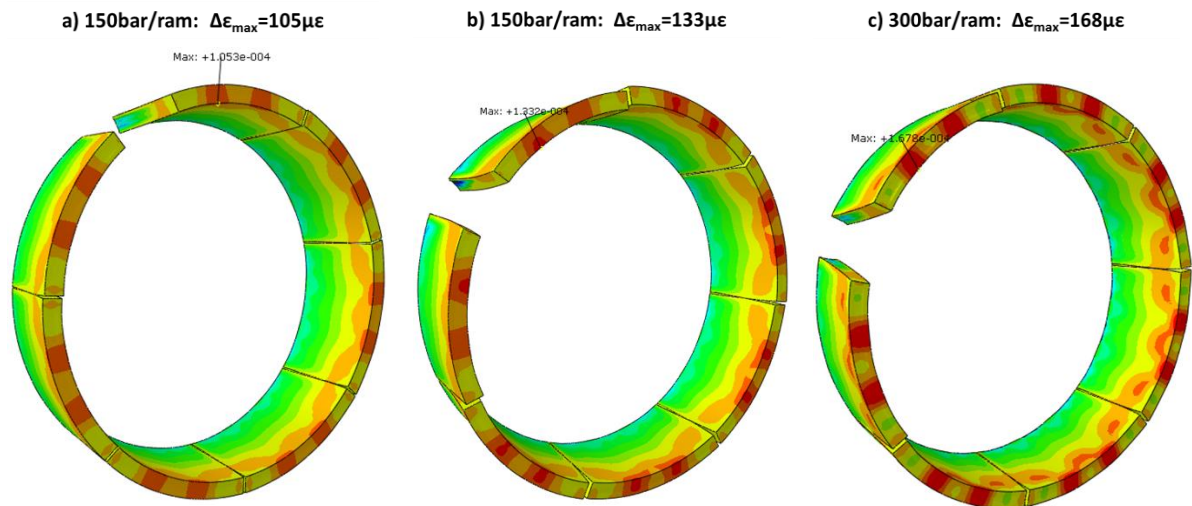


Figure 7.10: Concrete spalling during sequential loading

## 7.5. Sequential loading under axisymmetric conditions

### 7.5.7. Influence of ring joint design on segment damage

In a two-ring system under free conditions, the moment capacity of the segment circumferential joints delimits the magnitude of segment rotations during sequential loading. The moment-rotation relation depends on the packer material, size and distribution, i.e. number and spacing per segment, if the action of lock-in dowels is ignored.

Figures 7.11.a and 7.11.b show that peak rotations can be substantially reduced with the improvement of the lateral support. For example, when the packer depth is increased from 150mm to cover the entire joint depth of 170mm, the peak rotations of standard segments subjected to 700kPa sequential pressures and 150bar/ram applied with a -25mm ram pad eccentricity decrease from  $0.22^\circ$  to  $0.15^\circ$ . When the packer stiffness is 38GPa, equal to the concrete stiffness, the peak rotations are negligible.

However, the benefits of the enhanced lateral support are most notable for keystones: the deep packer can halve peak rotations, from  $0.070^\circ$  to  $0.035^\circ$  and drop residual rotations from  $0.040^\circ$  to  $0.030^\circ$ ; the peak rotations fall to  $0.010^\circ$  with the use of stiff packers while residual rotations become very small.

Given that the use of soft packers is desirable to correct contact deficiencies at ring joints (Cavalaro, 2009), a packer material that exhibits low initial stiffness and considerable stiffening under normal compression may optimise the lateral support of rings during construction. Otherwise, deep packers can still mitigate the extent of peak radial rotations and the residual tilt of keystones.

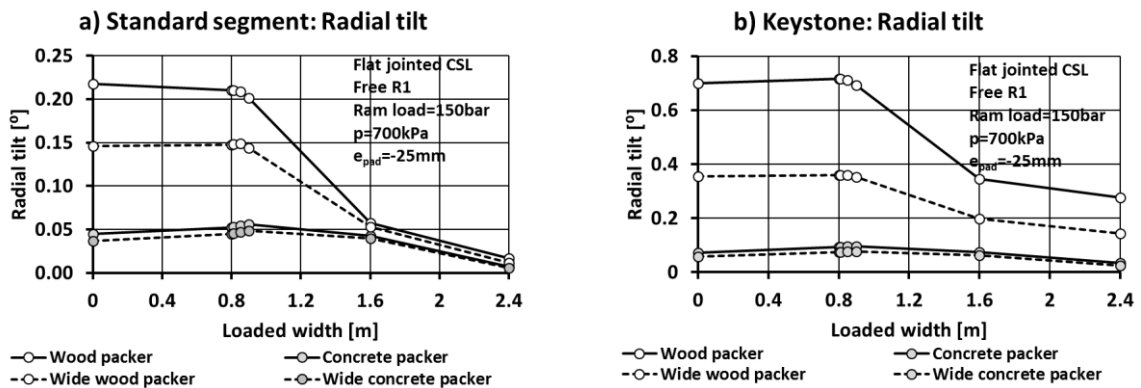


Figure 7.11: Influence of ring joint design on segment damage

## 7.6. The effect of ring selfweight on lining response

### 7.6. The effect of ring selfweight on lining response

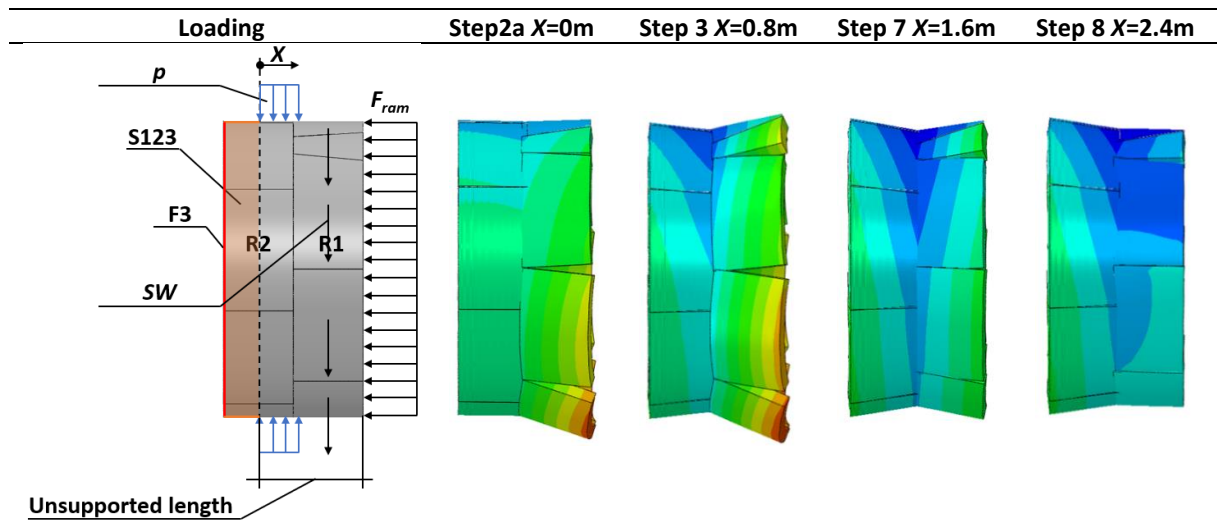
In a longitudinally compressed two-ring system under free conditions and subject only to the selfweight of R1, the R1 segments rotate downwards until segment equilibrium is reached through the vertical frictional forces developed at the packers and the moment reaction at the circumferential joint (see Table 7.4). At the crown, the segments rely partially on the support of the lower segments, which act as abutments of the top arch structure.

The arch behaviour of the top half ring results in smaller rotations at the crown, although the outward rotations induced by high longitudinal loads or negative ram pad eccentricities can counteract the beneficial arch effect. Conversely, positive ram eccentricities ensure the cooperative response of the upper segments and limited rotations.

The magnitude of maximum rotations at the invert segments depends on the moment capacity of the circumferential joint enabled by the ram loads and it is comprised between  $0.10^\circ$  and  $0.15^\circ$ . Overall, the peak invert rotations tend to exceed those at the crown by about  $0.10^\circ$ . The difference is corrected by the completion of sequential loading. Given the greater tendency of keystones to radial rotations, it may be beneficial to give preference during ring assembly to ring orientations where the keystones are placed at upper positions so that their own weight can mitigate outward rotations.

The effect of the R1 selfweight on the total load share between rings and the MN trajectories during sequential loading is minor. The peak contact stresses at the longitudinal flat joints of invert segments grow by 10MPa.

Table 7.4: Effect of selfweight on lining response





### 7.7. Validation of two-ring models

The validity of two-ring models as reliable engineering tools to examine CSL behaviour under axisymmetric conditions was confirmed through their comparison with ten-ring models (see Figure 7.12.a). Given that, under axisymmetric conditions, the tunnel unsupported length,  $L_u$ , is not a relevant parameter for lining response (see Figure 7.12.b), the validation is based on the comparison of R1 segment rotations in two-ring models and ten-ring models with  $L_u=1.5$  rings (see Figures 7.12.c and 7.12.d).

Figure 7.12.c evidences that there is an excellent agreement in the rotation of R1 standard segments of two-ring and ten-ring models through the whole loading sequence with discrepancies smaller than  $0.020^\circ$ . Figure 7.12.d show that the two-ring model also replicates with great accuracy the peak and residual rotations of keystones.

Overall, it can be inferred that the two-ring model is a valid tool for the analysis of CSLs under axisymmetric sequential loading.

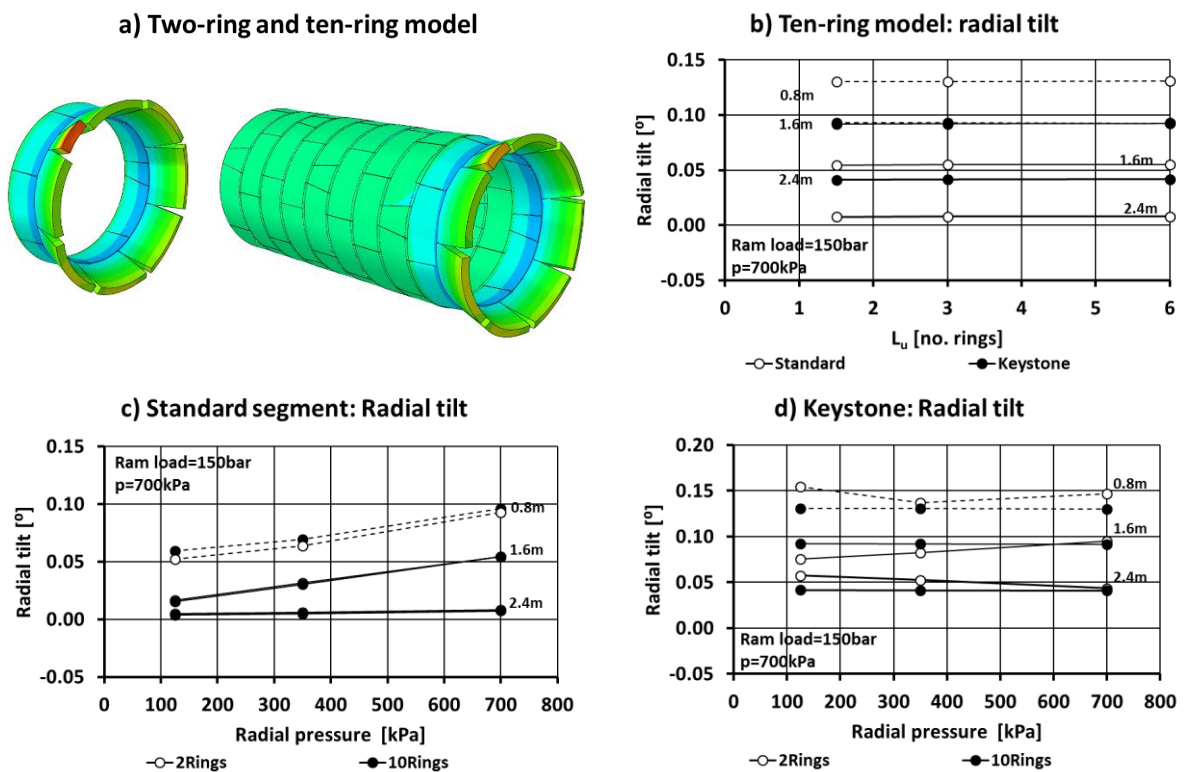


Figure 7.12: Validation of two-ring models

## 7.8. Sequential loading with vertical pressure gradients

### 7.8. Sequential loading with vertical pressure gradients

#### 7.8.1. Lining response with uniform ram pad-lining interface

##### 7.8.1.1. Free condition

In free conditions, the net uplift force of radial pressures applied with a vertical pressure gradient induces a cantilever-type response of the lining that activates the passive reaction of the ground within the supported tunnel length,  $L_s$  (see Table 7.5). The longitudinal moment grows within  $L_u$  and reaches a peak at the interface between  $L_u$  and  $L_s$ ; the maximum shear forces extend over most of  $L_u$ . Given that the CSL longitudinal pre-stressing during an advance prevents the shearing of the ring joints, the longitudinal deflection must be fundamentally caused by the longitudinal curvatures.

Longitudinal bending stresses in curved thin-wall cylinder shells can produce the squatting of the cross sections if the longitudinal curvatures are sufficiently high. In recent analytical models describing the flattening of tunnels induced by longitudinal differential settlements, the ovalisation loads in a cross-section induced by longitudinal bending were attributed a sinusoidal distribution with amplitude proportional to the longitudinal moment and curvature and inversely proportional to the ring moment of inertia (Huang et al., 2012; Gong et al., 2015).

According to the above, when  $L_u$  is short, the ring squatting caused by the longitudinal bending of the tunnel is of minor importance. Thus, the primary ovalisation loads resulting from the uplift pressures and ground subgrade reaction have a predominant role. The ring distortion is more pronounced near R1. When  $L_u$  is long, the secondary ovalisation loads are of greater magnitude by the end of  $L_u$ . The rings near the TBM hardly squat while the rings at the boundary with the supported length converge under both primary and secondary ovalisation loads.

Figures 7.13.a and 7.13.b show that there is nearly a linear correlation of R1 ring convergence with the vertical pressure gradient and the  $L_u$  so that when  $L_u=6\text{ring}$ , R1 is practically undeformed. Figure 7.13.c evidences that flat jointed CSLs undergo about half the convergence of curved jointed CSLs.

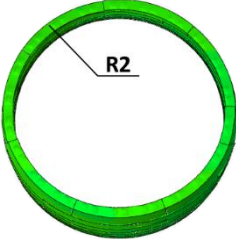
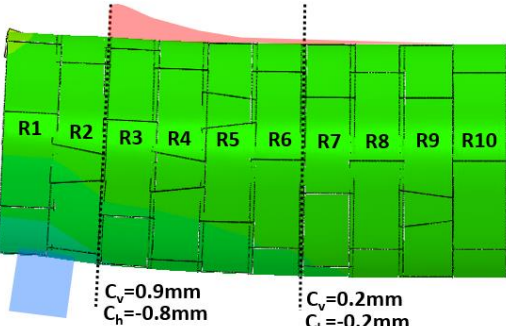
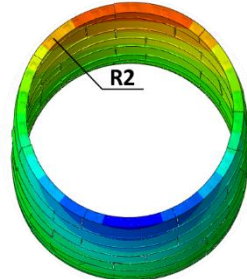
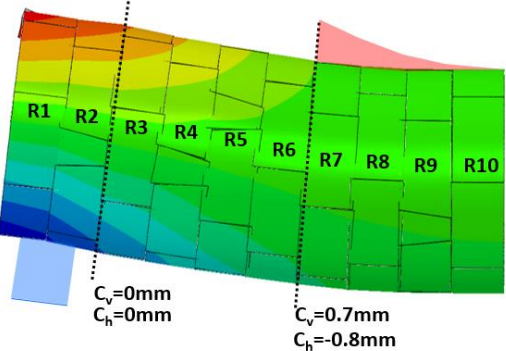
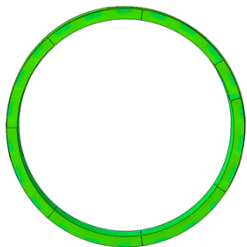
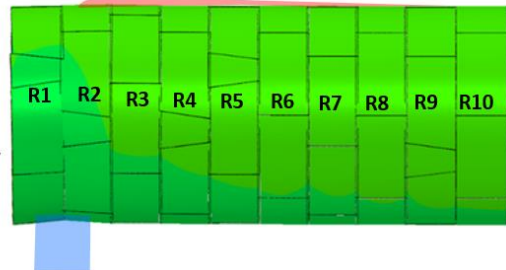
##### 7.8.1.2. Fixed condition

With fixed conditions, the longitudinal bending of the tunnel induced by the vertical gradients in lining pressure increments is almost entirely prevented and, like in the case of uniform compression, a great proportion of the ovalisation loads is sustained by the TBM (see Table 7.5). The TBM downward action is realised through tangential stresses at the circumferential face of the lining in contact with the ram pads, with a distribution along the ring circumference similar to that proposed by Gong et al. (2015). Consequently, radial displacements and ring squatting are small, with peak vertical convergence at the first circumferential joint in the order of 1.5mm, i.e. 0.02% of the ring mean diameter  $D$ .

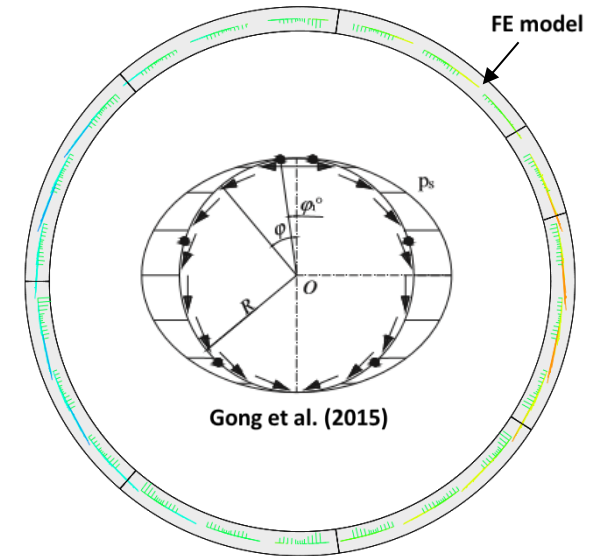


## 7.8. Sequential loading with vertical pressure gradients

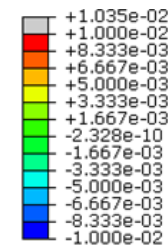
Table 7.5: Sequential loading with vertical pressure gradients and uniform ram pad-lining interface

Boundary conditions	Front view	Profile
Free Lu=1.5ring		
Free Lu=6ring		
Fixed Lu=1.5ring		

TBM downward action  
under fixed conditions



Radial displacements  
[m]



Upward vertical  
pressure gradient

Downward vertical  
pressure gradient

Net TBM downward  
action

## 7.8. Sequential loading with vertical pressure gradients

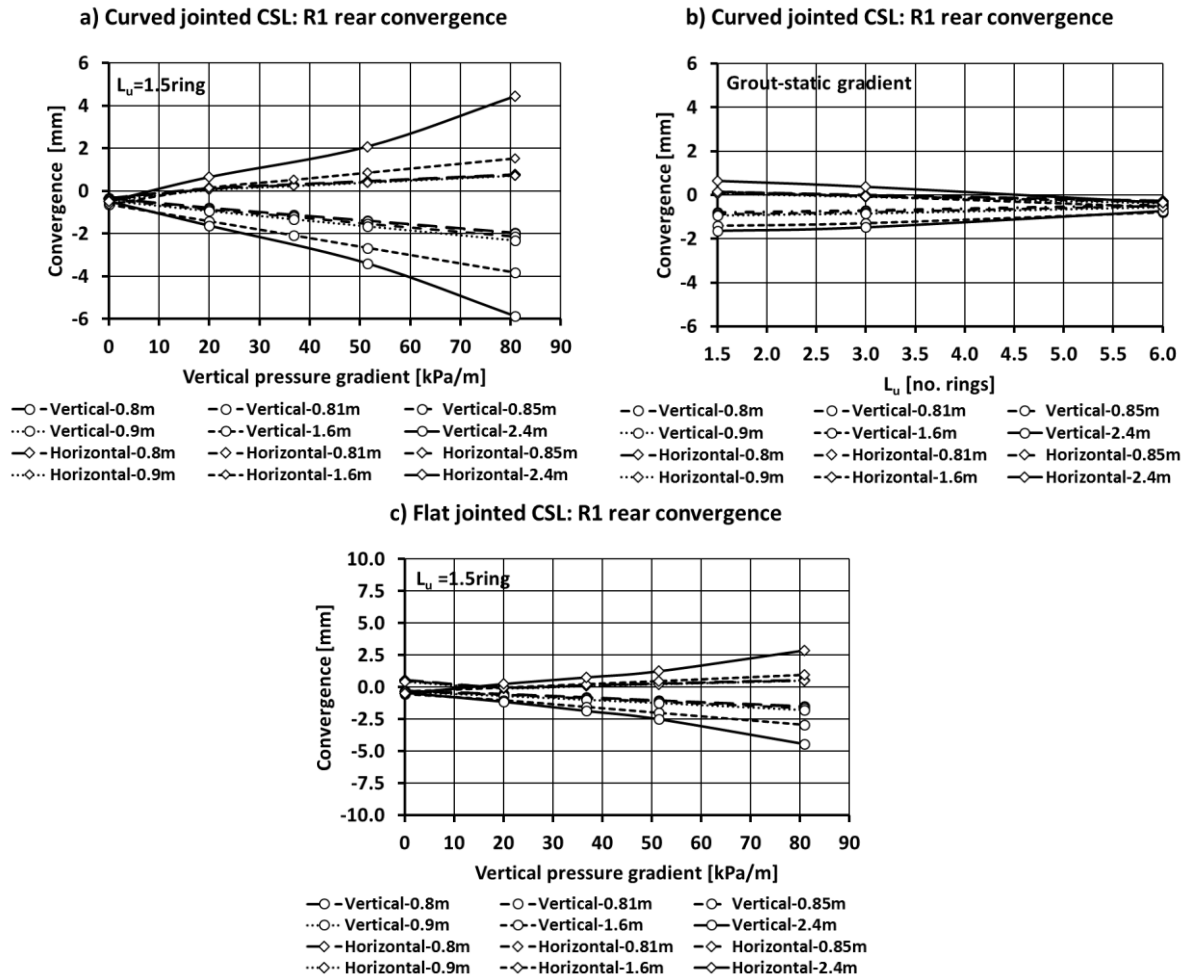


Figure 7.13: Convergence induced by vertical gradients in free TBM conditions

### 7.8.2. Lining response with uneven ram pad-lining interface

When the tunnel is subjected to an uneven fixity at the ram pad-lining interface, the upward movement of the lining is inhibited through transverse reaction forces delivered only along the circumference of the fixed segments, transverse forces whose distribution is no longer sinusoidal. The length and orientation of the fixed boundary determines the deformation mode of the rings within  $L_u$ .

It is reminded that the vertical tilt of segments is positive when the segment front is at a higher position than the back.

#### 7.8.2.1. Hoop ring behaviour with fixity at the invert

In the  $3UAB$  model, when the upward deflection of the tunnel is constrained by the ram pads at the invert, the rings tend to squeeze with an elliptical shape where the knees displace further up than the invert centre (see Figure 7.14.a). Consequently, the TBM downward reaction forces that prevent the movement of the fixed perimeter are concentrated at the knees; upward forces are required to keep the original ring shape at the front of the R1 invert (see Figure 7.14.b). The magnitude of the reaction forces is the greatest by end of the advance,  $X=1.6m$ , with the full application of the uplift loading.

## 7.8. Sequential loading with vertical pressure gradients

The tangential component of the downward reaction at the knees causes a local increase in hoop tensile strains of about  $+50\mu\epsilon$  at the ring front (see Figure 7.15.a) and a sharp drop in hoop compression to negligible values at the ring centreline (see Figure 7.15.b). Such rise in hoop tension is consistent with the short contact length of the knee joint instigated by the abrupt change in segment rotations between restrained and free segments (see Figure 7.15.d). Indeed, the peaks in hoop compression experienced at the rear of the ring knees indicate that the transfer of hoop force between segments is concentrated at this region (see Figure 7.15.c).

The radial component of the reaction forces induces positive and negative hoop curvatures at the knees and invert of the ring front,  $+0.50\%$  and  $-0.25\%$  respectively (see Figure 7.15.e). Further away from the transverse constraints, the hoop curvatures of the bottom ring respond to the typical diagrams of a squeezed tunnel with smoother profiles: positive curvatures at the invert and negative at the springline (see Figures 7.15.f and 7.15.g). The magnitude of the curvatures increases with distance from the ring front so that the peaks of  $\pm 0.50\%$  are reached at the ring rear. The influence of the reaction forces on the top part of the ring is negligible, which is reflected by both the ring shape and hoop curvatures.

The hoop curvature profiles of R2 agree with the general vertical elongation, with the difference given by the staggered position of the joints (see Figure 7.16). The effects of the ram pad restraints decay rapidly within the tunnel supported length in such a way that become negligible at the rear of R2.

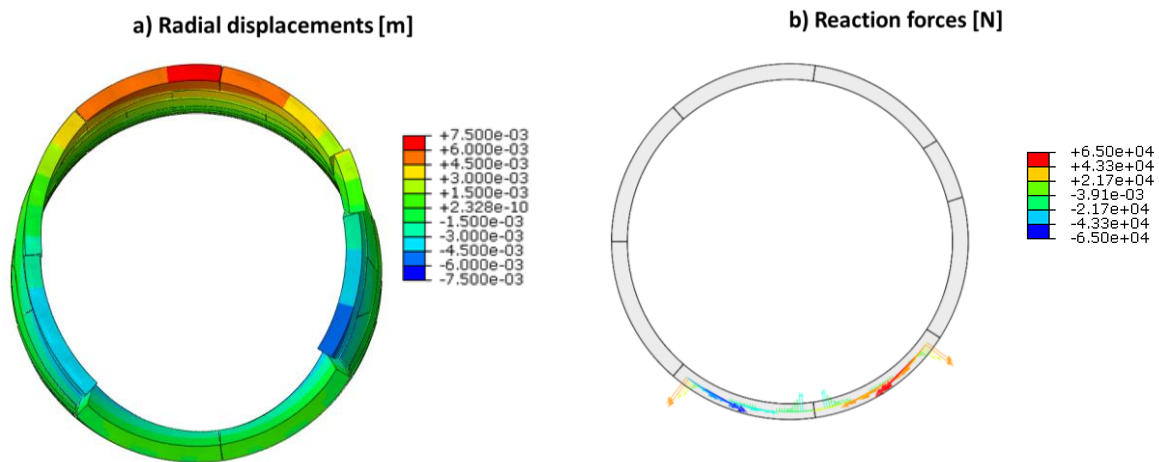
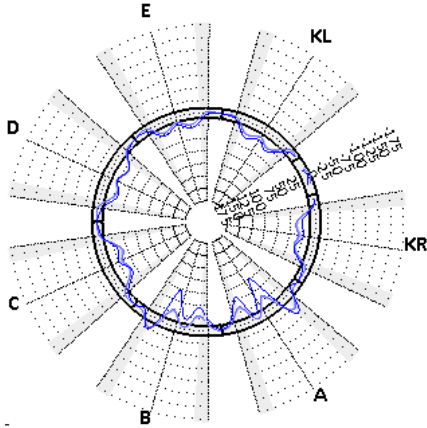


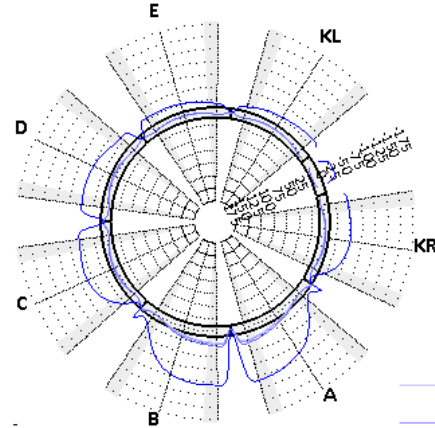
Figure 7.14: 3UAB model: R1 deformed shape and ram pad reaction forces

## 7.8. Sequential loading with vertical pressure gradients

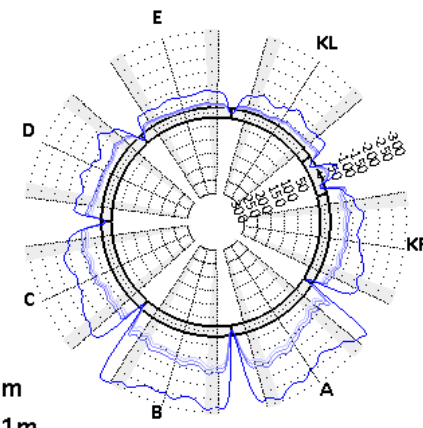
a) 3UAB Hoop Mean Strains TBM SIDE [ $\mu\epsilon$ ] - Ring 1



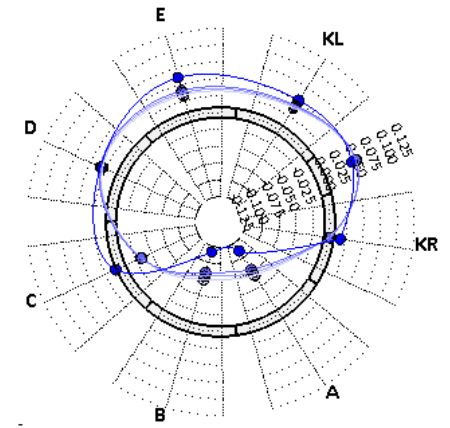
b) 3UAB Hoop Mean Strains CENTRE [ $\mu\epsilon$ ] - Ring 1



c) 3UAB Hoop Mean Strains LINING SIDE [ $\mu\epsilon$ ] - Ring 1

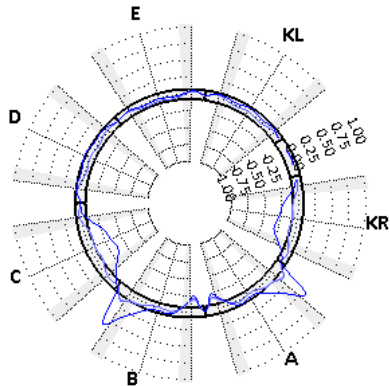


d) 3UAB Vertical Tilt [ $^{\circ}$ ] - Ring 1

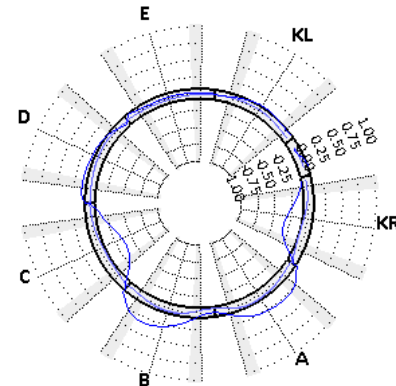


—  $X=0.8m$   
—  $X=0.81m$   
—  $X=0.85m$   
—  $X=0.9m$   
—  $X=1.6m$

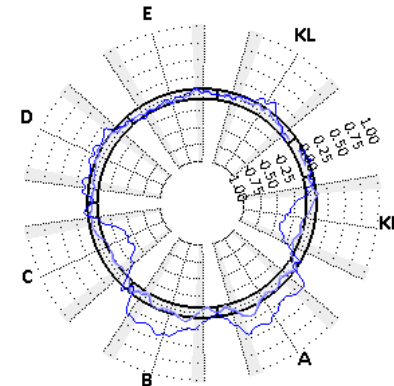
e) 3UAB Hoop Curvatures TBM SIDE [ $^{\circ}/\infty$ ] - Ring 1



f) 3UAB Hoop Curvatures CENTRE [ $^{\circ}/\infty$ ] - Ring 1



g) 3UAB Hoop Curvatures LINING SIDE [ $^{\circ}/\infty$ ] - Ring 1



h) 3UAB Longitudinal Curvatures CENTRE [ $^{\circ}/\infty$ ] - Ring 1

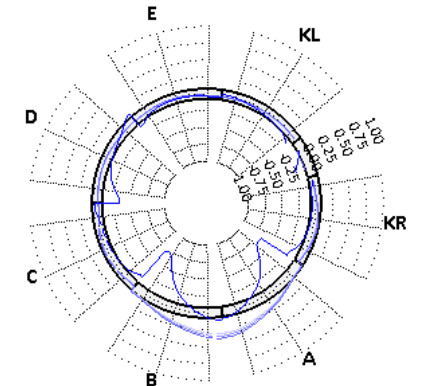
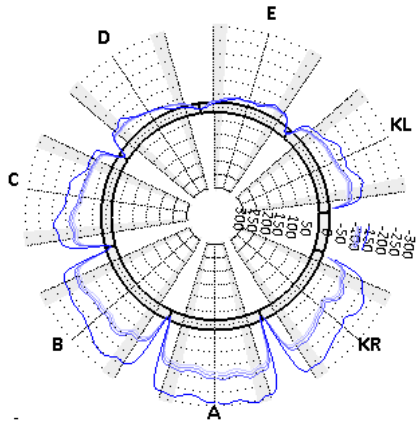


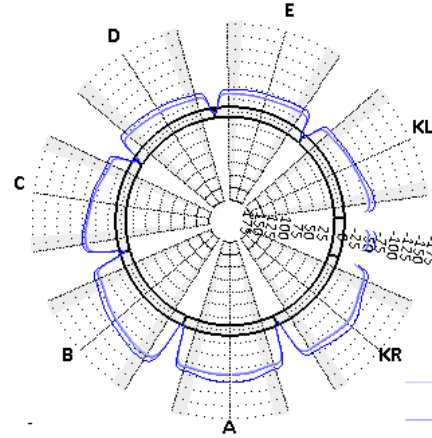
Figure 7.15: FEA results-3UAB-R1

## 7.8. Sequential loading with vertical pressure gradients

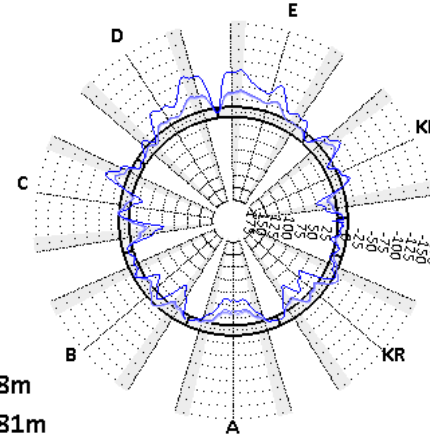
a) 3UAB Hoop Mean Strains TBM SIDE [ $\mu\epsilon$ ] - Ring 2



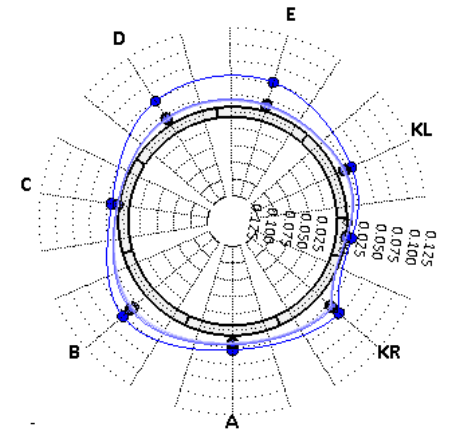
b) 3UAB Hoop Mean Strains CENTRE [ $\mu\epsilon$ ] - Ring 2



c) 3UAB Hoop Mean Strains LINING SIDE [ $\mu\epsilon$ ] - Ring 2

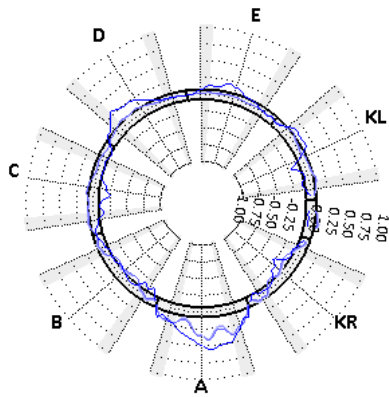


d) 3UAB Vertical Tilt [ $^\circ$ ] - Ring 2

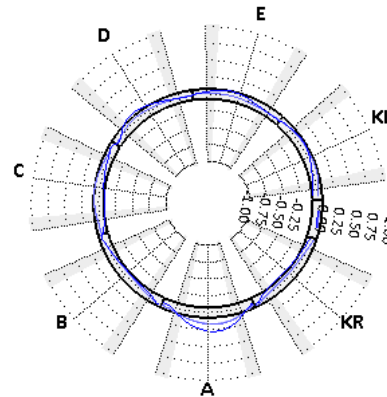


—  $X=0.8m$   
—  $X=0.81m$   
—  $X=0.85m$   
—  $X=0.9m$   
—  $X=1.6m$

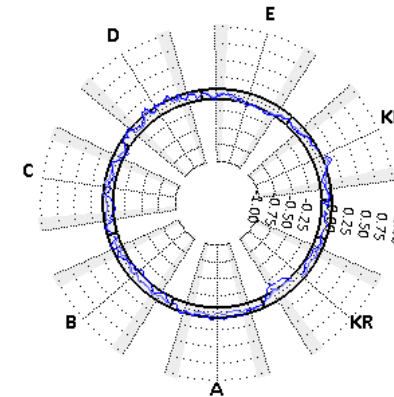
e) 3UAB Hoop Curvatures TBM SIDE [ $^\circ/100$ ] - Ring 2



f) 3UAB Hoop Curvatures CENTRE [ $^\circ/100$ ] - Ring 2



g) 3UAB Hoop Curvatures LINING SIDE [ $^\circ/100$ ] - Ring 2



h) 3UAB Longitudinal Curvatures CENTRE [ $^\circ/100$ ] - Ring 2

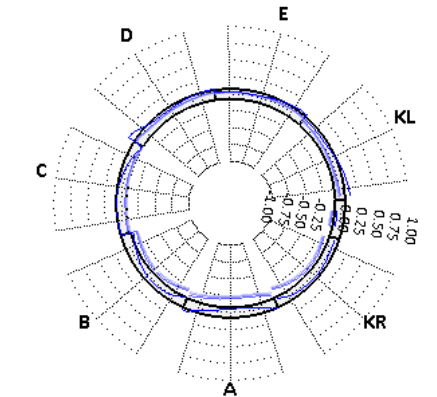


Figure 7.16: FEA results-3UAB-R2

## 7.8. Sequential loading with vertical pressure gradients

### 7.8.2.2. Hoop ring behaviour with fixity at the crown

When the crown segments are fixed, such as in the *3UEKL* model, the net uplift forces push the unrestrained segments upwards leading to a pronounced squatted shape near the ram pads that declines with distance (see Figure 7.17.a). The vertical and horizontal convergence at R1 are -16mm and +8mm respectively, i.e. -0.5%D and 0.25%D. The keystone is situated at the limit of the fixed perimeter. It must accommodate the change in deformation mode through significant rotation and lipping of its longitudinal joints and the local slipping of the ring joint.

Like in the *3UAB* model, the downward reaction forces are concentrated at the R1 shoulders (see Figure 7.17.b). This time, the orientation of the tangential component opposes the opening of longitudinal joints typical of sequential loading; thus, the hoop compression at the crown is more evenly distributed along the ring width (see Figures 7.18.a to 7.18.c). This is consistent with the downward tilt of the crown segments that promotes a more arch-like behaviour (see Figure 7.18.d). The peaks of hoop tension up to  $+75\mu\epsilon$  at the front of the springline segments are again associated with pronounced radial rotations.

The distribution of hoop curvatures in R1 are governed by the radial ram pad forces at the fixed perimeter (see Figures 7.18.e to 7.18.g). The peak values of -1.00‰ decay rapidly with distance, and the overall ovalisation of R1 and R2 free circumferences leads to maximum curvatures of +0.75‰ at the springline of R2 (see Figure 7.19).

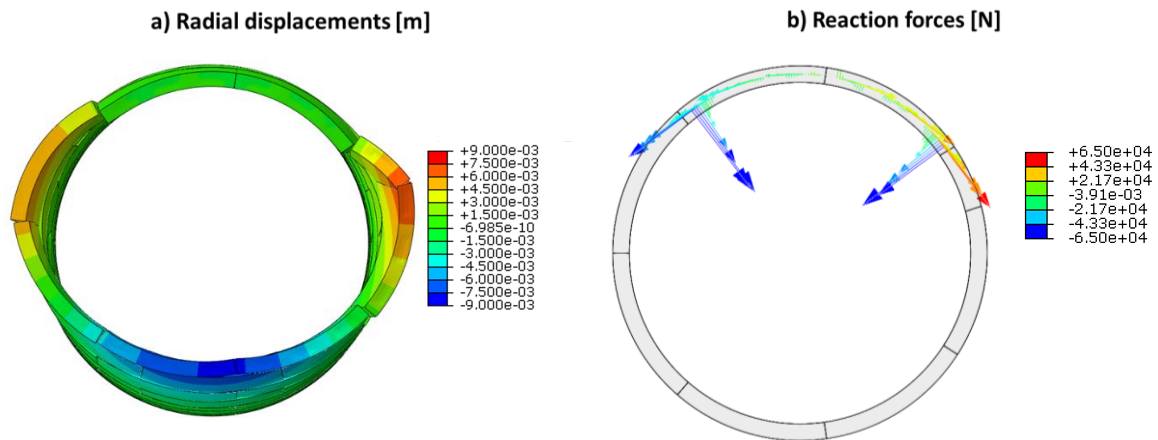
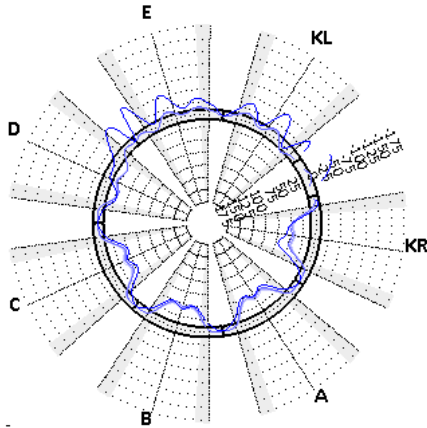


Figure 7.17: *3UEKL* model: R1 deformed shape and ram pad reaction forces

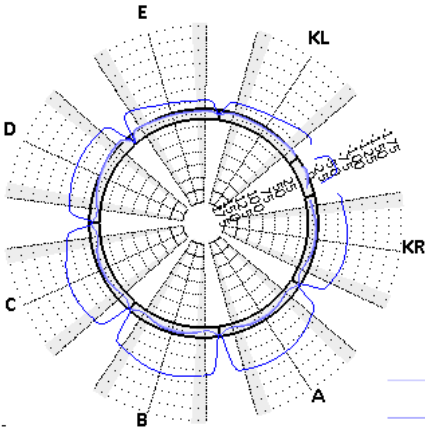


## 7.8. Sequential loading with vertical pressure gradients

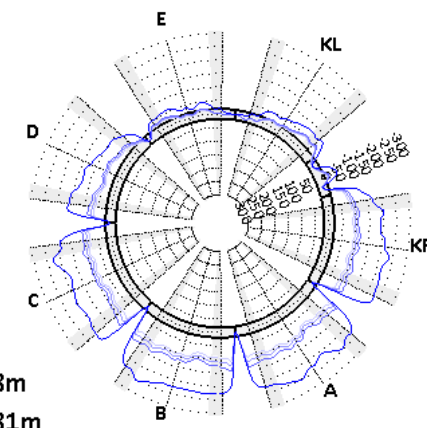
a) 3UEKL Hoop Mean Strains TBM SIDE [ $\mu\epsilon$ ] - Ring 1



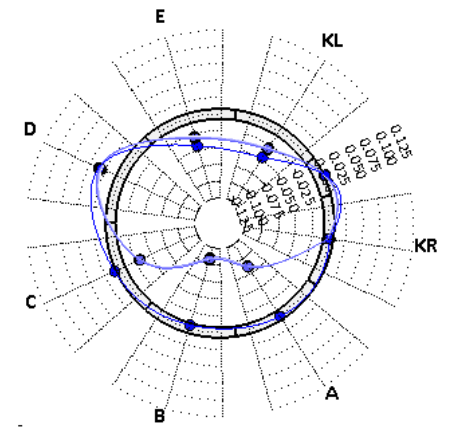
b) 3UEKL Hoop Mean Strains CENTRE [ $\mu\epsilon$ ] - Ring 1



c) 3UEKL Hoop Mean Strains LINING SIDE [ $\mu\epsilon$ ] - Ring 1

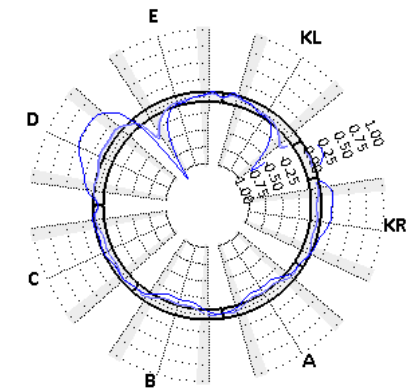


d) 3UEKL Vertical Tilt [ $^\circ$ ] - Ring 1

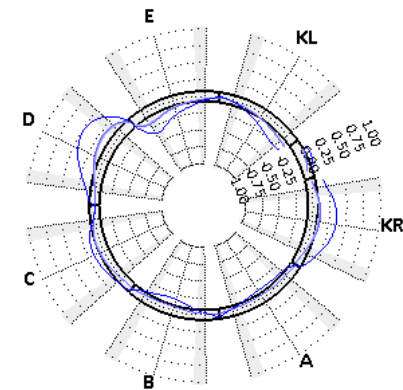


—  $X=0.8m$   
—  $X=0.81m$   
—  $X=0.85m$   
—  $X=0.9m$   
—  $X=1.6m$

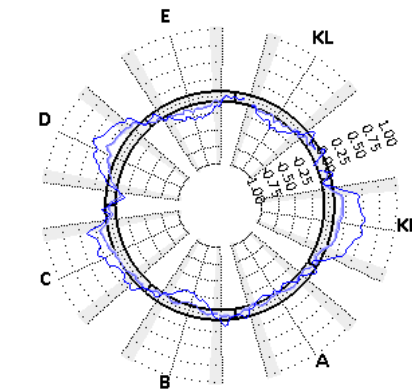
e) 3UEKL Hoop Curvatures TBM SIDE [ $^\circ/\infty$ ] - Ring 1



f) 3UEKL Hoop Curvatures CENTRE [ $^\circ/\infty$ ] - Ring 1



g) 3UEKL Hoop Curvatures LINING SIDE [ $^\circ/\infty$ ] - Ring 1



h) 3UEKL Longitudinal Curvatures CENTRE [ $^\circ/\infty$ ] - Ring 1

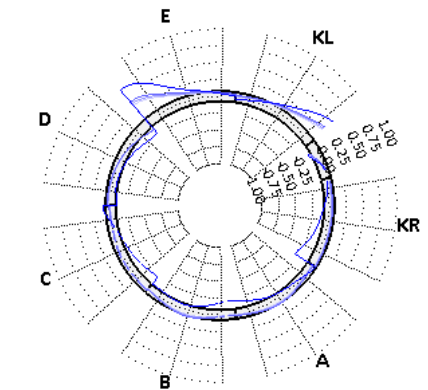
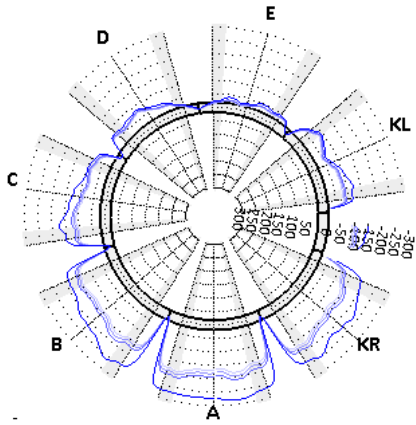


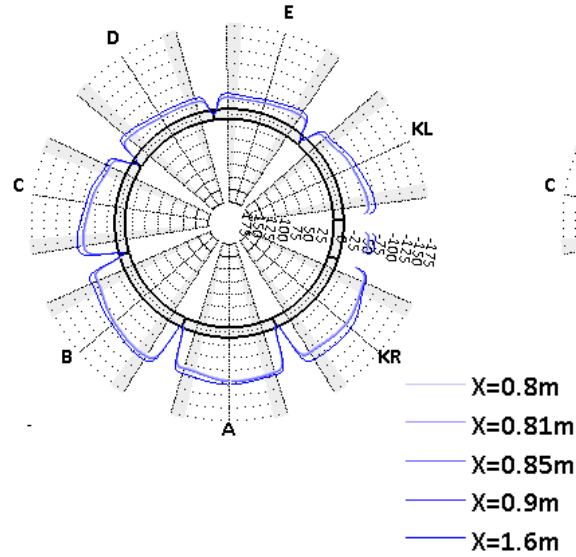
Figure 7.18: FEA results-3UEKL-R1

## 7.8. Sequential loading with vertical pressure gradients

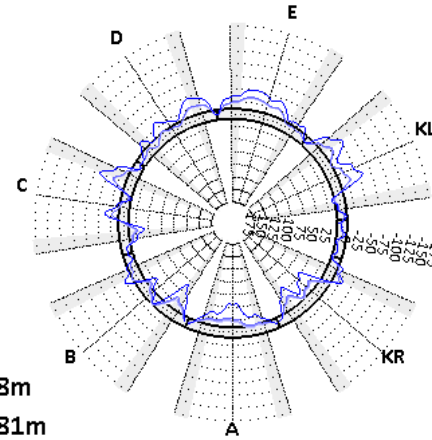
a) 3UEKL Hoop Mean Strains TBM SIDE [ $\mu\epsilon$ ] - Ring 2



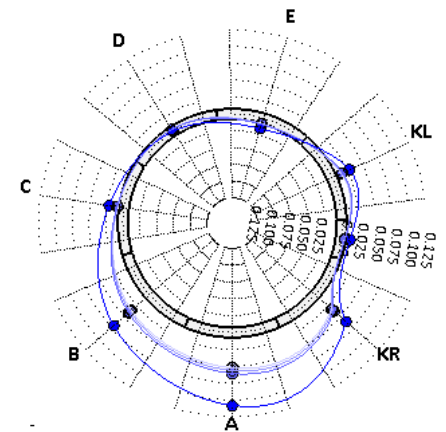
b) 3UEKL Hoop Mean Strains CENTRE [ $\mu\epsilon$ ] - Ring 2



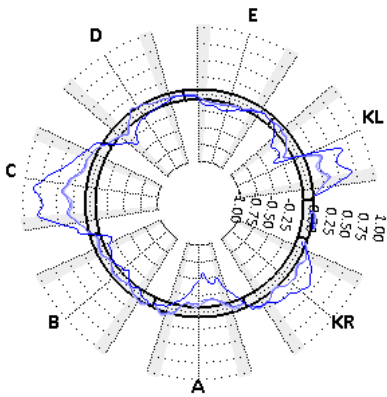
c) 3UEKL Hoop Mean Strains LINING SIDE [ $\mu\epsilon$ ] - Ring 2



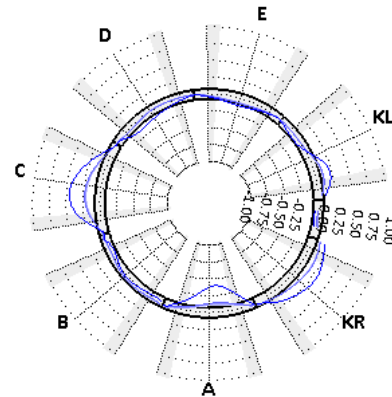
d) 3UEKL Vertical Tilt [ $^\circ$ ] - Ring 2



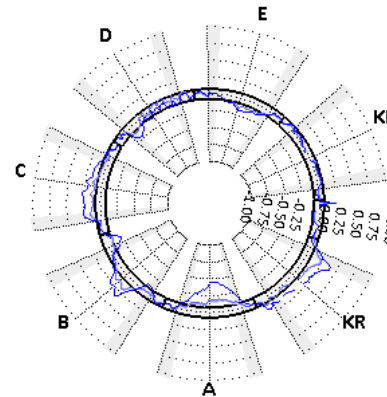
e) 3UEKL Hoop Curvatures TBM SIDE [ $^\circ/\infty$ ] - Ring 2



f) 3UEKL Hoop Curvatures CENTRE [ $^\circ/\infty$ ] - Ring 2



g) 3UEKL Hoop Curvatures LINING SIDE [ $^\circ/\infty$ ] - Ring 2



h) 3UEKL Longitudinal Curvatures CENTRE [ $^\circ/\infty$ ] - Ring 2

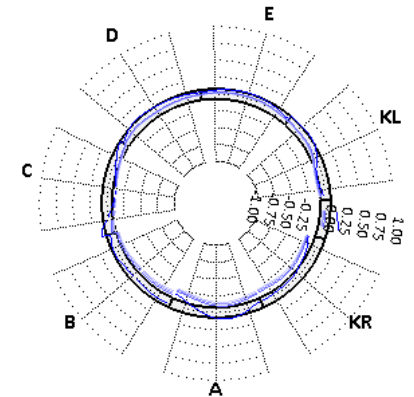


Figure 7.19: FEA results-3UEKL-R2



## 7.8. Sequential loading with vertical pressure gradients

### 7.8.2.3. Hoop ring behaviour with lateral fixity

When the R1 ring is subjected to lateral fixity, the free perimeter tends to move upwards under the action of the uplift forces, which results in a skewed oval shape of the unsupported rings (see Figure 7.20.a). The peak radial displacements are about  $\pm 5\text{mm}$  regardless of the orientation or length of the fixed perimeter.

In all models with lateral fixity, the downward action of the ram pads is mainly transferred through the R1 springline segment KR (see Figure 7.20.b), except for the *3UKRAB* model where the invert constraints play an important role in preventing upward movements. Consequently, the invert segment A becomes the most compressed segment in detriment of its adjacent segments, particularly the top part of KR (see Figures 7.21.a to 7.21.c).

The asymmetry in ring distortion caused by the upward movement of the free invert segments is coupled with the development of alternate hoop curvatures at the invert, positive in segment A and negative in B (see Figures 7.21.e to 7.21.f and 7.22.e to 7.22.f). At the front of R1, the difference in upward displacements between ring sides is bridged via hoop deformations and the lipping of longitudinal joints. However, the contribution of joint lipping declines with distance from the ram pads; thus, the curvatures reach peak values at the R1 rear and R2 front,  $+0.75\text{‰}$  and  $-0.25\text{‰}$ . In the rest of the ring circumference, the hoop curvatures are minor, with greatest values at the crown near the ring joint caused again by ring ovalisation.

The FE results of the *3UKR* model are also included to illustrate the similarities in ring behaviour of models with lateral fixity (see Figures 7.23 and 7.24).

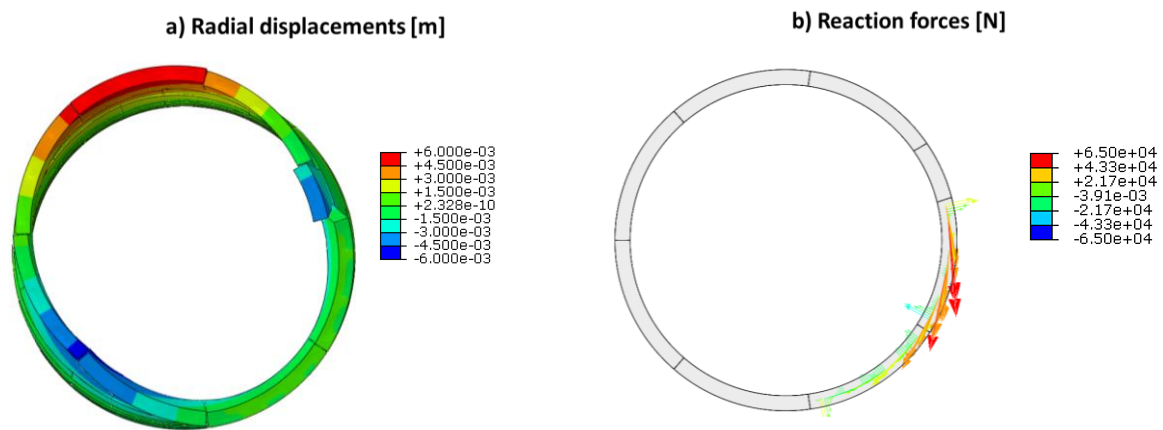
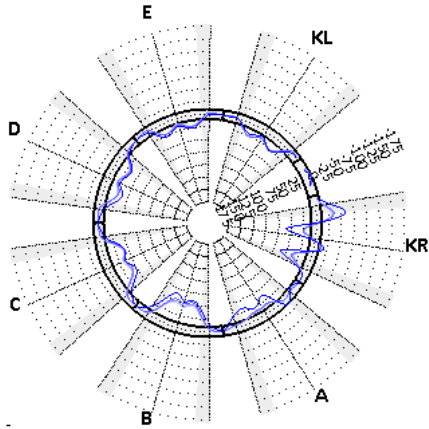


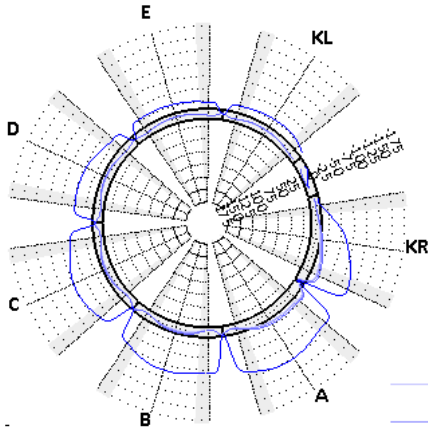
Figure 7.20: *3UKRA* model: R1 deformed shape and ram pad reaction forces

## 7.8. Sequential loading with vertical pressure gradients

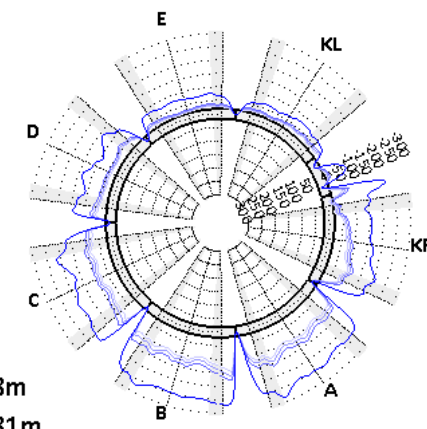
a) 3UKRA Hoop Mean Strains TBM SIDE [ $\mu\epsilon$ ] - Ring 1



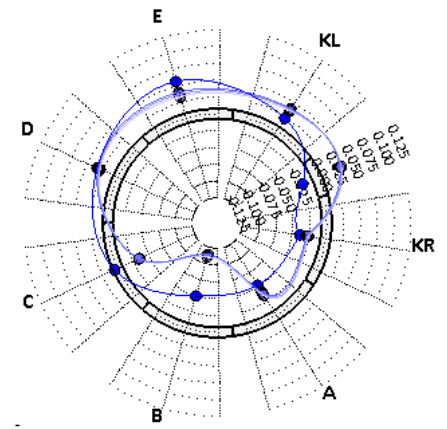
b) 3UKRA Hoop Mean Strains CENTRE [ $\mu\epsilon$ ] - Ring 1



c) 3UKRA Hoop Mean Strains LINING SIDE [ $\mu\epsilon$ ] - Ring 1

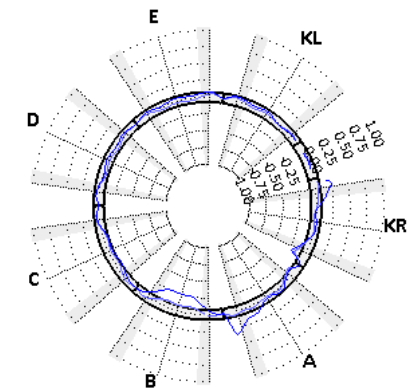


d) 3UKRA Vertical Tilt [ $^{\circ}$ ] - Ring 1

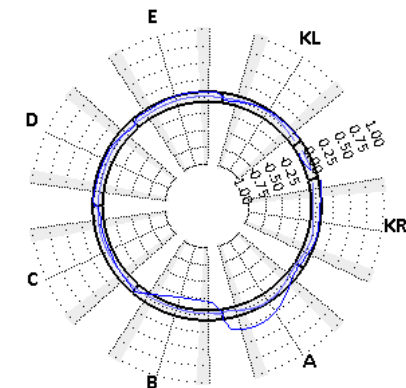


—  $X=0.8m$   
—  $X=0.81m$   
—  $X=0.85m$   
—  $X=0.9m$   
—  $X=1.6m$

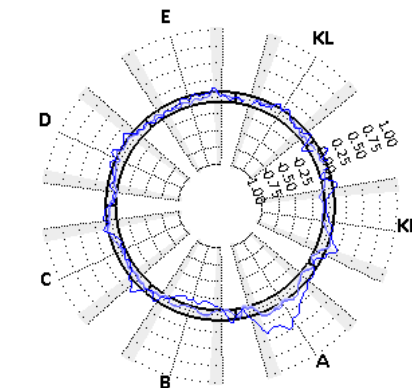
e) 3UKRA Hoop Curvatures TBM SIDE [ $^{\circ}/\infty$ ] - Ring 1



f) 3UKRA Hoop Curvatures CENTRE [ $^{\circ}/\infty$ ] - Ring 1



g) 3UKRA Hoop Curvatures LINING SIDE [ $^{\circ}/\infty$ ] - Ring 1



h) 3UKRA Longitudinal Curvatures CENTRE [ $^{\circ}/\infty$ ] - Ring 1

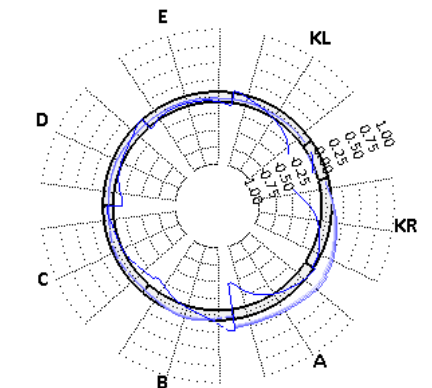
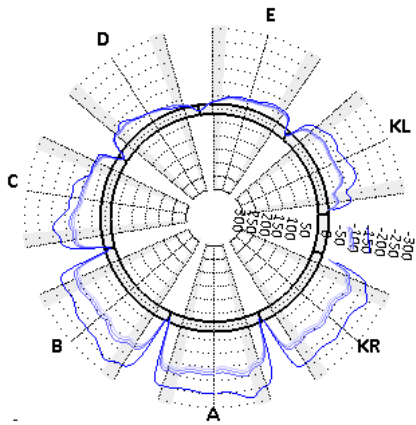


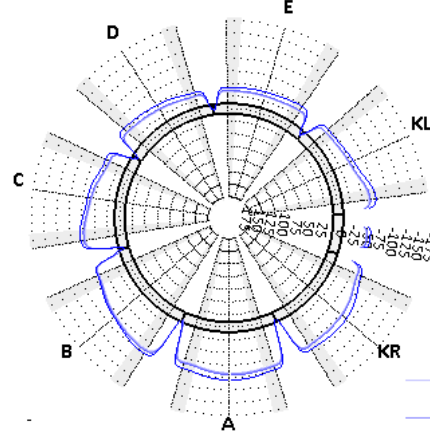
Figure 7.21: FEA results-3UKRA-R1

## 7.8. Sequential loading with vertical pressure gradients

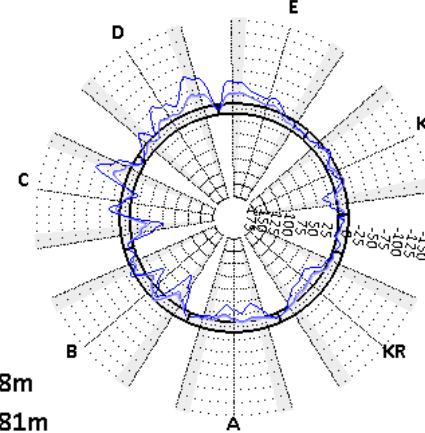
a) 3UKRA Hoop Mean Strains TBM SIDE [ $\mu\epsilon$ ] - Ring 2



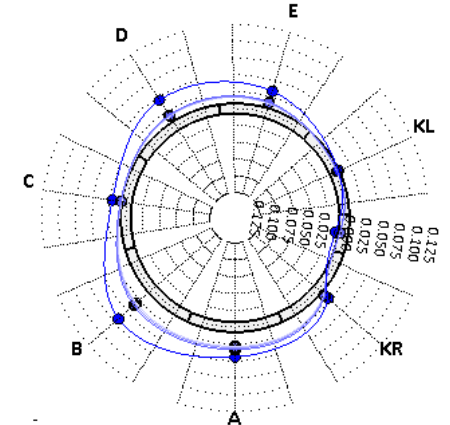
b) 3UKRA Hoop Mean Strains CENTRE [ $\mu\epsilon$ ] - Ring 2



c) 3UKRA Hoop Mean Strains LINING SIDE [ $\mu\epsilon$ ] - Ring 2

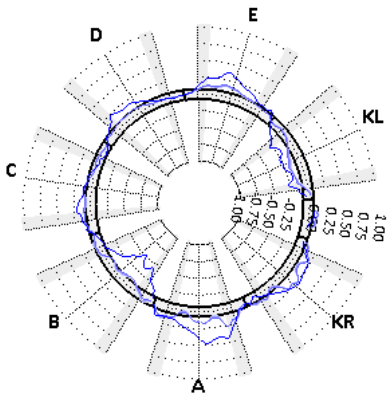


d) 3UKRA Vertical Tilt [ $^\circ$ ] - Ring 2

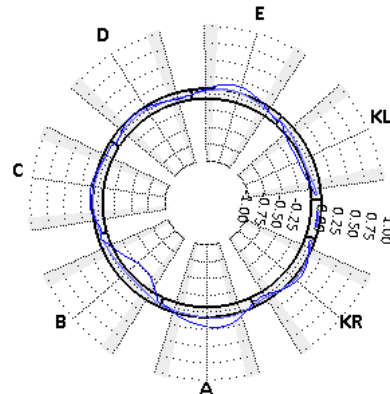


—  $X=0.8m$   
—  $X=0.81m$   
—  $X=0.85m$   
—  $X=0.9m$   
—  $X=1.6m$

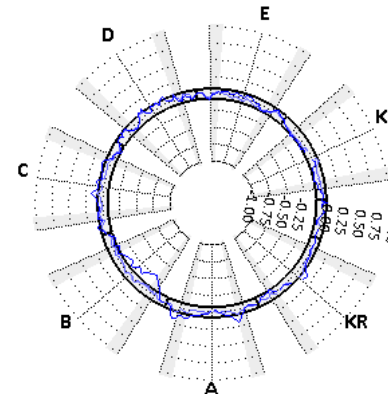
e) 3UKRA Hoop Curvatures TBM SIDE [ $^\circ/100$ ] - Ring 2



f) 3UKRA Hoop Curvatures CENTRE [ $^\circ/100$ ] - Ring 2



g) 3UKRA Hoop Curvatures LINING SIDE [ $^\circ/100$ ] - Ring 2



h) 3UKRA Longitudinal Curvatures CENTRE [ $^\circ/100$ ] - Ring 2

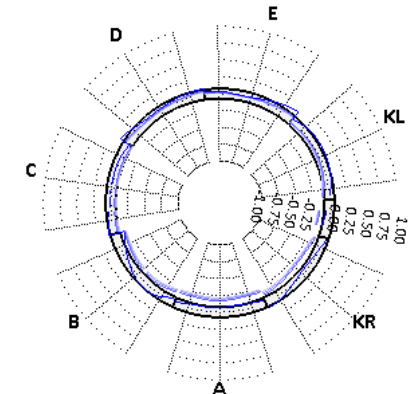
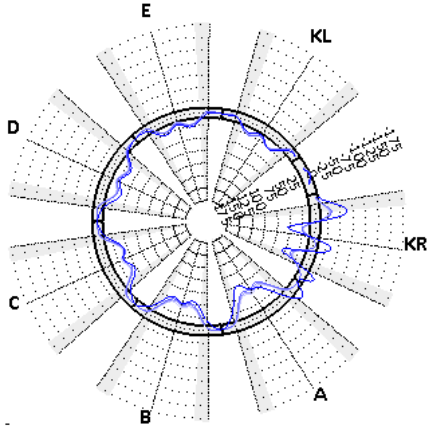


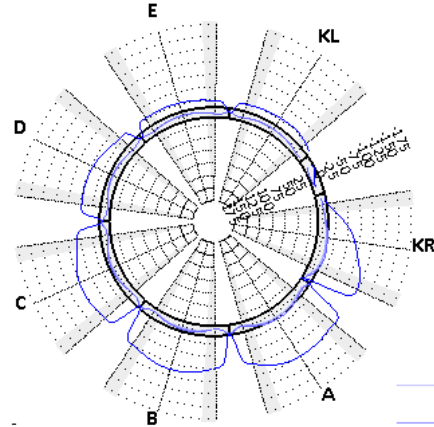
Figure 7.22: FEA results-3UKRA-R2

## 7.8. Sequential loading with vertical pressure gradients

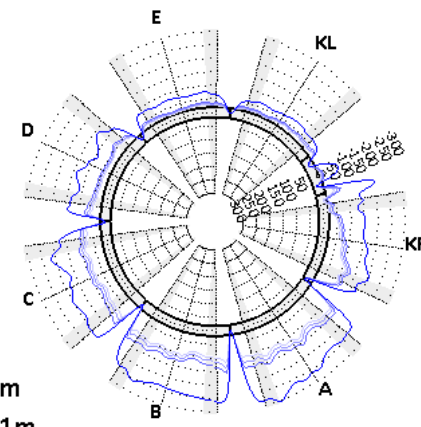
a) 3UKR Hoop Mean Strains TBM SIDE [ $\mu\epsilon$ ] - Ring 1



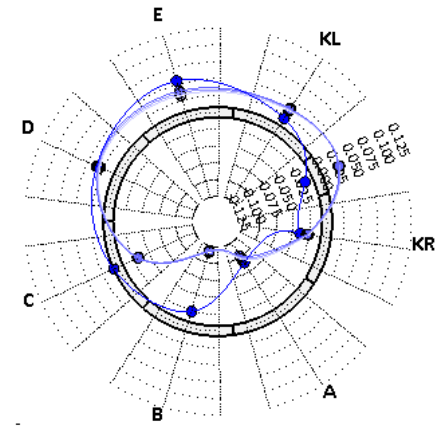
b) 3UKR Hoop Mean Strains CENTRE [ $\mu\epsilon$ ] - Ring 1



c) 3UKR Hoop Mean Strains LINING SIDE [ $\mu\epsilon$ ] - Ring 1

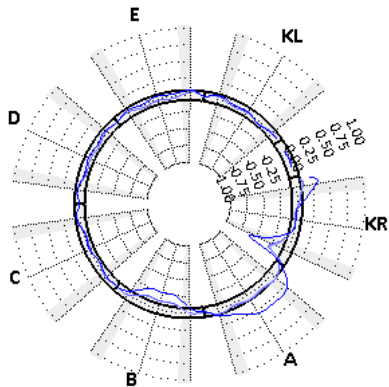


d) 3UKR Vertical Tilt [ $^{\circ}$ ] - Ring 1

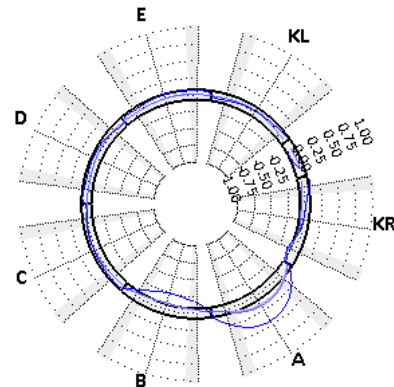


—  $X=0.8m$   
—  $X=0.81m$   
—  $X=0.85m$   
—  $X=0.9m$   
—  $X=1.6m$

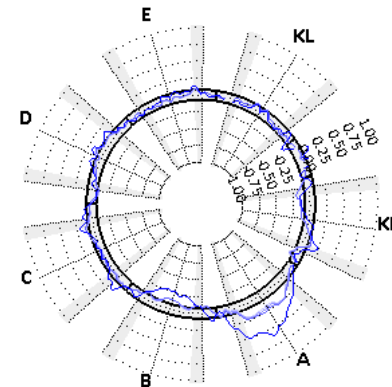
e) 3UKR Hoop Curvatures TBM SIDE [ $^{\circ}/\infty$ ] - Ring 1



f) 3UKR Hoop Curvatures CENTRE [ $^{\circ}/\infty$ ] - Ring 1



g) 3UKR Hoop Curvatures LINING SIDE [ $^{\circ}/\infty$ ] - Ring 1



h) 3UKR Longitudinal Curvatures CENTRE [ $^{\circ}/\infty$ ] - Ring 1

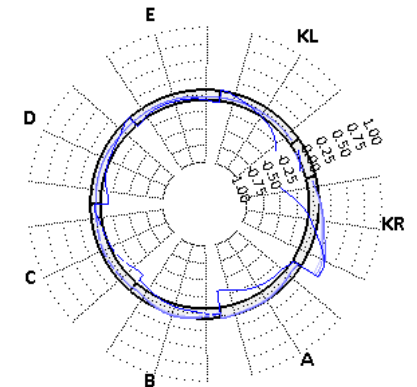
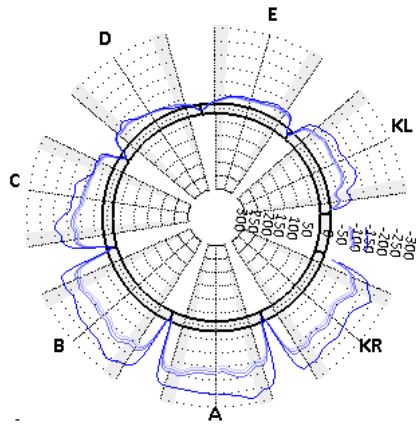


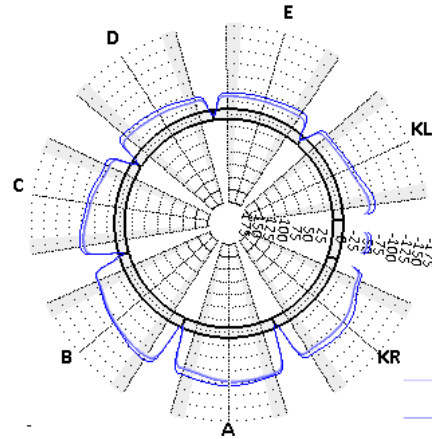
Figure 7.23: FEA results-3UKR-R1

## 7.8. Sequential loading with vertical pressure gradients

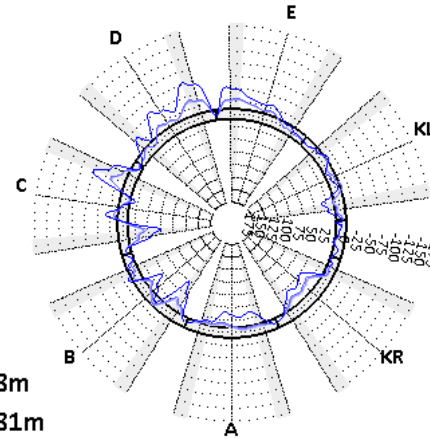
a) 3UKR Hoop Mean Strains TBM SIDE [ $\mu\epsilon$ ] - Ring 2



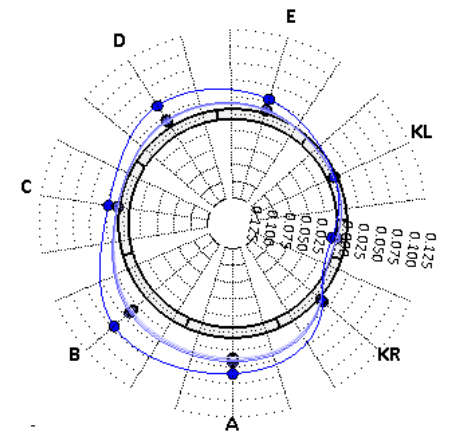
b) 3UKR Hoop Mean Strains CENTRE [ $\mu\epsilon$ ] - Ring 2



c) 3UKR Hoop Mean Strains LINING SIDE [ $\mu\epsilon$ ] - Ring 2

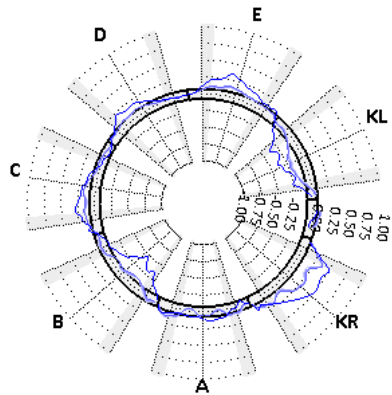


d) 3UKR Vertical Tilt [ $^{\circ}$ ] - Ring 2

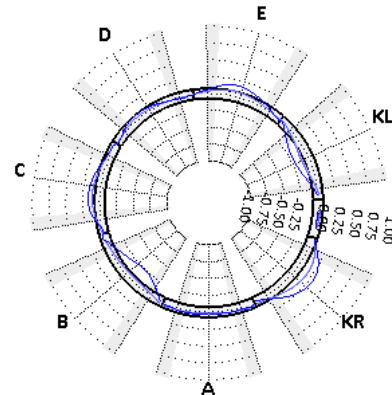


—  $X=0.8m$   
—  $X=0.81m$   
—  $X=0.85m$   
—  $X=0.9m$   
—  $X=1.6m$

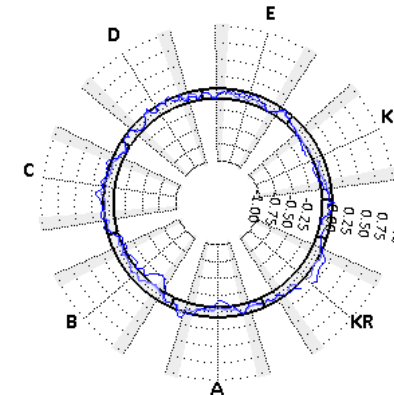
e) 3UKR Hoop Curvatures TBM SIDE [ $^{\circ}/100$ ] - Ring 2



f) 3UKR Hoop Curvatures CENTRE [ $^{\circ}/100$ ] - Ring 2



g) 3UKR Hoop Curvatures LINING SIDE [ $^{\circ}/100$ ] - Ring 2



h) 3UKR Longitudinal Curvatures CENTRE [ $^{\circ}/100$ ] - Ring 2

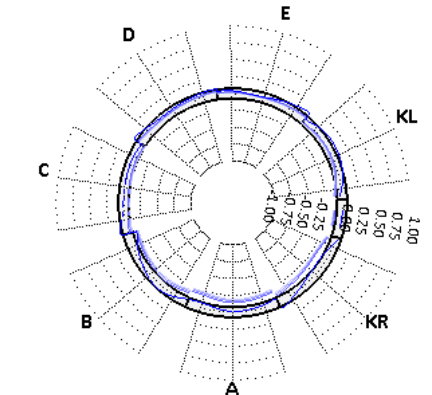


Figure 7.24: FEA results-3UKR-R2



## 7.8. Sequential loading with vertical pressure gradients

### 7.8.2.4. Longitudinal ring behaviour

The ram pad transverse action has also an impact on the local longitudinal behaviour of the unsupported rings.

Overall, at the ends of the fixed perimeters, the vertical tilt of R1 segments changes abruptly due to the transition from fixed to free segment rotations. For example, with invert fixity, the R1 top segments exhibit moderate vertical tilt, up to  $+0.050^\circ$ , while the restraints of invert segments accentuate the negative tilt up to  $-0.125^\circ$  values (see Figure 7.15.d). With crown fixity, the vertical tilt of top segments is reversed while the free invert segments develop negative tilt up to  $-0.125^\circ$ , which is corrected later to virtually null values when  $X=1.6\text{m}$  (see Figure 7.18.d). With lateral fixity, the constrained segments undergo small vertical tilt, the free invert segment B reaches values of  $-0.125^\circ$  before the completion of the advance while the top free segments exhibit moderate tilt of about  $0.050^\circ$  (see Figure 7.21.d).

Likewise, the radial ram pad reactions cause the longitudinal bending of the fixed segments in a cantilever-type mode and with sign opposite to their induced hoop curvatures, i.e. at the R1 centreline, the distribution of longitudinal curvatures mirrors the hoop curvatures of the R1 front (see Figures 7.15.g, 7.18.g and 7.21.g). Absolute peak values oscillate between  $0.50\text{‰}$  and  $1.00\text{‰}$ .

### 7.8.3. Potential damage during sequential loading

The numerical models evidenced that the sequential loading with uplift pressures under the condition of an uneven ram-pad interface can lead to two modes of concrete damage in the fixed segments: cracking near the rear corners and concrete spalling at the interspaces between ram pads (see Figure 7.25).

The contact length at the longitudinal joint separating the fixed and free condition of the R1 segments can be shortened by two mechanisms: the difference in radial rotation between the adjacent segments and the reduction in total hoop force induced by tangential ram pad reactions. The spread of the hoop force from a limited compression zone at the rear of the segment to the full segment width will generate transverse, longitudinal, tensile stresses within the disturbed region. Additionally, the radial ram pad reactions concentrated at the ends of the fixed perimeter yield longitudinal curvatures near the transitional longitudinal joint that reach peak values at the rear corners. When the spread of hoop forces at the back of the joint is combined with pronounced longitudinal bending, the fixed segment experiences high tensile longitudinal strains near the rear corner that may lead to concrete cracking, e.g.  $+390\mu\epsilon$  in model *3UAB*. The models show that the distribution of the ram pad reactions makes the cracking more likely at the intrados than extrados of the rear corners (see Figure 7.25.a).

Figure 7.25.b also illustrates that the peak spalling strains in the fixed segments can be increased by the additional hoop tension caused by the tangential ram pad reactions. For instance, in the *3UAB* model, the spalling strains reach a maximum of  $+220\mu\epsilon$  as opposed to the  $+105\mu\epsilon$  in axisymmetric free conditions.

## 7.8. Sequential loading with vertical pressure gradients

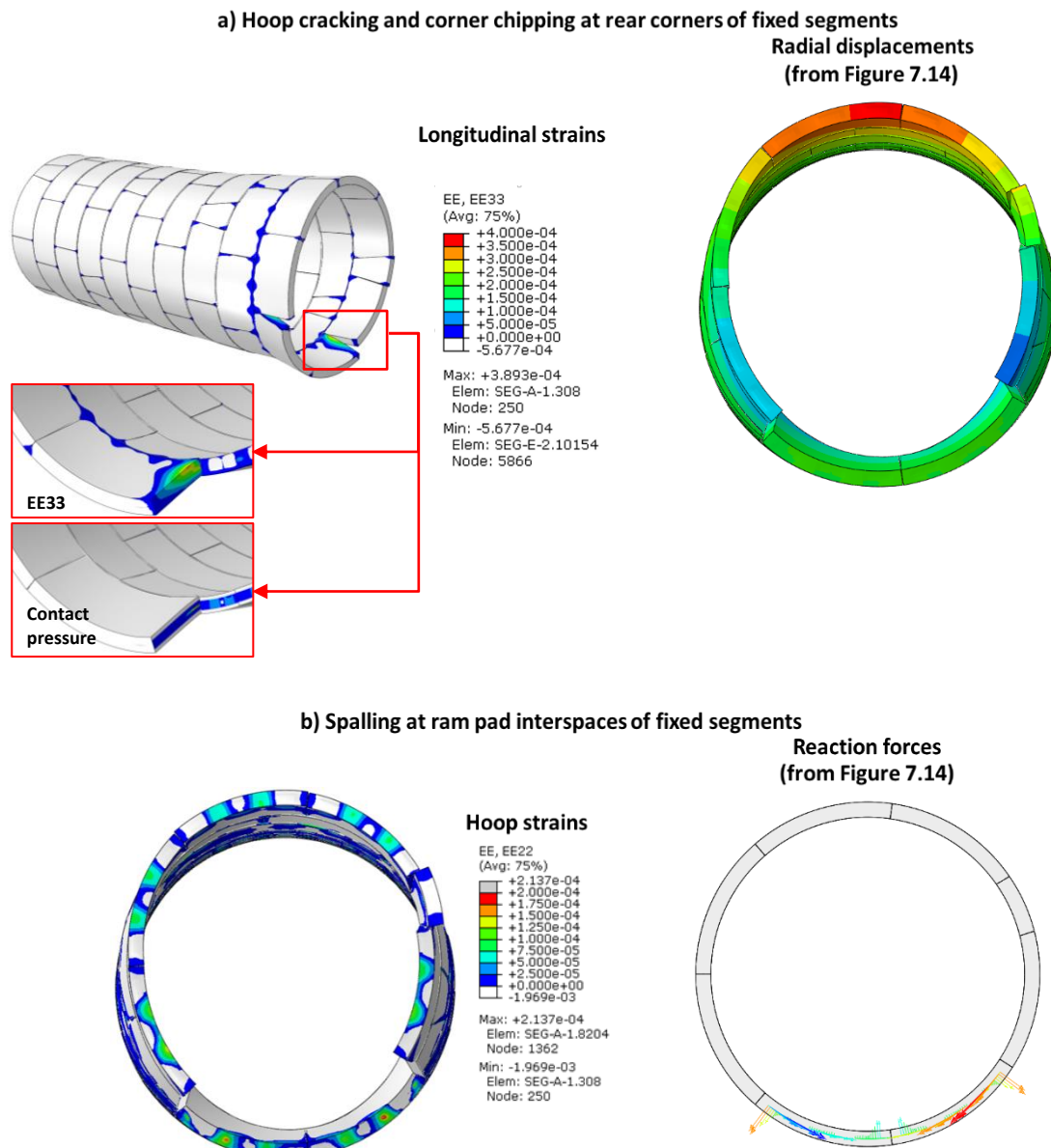


Figure 7.25: Damage modes in a CSL subjected to sequential loading with pressure gradients

### 7.8.4. Influence of other parameters on lining response

The effect of ram load distribution,  $L_u$ , and CSL features, such as the R1 rolling, the longitudinal joint geometry and the use of spear bolts, is evaluated here through indicators of ring behaviour and structural damage (see Figure 7.26). The parametric study is based on variations of the *3UKRA* model. However, all the models examined in section 7.8.2 are included in Figure 7.26 for completion.

The ring distortion is represented by R1 peak radial displacements and hoop moments. The likelihood of structural damage is assessed via spalling strains at the ring joints and peak longitudinal strains at the

## 7.8. Sequential loading with vertical pressure gradients

---

rear corners of R1 segments. The contact quality of R1 longitudinal joints by the end of the advance is considered through maximum joint rotations and lipping, contact pressures and minimum contact lengths. The watertightness is evaluated qualitatively via the gasket gaps and joint lipping remaining when  $X=1.6m$ .

When  $L_u$  is increased to 3 rings, the ring distortion is doubled, e.g. peak radial displacements grow from 6mm to 12mm. Consequently, the hoop moments also rise by  $\pm 40kN/m$  from the baseline values of  $+40kN/m$  and  $-20kN/m$ . The risk of structural damage is accentuated: both peak spalling strains and tensile strains at rear corners increase from  $+200\mu\epsilon$  to  $+250\mu\epsilon$ . The contact quality of longitudinal joints is deteriorated without undermining joint watertightness: peak joint rotations double from  $0.1^\circ$  to almost  $0.2^\circ$  and the joint lipping at the keystone joint triples to 12mm while gasket openings remain close to 1mm.

The temporary bolts modify locally the ring distortion where there is differential rotation between adjacent segments. Therefore, the above 12mm joint lipping drops to 4mm at the expense of a minor increase in maximum gasket opening from 1mm to almost 2.5mm.

The ring rolling can influence the tendency to crack formation at the rear corners of R1 segments since the peak tensile longitudinal strain of the 3UKRA model with the CAM4 rolling becomes  $+350\mu\epsilon$  as opposed to the  $+200\mu\epsilon$  baseline.

The ram loads applied to CAM3 and CAM4 rings in their first advance do not bring significant changes in the selected indicators, suggesting that the distribution of longitudinal loads with reasonable margins may be a secondary factor in ring behaviour during advance.

The use of flat longitudinal joints decreases the ring distortion by virtue of limited joint rotations, less than  $0.025^\circ$ , although the hoop moments are comparable with those of curved jointed CSLs. The required ram pad reactions to prevent movements along the ring perimeter are much smaller, which entails a reduction in spalling strains and longitudinal tensile strains. The latter strains are also benefited from the deep contact patches typical of flat joints without out-of-plane angularities. The short contact length and the wider gasket gaps exceeding 1mm may indicate a greater in-plane angularity of longitudinal joints by the end of the advance.



## 7.8. Sequential loading with vertical pressure gradients

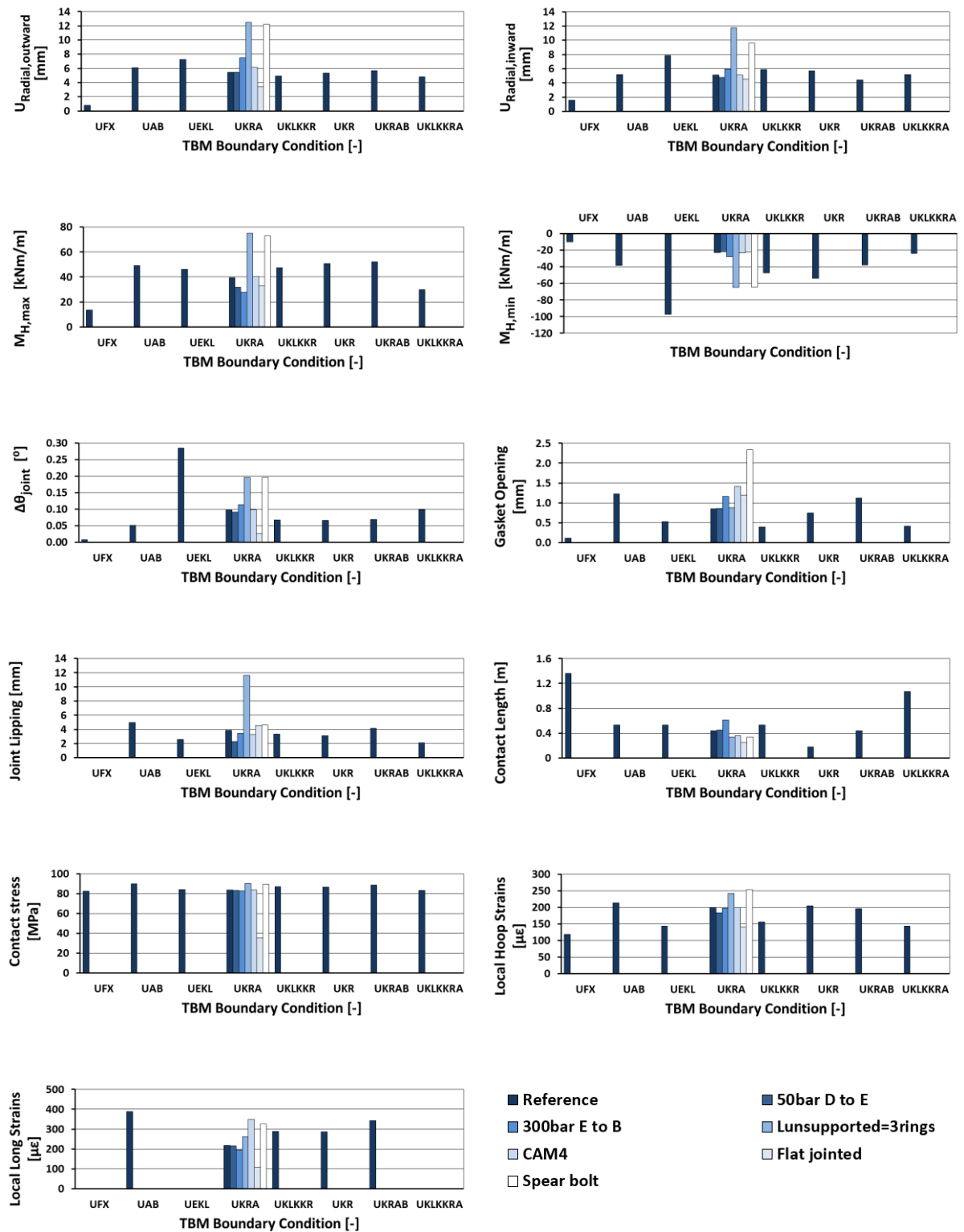


Figure 7.26: Parametric study on local lining response

### 7.9. Conclusions

The effect of ring sequential loading and uneven TBM-lining transverse interactions on ring behaviour and structural damage near the tail skin has been hardly researched despite the in situ evidence that it is precisely at the early TBM cycles when CSLs undergo most damage during construction (see chapter 1). In this chapter, a detailed investigation of ring behaviour under the sequential loading experienced in one TBM advance is conducted with the aid of 3D FE structural models of two and ten CSL rings. The study tackles two loading scenarios: sequential loading under axisymmetric conditions, representative of a ring concentric with the tail skin, and sequential loading with radial pressures with vertical gradients and uneven ram pad-lining interface, for an eccentric ring (see chapter 8).

The numerical study demonstrates that the damage modes in both scenarios are similar: corner chipping or cracking at the rear corners of R1 segments and spalling at the intrados of ram pad interspaces in the R1 front circumferential face. The case of an eccentric ring increases the risk of damage.

#### *a) Sequential loading under axisymmetric conditions:*

In structures made of several rings, when a ring is eccentrically compressed, there is longitudinal migration of hoop compression to neighbour rings through the development of radial coupling forces at circumferential joints. The load share between rings depends on the magnitude of longitudinal loads and type of ram pad boundary.

In free conditions, both the sequential ring compression and the offset of ram longitudinal loads relative to the packers cause the radial rotation of individual segments, which leads to the typical “tulip shape” observed on the field (Gruebl, 2006). In fixed conditions, the segment rotations are negligible.

The magnitude of radial tilt is given by the eccentric radial loading, the radial moment resulting from the longitudinal loads and the ram pad eccentricity applied, and the rotational stiffness of the circumferential joints. Keystones with poor lateral support experience high peak rotations and significant residual tilt at uniform ring compression, which suggests that they are more prone to chipping at rear corners under axisymmetric conditions. Negative (outward) ram eccentricities magnify outward rotations, particularly at the keystone. Positive (inward) eccentricities can fully compensate segment rotation.

The optimisation of the ring joint design can inhibit a great proportion of segment rotations. Packer depths equal to joint depths reduce rotations considerably. Packer materials with low initial stiffness and substantial stiffening under compression can prevent permanent “tulip shapes” without undermining the longitudinal load redistribution within packers.

Flat jointed rings may be more likely to develop permanent “tulip shapes” and chipping at corners under axisymmetric conditions. High longitudinal loads or medium longitudinal loads with negative ram pad eccentricity can increase the risk of concrete spalling.

It may be appropriate to prioritise ring orientations where keystones are placed at upper rather than lower positions to avoid greater rotations under selfweight.

***b) Sequential loading under vertical pressure gradients:***

The ram pad-lining interface determines the ring deformation modes and internal forces within the unsupported length of CSLs subjected to radial pressures with vertical gradients. With a fully fixed ram pad boundary, the ring deformations and hoop moments remain small. With mixed ram pad boundary conditions, ring deformations and curvatures within  $L_u$  can become substantial. For example, when the upward movements are restrained at the crown or invert, the ring either squats or squeezes onto a roughly elliptical shape that attenuates with distance from the TBM. The TBM reaction forces concentrated at the edges of the restrained circumference lead to the reduction of compression at either crown or invert and sharp hoop curvatures up to 1.00‰ at shoulders or knees. When the fixed boundaries are situated at one side of the ring, the ring deforms into a skewed oval shape with varying orientation depending on the boundary. The downward tangential stresses at the springline tend to dominate the TBM interaction with the lining, which have an impact on hoop force distribution. The asymmetric deformation mode produces alternate hoop curvatures up to 0.75‰ at the front of invert segments.

The amplitude of the ring response, conditioned by the quality of ram pad-lining interactions, and the risk of damage is directly related to the magnitude of the pressure gradients,  $L_u$  and the ring flexibility. The risk of damage is also influenced by the orientation of the constrained segments with respect to the pressure gradients and the R1 ring rolling.

The risk of cracking at the rear corners of constrained segments is caused by the combination of high negative longitudinal curvatures and short contact lengths at the ends of the R1 fixed perimeter caused by the radial action of the ram pads. The risk of concrete spalling in the constrained segments is increased by the tangential action of the ram pads on the circumferential face.

The higher rotational capacity of flat longitudinal joints lead to smoother ring distortions, which implies smaller joint rotations and spalling strains, at the expense of greater peak in-plane angularities of the longitudinal joints. The latter may suggest a greater propensity to corner chipping, particular at flat joints with initial contact imperfections.

Finally, the temporary bolts proved to be effective in limiting the differential radial rotations of adjacent segments in R1.

## Chapter 8

# Thames tunnel field data interpretation: local CSL response to sequential construction

### 8.1. Introduction

A great number of publications to date on the structural behaviour of CSLs during shield tunnelling focuses on the effects of grout pressures on lining response and neglects or oversimplifies the TBM-lining transverse interaction near the tail skin. For example, in the most complex numerical models targeting typical geotechnical problems associated with shield tunnelling such as surface settlement or the impact of tunnel construction on adjacent structures, the modelling efforts are concentrated on the support pressures of the tunnel cavity while sealing pressures are ignored, hydraulic jacks are represented by trusses and the tunnel segmental structure is simplified (Ninic et al., 2017). In sequential tunnel beam models, it is generally assumed that the net TBM transverse action on the tunnel is null (Hoefsloot, 2007; Talmon et al., 2009c), even though it is acknowledged that TBM transverse forces may be an important factor of longitudinal behaviour (Bezuijen and Talmon, 2009). In bedded 3D numerical models of multiple segmental rings simulating the effects of construction loads on lining performance, the interface between TBM and lining tends to be reduced to full in-plane fixity at the contact between ram pads and lining (Blom et al., 1999; Ishimura et al., 2013).

It can then be inferred that it is usually presumed that the transverse interaction between TBM and lining either does not exist or has little influence on the lining behaviour because it is expected to be evenly distributed along the ring circumference.

Conversely, the study on field pressure gradients in chapter 6 verified that both CTT instrumented rings, CAM3 and CAM4, were subjected to lining pressure gradients much greater than grout-static near the tail skin. The calibration of sequential beam models against the eccentricity of measured mean longitudinal strains also proved the need for net TBM transverse loads acting in the vertical direction in the six advances following CAM3 assembly and in the horizontal direction in the ten advances after CAM4 erection.

The analytical models based on the sequential assembly and loading of elastic rods (and beams) in shear (and transverse) interaction with elastic ground, however, can only provide information on the tunnel longitudinal response and cannot describe or predict ring behaviour. In order to facilitate the CTT field data interpretation on in situ ring behaviour near the tail skin, a 3D numerical study on CSL

## 8.2. CSL loading scenarios during construction

---

local response to sequential loading during one TBM advance was conducted in chapter 7. The study tackled the structural performance of rings subjected to axisymmetric sequential compression and boundaries; and rings subjected to high vertical pressure gradients with variable ram pad-lining interface. It was found that the latter case led to local ring distortion and bidirectional segment bending in those rings not bedded yet in the ground, which increased the risk of structural damage during sequential loading.

In this chapter, the in situ response of the CTT instrumented rings subjected to construction loads in early TBM cycles and how such response can determine long term behaviour are investigated in detail with the support of the numerical study performed in chapter 7. Based on the CTT field data interpretation, a theoretical framework for the development of limit state design methods that captures the effects of shield tunnelling on the CSL response is proposed: construction loading scenarios representative of field conditions where TBM-lining transverse interaction plays a key role are identified; the CSL structural response and damage mechanisms associated with these CSs are also described. The CSs are presented first for clarity purposes.

### 8.2. CSL loading scenarios during construction

Extensive research on lining pressures of CSLs simultaneously backfilled with MGs enabled the development of theoretical models of grout behaviour within the tail void (Talmon et al., 2001; Talmon and Bezuijen, 2006) that explained the mechanisms driving the history of lining pressures and provided a reliable estimation of in situ measurements (see chapter 6). However, in several tunnel projects where CSLs were backfilled with BGs, the field lining pressures exhibited high vertical pressure gradients in early advances beyond grout-static values that the grout models developed for MGs could not explain (Talmon and Bezuijen, 2005) and contradicted the uniform distribution expected from the material properties of BGs (see chapter 6). Talmon and Bezuijen (2005) attributed the high gradients to lining movements against hardened grout; Koyama (2003) correlated the high lining pressures with the contact between segments and steel wire brushes.

Steel brush seals can accommodate tail clearance tolerances, generally between  $\pm 20\text{mm}$  and  $\pm 40\text{mm}$  (Maidl et al., 2012), at the expense of deforming the steel stiffeners that support the wire brushes (see Figure 8.1). The pressures exerted by the steel plates onto the ring exiting the tail skin must depend on the tail clearance: the smaller the tail gap, the greater the reactive pressures. The sealing compound filling the sealing chambers is pressurised at least at 2bar greater than the grout injection pressures (Maidl et al., 2012). Being a fluid that can flow within the annular chambers, it is expected that the compound or grease pressures are not influenced by tail clearance. Consequently, any variations in tail clearance along the ring circumference in contact with the sealing system must result in an uneven distribution of sealing pressures through the variable deformation of the stiffeners.

## 8.2. CSL loading scenarios during construction

---



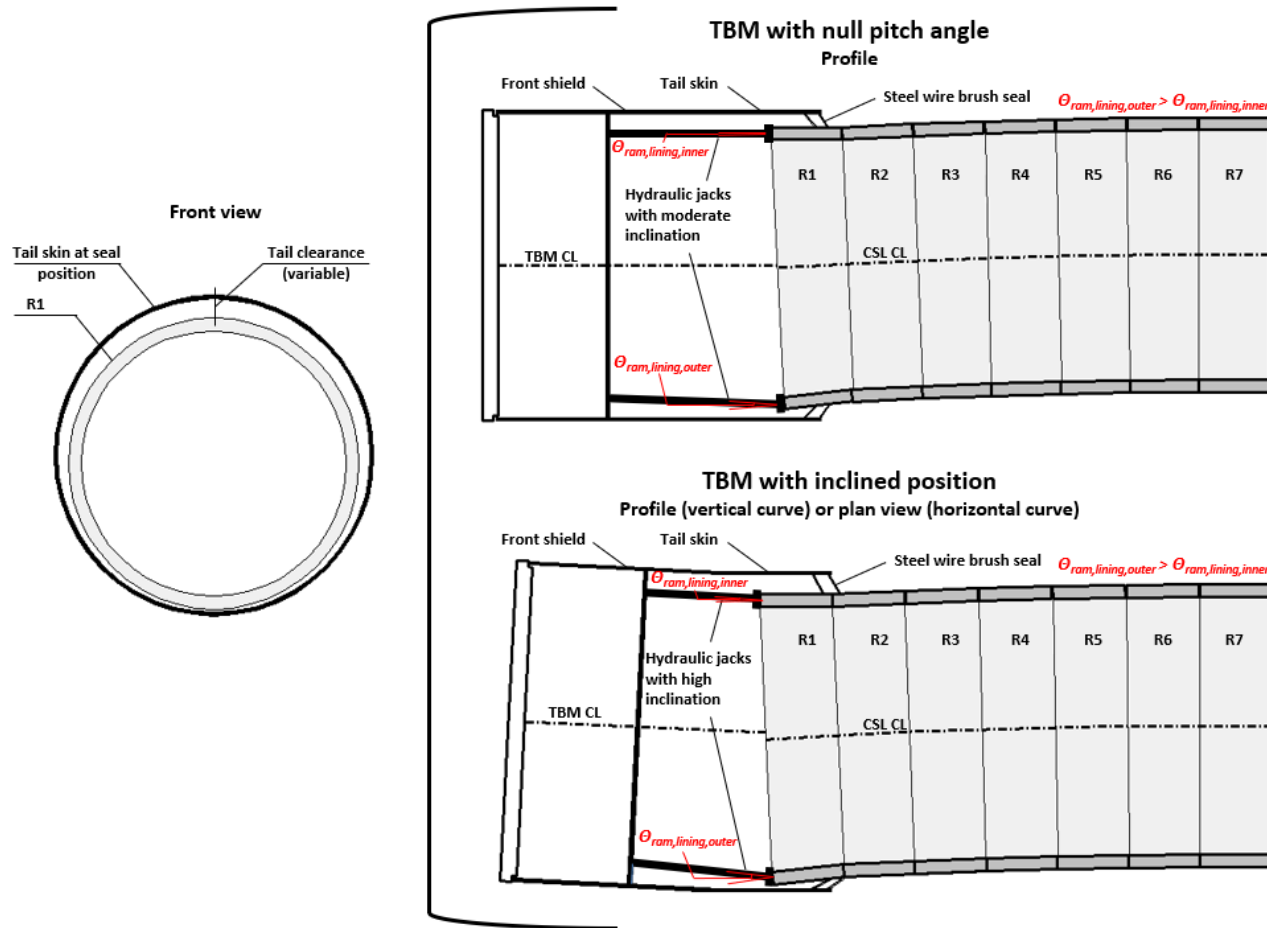
**Figure 8.1: Parts of TBM wire brush seal (after Shandong East Machinery & Equipment Co., 2017)**

Accordingly, when the tail skin and the tunnel share the same longitudinal axis and are concentric to each other, the sealing system pressures must be fundamentally axisymmetric and the hydraulic jacks applied with no inclination, providing lining imperfections and TBM tolerances are negligible. However, this is rarely the case on site. The clearance between tail skin and lining can change around the ring perimeter with the longitudinal deflection of the lining, the TBM steering and the deformation of the rings inside the shield tail.

Figure 8.2.a illustrates the changes in tail clearance caused by the offset position of the lining with respect to the tail skin. For example, in a tunnel section with straight alignment and no rotation of the TBM axis, the longitudinal response of the tunnel to uplift forces can lead to eccentricity between shield tail and lining and the inclined application of hydraulic jacks. When the TBM steers around a curve or rotates to rectify its position according to the planned alignment, the shield tail axis may exhibit a certain angle and offset against the nominal tunnel position at the tail chainage. The ram loads are applied at an oblique angle and are greater on the outer side than on the inner side of the curve, leading to a net longitudinal moment and transverse load that deflects the tunnel tube in the direction opposite to the TBM rotation (see Figure 6.18). The longitudinal response of the tunnel increases the relative inclination and eccentricity between tail skin and lining.

Figure 8.2.b. shows that in situ ring imperfections caused by assembly, sequential loading, the transverse component of ram loads or ram pad eccentricity can also alter the clearance between the tail skin and individual segments.

### a) Change in tail clearance due to ring eccentricity



### b) Change in tail clearance due to ring deformation

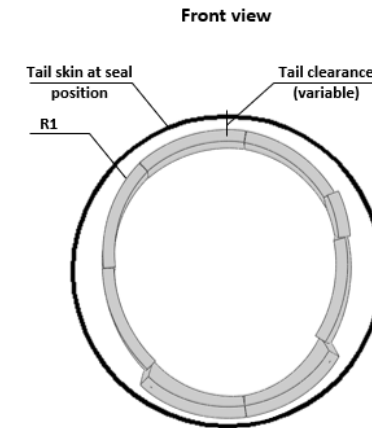


Figure 8.2: Causes of variable clearance between tail skin and lining

## 8.2. CSL loading scenarios during construction

---

The interpretation of the CTT field data undertaken in chapter 6 and in the following sections of this chapter led to the identification of three CSs near the tail skin, and their associated mechanisms of CSL response, where the TBM-lining transverse interaction is significant and may be conducive to structural damage:

*a) Construction scenario 1 (CS1): Concentric ring*

In this scenario, it is assumed that the last assembled ring, R1, remains roughly concentric with the shield tail, which implies that the TBM is driven through a straight alignment or the beginning of a transition curve and presents no deviation in axial orientation (see Figure 8.3.a). The TBM transverse reaction may be required to restore lining stability against uplift forces behind the TBM. Given R1's concentric position, the downward action must be delivered by the hydraulic jacks. In the case of CSLs simultaneously backfilled with BGs, the magnitude of the transverse reaction must be small since  $L_u$  is short and the grout pressure distribution fairly uniform (Peila et al., 2011).

The risk of structural damage during sequential loading, i.e. chipping or cracking at R1 rear corners and spalling at ram pad interspaces is lower than in the scenario of an eccentric ring (see chapter 7).

*b) Construction scenario 2 (CS2): Eccentric ring*

In this scenario, R1 has an eccentric position with respect to the tail skin, inherited from previous TBM cycles and/or developed during the following advance, AD1. The sealing pressures vary smoothly along the ring circumference and are inversely correlated to the tail clearance. The hydraulic jacks must exert an opposite action to ensure equilibrium against the net unbalanced pressures.

**Structural mechanism:**

For example, in a transition towards uphill excavation (see Figure 8.3.b), the TBM steering around the vertical curve results in an eccentric position of the lining where tail clearances are smaller at the invert and greater at the crown. The sealing pressures exhibit a positive vertical pressure gradient and, of course, are unrelated to the grout-static pressures.

The pitch angle of the TBM and the typical vertical deflection of a tunnel subjected to uplift forces also lead to a relative angle between tail skin and R1, which is exacerbated by both the longitudinal moment required to steer the TBM around the vertical curve and the net transverse action of the oblique hydraulic jacks.

The vertical pressure gradient tends to shift the ring upwards to approach a position concentric with the tail skin. This upward movement is opposed by the downward action of the oblique hydraulic jacks, mostly delivered at the bottom half of R1.



## 8.2. CSL loading scenarios during construction

---

The transverse component of the ram loads leads to the inward and outward rotation of top and bottom segments respectively, potentially increasing and decreasing the tail clearance in each case. The tendency of invert segments to rotate radially outwards impedes the release of the reactive sealing pressures exerted by the deformed stiffeners, which in turn limits the segment tilt to the minimum.

### **Structural damage:**

This scenario was studied and discussed in chapter 7 with the aid of simplified 3D numerical models. It was found that the combination of high seal pressures gradients and the uneven interaction with hydraulic jacks in one advance causes ring distortion within  $L_u$ , particularly in the ring in contact with the sealing pressures. The magnitude of ring deformations depends on  $L_u$ , the pressure gradients and the longitudinal joint stiffness; the deformation mode is governed by the relative orientation of pressure gradients and the length of ring circumference with active hydraulic jack transverse interaction. The risk of structural damage in the form of corner cracking or chipping and spalling is increased.

### *c) Construction scenario 3 (CS3): Rotated segment*

In this scenario, highly concentrated reactive pressures act on a R1 segment that has undergone significant outward radial rotation due to either the transverse component or eccentricity of ram loads.

### **Structural mechanism:**

For example, when the TBM steers around a horizontal curve, it can be generally assumed that all hydraulic jacks exhibit a similar inclination with respect to the lining given by the relative angles between TBM and lining (see Figure 8.3.c). The transverse loads delivered by the ram pads are proportional to the axial loads in the cylinders as long as the friction resistance of the ram pad-lining interface is not exceeded. The transverse loads are greater on the outer side of the curve than on the inner side and push the R1 outer segments outwards and the inner segments inwards.

The outer segment at the springline, with the lowest moment of inertia about the in-plane axis perpendicular to the transverse load, experiences the highest radial rotation. If the segment rotation is sufficiently high, the tolerance of the steel brush seal may be exhausted and there could be local concentration of normal sealing pressures on the segment due to the excessive deformation of the stiffeners.

In extreme cases, the rotated segment could make contact with the shield tail, thus a highly concentrated reaction would also act at the TBM edge of the segment extrados.

### **Structural damage:**

Figures 8.4.a and 8.4.b outline the loads acting on the rotated segment and its subsequent deflection diagrams.

## 8.2. CSL loading scenarios during construction

---

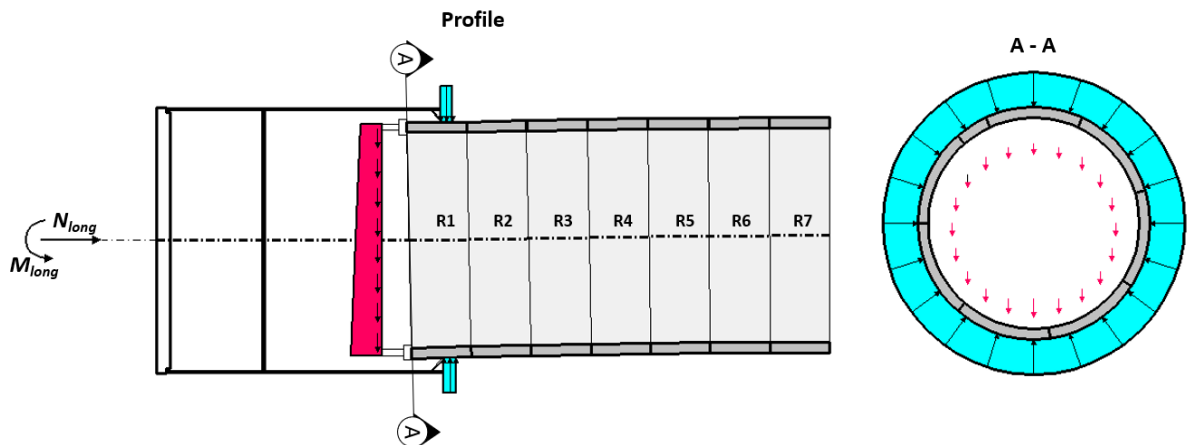
Without direct contact with the shield tail, the segment curvatures around the segment centroid are anticipated to be predominantly negative in both directions, being the longitudinal curvature  $k_l$  greater than the hoop curvature  $k_h$  as the segment width  $W$  is shorter than the segment length  $L$ .

When there is contact with the shield tail, the reaction load at the TBM segment edge would largely determine the magnitude of curvatures particularly in the longitudinal primary section. Positive longitudinal curvatures are expected along the longitudinal primary section whilst hoop curvatures at the segment centroid would tend to be fundamentally negative.

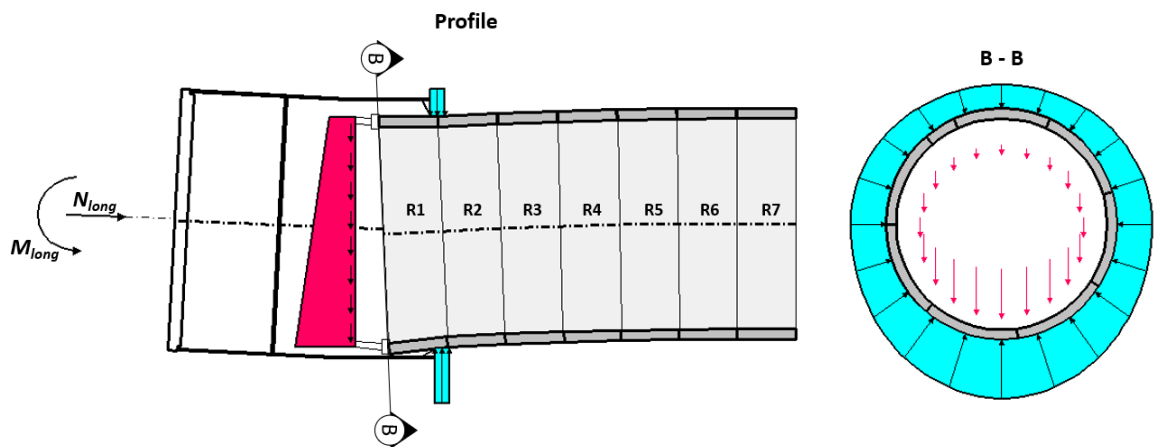
Despite peak curvatures being greater in longitudinal than hoop direction, the longitudinal compression of the hydraulic jacks mostly prevents the formation of hoop cracks in both loading cases. The segment, however, is prone to longitudinal cracking at the TBM side of the segment intrados due to the combined action of flexural cracking and pure tension. The former is mainly caused by the concentrated seal and/or tail loads described above; the latter is the result of the ring sequential loading and segment rotation (see chapter 7).

## 8.2. CSL loading scenarios during construction

### a) CS1: Concentric ring1 in straight alignment



### b) CS2 example: TBM steering around an uphill vertical curve



### c) CS3 example: TBM steering around a horizontal curve

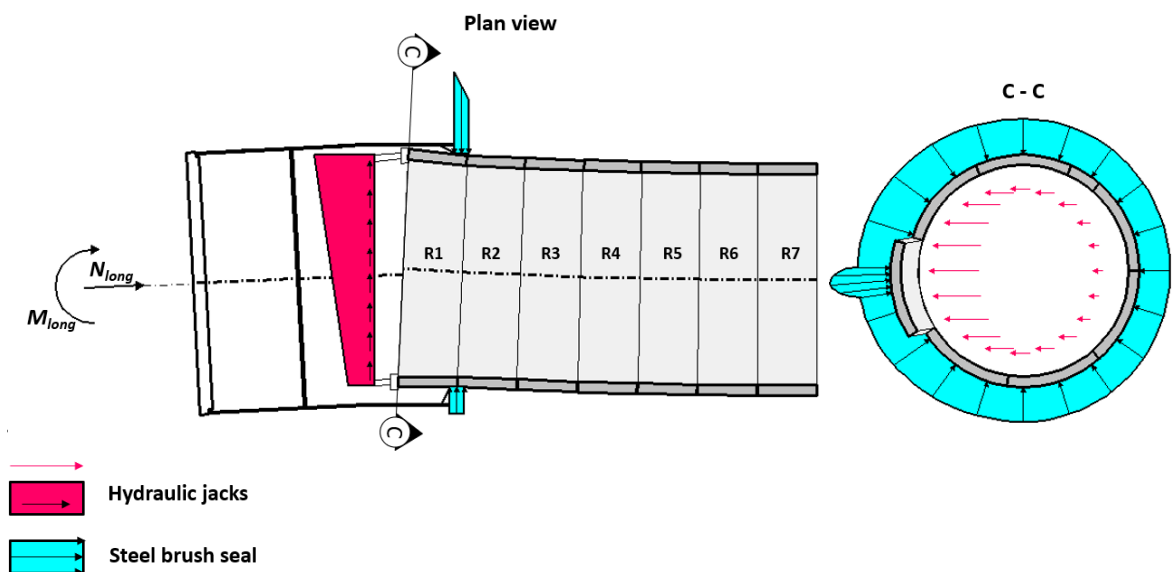


Figure 8.3. Construction scenarios

### 8.3. Further considerations on processed field data

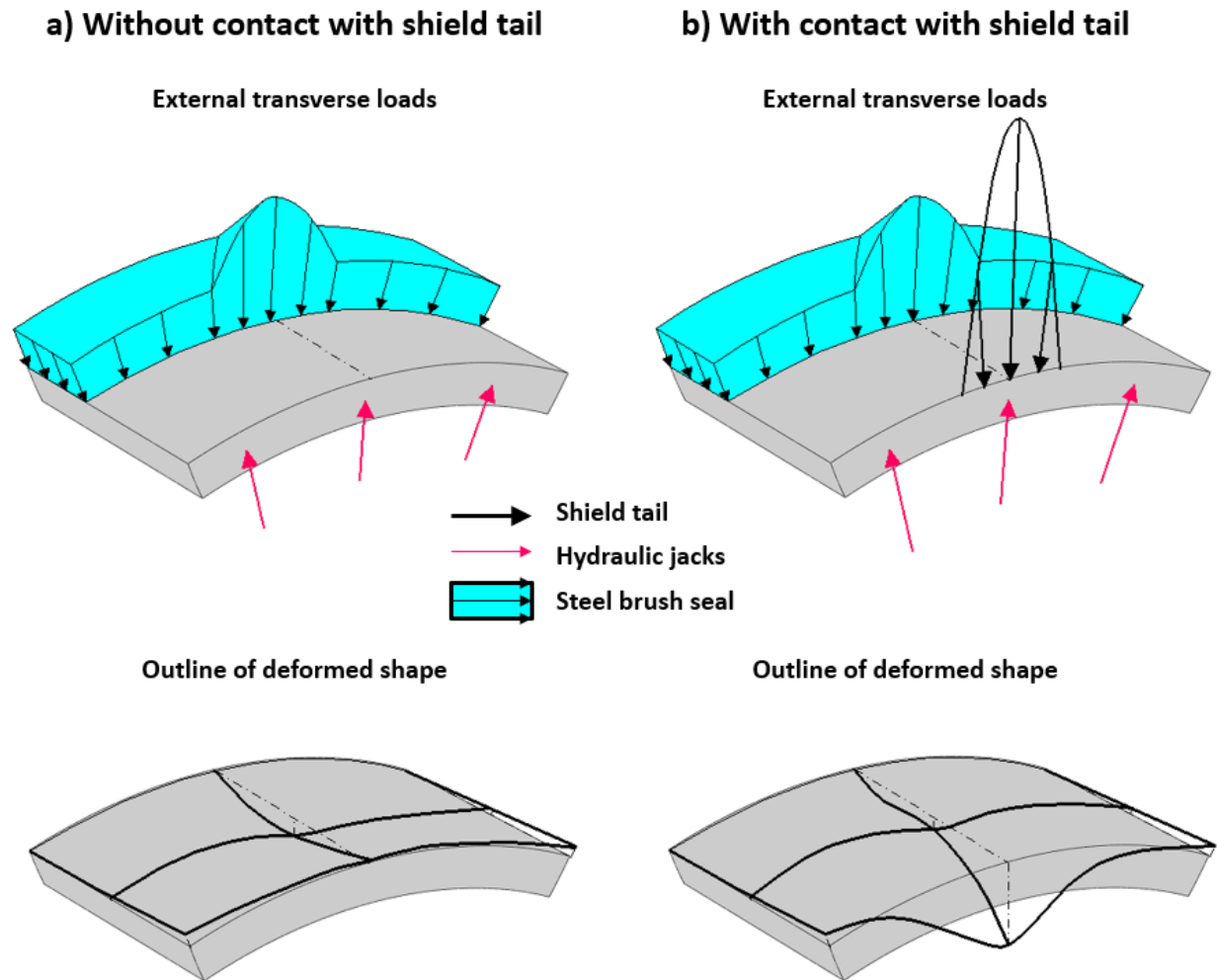


Figure 8.4. CS3 loading and segment response

### 8.3. Further considerations on processed field data

The discussion on hoop membrane behaviour is based on raw hoop mean strains along longitudinal primary sections after elimination of the Poisson effect. The influence of the load spread on these hoop strains is deemed small along this primary section (see chapter 5). The gradient of the linear hoop mean strain distribution is calculated as the best fit to measured BOTDR strains that crosses the VWSG strain, assuming that the measurement uncertainty of the latter is negligible. Total hoop forces, in-plane moments and mean lining pressures are derived from the distribution of zeroed hoop mean strains.

The transverse strains at the BOTDR lateral hoop sections associated with the longitudinal load spreading cannot be excluded from the processed data. The Poisson effect is not corrected for the BOTDR curvatures given that the corrections are much smaller than their nominal dispersion.

## 8.4. Field response to sequential assembly

---

When the data sets last captured in a certain advance correspond to a swept distance or time far from the advance completion, the next data set in the following assembly period may be more representative of CSL response by the end of the advance.

### 8.4. Field response to sequential assembly

Prior to the first TBM advance, the weight of the instrumented rings is sustained by the action of the hydraulic jacks plus the shear and normal reactions delivered by the compressed packers and dowels at the circumferential joints. No radial pressures are applied yet, and therefore the hoop compression of the segments must be fundamentally null unless there are significant contact deficiencies at their joints.

#### 8.4.1. CAM3 ring

The BOTDR hoop profiles of raw mean strain and curvature at the centreline and TBM side of CAM3 segments captured before CAM3 cycle1 are shown in Figure 8.5. Hoop mean strains and curvatures are consistently close to zero in all segments except for segment B3.

The sharp changes in B3 mean strain and curvature must be caused by the uneven distribution of the longitudinal thrust in a segment with contact deficiencies originated during ring erection, given that such strain patterns are perpetuated over the entire monitoring period. Since the adjacent segments in CAM3 exhibit uniform and almost null hoop deformations, the contact imperfections must take place at the circumferential joint with the previous ring, R2.

Cavalaro (2009) studied the structural response of segments with uneven support at one circumferential joint. When the deformation of the segment cannot close the gap at the imperfect circumferential joint, the segment behaves as a deep beam undergoing significant shear deformation. The longitudinal loads are transferred to the active supports leading to a state of plane stress within the segment body that can be effectively represented with strut and tie models (STMs). Figure 8.5.c shows Cavalaro's STM for a segment subjected to two sets of ram loads in one side and with a single support at the opposite side. The right load is transferred through a diagonal compression strut to the support, which causes hoop tension at the TBM side. Following the strut and tie analogy, local hoop compression must also be originated in the vicinity of the single support.

Figure 8.5.d and 8.5.e illustrate possible STMs and foreseeable crack patterns in a CTT segment subjected to three sets of longitudinal loads at one side and uneven support at the opposite side. In the case of a single support, the STM is equivalent to the superposition of two Cavalaro's STMs, one for each unbalanced load, which results in higher hoop tension between the ram pads closest to the support, RP1 and RP2; the segment will be prone to crack longitudinally at the TBM side between these two pads. The segment may also exhibit diagonal shear cracks isolating the compression struts

## 8.4. Field response to sequential assembly

(Nilson et al., 1991). There may be continuity between the longitudinal tension crack at the TBM side and the diagonal shear cracks along the mid strut. When the segment is provided with two supports, one compression strut is formed laterally and the same crack mechanisms will take place with the cracks situated this time between ram pads RP2 and RP3.

The B3 mean strain profiles would appear to accommodate better the state of stresses and crack patterns of Figure 8.5.d, where the segment lacks the longitudinal supports aligned with ram pads RP2 and RP3: at the TBM side, there is moderate hoop membrane tension with a peak of about  $+130\mu\epsilon$  between RP1 and RP2; at the segment centreline, the hoop membrane strains vary from about null strains in the vicinity of RP3 to almost  $+300\mu\epsilon$  between ram pads RP1 and RP2. Despite the difference in maximum mean tensile strains at the centreline and TBM side of the segment, the peak extreme fibre tensile strain in both primary sections is in the order of  $+400\mu\epsilon$  and situated at the segment extrados (see Figure 5.33.c, p.134), which indicates that both sections are crossed by concrete cracks at the extrados.

The B3 hoop curvatures computed from pairs of measured strains are quite variable along the segment length and width and reach peak values in the order of 1.5‰. The cause of such deformational patterns is not clear. First, there may be some measurement uncertainty associated with the identification and alignment of DFOS sections in parallel topologies. Second, cracks may not develop equally at the extrados and intrados of concrete segments due to material inhomogeneities or the action of contemporary loads applied in other directions. The disparity between the two profiles appears to suggest that the segment is subjected to torsion.

Figure 8.6 presents the history of raw hoop mean strain profiles along the longitudinal primary section for all CAM3 segments derived from BOTDR and VWG data. Segment B3 is omitted due to VWG data loss (see chapter 5).

Overall, the raw hoop mean strains at segment centroids before cycle1, i.e. the reference strains, are fairly close to zero, which evidences that the effect of contact deficiencies at circumferential joints near the centroid of all segments other than B3 is negligible, and therefore these are minor.

The limited raw hoop gradients exhibited by all segments prior to cycle1 indicates that contact imperfections at longitudinal joints after ring erection are also small. Segment D3 displays the greatest hoop strain gradient, with extreme membrane strains of about  $\pm 100\mu\epsilon$ .

### 8.4.2. CAM4 ring

The BOTDR hoop profiles before CAM4 AD1 in Figure 8.7 show that both mean strains and curvatures are uniformly distributed along the segment length with values close to zero in all hoop primary sections of CAM4 segments; which suggests that the erection of CAM4 segments against the previous ring has not caused significant contact imperfections.

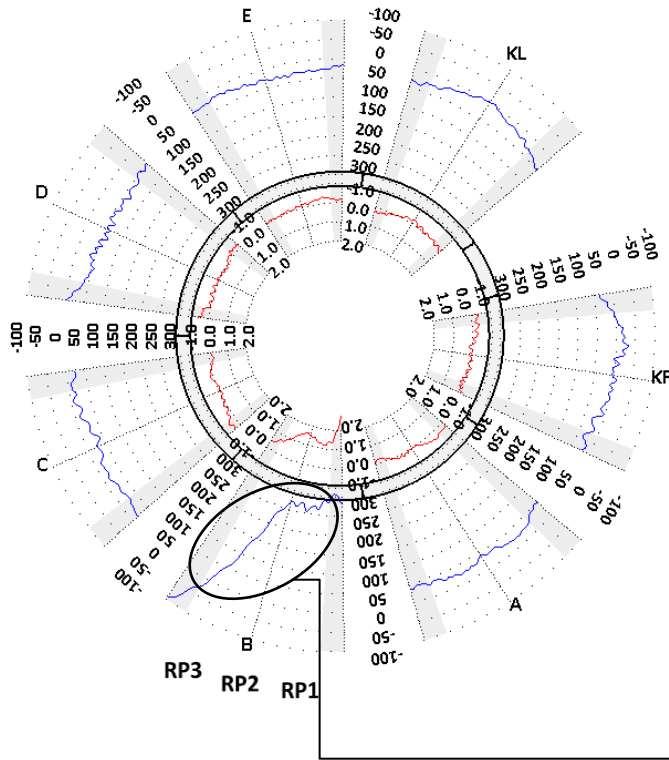
## 8.4. Field response to sequential assembly

---

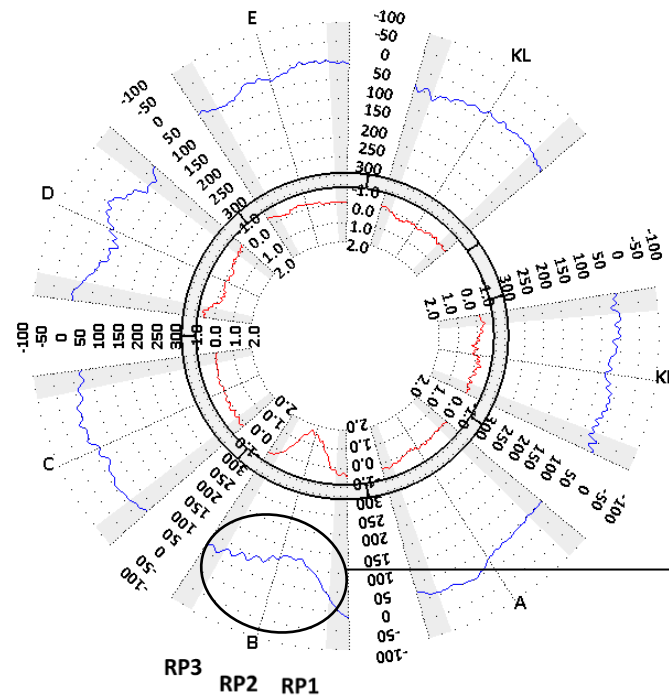
Like in CAM3, the hoop membrane strains at the longitudinal primary section prior to cycle1 are approximately null for most segments, with extreme fibre strains in the order of  $\pm 50\mu\epsilon$  except for segment C4, which exhibits  $\pm 100\mu\epsilon$  peak strains (see Figure 8.8.a).

## 8.4. Field response to sequential assembly

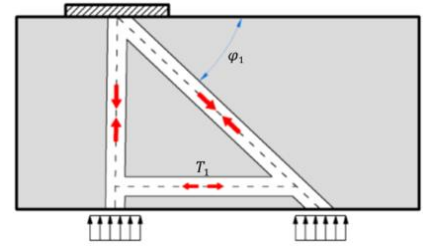
a) CAM3 Hoop Mean Strains [ $\mu\epsilon$ ] and Curvatures [ $^{\circ}/\infty$ ] prior to Cycle 1  
CENTRE



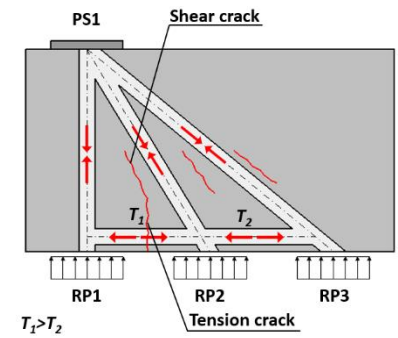
b) CAM3 Hoop Mean Strains [ $\mu\epsilon$ ] and Curvatures [ $^{\circ}/\infty$ ] prior to Cycle 1  
TBM SIDE



c) STM model for contact deficiencies at circumferential joint (after Cavalaro, 2009)



d) CTT STM model: one packer support



e) CTT STM model: two packer supports

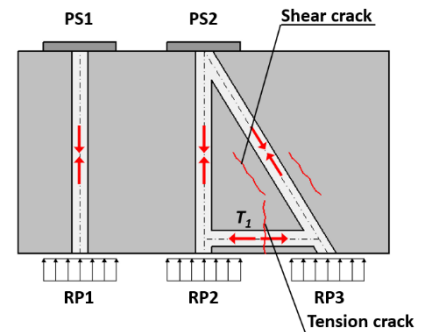


Figure 8.5: CAM3 hoop mean strains and curvatures prior to cycle1



## 8.4. Field response to sequential assembly

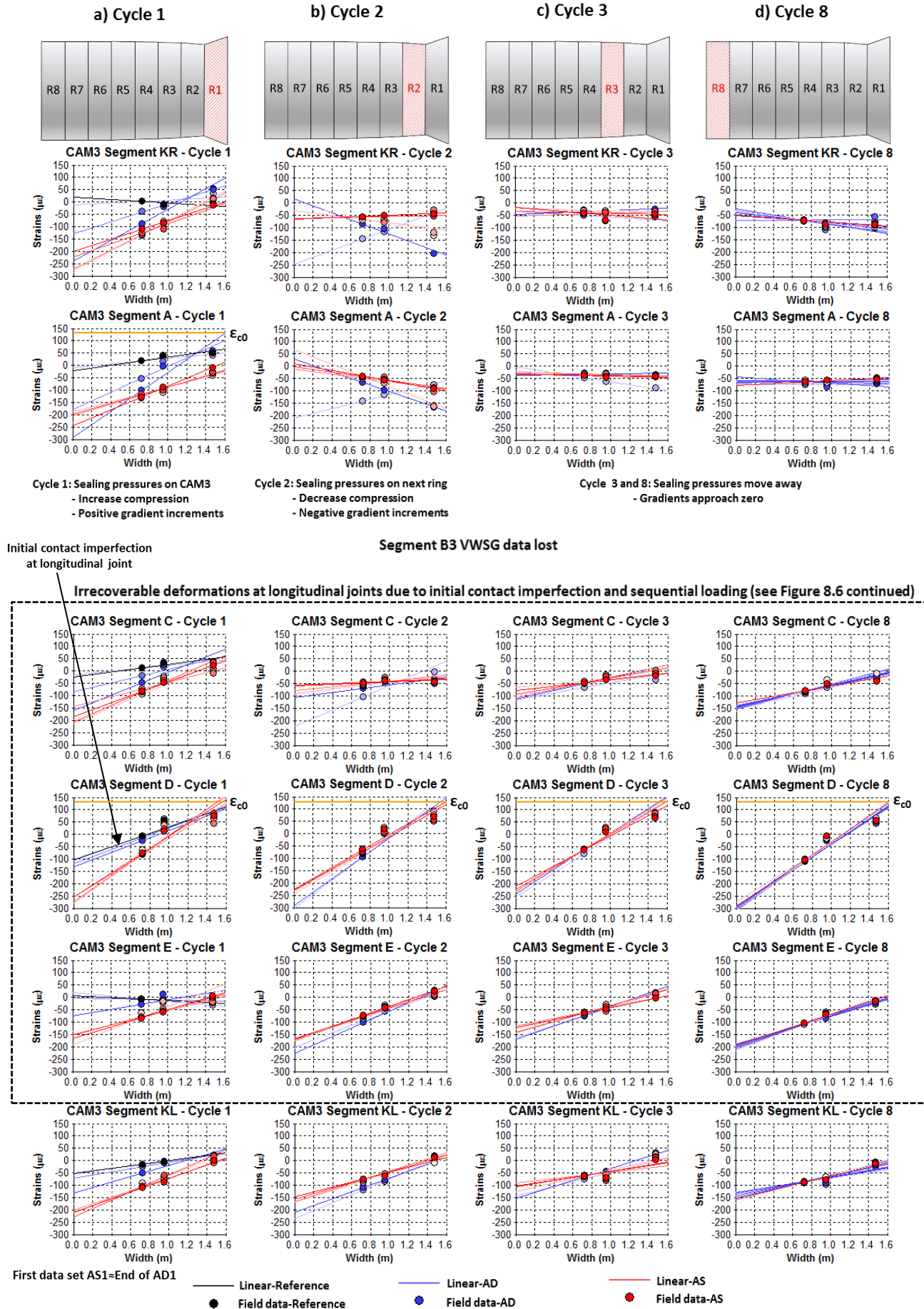


Figure 8.6: CAM3 raw hoop strains during sequential loading

## 8.4. Field response to sequential assembly

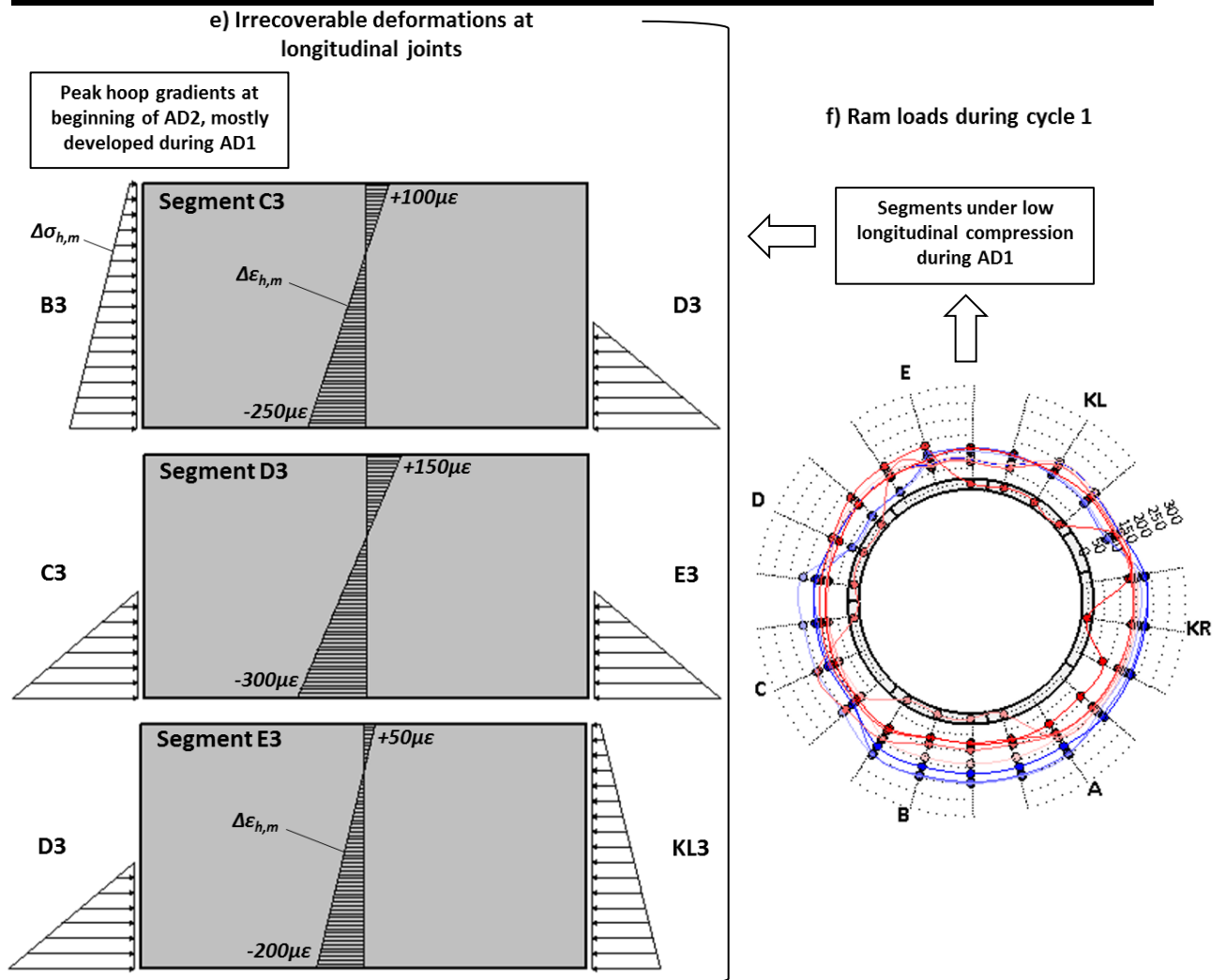
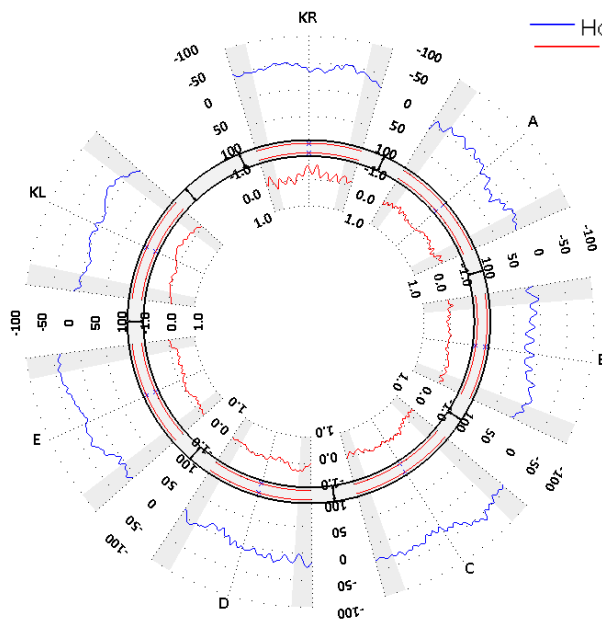


Figure 8.6 (continued)

a) CAM4 Hoop Mean Strains [ $\mu\epsilon$ ] and Curvatures [ $1/\text{mm}$ ] prior to Cycle 1 CENTRE



b) CAM4 Hoop Mean Strains [ $\mu\epsilon$ ] and Curvatures [ $1/\text{mm}$ ] prior to Cycle 1 TBM SIDE

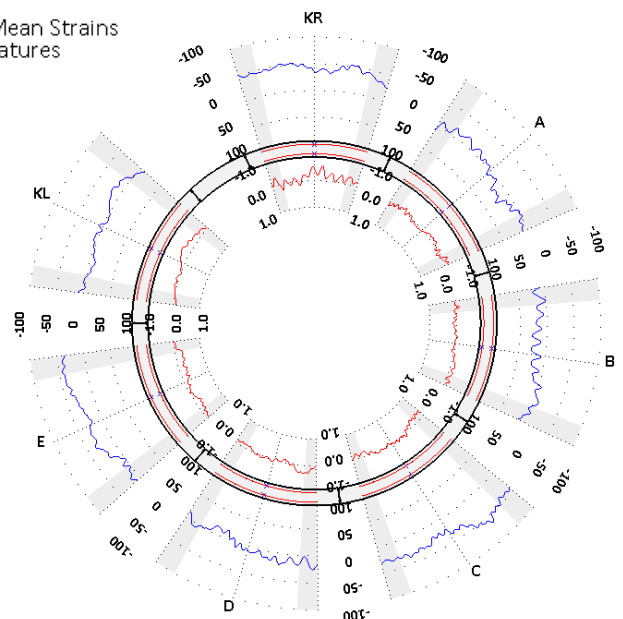


Figure 8.7: CAM4 hoop mean strains and curvatures prior to cycle1

## 8.4. Field response to sequential assembly

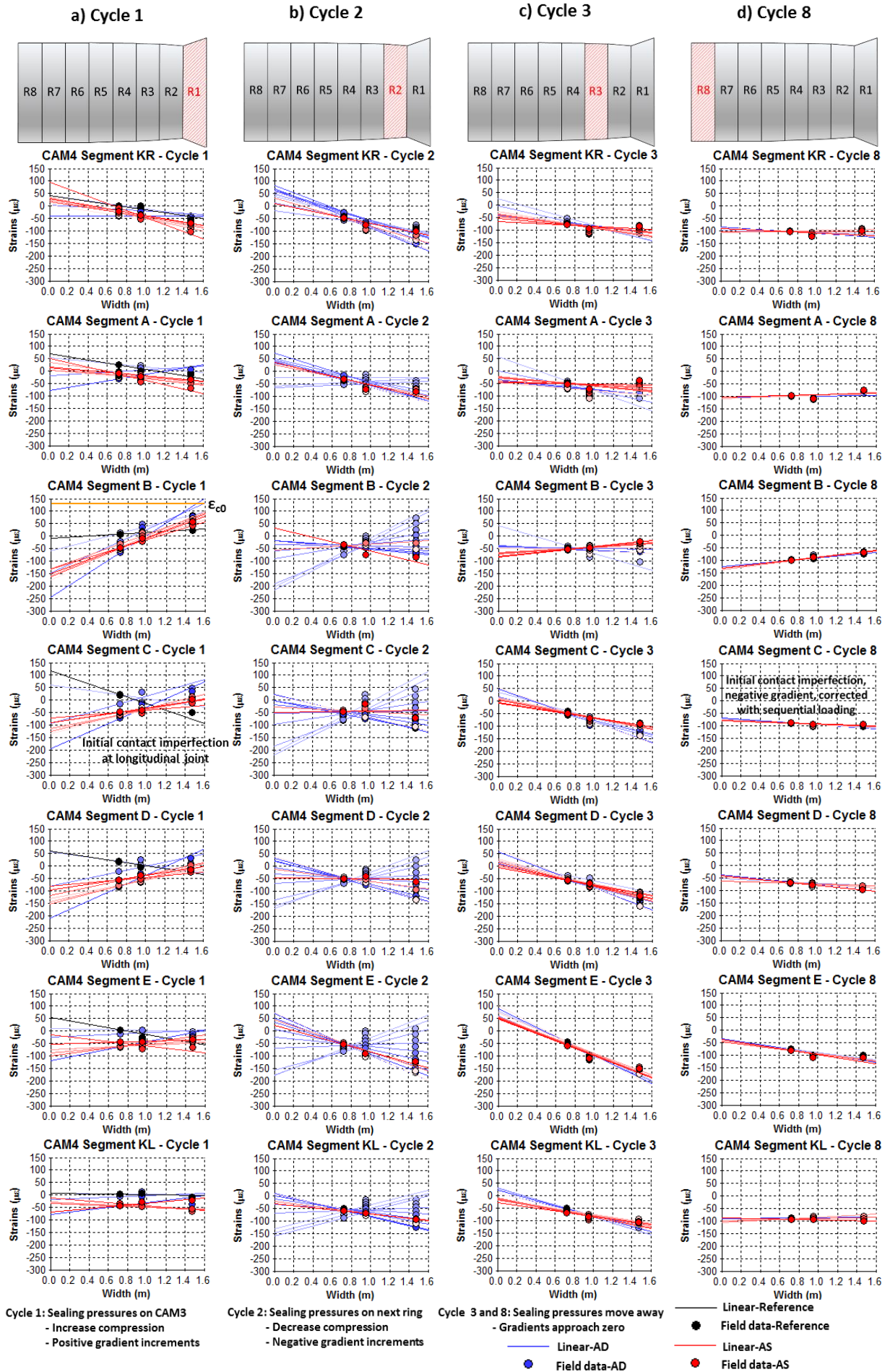


Figure 8.8: CAM4 RAW hoop strains

### 8.5. Field data interpretation on cycle 1

According to HMJV information on the tunnel drive, it is generally assumed in this study that the instrumented ring makes contact with the first row of steel wire brushes for the first time at about one fifth of AD1, i.e.  $SD \approx 0.3\text{m}$ . Since the width of the sealing system was in the order of  $0.875\text{m}$ , the ring would start to exit the tail skin and be surrounded by the annular grout at  $SD = 1.175\text{m}$ . The relative position of tail seal and lining along the tunnel axis, however, depends on the stroke of the hydraulic jacks and therefore it is expected to be slightly different for each TBM advance and to vary along the ring perimeter with TBM steering.

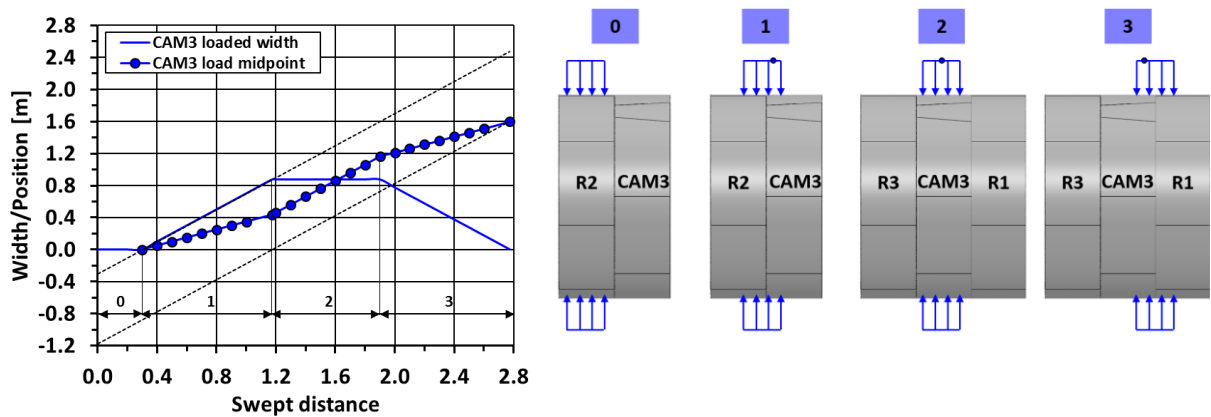


Figure 8.9: Sealing pressures with swept distance

The response of the rings immediately behind the TBM can be described through the construction scenarios defined in section 8.2 or their combination. The construction scenarios CS1 and CS2 for concentric and eccentric rings against the shield tail were examined in chapter 7 via 3D FE models of sequential loading in one TBM advance. The knowledge gained through the numerical study is applied here to interpret the set of field data gathered on cycle1 and validate the theoretical framework of construction loading scenarios outlined in section 8.2.

The numerical simulations performed the sequential application of a radial pressure distribution with either null or positive vertical gradient on a CSL longitudinally compressed by uniform ram loads and with in-plane displacement restraints along variable sections of the ring face in contact with the ram pads.

In field conditions, however, TBM transverse actions may imply partial rather than full constraints of ring displacements even in those segments with most active TBM-lining interfaces: indeed, the calibrated tunnel beam models predicted small lining movements of the instrumented rings at a one ring distance from the TBM (see chapter 6). Changes in shield steering or the lining response may influence the interactions between TBM and lining within the duration of a TBM cycle. In situ ram loads, even during straight tunnelling, tend to be unevenly distributed along the ring circumference and may be applied with certain eccentricity, which can also change during a TBM cycle.



## 8.5. Field data interpretation on cycle 1

It then follows that the FE reference models must be regarded as a guide for field data interpretation and some discrepancies with the numerical results must be expected. This may be particularly true for the vertical tilt and the longitudinal curvatures that may be more influenced by the unmonitored tilt during ring erection and ram pad eccentricity.

### 8.5.1. CAM3 ring

Figure 8.10 summarises the general conditions of CAM3 and CAM4 rings regarding planned tunnel alignment, recorded TBM ram loads and the net TBM transverse actions inferred from the field data interpretation on the CTT longitudinal response undertaken in chapter 6.

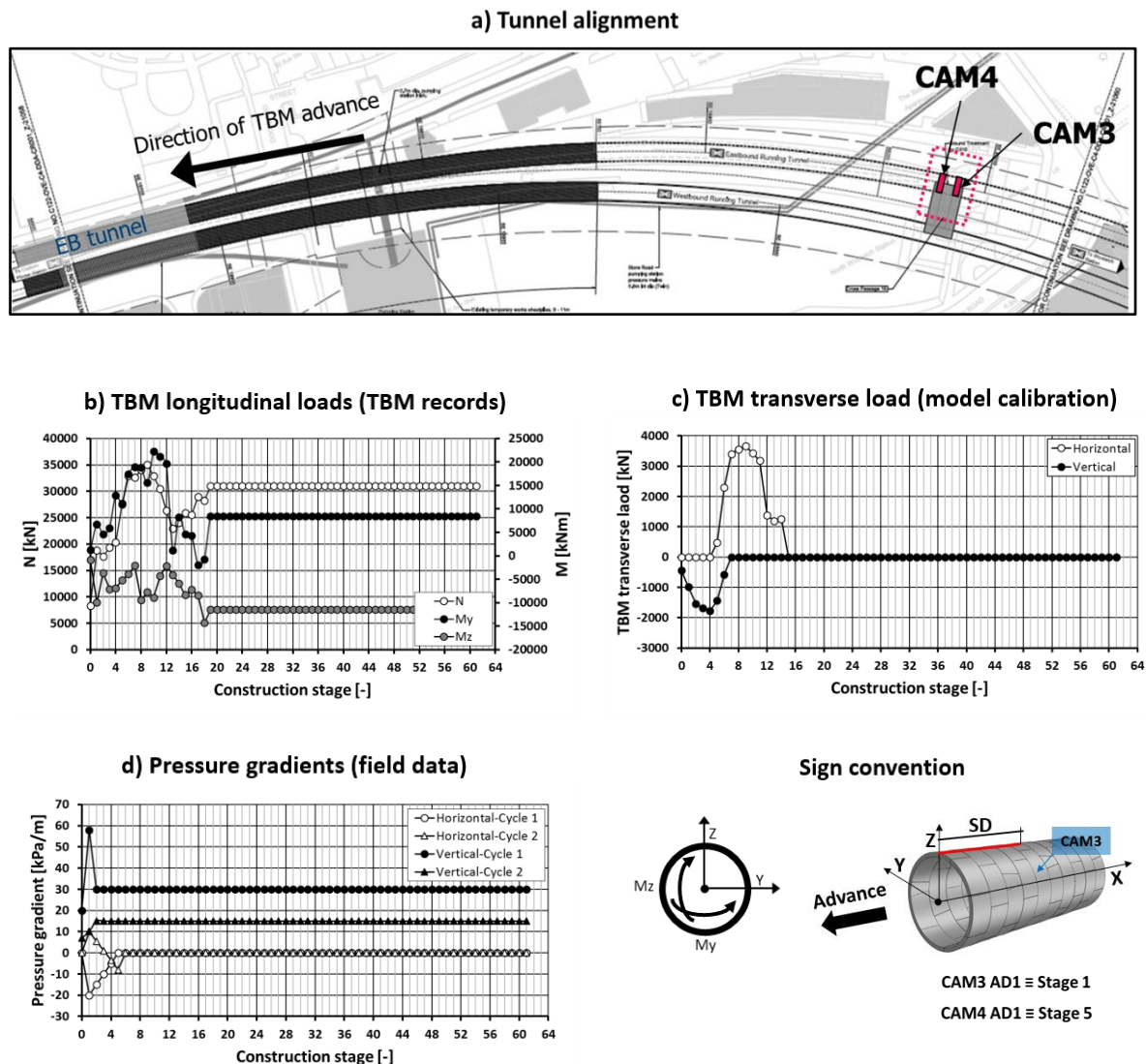


Figure 8.10: CAM3 and CAM4 general conditions

During AD1, CAM3 was subjected to moderate TBM longitudinal moments  $M_y$  and  $M_z$ , the mean lining pressures presented substantial vertical and horizontal gradients of about 60kPa/m and 20kPa/m respectively and additional net vertical TBM loads were required for the calibration of the sequential tunnel beam model. The magnitude of vertical and horizontal pressure gradients being greater than

## 8.5. Field data interpretation on cycle 1

---

grout-static suggests that CAM3 is subjected to the construction scenario typical of a ring eccentric with respect to the tail skin (CS2). The minimum tail clearance must be situated at the lower quarter of the ring outer side, near the invert, which is consistent with the expected position of a ring erected during uphill excavation and moderate TBM steering around a horizontal curve (see section 8.2).

The longitudinal ram loads present a stepped distribution that is roughly symmetrical about an axis passing through the A3 centroid, i.e.  $60^\circ$  below springline on the outer side of the tunnel horizontal curve (see Figure 8.11.e). Minimum ram loads of 50bar/ram take place at the inner shoulder; maximum ram loads of 200bar/ram are applied to the outer bottom ring quarter. Such loading profile remains roughly constant for the entire advance, with fluctuations smaller than 50bar/ram.

According to the construction scenario CS2, the transverse action of the hydraulic jacks preventing the movement of the lining towards a concentric position will be most effective at those segments where the rams exert the highest axial loads with greatest relative inclination with respect to the ring (see Figure 8.3). Both the field pressure gradients (see Figure 8.11.c and 8.11.d) and the ram load distribution point to A3, and KR3 to a lesser extent, as the segments with most active ram pad-lining interactions. The transverse action of the rams pushes these segments against the sealing system, locking their position and restraining their rotations. If the effect of horizontal pressure gradients is regarded as secondary, the above loading situation must be well described by the 3D FE model *3UKRA*, which can be considered the reference model for CAM3 field data interpretation during AD1.

In the following sections, the field data is analysed in detail to confirm the above hypotheses. Figure 8.11 illustrates the complete field data set on ring behaviour for CAM3 during its cycle1. Figure 7.22 is recalled here to facilitate the comparison between numerical results and field observations.

### 8.5.1.1. Lining pressures

The first CAM3 pressure data set takes place at  $SD < 0.3\text{m}$  (see Figures 8.11.a, 8.11.c and 8.11.d). The ring has not made contact yet with the sealing system and the lining pressures are virtually null.

At the next pressure profile, at  $SD \approx 0.9\text{m}$ , the first two rows of steel wire brushes are touching the ring with more than half the compound pressures directly applied onto CAM3. The lining pressures present a roughly linear gradient with depth of about 30kPa/m and slightly greater pressures at the outer than inner side of the ring. Such pressure distribution indicates that the ring may have encountered the steel wire brushes at an eccentric position: the greatest tail clearance occurs near the crown, where lining pressures are null; the narrowest gap, along segment A3, with peak pressures of about 200kPa.

At the field pressure data set with 1.2m swept distance, the full sealing system has just moved over the ring, particularly at the bottom part of the outer side where the ram stroke is longer. The pressure gradients increase further up to 50kPa/m and 12kPa/m in vertical and horizontal directions; the highest and lowest lining pressures are reached again at segment A3 and E3 respectively, i.e. 360kPa and 60kPa.

## 8.5. Field data interpretation on cycle 1

---

The next pressure profile, at  $SD \approx 1.6\text{m}$ , was captured at the beginning of AS1 and it can be deemed representative of lining pressures at the end of AD1. At this stage, the entire sealing system is in contact with the ring and roughly centred with the segment width,  $W$ , while the ring rear is surrounded by the annular grout. There is a general increase in lining pressures with respect to the previous data set of about 100kPa at the crown and 150kPa near the invert with a minor increase in vertical and horizontal pressure gradients. It can be inferred that at this stage the total action of the steel wire brushes has not changed substantially and thus the grout pressures near the TBM have a fairly axisymmetric distribution.

During AS1, the TBM advance is interrupted. The lining pressures and pressure gradients remain fundamentally constant besides very minor fluctuations that may be related to the repeatability of BOTDR measurements or partially caused by segment movements during the erection of the next ring.

### 8.5.1.2. Hoop membrane behaviour

It was explained in chapter 7 that the radial compression of R1 at its rear, typical of sequential loading during AD1, tends to open the longitudinal joints and to develop hoop tension at the ring front as a result of compatibility of deformations.

The hoop membrane profiles of CAM3 during AD1 are shown in Figures 8.11.i to 8.11.l. At  $SD \approx 0.9\text{m}$ , when the ring is mainly loaded at the rear end of the bottom segments, these lower segments experience significant hoop tensile strains at their front: the BOTDR profile at the TBM side displays peak tensile strains of  $+100\mu\epsilon$  at B3 and  $+50\mu\epsilon$  at KR3 and A3. The lateral hoop tension is corrected with the progressive compression of R1, and by the end of AD1 is reduced to  $+25\mu\epsilon$ .

Figure 8.6.a evidences that the hoop compressive membrane strain at the segment centroid, and thus the total hoop force in the segment, increases with advance. The peak tensile strains developed during AD1 at the TBM end of the longitudinal primary section are directly related to the magnitude of lining pressures acting on the segments except for D3; for example, peak strains barely reach  $+50\mu\epsilon$  at E3 and exceed  $+120\mu\epsilon$  at A3. Except for D3, at the end of AD1 (i.e. first data set of AS1), the hoop tension reduces to values close to  $+50\mu\epsilon$  as the ring carries greater hoop compression; the hoop gradients become smaller as the lining pressures are applied over a wider segment area.

The MN trajectories described by the CAM3 sequential loading during AD1 reflect the typical load paths obtained from FE models subjected to axisymmetric compression (see Figure 8.12.a). The internal force increments at  $SD \approx 1.2\text{m}$  conform quite well to the range delimited by the numerically computed PM lines; the latter represents the proportional relationship between internal force increments for a R1 loaded width of 0.8m, i.e. a total loaded width of 1.6m (see chapter 7). The agreement with the PM lines suggests that contact imperfections at longitudinal joints prior to AD1 are moderate at worst. Most deviations from the predicted load paths occur at the beginning of AD1 but are then partially corrected.

## 8.5. Field data interpretation on cycle 1

During AS1, the TBM stops the advance and the total hoop forces sustained by the ring must remain roughly constant with only minor variations caused by lining movements during the erection of the following ring. In this way, the changes in VWSG hoop strains at segment centroids are negligible and fluctuations in BOTDR strain profiles at the ring centreline can be assigned to the BOTDR repeatability.

Strain gradients are slightly affected by variations in longitudinal ram loads and boundary conditions during AS1. The BOTDR strain profiles experienced at the ring front show fluctuations wider than the dispersion observed in the central BOTDR profile, particularly at the segments subjected to higher ram loads during advance, i.e. KR3, A3 and B3.

The MN trajectories of AS1 in Figure 8.12.b evidence also the low sensitivity of hoop forces to ring assembly, although, like strain gradients, hoop in-plane moments are more variable. By the end of AS1, the MN pairs of most segments concur with the region delimited by the PM lines. The greatest divergences are exhibited by the segments with the narrowest tail clearance and thus with their rotations potentially restrained by the transverse action of hydraulic jacks, i.e. A3 and KR3.

D3 is the segment with the most uneven distribution of ram loads during AD1 with 25bar/ram for two ram sets and 150bar/ram for the third set. It is also the segment opposite to A3 with the lowest mean ram loads and, most likely, with the shortest ram stroke. Consequently, the peak tensile membrane strain in Figure 8.3.a is delayed to the end of AD1 (i.e. first data set of AS1). Despite the total peak tensile strain being quite high, about  $+150\mu\epsilon$ , the  $+50\mu\epsilon$  strain increment and associated increase in strain gradients experienced during AD1 correlate well with the small magnitude of D3 lining pressures.

### 8.5.1.3. Deformed shape, segment curvatures and vertical tilt

#### *a) Ring behaviour during AD1*

Figure 8.11.h illustrates the CAM3 deformed shape at the ring rear. The keystone joint *O* is placed coincident with that of the undeformed shape and therefore only changes in ring shape are relevant in this graph. It is shown that, during AD1, the ring experiences small deformations, particularly at the outer and most longitudinally compressed side, which result in an asymmetric mode of ring distortion. The vertical diameter converges by about 2mm and the horizontal diameter elongates by about 3mm, leading to peak distortion ratios of less than 0.05% the ring diameter *D*.

Figures 8.11.i to 8.11.l and Figures 8.11.m to 8.11.p present the hoop mean strains and curvature diagrams respectively at both the centreline and the TBM side of segments. The deformed ring shape is coupled with the mean strain and hoop curvature diagrams, which agree with the trends in ring behaviour observed in the 3UKRA FE model (see Figure 7.22).



## 8.5. Field data interpretation on cycle 1

---

In the *3UKRA* model, the downward action delivered by the ram pads at the interface with KR3 and A3 segments determined the deformation mode of the rings within  $L_u$ , particularly in the ring in direct contact with the ram pads. This downward action was mainly applied at the KR3 interface through high tangential loads that decreased from the ring springline through knee to invert. The effect of the tangential loads led to hoop tension at the TBM side of KR3 and A3 to a lesser extent together with a sharp drop in compression to almost null values at the keystone joint of KR3 centreline. The ram loads exerted radial reactions predominantly at those sections of the fixed perimeter with a greater tendency to radial displacements, namely outward action at the invert and above the springline. These radial actions resulted in local positive hoop curvatures. The lateral fixity of the ring while subjected to uplift pressures forced the asymmetric distortion of the ring and the upward displacement of B3, which in turn caused the constant hoop tension and negative hoop curvature of the latter. The ring deformations were the greatest for the R1 loaded width of 0.8m, equivalent to  $SD=1.1m$ .

All the above strain and curvature patterns were captured by CAM3 field data with reasonable discrepancies in magnitude given by differences in lining pressure distribution, i.e. vertical gradient and longitudinal profile, and the effectiveness of ram-pad lining restraints. Besides, the BOTDR profiles, with a spatial resolution of 500mm, were expected to smoothen the sharp changes in strain.

For example, at the TBM side, the field data shows tension increasing from KR3 through A3 to B3 with a uniform peak value of  $+75\mu\epsilon$  at B3 and maximum values up to  $+50\mu\epsilon$  in the lower half of A3; in the *3UKRA* model, the above values were  $+50\mu\epsilon$  and  $+25\mu\epsilon$  respectively. At the central profile, KR3 mean compressive strains vary from  $-0\mu\epsilon$  to  $-75\mu\epsilon$  and A3 shows a constant compression of about  $-100\mu\epsilon$  by the end of AD1; in the *3UKRA* model, maximum B3 mean compressive strains were  $-90\mu\epsilon$  and A3 was compressed at  $-100\mu\epsilon$ . The last BOTDR data set of AD1,  $SD\approx 1.6m$ , presents hoop curvatures of about  $+0.40\text{‰}$  at the TBM side and  $+0.65\text{‰}$  at the centreline of A3, whilst the last VWSG curvature at  $SD\approx 1.2m$  is  $0.40\text{‰}$ ; in the *3UKRA* model, peak curvatures were  $+0.30\text{‰}$  and  $+0.25\text{‰}$  at side and centreline respectively. B3 experiences peak field curvatures of about  $-0.50\text{‰}$  for both side and centreline by the end of AD1; the *3UKRA* model yielded  $-0.25\text{‰}$  peak curvatures.

The vertical tilt changes exhibited from ring erection up to a  $SD\approx 1.0m$  are similar to those numerically obtained for a R1 loaded width shorter than 0.8m (see Figure 8.11.b and 7.22). The restrained KR3 and A3 segments undergo a small vertical tilt of about  $-0.025^\circ$  in both cases. The vertical tilt of segment B3, which is free to rotate, oscillates between  $+0.060^\circ$  and  $+0.080^\circ$  while the *3UKRA* model predicted a value of  $+0.110^\circ$ . The discrepancy between measured and numerical vertical tilt of upper segments, particularly at the first half of the advance, may be caused by the inclination of hydraulic jacks (see section 8.2) or their own selfweight under a condition of poor longitudinal compression.

## 8.5. Field data interpretation on cycle 1

---

The longitudinal curvatures are small in all segments (see Figure 8.9.g): A3 displays the highest absolute curvatures at  $SD \approx 1.2\text{m}$ , i.e.  $-0.50\%$ , whilst the curvatures remain within the  $\pm 0.25\%$  interval in the rest of the segments.

Finally, Figure 8.11.f shows that all segment centroids exhibit compressive longitudinal mean strains, which suggests that the circumferential joint between CAM3 and the adjacent rings are fully closed during AD1.

### ***b) Ring behaviour during AS1***

During AS1, the TBM releases the hydraulic jacks sequentially, generally four rams per erected segment, to enable the construction of the new ring. The axial thrust in the active cylinders is evened during this process and the ram load distribution becomes roughly uniform by the end of AD1. There is a reduction in longitudinal loads of about 100bar/ram at KR3, A3 and B3 segments and an increase up to 100bar/ram at D3 and E3, which results in either balanced loads or greater compression at crown than invert (see Figure 8.11.e).

The redistribution of ram loads and the erection of the new ring change the boundary conditions of CAM3 at the TBM side, which by the end of AS1 is no longer in direct interaction with the ram pads. At mid stages of AS1, the ram loads at crown and invert are in the order of 100bar/ram while KR3 and the upper part of A3 maintain the highest loads of 150bar/ram this time. Consequently, the CAM3 crown and invert tend to converge due to the high vertical gradients of the sealing pressures, like in the *3UEKL* FE model (see chapter 7), but with greater squatting on the inner than outer side of the ring (see Figure 8.11.h). By the end of AS1, the ram loads at the invert and inner side decrease to 75bar/ram and so the ring squats further and again more at the inner side.

Overall, the vertical convergence reaches 5mm and the horizontal elongation at the springline grows from 3mm to 8mm, i.e. a ring distortion of 0.12%. This ring distortion ratio is already close to the lower bound recommended by the British Tunnelling Society (BTS) for the design and construction monitoring of circular flexible tunnels in stiff to hard clays, which may be also relevant to chalk tunnels (BTS, 2004). The squatted shape of the ring also proves that the effects of the nearly 60kPa/m vertical pressure gradient prevail over those of the 20kPa/m horizontal gradient.

The first vertical tilt profile of AS1, which corresponds to a ring shape not far from that arisen in AD1, is similar to the vertical tilt diagram of the *3UKRA* model at  $SD \approx 1.6\text{m}$ . However, the in situ vertical tilt at crown and invert segments is slightly smaller and greater respectively than the numerical tilt since the TBM sealing system is roughly centred with the segment width as opposed to the R1 loaded width in the FE model, which is applied at the ring rear.

The changes in ring shape and segment tilt developed in AS1 have an impact on the hoop curvature diagrams (see Figures 8.11.m to 8.11.p). Like in the *3UEKL* model, the ring squatting contributes to

## 8.5. Field data interpretation on cycle 1

the moderate increase in negative bending of KL3 with peak values in the order of -0.25‰. KR3 and A3 are subjected to the highest lining pressures and ram loads and remain the most restrained segments as evidenced by the ring deformed shape. As such, the alternate hoop curvatures of invert segments are kept with moderate increments in A3 VWSG hoop curvatures from +0.40‰ up to +0.70‰. However, KR3 experiences a sharp increase in negative curvatures from virtually -0.00‰ to -0.75‰ which cannot be explained solely by the general ring distortion.

The tilt sensor at KR3 was situated at an angle with the horizontal,  $\gamma$ , of about  $3.5^\circ$  (see Figure 8.13). If it is assumed that the vertical tilt  $\omega$  during AS1 is caused mainly by the radial rotation of segments, which can be particularly true near the springline, the radial rotations  $\theta_r$  and the subsequent change in tail clearance  $\Delta C$  at the TBM side can be calculated with Eq. 8.1 and Eq. 8.2:

$$\theta_r = \frac{\omega}{\sin \gamma} \quad (8.1)$$

and

$$\Delta C = -W \sin \left( \frac{\omega}{\sin \gamma} \right) \quad (8.2)$$

Accordingly, Figure 8.13.b shows the variations in tail clearance associated with the vertical tilt measured in cycle1. It is evidenced that during AD1 the radial rotation of KR3 contributes to increase the tail clearance at the TBM side in a range comprised between 5mm and 11mm. The trend reverses during AS1 where the gap between lining and shield tail narrows down to 5mm, 16mm from the end of AD1. Furthermore, the fluctuations in  $\Delta C$  are roughly synchronised with those exhibited by the centroid curvatures of KR3 in both directions: a reduction in tail gap produces an increase of segment curvatures.

The last VWSG data set at AS1 captures a decrease in curvatures despite the last tilt measurement indicating a reduction in tail gap. Such drop in segment curvatures could be caused by the temporary release of ram loads at KR3 centre, whose effects would not have been captured by the slightly anticipated tilt measurement.

It can be inferred from the above that the sudden increase in KR3 longitudinal curvatures from less than -0.25‰ to about -1.00‰ must be caused by changes in the interaction between the ring and the sealing system triggered by the reduction in tail clearance induced by the segment rotation.

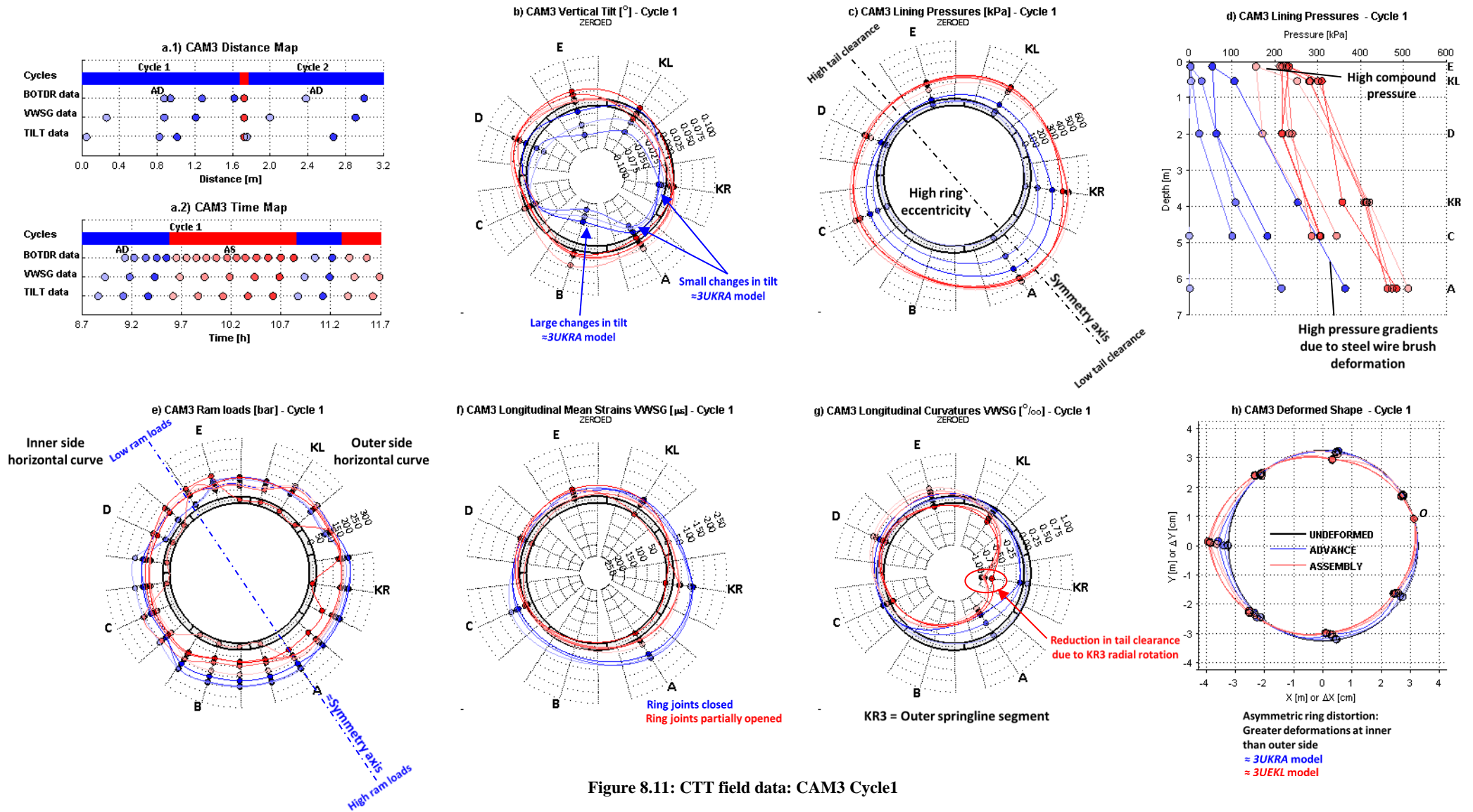
The above observations point clearly to the construction scenario (CS3) of rotated segments typical of outer springline segments in tunnel sections with curved horizontal alignments. Given that both curvatures at the segment centroid are negative, it can be inferred that the segment bending is caused by the sealing pressures acting near its centroid; thus, the direct contact between the shield tail and the segment is excluded.

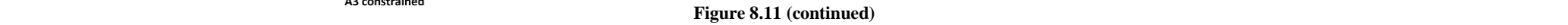
## 8.5. Field data interpretation on cycle 1

---

The changes in longitudinal curvatures of other CAM3 segments are small during AS1. The longitudinal mean strains drop during AS1 to null compression by the end of AS1 for most segments.

## 8.5. Field data interpretation on cycle 1









## 8.5. Field data interpretation on cycle 1

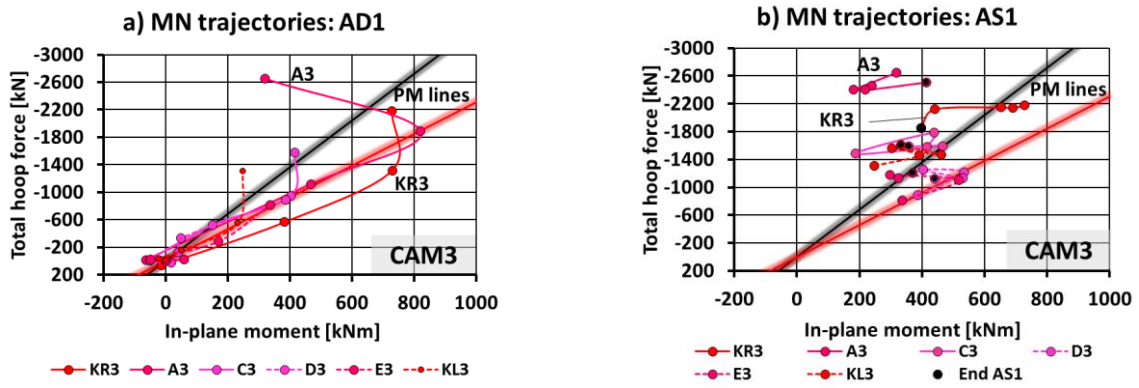


Figure 8.12: CAM3 MN trajectories in cycle1

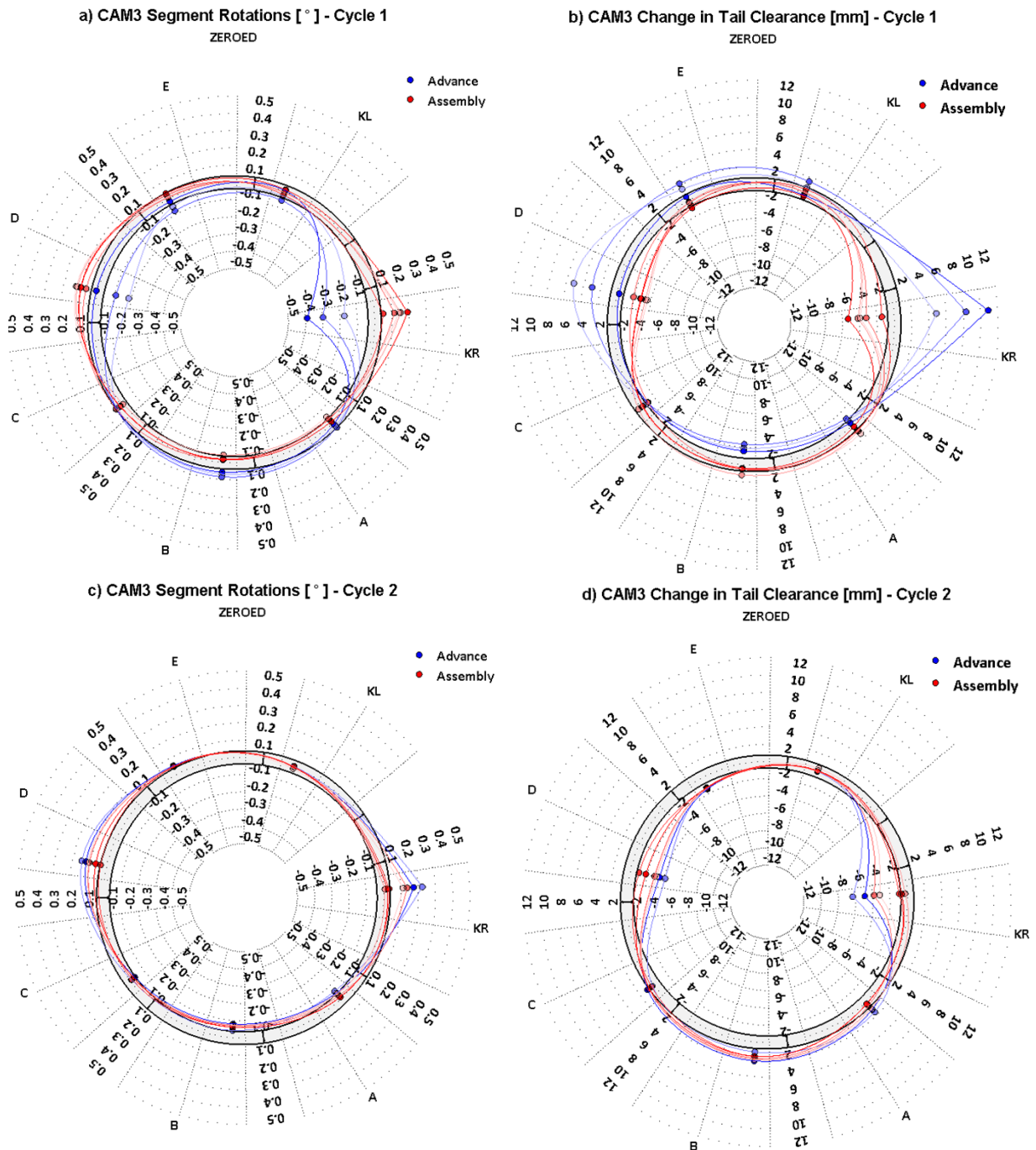


Figure 8.13: CAM3 segment rotation and change in tail clearance



### 8.5.2. CAM4 ring

During AD1, CAM4 was subjected to  $M_y$  moments in the order of 15MNm to facilitate the TBM steering around the horizontal curve and negligible  $M_z$  (see Figure 8.10). The lining pressures exhibited vertical gradients smaller than in CAM3, up to 25kPa/m, and virtually null horizontal gradients. The calibration of the sequential tunnel beam model revealed the need for net horizontal TBM loads in the ten advances following CAM4 erection.

The peak vertical pressure gradient suggests that CAM4 is also subjected to the construction scenario typical of a ring eccentric with respect to the tail skin (CS2). The minimum tail clearance must be situated around the centre of the ring invert this time. The moderate magnitude of peak vertical gradients, closer to the grout-static value of 12.5kPa/m, also points to a lesser eccentricity between the ring and the tail skin.

The ram load distribution during AD1 corresponds to the early stages of a period of pronounced TBM steering around a horizontal curve: on the outer and invert segments, ram loads are about 250bar/ram; in the remaining segments, loads are in the order of 150bar/ram. The symmetry axis is oriented at 8.2° below the outer side of the springline near the B4 centroid. The loading profile is kept constant during AD1 with limited variations of about 50bar/ram (see Figure 8.14.e).

The ring position relative to the tail skin inferred from the field pressure gradients suggests that the hydraulic jacks with greatest load inclination must be positioned at the invert, at least at the beginning of the advance. The ram load distribution indicates that, with the progress of AD1, the interface between the ring and hydraulic jacks may transition towards that typical of horizontal TBM steering where the horizontal angle between segments and rams should be expected to increase. Consequently, the in situ ring behaviour of CAM4 may respond to two foreseeable scenarios: one where there is a change in orientation of tail clearance in the original construction scenario CS2; or a second scenario where there is a combination of the initial CS2, i.e. ring eccentricity, and the construction scenario CS3 with the rotated segment situated at the outer side of the springline (see section 8.2).

The initial construction scenario CS2 can be described with the *3UAB* FE model bearing in mind that the magnitude of vertical pressure gradients on the field, 25kPa/m, is much smaller than in the numerical simulations,  $\approx 80$ kPa/m.

In the following sections, the field data is analysed in detail to confirm the above hypotheses. Figure 8.14 illustrates the complete field data set on ring behaviour for CAM4 during its cycle1. Figure 7.16 is recalled here to facilitate the comparison between numerical results and field observations.

#### 8.5.2.1. Lining pressures

The evolution of CAM4 lining pressures is similar to that of CAM3 with differences given by the relative position between ring and shield tail.

## 8.5. Field data interpretation on cycle 1

---

The first CAM4 pressure data set takes place at a  $SD < 0.3\text{m}$  (see Figures 8.14.a, 8.14.c and 8.14.d). The ring has not made contact yet with the sealing system and lining pressures are virtually null.

At  $SD \approx 0.8\text{m}$ , the first two rows of steel wire brushes are touching the ring with more than half the compound pressures directly applied onto CAM4. The lining pressures present a roughly linear gradient with depth less than  $10\text{kPa/m}$  and slightly greater pressures at the outer than inner side of the ring. Such pressure distribution indicates that the ring may have encountered the steel wire brushes at a moderate eccentric position: the greatest tail clearance occurs near the crown, where lining pressures are  $40\text{kPa}$ ; the narrowest gap, along segment D4, with peak pressures of about  $100\text{kPa}$ .

At the field pressure data set with  $SD \approx 1.4\text{m}$ , the full width of the sealing system acts roughly centred with  $W$ . The vertical pressure gradients increase further up to  $25\text{kPa/m}$  at negligible horizontal gradients; the highest and lowest lining pressures are reached again at segment KR4 and D4 respectively, i.e.  $120\text{kPa}$  and  $300\text{kPa}$ . The KR4 lining pressure is smaller than the CAM3 pressure at the narrowest tail clearance, which may indicate that the sealing compound pressure during CAM4 cycle1 remained about 1bar lower than in CAM3 cycle1 after the groundwater leakage experienced through the sealing system right before CAM4 ring erection (see Figure 8.14.d).

During AS1, the lining pressures and vertical pressure gradients have greater fluctuations than in CAM3 AS1: the dispersion of lining pressures at the crown, invert and the outer springline segment B3 over this period is around  $100\text{kPa}$ .

### 8.5.2.2. Hoop membrane behaviour

The CAM4 profiles of hoop membrane strains during AD1 are illustrated in Figures 8.14.i to 8.14.l. The initial hoop mean strains at segment centroids in Figure 8.14.i evidence that there is no net hoop compression in the ring before it is directly loaded by the sealing pressures. In following profiles, the total hoop force sustained by the ring increases progressively with lining pressures, and thus the strain distribution is roughly symmetric about the ring vertical axis.

The BOTDR ring profiles include the lateral deformations caused by the longitudinal compression of the hydraulic jacks. Consequently, the ring exhibits high hoop tension at the most longitudinally loaded segments even at central profiles, e.g. C4 experiences tensile strains close to  $+100\mu\epsilon$  at the beginning of AD1. At the ring centreline the hoop tension is uniformly distributed over the length of all segments, except for B4; at the TBM side the BOTDR captured the sinusoidal-like fluctuations caused by the ram load spread at invert segments.

Like in CAM3, Figure 8.8.a shows that the peak tensile strain increments developed during AD1 at the TBM end of the longitudinal primary section are directly related to the magnitude of lining pressures acting on the segments; for example, peak strains grow by less than  $+50\mu\epsilon$  at KR4 and exceed the  $+100\mu\epsilon$  increments at invert segments. Both segments C4 and D4 reach peak tensile strains of about  $+75\mu\epsilon$  during AD1, even though C4 exhibits a marked negative hoop gradient after ring erection. It

## 8.5. Field data interpretation on cycle 1

may be inferred that the initial in-plane angularities at longitudinal joints with contact at the front of segments can be corrected by the sequential loading of the ring near the tail skin.

By the end of AD1 (i.e. first data set of AS1), the hoop gradients become smaller as the lining pressures are applied over a wider segment area. All longitudinal primary sections are in full compression except for B4, which displays hoop tension at the TBM side greater than  $+50\mu\epsilon$ .

In CAM4 there is a wider scatter in MN trajectories than in CAM3 (see Figure 8.15.a). Most deviations from predicted trends occur at the beginning of AD1 but are partially corrected by the end of it. B4 presents the greatest divergence from the PM line region, with too high in-plane moments for the magnitude of hoop force. Given the proximity of the longitudinal primary section to the longitudinal crack/s detected by BOTDR strain measurements (see chapter 5), it is reasonable to deduct that the hoop strains calculated at mid lining depth may be biased by the uneven cross-sectional strain distribution in the cracked region, leading to longer segment widths with apparently higher membrane tension. This is also reflected by the hoop mean strain distribution of BOTDR profiles at B4 with marked tensile peaks at the location of the longitudinal crack/s.

Like in CAM3, the changes in VWSG hoop strains at segment centroids observed during AS1 are small and the fluctuations in BOTDR strain profiles at the ring centreline can be assigned to the BOTDR repeatability. Again, strain gradients are slightly affected by variations in longitudinal ram loads and boundary conditions with the erection of the next ring. The BOTDR strain profiles at the ring front show also fluctuations wider than at centreline profiles, in this occasion mainly at the upper segments and with the temporary release of hydraulic jacks.

The MN trajectories during AS1 in Figure 8.15.b display greater oscillations in total hoop forces than in CAM3 at comparable variations of hoop in-plane moments. By the end of AS1, when the sealing pressures are roughly centred with  $W$ , the MN pairs of all segments but B4 are comprised within the region delimited by the numerical PM lines. B4 is this time the segment with the greatest disparity by the end of AS1 due to an excessive in-plane moment. Drawing an analogy with the CAM3 MN pairs, it could be deducted that B4 is the segment with the narrowest tail clearance and greatest restraints in segment rotations imposed by the transverse action of hydraulic jacks, at least by the end of AS1.

### 8.5.2.3. Deformed shape, segment curvatures and vertical tilt

#### a) *Ring behaviour during AD1*

Figure 8.14.h illustrates the CAM4 deformed shape at the ring rear. The moderate vertical pressure gradients of about 25kPa/m exerted by the sealing system during AD1 and the effective ring coupling ensured by the high loads applied by the hydraulic jacks translate into a very limited ring distortion of less than 0.03%. Both the squeezed ring shape and the hoop diagrams presented in Figures 8.14.i to 8.14.p agree with the trends in ring behaviour observed in the 3UAB FE model, with in-plane ring fixity at the invert segments A and B (see Figure 7.16).

## 8.5. Field data interpretation on cycle 1

---

In the *3UAB* model, the downward action delivered by the ram pads at the interface with the invert segments determined the deformation mode of the rings within  $L_u$ , particularly in the ring in direct contact with the ram pads. This downward action was mainly applied at the far ends of both invert segments, near the ring knees through high tangential loads that decreased towards the invert. The effect of the tangential loads led to hoop tension at the TBM side of the invert segment together with a sharp drop in compression to almost null values at the centreline of knee joints. The ram loads exerted radial reactions predominantly at those sections of the fixed perimeter with a greater tendency to radial displacements, namely outward action at the knees and inward action at the invert. These radial actions resulted in predominantly positive hoop curvatures at invert segments with minor negative spikes near the invert. The vertical elongation of the ring also led to negative hoop curvatures of the bottom segments adjacent to the invert segments. The ring deformations were the greatest for the R1 loaded width of 0.8m, equivalent to  $SD \approx 1.1\text{m}$ .

The above strain and curvature patterns can be generally observed in the CAM4 field data considering the limitations given by the monitoring technology and the differences between lining pressures and ram-pad lining restraints in the field and in the numerical simulation. At the last BOTDR and VWSG data sets, with  $SD \approx 1.5\text{m}$ , the total width of the sealing pressures is applied on the ring at a roughly centred position. The numerical simulations terminate with a 0.8m R1 loaded width placed at the ring rear. Consequently, there must be some additional disparity between numerical and field strain quantities at this last data set.

The BOTDR hoop mean strain profile at the TBM side evidences fluctuations in tensile strains very similar to those in the *3UAB* model if the influence of B4 longitudinal cracks is ignored. At the centreline, the reduction in hoop compression at the knees is clearly captured at the inner side of the ring, i.e. segments D4 and E4, but it appears to be masked at the outer side. As discussed, the BOTDR strains comprise lateral hoop deformations caused by the Poisson effect and therefore reach tensile values greater than those numerically predicted in both ring profiles, particularly at the most longitudinally loaded segments.

The VWSG hoop curvatures, excluding the last data set, are in good agreement with the *3UAB* model: the second ring diagram at  $SD \approx 0.8\text{m}$  shows positive hoop curvatures of about 0.25‰ at the centroid of invert segments as in the *3UAB* model. At the lower sides, the hoop curvatures grow in B4 from -0.07‰ to -0.55‰ and are kept close to zero in E4; in the *3UAB* model both segments experience similar negative hoop curvatures around -0.40‰. In the upper segments, the hoop curvatures are small in both cases. The BOTDR strain profiles, excluding the last one, display a similar resemblance with the numerical diagrams of hoop curvatures.

In the last data set of field curvatures, the positive hoop curvatures at invert segments either become almost null keeping the vertical symmetry, like in the VWSG ring profile, or change to a distribution

## 8.5. Field data interpretation on cycle 1

---

with alternate curvatures, which were typical of the numerical models with lateral fixity such as the *3KRA* model recalled in 8.5.1 or the *3UKR* model with ram pad restraints only at the springline segment KR (see chapter 7). From  $SD \approx 0.8\text{m}$  onwards, there is a pronounced negative curvature at the TBM side of the springline segment, B4, and the hoop tension increases evenly along the length of the invert segments at the TBM side; both patterns can be observed in the *3UKR* model.

The coexistence of the above trends in hoop deformations with significant vertical pressure gradients suggests that there is indeed a shift in the position of constrained segments towards the outer springline segment B4 without a substantial change in the overall ring eccentricity; that is, the initial CS2 scenario is later combined with the CS3 scenario of a rotated segment situated at the outer springline of a horizontal curve (see section 8.2).

The evolution in tail clearance during AD1 contributes to the validation of the above hypothesis (see Figure 8.16.b). At  $SD \approx 0.5\text{m}$ , the tail clearance at the front of B4 is already reduced by 5.5mm due to the radial rotation of the segment. At  $SD \approx 1.1\text{m}$ , the tail clearance is decreased by 8.8mm. By the end of AD1, i.e. at the first data set of AS1, the tail gap reduction reaches a peak of 11.2mm. Conversely, the radial rotation of the other segments does not influence their tail clearance significantly.

The history of B4 curvatures during AD1 is synchronised with the changes in tail clearance. There is a progressive increase in VWSG negative curvatures with advance, e.g. from null values to about -0.76‰ and -1.10‰ in hoop and longitudinal directions respectively (see Figure 8.14.g). Given the nature of the biaxial bending with negative curvatures in both directions, it can be ascertained that there is local concentration of sealing pressures around the segment centroid but no contact with the shield tail.

These local loads of the sealing system on B4 have also an influence on the response of the adjacent segments. The inward radial action squeezes mildly the outer side of the ring (see Figure 8.9.h), particularly at the upper part given that the invert must be partially restrained by the ring eccentricity. In this line, segment A4 experiences an increase in positive hoop curvatures up to +0.30‰ that is simultaneous with that of B4 curvatures.

It was discussed in chapter 5 that the DFOS mapping of hoop strains enabled the detection of temporary longitudinal cracking at the intrados of segment B4 near its midlength. The tensile strain at imminent cracking was first exceeded at the second BOTDR measurement, at  $SD \approx 0.8\text{m}$ , where the peak intrados raw strain at the TBM side approached +150µε. In the following data set, the crack/s propagated towards the segment centroid without reaching the strain gauge position and the peak tensile strains were kept around +300µε and +250µε at the TBM side and centreline respectively for the rest of the advance (see Figure 5.33.a, p.134). This longitudinal flexural cracking affected the BOTDR profiles of segment B4, which are characterised by a computed loss of hoop compression and marked negative curvatures at the segment midlength.

## 8.5. Field data interpretation on cycle 1

---

The vertical tilt of segments C4 and D4 follows a trend similar to that of the invert segments in the 3UAB model. Their negative tilt peaks only to about  $-0.050^\circ$  given the smaller magnitude of field vertical pressure gradients. However, the evolution of vertical tilt in the remaining segments diverges from the numerical diagram, particularly at the crown and outer side segments.

Figure 8.16.a shows the radial rotations inferred from the vertical tilt measurements during cycle1. The A4 and B4 segments at the outer side rotate outwards during AD1, particularly B4 with peak rotations of  $0.31^\circ$ . The outward rotations of the outer side segments with highest values at the springline agree with the hypothesis built for the construction scenario CS3: with pronounced TBM steering around a horizontal curve, the oblique inclination of the hydraulic jacks against the ring drives the outer side segments towards the shield tail, especially near the springline (see section 8.2). The vertical and radial rotations of crown and invert segments are hardly affected by the transverse action of the ram pads. The crown segment, however, rotates inwards up to about  $-0.050^\circ$  by the end of AD1.

The changes in longitudinal curvatures along the ring circumference during AD1, besides the case of B4, could be caused by an increase in the angle between hydraulic jacks and lining due to the TBM steering around the horizontal curve and the longitudinal deflection of the lining (see section 8.2). The transverse action of the ram pads is proportional to the ram loads and is directed towards the outer side of the curve. Consequently, the outer side should experience negative increments in longitudinal curvature of greater magnitude than the positive increments undergone by the inner side (see Figure 8.14.g).

### ***b) Ring behaviour during ASI***

In CAM4, the sequential erection of the next ring was roughly coordinated with the VWSG data collection. The fluctuations in segment curvatures, vertical tilt and radial rotation plus the minor changes in ring distortion are directly related to the sequence of ram load changes.

For example, in the first VWSG data set, four hydraulic jacks are released between KR4 and A4. The two segments rotate slightly inwards due to selfweight, and the absence of transverse loads in the case of A4, while the negative longitudinal curvatures drop proportionately by 0.25‰ and 0.40‰ respectively. In the second data set, the next ram set is released from A4 and B4 segments and the previous loads restored to 100bar/ram. The radial rotation decreases at B4 and both A4 and B4 segments experience a reduction in hoop and longitudinal curvatures. Then, the ram set between B4 and C4 is released and the preceding set reloaded. The radial rotation in B4 becomes almost null, which reinstates the tail clearance close to initial values. The B4 curvatures are thus further decreased to -0.55‰ and -0.25‰ in longitudinal and hoop directions and the squeezed ring distortion is partially corrected at the outer side. In the following stages, the invert segments reach roughly null vertical tilt while the longitudinal curvatures become smaller.

## 8.5. Field data interpretation on cycle 1

---

By the end of AS1, the ram loads are evenly distributed at 100bar/ram. The longitudinal curvatures are generally smaller. The reduction in hoop curvatures at segment B4 is coupled with a decrease in hoop tension, which indicates that the longitudinal crack partially closed during AS1.

## 8.5. Field data interpretation on cycle 1

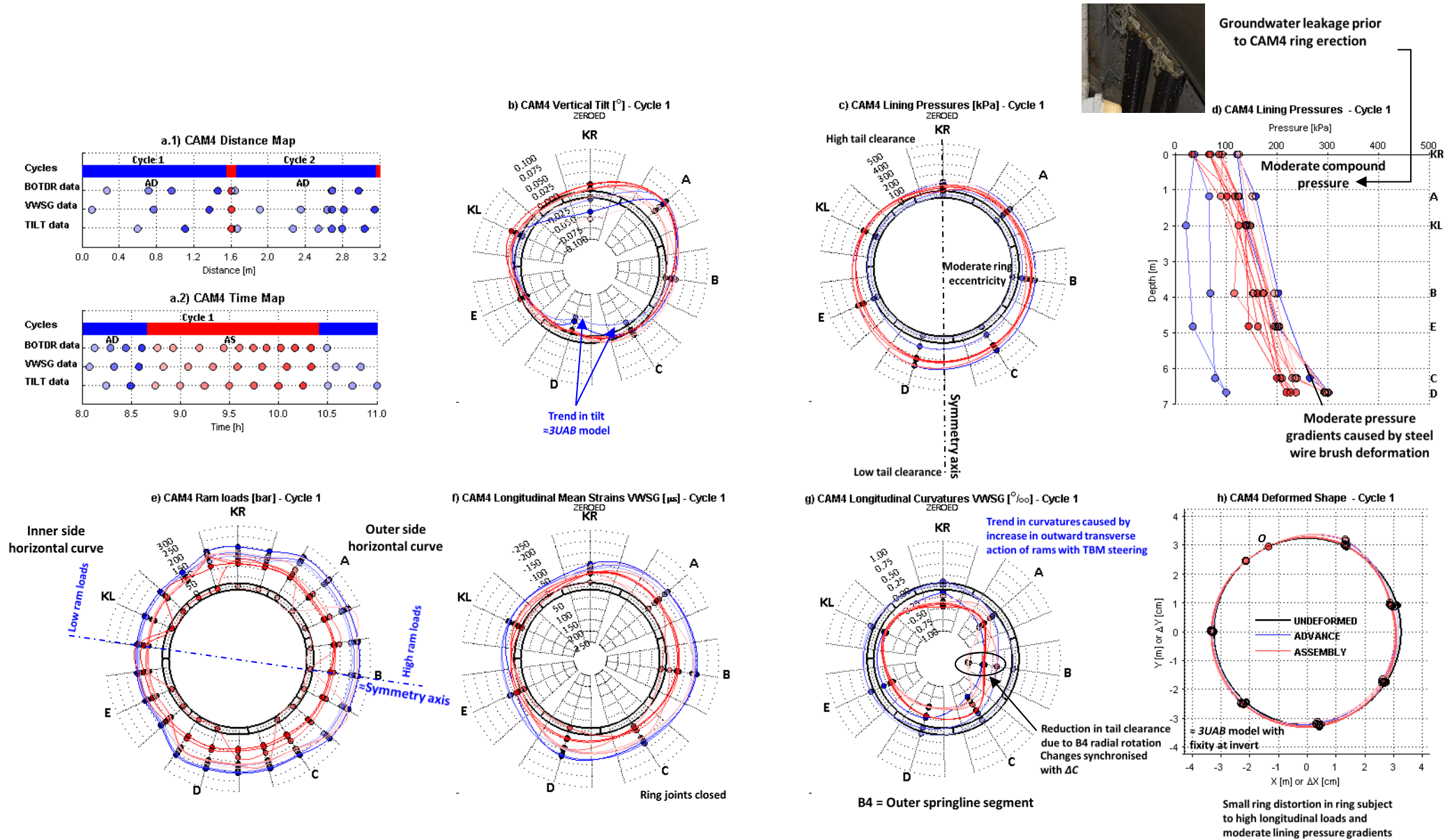


Figure 8.14: CTT field data: CAM4 Cycle1



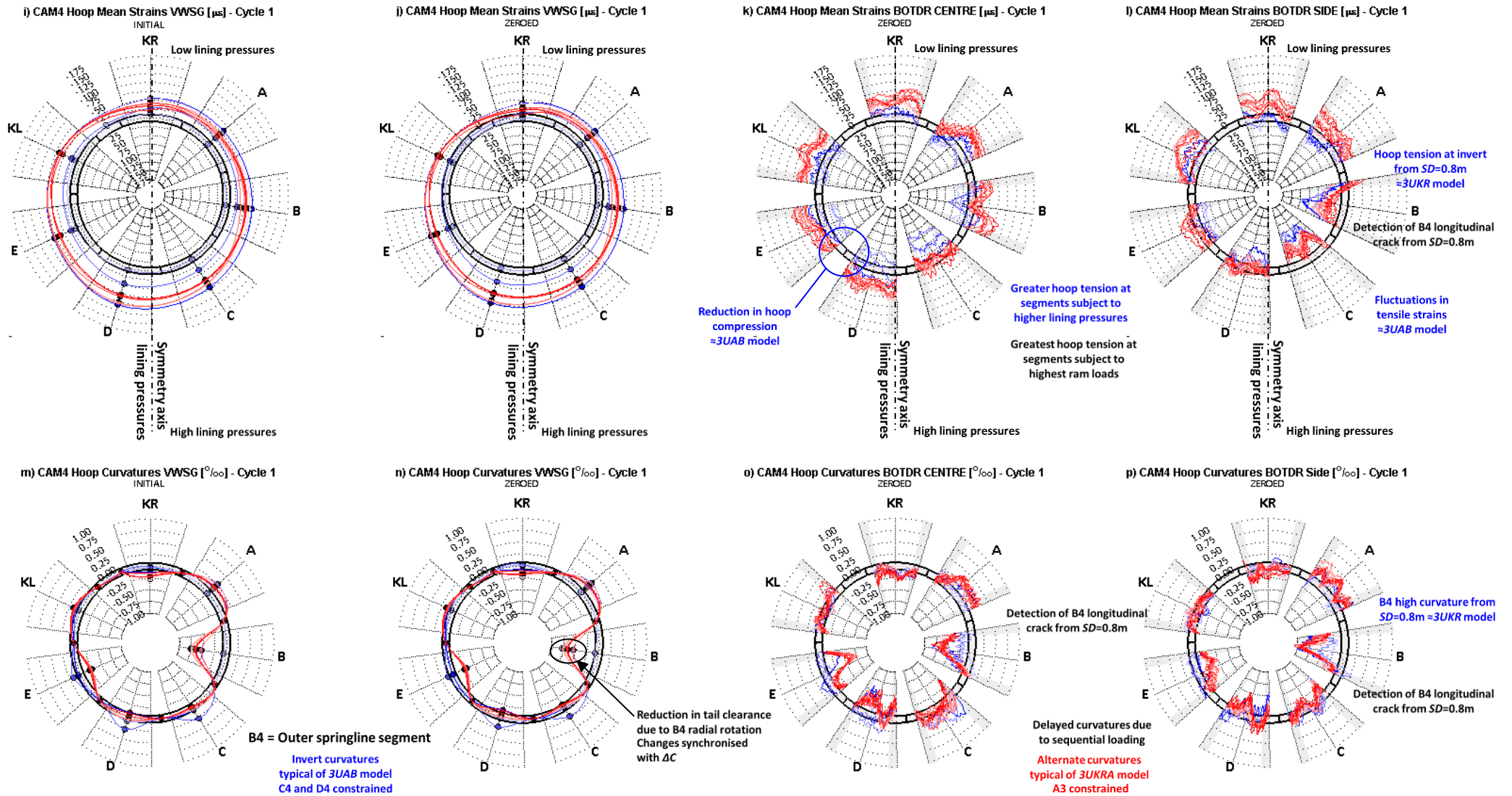


Figure 8.14 (continued)

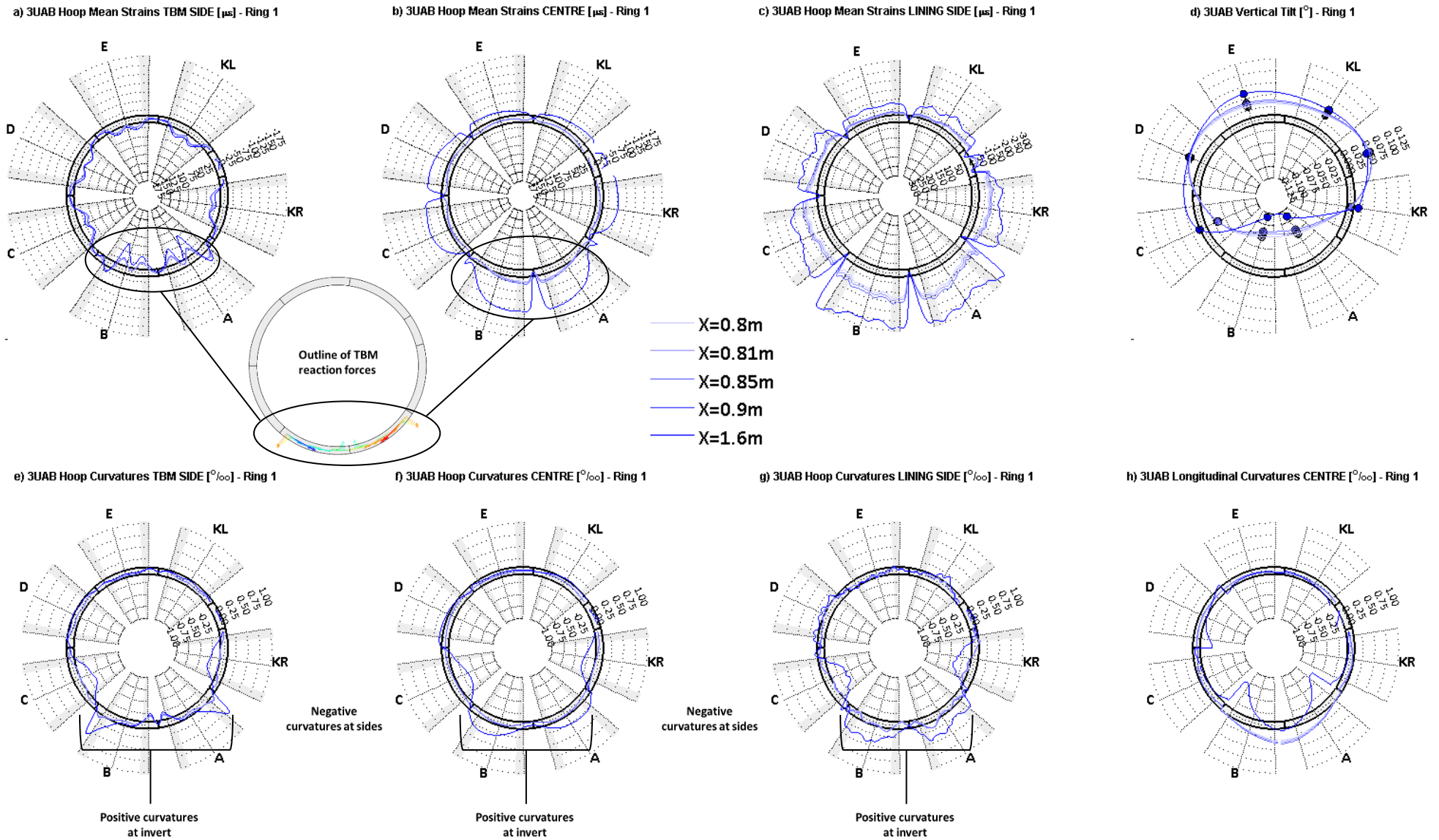


Figure 7.16 (repeated): 3UAB model

## 8.5. Field data interpretation on cycle 1

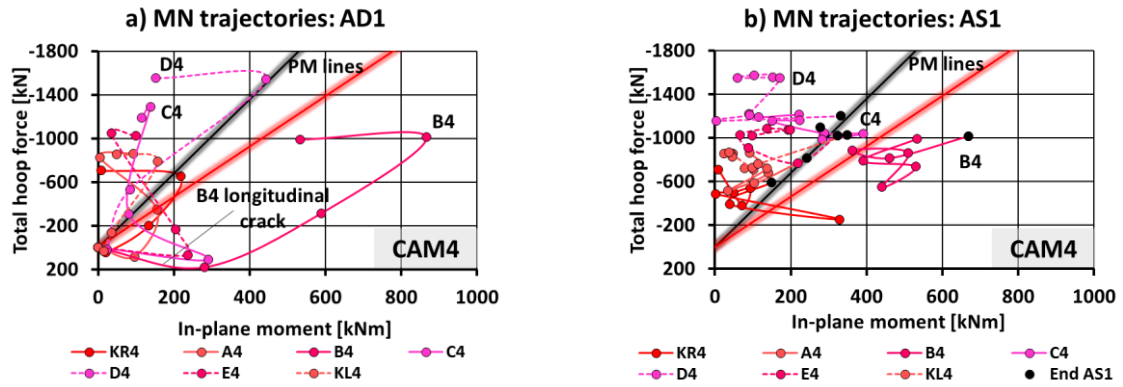


Figure 8.15: CAM4 MN trajectories in cycle1

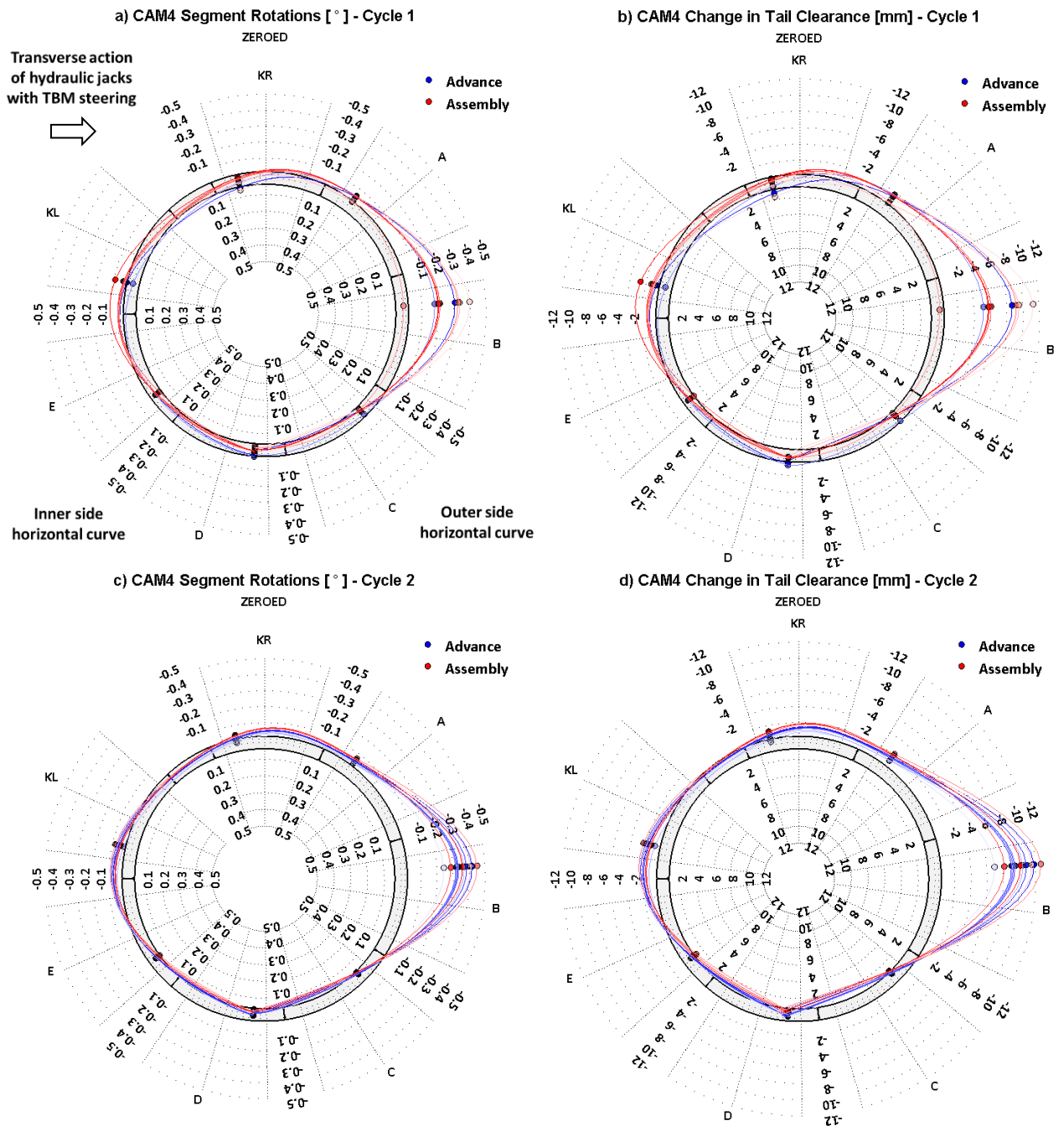


Figure 8.16: CAM4 segment rotation and change in tail clearance

### 8.6. Field data interpretation on cycle 2

#### 8.6.1. CAM3 ring

##### 8.6.1.1. Lining pressures

At the first pressure data set in AD2, with  $SD \approx 2.0\text{m}$ , a  $0.775\text{m}$  ring width is still directly loaded by the sealing system, the first row of steel wire brushes has shifted to the following ring, but is very near the CAM3 ring, and more than half of the ring is subjected to tail void pressures at its rear (see Figures 8.17.a, 8.17.c and 8.17.d). Consequently, the computed lining pressures continue to grow with constant vertical gradients by about  $50\text{kPa}$ . The calculated lining pressures at KR3 increase by  $120\text{kPa}$  from the last data set in AS1 with the reinstatement of the outward radial rotations (see Figure 8.13).

At the next data set, with  $SD \approx 2.9\text{m}$ , the ring has fully emerged from the tail skin. Without the direct action of the steel wire brushes, the vertical and horizontal pressure gradients drop dramatically. There is no significant change in E3 pressures at the crown, which is consistent with the assumption that crown segments were erected with the widest tail clearance. The residual values of vertical and horizontal gradients,  $10\text{kPa/m}$  and  $7\text{kPa/m}$  respectively, are caused by the proximity of the sealing pressures acting on the following ring.

At the first AS2 data set, captured at  $SD \approx 3.3\text{m}$ , the back of the sealing system is about  $0.325\text{m}$  away from the ring. There is a roughly uniform decrease of lining pressures, with crown pressures reducing from  $280\text{kPa}$  to  $230\text{kPa}$ . The pressure gradients become null, evidencing that there is already ring equilibrium against uplift forces.

By the end of AS2, the lining pressures are slightly reduced in a uniform manner so that the crown pressures reach values close to hydrostatic, i.e.  $190\text{kPa}$ . The  $100\text{kPa}$  decay in lining pressures up to hydrostatic values since AD2 and over the  $1.25\text{h}$  duration of AS2 suggests that BGs in the tail void of tunnels excavated in stiff and permeable grounds can be subjected to a relatively quick grout consolidation.

##### 8.6.1.2. Hoop membrane behaviour

The evolution of hoop membrane strains at the mid length of CAM3 segments is consistent with the assumed displacement of sealing pressures with the TBM advance.

At  $SD \approx 2.0\text{m}$ , with the front half of the ring loaded by sealing pressures and the rear half by grout pressures, there is a general increase in centroid compressive strains with the rise of mean lining pressures (see Figure 8.6.b). The positive hoop strain gradient becomes slightly smaller in KR3 and A3 as the sealing system shifts towards the next ring. However, as discussed in section 8.5.1.2, the shortest stroke at the inner side of the curve delays the advance of the sealing pressures, and therefore the segments in this region still experience a slight increase in positive hoop gradients.

## 8.6. Field data interpretation on cycle 2

---

At the next data set, the sealing pressures are fully acting on the following ring. The hoop strains at the segment centroid denote a reduction in total hoop compression in consonance with the release of mean lining pressures. The hoop strain gradients are clearly reversed at segments KR3 and A3, which exhibit compressive strains in the order of  $-200\mu\epsilon$  at the rear extreme fibre. The peak tensile strains, this time at the ring rear are very small. Conversely, the changes in hoop gradients of upper segments are negligible and therefore peak tensile strains are still in the order of  $+150\mu\epsilon$  in the cracked D3 and around  $+50\mu\epsilon$  in the other segments. The above changes suggest that the next ring is subjected to a lining pressure distribution similar to that of CAM3 in cycle1 and thus it must present a similar ring eccentricity.

Figures 8.17.i to 8.17.l also confirm that at the ring outer side there is first a progressive shift of hoop compression from the ring front to the ring rear followed by a trend towards uniform hoop compression along the ring width. The ring diagrams also show that there is a good correlation of VWSG and BOTDR hoop mean strains near the ring centreline.

At the first data set of AS2, with a greater distance of the sealing system, the total hoop force in the segments is further decreased (see Figure 8.6.b). The negative gradient of hoop strains is also attenuated in all segments, particularly at KR3 and also A3 with a certain delay.

During AS2, the fluctuations in both total hoop force and hoop gradients are small for all the segments. The numerous BOTDR profiles captured during AS2 show the progressive reduction in mean hoop strains at the TBM side of KR3 and A3. By the end of AS2, the lower segments present a fairly uniform distribution of hoop strains at mid length; the upper segments display substantial positive gradients as the tensile strains reached by the end of AD2 were hardly corrected.

### 8.6.1.3. Deformed shape, segment curvatures and vertical tilt

#### a) *Ring behaviour during AD2*

During AD2, the ram load distribution is fairly uniform in the order of 150bar/ram with slightly greater compression at the outer side than the inner side of the ring, 170bar/ram against 100bar/ram respectively (see Figure 8.17.e).

Despite the vertical and horizontal pressure gradients decreasing from about 55kPa/m and 20kPa/m to 10kPa/m and 7kPa/m respectively within the advance, the deformed shape remains unchanged (see Figure 8.17.h). This insensitivity of the ring to drastic changes in lining pressures indicate that the joint rotations developed in cycle1 are hardly recoverable and will tend to become permanent features of the constructed tunnel.

The vertical tilt diagram resembles quite well the numerical results of R2 in the 3UKRA model, where the crown and invert segments of R2 tilt positively with the sequential loading of R1 (see Figure 5.17.b). The position of A3 and B3 tilt sensors at the knee and invert respectively can explain partially

## 8.6. Field data interpretation on cycle 2

---

the difference in vertical tilt between the two. However, given that the radial rotations are greater at B3, the tilt measurements may indicate that there is also fixity in the next ring at the bottom outer side.

The VWSG hoop curvature diagram at  $SD \approx 2.0\text{m}$  is almost identical to that displayed at the first data set of AS1, particularly at the outer side of the ring, and therefore exhibits curvatures at KR3, A3 and KL3 greater than those by the end of AS1 (see Figure 8.17.n). When the ring is finally outside the tail skin, at  $SD \approx 2.9\text{m}$ , the hoop curvatures at the outer side return to values either equal to those reached by the end of AS1, e.g.  $+0.5\text{‰}$  at A3 centroid, or smaller,  $-0.25\text{‰}$  for both KR3 and KL3 segments (see Figures 8.17.n to 8.17.p).

The evolution of hoop curvature diagrams supports the shift of the uneven sealing pressures with swept distance. In the first half of AD2, the hoop curvatures at the outer side segments are distributed quite uniformly along the ring width, particularly at A3. However, in the second half of AD2, the A3 peak curvatures are greater at the ring front by about  $+0.25\text{‰}$  than at the centreline. Likewise, in KR3, peak curvatures of  $-0.75\text{‰}$  are now reached at the TBM side while dropping to  $-0.25\text{‰}$  at the centreline.

The radial rotation of the KR3 segment narrows slightly the tail gap at the very beginning of AD2 leading to a total reduction of 6.3mm (see Figures 8.13.c and 8.13.d). In this way, the reinstatement of the concentrated sealing pressures at KR3 can explain the increase in the hoop curvatures of the first data set during AD2. At  $SD \approx 2.7\text{m}$ , only the last row of steel wire brushes is still in contact with the ring front and the tail clearance widens back to initial values. Consequently, the hoop curvatures at the outer side become smaller.

The longitudinal curvatures at the beginning of AD2 are very similar to those experienced by the end of AS2 (see Figure 8.17.g). There is only a minor increment in the negative curvature of the KR3 segment that brings it back to the value reached at the beginning of AS1. It is again caused by the bidirectional flexure of the segment under the higher local sealing pressures. At  $SD \approx 2.9\text{m}$ , there is a sudden change in the longitudinal curvatures of KR3 and A3 towards  $+0.25\text{‰}$  and  $0.00\text{‰}$  as a result of the total release of the sealing pressures directly acting on the ring.

### ***b) Ring behaviour during AS2***

In the second ram load data set, the longitudinal loads are generally 50bar/ram smaller than during AD2, which brings the ram loads at segments C3, D3 and E3 to values close to 50bar/ram. With such distribution, it can be inferred that most of the action of the hydraulic jacks is still delivered at the outer side of the ring at this stage. The next ring may tend to squat under the uplift action of sealing pressures in a way similar to CAM3 during AS1, dragging CAM3 into further ring distortion. In this line, the CAM3 deformed shape at the second tilt measurement within AS2 shows that the inner side of the ring moves upwards, particularly at the knee joint, without any significant changes in deformed

## 8.6. Field data interpretation on cycle 2

---

shape at the outer side. The vertical convergence increases to about 5mm and the horizontal convergence is kept constant.

By the end of AS2, the ram loads become roughly axisymmetric with values close to 100bar/ram in all segments. The reduction of hoop curvatures in 0.25‰ at the ring front of A3 by the end of AS2 may be caused by the decrease in the radial forces applied by the oblique hydraulic jacks onto the restrained segments. In the same way, the weaker ring interaction reduces the magnitude of vertical tilt in all segments and of the positive longitudinal curvatures except at the invert.



## 8.6. Field data interpretation on cycle 2

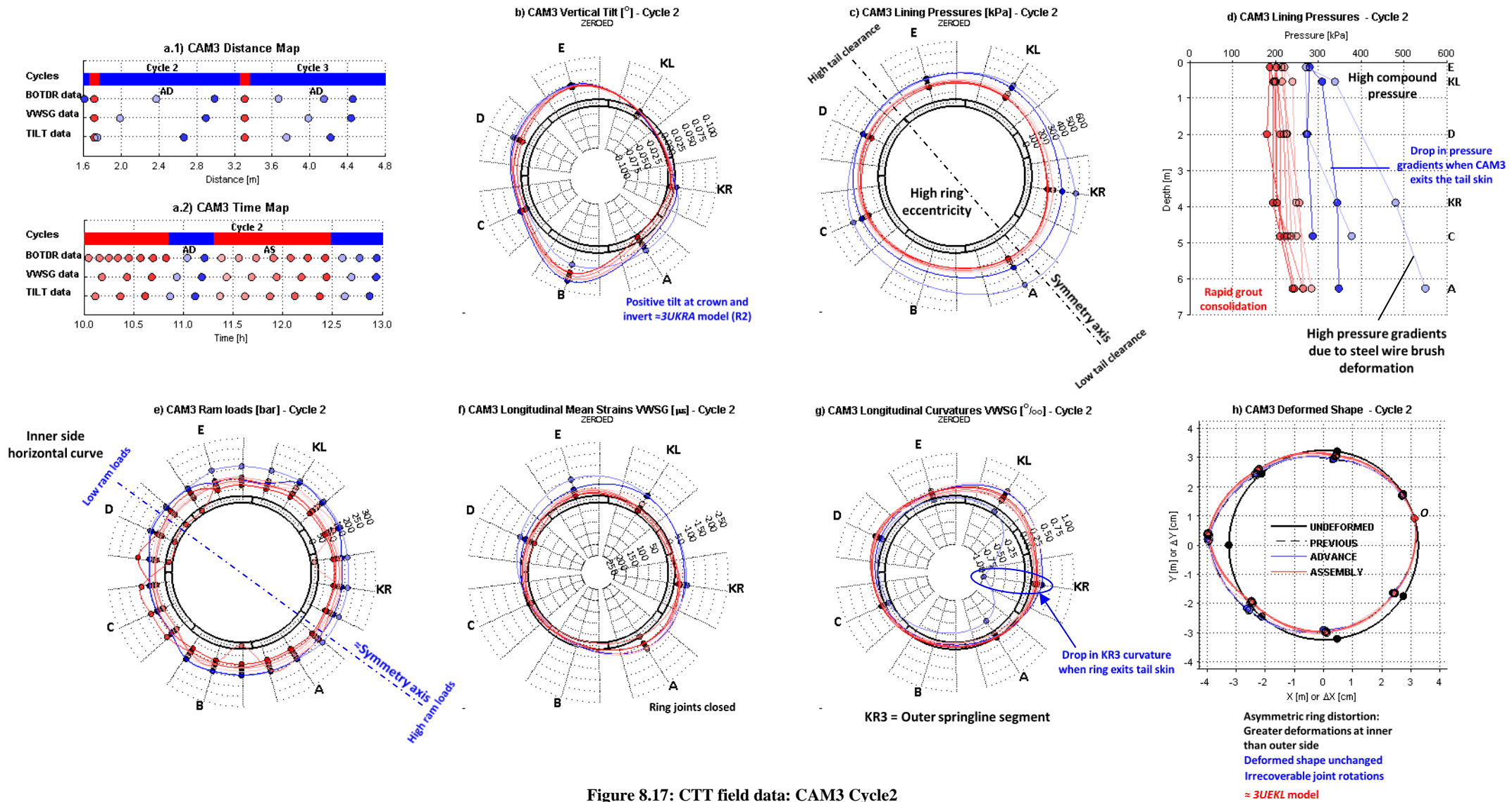


Figure 8.17: CTT field data: CAM3 Cycle2



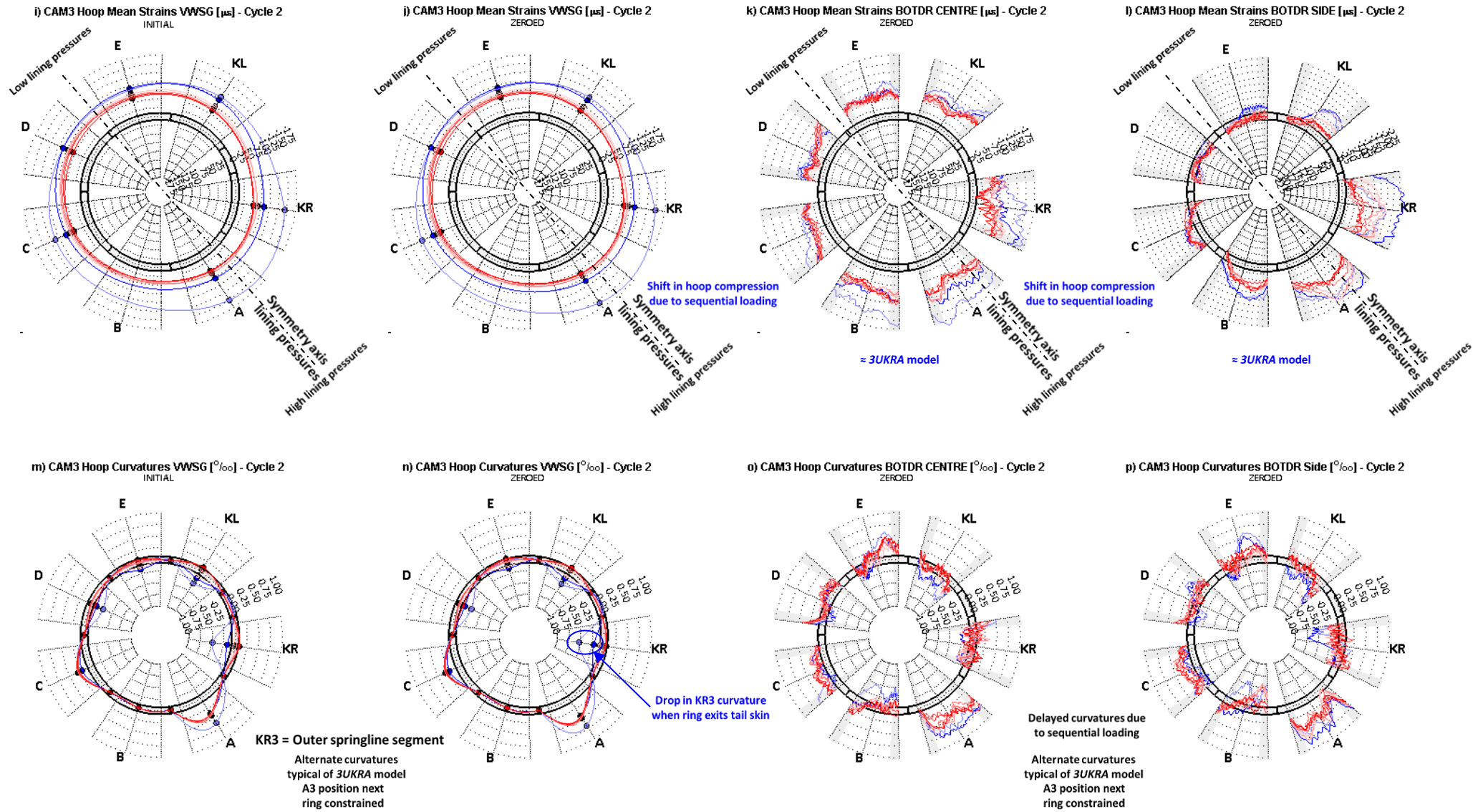


Figure 8.17 (continued)

### 8.6.2. CAM4 ring

#### 8.6.2.1. Lining pressures

The comparison of CAM4 time and distance maps in Figure 8.18.a evidences that the TBM interrupted the AD2 for nearly an hour when the ring was about to complete its exit from the tail skin, i.e. at  $SD \approx 2.7\text{m}$ . The grout injection pressures recorded by the TBM sensors show that, before the pause, the injection pressures reached peaks of 6.5bar and 6.0bar at the two injection lines, which exceeded the general limit value of 5bar delivered in most TBM advances (see Figure 8.19). The injection pressure stopped during the standstill period to be later recovered to erratic values comprised between 1bar and 6bar until the end of AD2. The total duration of effective grout injection almost doubled the 1h typical of common TBM advances. It becomes apparent that the AD2 was conducted with certain technical difficulties, which could have compromised the quality of the backfilled grout in terms of its completeness and homogeneity.

Figures 8.18.c and 8.18.d show the lining pressures in cycle2. At the first pressure data set in AD2, with  $SD \approx 1.9\text{m}$ , the full width of sealing pressures is loading the ring with the first row of steel wire brushes at the front edge of the ring. The lining pressure distribution is similar to that exhibited by the end of AS2 with the greatest difference being the increment in crown pressures from about 80kPa to 100kPa. The vertical gradient reduces from 25kPa/m to 20kPa/m.

At the next field data set, with  $SD \approx 2.4\text{m}$ , the ring front is directly loaded by the sealing pressures over a 0.4m width while the rest of the ring is subjected to the grout pressures at the tail void. The lining pressures undergo a roughly uniform increase of about 50kPa at constant vertical gradient as in the first half of CAM3 AD2.

At  $SD \approx 2.65\text{m}$  and time equal to 11.07h, the ring is almost fully surrounded by the annular grout with only a 0.1m width at the ring front is in contact with the back of the sealing system. The lining pressures remain constant at the bottom segments (B4, C4 and D4) and increase up to 40kPa at the rest of the segments. The vertical profile of lining pressures in Figure 8.18.d shows modest peaks at the segments closest to the two injection ports, i.e. KL4 and A4. According to the TBM records, the peak injection pressures occurred a few minutes before the field measurement. If it is accepted that there could be a short lag between the TBM and field data, the peaks at the ring shoulders could be correlated to the high injection pressures delivered by the grout ports.

The next four data sets take place during the TBM standstill at  $SD \approx 2.7\text{m}$ . The drop in lining pressures of about 100kPa at roughly constant vertical gradients could be caused by a uniform grout consolidation in the tail void during the 1h period where the TBM advance was stopped and the grout injection interrupted. The magnitude of pressure decay and the duration of consolidation correlate well with those observed in CAM3 during its AS2.

## 8.6. Field data interpretation on cycle 2

---

Once the AD2 is resumed, the lining pressures increase progressively at the upper segments with pressure increments at the crown of about 100kPa. At the lower segments, the lining pressures are less sensitive to grout injection and grow only up to 20kPa. The vertical gradients decrease to about 7kPa/m and the computed crown pressures of 160kPa are near hydrostatic values.

During AS2, the lining pressures remain generally the same with a further reduction in vertical gradients to almost zero, which suggests that also CAM4 is in ring equilibrium against uplift forces and there is no longer grout consolidation.

### 8.6.2.2. Hoop membrane behaviour

The progressive change in hoop strain gradients caused by the displacement of sealing pressures is clear at CAM4 segments, which exhibit negative gradients by the end of AD2 (see Figure 8.8.b). The magnitude of change is directly related to the lining pressures. The peak tensile strains arising now at the ring rear are greater than in CAM3 given the generally lower total hoop force acting on the segments, above +50 $\mu\epsilon$  up to +75 $\mu\epsilon$ .

During AS2, the fluctuations in total hoop force and strain gradients are minor and the latter tend to be attenuated. The greatest variations occur at B4, C4 and D4, the last two segments reaching uniform hoop compression by the end of AS2.

### 8.6.2.3. Deformed shape, segment curvatures and vertical tilt

The general trends of CAM4 ring within cycle2 resemble those encountered in CAM3 despite their disparate ram load distribution and ring eccentricity.

The pronounced TBM steering around the horizontal curve that initiates after CAM4 erection results in very high ram loads at the crown, invert and outer side of the ring during AD2, comprised between 200bar/ram to 300bar/ram, whilst E4 and KL4 support smaller ram loads between 100bar/ram to 200bar/ram. During AS2, the longitudinal action of the ram pads tends to be uniformly distributed (see Figure 8.18.e).

The deformed shape barely changes within cycle2 and the ring convergence at vertical and horizontal diameters is kept constant. Given the lower gradients of lining pressures, it is natural that the ring shape is less sensitive to changes in boundary conditions than CAM3.

The vertical tilt diagram at the beginning of AD2 is the same exhibited at the end of AS1 (see Figure 8.18.b). During the advance, the vertical tilt at the outer segments increases further due to the outward rotations induced by the transverse action of the inclined hydraulic jacks (see Figure 8.16, section 8.2 and chapter 6); the opposite behaviour takes place at the inner segments; and the vertical tilt of the restrained segments at the invert is very small. The changes in longitudinal compression in AS2 increase vertical tilt at KR3 and A3; their total increment is of 0.050° and 0.030° respectively.

## 8.6. Field data interpretation on cycle 2

---

The VWSG hoop curvature diagram at  $SD \approx 1.9\text{m}$  is again very similar to that displayed by the end of AS1 (see Figure 8.18.n). The tail clearance at B4 until the exit of the ring from the tail skin decreases with advance (see Figure 8.16.d). However, the progressive reduction in the width of sealing pressures directly applied to the ring front causes the decrease of B4 hoop curvatures from  $-0.65\text{‰}$  to  $-0.35\text{‰}$ . Once the ring is surrounded by the annular grout, the curvatures decrease further to about  $-0.25\text{‰}$ . The curvatures at the ring front decrease with the displacement of the sealing system. By the end of AD2, the longitudinal crack appears to have closed.

The longitudinal curvatures at  $SD \approx 1.9\text{m}$  are identical to those developed by the end of cycle1 (see Figure 8.18.g). The diagram of centroid curvatures undergoes a drastic change at the next field data set when the ring centreline is no longer in contact with the sealing system. With the displacement of the sealing system towards the ring front, the segments tend to bend gradually with opposite curvature. The analogy of a continuous beam subjected to a moving load clarifies the above trend (see Figure 8.18.g). The magnitude of positive curvature increments is directly related with the lining pressures, i.e. greater at invert than crown. Being B4 the segment subjected to highly concentrated sealing pressures, it undergoes the greatest change in longitudinal curvature.

The mean longitudinal strains during AS2 evidence again that the CAM4 circumferential joints are susceptible to partial opening in the assembly stages (see chapter 6).

## 8.6. Field data interpretation on cycle 2

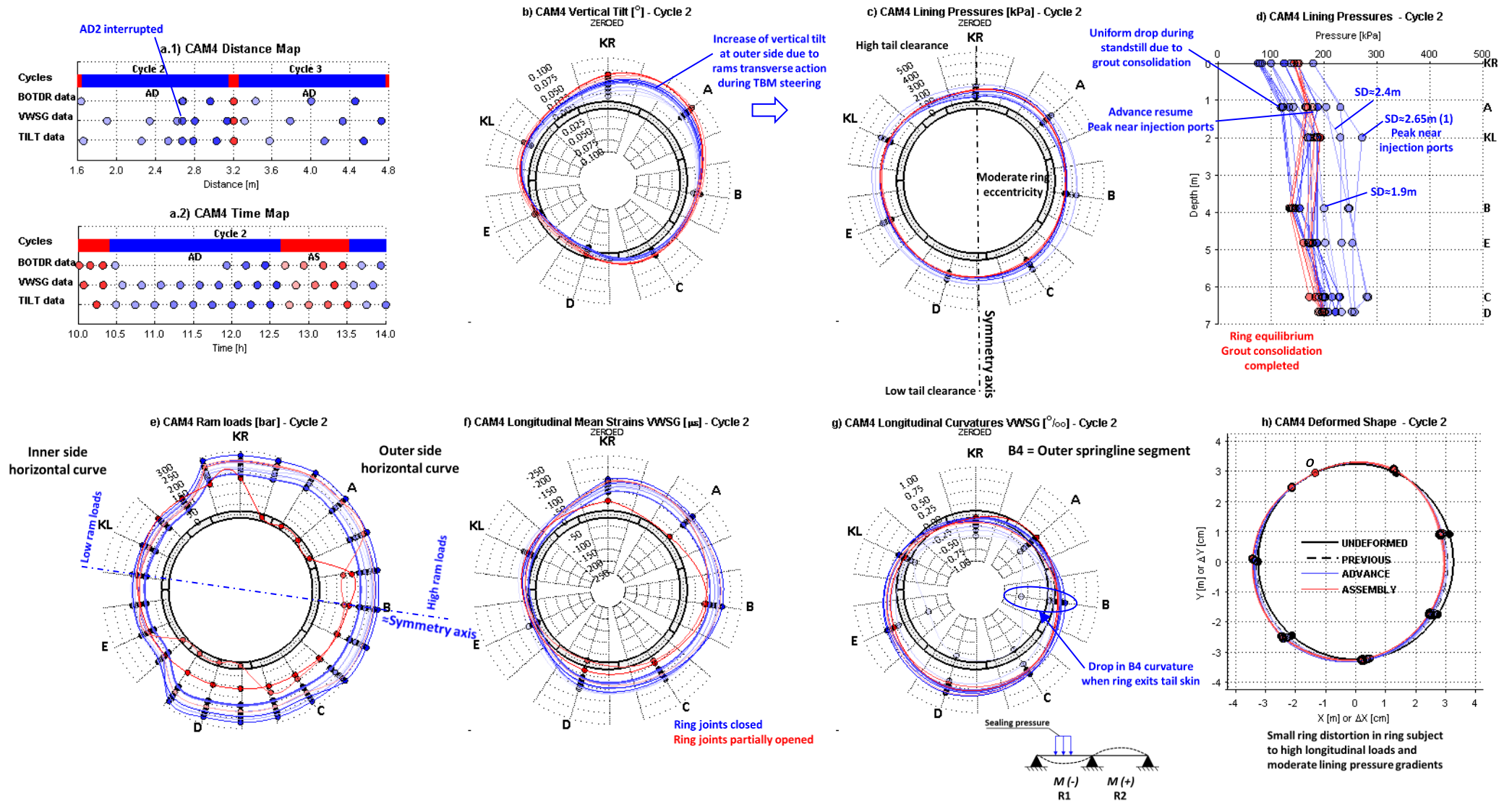


Figure 8.18: CTT field data: CAM4 Cycle2

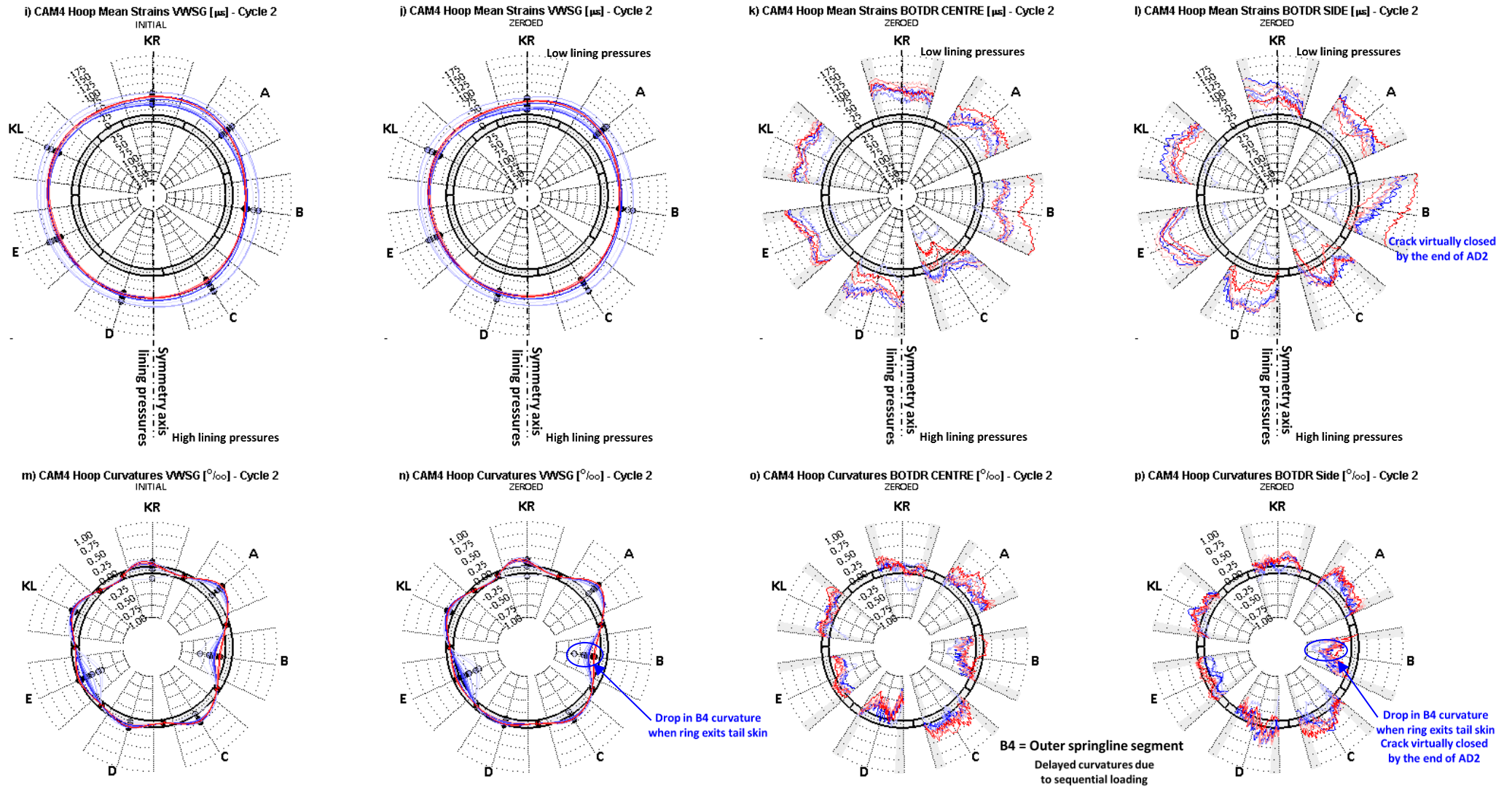


Figure 8.18 (continued)

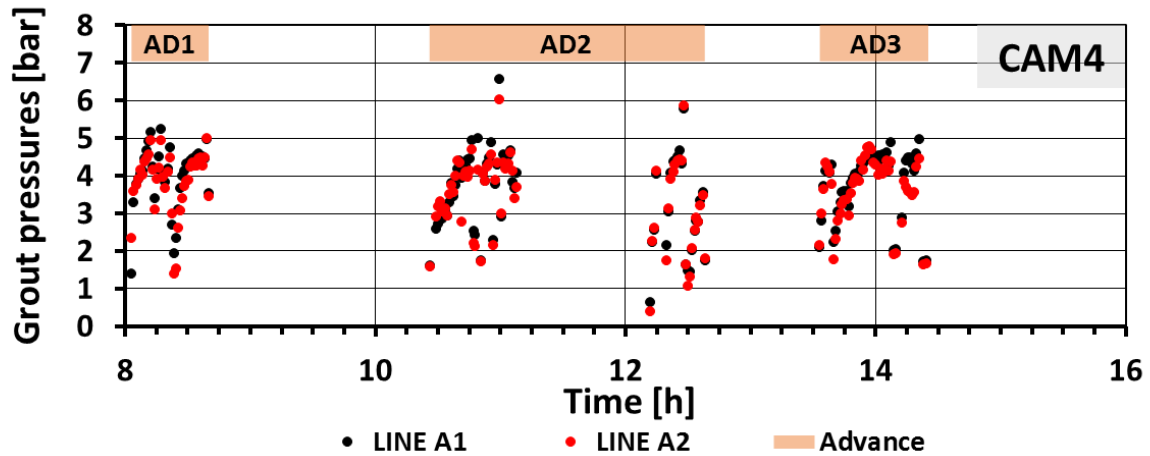


Figure 8.19: CAM4 grout injection pressures

### 8.7. Field data interpretation on following cycles

In accordance with the evolution of field pressure gradients (see chapter 6), it was generally assumed that the instrumented rings were founded on the ground from cycle3 onwards. Thus, the lining pressures acting on the rings are conditioned by the ground support (see chapter 6) and the influence of the TBM-lining transverse interaction on the ring behaviour is minor (see chapter 7).

#### 8.7.1. Lining pressures

Figure 8.20 presents the history of the CTT lining pressures. In AD3 there is a uniform rise in lining pressures of about 30kPa in both rings, only in the first half of the advance for CAM3. Such uniform pressure increments may indicate that the grout pressures are still affected by the injection of the fresh grout at this stage.

In CAM4, the lining pressure at A4 exhibits a greater increase of 110kPa, from 160kPa to 270kPa, which results in a peak at the outer shoulder that is later dissipated during AS3. Such localised and temporary increase in lining pressures situated in front of a grout port and which decays after the end of grout injection may suggest that it is caused by the partial refill of the annulus surrounding the ring at this area. Given the interruption in grout injection experienced in AD2, the quality of the grout layer may have been jeopardised by either an incomplete backfill or a degraded bond at the interfaces of the hardened grout. Thus, the fresh grout in AD3 may have been able to penetrate the annular grout through the most accessible paths.

The evolution of lining pressure gradients after cycle2 is influenced by the sequence of longitudinal deflections in the tunnel beam (see chapter 6). The displacement of a ring fully founded in elastic ground activates a total ground reaction  $F$  that opposes the lining movement and is proportional to the pressure gradient  $g$ :

$$F = -K_{tot}\Delta\delta = g\pi R_e^2$$



## 8.7. Field data interpretation on following cycles

---

where  $\Delta\delta$  is the ring displacement after being fully founded on the ground and  $R_e$  the external radius of the tunnel.

In CAM3, the vertical gradient evolves from near 8kPa/m in AD3 to 12kPa/m by the end of AS4, i.e. during the CAM4 ring erection, and returns to negative gradients close to zero in cycle8 (see Figure 8.20.a). The reduction in vertical gradient from cycle4 to cycle8 yields a downward ring displacement of about -0.3mm for a fully bonded tunnel (see chapter 6). The history of vertical displacements estimated with the tunnel beam model (see Figure 8.20.i) shows that there is a tendency of rings near CAM3 to move downwards from stage 5 (CAM4 ring erection) to stage 61 (long term).

The CAM3 horizontal gradients increase from 0kPa/m to 12kPa/m in AD3, then reduce to 5kPa/m in AD4 to return to 10kPa/m in cycle8. The increase in vertical gradient from AD2 to AD3 results in an horizontal displacement towards the inner side of the curve around -0.4mm; the beam model predicts increments in inner movements of less than -1mm.

In CAM4, the skewed distribution of lining pressures is the result of the abnormal grout injection and the biaxial longitudinal deflection of a tunnel tube subjected to a pronounced TBM steering around a horizontal curve. The TBM steering forces increase the horizontal pressure gradients from 0kPa/m to -12kPa/m from AD3 to cycle8. The associated horizontal displacements near +0.8mm agree well with those estimated by the beam model between stage 7 (CAM4 AD3) and stage 61 (long term), which are less than +1mm.

In the vertical direction, the skewed shape of the lining pressure distribution hampers the identification of pressure gradients. Taking D4 as the segment representative of invert pressures, the gradients grow from 0kPa/m to -7.4kPa/m between AD3 and cycle8. The +0.5mm displacement obtained from the increase in pressure gradients are again similar to the +1mm increment in longitudinal deflection.

In cycle8, the lining pressures do not undergo significant fluctuations. The residual non-zero gradients, fundamentally in the horizontal direction, are mainly caused by the longitudinal deflections locked in the tunnel tube.

The link between tunnel deflections and pressure gradients in the tail void is also evidenced by the dissipation of horizontal gradients with the reduction of  $M_y$  during assembly periods while the tunnel still experiences changes in tunnel deflection, i.e. in AS3 and AS4.

Besides, the figures show that the computed lining pressures grow uniformly and gradually with time. However, such increase may reflect the influence of concrete creep on the measured CSL strains rather than the long term pressures acting on the lining (see Figure 8.21). The trace of the tidal fluctuations on the measured strains indicates that the chalk surrounding the CTT is very permeable and the grout consolidation against changes in field stresses is almost instantaneous. If the effect of tidal fluctuations is ignored, the increasing monotone strain curves can be approximated with the strain curves derived



## 8.7. Field data interpretation on following cycles

---

from the CTT concrete creep tests. The creep strains inferred from the EC2 creep factor overestimate the long term hoop strains.

## 8.7. Field data interpretation on following cycles

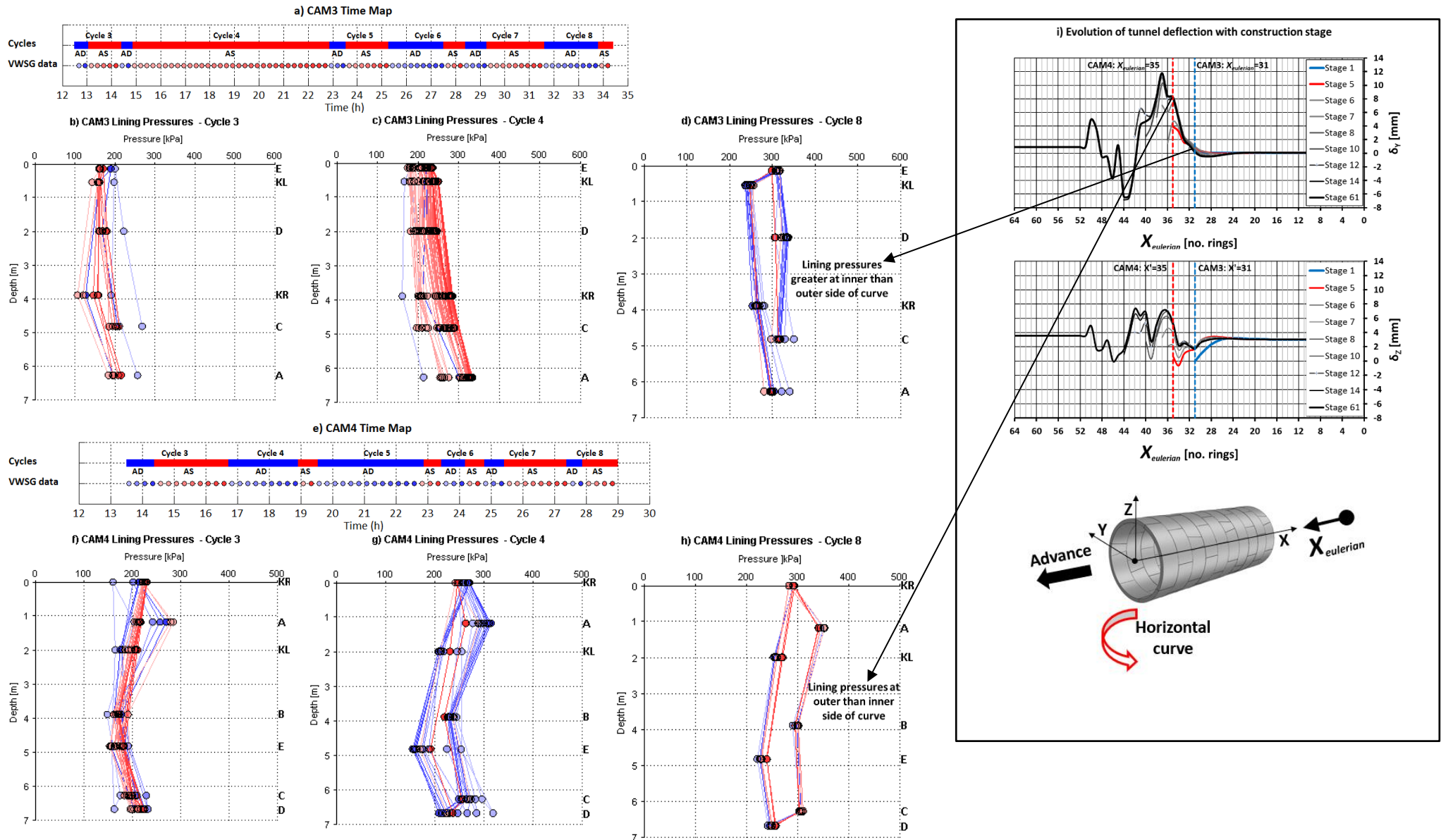


Figure 8.20: History of the CTT lining pressures

## 8.7. Field data interpretation on following cycles

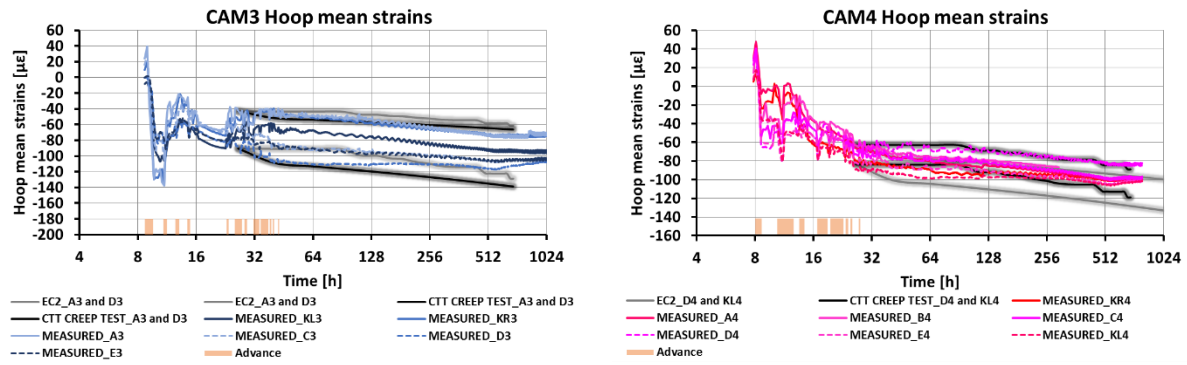


Figure 8.21: History of the CTT hoop mean strains

### 8.7.2. Hoop membrane behaviour

Hoop membrane strains at segment centroids rise notably from AD3 onwards in accordance with lining pressures. As discussed previously, the deferred increase in hoop membrane strains is influenced by concrete creep under sustained radial compression (see Figures 8.6.c and 8.8.c).

Strain gradients are gradually flattened with *SD* in all segments, although negative gradients still persist by the end of cycle3 in most segments, given the proximity of the sealing pressures to the instrumented rings.

At cycle8, all segments exhibit a relatively uniform hoop strain distribution, except for C3, D3 and E3, which are the segments under the lowest longitudinal compression during cycle1. In these segments, the positive strain gradients developed in AS1 remain roughly invariable through the following sequence of loads. Subsequent increments in lining pressures are insufficient to close the in-plane angularity developed at their longitudinal joints in cycle1 and compensate the concentration of ring compression at their rear. Thus, an initial in-plane angularity with contact at the ring rear may be perpetuated or accentuated in time by sequential loading. The least longitudinally compressed segments may be the most prone to the in-plane angularities arising during sequential loading.

Conversely, the evolution of C4 membrane strains reveals that the initial in-plane angularities of opposite sign may be corrected with the sequential compression of the ring rear in AD1.

### 8.7.3. Deformed shape, segment curvatures and vertical tilt

The CAM3 ring distortion grows until cycle3 with the same pattern exhibited in cycle2 but with attenuated amplitudes: the increment in joint rotation at the inner knee in AS3 is 1mm as opposed to the 3mm detected in AS2 (see Figures 8.22.h and 8.23.h). In CAM4, the ring deformations were already constant during cycle2 (see Figures 8.24.h and 8.25.h).

After cycle2, there is a period of alternate increase and decrease in the hoop curvatures of lower segments for both rings without significant variations in hoop curvatures at upper segments. In general, the curvatures rise at the beginning of the advances and fall progressively with *SD* from about

## 8.7. Field data interpretation on following cycles

---

0.25‰ to negligible values. During standstill, the curvatures remain constant, suggesting that the changes are induced by the variable TBM loads applied during advance, including the passage of the TBM backup trail. The residual curvatures by the end of cycle8 are similar to those developed by the end of AS2, e.g. 0.5‰ at A3, 0.25‰ at C3 (see Figures 8.22.n and 8.23.n) and -0.25‰ at B3; and 0.25‰ or less in CAM4 lower segments (see Figures 8.24.n and 8.25.n).

In cycle8, there is no change in hoop curvatures at CAM4, while variations are still detected by BOTDR and strain gauge sensors in CAM3. Given that CAM4 was assembled four rings after CAM3 and that the monitoring works delayed tunnelling by about 8h, the grout annulus behind CAM4 is around 8h older than behind CAM3, if the middle four rings are excluded. It may be inferred that the tunnel tube at CAM4 cycle8 is more firmly founded on the chalk than at CAM3 cycle8 and, thus, less sensitive to beam behaviour and subsequent loading.

Likewise, vertical tilt increments experienced by both rings from cycle3 onwards dissipate with *SD* from 0.25° in cycle3 to negligible values in cycle8 (see Figures 8.22.b to 8.25.b). Overall, the individual rotations of segments dominate vertical tilt in the first two cycles, where TBM-lining transverse interaction is key. Tunnel beam behaviour governs the evolution of vertical tilt in the following cycles, with residual values being the summation of the vertical increments developed in each cycle.

The longitudinal curvature diagram does not significantly change from cycle3 onwards (see Figures 8.22.g to 8.25.g). By the end of cycle8, the diagram of longitudinal mean strains evidences that the circumferential joints adjacent to CAM3 are closed; the imminent ring joint opening around the CAM4 inner knee is not corrected with *SD* (see Figures 8.22.f to 8.25.f).

## 8.7. Field data interpretation on following cycles

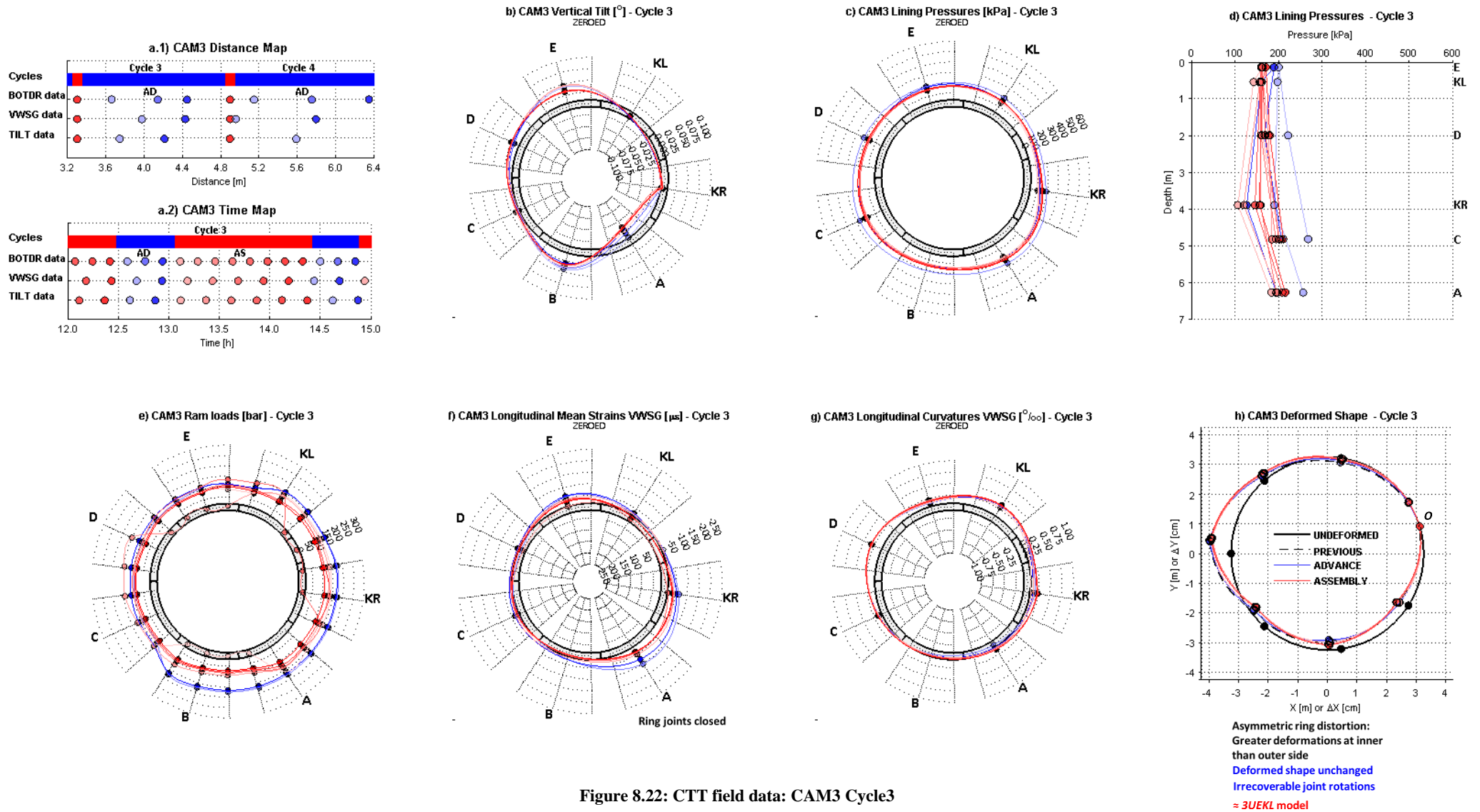
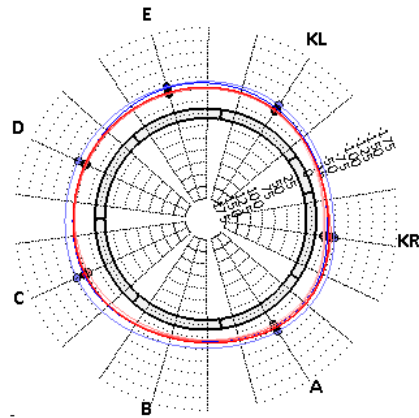


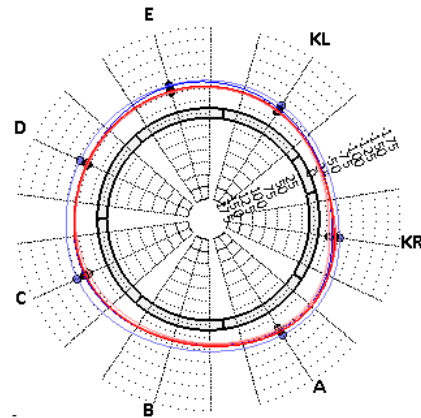
Figure 8.22: CTT field data: CAM3 Cycle3

## 8.7. Field data interpretation on following cycles

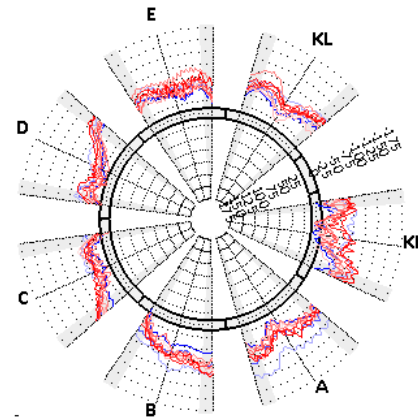
i) CAM3 Hoop Mean Strains VWSG [ $\mu\epsilon$ ] - Cycle 3  
INITIAL



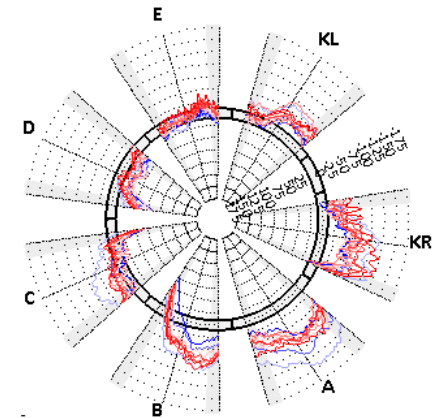
j) CAM3 Hoop Mean Strains VWSG [ $\mu\epsilon$ ] - Cycle 3  
ZEROED



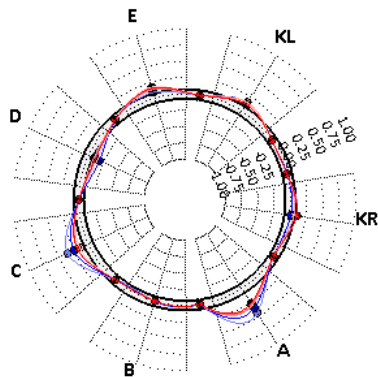
k) CAM3 Hoop Mean Strains BOTDR CENTRE [ $\mu\epsilon$ ] - Cycle 3  
ZEROED



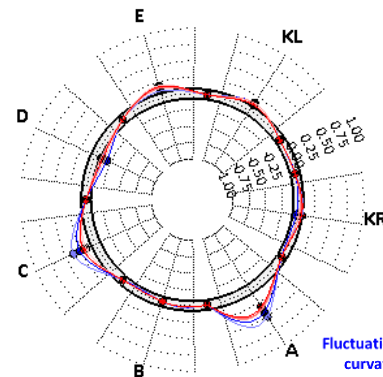
l) CAM3 Hoop Mean Strains BOTDR SIDE [ $\mu\epsilon$ ] - Cycle 3  
ZEROED



m) CAM3 Hoop Curvatures VWSG [ $10^{-6}$ ] - Cycle 3  
INITIAL

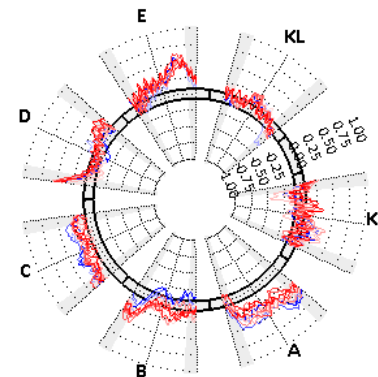


n) CAM3 Hoop Curvatures VWSG [ $10^{-6}$ ] - Cycle 3  
ZEROED



Fluctuation in hoop  
curvatures at  
bottom segments

o) CAM3 Hoop Curvatures BOTDR CENTRE [ $10^{-6}$ ] - Cycle 3  
ZEROED



p) CAM3 Hoop Curvatures BOTDR Side [ $10^{-6}$ ] - Cycle 3  
ZEROED

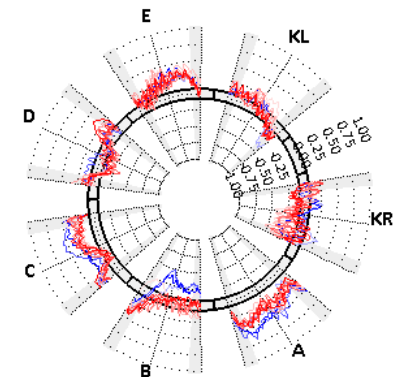


Figure 8.22 (continued)

## 8.7. Field data interpretation on following cycles

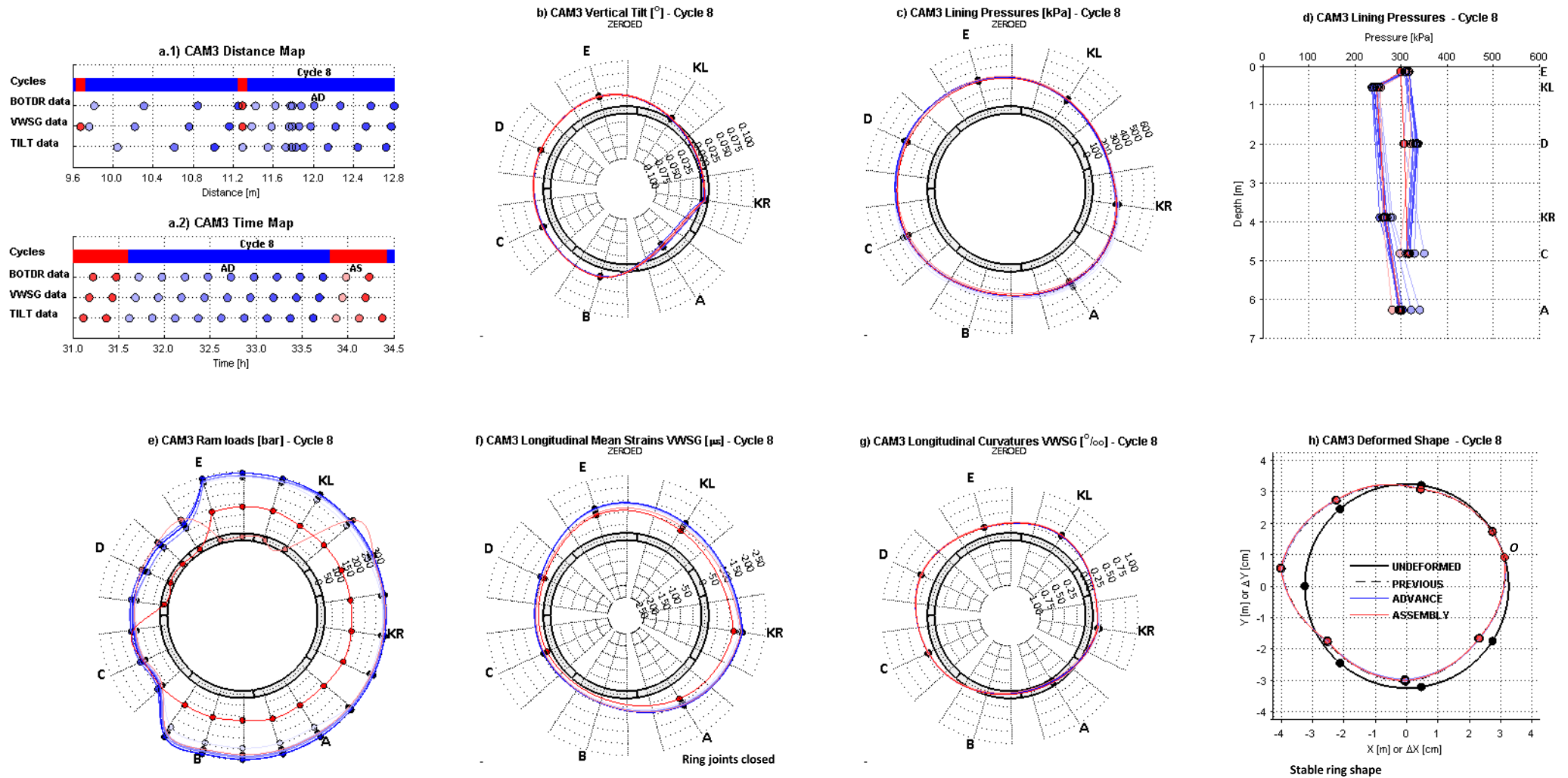
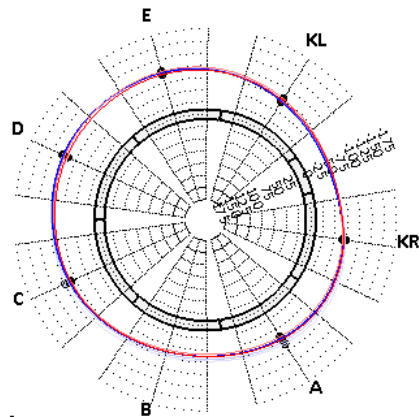


Figure 8.23: CTT field data: CAM3 Cycle8

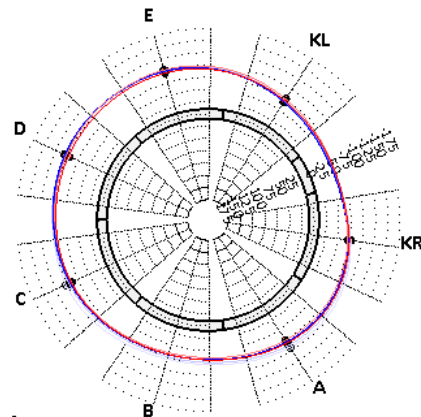


## 8.7. Field data interpretation on following cycles

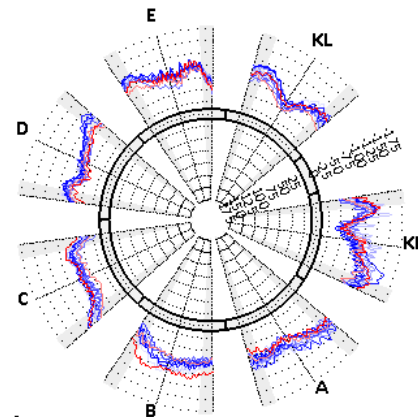
i) CAM3 Hoop Mean Strains VWSG [ $\mu\epsilon$ ] - Cycle 8  
INITIAL



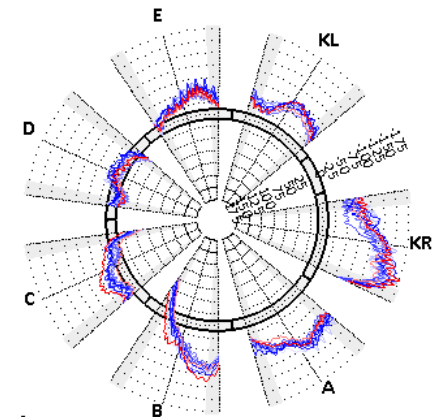
j) CAM3 Hoop Mean Strains VWSG [ $\mu\epsilon$ ] - Cycle 8  
ZEROED



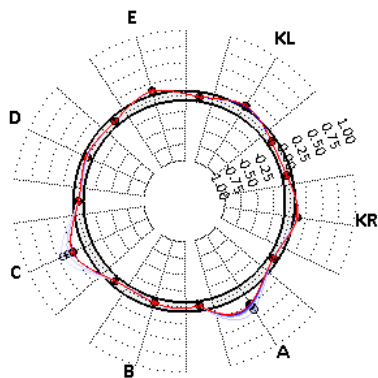
k) CAM3 Hoop Mean Strains BOTDR CENTRE [ $\mu\epsilon$ ] - Cycle 8  
ZEROED



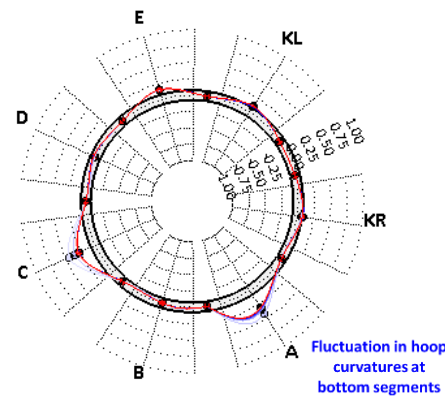
l) CAM3 Hoop Mean Strains BOTDR SIDE [ $\mu\epsilon$ ] - Cycle 8  
ZEROED



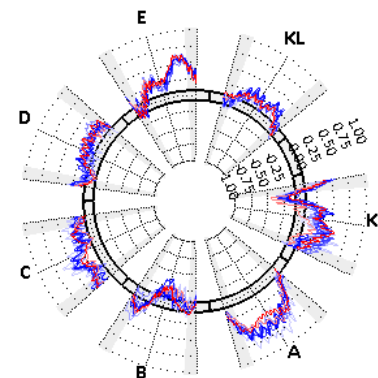
m) CAM3 Hoop Curvatures VWSG [ $10^{-6}$ ] - Cycle 8  
INITIAL



n) CAM3 Hoop Curvatures VWSG [ $10^{-6}$ ] - Cycle 8  
ZEROED



o) CAM3 Hoop Curvatures BOTDR CENTRE [ $10^{-6}$ ] - Cycle 8  
ZEROED



p) CAM3 Hoop Curvatures BOTDR Side [ $10^{-6}$ ] - Cycle 8  
ZEROED

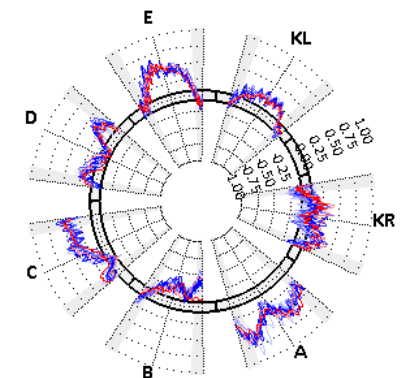


Figure 8.23 (continued)



## 8.7. Field data interpretation on following cycles

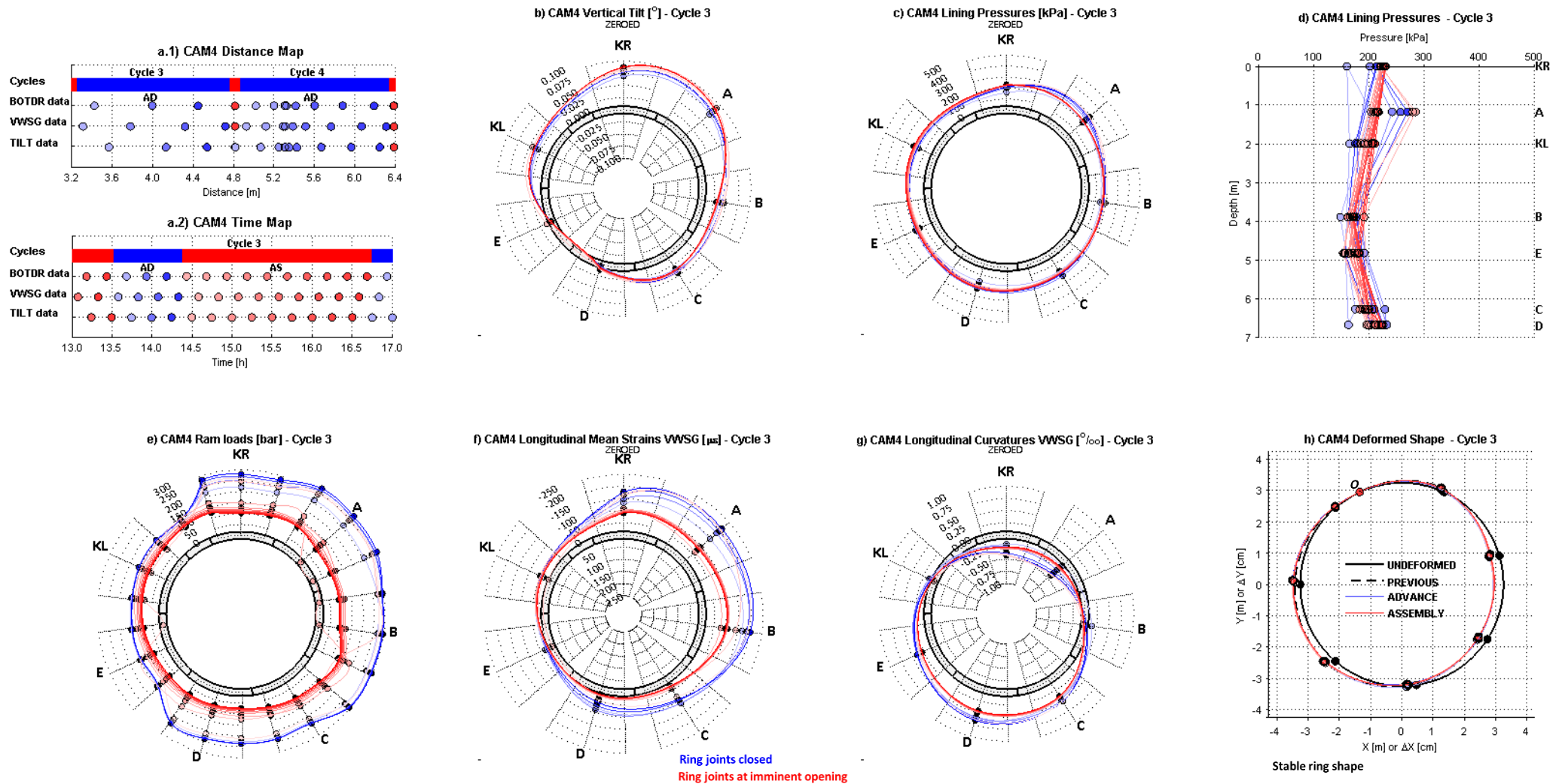


Figure 8.24: CTT field data: CAM4 Cycle 3

## 8.7. Field data interpretation on following cycles

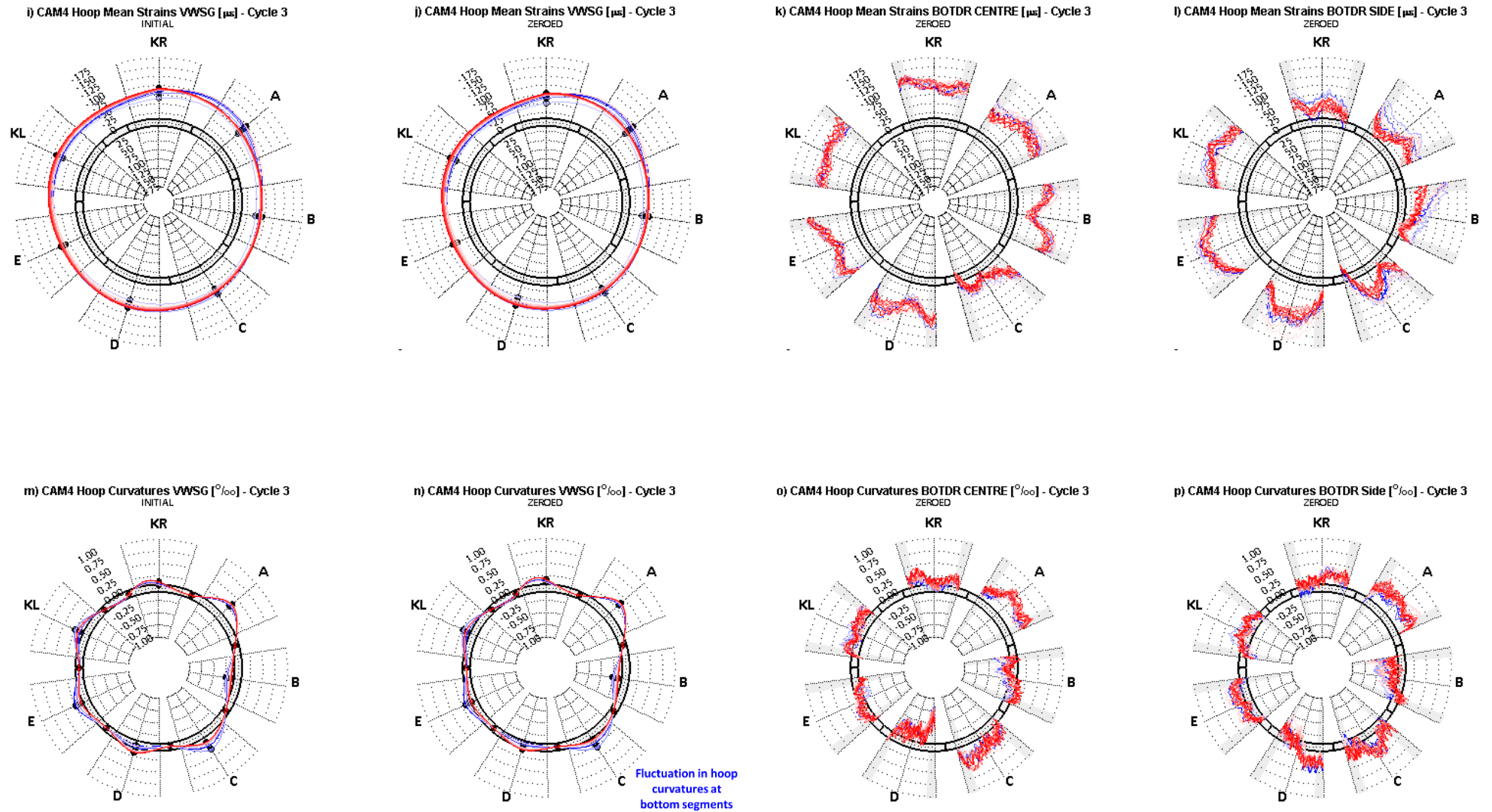


Figure 8.24 (continued)

## 8.7. Field data interpretation on following cycles

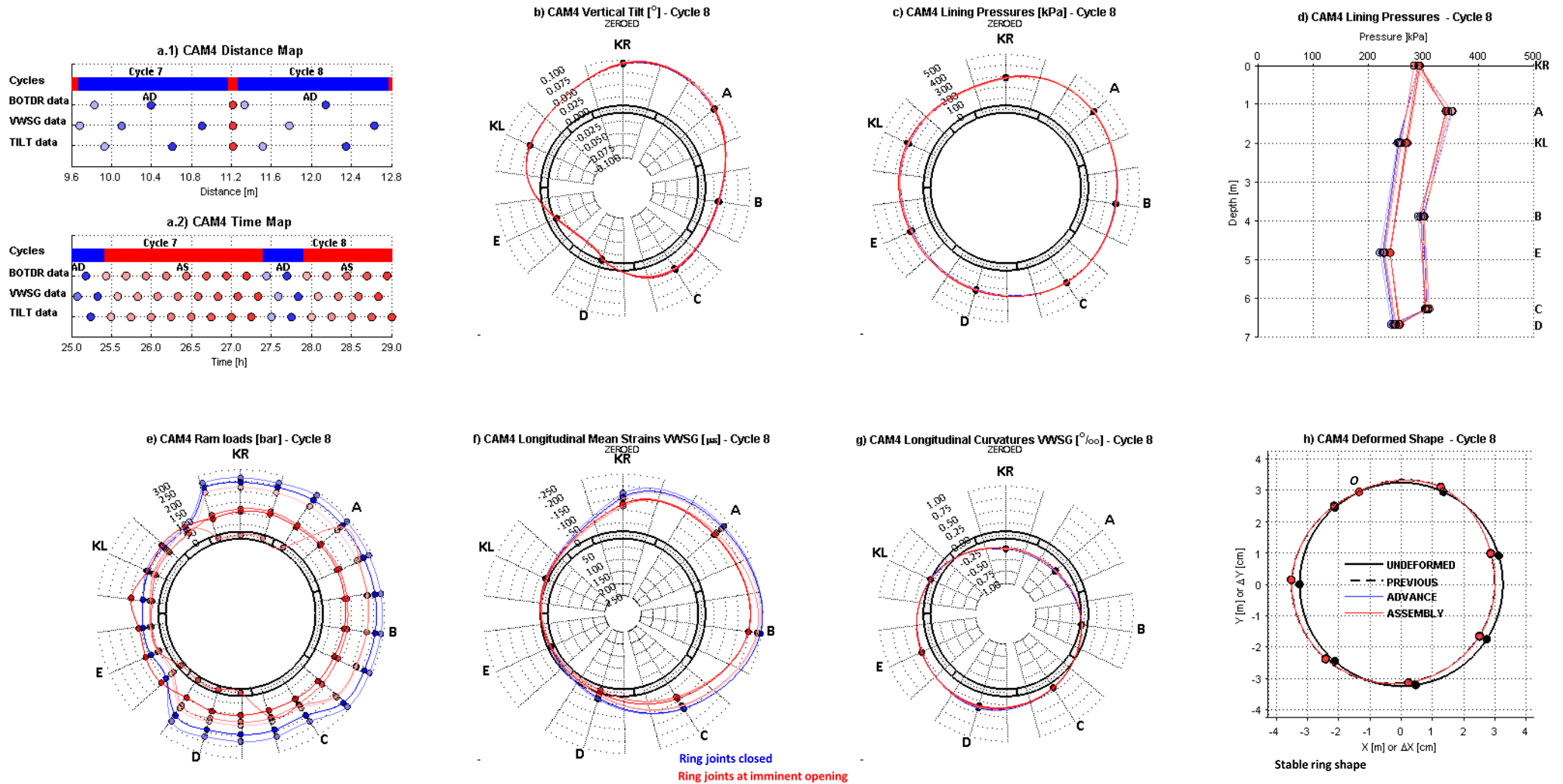


Figure 8.25: CTT field data: CAM4 Cycle8

## 8.7. Field data interpretation on following cycles

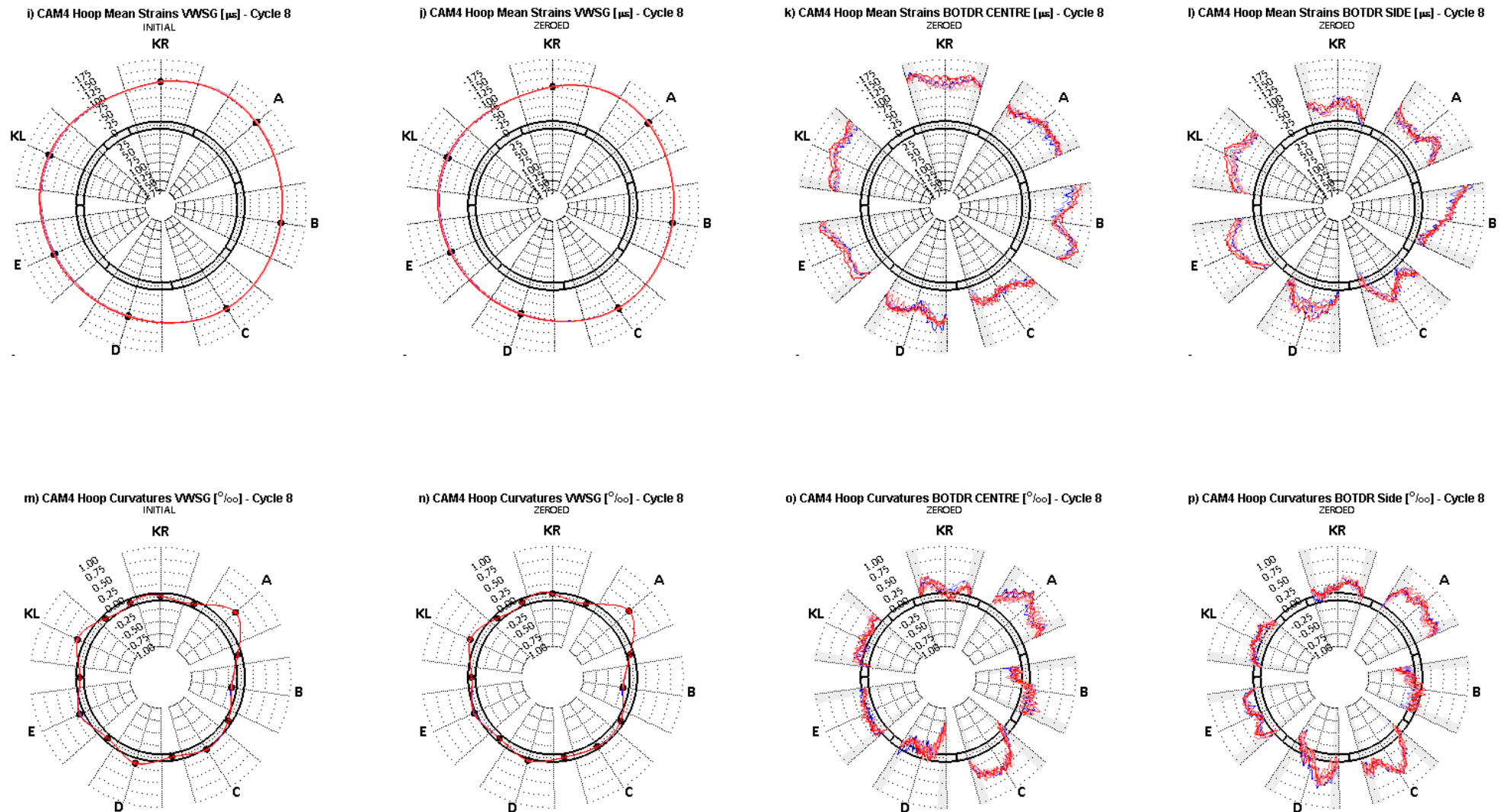


Figure 8.25 (continued)

## 8.8. Conclusions

The CTT field data interpretation proved that the TBM-lining transverse interaction near the tail skin determines CSL ring behaviour at the early stages of tunnelling, e.g. the first three and two TBM cycles in CAM3 and CAM4 respectively. The ring response resultant from this interaction is irrecoverable and contributes to the total deformations and internal forces developed in the long term; in tunnels excavated in grounds with  $K_o \approx 1$ , they become the main source of ring distortion. The grout pressures within  $L_u$  of CSLs simultaneously backfilled with BGs play only a secondary role in ring response. The longitudinal beam response to construction loads in CSLs where deflections are constrained by the TBM hardly affects ring distortion.

The above conclusion can become a turning point in the design approach to CSLs (and TBMs) and in future research tackling lining behaviour during mechanised shield tunnelling, which to date has been mainly focused on the influence of grout pressures on the longitudinal and transverse response of CSLs.

The TBM transverse action onto the lining can be delivered through the sealing system, the hydraulic jacks and in extreme cases the contact with the shield tail. The sealing pressures are the sum of sealing compound pressures and the pressures of the steel stiffeners, which are inversely related to the tail clearance. The transverse load of oblique hydraulic jacks is proportional to the magnitude of their thrust and the relative inclination of the rams.

Based on the CTT field data interpretation and with the aid of the numerical study conducted in chapter 7, a theoretical framework for the development of limit state design methods that captures the effects of the TBM-lining transverse interaction has been proposed: the construction loading scenarios representative of field conditions, together with their associated CSL structural response and damage mechanisms, were identified and described:

**a) CS1: Concentric ring**

The sealing pressures acting on the lining are uniform and the downward action of the hydraulic jacks against uplift forces is small, at least in CSLs backfilled with BGs. This CS is equivalent to the case of sequential loading under axisymmetric conditions studied in chapter 7.

**b) CS2: Eccentric ring**

This case may be representative of a tunnelling scenario with TBM steering, for example around a curve. The lining is eccentric relative to the tail skin. The sealing pressures are smoothly distributed with pressure gradients proportional to the ring eccentricity. The transverse action of the oblique hydraulic jacks locks the relative position of the ring. The radial rotation of the segments with the lowest tail clearance is constrained.

This case is equivalent to that of the sequential radial loading with pressure gradients and an uneven ram pad-lining interface (see chapter 7), where the ring deforms under the action of the pressure gradients combined with uneven constraints. The numerical results in chapter 7 confirmed that the magnitude of the ring distortion was directly related to the pressure gradients and that the deformation mode depended on the relative orientation of pressure gradients and constraints. The numerical models were able to replicate the in situ ring behaviour during AD1 and were deployed as an effective tool to describe the underlying mechanics.

The tensile concrete cracking at the ring front was observed in segments A3, D3 and B4, which, when combined with the spalling strains between ram pads, could increase the risk of spalling cracks, as explained in chapter 7. Permanent in-plane angularities were also detected in the least longitudinally compressed segments of CAM3, indicating that these segments may be more prone to splitting failure at longitudinal joints or corner chipping at the ring rear, particularly near the keystone. The concrete damage types associated with this CS, i.e. hoop cracking near rear joints and spalling between ram pads, could not be detected with the designed ring instrumentation.

**c) CS3: Rotated segment**

This tunnelling scenario is typical of pronounced TBM steering, such as in the case of CAM4. The newly erected ring is subjected to high TBM longitudinal moments and transverse loads delivered by the oblique hydraulic jacks. The segment subjected to the highest radial ram loads, for example the outer springline segment in a horizontal curve, undergoes significant outward rotations that reduce locally the tail clearance. The segment is subjected to a high concentration of sealing pressures, or tail reaction if it makes contact with the tail skin, and bends biaxially. The high longitudinal compression of the hydraulic jacks prevents hoop flexure cracking. However, the hoop curvatures combined with the hoop tension near the ring front typical of sequential loading may result in the longitudinal cracking of the segment intrados at the ring front. This cracking pattern was detected in the outer springline segment of CAM4, although it appeared to close progressively in the following advances.

Finally, it was found that the initial in-plane angularities of longitudinal joints with contact at the ring front may be corrected with sequential loading. The uneven strain field detected in segment B3 agreed with the STM and crack patterns of unevenly supported segments with one instead of three packer supports.

# Chapter 9

## Conclusions

The study investigated the longitudinal and transverse behaviour of CSL structures simultaneously backfilled with BGs during tunnelling, and the influence of this short term behaviour on the long term response. It was also sought to advance in the development of a theoretical framework for CSL design and management that captured the effects of radial ring loading and TBM-lining transverse interaction near the tail skin. Despite empirical evidence proving that most damage in CSLs during construction takes place at the early stages of tunnelling (Chen and Mo, 2009; Sugimoto, 2006; Gruebl, 2006), the conventional CSL design methods in use today ignore the tunnelling effects on CSL performance and thus can lead to either overdesigned structures or structural damage. Furthermore, most research to date on CSL behaviour during construction focuses on the impact that grout pressure distributions in the tail void have on the lining response, entirely neglecting the sequential ring loading and TBM-lining transverse interaction that this study proved to be key in the short and long term behaviour of CSLs.

The study was supported on the interpretation of the CTT field data collected during tunnelling, which included BOTDR data. The research works comprised the development of installation procedures for BOTDR sensing in CSLs during tunnelling and a performance-based assessment of the BOTDR data.

The CTT lining was a curved jointed CSL furnished with spear bolts. Since most published literature to date is based on flat jointed CSLs and the function of spear bolts in current CSL configurations was unclear (Harding et al., 2014), the study included the evaluation of the impact of joint geometry on CSL behaviour and the identification of the bolt's role during construction.

In this chapter, the findings are described, explaining their limitations and implications for the design and management of CSL tunnels. Then, the lines of future research that stem from this study are outlined.

### 9.1. Findings

In chapter 1, the research objectives were specified. In this section, the findings of this study are referred to the defined objectives.

### 9.1.1. CSL behaviour

#### 9.1.1.1. Longitudinal behaviour

The study of the CTT longitudinal response during construction described in chapter 6 revealed that CSLs simultaneously backfilled with cementitious grouts undergo an early relaxation of the longitudinal pre-stressing force due to the temperature changes induced by grout hardening. For a given tunnel system, the magnitude of relaxation depends mainly on the temperature profile given by the grout mix and the ambient temperatures. In the CTT tunnel, a chalk tunnel backfilled with BGs, the longitudinal mean strains were reduced by 50%, equivalent to 85bar/ram, in the months following ring erection. The combination of early thermal relaxation with the deferred creep decompression that develops with loading time (Arnau, 2012) could result in small long term longitudinal forces, which undermines ring interaction and increases long term ring misalignments in tunnels subjected to deviatoric pressures (**Objective 1.1**).

It was also found that the residual moments and shear forces after sequential CSL construction are highly dependent on the TBM moments and transverse actions near the tail skin. The tunnel tends to bend when subjected to pronounced TBM steering around curves and is prone to shearing under the cumulative effect of uplift forces. The internal forces remaining in the tunnel after its construction may lead to delayed ring joint opening or lipping as the tunnel pre-stressing force is lost. During tunnelling, the greater internal forces can also originate ring joint damage, with higher risk during the ring assembly periods in the TBM cycles following ring erection due to the reduction in total longitudinal force (**Objective 1.2**).

The deployment of analytical models enhanced the field data interpretation. The solution developed for a sequential elastic rod subjected to trilinear temperature and in shear interaction with the elastic ground enables the accurate prediction of tunnel relaxation caused by grout hardening. The proposed sequential elastic beam model incorporates the effects of stage-varying net TBM moments, transverse loads and lining pressure gradients within  $L_u$ . It was proved to estimate satisfactorily the history of tunnel beam response during construction with the derived expression of  $EI_0$ . The improved tunnel beam solution eliminates the need for the ad hoc selection of stiffness parameters to match field measurements as done in previous works (Hoefsloot, 2009; Talmon et al., 2009c) (**Objectives 1.3 and 1.4**).

Following the validation of these two models as effective tools for the prediction of longitudinal lining response, a PDA method for the early detection of tunnel sections prone to ring joint damage was proposed (see Figure 6.19 repeated). Given the reliance of this PDA method on elastic solutions, it is envisaged as a preliminary assessment method for the identification of future problematic areas in a tunnel immediately after its construction. Then, asset owners can focus on the detailed analysis of these areas with more sophisticated methods and on developing monitoring, inspection and



maintenance plans that target these areas. The method requires that the TBM is equipped with transducers that can measure the transverse ram loads and sealing pressures, that the TBM records on the above loads and longitudinal ram loads are available and that the in situ lining temperatures are either monitored from early construction or estimated (**Objective 1.5**).

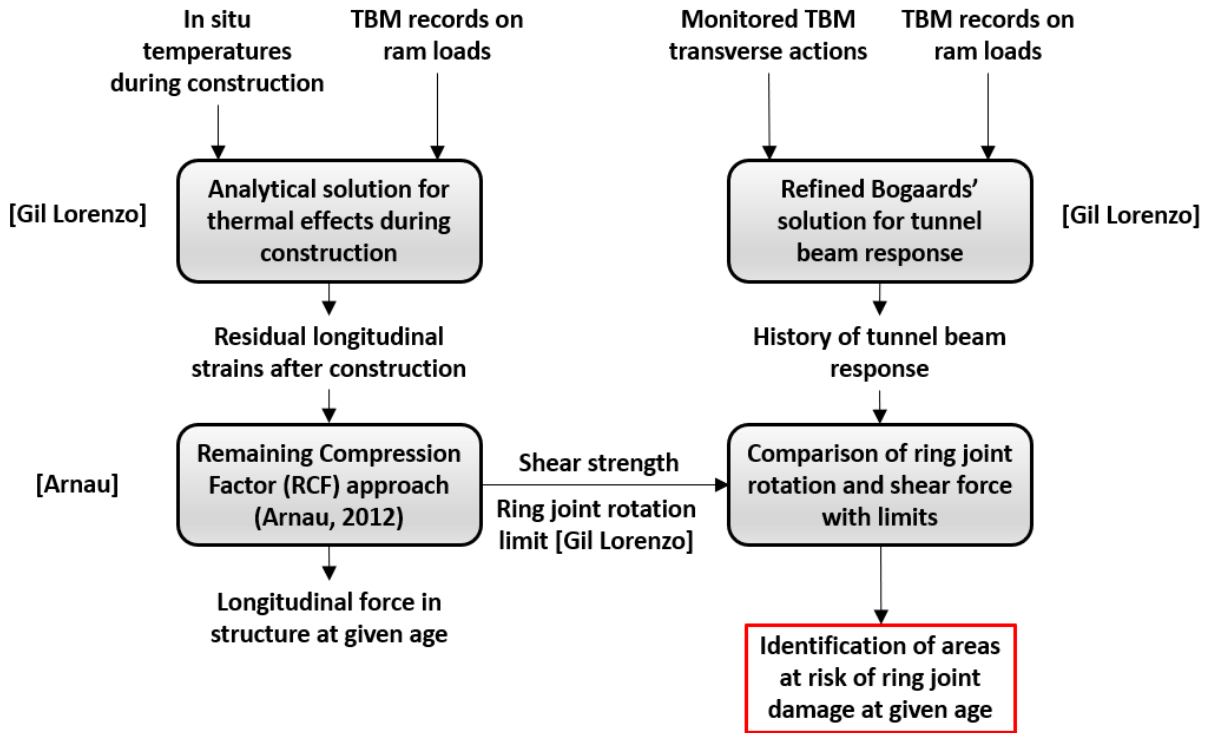


Figure 6.19 (repeated): PDA method for preliminary assessment

The proposed rod and beam models could enable tunnel designers to customise ring joint design in accordance with the predicted history of longitudinal lining response. However, a reliable method for the prediction of TBM ram loads and net transverse TBM-lining interactions based on the knowledge of the proposed tunnel drive, i.e. possibly alignment and geology, and foreseeable operations would be needed beforehand.

### 9.1.1.2. Transverse behaviour

The CTT field data interpretation proved that the TBM-lining transverse interaction near the tail skin determines CSL ring behaviour at the early stages of tunnelling, e.g. the first three and two TBM cycles in CAM3 and CAM4 respectively. The ring response resultant from this interaction is irrecoverable and contributes to the total deformations and internal forces developed in the long term; in tunnels excavated in grounds with  $K_o \approx 1$ , it becomes the main source of ring distortion. The grout pressures within  $L_u$  of CSLs simultaneously backfilled with BGs play only a secondary role in ring response. The longitudinal beam response to construction loads in CSLs where deflections are constrained by the TBM hardly affects ring distortion (**Objective 1.6**).

The above conclusions can become a turning point in the design approach to CSLs (and TBMs) and in future research tackling lining behaviour during mechanised shield tunnelling, which, to date, has been mainly focused on the influence of grout pressures on the longitudinal and transverse response of CSLs.

The TBM transverse action onto the lining can be delivered through the sealing system, the hydraulic jacks and in extreme cases the contact with the shield tail. The sealing pressures are the sum of sealing compound pressures and the pressures of the steel stiffeners, which are inversely related to the tail clearance. The transverse load of oblique hydraulic jacks is proportional to the magnitude of their thrust and the relative inclination of the rams.

Based on the CTT field data interpretation and the 3D numerical study conducted in chapters 7 and 8 respectively, a theoretical framework for the development of limit state design methods that captures the effects of the TBM-lining transverse interaction was proposed (see Table 9.1): the construction loading scenarios representative of field conditions, together with the associated CSL structural response and damage mechanisms, were identified and described (**Objectives 1.7 and 1.8**):

*a) CS1: Concentric ring*

The sealing pressures acting on the lining are axisymmetric and the downward action of the hydraulic jacks against uplift forces is small, at least in CSLs backfilled with BGs. This CS is equivalent to the case of sequential loading under axisymmetric conditions studied in chapter 7. The numerical models revealed that there is longitudinal migration of hoop compression to neighbouring rings during sequential ring loading until the ring is eventually subjected to uniform compression. There is a tendency for segments not fully constrained by the ram pads to rotate radially.

There are two potential damage mechanisms:

1. Residual in-plane angularities, particularly at keystone joints, such as those observed in the least longitudinally compressed segments of CAM3. These permanent deformations can increase the risk of splitting failure at longitudinal joints or corner chipping at the ring rear;
2. Spalling at the ram pad interspaces of the front circumferential face accentuated by hoop tension at the ring front. The concrete spalling could not be detected with the CTT instrumentation layout, but the segments A3, D3 and B4 experienced hoop tensile strains exceeding the CTT elastic limit at the ring front.

*CS2: Eccentric ring*

The lining is eccentric relative to the tail skin. The sealing pressures are smoothly distributed with pressure gradients proportional to the ring eccentricity. The transverse action of the oblique hydraulic jacks locks the relative position of the ring. The radial rotation of the segments with the lowest tail clearance is constrained. The ring deforms under the action of

the pressure gradients combined with uneven constraints. This CS may be representative of a tunnelling scenario with moderate TBM steering, for example around a curve.

CS2 is well represented by the FE models simulating sequential radial loading with pressure gradients and uneven ram pad-lining interfaces examined in chapter 7. The numerical results confirmed that the magnitude of the ring distortion was directly related to the pressure gradients,  $L_u$  and the ring flexural stiffness, i.e. the curved jointed CSLs deformed more than the flat jointed CSLs. The deformation mode depended on the relative orientation of pressure gradients and ram pad constraints. The reference numerical models, selected from credible in situ boundary conditions inferred from the field data, were able to replicate the in situ ring behaviour during AD1 and were deployed as an effective tool to describe the underlying mechanics of the instrumented rings.

There is one concrete damage mechanism characteristic of this CS that adds to those of CS1: hoop cracking near the rear joints of constrained segments due to the hoop force spread at longitudinal joints with short contact lengths combined with the longitudinal bending induced by the radial ram loads. The risk of concrete spalling in constrained segments is also increased. The amplitude of the ring distortion magnifies the risk associated with both damage modes. The ring rolling and the relative orientation of pressure gradients and constraints affects the likelihood of damage. None of the above damage types could be detected with the designed ring instrumentation.

The evolution of field lining pressures of both rings confer credibility to the CS2 proposed: both rings were subjected to vertical pressure gradients much higher than grout-static, 60kPa/m and 25kPa/m for CAM3 and CAM4, and horizontal pressure gradients near the tail skin. The pressure gradients dissipated abruptly when the ring emerged fully from the shield tail.

### **b) CS3: Rotated segment**

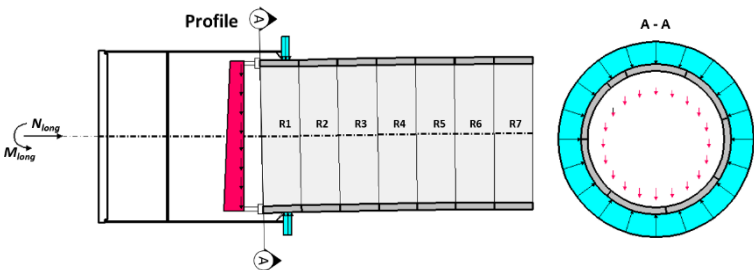
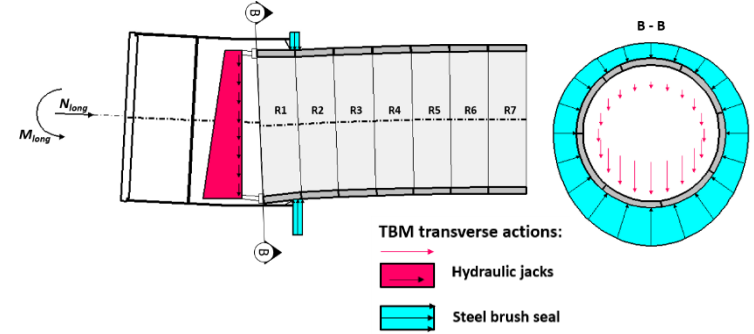
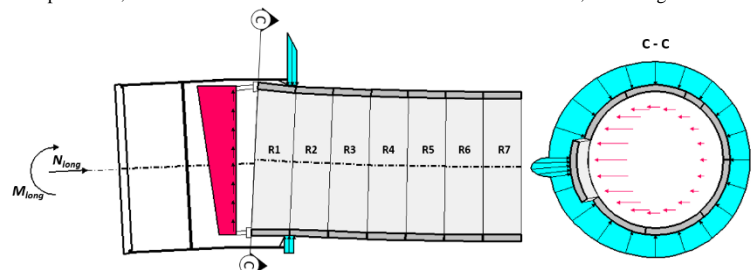
This tunnelling scenario is typical of pronounced TBM steering around curves, such as in the case of CAM4. The newly erected ring is subjected to high TBM longitudinal moments and transverse loads delivered by the oblique hydraulic jacks. The segment subjected to the highest radial ram loads, for example the outer springline segment in a horizontal curve, undergoes significant outward rotations that reduce locally the tail clearance. The segment is subjected to a high concentration of sealing pressures, or tail reaction if it makes contact with the tail skin, and bends biaxially. The high longitudinal compression of the hydraulic jacks prevents hoop flexure cracking. However, the hoop curvatures combined with the hoop tension near the ring front typical of sequential loading may result in the longitudinal cracking of the segment intrados at the ring front.

This cracking pattern was detected in the outer springline segment of CAM4, although it appeared to close progressively in the following advances. Sugimoto (2006) also reported that 72% of the longitudinal cracks recorded in his statistical study were formed while the ring had not fully emerged from the shield tail; 70% took place in tunnel sections with curved alignments and frequently at the springline segments.

It was proved that the numerical models could predict well the R1 ring behaviour during one TBM advance despite the simplified simulation of the TBM-lining transverse interactions: the radial pressures in the models were uniformly distributed along the longitudinal axis and the transverse action of the ram pads on the constrained segments were simulated with ring plane fixity. A more sophisticated modelling of the TBM-lining transverse interaction could have improved the reliability or the quantity of these findings. However, the required information on the TBM parts relevant to the TBM-lining transverse interaction was not available at the time.

The data captured in the CTT field trials provided key evidence that confirmed the importance of the TBM-lining transverse interaction on the CSL response, especially because the CTT was excavated in a chalk stratum whose primary in situ stresses were characterised by  $K_0 \approx 1$ , meaning that the construction effects were not biased by the tunnel deformations under deviatoric earth pressures. The strain data, however, was affected by concrete creep effects and the quality of BOTDR measurements (see section 9.2). The tail clearance, hydraulic jack inclination and ram pad eccentricity could not be measured.

**Table 9.1: Construction loading scenarios representative of field conditions near the tail skin**

Construction loading scenarios near the tail skin					
No.	Description	Ring behaviour near the tail skin	Structural damage in R1	In situ evidence	Structural analysis
1	<b>Concentric ring:</b> Sequential radial compression under roughly axisymmetric conditions. 	<p>This case is typical of <b>straight alignments</b>. There is longitudinal migration of hoop compression to neighbouring rings. Also, radial rotation of free segments under eccentric ring compression and offset ram loads relative to the packers.</p>	<p>1. Permanent ring deformations when the segments are free to rotate radially with sequential loading; they may lead to concrete splitting or chipping near the rear corners of segments during or after construction.</p> <p>2. Spalling at the interspaces between ram pads of the circumferential face exacerbated by tensile concrete cracking at the ring front.</p>	<p>1. Permanent in-plane angularities at least longitudinally compressed segments of CAM3;</p> <p>2. Hoop tensile membrane strains greater than the CTT yield tensile strain of <math>+130\mu\epsilon</math> observed at A3, D3 and B4 segments.</p>	<p>3D FE models for the sequential loading of two coupled rings under axisymmetric conditions</p>
2	<b>Eccentric ring:</b> Sequential radial compression under a smooth distribution of sealing pressures with vertical and horizontal pressure gradients proportional to the tail clearance. 	<p>This case is typical of tunnel sections subjected to <b>moderate TBM steering</b>, e.g. at <b>curved alignments</b>. The ring deforms under the action of pressure gradients and uneven ram pad-lining interface. The deformation mode depends on the orientation of pressure gradients and the ring perimeter subjected to ram pad constraints. The magnitude of ring distortion and hoop moments depends on <math>L_u</math>, the value of pressure gradients and longitudinal joint geometry.</p>	<p>1. Hoop cracks at the intrados of rear corners of constrained segments;</p> <p>2. Higher risk of spalling at the interspaces between ram pads of the circumferential face.</p>	<p>Evidence of sealing pressures in eccentric rings: CAM3 and CAM4 vertical pressure gradients greater than grout-static and horizontal gradients near the tail skin that drop abruptly once the ring exits from the shield tail;</p> <p>Evidence of ring behaviour: Good correlation between the in situ ring distortion, vertical til, hoop curvatures and hoop mean strains of CAM3 and CAM4 during AD1 with those predicted by the 3D FE reference models, the 3UKRA model and the 3UAB model. The reference models were selected beforehand in accordance with the most credible boundary conditions inferred from the field data.</p>	<p>3D FE models for the sequential loading of ten coupled rings under radial pressures with vertical gradient, variable ram pad-lining interface and R1 selfweight.</p>
3	<b>Rotated segment:</b> The segment subjected to the greatest outward radial ram load rotates outwards. The local reduction of tail clearance results in highly concentrated sealing pressures, and tail reaction if it is in direct contact with the shield tail, on the segment. 	<p>This case is typical of tunnel sections subjected to <b>pronounced TBM steering</b> such as in <b>curved alignments</b>. The segment undergoes biaxial bending due to the concentrated pressures combined with hoop membrane tension at the segment front due to segment rotation. There are two modes of bending depending on whether there is direct contact with the shield tail.</p>	<p>1. Longitudinal flexural crack at the intrados of the rotated segment.</p>	<p>Detection of a temporary crack at the intrados and front of the CAM4 springline segment located at outer side of the horizontal curve, i.e. B4;</p> <p>70% of the longitudinal cracks in Sugimoto's (2006) statistical study appeared in curved alignment and frequently at springline segments.</p>	<p>#N/A</p>

### 9.1.2. SHM systems for CSLs

The CTT deployment study evidenced that the development of FO connectors that can be connected quickly and perform effectively and reliably in hard construction environments is essential for the conventional use of DFOS sensing in CSLs, at least, for research projects. The development of small and cost-effective interrogators may facilitate the deployment of DFOS sensing techniques by the tunnel industry in a somewhat systematic manner (**Objective 2.1**).

In the CTT case study, the BOTDR measurement specification was adequate for the optical budget of DFOS circuits, although the repeatability governed by the interrogator was quite high when compared to the range of measured strains (**Objective 2.3**). It was, however, showcased the capability of BOTDR measurements with 500mm gauge length to detect concrete cracks in segments working at serviceable states with the centroid fitting method (**Objective 2.4**).

It was found that, in CSLs with staggered joints, temperature compensated mean strains represent net mechanical strains in hoop direction and total mechanical strains in longitudinal direction. Total curvatures in both directions could be representative of net mechanical curvatures (**Objective 2.2**).

A new double cross-correlation method based on normalised BFS and BFS increments can compensate the lack of local DFOS pre-tensioning as a spatial reference technique in the optical circuit (**Objectives 2.1 and 2.2**).

### 9.1.3. Joints and bolts

A new analytical method for longitudinal joint design that predicts joint performance against bursting and watertightness criteria for variable out-of-plane rotations was proposed in chapter 2. This inexpensive method enables tunnel designers to make rational decisions on the geometry of longitudinal joints by inserting the results of global CSL structural analysis on the proposed NR diagrams. The selection of joint geometry no longer needs to rely on general guidelines supported on past performance (Baumann, 1992). When more than one option is possible, then the evaluation of other criteria such as cost or the impact on the environment can be pondered. The method cannot cope with the effects of in-plane angularity (**Objective 3.2**).

The analytical estimation of bursting capacity and forces at imminent cracking can be a powerful tool in the preliminary stages of joint design, as it can help designers to minimise or avoid the need for costly full-scale tests and FE analyses and identify opportunities to reduce or eliminate bursting reinforcement in accordance with the expected global behaviour of the tunnel. However, the method proposed here relies on Zhou's (2015) polynomial approximation to ILCs, which overestimates  $\sigma_{t,max}$  in eccentrically loaded joints. The development of more accurate analytical expressions for transverse stresses is needed and should be encouraged in future research (**Objective 3.1**).

The bursting capacity before cracking depends mainly on the joint curvature and  $f_{ct}$ . Curved joints with radius in the order of 3.5m tolerate larger rotations than flat joints. The splitting cracks in flat joints tend to develop near the joint edge, which can trigger rebar corrosion and loss of lateral confinement. Conversely, the splitting cracks of curved joints would tend to be close to the joint mid depth. High strength concretes, with generally superior  $f_{ct}$ , ensure a greater bursting capacity before cracking.

The influence of joint geometry on the resilience to in-plane imperfections was briefly investigated through flat and curved joints with either a straight or rounded extrusion. Overall, the rounded flat joints exhibited the best resilience to high  $\alpha_j$ , followed by joints with one single curvature. The out-of-plane rotation of rounded flat joints, however, may undermine their resilience to  $\alpha_j$ .

The impact of longitudinal joint geometry on the global performance of CSLs in soft ground, i.e. with moderate  $\alpha$ , was examined in chapter 4 through a ten-ring model subjected to variable longitudinal and ovalisation loads. Given the longitudinal relaxation of tunnels with time (see section 9.1.1), the uncoupled rings could represent the long term condition while the strongly coupled CSLs could approximate the short term condition.

It was found that the CM solution underestimates the ring convergence of uncoupled segmental rings, particularly in those with curved joints, and provides a good estimation of peak hoop moments in flat jointed rings without substantial joint opening and in curved jointed rings, in the latter case when applied with smeared lining stiffness. With ring coupling, the vertical convergence approached the CM predictions at the expense of increasing hoop moments. The maximum moments at infinite ring coupling were linearly correlated with the CM peak moments through a lining stiffness factor  $f_{CSL}$  greater than 1, independent from  $K_o$  and inversely related to the longitudinal joint stiffness.

The detailed study on the role of spear bolts during construction, conducted in chapter 3, concluded that these bolts have two functions:

1. To impose a physical constraint to longitudinal joint lipping during ring build;
2. To reduce the risk of chipping at segment corners and differences in the radial rotation of adjacent segments while the ring exits the tail skin.

Contrarily to industry opinion, spear bolts have a secondary role in holding longitudinal gaskets closed, particularly in CSLs equipped with dowels at circumferential joints (**Objective 3.3**).

### 9.1.4. Recommendations for joint design

#### 9.1.4.1. Long term performance

The longitudinal joint geometry is only a relevant parameter of long term performance in tunnels excavated in soft ground, i.e. with at least moderate  $\alpha$ . Curved jointed CSLs reduce the risk of a consistent development of bursting cracks. However, in tunnels in soft ground under high ovalisation loads, the long term watertightness may be undermined due to excessive ring misalignments. The use

of dowels at circumferential joints limits the magnitude of ring misalignments. Flat jointed CSLs in soft ground under high ovalisation loads generally demand the use of concretes with higher  $f_{ct}$  and more bursting reinforcement than curved jointed CSLs.

### 9.1.4.2. Performance during construction

Table 9.2 summarises the implications that the selection of the longitudinal joint geometry may have on the CSL performance and risk of damage during construction, including recommendations on packer design, bolt deployment and TBM operations as a way to mitigate the risk of damage.

Packer depths equal to joint depths minimise segment rotations during sequential loading. Packer materials with low initial stiffness and substantial hardening under compression can prevent permanent tulip shapes without undermining the distribution of longitudinal loads within packers.

Boltless CSLs can be adopted in favourable tunnelling conditions with the benefit of removing the risk of localised cracking near bolt pockets (Chen and Mo, 2009) and cutting costs. Curved jointed CSLs may require the use of spear bolts to reduce the differential rotation of adjacent segments in non-bedded eccentric rings.



Table 9.2: Influence of longitudinal joint geometry on risk of concrete damage

Potential damage	Triggered by	Response	Curved jointed CSL		
			Damage		Mitigation
			Likelihood	Severity	
Chipping/cracking of segment corners or bursting cracks at longitudinal joints	Initial joint rotations	Peak contact pressures near the joint mid depth are stable and equal to those in perfect joints.	Low	Low	N/A
	In-plane angularities	They can originate at assembly stage, less likely during sequential loading. Resistance to bursting and shear decrease sharply.	Moderate	Permanent	1) Careful assembly.
	CS1: Concentric ring	Peak contact pressures near the joint mid depth are stable and equal to full ring compression.	Low	Low	N/A
	CS2: Eccentric ring	The low $I_R$ amplifies ring distortion, which increases the radial and tangential TBM reaction forces and in turn increase the longitudinal bending and decrease hoop compression respectively at the extremities of the restrained ring perimeter.	Low at straight alignments or with diligent steering. Moderate at curved alignments or with substantial TBM steering.	Temporary action but permanent damage	1) Diligent steering; 2) Short $L_u$ ; 3) Deploy spear bolts;
Spalling at ram pad interspaces	CS1: Concentric ring with negative ram pad eccentricity	Peak hoop tensile strains at ram pad interspaces in standard segments increase with negative ram pad eccentricity.	Moderate with high ram loads: e.g. in deep tunnels with high H/D ratio or substantial TBM steering. Low in other cases.	Temporary action but permanent damage	1) Careful assembly; 2) Diligent steering; 3) Apply moderate positive ram pad eccentricity by default.
	CS2: Eccentric ring	The low $I_R$ amplifies ring distortion, which increases tangential TBM reaction forces and in turn increase the peak tensile strains at the ram pad interspaces of restrained standard segments.	Low at straight alignments or with diligent steering. Moderate at curved alignments or with substantial TBM steering.	Temporary action but permanent damage	1) Diligent steering; 2) Short $L_u$ .
Longitudinal flexural cracking at segment intrados	CS3: Rotated segment	The segment bends biaxially. The high longitudinal compression of ram loads prevents flexural cracking in hoop direction. The hoop curvatures combined with the hoop tension at the ring front results in longitudinal flexural cracking at the segment intrados.	Low at straight alignments or with diligent steering. Moderate at curved alignments or with substantial TBM steering.	Temporary action and, at least, the damage may be partially reversible.	1) Diligent steering; 2) Short $L_u$ ; 3) Deploy spear bolts in segments with foreseeable high rotations, e.g. outer springline segments at curved alignments; 4) Maximise $K_j$ through packer number, depth and material; 5) Apply moderate positive ram pad eccentricity by default; 6) Avoid keystones at areas with foreseeable high segment rotations.

Table 9.2 (continued)

Potential damage	Triggered by	Response	Flat jointed CSL		
			Likelihood	Damage Severity	Mitigation
Chipping/cracking of segment corners or bursting cracks at longitudinal joints	Initial joint rotations	Peak contact stresses increase with joint rotation at joint edge.	Moderate	Permanent	1) Careful assembly.
	In-plane angularities	They can originate at assembly stage or the sequential loading of eccentric rings. Resistance to bursting and shear decrease sharply.	Moderate	Permanent	1) Careful assembly.
	CS1: Concentric ring	Contact stresses at joint edge increase with radial segment rotations. Segment rotations depend on the segment length, the rotational capacity of circumferential joints, ram pad eccentricity and, to a lesser extent, radial pressures.	Moderate Higher at keystone	Temporary action but permanent damage	1) Maximise $K_j$ through packer number, depth and material; 2) Apply moderate positive ram pad eccentricity by default; 3) Maximise keystone length; 4) Careful assembly; 5) Deploy spear bolts at keystone longitudinal joints; 6) Design packers specific for keystones.
	CS2: Eccentric ring	The high $I_R$ limits the ring distortion, which leads to reduced radial and tangential TBM reaction forces and in turn results in low longitudinal bending and hoop compression at the extremities of the restrained ring perimeter.	Low, but the risk increases when combined with 2D or 3D imperfections.	Permanent	1) Careful assembly; 2) Diligent steering; 3) Short $L_u$ ; 4) Deploy spear bolts (minor).
Spalling at ram pad interspaces	CS1: Concentric ring with negative ram pad eccentricity		Same as curved jointed CSL.		
	CS2: Eccentric ring	The high $I_R$ limits the ring distortion, which leads to reduced tangential TBM reaction forces and in turn results in low peak tensile strains at the ram pad interspaces of restrained standard segments.	Low	Permanent	1) Careful assembly; 2) Diligent steering; 3) Short $L_u$ .
Longitudinal flexural cracking at segment intrados	CS3: Rotated segment		Same as curved jointed CSL.		

### 9.2. Future works

This study represents a qualitative leap towards the optimisation of CSL design, shifting the attention of researchers and designers from tail void pressures to TBM-lining transverse interactions as the most determinant factor of structural response during construction in CSLs simultaneously backfilled with BGs. Further work is, however, required to develop the theoretical framework proposed here into limit state design methods, with clearly defined input loads and structural models, that can be deployed systematically by designers.

Figure 9.1. illustrates the research workflow needed to incorporate the effects of TBM-lining transverse interaction into design procedures. It integrates the findings in this study with the lines of future research:

1. Development of a TBM monitoring system fitted into the tail skin for the measurement of tail clearance, hydraulic jack inclination and ram pad eccentricity during tunnelling.

With the measurement of the quantities outlined in Figure 9.1, it would be possible to calculate the relative inclination between ram pads and lining, which should determine the transverse component of ram loads providing there is no lipping of the pads, and the distribution of sealing pressures derived as a function of the tail clearance. The history of TBM-lining transverse interactions captured during tunnelling would become an input for the preliminary PDA method of ring joints and would provide valuable field data for the development and validation of line research 3.

The plan should include the development and verification of a prototype and the in situ validation of the underpinning hypotheses with a structural monitoring system;

2. Definition of the correlation between tail clearance and sealing pressures through laboratory loading tests of sealing systems. The knowledge of this relationship would contribute to validate the line of research 1 and obtain credible input loads for the analysis of CS3;
3. Development of engineering models that can predict a range of working transverse loads from input tunnelling conditions, e.g. geology and tunnel alignment. These working loads could then be used as input loads for the analysis of CS2 and help designers to optimise ring joint design with the aid of the tunnel beam models proposed in this study;
4. Development of CSL structural models for limit state design representative of CS2;
5. Development of segment structural models for limit state design representative of CS3.

Other secondary lines of research are:

6. Study on the impact of nonlinear strain profiles and concrete cracks on the BOTDR measurement accuracy and the influence of DFOS attachment methods on crack detection and measurement of average steel strains in cracked concrete;

7. Development of accurate analytical expressions for transverse stresses required for the calculation of joint bursting capacity;
8. Study on the impact of joint geometry and ring sequential loading on the resilience of longitudinal joints to angular imperfections. The brief investigation conducted in chapter 2 evidenced differences in resilience between joint geometries. Additionally, the CTT field data interpretation showed that the sequential ring loading may correct the initial in-plane angularities of joints with contact at the ring front and exacerbate the angular imperfections of opposite sign.

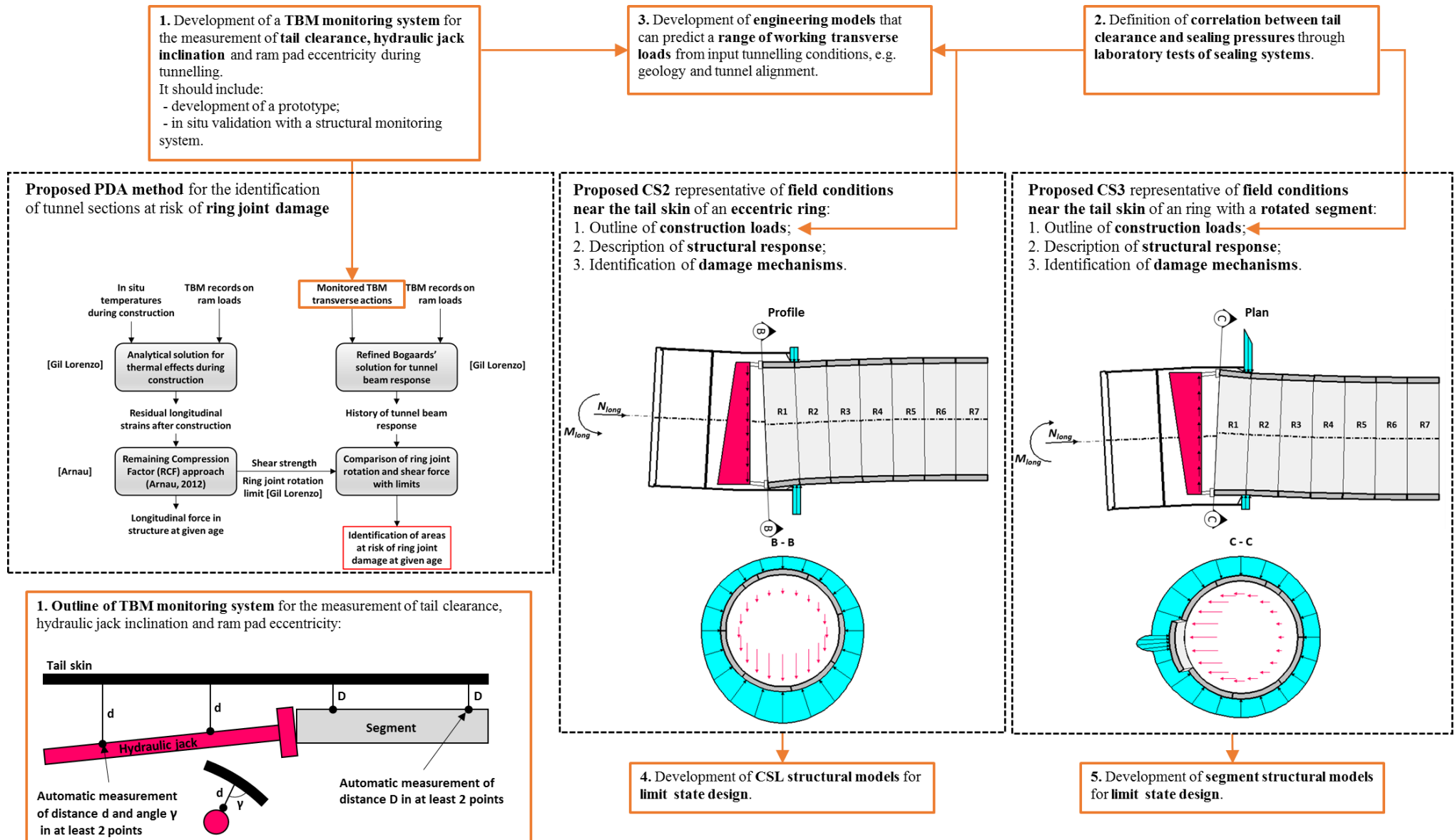


Figure 9.1: Future works

---

## References

- ABAQUS (2012). *Abaqus Manual (6.12)*. Dassault Systèmes Simulia Corp., Providence, RI, USA.
- Anixter (2014). *Technical Reports*. France.
- Antunes, P. (2012). Testing procedures for two-component annulus grouts. *North American Tunnelling 2012 Proceedings*. Matthre Fowler, SMME, 14-23.
- Arnau, O. (2012). *Structural response of precast concrete segmental tunnel linings*. Ph.D. Thesis. Universitat Politècnica de Catalunya.
- Bakker, K.J. (2003). *Structural design of linings for bored tunnels in soft ground*. Heron, 48(1):33-63.
- Bassett, R. (2012). *A guide to field instrumentation in geotechnics-Principles, installation and readings*. Spon Press, England.
- Bengtsson, C. (2000). Creep of timber in different loading modes-material property aspects. *The 7<sup>th</sup> Works Conference on Timber Engineering*, Malasya.
- Baumann, T. (1992). Tunnelauskleidungen mit Stahlbetontubbingen. *Bautechnik*, 69:11-20.
- Bazant, Z.P., Murphy, W.P. (1995). Creep and shrinkage prediction model for analysis and design of concrete structure-Model B3\*. *Materials and Structures*, 28:357-365.
- Berwanger, C., Sarkar, F. (1976). Thermal expansion of concrete and reinforced concrete. *ACI Structural Journal Proceedings*, 73(11):618-621.
- Bezuijen, A., Talmon, A.M. (2003). Grout, the foundation of a bored tunnel. *BGA International Conference on Foundations*, Thomas Telford, London
- Bezuijen, A., Talmon, A.M., Kaalberg, F.J., Plugge, R. (2004). Field measurements of grout pressures during tunnelling of the Sophia rail tunnel. *Soils and Foundations*, 44(1):39-48.
- Bezuijen, A., Talmon, A.M. (2005). Laboratory testing of grout properties and their influence on back fill grouting. *Proceedings of the 31st ITA-AITES World Tunnel Congress*, Y. Erdem & T. Solak, 941-948.
- Bezuijen, A., Talmon, A.M. (2009). Processes around a TBM. *Geotechnical Aspects of Underground Construction in Soft Ground*, Taylor & Francis Group, London.
- Bishnoi, S., Uomoto T. (2008). Strain-temperature hysteresis in concrete under cyclic freeze-thaw conditions. *Cement & Concrete Composites*, 30:374-380.
- Blanchard, B.S., Fabrycky, W.J. (2011). *Systems engineering and analysis*. Pearson International Edition, USA.

- Blom, C.B.M. (2002). *Design philosophy of concrete linings for tunnels in soft soils*. Ph.D Thesis, TU Delft.
- Blom, C.B.M., Van der Horst, E.J., Jovanovic, P.S. (1999). Three-dimensional structural analyses of the shield-driven “Green Heart” tunnel of the high-speed line South. *Tunnelling & Underground Space Technology*, 14(2):217-224.
- Bogaards, P.J., Bakker, K.J. (1999). Longitudinal bending moments in the tube of a bored tunnel. *NUMOG VII*, Balkema, 317-321.
- Brown, A.W., DeMerchant, M.D., Bao X., Bremner, T.W. (1999). Spatial resolution enhancement of a Brillouin-distributed sensor using a novel signal processing method. *Journal of Lightwave Technology*, 17(7):1179-1183.
- BSI (2010). *Eurocode 2: Design of concrete structures-Part1-1: General rules and rules for building (BS EN 1992-1-1)*.
- BTS (2011). *Monitoring Underground Construction-A best practice guide*. ICE, London.
- BTS (2004). *Tunnel lining design guide*. ICE, London.
- Cavalero, S.H.P. (2009). *Aspectos tecnológicos de túneles construidos con tuneladora y dovelas prefabricadas de hormigón*. Ph.D. Thesis, Universitat Politècnica de Catalunya.
- Chen, J.S., Mo, H.H. (2009). Numerical study on crack problems in segments of shield tunnel using finite element method. *Tunnelling and Underground Space Technology*, 24:91-102.
- Chen, W.F. (1982). *Plasticity in reinforced concrete*. McGraw-Hill, USA.
- Colton, J. (2013). *Fibre optic connector investigation*. Lucid Ltd., UK.
- Craig, R.N., Muir-Wood, A.M. (1978). *A review of tunnel lining practice in the United Kingdom. TRRL Supplementary Report 335*.
- Crossrail (2014). *Internal reports*. London.
- CSIC (2016). *Distributed Fibre Optic Strain Sensing for Monitoring Civil Infrastructure-A practical guide*. ICE, UK.
- Curtis, D.J. (1976). Discussion of “The circular tunnel in elastic ground” by A.M. Muir Wood”. *Géotechnique*, 26(1):231-237.
- Debrauwer, R., Bakker, K.J., Aartsen, R.J. (2003). Improved grout pressure model for tunnel linings in soft soil conditions. *(Re)Claiming the Underground Space*, Saveur, Swets & Zeitlinger, Lisse.
- Deif, A., Martin Perez, B., Cousing, B., Zhang, C., Bao, X., Li, W. (2010). Detection of cracks in reinforced concrete beam using distributed Brillouin fibre sensors. *Smart Materials and Structures*, 19:1-7.

- Ding, W.Q., Peng, Y.C., Yan, Z.G., Shen, B.W., Zhu, H.H., Wei, X.X. (2013). Full-scale testing and modelling of the mechanical behaviour of shield TBM tunnel joints. *Structural Engineering and Mechanics*, 45(3):333-350.
- Do, N.A., Dias, D., Oreste, P., Djeran-Maigre, I. (2013). 2D numerical investigation of segmental tunnel lining behaviour. *Tunnelling and Underground Space Technology*, 37:115-127.
- Duddeck, H., Erdmann, J. (1982). Structural design models for tunnels. *Tunnelling'82: Proceedings*, 83-91, London.
- Dunnicliff, J. (1993). *Geotechnical instrumentation for monitoring field performance*. Wiley Interscience, USA.
- Dunnicliff, J. (2008). *Geotechnical instrumentation news (GIN)*. Geotechnical News.
- El-Tayeb, E.H., El-Metwally, S.E., Askar, H.S., Yousef, A.M. (2015). Thermal analysis of reinforced concrete beams and frames. *HBRC Journal*, 1-17.
- Feddema A., Van der Zon, W.H., Möller, M., Hashimoto, T. (2006). ETAC two-component grout field test at Botlek rail tunnel. *Tunnelling, A Decade of Progress - GeoDelft 1995-2005*, Taylor & Francis, 19-25.
- Firesmith (2011). *Using V Models for Testing*. Retrieved 2015, from: [https://insights.sei.cmu.edu/sei\\_blog/2013/11/using-v-models-for-testing.html](https://insights.sei.cmu.edu/sei_blog/2013/11/using-v-models-for-testing.html)
- Gambhir, M.L. (2013). *Concrete Technology: Theory and Practice*. 5<sup>th</sup> edition, McGraw-Hill Education, India.
- Gijsbers, F.B.J., Hordijk, D.A. (1997). *Experimental research on shear between ring joints*. COB.
- Gladwell, G.M.L. (1980). *Contact problems in the classical theory of elasticity*. Springer Science & Business Media.
- Glisic, B. (2011). Influence of the gauge length on the accuracy of long-gauge sensors employed in monitoring of prismatic beams. *Measurement Science and Technology*, 22:1-13.
- Glišić, B., Inaudi, D. (2007). *Fibre Optic Methods for Structural Health Monitoring*. John Wiley and Sons Ltd., England.
- Gong, W., Juang, C.H., Huang, H., Zhang, J., Luo, Z. (2015). Improved analytical model for circumferential behaviour of jointed shield tunnels considering the longitudinal differential settlements. *Tunnelling and Underground Space Technology*, 45:153-165.
- Grose, W.J., Benton, L. (2005). Hull wastewater flow transfer tunnel: tunnel collapse and causation investigation. *Proceedings of the Institution of Civil Engineers - Geotechnical Engineering*, 158(4): 179-185.



- Gruebl, F. (2006). Segmental rings (Critical loads and damage prevention). *International Symposium on Underground Excavation and Tunnelling*, Bangkok, Thailand.
- Guyon, Y. (1953). *Prestressed concrete*. F.J. Parsons, London.
- Haack, A. (1991). Water leakages in subsurface facilities: required watertightness, contractual matters, and methods of redevelopment. *Tunnelling Underground Space Technology Incorporating Trenchless*, 6(3):273–282.
- Harding, A., Chappel, M., King, M. (2014). Myth and reality: bolts in modern concrete segmental tunnel linings. *North American Tunneling, Proceedings, SME, USA*.
- Hashimoto, T., Brinkman, J., Konda, T., Kano, Y., Feddema, A. (2006). Simultaneous backfill grouting, pressure development in construction phase and in long term. *Tunnelling, a decade of progress - GeoDelft 1995-2005*, Taylor & Francis, 101-107.
- Hashimoto, T., Nagaya, J., Konda, T., Tamura, T. (2002). Observation of lining pressure due to shield tunnelling. *Geotechnical Aspects of Underground Construction in Soft Ground*, Kastner, Lyon.
- Henn, R.W. (2003). *AUA Guidelines for Backfilling and Contact Grouting of Tunnels and Shafts*. ASCE.
- Herrenknecht, M., Bappler, M.S. (2003). Segmental concrete lining design and installation. *Soft Ground and Hard Rock Mechanical Tunneling Technology Seminar*, Colorado School of Mines.
- Hoefsloot, F.J.M., Bakker, K.J. (2002). Longitudinal effects bored Hubertus tunnel in The Hague. *Geotechnical Aspects of Underground Construction in Soft Ground*, Kastner, Lyon.
- Hoefsloot, F.J.M. (2007). *Boortunnel Groene Hart, Analytische oplossing liggerwerking*. Fugro Ingenieursbureau B.V.
- Hoefsloot, F.J.M. (2009). Analytical solution of longitudinal behaviour of tunnel lining. *Geotechnical Aspects of Underground Construction in Soft Ground*, Taylor & Francis, London.
- Holzer, S.M., Loferski, J.R., Dillard, D.A. (1989). A review of creep in wood: Concepts relevant to develop long-term behaviour predictions for wood structures. *Wood and Fiber Science*, 21(4):376-392.
- Hordijk, D.A., Gijsbers, F.B.J. (1996). *Laboratoriumproeven tunnelsegmenten*, K100-W-026, COB.
- Huang, X., Huang, H., Zhang, J. (2012). Flattening of jointed shield-driven tunnel induced by longitudinal differential settlements. *Tunnelling and Underground Space Technology*, 31:20-32.
- Ibell, T.J. (1992). *Behaviour of anchorage zones for prestressed concrete*. Ph.D Thesis, Cambridge University.

- Ishimura, T., Mashimo, H., Morimoto, S. (2013). Influence of construction load for segmental lining by result of in-situ measurement and numerical analysis. *World Tunnel Congress 2013*, Anagnostou, Taylor & Francis, London.
- ITA (2000). Guidelines for the design of shield tunnel lining. *Tunnelling and Underground Space Technology*, 15(3):303-331.
- Kim, S.H., Lee, J.J., Kwon, I. B. (2002). Structural monitoring of a bending beam using Brillouin optical fiber sensors. *Smart Materials and Structures*, 11:396-403.
- Koek, A.J. (2005a). *Axiale voorspanning in de lining van een geboorde tunnel*. Student thesis, TU Delft.
- Koek, A.J., Bakker, K.J., Blom, C.B.M. (2005b). Axial pre-stresses in the lining of a bored tunnel. *Geotechnical aspects of underground construction in soft ground*, 559-564.
- Kolic, D., Wagner, H., Schulter, A. (2000). Development of dowelled connectors for segmental linings. *Felsbau* 18(6):32-40.
- Kolymbas, D. (2005). *Tunelling and tunnel mechanics-A rational approach to tunnelling*. Springer, Germany.
- Koyama, Y. (2003). Present status and technology of shield tunneling method in Japan. *Tunnelling and Underground Space Technology*, 18:145-159.
- Kwak, H., Song, J. (2002). Cracking analysis of RC members using polynomial strain distribution function. *Engineering Structures*, 24(4):455-468.
- Li, M., Jiao, W., Liuwu, X., Song, Y., Chang, L. (2015). A method for peak-seeking of BOTDR based on the incomplete Brillouin spectrum. *IEEE Photonics Journal*, 7(5).
- Li, Q., Gan, J., Wu, Y., Zhang, Z., Li, J., Yang, Z. (2016). High spatial resolution BOTDR based on differential Brillouin spectrum technique. *IEEE Photonics Technology Letters*, 28(14).
- Li, X., Yan, Z., Wang, Z., Zhu, H. (2015). Experimental and analytical study on longitudinal joint opening of concrete segmental lining. *Tunnel and Underground Space Technology*, 46:52-63.
- Li, Z. (2014). *Long-term behaviour of cast-iron tunnel cross passage in London Clay*, Ph.D. Thesis, Cambridge University.
- Liao, S.M., Peng, F.L., Shen, S.L. (2008). Analysis of shearing effect on tunnel induced by load transfer along longitudinal direction. *Tunnelling and Underground Space Technology*, 23:421-430.
- Lofgren, I. (2007). Calculation of crack width and crack spacing. *Proceedings of the Nordic Mini-Seminar on Fibre reinforced concrete*, Workshop proceeding no. 6, Trondheim.
- Lord, J.A., Clayton, C.R.I., Mortimore, R.N. (2002). *Engineering in chalk*. CIRIA, London.

- Luttikholt, A. (2007). *Ultimate limit state analysis of a segmented tunnel lining—Results of full-scale tests compared to finite element analysis*. Master Thesis, TU Delft.
- Maidl, B., Herrenknecht, M., Maidl, U., Wehrmeyer, G. (2012). *Mechanised shield tunnelling*, Ernst & Sohn, A Wiley Company, 2<sup>nd</sup> ed, Berlin.
- Mashimo, H., Ishimura, T. (2005). Numerical modelling of the behaviour of shield tunnel lining during assembly of a tunnel ring. *Geotechnical Aspects of Underground Construction in Soft Ground*, 587-594.
- Mayer, P., Klotz, C., Franzius, J.N., Hörrle D. (2009). *A tool to improve risk analysis of TBM tunnelling processes*. ITA-AITES World Tunnel Congress 2009, Budapest.
- Muir-Wood, A.M. (1975). The circular tunnel in elastic ground. *Géotechnique* 25(1):115-127.
- Murayama, H., Kageyama, A., Shimada, A., Nishiyama, A. (2005). Improvement of spatial resolution for strain measurements by analysing Brillouin gain spectrum. *17<sup>th</sup> International Conference on Optical Fibre Sensors*, Proc. SPIE, 5855:552-554.
- Neville, A.M., Brooks, J.J. (2010). *Concrete Technology*. Longman, UK.
- Neville, A.M., Dilger, W.H., Brooks, J.J. (1983). *Creep of plain and structural concrete*. Construction Press, New York, USA.
- Neubrex (2015). *NBX-5000 Specifications*. Retrieved in 2015, from: <http://www.neubrex.com/htm/products/pro-nbx5001.htm>
- Nilson, A.H., Winter, G. (1991). *Design of Concrete Structures*. McGraw-Hill International Editions.
- Ninic, J., Freitag, S., Mecshke, G. (2017). A hybrid finite element and surrogate modelling approach for simulation and monitoring supported TBM steering. *Tunnelling and Underground Space Technology*, 63:12-28.
- Peila, D., Borio, L., Pelizza, S. (2011). The behaviour of a two-component backfilling grout used in a tunnel boring machine. *Acta Geotechnica Slovenica*, 1:5–15.
- Phoenix (2014). *Seals for tunnel construction*. Retrieved in 2014, from: <http://www.file.seekpart.com/keywordpdf/2011/3/20113221441482.pdf>
- Purkiss, J. A. (1987). Thermal expansion of steel fibre reinforced concrete up to 800°C. *Composite Structures* 4, 1:404-415, Springer, Netherlands.
- Reschke, A., Noppenberger, C. (2011). Brisbane Airport Link Earth Pressure Balance machine two component tailskin grouting—A new Australian record, *14<sup>th</sup> Australasian Tunnelling Conference*, Auckland, New Zealand.

- Rodrigues, C., Inaudi, D., Glisic, B. (2013). Long-gauge fibre optic sensors: performance comparison and applications. *Int. J. Lifecycle Performance Engineering*, 1(3).
- Rogers, A. (1999). Review article–Distributed optical-fibre sensing. *Journal of Measurement Science Technology*, 10:75-79.
- Shalabi, F.I. (2001). *Behaviour of gasketed segmental concrete tunnel lining*, Ph.D. Thesis, University of Illinois.
- Shandong East Machinery & Equipment Co. (2017). *Wire Seal Brushes for Tunnel Boring Machines, Tbm Cutter*. Retrieved 01/08/2018, from: <https://rockbits.en.made-in-china.com/product/sqKQXmaJXNUy/China-Wire-Seal-Brushes-for-Tunnel-Boring-Machines-Tbm-Cutter.html>
- Shang, Q.F., Liu, J., Li, Y.Q. (2009). *Influence of temperature gradient on measurement accuracy of BOTDR system*, IEEE, 1-4.
- Sheahan, T., Mazzel, D., McRae, J. (2008). Performance testing of MEMS-based tilt sensors. *Geotechnical Instrumentation News (GIN)*.
- Soto, M.A., Thévenaz, L. (2013). Modelling and evaluating the performance of Brillouin distributed optical fiber sensors. *Optics Express*, 21(25):31347-31366.
- Sugimoto, M. (2006). Causes of shield segment damages during construction. *International Symposium on Underground Excavation and Tunnelling*, International Tunneling Association (ITA) Bangkok, Thailand, 67-74.
- Swartz, S., Lum, H., McRae, M., Curtis, D.J., Shamma, J. (2002). Structural design and testing of a bolted and gasketed pre-cast concrete segmental lining for high external hydrostatic pressure. *North American Tunnelling*.
- TAC Corporation (2017). *TAC Backfill Grout Injection: Two Component Backfill Grout Injection*. Retrieved 27/06/2017, from: <http://www.tac-co.com/enoutline/TAC%20Presentation.pdf>
- Talmon, A.M., Aanen, L., Bezuijen, A., Van der Zon, W.H. (2001). Grout pressures around a tunnel lining. *Modern Tunneling Science and Technology*. Balkema, Kyoto.
- Talmon, A.W., Aanen, L., Van der Zon, W.H. (2002). *Stromingsgedrag groutinjectie*. Delft Cluster.
- Talmon, A.M., Bezuijen, A. (2005). Grout properties and their influence on back fill grouting. *Geotechnical aspects of underground construction in soft ground*, Rotterdam, A.A. Balkema, 7-12.
- Talmon, A.M., Bezuijen, A. (2006). Grouting the void of bored tunnels: the role of hardening and consolidation of grouts. *Geotechnical Aspects of Underground Construction in Soft Ground*, Taylor & Francis, London, 319-325.

- Talmon, A.M., Bezuijen, A. (2009a). Backfill grouting research at Groene Hart Tunnel. *Geotechnical Aspects of Underground Construction in Soft Ground*, Taylor & Francis, London.
- Talmon, A.M., Bezuijen, A. (2009b). Simulating consolidation of TBM grout at Noordplaspolder. *Tunnelling and Underground Space Technology*, 24(5):493-499.
- Talmon, A.M., Bezuijen, A., Hoefsloot, F.J.M. (2009c). Longitudinal tube bending due to grout pressures. *Geotechnical Aspects of Underground Construction in Soft Ground*, Taylor & Francis, London.
- USACE (1997). *EM Tunnels and Shafts in Rock*. Washington, USA.
- Vimalanathan, Y.K. (2007). Development in pre-cast concrete segmental circular tunnel linings. *33<sup>rd</sup> World tunnel congress - Underground space: the 4<sup>th</sup> dimension of metropolises*, Prague, Taylor & Francis Group, London, 2: 1451-1456.
- Wang, F., Huang, H., Soga, K., Li, Z., Zhang, D., Tsuno, K. (2012). Deformation analysis of a tunnel with concrete segmental lining subjected to ground surface loading novel joint model. *ITA-AITES World Tunnel Congress*, Bangkok, Thailand.
- Webb, G.T., Vardanega, P.J., Middleton, C.R. (2015). Categories of SHM Deployments: Technologies and Capabilities. *Journal of Bridge Engineering*, 20(11):1-15, ASCE.
- Williams, J. (2005). *Engineering tribology*. Cambridge University Press.
- Winterton, T.R. (1994). Developments in precast concrete tunnel linings in the United Kingdom. *Tunnelling '94*, 601-633, London.
- Young, W.C., Budynas, R.G. (2002). *Roark's formulas for stresses and strain*, McGraw-Hill International Edition, 7<sup>th</sup> Ed.
- Zhao, L., Li, Y., Xu, Z., Yang, Z., Lu, A. (2014). On-line monitoring system of 110kV submarine cable based on BOTDR. *Sensors and Actuators A 216*, pp.28-35.
- Zhou, L.Y., Liu, Z., He, Z.Q. (2015). Further investigation of transverse stresses and bursting forces in post-tensioned anchorage zones. *Structural Concrete 1*, 84-92.

## **Appendix 1**

# **Manufacturer's technical specifications of CTT monitoring instrumentation**

## VW Strain Gauge Embedment VWS-2100 Series

Designed for direct embedment in concrete. Can be used within mass concrete with coarse aggregates as its heavy duty construction resists bending and the large end flanges provide a high contact area.



# VW Strain Gauge Embedment VWS-2100 Series

## Overview



Geosense® VWS-2100 series vibrating wire embedment strain gauges are designed for direct embedment in concrete.

The strain gauge operates on the principle that a tensioned wire, when plucked, vibrates at its resonant frequency. The square of this frequency is proportional to the strain in the wire.

The gauge consists of two end blocks with a tensioned steel wire between them.

Around the wire is a magnetic coil which when pulsed by a vibrating readout or data logger interface plucks the wire and measures the resultant resonant frequency of vibration.

Deformation within the concrete will cause the two end blocks will move relative to each other. The tension in the wire between the blocks will change accordingly thus altering the resonant frequency of the wire.

VWS-2125 can be used within mass concrete with coarse aggregates as it's heavy duty construction resists bending and the large end flanges provide a high contact area.

### APPLICATIONS

Measurement of stress and strain deformation in:

Driven and bored piles

Tunnels and deep excavations

Mass concrete pours

Precast piles

Concrete dams

Retaining walls

Dynamic measurements with auto resonant version

Building foundations

### FEATURES

Reliable long-term performance

Rugged, suitable for demanding environments

High accuracy

Insensitive to long cable lengths

Totally waterproof

Direct embedment in concrete

Auto resonant units available





# VW Strain Gauge Embedment VWS-2100 Series

## Specifications

### GENERAL

Model number	VWS-2100	VWS-2120	VWS-2125
Gauge length	150mm	50mm	250mm
Overall length	156mm	54mm	260mm
Resolution	1 $\mu\epsilon$	1 $\mu\epsilon$	1 $\mu\epsilon$
Strain range	3000 $\mu\epsilon$	3000 $\mu\epsilon$	3000 $\mu\epsilon$
Accuracy <sup>1</sup>	$\pm 0.1\%$ to $\pm 0.5\%$ FS	$\pm 0.1\%$ to $\pm 0.5\%$ FS	$\pm 0.1\%$ to $\pm 0.5\%$ FS
Non linearity	<0.5% FS	<0.5% FS	<0.5% FS
Coil resistance	180 $\Omega$	180 $\Omega$	180 $\Omega$
Coefficient of thermal expansion	12.0 ppm/ $^{\circ}$ C	12.0 ppm/ $^{\circ}$ C	12.0 ppm/ $^{\circ}$ C
Thermal factor K	<0.1% FS/ $^{\circ}$ C	<0.1% FS/ $^{\circ}$ C	<0.1% FS/ $^{\circ}$ C
Temperature range	-20 $^{\circ}$ C to +80 $^{\circ}$ C	-20 $^{\circ}$ C to +80 $^{\circ}$ C	-20 $^{\circ}$ C to +80 $^{\circ}$ C
Frequency range	850-1550	850-1550	850-1550
Cable type	2 pair x Type 900 - VW Sensor with Foil Screen & Drain Wire		
Cable sheath	Orange PUR 5mm $\varnothing$		

### ORDERING INFORMATION

Gauge length
Cable length
Readout

<sup>1</sup>  $\pm 0.1\%$  with individual calibration,  $\pm 0.5\%$  FS with standard batch calibration

# VW Strain Gauge Embedment VWS-2100 Series

---

## Further Information

### READOUTS

---

VWS-2100 vibrating wire strain gauges may be read by the VWR-1 or any vibrating wire readout device and may be readily data logged using the GeoLogger G8-Plus or any other data loggers with vibrating wire interface modules.

### CABLES

---

therefore insensitive to resistance changes in connecting cables caused by contact resistance or leakage to ground.

Cable may be readily and simply extended on site without special precautions. Gauges may be read up to 1000 metres away from their installed location without change in calibration.

### FULLY WATERPROOF

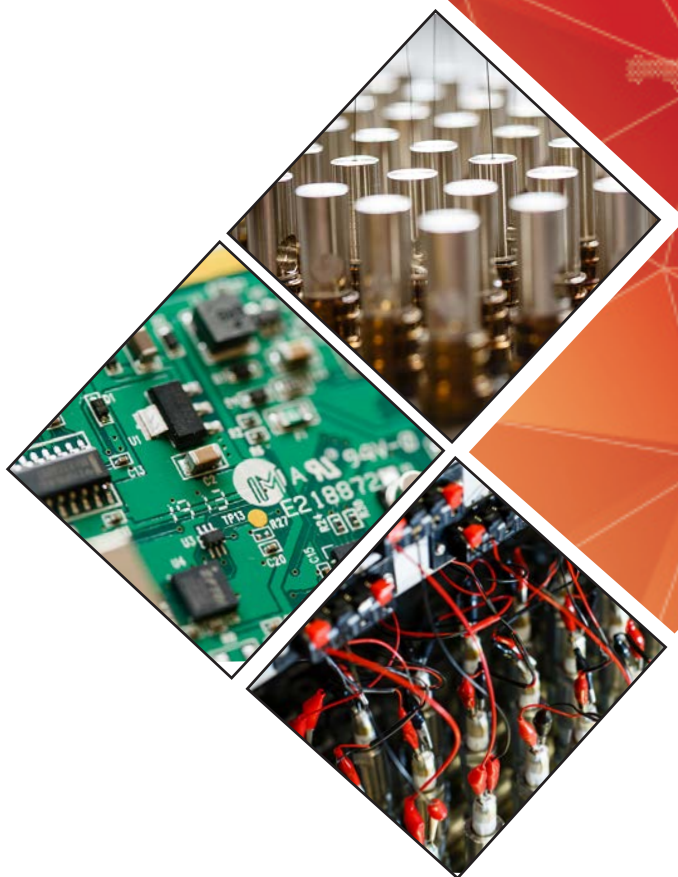
---

VWS-2100 strain gauges are fully waterproof all stainless steel construction with coils encapsulated with epoxy resin. The protective tube assembly is totally sealed to the embedment flanges by laser welding, thus eliminating any possibility of seal degradation. During the testing and stressing procedures, the welds are fully checked by tensile testing carried out in excess of the elastic limit of the protective tube assembly.

### ROSETTES & ZERO STRAIN CONTAINERS

---

Strain gauge rosettes and zero strain containers are available for VWS-2100 gauge series.



Geosense Ltd, Nova House, Rougham Industrial Estate, Rougham, Bury St Edmunds, Suffolk IP30 9ND, England

[www.geosense.co.uk](http://www.geosense.co.uk) e [sales@geosense.co.uk](mailto:sales@geosense.co.uk) t +44(0)1359 270457



DATE Aug. 8, 2006

NO. JFT-02323

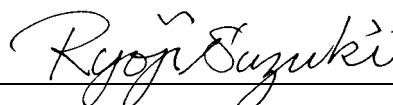
Supersedes None

**Messrs. University of Cambridge**

**SPECIFICATION  
FOR  
SINGLEMODE OPTICAL FIBER RIBBON  
(FutureGuide®-SM 8 FIBER RIBBON)**

A handwritten signature in cursive script, reading 'Hideo Komiyama'.

Prepared by **H. KOMIYAMA**  
Manager  
Optical Fiber & Cable Dept.  
Optical Fiber and Cable System Div.

A handwritten signature in cursive script, reading 'Ryoji Suzuki'.

Approved by **R. SUZUKI**  
Manager  
Optical Fiber & Cable Dept.  
Optical Fiber and Cable System Div.

**Fujikura**

# FUJIKURA'S SPECIFICATION FOR SINGLEMODE OPTICAL FIBER RIBBON (Fujikura's Designation: FutureGuide®-SM 8 FIBER RIBBON)

## 1. General

This specification covers singlemode 8 optical fiber ribbon optimized at a wavelength of 1310 nm but also can be used at 1550 nm, complying with the subcategory G.652.B in the ITU-T recommendation G.652 June 2005.

## 2. Specifications

Unless otherwise stated, the following characteristics are measured at ambient temperature ( $25 \pm 5^\circ\text{C}$ ).

### 2-1. Fiber Material

- (i) Core: Silica ( $\text{SiO}_2$ ) doped with Germanium Dioxide ( $\text{GeO}_2$ )
- (ii) Cladding: Silica ( $\text{SiO}_2$ )
- (iii) Coating: Dual layers of UV-cured Acrylate (Non-colored)  
The 3rd layer of color-coded UV-cured Acrylate

### 2-2. Fiber Structure

Refer to Fig. 1.

#### 2-2-1. Dimensions

- (i) Mode Field Diameter:  $9.2 \pm 0.4\mu\text{m}$  at 1310 nm  
 $10.4 \pm 0.8\mu\text{m}$  at 1550 nm
- (ii) Cladding Diameter:  $125 \pm 1.0\mu\text{m}$
- (iii) Outer Coating Diameter:  $255 \pm 10\mu\text{m}$

#### 2-2-2. Refractive Index Profile

The fiber shall have a matched clad, **step index profile**, and the difference between the maximum refractive index of the core and that of the cladding **shall be typical 0.36 %**. (Refer to Fig. 2.)

#### 2-2-3. Core Concentricity Error

$\leq 0.6\mu\text{m}$

#### 2-2-4. Cladding Non-Circularity

$\leq 1.0 \%$

#### 2-2-5. Coating / Cladding Concentricity Error

Not more than  $12.5 \mu\text{m}$

#### 2-2-6. Fiber Curl

Radius of Curvature:  $\geq 4.0 \text{ m}$

### 2-2-7. Coloring\* (Refer to Figs. 3.)

The each fiber of the ribbon shall be colored appropriately for identification.  
Color codes are shown in Table 1.

Table 1. Color Codes for 8 Fiber Ribbon

Ribbon Type	1	2	3	4	5	6	7	8
8 fiber	Blue	White	White	Pink	Yellow	White	White	Pink

\* Another color code is available on request.

### 2-3. Ribbon Configuration (Refer to Figs. 3.)

#### 2-3-1. Overall Jacket (Encapsulated Ribbon Structure)

8 fibers shall be laid parallel and coated with overall UV-cured acrylate.

#### 2-3-2. Ribbon Dimensions (Refer to Fig. 4.)

The ribbon dimensions and structural geometry of optical fiber ribbons are shown in Table 2.

Table 2. Ribbon Dimensions

Number of fibers	Width <b>w</b>	Thickness <b>t</b>	Fiber alignment		
			Horizontal separation		Planarity <b>p</b>
			Adjacent fibers <b>d</b>	Extreme fibers <b>b</b>	
	$\mu\text{m}$	$\mu\text{m}$	$\mu\text{m}$	$\mu\text{m}$	$\mu\text{m}$
8	$\leq 2200$	$320 \pm 20$	$\leq 280$	$\leq 1880$	$\leq 25$

### 2-4. Optical Characteristics

Unless otherwise stated, the following characteristics are effective for each fiber in ribbon.

#### 2-4-1. Attenuation (Refer to Fig. 5.)

(a) Under the Condition of **Free-Tension** (Uncoiled/Linear)

(i)  $\leq 0.35$  dB/km at 1310 nm

(ii)  $\leq 0.22$  dB/km at 1550 nm

(b) Under the Condition of **High-Tension** \*\* (Coiled/Wound on the reel)

(i)  $\leq 0.50$  dB/km at 1550 nm

\*\* Remarks)

(b) Since fiber ribbon is tightly wound on the reel with high-tension in order to avoid becoming loose and/or being entangled during transportation, the values of attenuation become higher than those under tension-free condition (a), due to the microbending. However, these attenuation values recover completely down to the tension-free level of (a), if the ribbon is put back to the uncoiled tension-free condition.

#### 2-4-2. Attenuation vs. Wavelength (Fiber Prior to Ribbonization)

The attenuation in a given wavelength range does not exceed the attenuation of the reference wavelength ( $\lambda$ ) by more than the value  $\alpha$ .

Attenuation vs. Wavelength		
Range (nm)	Ref. $\lambda$ (nm)	Max. Increased $\alpha$ (dB/km)
1285 to 1330	1310	0.05
1525 to 1575	1550	0.05

#### 2-4-3. Attenuation with Bending (Fiber Prior to Ribbonization)

The induced attenuation due to fiber wrapped around a mandrel of a specified diameter shown in the table below.

Attenuation with Bending			
Mandrel Diameter (mm)	Number of Turns	Wavelength (nm)	Induced Attenuation (dB)
32	1	1550	$\leq 0.50$
60	100	1310	$\leq 0.05$
60	100	1550	$\leq 0.10$

#### 2-4-4. Attenuation Uniformity

##### (a) Under the Condition of Free-Tension (Uncoiled/Linear)

No point discontinuity greater than 0.1 dB at either 1310 nm or 1550 nm in the OTDR trace.

##### (b) Under the Condition of High-Tension \*\*\* (Coiled/Wound on the reel)

No point discontinuity greater than 1.0 dB at either 1310 nm or 1550 nm in the OTDR trace.

#### \*\*\* Remarks)

(b) Since the starting wound portion of fiber ribbon (about 400 m) touches directly and tightly on the surface of reel barrel, the value of point discontinuity become higher than that under tension-free condition (a). However, this point discontinuity value recovers completely down to the tension-free level of (a), if the ribbon is put back to the uncoiled tension-free condition.

#### 2-4-5. Cable Cut-off Wavelength $\lambda_{cc}$

$$\lambda_{cc} \leq 1260 \text{ nm}$$

#### 2-4-6. Chromatic Dispersion

- (i)  $\leq 3.5 \text{ ps}/(\text{km}\cdot\text{nm})$ , when measured in the wavelength range of 1285 to 1330 nm
- (ii)  $\leq 18.0 \text{ ps}/(\text{km}\cdot\text{nm})$ , when measured at a wavelength of 1550 nm

2-4-7. Zero-dispersion wavelength  $\lambda_0$   
 $1300 \leq \lambda_0 \leq 1324 \text{ nm}$

2-4-8. Zero-dispersion slope  
 $\leq 0.092 \text{ ps}/(\text{km} \cdot \text{nm}^2)$

2-4-9. Effective Group Index of Refraction  $N_{\text{eff}}$  (Typical Values)

(i) 1.4675 at 1310 nm

(ii) 1.4681 at 1550 nm

2-5. Mechanical Characteristics (Fiber Prior to Ribbonization)

2-5-1. Proof Test

The entire optical fiber length shall be tested with regard to the tensile strength in accordance with IEC 60793-1-30, July 2001. The screening test value is equal to or not less than 100 kpsi (0.7GPa= 1% elongation).

3. Environmental Specifications

3-1. Temperature Dependence of Attenuation (Uncoiled/Linear Ribbon)

The induced attenuation from -40 to +85°C shall be  $\leq 0.05 \text{ dB/km}$  at either 1310 or 1550 nm.

3-2. Storage Environment (on the shipping reel)

-20 to +55°C, at < 98% RH.

4. Packing

The reel lengths are the following.

8 Fiber Ribbon: 1, 2, 3, 4, 5, 6 and 8 km (Max. 8 km)

The reel size shall be standardized by Fujikura Ltd. as shown in Fig.6.

A Fujikura label(s) with the manufacture's name, the production No., the type of fiber and the fiber length shall be shown on each reel.

Other lengths are also available upon request.

5. Measurement Data

If so requested by the customer, fiber data shall be transmitted electrically and precede each shipment (Microsoft Windows, diskette).



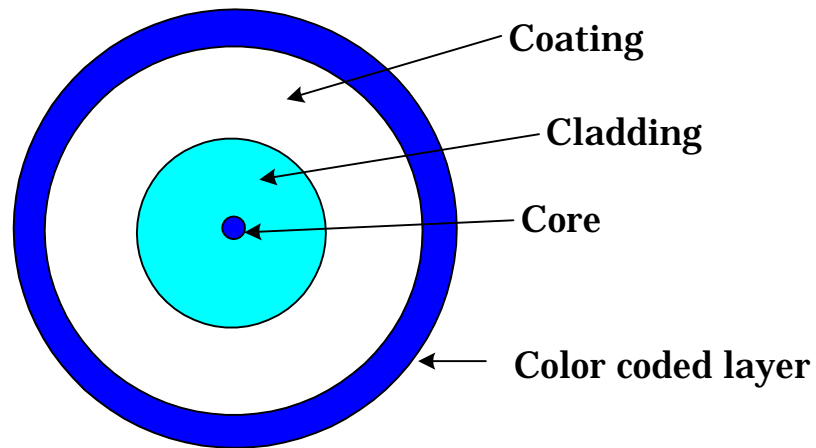


**Fig. 1. Structure of UV-Cured Acrylate Fiber**

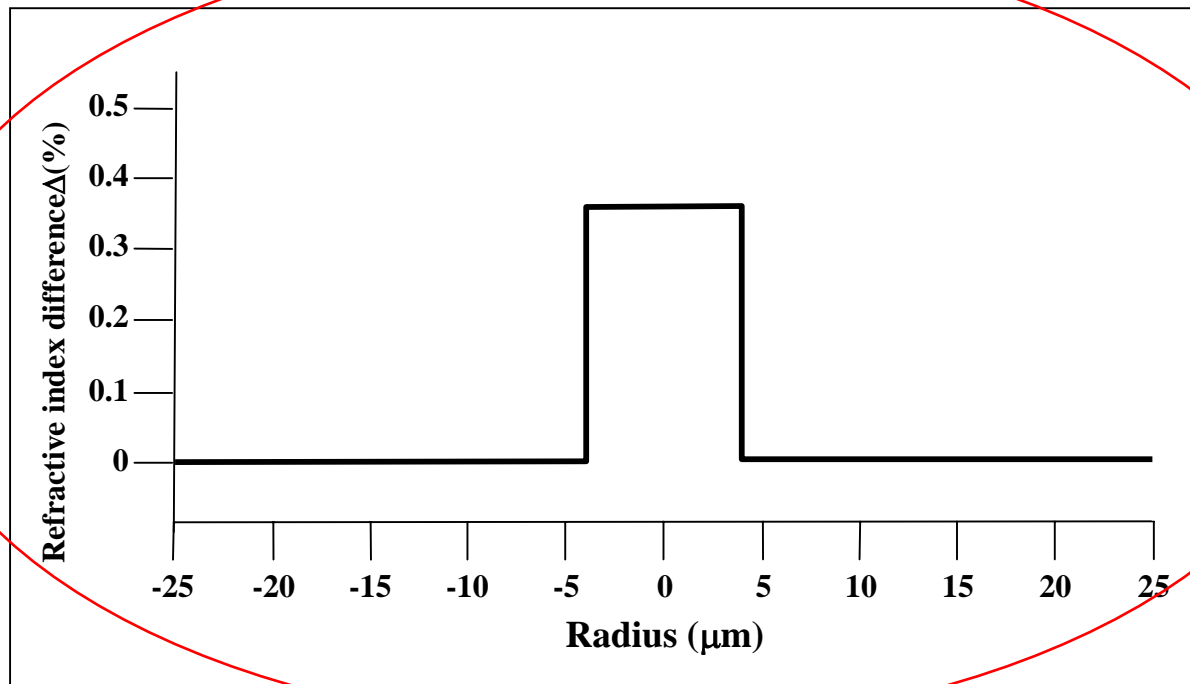


**Fig. 2. Refractive Index Profile ( Typical Fiber)**

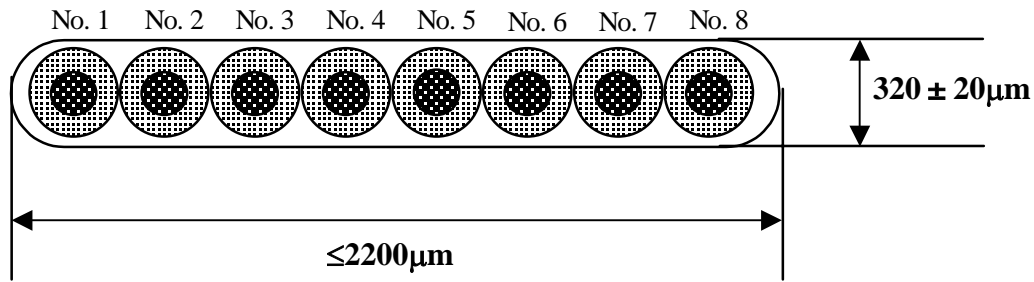
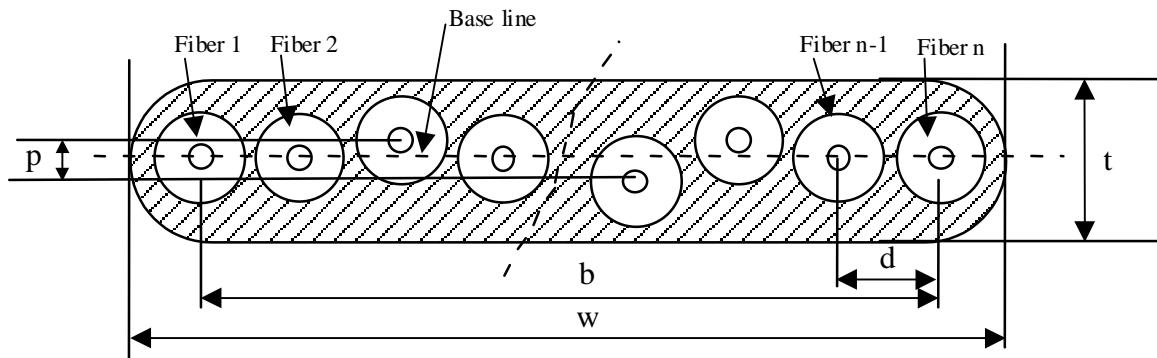


**Fig. 3. 8 Fiber Ribbon**



w : Width  
 t : Thickness  
 d : Horizontal Separation (Adjacent fibers)  
 b : Horizontal Separation (Extreme fibers)  
 p : Planarity

**Fig. 4. Schematic Cross-sectional Drawing for Fiber Ribbon Geometry**

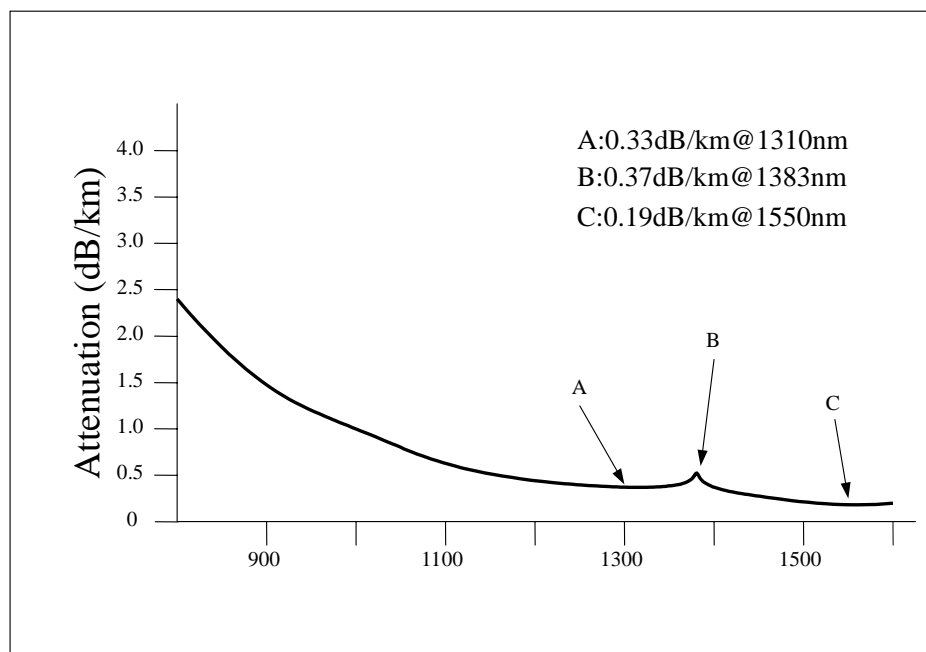


**Fig. 5. Spectral Attenuation (Typical Fiber)**

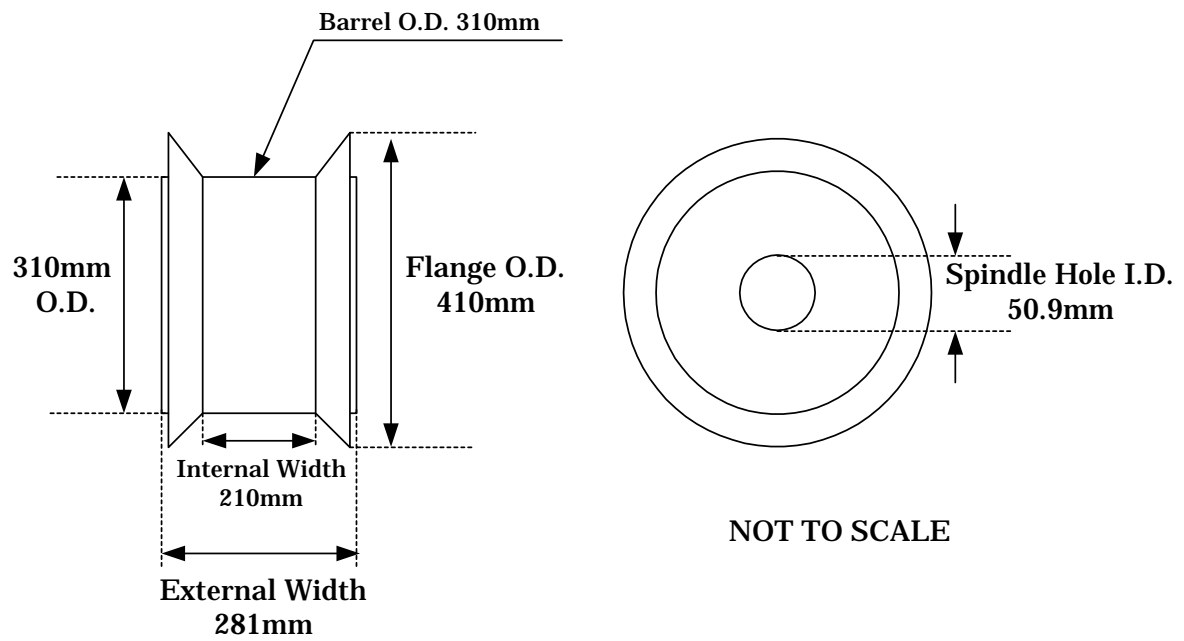


**Fig. 6. Ribbon Reel**

**++ END OF SPECIFICATION ++**

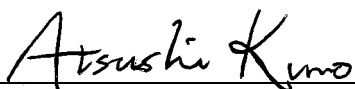
DATE : Mar. 16, 2009No. : JBT-03813**Messrs.**

---

# **SPECIFICATION**

FOR

SINGLEMODE OPTICAL FIBER SENSOR CABLE  
FOR PILE FOUNDATION MONITORING SYSTEM  
SM ×4C



Prepared by A. Kuno

Optical Fiber and Cable Department  
Global Telecommunication Strategy  
and Marketing Division

Approved by H. Komiyama  
Manager

Optical Fiber and Cable Department  
Global Telecommunication Strategy  
and Marketing Division

## 1. General

This specification covers the optical fiber sensor cable for pile foundation monitoring system.

## 2. Singlemode optical fiber

### Fiber characteristics

Item		Construction
Mode field diameter	at 1310 nm	$9.5 \pm 1 \mu\text{m}$
Cladding diameter		$125 \pm 2 \mu\text{m}$
Core concentricity error		$\leq 1 \mu\text{m}$
Cladding non-circularity		$\leq 2 \%$
Primary coating diameter		$250 \pm 15 \mu\text{m}$
4-fiber ribbon jacketing diameter		Nom. 1.1 mm $\times$ 0.3 mm

### Transmission characteristics

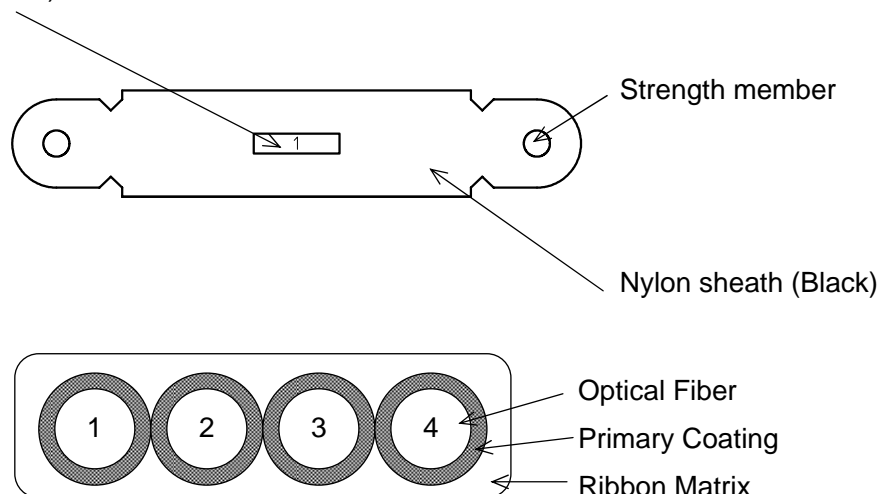
Item	Performance		
Attenuation at 1550 nm	$\leq 0.5 \text{ dB/km}$	$0.2 \leq L < 1$	$\leq 0.375 \times L + 0.125 \text{ dB}$
		$L < 0.2$	$\leq 0.2 \text{ dB}$
Cutoff Wavelength	1100 - 1350 nm		

L= Cable Length (km)

### 3. Optical Fiber Cable

#### **Construction (Optical Fiber Sensor Cable SM x 4C)**

4-fiber ribbon (Ribbon No.)



Item	Construction
Fiber count	4
Number of 4-fiber ribbons / slot	1
Cable diameter	Approx. 1.3 × 5.0 mm
Cable weight	Approx. 8 kg/km

#### **Ribbon identification**

Ribbon No.	Fiber No.			
	1	2	3	4
1	Blue	White	Brown	Slate

#### **Mechanical performance**

Item	Performance
Permissible tensile strength	70 N
Permissible bending radius	30 mm

## 4. Packing

Each factory length of the cable is coiled on a suitable drum. The drum is durable and constructed so as to prevent damage to the cables during shipment and handling. Lags or other suitable means of protection are applied to the drum to prevent damage to the cables during shipment and storage. The drums are non-returnable.

After completion of the tests, both ends of the cable are sealed by a suitable method. The cable ends are fastened so as not to protrude beyond any portion of the drum and to prevent the cable from becoming loose in transport.

If necessary, the cable end(s) will be provided with pulling eye(s) by extra charge.

Specifications NBX-5000

Function		BOTDR				
Laser Wavelength		1550 ±2 nm				
Distance Range		50 m, 100 m, 250 m, 500 m, 1 km, 2.5 km, 5 km, 10 km, 27 km				
Measurement Frequency Range		9~13 GHz				
Range of Strain Measurement		-30,000 to +40,000 με (-3 % to +4 %)				
Measurement Frequency Scan Step		1, 2, 5, 10, 20, 50 MHz				
Readout Resolution		5 cm (minimum)				
Sampling Points		600,000 (default)				
Average Count Settings		2 <sup>5</sup> ~ 2 <sup>23</sup> times (inc. Hardware Average Count 2 <sup>16</sup> )				
Pulse Width		5 ns	10 ns	20 ns	50 ns	100 ns
Spatial Resolution		50 cm	1 m	2 m	5 m	10 m
Dynamic Range <sup>(1)</sup>		2 dB	5 dB	8 dB	10 dB	13 dB
Max. Measurement Distance <sup>(2)</sup>		5 km	15 km	20 km	27 km	27 km
Optical Budget <sup>(1)(6)</sup>		4 dB	7 dB	10 dB	12 dB	15 dB
Measurement Accuracy <sup>(3)(4)</sup>		50 με / 2.5 °C	30 με / 1.5 °C			
Repeatability <sup>(3)(4)(5)</sup>		20 με / 1.0 °C				
Measurement Time <sup>(7)</sup>		5 second (minimum)				
Signal Terminal	Input-Output Fiber	Single mode optical fiber				
	Fiber Connector	FC-APC / SC-APC (factory option)				
Suitable Fiber		Single mode optical fiber				
Remort Control Interface		TCP/IP / GPIB (factory option)				
Power Supply		AC100 ~ 240V 50/60Hz 250VA				
Dimensions / Weight		approx. 456 (W) × 485 (D) × 286 (H) mm / 30 kg				
Operating Temperature		10~35 °C, Humidity below 85 % (no dew condensation)				
Storage Temperature		0~50 °C				
Place of Production		Japan				

(1) Based on  $2^{15}$  average cycles.  
(2) Based on average fiber loss of 0.3 dB/km using Single mode fiber.  
(3) Based on the measurement of strain free, UV coated fiber.  
(4) Based on the measurement of strain free, UV coated fiber and in constant temperature environment.  
(5) The maximum standard deviation of measurement value in 5 consecutive measurements for 100 consecutive points.  
(6) Within the allowable range adjusted by the optical power excluding the case of nonlinear phenomena.  
(7) The settings of 50 m distance range,  $2^8$ - $2^{14}$  count settings, 41 scanning steps excluding the time for Pulse Adjustment.  
(1)-(6) are all based on a frequency scan step of 5 MHz and with Pulse Adjustment and Auto Frequency Adjustment on.

\* Specifications are subject to change without notice.

Give you a feel<sup>®</sup>  
When every point of the optical fiber is a sensor

Neural Optical Fiber Scope  
**NEUBRESCOPE NBX-5000**  
Single-end technology (BOTDR) to measure strain and / or temperature

NEW

Now operated from  
laptop computer  
for easy in-the-field use



Spatial resolution: **50 cm** / Sampling resolution: **5 cm**

Repeatability of strain measurement: **20  $\mu\epsilon$**

Repeatability of temperature measurement: **1.0 °C**

Contact Address

Neubrex Co., Ltd.

Sakae-machi-dori 1-1-24, Chuo-ku, Kobe, Hyogo 650-0023, Japan  
Tel: +81-78-335-3510 Fax: +81-78-335-3515

(20160613)

[www.neubrex.com](http://www.neubrex.com)







Segment 1

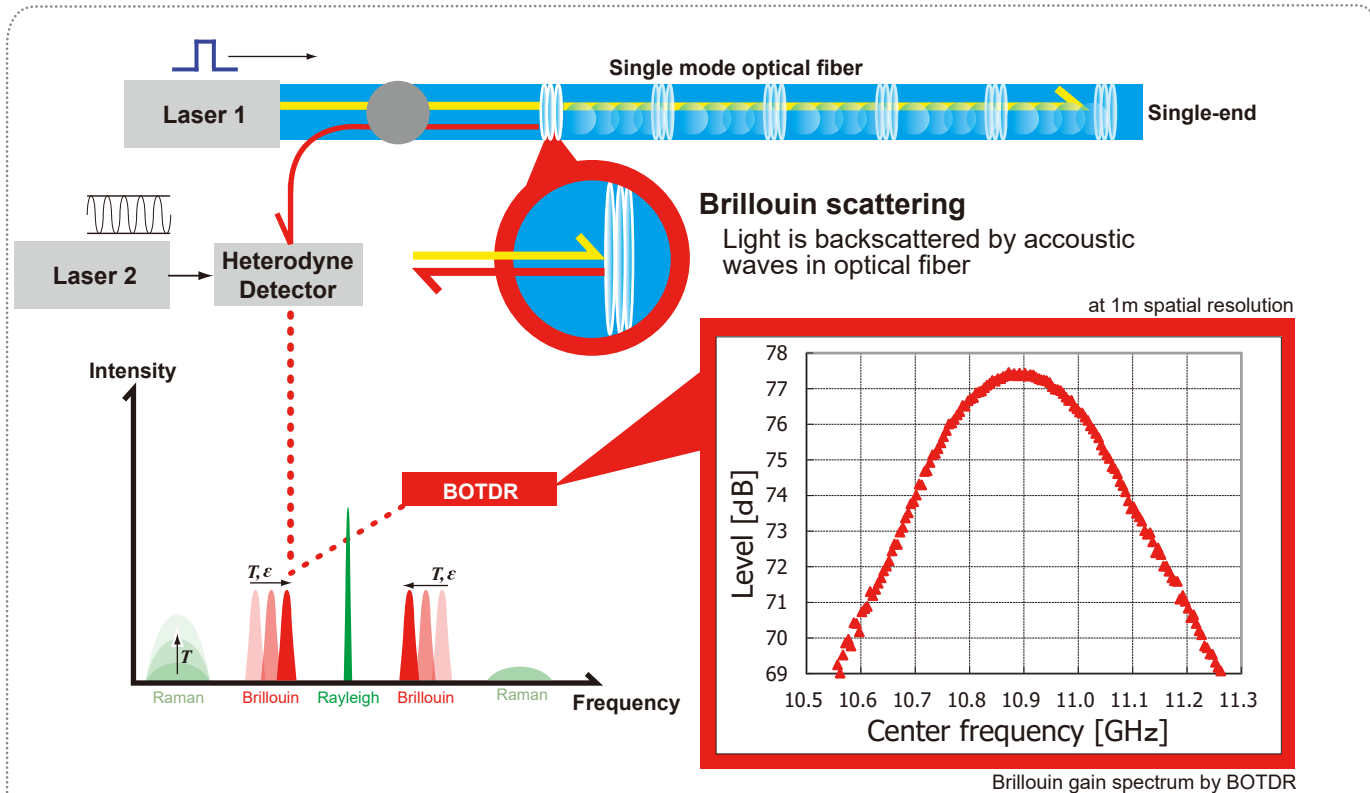
Segment 2

Segment 3

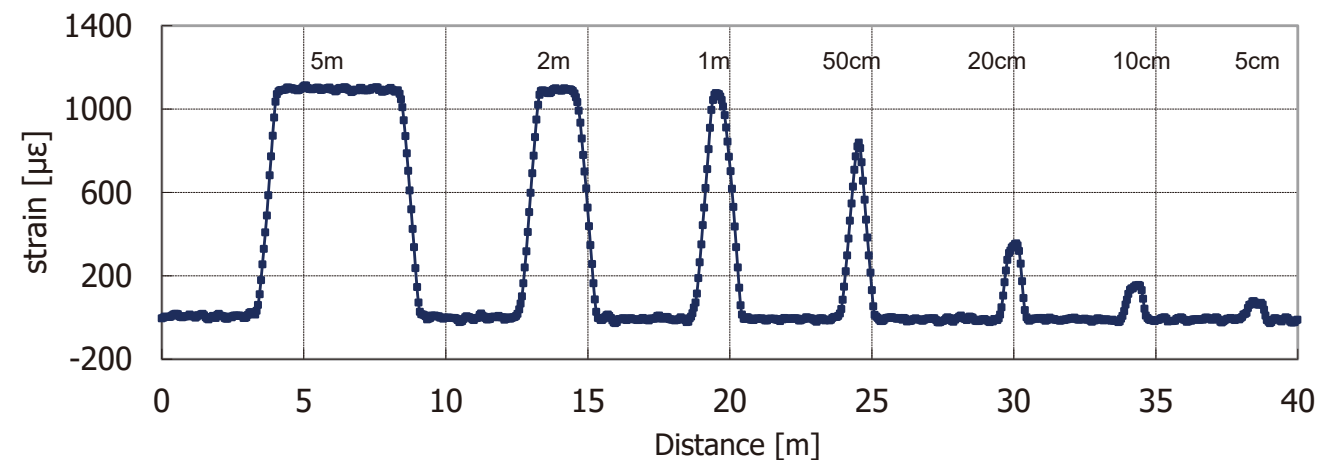
## Key features

- High cost/performance Brillouin Optical Time Domain Reflectometry (BOTDR)
- Measurement of strain and / or temperature at each point in any single mode optical fiber
- Long distance measurement up to 25 km

## Principles of BOTDR



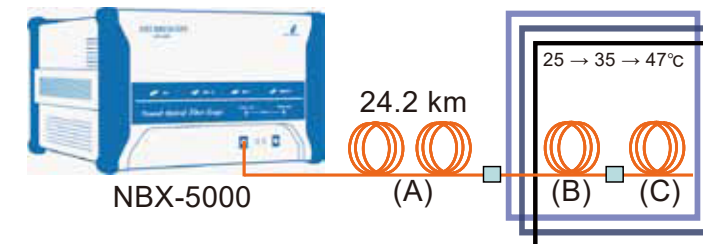
Example of strain distribution measured in spatial resolution and accuracy test fiber with resolution of 1 m



The NBX-5000 sensing system uses Brillouin backscattering phenomena, which employs single-end technology for long distance up to 25 km of Brillouin Optical Time Domain Reflectometry (BOTDR). It provides, in standard single-mode fiber, frequency shifts due to strain/temperature changes. Dynamic sensing (rates up to 200Hz) is also optionally available (NBX-5000A).

## Long Distance Measurement

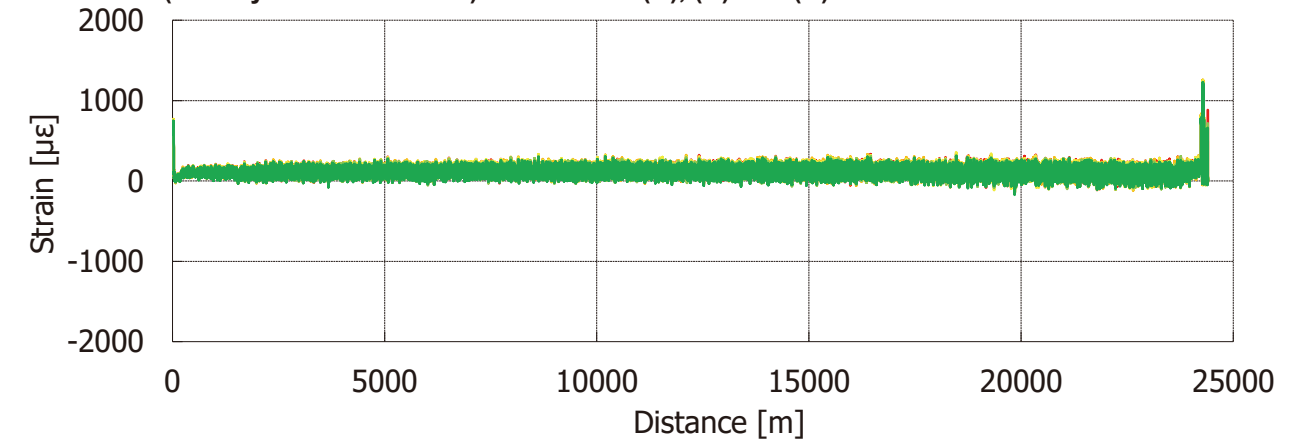
Evaluation test



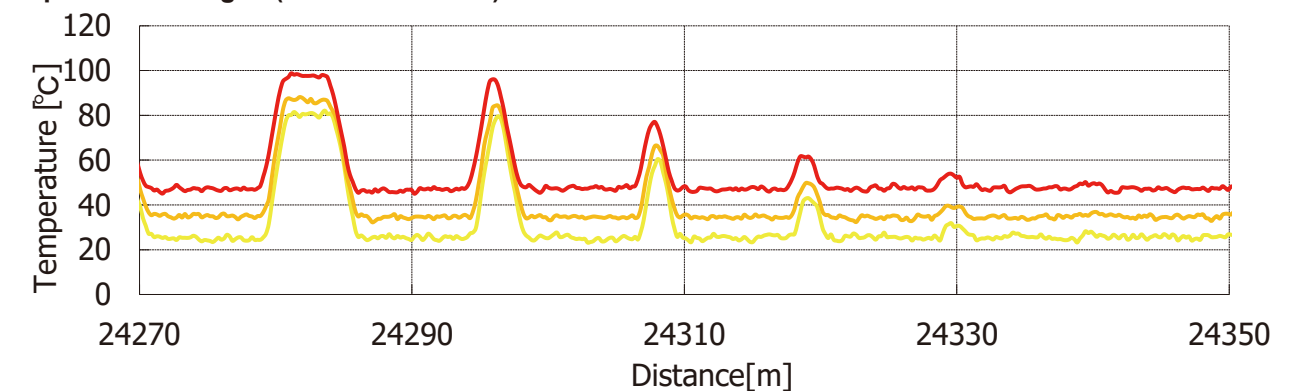
Experiment setup

- (1) Fiber (A) is long distance fiber (24.2 km), (B) is for spatial resolution and accuracy, and (C) is for repeatability evaluation. No strain changes applied on the fiber.
- (2) Continuously measured for five times.
- (3) Temperature change from 25 to 47°C applied for the fiber (B) and (C).

Strain distribution (overlayed for five times) for the fiber (A), (B) and (C) with 2 m resolution



Temperature distribution for (B) using spatial resolution and accuracy test fiber (same fiber used in the left page) when temperature changed (25 → 35 → 47°C).



## Accuracy and Repeatability

Measured strain distribution (overlayed for five times) for the fiber (B) and (C) (left) at the same temperature, and strain difference (right) for the fiber (C) at the same condition.

